APPENDIX A

DESIGN AND CONSTRUCTION OF THE TEST BUILDING

Within this appendix further details are provided for the design and construction of the two-storey test building, which was introduced in Chapter 4. Design lateral forces for a (full-scale) prototype building are determined. These lateral forces are scaled according to similitude criteria for the two-third scale test building. The section sizes and reinforcement requirements for test building are determined using the scaled lateral forces. Subsequently, the actual strength, rather than the design strength, of the test building is predicted with and without additional reinforcement. The construction process for the test building is documented and structural drawings plus specifications for the test building are provided. Details of the materials used in the test building are provided.

A.1. LATERAL FORCE DESIGN OF PROTOTYPE

The prototype building is designed using a displacement-based design (DBD) procedure (Priestley et al. 2007) with design parameters that are defined in Chapter 4. Firstly, the frame system is idealized as an equivalent single-degree-of-freedom (SDOF):

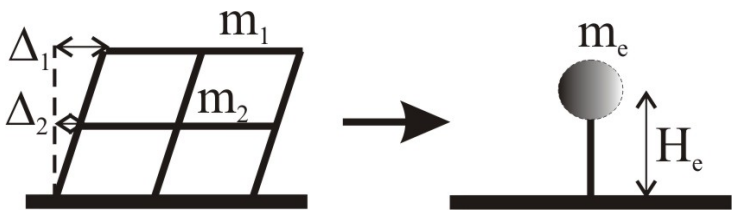

Figure A.1.1 – SDOF representation of prototype building

Step 1: Determine the design displacement Δ_d, the effective mass m_e and effective height H_e

The peak design displacement for the SDOF representation:

$$\Delta_d = \sum_{i=1}^{n}\left(m_i\Delta_i^{\,2}\right)\Big/\sum_{i=1}^{n}\left(m_i\Delta_i\right)$$

Where:

$$\Delta_i = \delta_i\frac{\Delta_1}{\delta_1}$$

And:

$$\frac{\delta_i}{\delta_1} = \frac{H_i}{H_n} = \text{the mode shape (linear displacement profile)}$$

So:

$$\Delta_i = \frac{H_i\Delta_1}{H_n}$$

And:

$$\Delta_1 = H_1\cdot\theta_d = 3.0\times 0.02 = 0.06m$$

The effective mass:

$$m_e = \sum_{i=1}^{n}\left(m_i\Delta_i\right)\Big/\Delta_d$$

The effective height:

$$H_e = \sum_{i=1}^{n}\left(m_i\Delta_i H_i\right)\Big/\sum_{i=1}^{n}\left(m_i\Delta_i\right)$$

Table A.1.1 – DBD calculations

Storey, i	Height, Hi (m)	Weight, wi (KN)	Mass, mi (tonnes)	Δi (m)	mi*Δi	mi*Δi^2	mi*Δi*Hi
2	6	823	83.9	0.120	10.1	1.21	60.4
1	3	823	83.9	0.060	5.0	0.30	15.1
Sum		**1646**	**167.8**		**15.10**	**1.51**	**75.5**

Therefore:

$$\Delta_d = \sum_{i=1}^{n}\left(m_i\Delta_i^{\,2}\right)\Big/\sum_{i=1}^{n}\left(m_i\Delta_i\right) = \frac{1.51}{15.1} = 0.1m$$

$$m_e = \sum_{i=1}^{n}\left(m_i\Delta_i\right)\Big/\Delta_d = \frac{15.1}{0.1} = 151tonne \text{ (90\% of the total mass)}$$

$$H_e = \sum_{i=1}^{n}(m_i \Delta_i H_i) \Big/ \sum_{i=1}^{n}(m_i \Delta_i) = \frac{75.5}{15.1} = 5.0m \text{ (83\% of the total height)}$$

Step 2: Determine the system damping

An elastic damping, ξ_{el}, of 5% of critical damping is assumed, as considered for equivalent static (force-based) design according to NZS1170.5 (2004). It is assumed that the elastic damping remains constant at all displacements and is not reduced in proportion to the tangent stiffness of the system as proposed by Priestley *et al.* (2007). Because the building is designed with post-tensioned connection, there is effectively no hysteretic damping for the system. This may be conservative if energy-dissipating reinforcement is provided at the base of the columns.

$$\xi_{eq} = \kappa \xi_{el} + \xi_{hyst} = 5\% + 0 = 5\%$$

Step 3: Determine the effective period from the design displacement spectrum

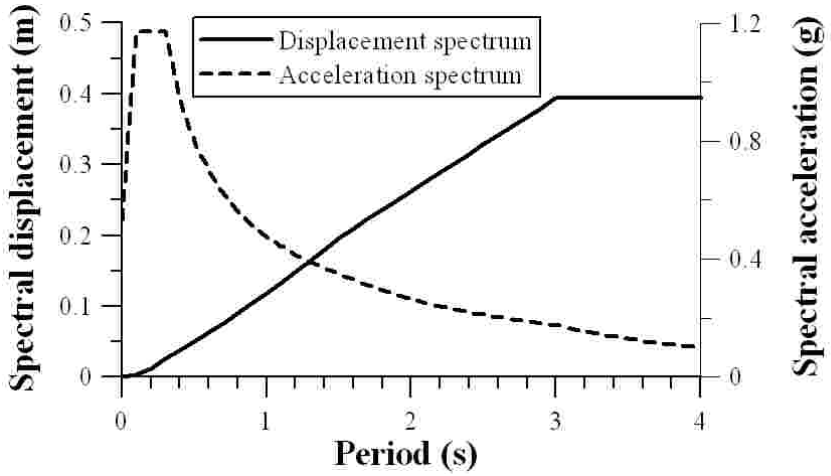

Figure A.1.2 – Design acceleration and displacement spectrum

By entering the displacement spectrum with the design displacement the effective period is obtained: $\mathbf{T_e = 0.94s}$.

Step 4: Obtain the equivalent lateral stiffness

$$K_e = \frac{4\pi^2 m_e}{T_e^2} = 4\pi^2 \frac{151}{0.94^2} = 6750kN/m$$

Note; this is a secant elastic stiffness to the peak displacement response.

Step 5: Determine the base shear

$$V_b = K_e \Delta_d = 6750 \times 0.1 = 675kN$$

Step 6: Distribute the base shear up the structure

For a two-storey structure is reasonable to distribute the forces according to first mode response. Hence, additional forces at the roof level are not required to account for higher modes of response:

$$F_i = V_b \left(m_i \Delta_i\right) \Big/ \sum_{i=1}^{n} \left(m_i \Delta_i\right)$$

Table A.1.2 – Design lateral forces for the prototype

Storey, i	Floor Force (KN)
2	450
1	225
Sum (Vb)	**675**

A.2. DETERMINATION OF THE FRAME ACTIONS

The lateral loads for the test model are scaled from the prototype design according to similitude requirements (see Chapter 4). The lateral forces are distributed evenly to each frame, ignoring any accidental eccentricity (NZS1170.5 2004).

Table A.2.1 – Design lateral forces for one frame

Storey, i	Floor Force, F_i (KN)
2	100
1	50
Sum (Vb)	**150**

An equilibrium-based approach (Priestley et al. 2007), apposed to member stiffness, is used to distribute strength throughout the frame.

Step 1: Determine the total overturning moment (OTM)

$$OTM = \sum_{i=1}^{n} F_i H_i$$

Table A.2.2 – Calculation of OTM

Storey, i	Hi (m)	Fi (kN)	Fi.Hi (kN.m)
2	4.0	100	400
1	2.0	50	100
Sum		**V_b=150**	**OTM=500**

Step 2: Decide how much of the OTM will be taken by the column bases:

$$OTM = \sum_{j=1}^{n} M_{c,j} + TL_{base}$$

Where: $\sum_{j=1}^{n} M_{c,j}$ = the sum all column-base moments

T = the tension force induced by lateral load in the exterior column

L_{base} = the total frame length (to column centrelines)

Hence, the sum of the column base moments must be decided. As recommended by Priestley *et al*. (2007), a reasonable approach is to ensure that the point of contra-flexure in the column is at 60% of the interstorey height at the bottom level. Hence:

$$\sum_{j=1}^{n} M_{c,j} = 0.6 V_b H_1 = 0.6 \times 150 \times 2.0 = 180 kN.m$$

Therefore, the column-base moments are 36% of the total overturning moment.

Step 3: Determine the remaining tension and compression force in the exterior columns:

$$T = C = \frac{OTM - \sum_{j=1}^{n} M_{c,j}}{L_{base}} = \frac{500 - 180}{8.38} = 38.2 kN$$

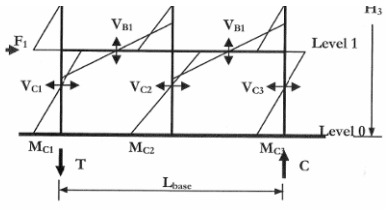

Step 4: Proportion the seismic axial forces to each beam up the height of the building

A rational way to proportion the seismic axial forces into beam shears is to use the total shear force diagram (Priestley et al. 2007). This will ensure that an effectively linear displacement profile is maintained.

Hence:

$$V_{B,i} = T\frac{V_{S,i}}{\sum_{i=1}^{n} V_{S,i}}$$

Where: $V_{B,i}$ = the beam shear at the i[th] floor

Table A.2.3 – Calculation of beam shears

Storey, i	Fi (kN)	Vsi (kN)	VBi (kN)
2	100	100	15.3
1	50	150	22.9
Sum	**V_b=150**	**∑Vsi=250**	**∑VBi=38.2**

Step 5: Calculate beam design moments

$$M_{B,i} = V_{B,i}\frac{L_b}{2}$$ (At the column centerlines)

Where L_b = the length of the bay from column centerline to column centerline (4.19m)

The beam-column connection design moments at the column face are:

$$M_{cf,i} = M_{B,i}\frac{L_b - h_c}{L_b}$$

Where h_c = the column width (400mm assumed)

Table A.2.4 – Calculation of beam moments

Storey, i	VBi (kN)	MBi (kN.m)	Mcfi (kN.m)
2	15.3	32.1	29.0
1	22.9	48.0	43.4

Step 6: Calculate column design moments

The sum of the column moments above and below a given floor must equal the sum of the beam moments.

$$\sum M_{c,i,above} + \sum M_{c,i,below} = \sum M_{B,i}$$

It is reasonable to assume that the column moments, immediately above and below the i^{th} floor, are equal. Making this assumption, the following equations are derived:

For the 1st storey:

$$\sum_{j=1}^{n} M_{C,j} = n_b M_{B,i}$$

For the 2nd storey (the roof):

$$\sum_{j=1}^{n} M_{C,j} = 2n_b M_{B,i}$$

Where n_b = the number of bays

Table A.2.5 – Calculation of total column moments

Storey, i	MBi (kN.m)	∑Mc (kN.m)
2	32.1	128
1	48.0	96.0

Hence, the worst-case column moment is on the top floor. By equilibrium, the moments induced in the interior and exterior columns can be determined:

Table A.2.6 – Calculation of interior and exterior column moments

Storey, i	Mc,ext (kN.m)	Mc,int (kN.m)
2	32.1	64.2
1	24	48.0

A.3. DETAILED DESIGN OF TEST BUILDING

The test building is designed considering purely post-tensioned frame and wall connections. The design takes into strength reduction factors and over-strength design.

A.3.1. Frame design

The frames were designed using existing connection modeling procedures (Newcombe et al. 2008) and improved methodologies, discussed in Chapter 6, to determine the member deformations.

Beam-column connections on Level 2

The actions on an internal beam-column joint are considered to estimate the member deformations.

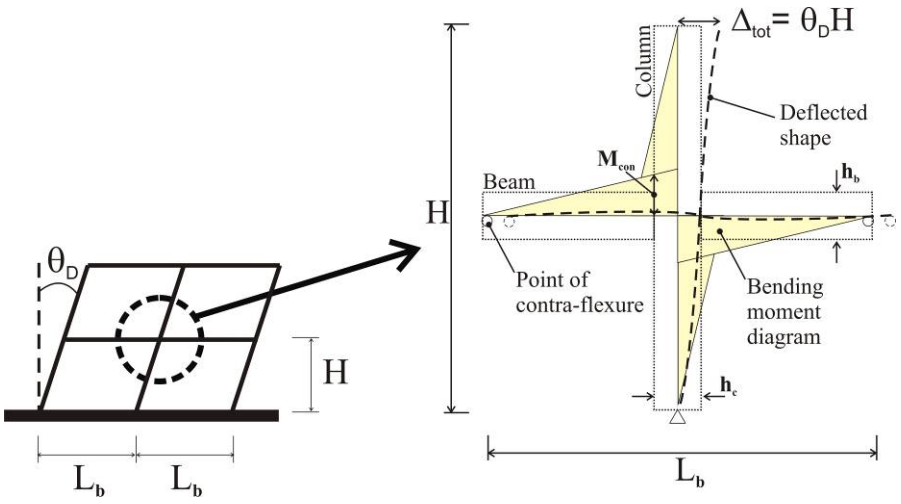

Figure A.3.1 – Internal beam-column joint idealization

The deflection of the frame can be broken into its components:

$$\theta_D = \theta_b + \theta_c + \theta_j + \theta_{con}$$

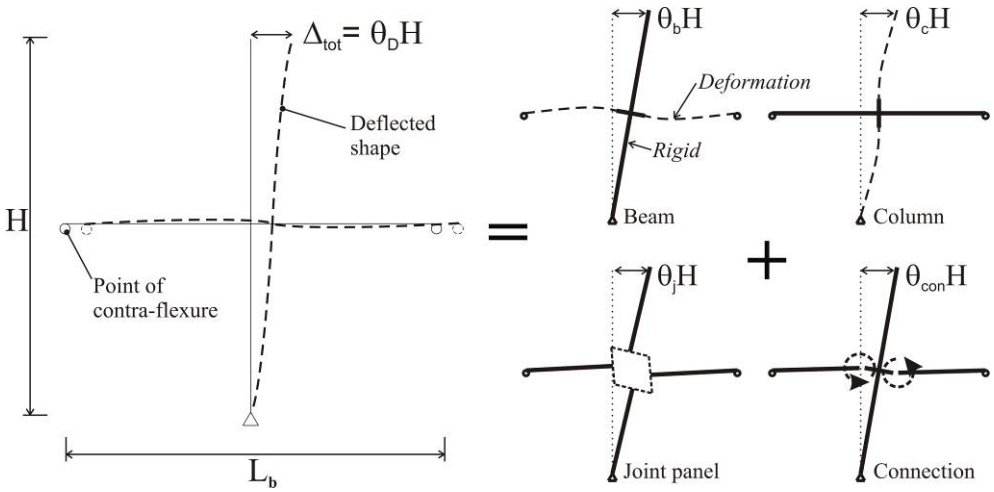

Figure A.3.2 – Deflection components of timber frame

Step 1: Calculate the beam and column deformation

If it is assumed that the beam and column sections are solid, that the points of contra-flexure for the beams and columns are at half the bay length and half the interstorey height respectively, the following expressions are appropriate:

$$\theta_b = \frac{\phi_b}{L_b}\left(\frac{(L_b - h_c)^2}{6} + \frac{E_t}{G}\frac{h_b^{\,2}}{4}\right) \text{ And } \theta_c = \frac{\phi_c}{H}\left(\frac{(H - h_b)^2}{6} + \frac{E_t}{G}\frac{h_c^{\,2}}{4}\right)$$

Where: E_t and G are the bending and shear elastic modulus respectively
h_b = the depth of the beam
h_c = the depth of the column.

The bending and shear modulus are 10500 MPa and 660 MPa respectively (see section A.8). Furthermore, it is assumed that the beam and column have a width (b_c and b_b) of 240mm and depth (h_c and h_b) of 400mm. These dimensions will be used at both levels.

The curvature in the beam and column is:

$$\phi_b = \frac{M_{con}}{E_t I_b} \text{ And } \phi_c = \frac{M_{con}}{E_t I_c}\frac{L_b(H - h_b)}{H(L_b - h_c)}$$

Where: I_b and I_c are the second moment of area of the beam and column respectively.

$$\phi_b = \frac{43.4\times10^6}{10500\times\dfrac{240\times400^3}{12}} = 3.23\times10^{-6}\,\frac{1}{mm}$$

$$\phi_c = \frac{43.4\times10^6}{10500\times\dfrac{240\times400^3}{12}}\,\frac{4191(2000-400)}{2000(4191-400)} = 2.86\times10^{-6}\,\frac{1}{mm}$$

Hence:

$$\theta_b = \frac{3.23\times10^{-6}}{4191}\left(\frac{(4191-400)^2}{6} + \frac{10500}{660}\frac{400^2}{4}\right) = 0.0023$$

$$\theta_c = \frac{2.86\times10^{-6}}{2000}\left(\frac{(2000-400)^2}{6} + \frac{10500}{660}\frac{400^2}{4}\right) = 0.0015$$

Step 2: Calculate the joint panel zone deformation

The joint panel deformation can be significant for unreinforced columns. However, on Level 2 extensive steel reinforcement is provided by an internal steel plate arrangement (see Chapter 4). Therefore, it is assumed that joint panel zone deformation can be ignored:

$$\theta_j = 0$$

Step 3: Determine the allowable connection rotation

To minimize the required post-tensioning reinforcement the maximum allowable connection rotation should be used for design of the post-tensioning.

$$\theta_{con} = \theta_d - \left(\theta_b + \theta_c + \theta_j\right) = 0.020 - \left(0.0023 + 0.0015 + 0\right) = 0.020 - 0.0038 = 0.0162$$

The actual imposed connection rotation at the connection, θ_{imp}, is slightly higher than the interstorey rotation due to the connection, θ_{con}:

$$\theta_{imp} = \frac{\theta_{con}}{\left(1 - \frac{h_c}{L_b}\right)} = \frac{0.0162}{\left(1 - \frac{400}{4191}\right)} = 0.018$$

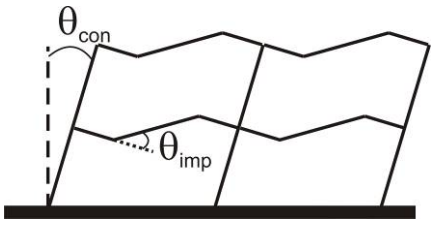

Step 4: Design beam-column connections

The connection moment capacity is calculated at the allowable imposed connection rotation. Sufficient post-tensioning force must be applied so that the beam-column connections have sufficient moment capacity, within the allowable connection rotation. If the moment capacity of the connection is more than required (due to strength reduction factors and over design) the actual connection rotation, and hence, the total frame deformation, will be less than considered for design. Existing procedures (Newcombe et al. 2008) are used to determine the connection moment capacity.

Impose connection rotation

The allowable connection rotation θ_{imp} is applied to the connection. A preliminary estimate of the post-tensioning is made: 4-0.5 inch (12.7mm) post-

tensioning tendons symmetrically spaced at 60mm centre-to-centre. The tendons are stressed to 60% of their yield stress.

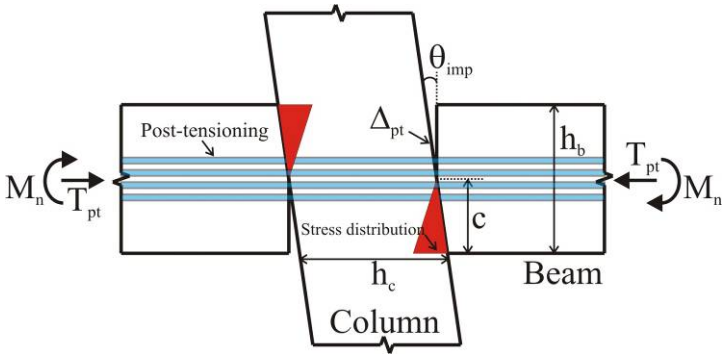

Figure A.3.3 – Rocking post-tensioned connection

Estimate the neutral axis depth, c

Say:

$c = 140mm$

Apply member compatibility:

The elongation of the tendon:

$$\Delta_{pt} = \theta_{imp}\left(y_i - c\right) = 0.018 \times \begin{pmatrix} 290-140 \\ 230-140 \\ 170-140 \\ 110-140 \end{pmatrix} = \begin{pmatrix} 2.70 \\ 1.62 \\ 0.54 \\ -0.54 \end{pmatrix} mm$$

Where: y_i = the distance to the centroid of the tendon from the base of the beam

According to Newcombe (2008) tendon shortening can be ignored. The strains due to gap openings are:

$$\Delta\varepsilon_{pt} = \sum \frac{n\Delta_{pt}}{l_{ub}} = \frac{2}{9280}\begin{pmatrix} 2.70 \\ 1.62 \\ 0.54 \\ 0 \end{pmatrix} + \frac{2}{9280}\begin{pmatrix} 0 \\ 0.54 \\ 1.62 \\ 2.70 \end{pmatrix} = \begin{pmatrix} 0.00058 \\ 0.00047 \\ 0.00047 \\ 0.00058 \end{pmatrix}$$

Where: n = the number of connections subject to the same rotation
l_{ub} = the unbonded length of the tendon

The stress in the tendon is checked at the design rotation. The stress in the tendon should be less than 90% of the yield stress:

$$\varepsilon_{pt} = \varepsilon_{pt,i} + \Delta\varepsilon_{pt} \leq 0.9\varepsilon_y$$

Where: $\varepsilon_{pt,i} = \dfrac{T_{pti}}{A_{pt}E_{pt}}$ and,

$T_{pti} = 0.7 f_y A_{pt}$

A_{pt} = 396mm^2 = the area of a tendons

E_{pt} = 190000 MPa = the elastic modulus of the tendons

f_y = 1560 MPa = the yield stress of the tendons

Hence:

$$T_{pti} = 0.6 f_y A_{pt} = 0.6 \times 1560 \times 396 = 371kN$$

$$\varepsilon_{pt,i} = \frac{371 \times 10^3}{396 \times 190000} = 0.00493$$

For the top and bottom tendons:

$$\varepsilon_{pt} = 0.00493 + 0.00058 = 0.0055 \leq 0.0074$$

The monolithic beam analogy (Palermo et al. 2005b) is applied assuming the timber remains elastic, as proposed by Newcombe (2008):

$$\varepsilon_t = \left(3\frac{\theta_{imp}}{L_{cant}} + \phi_{dec} \right) c$$

Where: ϕ_{dec} = the decompression curvature

L_{cant} = the shear span = (4191 – 400)/2 = 1896mm

The decompression curvature is:

$$\phi_{dec} = \frac{2T_{pti}}{E_t b_b {h_b}^2} = \frac{2 \times 371 \times 10^3}{10500 \times 240 \times 400^2} = 1.84 \times 10^{-6} \frac{1}{mm}$$

Hence:

$$\varepsilon_t = \left(3\frac{0.018}{1896} + 1.84 \times 10^{-6} \right) 140 = 0.0042$$

To determine the stress in the timber Newcombe *et al*. (2008) proposes an calibrated effective connection modulus is used. For armored connections,

where the perpendicular to grain timber of the column is protected by steel plates:

$$E_{con} = 0.55E_t = 0.55 \times 10500 = 5775MPa$$

The stress in the timber is checked. Note, since there is steel armoring in the connection the parallel-to-grain yield stress can be considered. Hence:

$$\varepsilon_y = \frac{f_c}{E_{con}} = \frac{45}{5775} = 0.0078 > 0.0042 \Rightarrow O.K! \text{ (Not yielding)}$$

Calculate the forces in the connection

Since the timber is elastic we can assume a linear distribution of the stress within the compression region of the timber, hence:

$$C_t = 0.5\varepsilon_t E_{con} c_i b = 0.5 \times 0.0042 \times 5775 \times 140 \times 240/10^3 = 407kN$$

For the post-tensioning:

$$T_{pt} = T_{pt,i} + \Delta T_{pt} = 0.7 f_y A_{pt} + \sum \varepsilon_{pt} E_{pt} A_{pt1}$$
$$= 371 + (0.00058 + 0.00047) \times 2 \times 99 \times 190000/10^3 = 411kN$$

Check force equilibrium

By equilibrium:

$$C_t = T_{pt}$$

$$\therefore 407 \approx 411 \Rightarrow OK! \text{ (Within 5\%)}$$

Evaluate the moment capacity

For the design of the test building a strength reduction factor of 0.9 was considered. This aims to take into account uncertainties in the prediction of the moment capacity of the connection. The moment capacity is:

$$\phi M_n = \phi T_{pt}\left(\frac{h_b}{2} - \frac{c}{3}\right) = 0.9 \times 411 \times \left(\frac{400}{2} - \frac{140}{3}\right) = 57kN.m$$

$$M^* \le \phi M_n$$

$$43 \le 57 \Rightarrow O.K!$$

Therefore, the preliminary section sizes and specified post-tensioning are sufficient. Note, some conservatism is built into the design to allow for losses in tendon force during testing and inaccuracies in the calculation of the section properties (i.e. the beams are box sections rather than solid).

Beam-column connections on Level 3

Again, the actions on the internal beam-column joint are considered to estimate the member deformations.

$$\theta_D = \theta_b + \theta_c + \theta_j + \theta_{con}$$

Step 1: Calculate the beam and column deformation

Because is the Level 3 top of the frame, to column deformation can be reduced. It is still reasonable to assume that the point of contra-flexure in the columns is at approximately half the interstorey height.

$$\theta_b = \frac{\phi_b}{L_b}\left(\frac{(L_b - h_c)^2}{6} + \frac{E_t}{G}\frac{h_b^{\,2}}{4}\right) \text{ And } \theta_c = \frac{\phi_c}{2H}\left(\frac{(H - h_b)^2}{6} + \frac{E_t}{G}\frac{h_c^{\,2}}{4}\right)$$

$$\phi_b = \frac{29\times10^6}{10500\times\dfrac{240\times400^3}{12}} = 2.16\times10^{-6}\,\frac{1}{mm}$$

$$\phi_c \approx \frac{2\times29\times10^6}{10500\times\dfrac{240\times400^3}{12}}\,\frac{4191(2000-400)}{2000(4191-400)} = 3.82\times10^{-6}\,\frac{1}{mm}$$

Hence:

$$\theta_b = \frac{2.16\times10^{-6}}{4191}\left(\frac{(4191-400)^2}{6} + \frac{10500}{660}\frac{400^2}{4}\right) = 0.0016$$

$$\theta_c = \frac{3.82\times10^{-6}}{2\times2000}\left(\frac{(2000-400)^2}{6} + \frac{10500}{660}\frac{400^2}{4}\right) = 0.0010$$

Step 2: Calculate the joint panel zone deformation

On Level 3 light reinforcement is provided by large SPAX wood screws (see Chapter 4). These were provided to reinforcement the column surrounding steel pins, which

anchor additional external reinforcement (see Chapter 6). However, it was not expected that the screws would provide a significant increase to the stiffness of the joint panel region. Hence, they are ignored in the design.

A simplified approach, proposed in Chapter 6, is used for determining this joint panel deformation:

$$\theta_j = \gamma\left(1 - \frac{h_c}{L_b} - \frac{2h_b}{H}\right)$$

Where: $\gamma = \gamma_h + \gamma_v$, γ_h and γ_v are the horizontal and vertical joint distortion respectively.

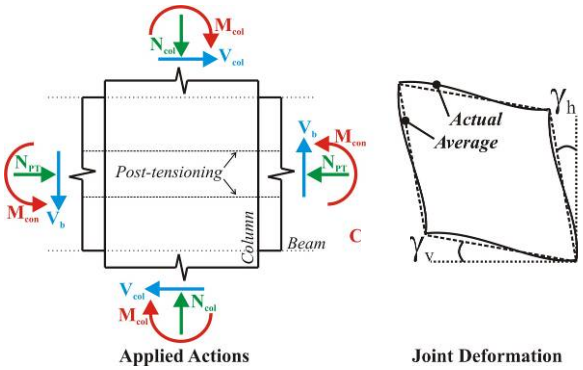

Figure A.3.4 – Horizontal and vertical joint distortion

The vertical joint distortion can be ignored. For a rectangular section, the horizontal joint distortion can be approximated as:

$$\gamma_h = \frac{\overline{V}_{jh}}{GA_{sh}}$$

Where: $\overline{V}_{jh}$ = the average horizontal shear force within the joint panel region.

$A_{sh} = b_c h_c$ = the horizontal shear area within the joint panel.

And:

$$\overline{V}_{jh} = \frac{2M_{con}}{h_b} - V_{col} \text{ (See Chapter 6)}$$

$$\text{Where } V_{col} \approx \frac{2M_{c,\text{int}}}{H} = \frac{2 \times 64}{2.0} = 64kN$$

Hence:

$$\overline{V}_{jh} = \frac{2 \times 29}{0.40} - 64 = 81kN$$

Therefore:

$$\gamma = \gamma_h = \frac{81 \times 10^3}{660 \times 400 \times 240} = 0.0013$$

And:

$$\theta_j = 0.0013\left(1 - \frac{400}{4191} - \frac{400}{2 \times 2000}\right) = 0.0010$$

Step 3: Determine the allowable connection rotation

To minimize the required post-tensioning reinforcement the maximum allowable connection rotation should be used for design of the post-tensioning.

$$\theta_{con} = \theta_d - \left(\theta_b + \theta_c + \theta_j\right) = 0.020 - \left(0.0016 + 0.0010 + 0.0010\right) = 0.020 - \left(0.0036\right) = 0.0164$$

And:

$$\theta_{imp} = \frac{\theta_{con}}{\left(1 - \frac{h_c}{L_b}\right)} = \frac{0.0164}{\left(1 - \frac{400}{4191}\right)} = 0.018$$

Step 4: Design beam-column connections

Existing procedures (Newcombe et al. 2008) are used to determine the connection moment capacity.

Impose connection rotation

The allowable connection rotation θ_{imp} is applied to the connection. A preliminary estimate of the post-tensioning is made: 4-0.5 inch (12.7mm) post-tensioning tendons symmetrically spaced at 60mm centre-to-centre, identical to Level 2. The tendons are stressed to 60% of their yield stress.

Estimate the neutral axis depth, c

Say:

$c = 270mm$

Apply member compatibility:

The elongation of the tendons, ignoring shortening (Newcombe 2008):

$$\Delta_{pt} = \theta_{imp}\left(y_i - c\right) = 0.018 \times \begin{pmatrix} 290-270 \\ 230-270 \\ 170-270 \\ 110-270 \end{pmatrix} = \begin{pmatrix} 0.36 \\ 0 \\ 0 \\ 0 \end{pmatrix} mm$$

$$\Delta\varepsilon_{pt} = \sum \frac{n\Delta_{pt}}{l_{ub}} = \frac{2}{9280}\begin{pmatrix} 0.36 \\ 0 \\ 0 \\ 0.36 \end{pmatrix} = \begin{pmatrix} 0.00008 \\ 0 \\ 0 \\ 0.00008 \end{pmatrix}$$

And:

$$\varepsilon_{pt} = \varepsilon_{pt,i} + \Delta\varepsilon_{pt} \le 0.9\varepsilon_y$$

Where: $\varepsilon_{pt,i} = \dfrac{T_{pti}}{A_{pt}E_{pt}}$ and,

$T_{pti} = 371kN$ (same as Level 2)

Hence:

$$\varepsilon_{pt,i} = \frac{371\times10^3}{396\times190000} = 0.00493$$

And:

$$\varepsilon_{pt} = 0.00493 + 0.00008 = 0.0050 \le 0.0074$$

The monolithic beam analogy (Palermo et al. 2005b) is applied assuming the timber remains elastic:

$$\varepsilon_t = \left(3\frac{\theta_{imp}}{L_{cant}} + \phi_{dec}\right)c$$

Hence:

$$\varepsilon_t = \left(3\frac{0.018}{1896} + 1.84\times10^{-6}\right)270 = 0.0082$$

Again, to determine the stress in the timber Newcombe *et al*. (2008) proposes an calibrated effective connection modulus. This aims to account for the interaction of parallel and perpendicular to grain timber of each side of the connection. In Newcombe *et al*, (2008), the

connection modulus was proposed as a ratio of the parallel to grain elastic modulus. However, there is little correlation between the parallel and perpendicular to grain modulus in timber. Hence, the calibrated numerical value from Newcombe (2008) is used here instead:

$$E_{con} = 1400MPa$$

The stress in the timber is checked. Note, since there is no steel armoring in the connection the perpendicular to grain yield stress should be considered. Hence:

$$\varepsilon_y = \frac{f_c}{E_{con}} = \frac{12}{1400} = 0.0086 > 0.0082 \Rightarrow O.K! \text{ (Not yielding)}$$

Calculate the forces in the connection

Since the timber is elastic we can assume a linear distribution of the stress within the compression region of the timber, hence:

$$C_t = 0.5\varepsilon_t E_{con} c_i b = 0.5 \times 0.0082 \times 1400 \times 270 \times 240 / 10^3 = 372kN$$

For the post-tensioning:

$$T_{pt} = T_{pt,i} + \Delta T_{pt} = 0.7 f_y A_{pt} + \sum \varepsilon_{pt} E_{pt} A_{pt_1}$$
$$= 371 + 3 = 374kN$$

Check force equilibrium

By equilibrium:

$C_t = T_{pt}$:

$\therefore 372 \approx 374 \Rightarrow OK!$ (Within 5%)

Evaluate the moment capacity

$$\phi M_n = \phi T_{pt}\left(\frac{h_b}{2} - \frac{c}{3}\right) = 0.9 \times 374 \times \left(\frac{400}{2} - \frac{270}{3}\right) = 37kN.m$$

$$M^* \le \phi M_n$$

$$29 \le 37 \Rightarrow O.K!$$

Therefore, the preliminary section sizes and specified post-tensioning are sufficient.

Column-base connections

The column-base connections are designed in a similar manner as the beam-column connections. Axial loads are induced by gravity loading, and seismic tension/compression on the exterior columns. The sum of moment capacity of the columns must be at least than $0.6V_bH_1$, according to the assumptions for the frame analysis (section A.2). However, due to laboratory constraints the interstorey height of the first floor is restricted. Hence, the column connections are effectively moved up the height of the column by 300mm (to allow for the steel foundations). Therefore, the actual connection design moment is reduced to:

$$\sum M_{col,actual} = \frac{0.6\times 2000 - 300}{0.6\times 2000} 0.6V_bH_1 = 0.75\left(0.6V_bH_1\right) = 0.75\times 180 = 135kN.m$$

It is assumed the reduction and increase in moment capacity for the columns subjected to seismic tension and compression forces respectively is similar. Hence, the interior column base connections were designed to have a moment capacity of at least $0.2V_bH_1$ (reduced by 25%): 45kN.m. For the interior connection the gravity induced axial load is approximately 37kN.

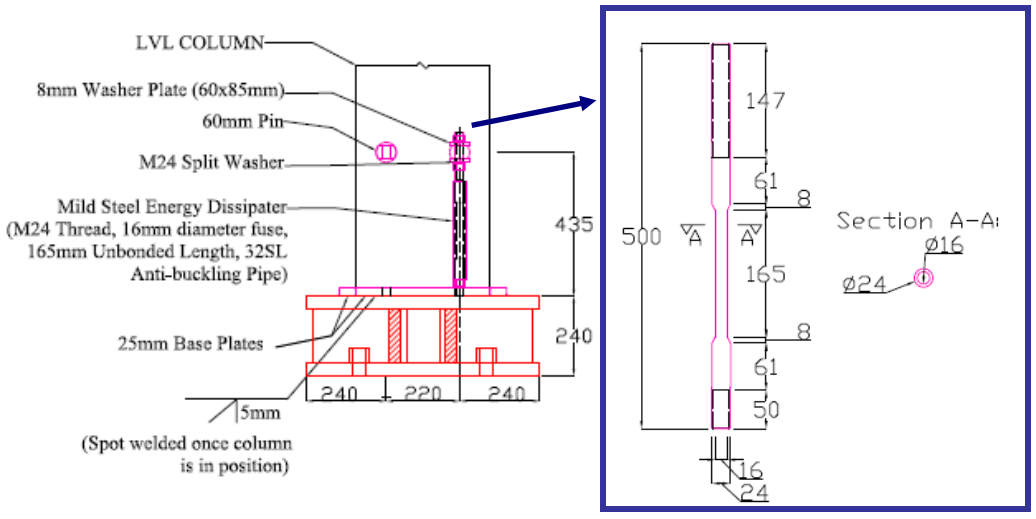

Figure A.3.5 – Column-base external reinforcement

Impose connection rotation

The allowable connection rotation θ_{imp} is applied to the connection. Here it is assumed that the elastic deformation of the column is negligible. Hence, the full design rotation of 2.0% is applied to the connection. A preliminary estimate of the external reinforcement is made: 2-16mm diameter fused mild steel bars per side, spaced at 220mm (see Figure A.3.5).

Estimate the neutral axis depth, c

Say:

$c = 70mm$

Apply member compatibility:

The elongation of the bars:

$$\Delta_s = \theta_{imp}\left(y_i - c\right) = 0.02 \times \begin{pmatrix} 310 - 70 \\ 90 - 70 \end{pmatrix} = \begin{pmatrix} 4.8 \\ 0.4 \end{pmatrix} mm$$

Where: y_i = the distance to the centroid of the bars from the edge of the column.

The strains due to gap openings are (Newcombe et al. 2008):

$$\varepsilon_s = \frac{\Delta_s - 2\Delta_{sp}}{l'_{ub}}$$

Where: Δ_{sp} = the strain penetration or slippage of the anchorages

$l'_{ub} = 165mm$ = the unbonded (fuse) length of the bars.

It is assumed that the slippage of the anchorage pin and the bolted connections is 0.5mm. Because the deformation of the bars closest to the neutral axis is less than the slippage deformation their contribution can be ignored. Hence:

$$\varepsilon_s = \begin{pmatrix} (4.8 - 0.5)/165 \\ 0 \end{pmatrix} = \begin{pmatrix} 0.0261 \\ 0 \end{pmatrix}$$

The maximum strain of the bar (at the design displacement of the structure) should not exceed 5% strain for mild steel (Marriott 2009).

$\varepsilon_s = 2.5\% \leq 5\%$

The monolithic beam analogy (Palermo et al. 2005b) is applied assuming the timber remains elastic, as proposed by Newcombe (2008):

$$\varepsilon_t = \left(3\frac{\theta_{imp}}{L_{cant}} + \phi_{dec} \right) c$$

Where: ϕ_{dec} = the decompression curvature

L_{cant} = the shear span = $0.6H_1$ - 300 = 900mm

The decompression curvature negligible due to low axial forces:

$$\phi_{dec} \approx 0$$

Hence:

$$\varepsilon_t = \left(3\frac{0.02}{900} + 0 \right) 70 = 0.0047$$

To determine the stress in the timber Newcombe *et al*. (2008) proposes an calibrated effective connection modulus is used for column-base connections:

$$E_{con} = 0.55E_t = 0.55 \times 10500 = 5775MPa$$

The stress in the timber is checked. Note, the parallel-to-grain yield stress should be considered. Hence:

$$\varepsilon_y = \frac{f_c}{E_{con}} = \frac{45}{5775} = 0.0078 > 0.0047 \Rightarrow O.K! \text{ (Not yielding)}$$

Calculate the forces in the connection

Since the timber is elastic we can assume a linear distribution of the stress within the compression region of the timber, hence:

$$C_t = 0.5\varepsilon_t E_{con} c_i b = 0.5 \times 0.0047 \times 5775 \times 70 \times 240 / 10^3 = 228kN$$

For the steel bars, an elasto-perfectly-plastic steel relationship is assumed, with a yield stress of 430MPa.

$$T_s = A_s f_y = 2 \times \frac{\pi}{4} 16^2 \times 430 / 10^3 = 173kN$$

Check force equilibrium

By equilibrium:

$$C_t = T_s + N^*$$

$$\therefore 228 \approx 173 + 37 = 210 \Rightarrow OK! \text{ (Within 10\%)}$$

Evaluate the moment capacity

$$\phi M_n = \phi\left[T_s\left(y_i - \frac{c}{3}\right) + N^*\left(\frac{h_c}{2} - \frac{c}{3}\right)\right] = 0.9\left[173 \times \left(310 - \frac{70}{3}\right) + 37 \times \left(200 - \frac{70}{3}\right)\right]$$

$$= 50kN.m$$

$$M^* \le \phi M_n$$

$$45 \le 50 \Rightarrow O.K!$$

Therefore, the preliminary section sizes and specified reinforcement are sufficient.

Design pin-anchorage

The pins used to anchor the external reinforcement to the column were designed using Eurocode 5 (EC5 1994) equations for a pure embedment failure. The axial capacity of a pin according Eurocode 5 is:

$$\phi V_n = 0.9 \times 703 = 632kN$$

The peak demand is derived from the two rods yielding in tension (ignoring overstrength):

$$V^*_{pin} = 346kN$$

$$V^* \le \phi V_n$$

$$346 \le 632 \Rightarrow O.K!$$

Beam and column section capacity

The critical section capacity check is for the interior column on Level 3, with a moment demand of 64kN.m.

Flexure:

For column design, it has been proposed (Newcombe 2008) that a dynamic amplification factor, ω, of 1.6 should be considered. In addition, an overstrength factor, ϕ^0, of 1.25 is assumed to take into

account inaccuracies in for the prediction of post-tensioned connection moment capacity and over-design.

The nominal moment capacity is:

$$\phi M_n = \phi k Z f_b$$

The bending strength, f_b, is 45MPa. For large timber members at size factor, k_{24}, should be considered. From NZS 3604, for a 400mm deep section; k_{24} = 0.95. Since the beam is subjected to axial load, the buckling factor, k_8, is computed; k_8 = 1.0. No other k-factors are required for short term earthquake loading. The lowest section modulus, Z, is within the joint panel region, between beams. Here, the section width is reduced to allow the post-tensioning to pass through the column. According to New Zealand Standards, a strength reduction factor need not be considered for overstrength design.

$$\therefore \phi M_n = 1.0 \times 0.95 \times 45 \times \frac{180 \times 400^2}{6} = 205 kN.m$$

$$\omega \phi^0 M^*_{cl} \le \phi M_n$$
$$1.6 \times 1.25 \times 64 \le 205$$
$$128 \le 205 \Rightarrow O.K!$$

Shear:

The maximum shear applied to the column will be within the joint panel region at Level 2. However, this is heavily reinforced with internal steel plates (see Chapter 4). Therefore, the critical shear demand will occur within the joint panel region on Level 3. The peak shear is determined using the previous section analysis:

$$V^* = C_t - V_{col} = 228 - \frac{64}{1.0} = 164 kN$$

It is tentatively recommended that the shear force dynamic amplification factor, ω_v, for the design of reinforced concrete frames (NZS3101 2006) of 1.3 can be used.

The shear capacity is:

$\phi V_n = \phi k f_s A_s$

Where: $f_s = 5.3MPa$ = the shear strength of the timber

Within the joint panel region, the internal stresses are predominately due to shear; hence, the shear area, A_s, is the full section area:

$\therefore \phi V_n = 1.0 \times 1.0 \times 5.3 \times 180 \times 400 / 10^3 = 382kN$

$\omega_v \phi^0 V^* \leq \phi V_n$

$1.3 \times 1.25 \times 164 \leq 382$

$267 \leq 382 \Rightarrow O.K!$

Therefore, the section capacity of the beams and columns is sufficient. With the addition of external mild steel reinforcement (see Chapter 4), the moment demand on the sections may increase by a factor of approximately 1.5. Even if this occurs there will be sufficient section capacity.

A.3.2. Wall design

The elastic member deformations for timber walls can also be significant (depending on geometry). Again, improved methodologies, discussed in Chapter 7, were used to determine the wall deformation for the test building and existing procedures were used to describe the connection response (Newcombe et al. 2008). It was assumed in the design that the concrete slab or edge beams provide no coupling action to the walls.

Determination of the wall actions

The actions (forces, shears and moments) on each wall are assumed to be simply the building actions from the prototype divided by eight and reduced according to similitude. Hence, no eccentricities are considered for proportioning load to each wall.

Table A.3.1 – Calculation of wall actions

Storey, i	Fi (kN)	Vsi (kN)	Msi (kN.m)
2	25	25	50
1	13	38	114
Sum	**V_b=38**		

Base connections

The actions on a wall are considered to estimate the member deformations and determine allowable connection rotation. It is assumed that the wall deformation profile is effectively linear. Hence, the rotation to the top of the wall is essentially the same as to the effective height.

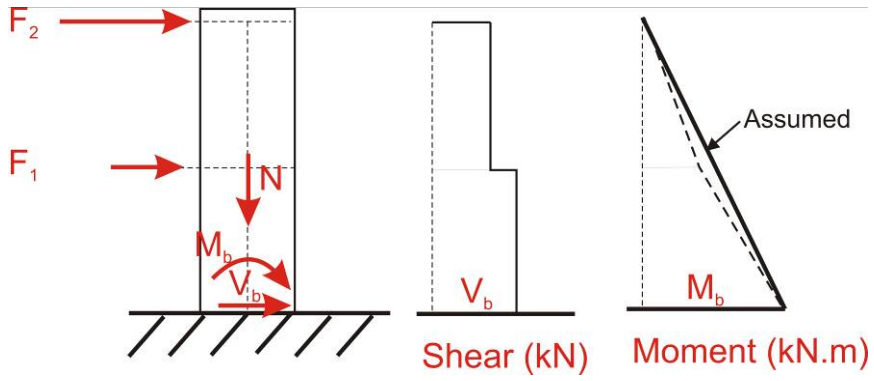

Figure A.3.6 – Wall actions

The deflection of the wall can be broken into its significant components:

$$\theta_D = \theta_f + \theta_s + \theta_{con}$$

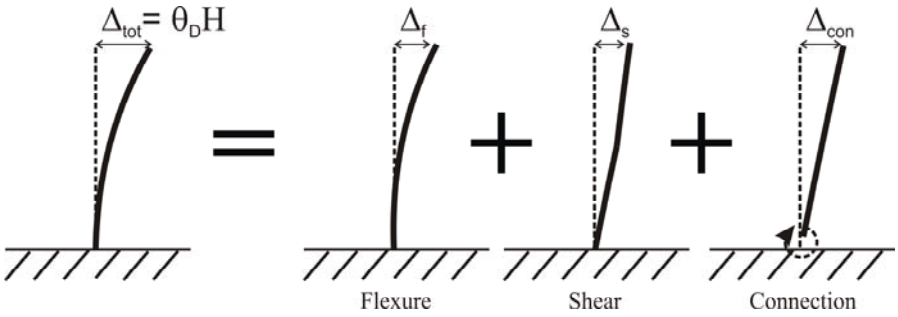

Figure A.3.7 – Deflection components of timber frame

Step 1: Calculate flexural deformation

It is assumed that the bending moment diagram is effectively linear.

$$\Delta_f = \frac{M_b {H_{total}}^2}{3E_t I_w}$$

Where: H_{total} = 3.7m = the height from the wall base to the top floor.

The walls sections are 800×144mm and have a void of 400x50mm. Therefore:

$$I_w = \frac{1}{12}\left(144\times 800^3 - 50\times 400^3\right) = 5.88\times 10^9\, mm^4$$

Hence:

$$\Delta_f = \frac{114\times 10^6 \times 3700^2}{3\times 10500\times 5.88\times 10^9} = 8.4mm$$

Therefore, the drift due to flexure is approximately:

$$\theta_f = \frac{\Delta_f}{H_{total}} = \frac{8.4}{3700} = 0.0023$$

Step 2: Calculate shear deformation

Again, it is assumed that shear deformation is approximately linear with height. The shear deformation is the sum of the shear deformation at each floor, Δ_{si}. Hence:

$$\Delta_s = \sum \Delta_{si} = \sum \frac{V_{si} H_i}{GA_s}$$

Where: H_i = 1.7m and 2.0m for Level 1 and Level 2 respectively

The shear area is approximately:

$$A_s = \frac{2}{3}\left(144\times 800 - 50\times 400\right) = 63.5\times 10^3\, mm^2$$

Hence:

$$\Delta_s = \frac{1}{660\times 63.5\times 10^3}\left(38\times 10^3 \times 1700 + 25\times 10^3 \times 2000\right) = 2.7mm$$

Therefore, the drift due to shear is approximately:

$$\theta_s = \frac{\Delta_s}{H_{total}} = \frac{2.7}{3700} = 0.0007$$

Step 3: Determine the allowable connection rotation

To minimize the required post-tensioning reinforcement the maximum allowable connection rotation should be used for design of the post-tensioning.

$$\theta_{con} = \theta_d - (\theta_f + \theta_s) = 0.020 - (0.0023 + 0.0007) = 0.020 - 0.0030 = 0.017$$

The actual imposed connection rotation at the connection, θ_{imp}, is equal to the interstorey rotation due to the connection, θ_{con}:

$$\theta_{imp} = \theta_{con} = 0.017$$

Step 4: Design wall base connections

Existing procedures (Newcombe et al. 2008) are used to determine the connection moment capacity. The gravity load on each wall will be approximately 9kN.

Impose connection rotation

The allowable connection rotation θ_{imp} is applied to the connection. A preliminary estimate of the post-tensioning is made: 5-0.5 inch (12.7mm) post-tensioning tendons symmetrically spaced at 60mm centre-to-centre. The tendons are stressed to 60% of their yield stress.

Estimate the neutral axis depth, c

Say:

$c = 270mm$

Apply member compatibility

The elongation of the tendons, ignoring shortening (Newcombe 2008) is:

$$\Delta_{pt} = \theta_{imp}\left(y_i - c\right) = 0.017 \times \begin{pmatrix} 520-270 \\ 460-270 \\ 400-270 \\ 340-270 \\ 280-270 \end{pmatrix} = \begin{pmatrix} 4.25 \\ 3.23 \\ 2.21 \\ 1.19 \\ 0.17 \end{pmatrix} mm$$

$$\Delta\varepsilon_{pt} = \sum \frac{n\Delta_{pt}}{l_{ub}} = \frac{1}{4250}\begin{pmatrix} 4.25 \\ 3.23 \\ 2.21 \\ 1.19 \\ 0.17 \end{pmatrix} = \begin{pmatrix} 0.00100 \\ 0.00076 \\ 0.00052 \\ 0.00028 \\ 0.00004 \end{pmatrix}$$

And:

$$\varepsilon_{pt} = \varepsilon_{pt,i} + \Delta\varepsilon_{pt} \le 0.9\varepsilon_y$$

Where: $\varepsilon_{pt,i} = \dfrac{T_{pti}}{A_{pt}E_{pt}}$ and,

$$T_{pti} = 464kN$$

Hence:

$$\varepsilon_{pt,i} = \frac{464 \times 10^3}{495 \times 190000} = 0.00493$$

And, for the worst-case tendon:

$$\varepsilon_{pt} = 0.00493 + 0.00100 = 0.0059 \le 0.0074$$

The monolithic beam analogy (Palermo et al. 2005b) is applied assuming the timber remains elastic, as proposed by Newcombe (2008):

$$\varepsilon_t = \left(3\frac{\theta_{imp}}{L_{cant}} + \phi_{dec}\right)c$$

Where: L_{cant} = the shear span = H_e – 300mm = 3333-300 = 3033mm
The decompression curvature is:

$$\phi_{dec} = \frac{2T_{pti}}{E_t b_w {l_w}^2} = \frac{2 \times 464 \times 10^3}{10500 \times 144 \times 800^2} = 0.96 \times 10^{-6}\,\frac{1}{mm}$$

Hence:

$$\varepsilon_t = \left(3\frac{0.017}{3033} + 0.96 \times 10^{-6}\right)270 = 0.0048$$

To determine the stress in the timber Newcombe *et al*. (2008) proposes an calibrated effective connection modulus, similar to column-base connections, is used.

$$E_{con} = 5775MPa$$

The yield stress of the timber:

$$\varepsilon_y = \frac{f_c}{E_{con}} = \frac{45}{5775} = 0.0078 > 0.0048 \Rightarrow O.K! \text{ (Not yielding)}$$

Calculate the forces in the connection

Since the timber is elastic we can assume a linear distribution of the stress within the compression region of the timber. Because the neutral axis passes through the void in wall, the total wall width can not be considered for calculating the force applied by the timber. Instead the following expression applies:

$$C_t = 0.5\varepsilon_t E_{con}\left(c_i b - \frac{(c-x)^2}{c} b_v\right)$$

Where: b_v = 50mm = the width of the void
x = 200mm = the length of the solid part of the wall

$$C_t = 0.5 \times 0.0048 \times 5775\left(270 \times 144 - \frac{(270-200)^2}{270} 50\right) / 10^3 = 526kN$$

For the post-tensioning:

$$T_{pt} = T_{pt,i} + \Delta T_{pt} = 0.7 f_y A_{pt} + \sum \varepsilon_{pt} E_{pt} A_{pt_1}$$
$$= 464 + (0.00100 + 0.00076 + 0.00052 + 0.00028 + 0.00004) \times 190000 \times 99 / 10^3$$
$$= 464 + 19 + 14 + 10 + 5 + 1 = 513N$$

Check force equilibrium

By equilibrium:

$C_t = T_{pt} + N^*$:

$\therefore 526 \approx 522 \Rightarrow OK!$ (Within 5%)

Evaluate the moment capacity

$$\phi M_n = \phi\left[\sum T_{pti}\left(y_i - \frac{c}{3}\right) + N^*\left(\frac{l_w}{2} - \frac{c}{3}\right)\right]$$

$$= 0.9\left[\begin{array}{l} 112\times\left(520-\frac{270}{3}\right)+107\times\left(460-\frac{270}{3}\right)+103\left(400-\frac{270}{3}\right)+98\left(340-\frac{270}{3}\right)... \\ +94\left(280-\frac{270}{3}\right)+9\left(400-\frac{270}{3}\right) \end{array}\right]/10^3$$

$$= 148kN.m$$

$$M^* \le \phi M_n$$

$$114 \le 148 \Rightarrow O.K!$$

Therefore, the preliminary section sizes and specified post-tensioning are sufficient for the connection response.

Wall section capacity

The critical section capacity is at the base of wall, with a moment demand of 114kN.m.

Flexure:

The section sizes were defined in the preliminary design to minimize deflection, now the section strength must be checked. The wall section will be subjected higher modes of amplification of moments and shears. Since there is no tension shift mechanism for timber walls, it is assumed that it is appropriate to use the reinforced concrete column amplification factors (ω = 1.0 at the ground floor). In addition, an overstrength factor, ϕ^0, of 1.25 is assumed to take into account inaccuracies in for the prediction of post-tensioned connection moment capacity and over-design.

$$\phi M_n = \phi k f_b Z$$

Where: $k = k_1 k_8 k_{23}$

k_1= 1.0 for short term loads

k_8= 1.0 (no buckling)

k_{23}= 0.85 for size effect

$$Z = \frac{2I_w}{l_w} = \frac{2\times 5.88\times 10^9}{800} = 14.7\times 10^6 mm^3$$

$$\therefore \phi M_n = 1.0 \times 0.85 \times 45 \times 14.7 = 562 kN.m$$

$$\omega \phi^0 M^* \le \phi M_n$$
$$1.0 \times 1.25 \times 114 \le 562 \Rightarrow O.K!$$

Shear:

Again the wall must be designed for increased forces due to higher modes. It is tentatively recommended that the dynamic amplification factor for the design of reinforced concrete walls is used herein:

$$\omega_v = 0.9 + \frac{n_t}{10} = 0.9 + \frac{2}{10} = 1.1$$

Where: n_t= number of floors

$$V^* = 38 kN$$
$$\phi V_n = \phi k f_s A_s$$

Where: k = 1.0 for short term loads
f_s = 5.3MPa

$$\therefore \phi V_n = 1.0 \times 1.0 \times 5.3 \times 63.5 = 337 kN$$

$$\omega_v \phi^0 V^* \le \phi V_n$$
$$1.1 \times 1.25 \times 38 \le 337$$

Therefore the section size is sufficient. With the addition of external mild steel reinforcement (see Chapter 4), the moment demand on the walls may increase by a factor of approximately two. Even if this occurs there will be sufficient section capacity.

A.3.3. Design of the floor diaphragm

The floor diaphragm is designed to remain essentially elastic for all tests performed on the test building. There are several methodologies for determination of the design forces for the diaphragm (see Chapter 3 and 8). The upper limit for diaphragm design forces according to the UBC (UBC 1997) and IBC (IBC 2003) codes are one times the peak ground acceleration (PGA). However, research has shown this to be non-conservative (see Chapter 3). For flexible diaphragms, it is proposed that each floor is design for

three times the design peak ground acceleration. This corresponds with the parts and portions section in NZS1170.5. Hence, for the prototype structure:

$$F_{dia} = 3pga \cdot m_i = 3 \times 0.532 \times 9.81 \times 84 = 1315kN$$

Scaling to the test building:

$$F_{dia} = 585kN$$

While this may be appropriate for dynamic earthquake loading, under quasi-static earthquake loading the floor forces not related to the design PGA but the achievable strength of the lateral load resisting systems. Hence, to ensure the floor diaphragm and diaphragm connections remain elastic the base shear from Stage 1 experimental testing are used to design the diaphragm.

$V_b = 666kN$ (in the EW direction)

This force is increased by 15% to account for the increases in frame strength due to interaction of the floor slab:

$V_b = 766kN$ (in the EW direction)

This force must be split to level 3 and 2. Hence, the peak diaphragm force is on the Level 3 with:

$F_{dia,L3} = 511kN$ (in the EW direction)

$F_{dia,L2} = 256kN$

It is conservatively assumed that this diaphragm force acts in both the NS and EW directions. A depiction of the floor diaphragm connections are given below. Further detail is given in the structural drawings within this Appendix.

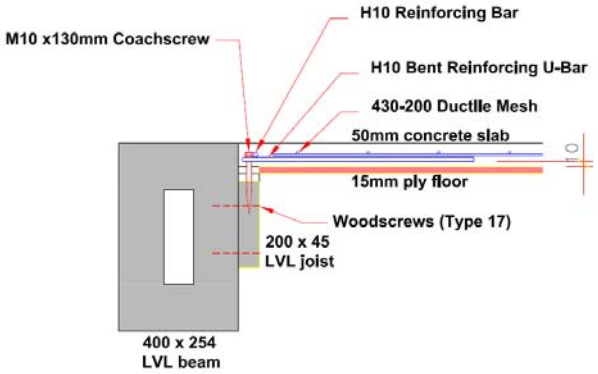

Figure A.3.8 – Diaphragm connection detail

Slab reinforcement

The slab reinforcement was designed using strut and tie analysis, considering clauses in NZS3101 (2006) for maximum and minimum reinforcement. The mesh was designed to transfer ram induced forces throughout the floor. The worst-case demand on the slab reinforcement was due to loading in the EW direction, illustrated in Figure A.3.9 below.

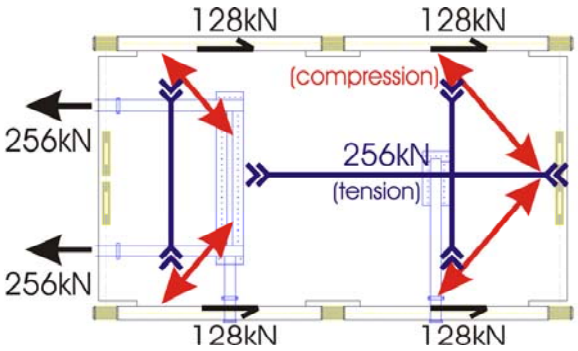

Figure A.3.9 – Slab reinforcing mesh design forces (floor plan)

430 MDT – 200 ductile mesh is specified, which has a bar diameter of 8mm at 250mm centers with a minimum tensile stress, f_u, of 430MPa. Ignoring the tensile strength of the concrete, the mesh must provide:

$$F^* = 255kN$$

Hence:

$$\phi F = \phi f_u A_s b_{slab}$$

Where: $A_s = 201mm^2/m$ = area per meter width
b_{slab} = 4.35m = width of slab

Therefore:

$$\therefore \phi F = 0.9 \times 430 \times 201 \times 4.35 = 343kN \geq 255kN$$

Bent 'U-bars' were designed ensure adequate transfer of slab forces, to notched shear key connections in edge joists (see the structural drawings below). These U-bars provide a shear transfer mechanism, even if the concrete slab is cracked due to out-of-plane loading. Simple shear capacity and development length formula from NZS3101 (2006) are used to design the U-bars.

Additional reinforcing (drag) bars are provided along the edge joists, which distributes the slab forces evenly to the notched connections (see the structural drawings below).

Notched joist connections

The notched connections in edge joists (and edge beams) are used to transfer diaphragm forces. These notched connections are identical to those used to provide composite action for gravity loading. The shear capacity of the notch connection was determined considering Yeoh (2010).

Edge joist-to-frame connections

The notched edge joists are screwed to the beams (within the seismic frames). The number of screws was determined using equations presented in Chapter 3 (Bejtka and Blass 2002; EC5 1994). On Level 3, screws inclined at 45 degrees were used. On Level 2, screws were placed perpendicular to the beams.

Edge beam-to-wall connections

The edge beams were screwed to the walls using orthogonal wood screws (see Chapter 4). The wood screws were positioned into a square pattern, to allow rotation of the wall relative to the edge beam while avoiding screw fracture due to excessive displacement. Standard Eurocode 5 (1994) equations were used to determine the number of screws required.

A.3.4. Other design

For brevity, details of the design of several other components are not presented in this Appendix. Some further information is provided below:

- The timber-concrete composite floor system for the prototype structure was designed according to Yeoh (2010) and TDG (2008). The prototype design was scaled (by 2/3) for the test building.
- Gravity corbels and top-hung joist hangers were designed using bearing formula and shear/axial pull-out wood screw capacities from NZS3603 (1999). These joist hanger connection and corbels were tested by Carradine *et al*, (2010; 2009).
- The anchorage of the external reinforcement for the frames and walls was designed according to Eurocode 5 (EC5 1994). The frame anchorage pins were designed remain elastic, with timber bearing as the critical mechanism. The screws used to anchor the UFPs to the walls were designed for axial pullout and shear. Pull-out forces were induced because the UFPs were anchored on only one side of the wall (for ease of construction).
- Steel shear keys were used at the column and wall bases, which were designed according to NZS 3404 (1997).
- SPAX screws were used to reinforce the timber surrounding steel anchorage pins in the columns on Level 3. Sufficient screws were provided to prevent timber fracture due to limited edge distances, according to NZS 3603 (1999). Stut and tie analysis was employed to evaluate the force demands on the screws.
- An internal steel plate arrangement was detailed for the columns at Level 2. This was designed to distribute compressive bearing stresses, applied by the rocking beams, and to avoid loading of the column perpendicular to grain. The steel components were designed according to NZS 3404 (1997) and the bearing capacities of the timber were determined using TDG (2008).

A.4. CAPACITY PREDICTION

Using a similar procedure to that shown for design, the capacity of the frame and wall system at 2% drift can be predicted, with and without additional external steel reinforcement. Due to the presence of additional reinforcement, over-design and strength reduction factors, the actual frame and wall capacity will be greater than required by the design. These predictions are compared with experimental results later in this appendix and in Chapter 5.

To make accurate predictions of the frame and wall capacity, iteration of the modeling procedure is required. This is because elastic deformation of the members depends on the moment capacity of the connections. To perform this task the modeling procedure was implemented into a numerical analysis computer package (MATLAB) which could predict the response of the frame and walls at any interstorey drift. Multiple design drift limit states and more accurate calculation of the section properties were used in the MATLAB analyses.

From the predicted response, the hysteretic area-based damping of the system can be evaluated (Jacobsen 1960; Priestley et al. 2007). The area-based equivalent viscous damping, $\xi_{hyst,ab}$, is described in the figure below.

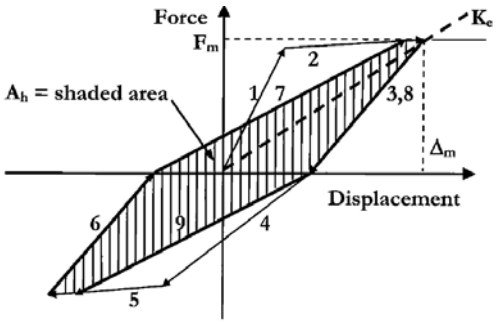

$$\xi_{hyst,ab} = \frac{A_h}{2\pi F_m \Delta_m}$$

Figure A.4.1 – Area-based equivalent viscous damping (Priestley et al. 2007)

According to Priestley *et al* (2007), the total system damping can be determined by taking a weighted average of the damping provided by individual components, where the weighting is defined by the overturning moment (OTM) contribution. For the frame system, the column-base connections and the additional external reinforcement will

provide some hysteretic damping, which can be weighted to approximate the total system damping of the frame.

Assuming that the hysteretic response of the column-base connections and additional reinforcement is essentially elasto-plastic, the following formula can be used to determine the component area-based damping (Blandon and Priestley 2005):

$$\xi_{hyst,comp} = \frac{2(\mu - 1)}{\mu\pi(1 + r(\mu - 1))}$$

Where: μ = the ductility achieved by the component
r = the bi-linear factor.

The overall system damping can be determined by taking the weighted average of **n** components using the following relation:

$$\xi_{hyst,ab} = \frac{\sum_{i=1}^{n} \xi_{hyst,comp,i} M_{b,comp,i}}{OTM}$$

Where: $\xi_{hyst,comp,i}$ = the hysteretic damping of the ith component
$M_{b,comp,i}$ = the base moment contribution from the component.

A.4.1. Post-tensioned frame

The resultant connection capacities are illustrated in Figure A.4.2. Some of the MATLAB output is shown in Figure A.4.3, Figure A.4.4 and Figure A.4.5.

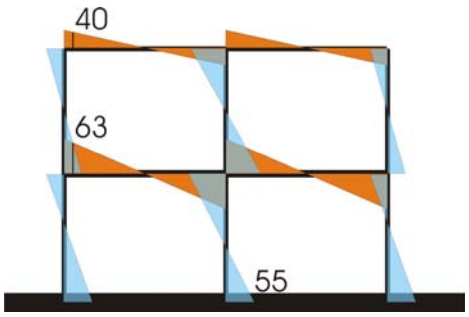

Figure A.4.2 – Post-tensioned frame bending moment diagram at 2% drift

The total overturning moment (OTM) for each frame is 619kN.m. This equates to a total base shear (or ram force) of 188kN and 199kN for Stage 1 and 2 respectively.

The base connections are the only components which have hysteretic energy dissipation potential for the post-tensioned frame (according to this simplified analysis). The connections achieve a ductility of approximately 6, with a bi-linear factor of 0.03, giving an area-based damping of approximately 46% (assuming an elasto-plastic hysteresis). Hence, the system area-based damping is approximately:

$$\xi_{hyst,ab} = \frac{46 \times 3 \times 55}{620} = 12\%$$

The re-centering ratio, λ, (as defined in Chapter 2) for post-tensioned only frame at 2% drift is:

$$\lambda = \frac{M_{pt} + M_N}{M_s} \geq \alpha_0$$

Where: $M_{pt} = TL_{base} = \left(\frac{40+63}{4.19/2}\right) 4.19 \times 2 = 412 kNm$;

$M_s = \sum M_{col} = 55 \times 3 = 165 kNm$;

$M_N = 0$.

Hence:

$$\therefore \lambda = \frac{412}{165} = 2.5$$

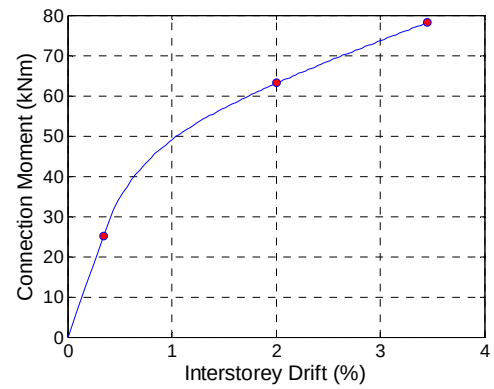

a)

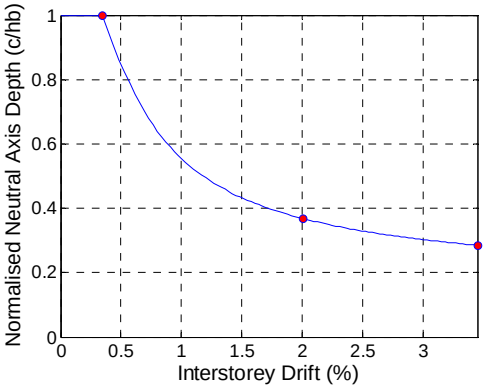

b)

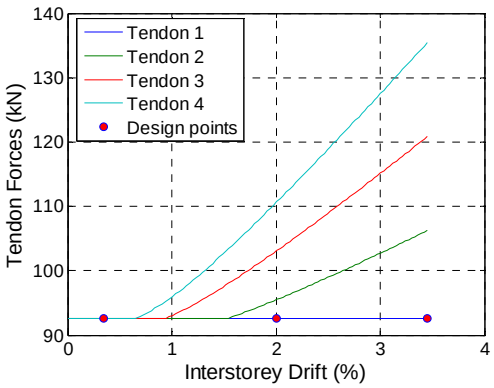

c)

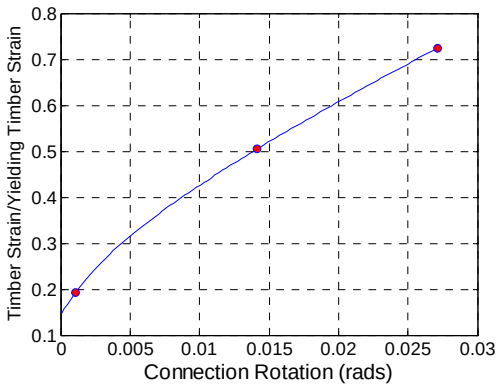

d)

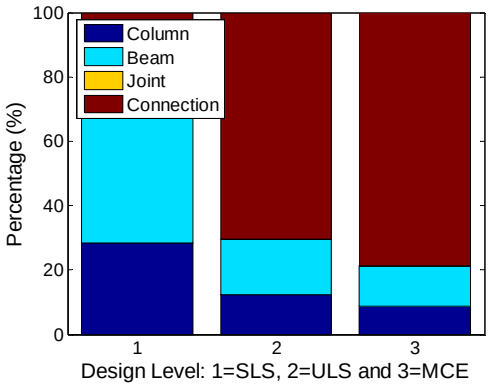

e)

Figure A.4.3 – Analysis output for Level 2 post-tensioned connections at 3 design points a) Connection moment b) Neutral axis depth c) Tendon forces d) Timber strain e) Deformation components at 3 design points

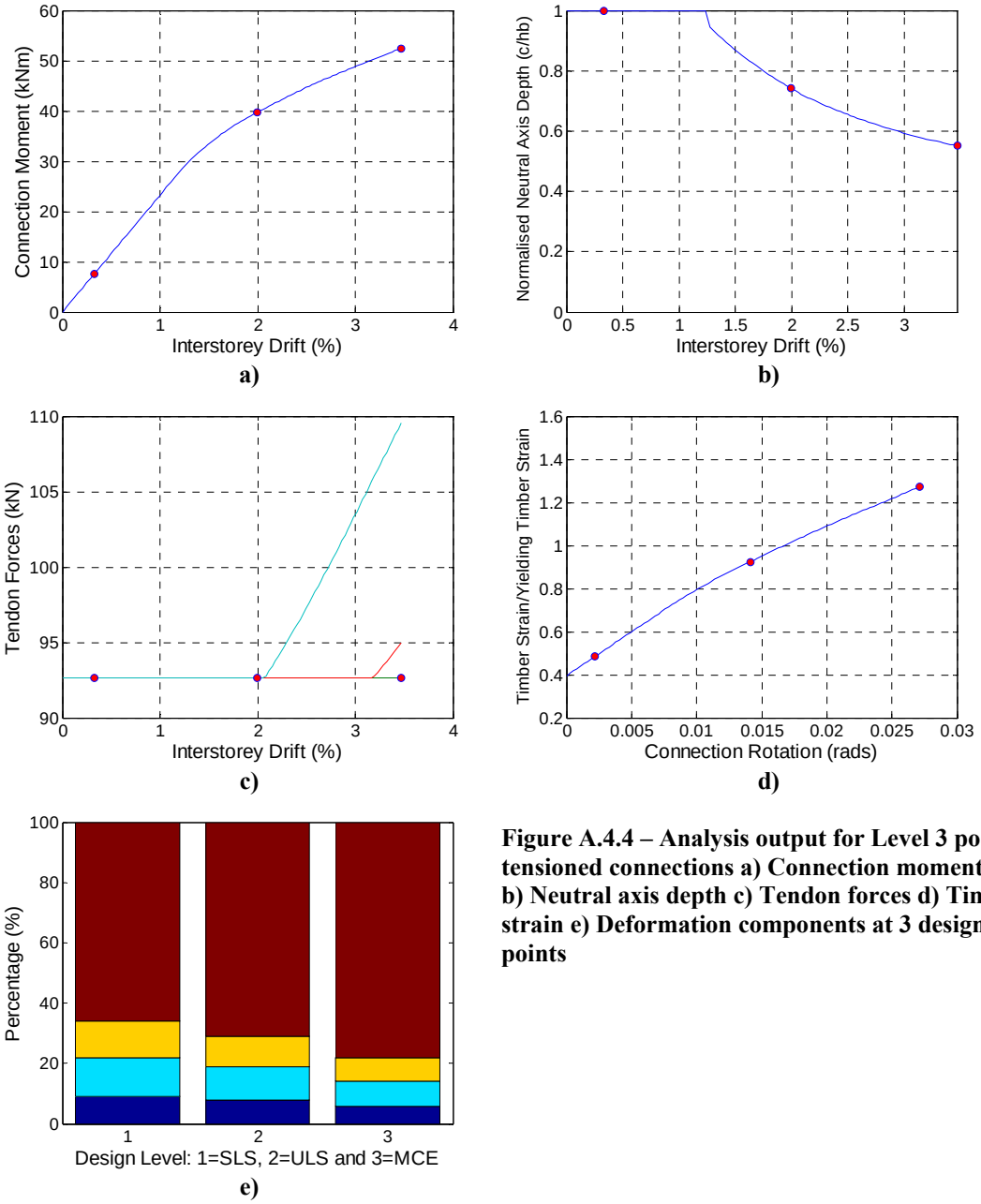

Figure A.4.4 – Analysis output for Level 3 post-tensioned connections a) Connection moment b) Neutral axis depth c) Tendon forces d) Timber strain e) Deformation components at 3 design points

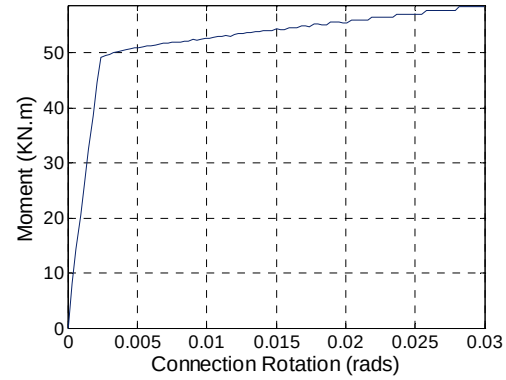

a)

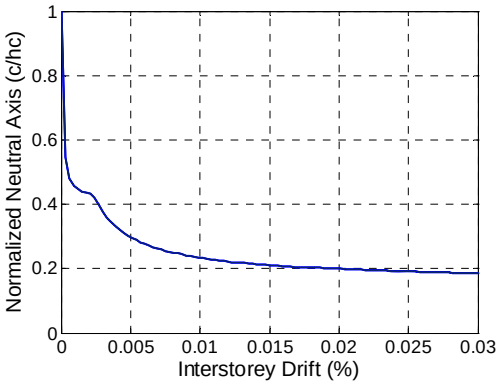

b)

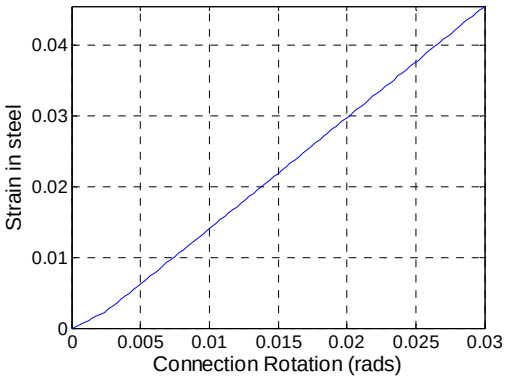

c)

Figure A.4.5 – Analysis output for column-base connections a) Connection moment b) Neutral axis depth c) Strain in steel bars

A.4.2. Hybrid post-tensioned frame

With the addition on the mild steel reinforcement between the beam-column connections (creating a hybrid system), the capacity of the frame system will increase. This can be predicted, using a similar design procedure to that shown above, with additional details from Newcombe *et al.* (2008).

It is assumed that the external reinforcement has a yield stress of 430MPa, a bi-linear stress-strain relationship and anchorage slippage of 0.5mm. The response of the column base connections is unchanged from the post-tensioned frame.

The resultant connection capacities are illustrated in Figure A.4.6. Some of the MATLAB output is shown in Figure A.4.7 and Figure A.4.8.

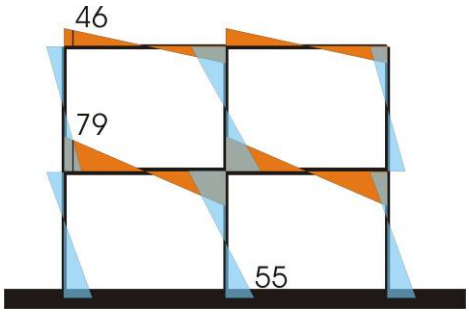

Figure A.4.6 – Hybrid post-tensioned frame bending moment diagram at 2% drift

The total overturning moment (OTM) for each frame is 720kN.m. This equates to a total base shear (or ram force) of 218kN and 232kN for Stage 1 and 2 respectively.

The base connections and additional beam-column reinforcement provide hysteretic energy dissipation to the system. Once activated, the beam-column reinforcement achieves a ductility of approximately 2.2 and 1 on Level 2 and 3 respectively. Hence, the steel does not yield on Level 3 according to the analytical predictions. The bi-linear factor is approximately 0.01, giving an area-based damping of approximately 34% for the Level 2 connections. The contribution of mild steel from the Level 1 connections to the OTM is 83kN.m (12%). Hence, adding the dissipative contributions of the base-

connection and mild steel reinforcement from the beam-column connections, the system area-based damping is approximately:

$$\xi_{hyst,ab} = \frac{46 \times 165 + 83 \times 34}{720} = 14\%$$

The re-centering ratio, λ, (as defined in Chapter 2) for hybrid frame at 2% drift is:

$$\lambda = \frac{M_{pt} + M_N}{M_s} \geq \alpha_0$$

Where: $M_{pt} = \left(\frac{41+61}{4.19/2}\right) 4.19 \times 2 = 408 kNm$;

$M_s = 55 \times 3 + \left(\frac{19+5}{4.19/2}\right) 4.19 \times 2 = 261 kNm$;

$M_N = 0$.

Hence:

$$\therefore \lambda = \frac{408}{261} = 1.6$$

The re-centering ratio is greater than minimum value, α_0, suggested by current precast concrete design (NZCS 2010) of 1.5.

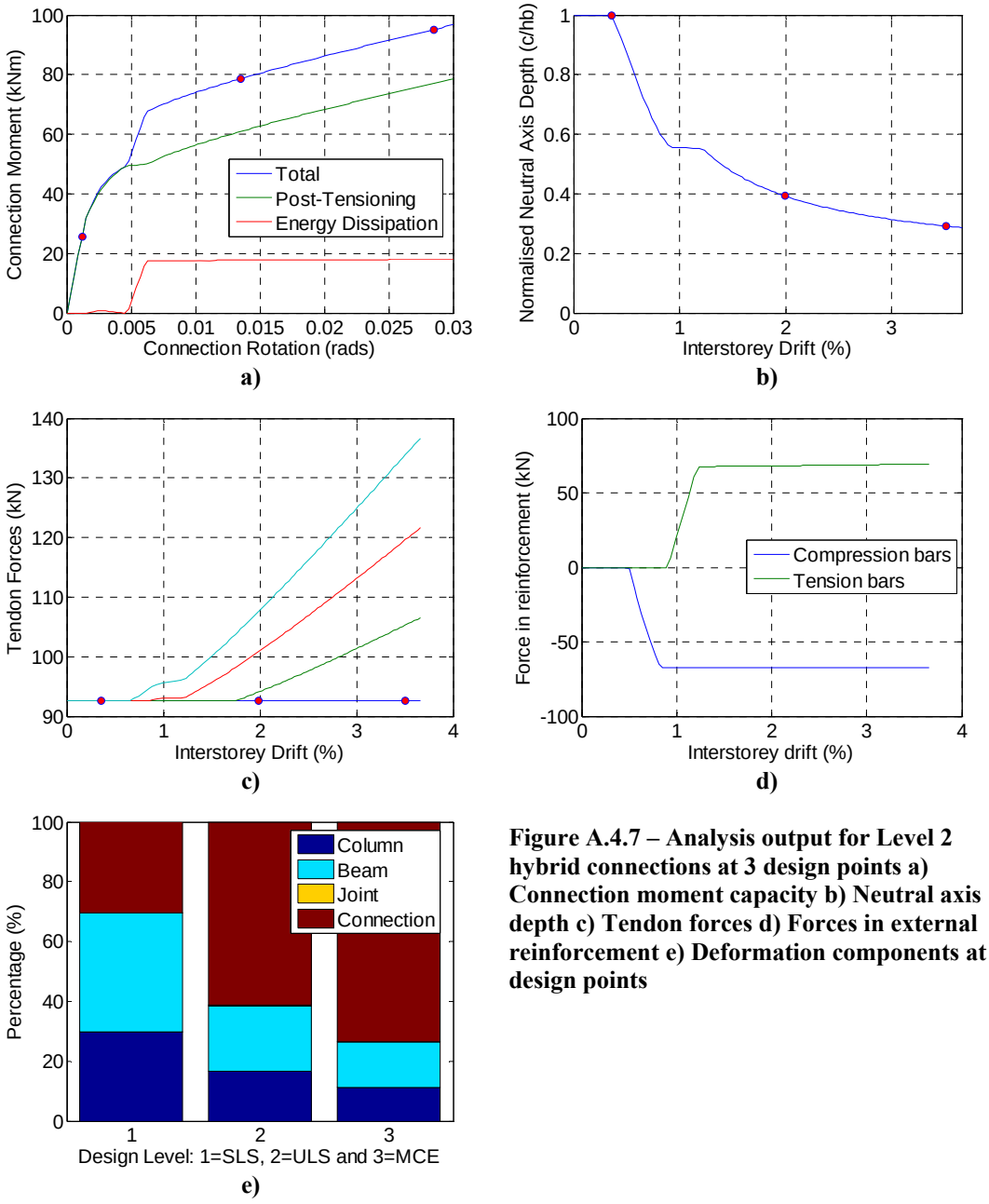

Figure A.4.7 – Analysis output for Level 2 hybrid connections at 3 design points a) Connection moment capacity b) Neutral axis depth c) Tendon forces d) Forces in external reinforcement e) Deformation components at 3 design points

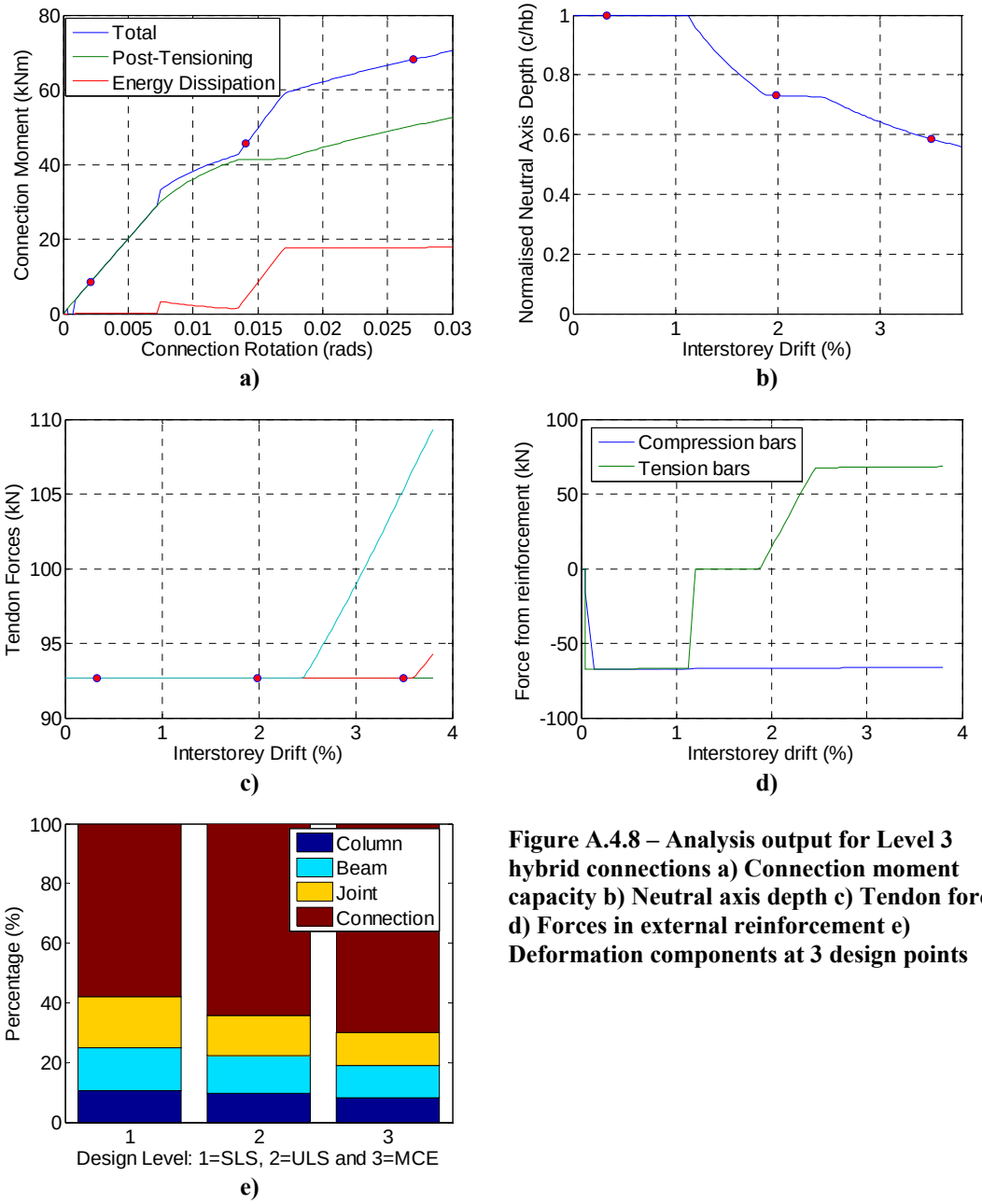

Figure A.4.8 – Analysis output for Level 3 hybrid connections a) Connection moment capacity b) Neutral axis depth c) Tendon forces d) Forces in external reinforcement e) Deformation components at 3 design points

A.4.3. Post-tensioned wall

The wall capacity is predicted using MATLAB, following a similar approach to that of the frame design (see the previous section). The resultant connection capacity is illustrated in Figure A.4.9. Some of the MATLAB output is shown in Figure A.4.10.

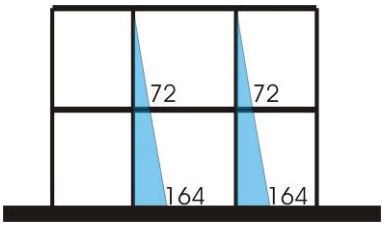

Figure A.4.9 – Post-tensioned wall bending moment diagram at 2% drift

Both walls provide an overturning moment (OTM) of 328kN.m. This equates to a total base shear (or ram force) of 105kN (53kN per wall).

The hysteretic area-based damping for this system is zero, according to this analysis.

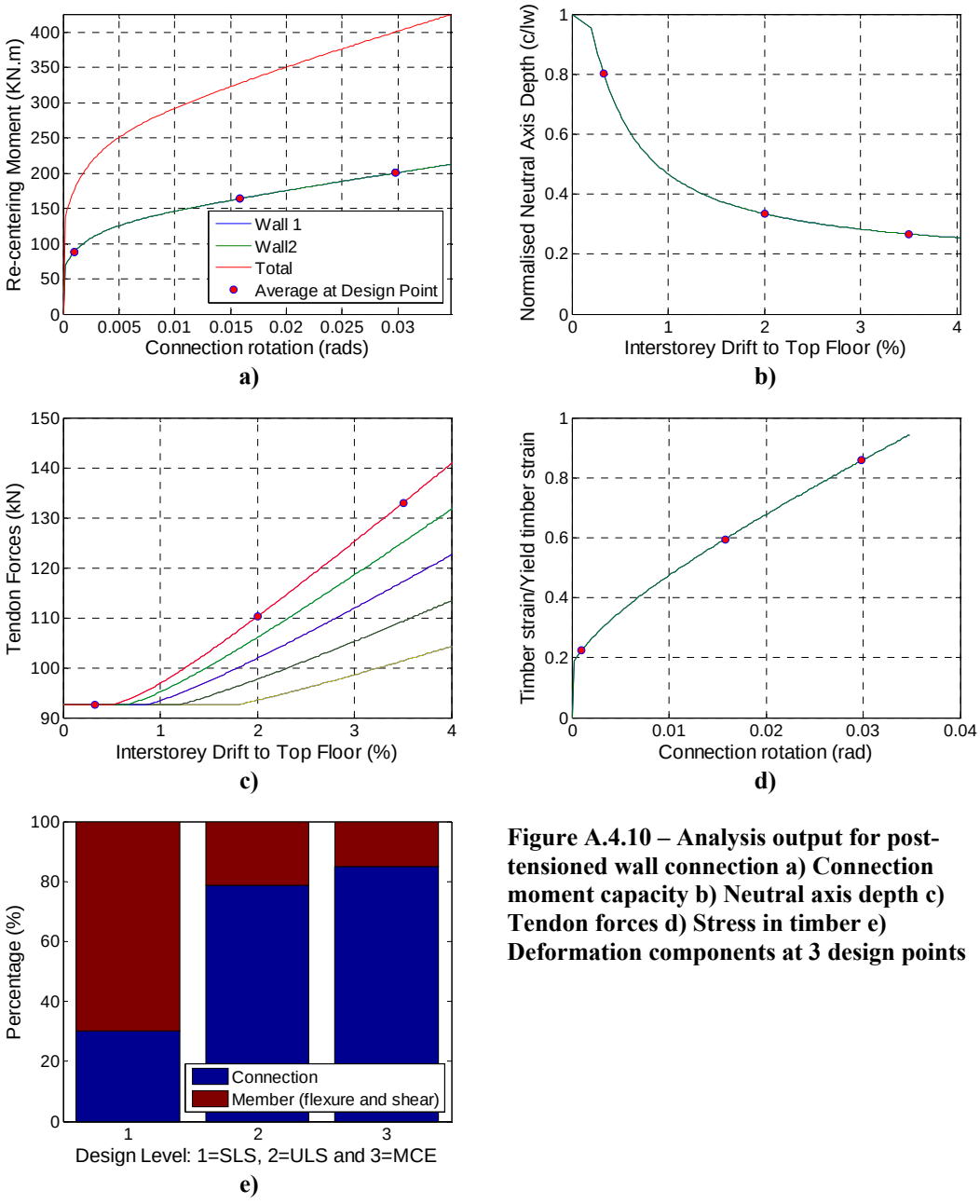

Figure A.4.10 – Analysis output for post-tensioned wall connection a) Connection moment capacity b) Neutral axis depth c) Tendon forces d) Stress in timber e) Deformation components at 3 design points

A.4.4. Hybrid post-tensioned wall

For the hybrid wall, UFP coupling devices positioned between the walls generate additional axial tension and compression forces in the respective walls (Kelly et al. 1972). This increases the capacity of the wall system and results in additional shear forces in the walls and increased elastic deformation. Design and modeling procedures for the coupled wall systems are provided in Chapter 7. The resultant connection capacity and coupling forces are illustrated in Figure A.4.11. Some of the MATLAB output is shown in Figure A.4.12.

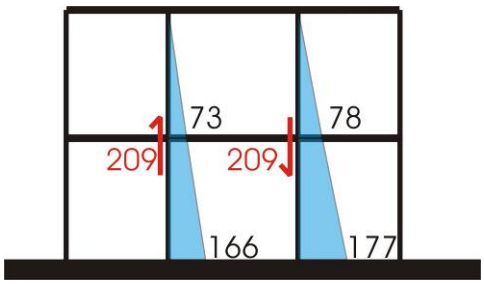

Figure A.4.11 – Hybrid post-tensioned wall bending moment diagram and UFP shears at 2% drift

Both walls provide an overturning moment (OTM) of 503kN.m (177kN.m from Wall 1, 166kN.m from Wall 2 and 160kN.m from the coupling action provided by the UFPs). This equates to a total base shear (or ram force) of 161kN (53kN per wall).

The UFP provide hysteretic energy dissipation potential to the wall system. The connections achieve a ductility of approximately 8, with a bi-linear factor of 0.01, giving an area-based damping of approximately 52%. Hence, the system area-based damping is approximately:

$$\xi_{hyst,ab} = \frac{52 \times 160}{503} = 17\%$$

The re-centering ratio, λ, (as defined in Chapter 2) for coupled walls at 2% drift is:

$$\lambda = \frac{M_{pt} + M_N}{M_s} \geq \alpha_0$$

Where: $M_{pt} + M_N = 177 + 166 = 343kNm$;
$M_s = 160kNm$.

Hence:

$$\therefore \lambda = \frac{343}{160} = 2.1$$

The re-centering ratio is greater than minimum value, α_0, suggested by current precast concrete design (NZCS 2010) of 1.5.

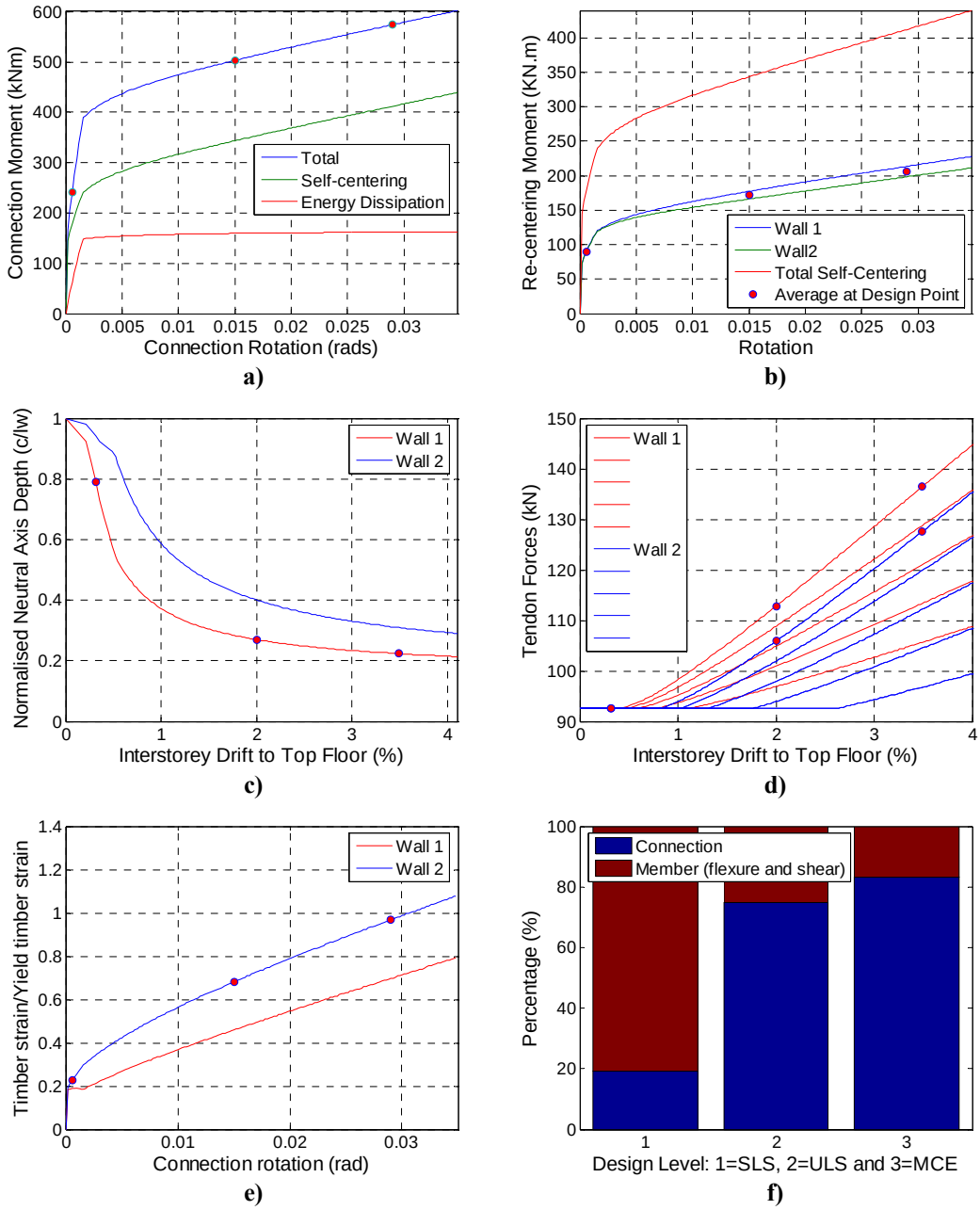

Figure A.4.12 – Analysis output for hybrid post-tensioned wall connection a) Connection moment capacity b) Moment demand in each wall c) Neutral axis depth c) Tendon forces d) Stress in timber e) Deformation components at 3 design points

A.5. EXTERNAL REINFORCEMENT TESTS

A.5.1. Introduction

Material tests were performed on the column-base external reinforcement (energy dissipaters) depicted in Figure A.5.1. Similar steel and detailing was used for the beam-column external reinforcement; therefore, material tests were only performed on the column-base reinforcement. Twenty seven devices were fabricated; twenty-four were used for the building and three were tested under cyclic loading to ensure they perform satisfactorily.

Each mild steel energy dissipater had a 24mm thread and was machined down to 16mm over a central fuse length. The dissipater was incased by a 32mm diameter pipe and filled with epoxy resin to prevent buckling in compression.

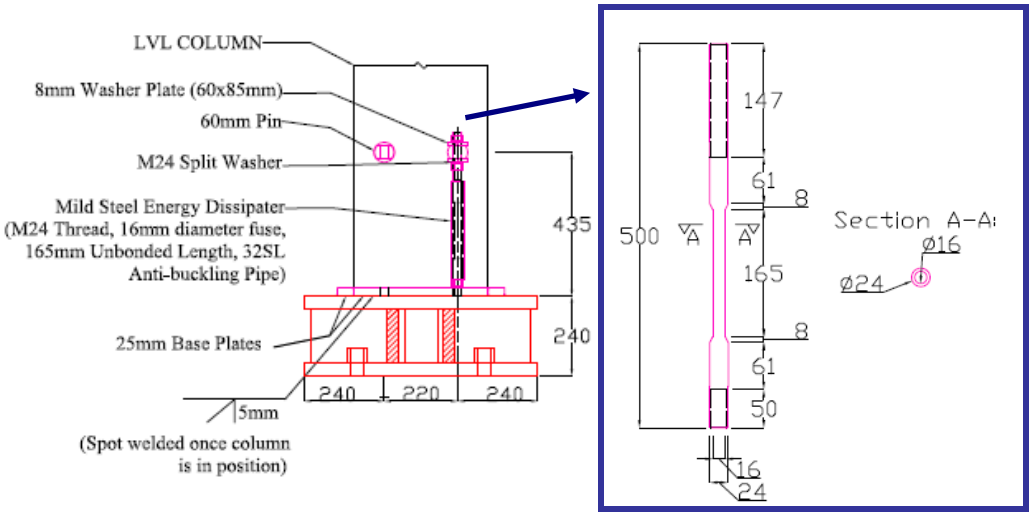

Figure A.5.1 – Column-base external reinforcement

A.5.2. Test setup

The test setup was designed to simulate the actual building anchorage details as close as possible (see Figure A.5.1). Two pots were attached to fixing nuts at the top and bottom

of the dissipaters. Two strain gauges were attached at the center of the fuse length on opposite sides. One strain gauge was placed at the base of dissipater, in the section of rod that was 24mm in diameter (without any thread).

Figure A.5.2 – Column-base external reinforcement test setup

A.5.3. Loading protocol

The loading protocol was based on ACI T1.1 (2001). Three cycles were performed at different displacement amplitudes. The displacement amplitude was increased by 1.5 times the previous amplitude (see Figure A.5.3).

Only elongations (or positive displacements) were considered. From section analysis of the column-base connection (Newcombe et al. 2008), as shown in the previous section, it was determined the dissipaters will not be subject to significant negative or compressive displacements. At small displacements, the neutral axis is larger than the depth of the dissipation devices but the negative displacement demand will be negligible.

A.5.4. Measured properties

The diameter of the fuse length was measured in three locations to gain an accurate estimate of the stress in the steel. The length between fixing nuts on the top and bottom of the dissipater is also recorded.

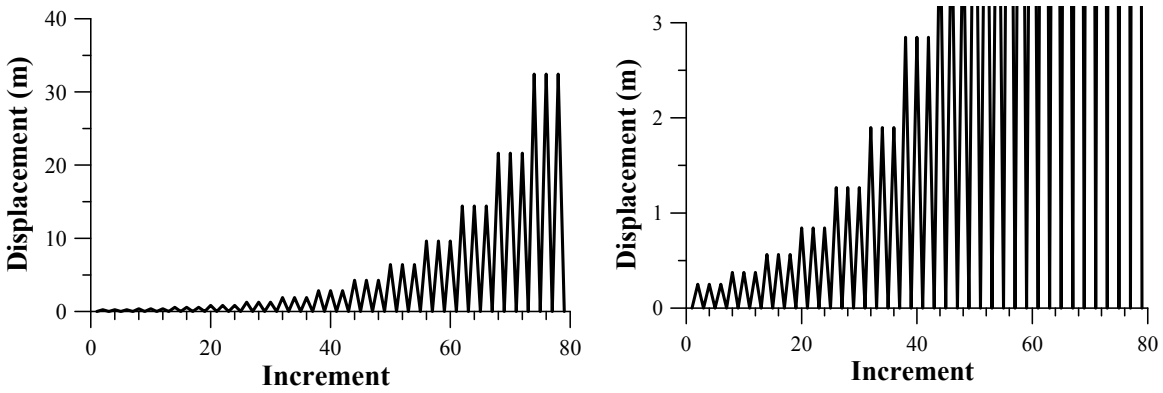

Figure A.5.3 – Loading protocol a) Large cycles b) Small cycles

Table A.5.1 – Fuse diameter measurements

Test #	Diameter Measurement (mm)				Average (mm)	Area (mm^2)
	1	2	3	4		
1	16.04	16.04	15.96	16.06	**16.03**	**201.82**
2	16.04	16.03	16.03	16.05	**16.04**	**202.07**
3	16.00	16.01	16.03	16.02	**16.02**	**201.56**

Table A.5.2 – Gauge length between pots

Test #	Overall gauge length (mm)
T1	**362**
T2	**361**
T3	**362**

A.5.5. Summary of test results

For all tests, the stable hysteretic loops were achieved until above 5% strain, no compression buckling occurred and yielding was localized to the fuse length. The yield strength of the steel was approximately 420MPa on average. Some specific conclusions are given below with reference to Figure A.5.4.

For Test 1:

- The strain gauges stopped recording at a maximum displacement of approximately 10mm.
- A 14mm stable displacement was achieved.
- Therefore, stable loops were achieved at approximately 5% strain. No buckling of the dissipaters occurred.

For Test 2:

- The strain gauges stopped recording at a maximum displacement of approximately 4.3mm.
- A 14mm stable displacement was achieved.
- Maximum stable strain is approximately 6%. No buckling of the dissipaters occurred.
- There were slightly lower stresses in compression. This indicates that there is some load sharing from the tube. This could be via friction between the tube, epoxy and bar.

For Test 3:

- The testing methodology was altered slightly. The potentiometer (which was attached to the nuts) and not the loading bridge followed the displacement protocol. In the previous tests, there was a small amount of elastic deformation in the test apparatus, which prevented the energy dissipaters from achieving

zero displacement after the first cycle. This may be slightly non-conservative as higher compressive strains may result in a tendency for the devices to buckle.

- The strain gauges stopped recording at a maximum displacement of approximately 7mm.
- A 14mm stable displacement was achieved.
- Hence, the maximum stable strain is approximately 7% with no buckling of the dissipaters.
- As in test 2, there were slightly lower stresses in compression

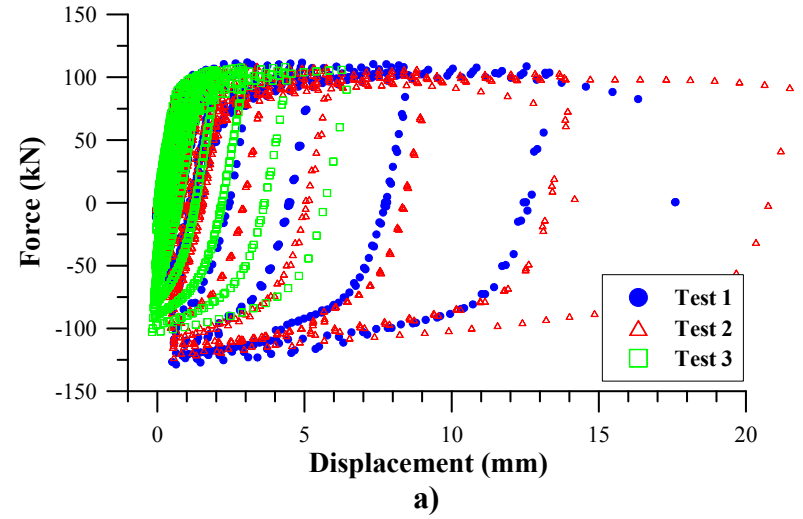

a)

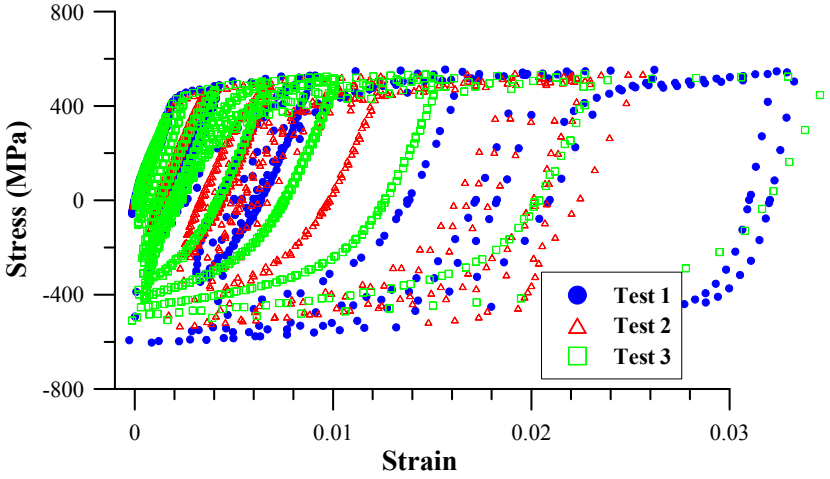

b)

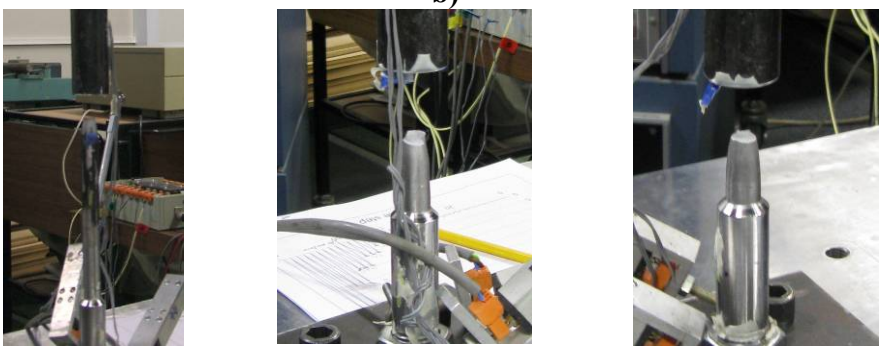

c) d) e)

Figure A.5.4 – Steel material test results a) Force-displacement response b) Stress-strain response c), d) & e) Failure mode of Test 1, 2 & 3 respectively

A.6. STRUCTURAL DRAWING OF TEST BUILDING

A.6.1. Timber components

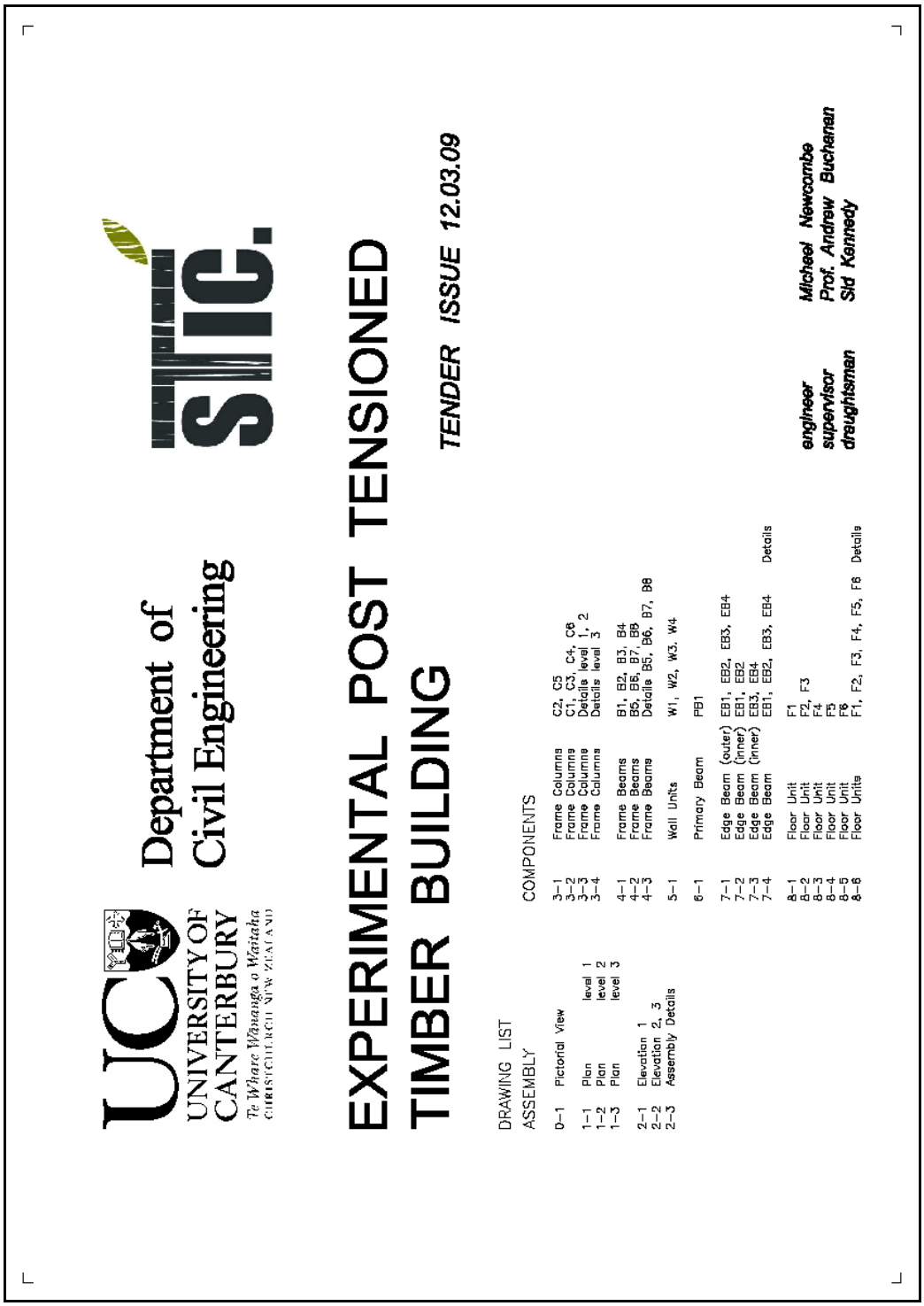

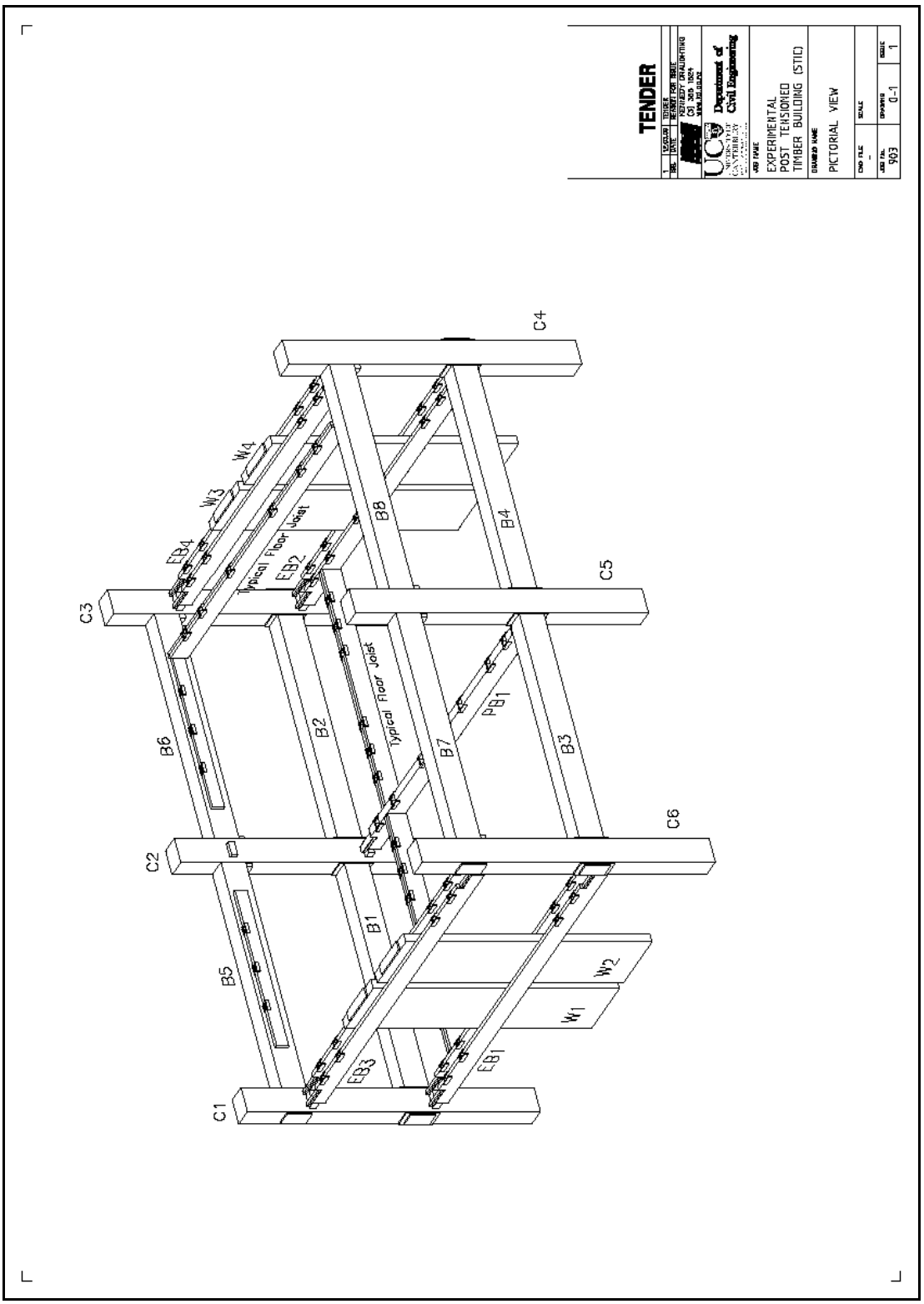
TENDER
Department of Civil Engineering
EXPERIMENTAL POST TENSIONED TIMBER BUILDING (STIC)
PICTORIAL VIEW
903
0-1
C1
C2
C3
C4
C5
C6
B1
B2
B3
B4
B5
B6
B7
B8
PB1
EB1
EB2
EB3
EB4
W1
W2
W3
W4
Typical Floor Joist
Typical Floor Joist

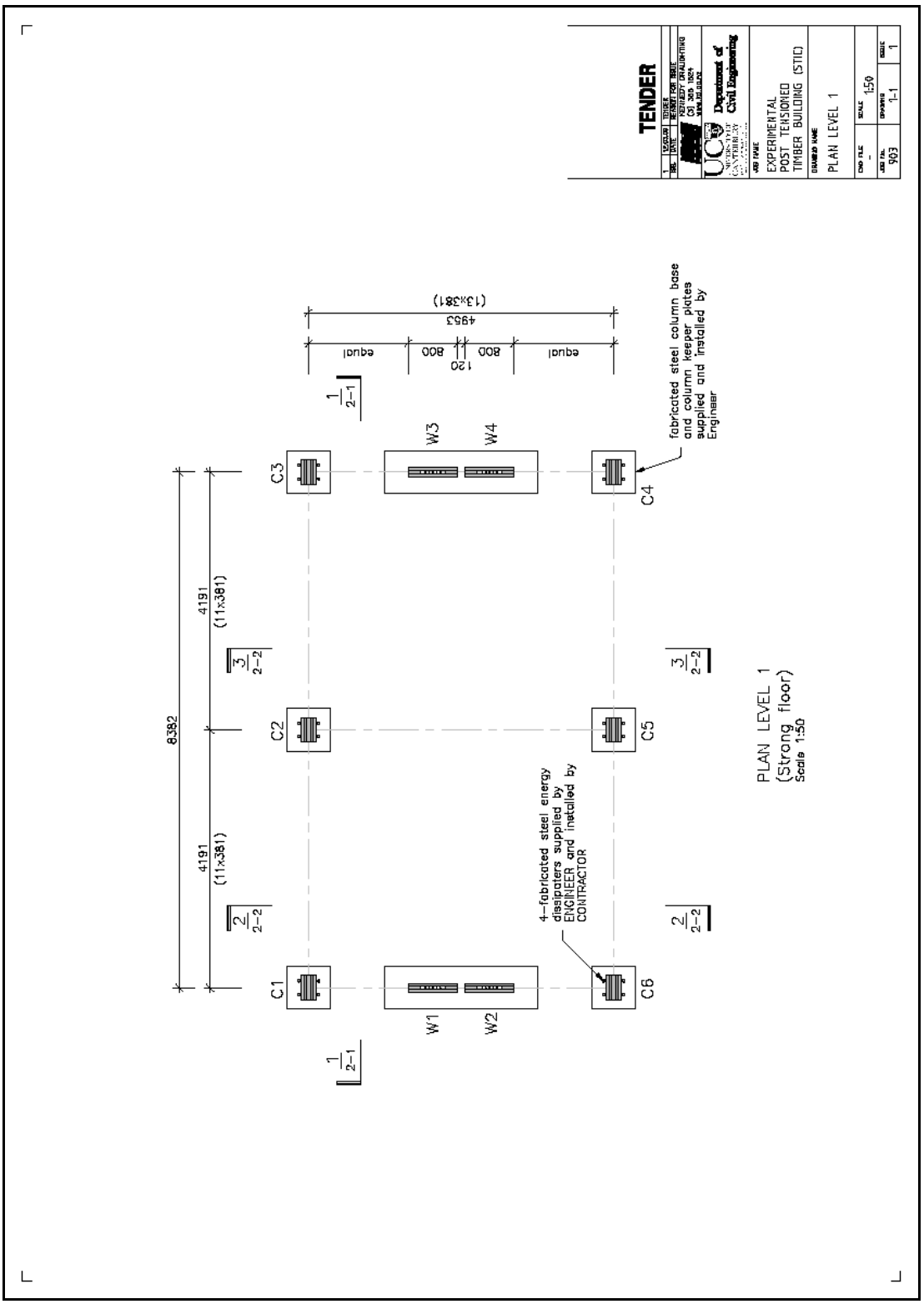
TENDER
Department of Civil Engineering
EXPERIMENTAL
POST TENSIONED
TIMBER BUILDING (STIC)
PLAN LEVEL 1
1:50
903
1-1
(13x381)
4953
equal
800
120
800
equal
fabricated steel column base and column keeper plates supplied and installed by Engineer
C1
C2
C3
C4
C5
C6
W1
W2
W3
W4
8382
4191
(11x381)
4191
(11x381)
4-fabricated steel energy dissipaters supplied by ENGINEER and installed by CONTRACTOR
PLAN LEVEL 1
(Strong floor)
Scale 1:50

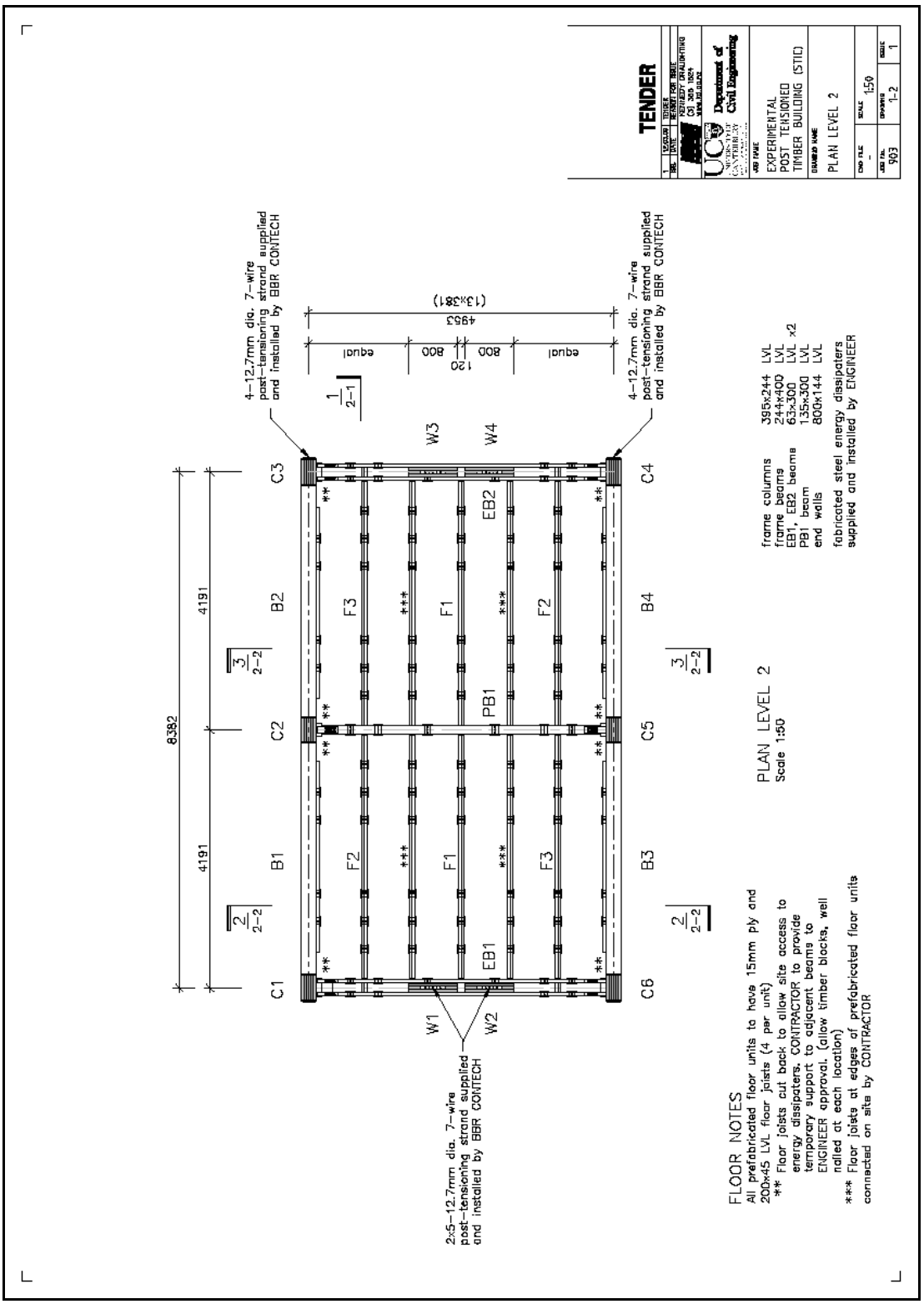
TENDER
Department of Civil Engineering
EXPERIMENTAL POST TENSIONED TIMBER BUILDING (STIC)
PLAN LEVEL 2
1:50
903
1-2
PLAN LEVEL 2
Scale 1:50
8382
4191
4191
(13x381)
4953
equal
800
120
800
equal
4–12.7mm dia. 7–wire post–tensioning strand supplied and installed by BBR CONTECH
2×5–12.7mm dia. 7–wire post–tensioning strand supplied and installed by BBR CONTECH
C1
C2
C3
C4
C5
C6
B1
B2
B3
B4
W1
W2
W3
W4
EB1
EB2
PB1
F1
F2
F3
frame columns 395x244 LVL
frame beams 244x400 LVL
EB1, EB2 beams 63x300 LVL x2
PB1 beam 135x300 LVL
end walls 800x144 LVL
fabricated steel energy dissipaters supplied and installed by ENGINEER
FLOOR NOTES
All prefabricated floor units to have 15mm ply and 200x45 LVL floor joists (4 per unit)
** Floor joists cut back to allow site access to energy dissipaters. CONTRACTOR to provide temporary support to adjacent beams to ENGINEER approval. (allow timber blocks, well nailed at each location)
*** Floor joists at edges of prefabricated floor units connected on site by CONTRACTOR

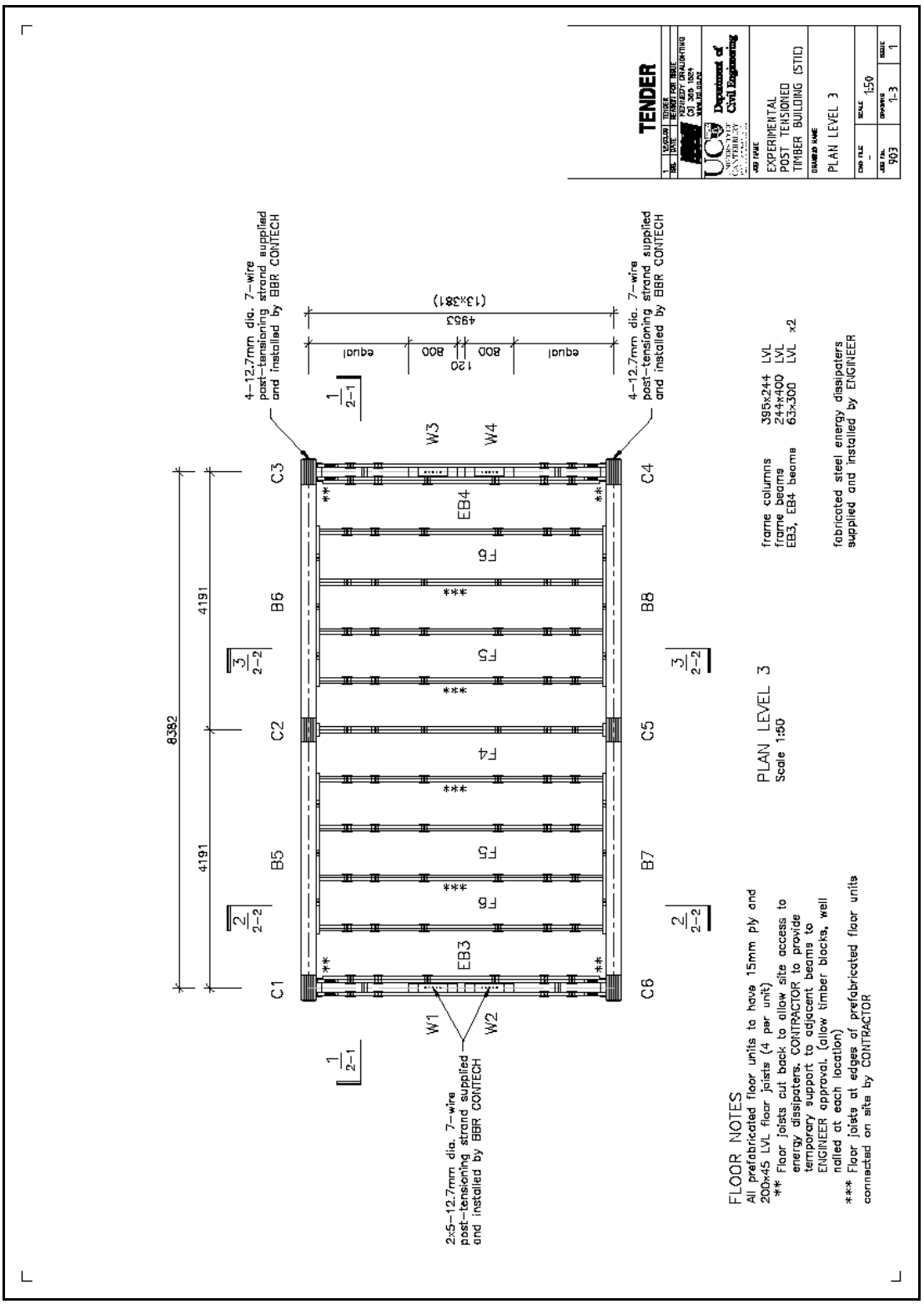
TENDER
Department of Civil Engineering
EXPERIMENTAL POST TENSIONED TIMBER BUILDING (STIC)
PLAN LEVEL 3
SCALE 1:50
903
PLAN LEVEL 3
Scale 1:50
frame columns 395x244 LVL
frame beams 244x400 LVL
EB3, EB4 beams 63x300 LVL x2
fabricated steel energy dissipaters supplied and installed by ENGINEER
4–12.7mm dia. 7–wire post–tensioning strand supplied and installed by BBR CONTECH
2x5–12.7mm dia. 7–wire post–tensioning strand supplied and installed by BBR CONTECH
8382
4191
4191
4953
(13x381)
equal
800
120
800
equal
C1
C2
C3
B5
B6
B7
B8
C4
C5
C6
EB3
EB4
W1
W2
W3
W4
T5
T4
FLOOR NOTES
All prefabricated floor units to have 15mm ply and 200x45 LVL floor joists (4 per unit)
** Floor joists cut back to allow site access to energy dissipaters. CONTRACTOR to provide temporary support to adjacent beams to ENGINEER approval. (allow timber blocks, well nailed at each location)
*** Floor joists at edges of prefabricated floor units connected on site by CONTRACTOR

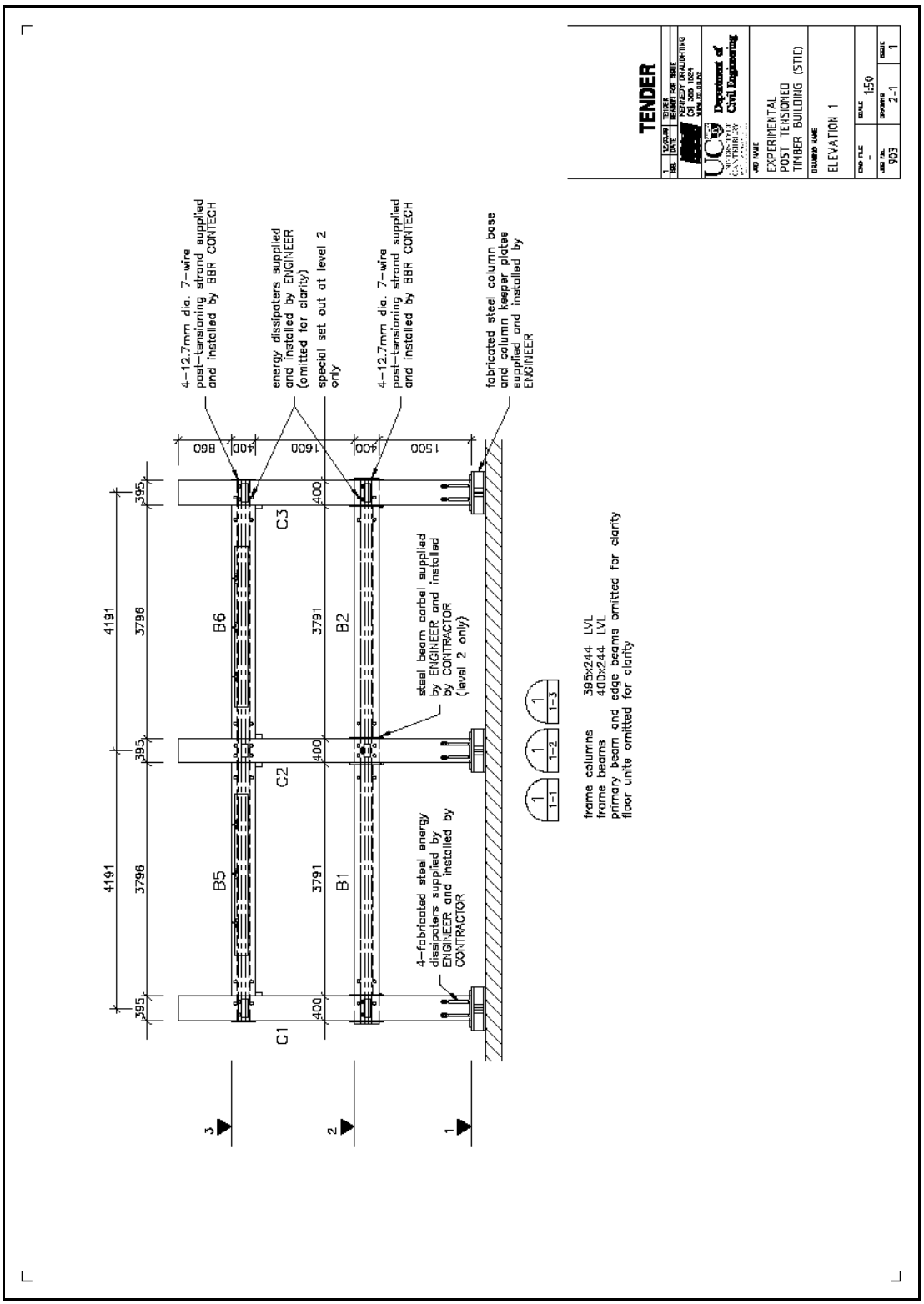
TENDER
Department of Civil Engineering
EXPERIMENTAL
POST TENSIONED
TIMBER BUILDING (STIC)
ELEVATION 1
4–12.7mm dia. 7–wire post–tensioning strand supplied and installed by BBR CONTECH
energy dissipaters supplied and installed by ENGINEER (omitted for clarity)
special set out at level 2 only
4–12.7mm dia. 7–wire post–tensioning strand supplied and installed by BBR CONTECH
fabricated steel column base and column keeper plates supplied and installed by ENGINEER
steel beam corbel supplied by ENGINEER and installed by CONTRACTOR (level 2 only)
4–fabricated steel energy dissipaters supplied by ENGINEER and installed by CONTRACTOR
B5
B6
B1
B2
C1
C2
C3
4191
3796
395
400
1600
1500
860
frame columns 395x244 LVL
frame beams 400x244 LVL
primary beam and edge beams omitted for clarity
floor units omitted for clarity

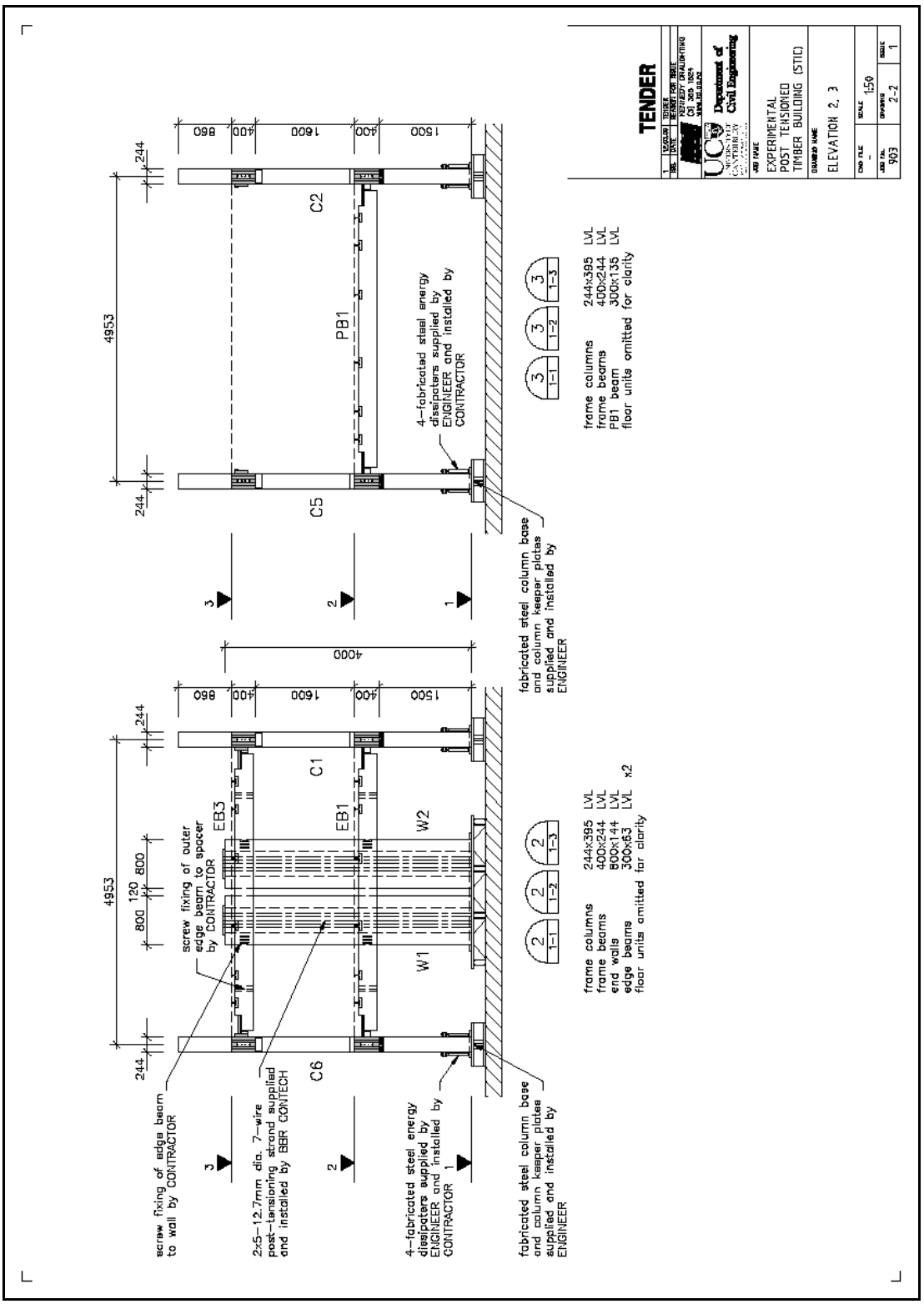
TENDER
Department of Civil Engineering
EXPERIMENTAL POST TENSIONED TIMBER BUILDING (STIC)
ELEVATION 2, 3
4953
4000
1500
1600
860
400
244
800
120
C1
C2
C5
C6
PB1
EB1
EB3
W1
W2
screw fixing of edge beam to wall by CONTRACTOR
screw fixing of outer edge beam to spacer by CONTRACTOR
2×5–12.7mm dia. 7–wire post–tensioning strand supplied and installed by BBR CONTECH
4–fabricated steel energy dissipaters supplied by ENGINEER and installed by CONTRACTOR
fabricated steel column base and column keeper plates supplied and installed by ENGINEER
frame columns 244×395 LVL
frame beams 400×244 LVL
end walls 800×144 LVL
edge beams 300×63 LVL x2
floor units omitted for clarity
PB1 beam 300×135 LVL

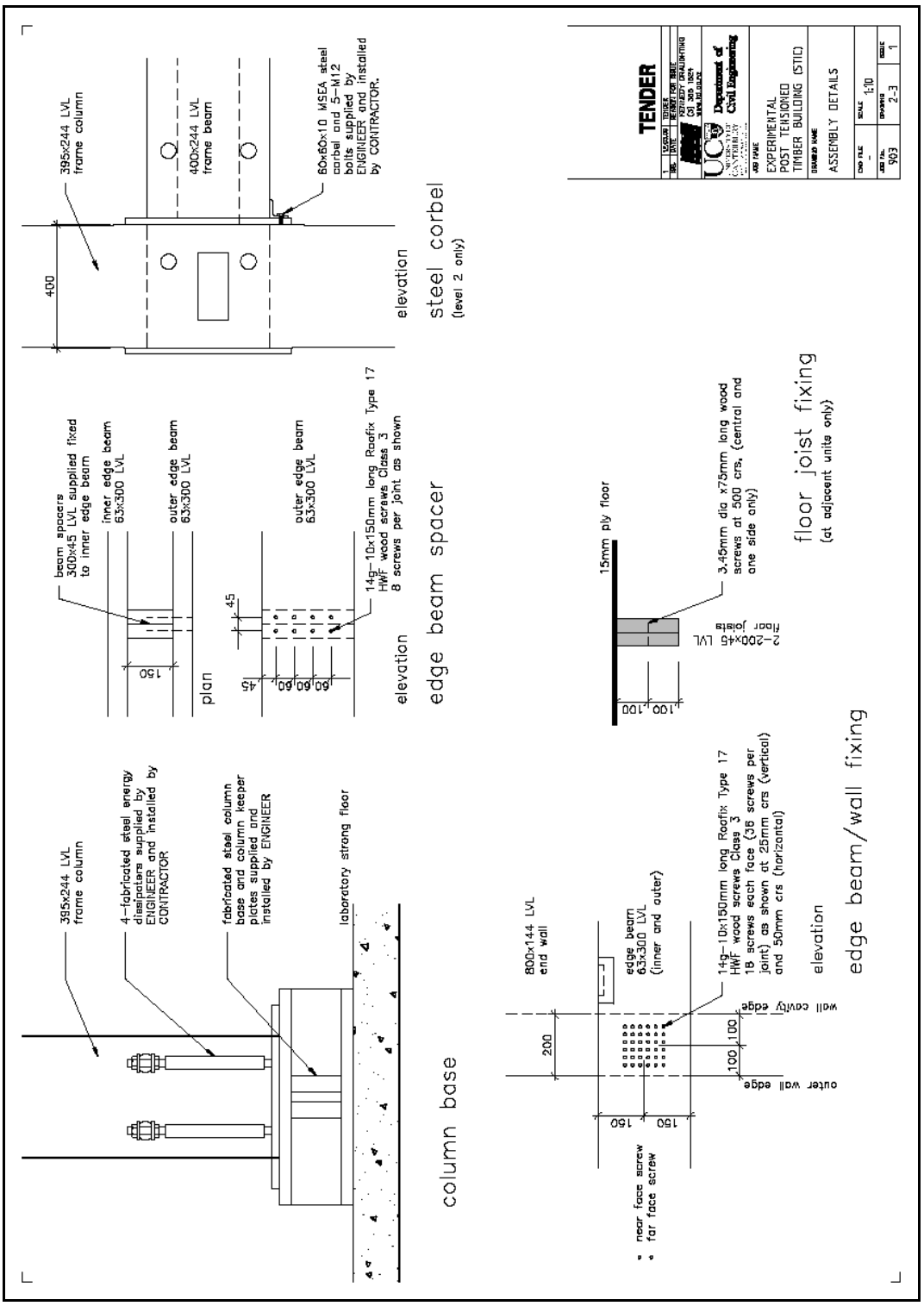
395x244 LVL frame column
4-fabricated steel energy dissipators supplied by ENGINEER and installed by CONTRACTOR
fabricated steel column base and column keeper plates supplied and installed by ENGINEER
laboratory strong floor
column base
beam spacers 300x45 LVL supplied fixed to inner edge beam
inner edge beam 63x300 LVL
outer edge beam 63x300 LVL
plan
14g-10x150mm long Roofix Type 17 HWF wood screws Class 3 8 screws per joint as shown
elevation
edge beam spacer
395x244 LVL frame column
400x244 LVL frame beam
60x60x10 MSEA steel corbel and 5-M12 bolts supplied by ENGINEER and installed by CONTRACTOR.
elevation
steel corbel
(level 2 only)
800x144 LVL end wall
edge beam 63x300 LVL (inner and outer)
14g-10x150mm long Roofix Type 17 HWF wood screws Class 3 19 screws each face (36 screws per joint) as shown at 25mm crs (vertical) and 50mm crs (horizontal)
wall cavity edge
outer wall edge
near face screw
far face screw
elevation
edge beam/wall fixing
15mm ply floor
3.45mm dia x75mm long wood screws at 500 crs. (central and one side only)
2-200x45 LVL floor joists
floor joist fixing
(at adjacent units only)
TENDER
Department of Civil Engineering
EXPERIMENTAL POST TENSIONED TIMBER BUILDING (STID)
ASSEMBLY DETAILS
1:10
903
2-3
1

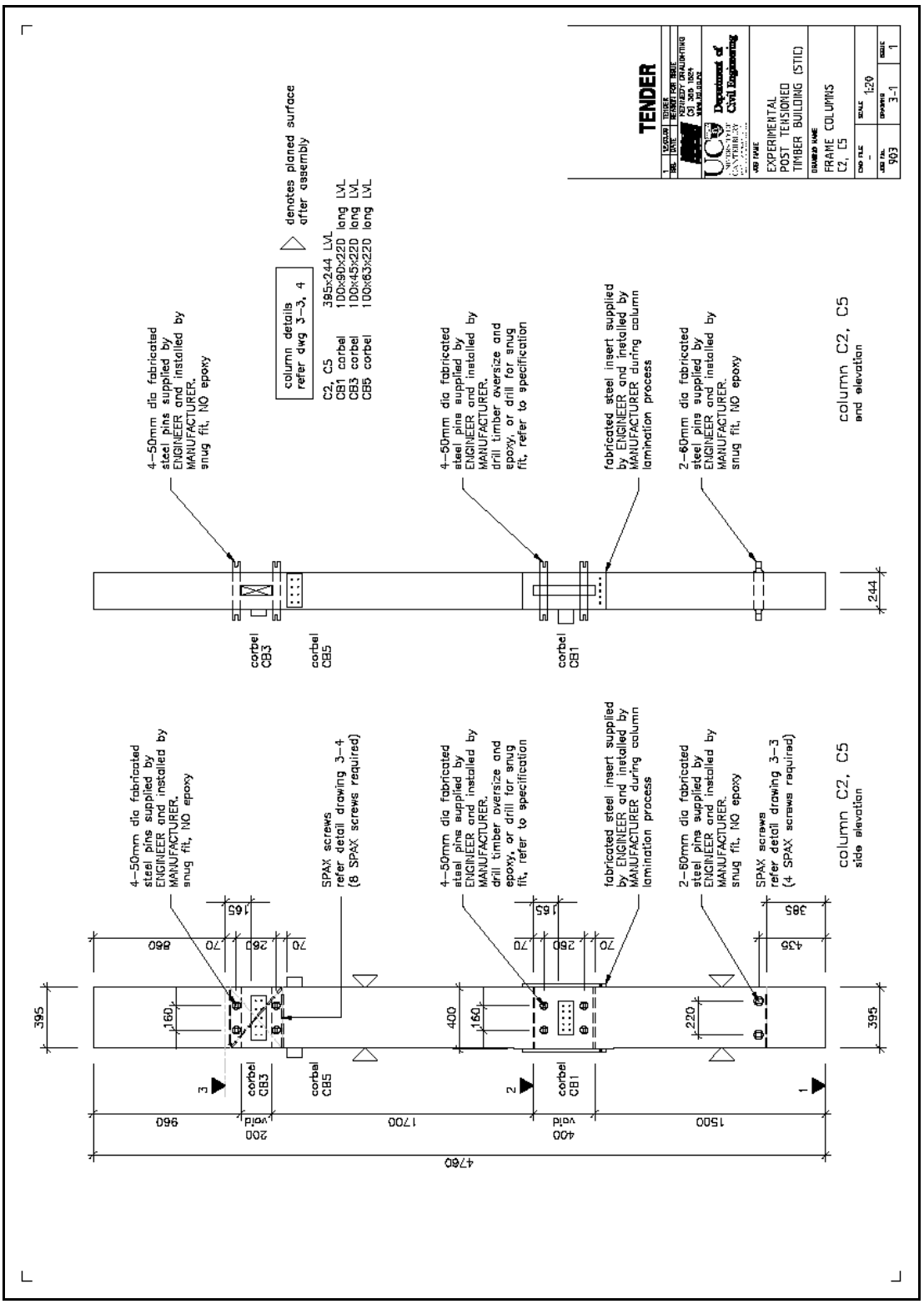
TENDER
Department of Civil Engineering
EXPERIMENTAL POST TENSIONED TIMBER BUILDING (STIC)
FRAME COLUMNS C2, C5
903
3-1
1:20
column details refer dwg 3-3, 4
denotes planed surface after assembly
C2, C5 395x244 LVL
CB1 corbel 100x90x22D long LVL
CB3 corbel 100x45x22D long LVL
CB5 corbel 100x63x22D long LVL
4-50mm dia fabricated steel pins supplied by ENGINEER and installed by MANUFACTURER. snug fit, NO epoxy
4-50mm dia fabricated steel pins supplied by ENGINEER and installed by MANUFACTURER. drill timber oversize and epoxy, or drill for snug fit, refer to specification
fabricated steel insert supplied by ENGINEER and installed by MANUFACTURER during column lamination process
2-60mm dia fabricated steel pins supplied by ENGINEER and installed by MANUFACTURER. snug fit, NO epoxy
column C2, C5 end elevation
SPAX screws refer detail drawing 3-4 (8 SPAX screws required)
SPAX screws refer detail drawing 3-3 (4 SPAX screws required)
column C2, C5 side elevation
corbel CB3
corbel CB5
corbel CB1
244
395
160
400
220
165
155
385
435
860
280
70
960
200 void
1700
400 void
1500
4760

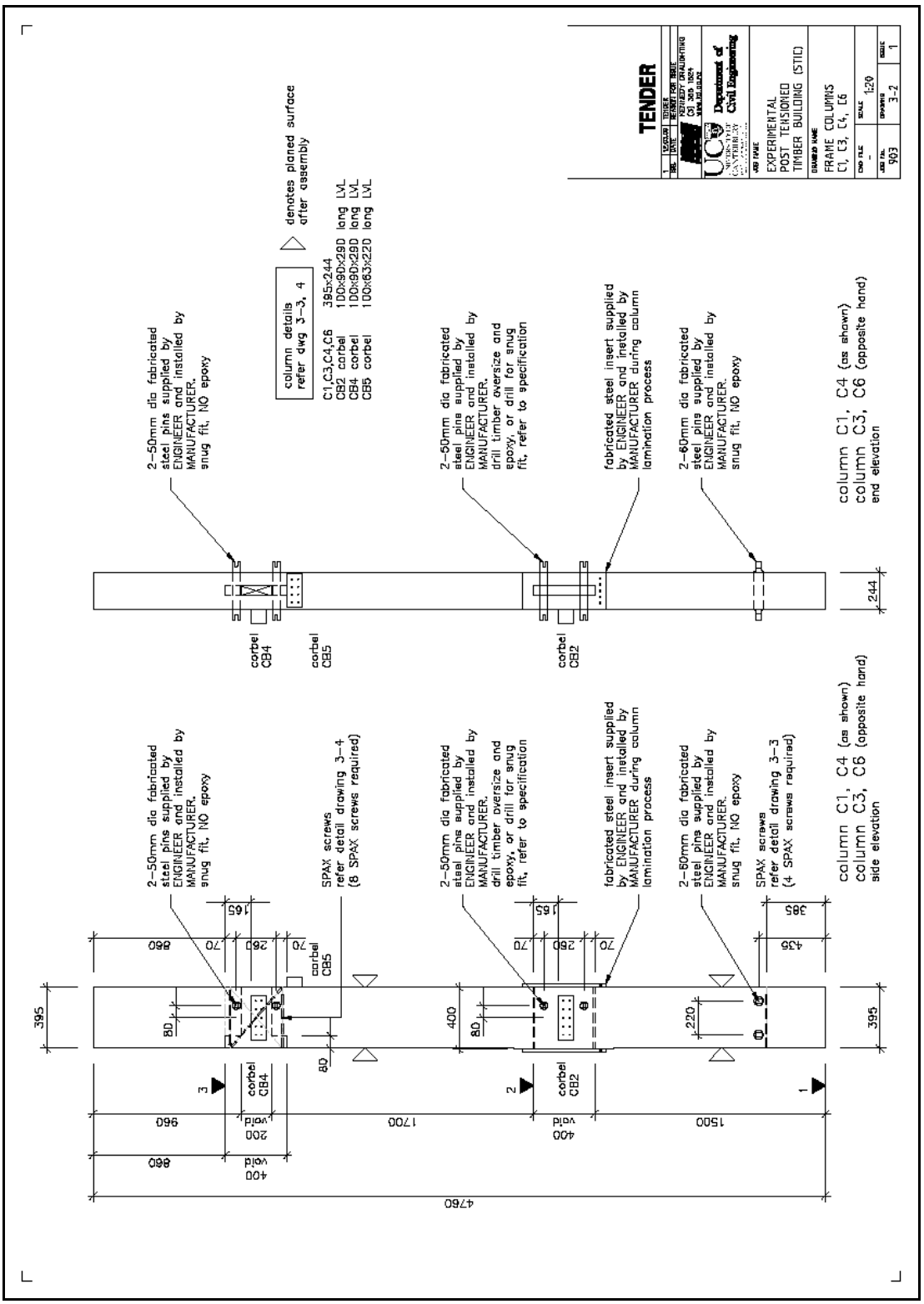
TENDER
Department of Civil Engineering
EXPERIMENTAL POST TENSIONED TIMBER BUILDING (STIC)
FRAME COLUMNS C1, C3, C4, C6
1:20
903
3-2
denotes planed surface after assembly
column details refer dwg 3-3, 4
C1,C3,C4,C6 395x244
CB2 corbel 100x90x290 long LVL
CB4 corbel 100x90x290 long LVL
CB5 corbel 100x65x220 long LVL
2-50mm dia fabricated steel pins supplied by ENGINEER and installed by MANUFACTURER. snug fit, NO epoxy
2-50mm dia fabricated steel pins supplied by ENGINEER and installed by MANUFACTURER. drill timber oversize and epoxy, or drill for snug fit, refer to specification
fabricated steel insert supplied by ENGINEER and installed by MANUFACTURER during column lamination process
2-60mm dia fabricated steel pins supplied by ENGINEER and installed by MANUFACTURER. snug fit, NO epoxy
SPAX screws refer detail drawing 3-4 (8 SPAX screws required)
SPAX screws refer detail drawing 3-3 (4 SPAX screws required)
corbel CB4
corbel CB5
corbel CB2
column C1, C4 (as shown)
column C3, C6 (opposite hand)
end elevation
side elevation
395
80
400
220
165
70
260
860
385
435
960
200 void
400 void
1700
1500
4760
244

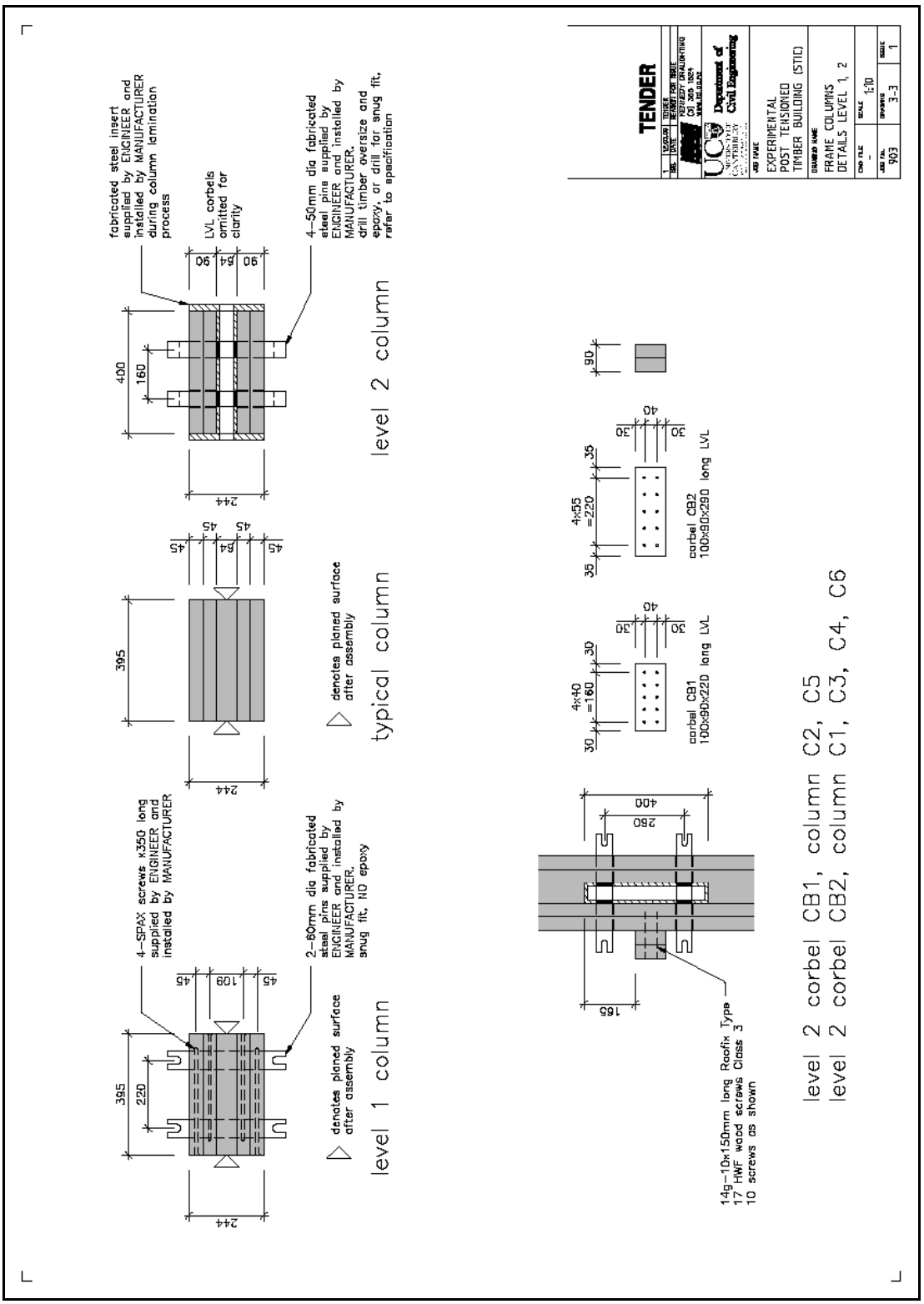
TENDER
Department of Civil Engineering
EXPERIMENTAL POST TENSIONED TIMBER BUILDING (STIC)
FRAME COLUMNS DETAILS LEVEL 1, 2
level 1 column
level 2 column
typical column
level 2 corbel CB1, column C2, C5
level 2 corbel CB2, column C1, C3, C4, C6
corbel CB1 180x90x220 long LVL
corbel CB2 180x90x290 long LVL
14g–10x150mm long Rooftx Type 17 HWF wood screws Class 3 10 screws as shown
4–SPAX screws x350 long supplied by ENGINEER and installed by MANUFACTURER
2–80mm dia fabricated steel pins supplied by ENGINEER and installed by MANUFACTURER. snug fit, NO epoxy
denotes planed surface after assembly
fabricated steel insert supplied by ENGINEER and installed by MANUFACTURER during column lamination process
LVL corbels omitted for clarity
4–50mm dia fabricated steel pins supplied by ENGINEER and installed by MANUFACTURER. drill timber oversize and epoxy, or drill for snug fit, refer to specification

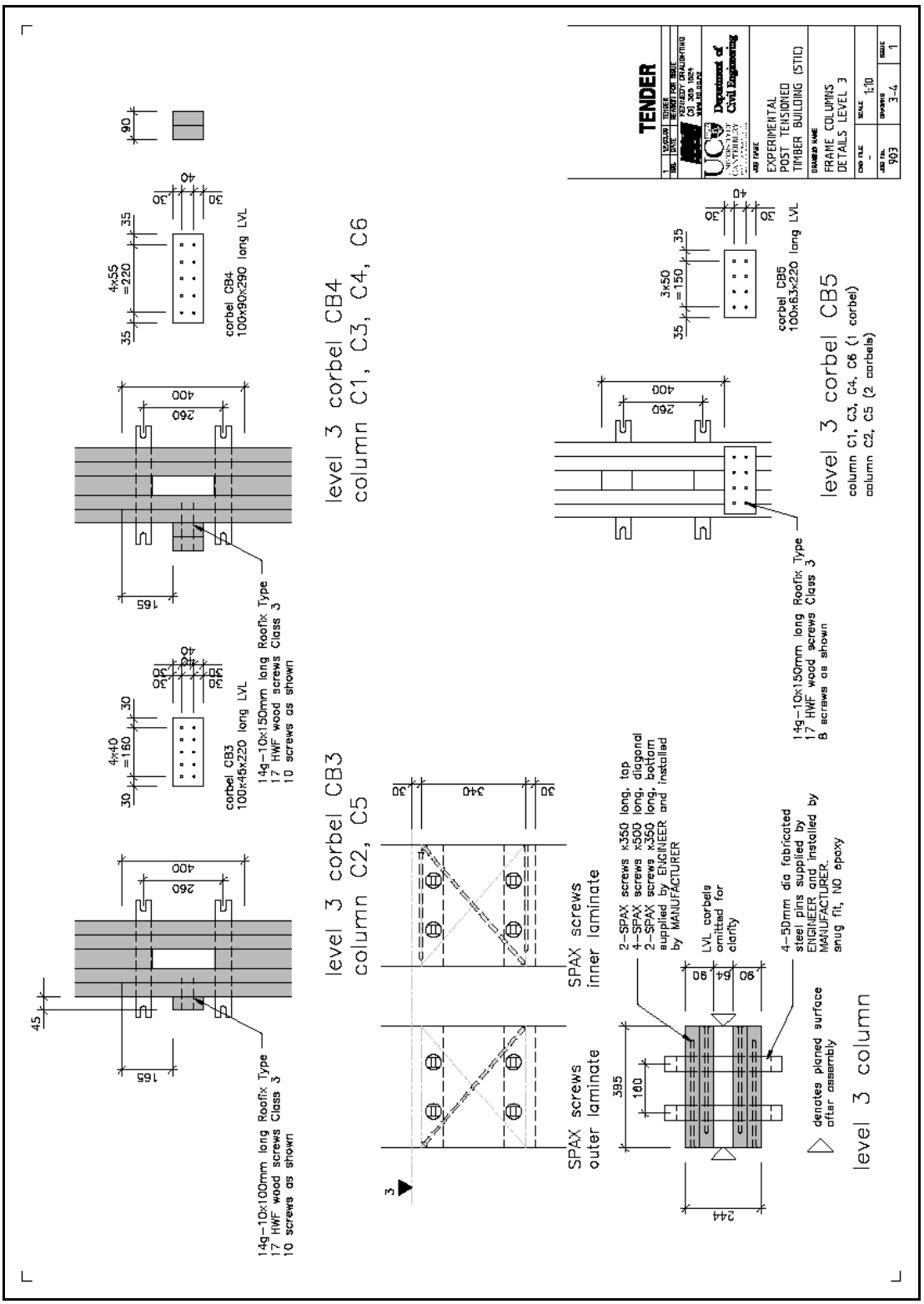
TENDER
Department of Civil Engineering
EXPERIMENTAL POST TENSIONED TIMBER BUILDING (STIC)
FRAME COLUMNS DETAILS LEVEL 3
level 3 corbel CB4
column C1, C3, C4, C6
level 3 corbel CB3
column C2, C5
level 3 corbel CB5
column C1, C3, C4, C6 (1 corbel)
column C2, C5 (2 corbels)
level 3 column
corbel CB4 100x90x290 long LVL
corbel CB3 100x45x220 long LVL
corbel CB5 100x63x220 long LVL
14g-10x150mm long Rooftx Type 17 HWF wood screws Class 3 10 screws as shown
14g-10x100mm long Rooftx Type 17 HWF wood screws Class 3 10 screws as shown
SPAX screws inner laminate
SPAX screws outer laminate
2-SPAX screws x350 long, tap 4-SPAX screws x500 long, diagonal 2-SPAX screws x350 long, bottom supplied by ENGINEER and installed by MANUFACTURER
LVL corbels omitted for clarity
4-50mm dia fabricated steel pins supplied by ENGINEER and installed by MANUFACTURER. snug fit, NO epoxy
denotes planed surface after assembly

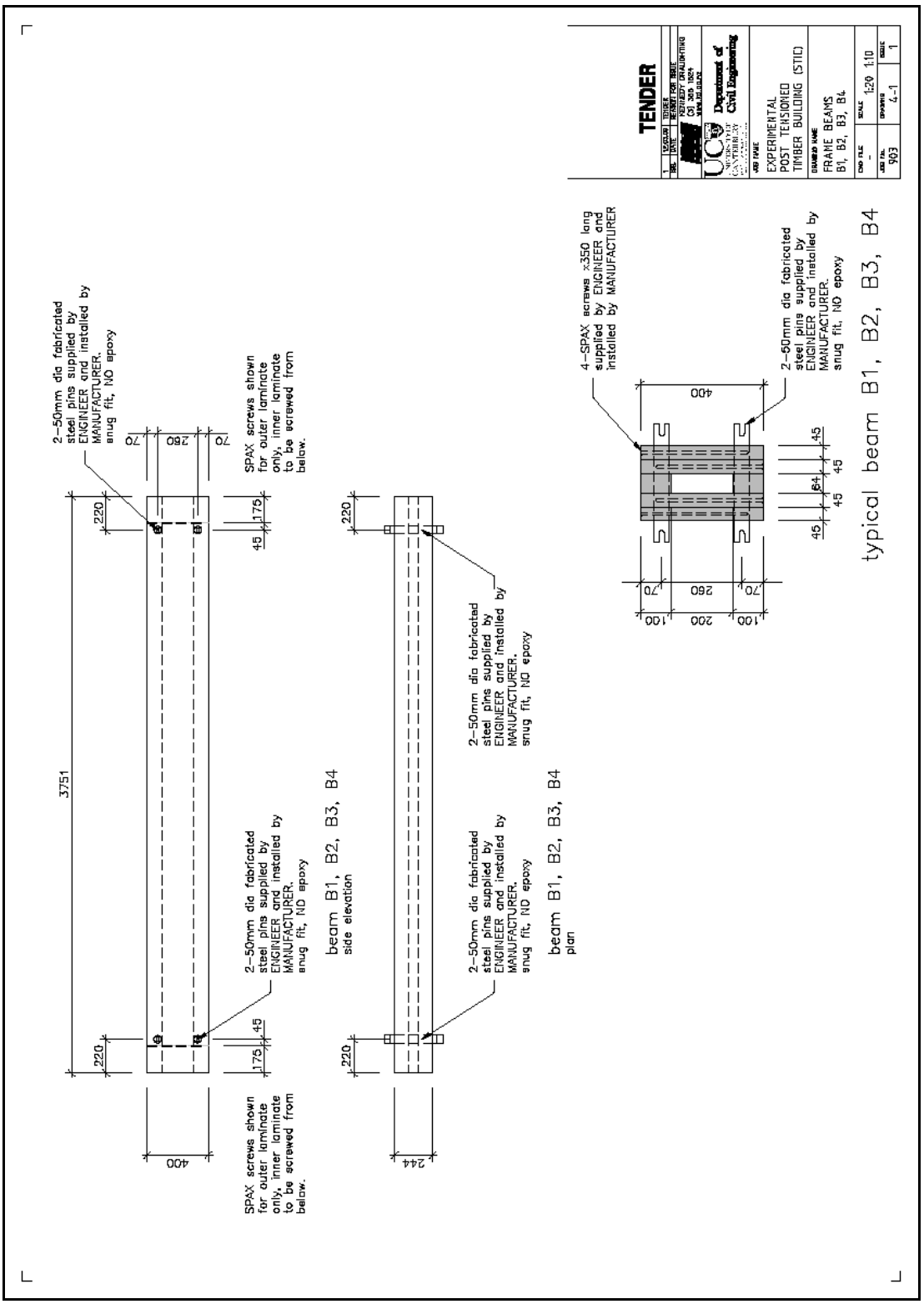
TENDER
Department of Civil Engineering
EXPERIMENTAL
POST TENSIONED
TIMBER BUILDING (STIC)
FRAME BEAMS
B1, B2, B3, B4
1:20 1:10
903
4-1
typical beam B1, B2, B3, B4
beam B1, B2, B3, B4
side elevation
beam B1, B2, B3, B4
plan
2-50mm dia fabricated steel pins supplied by ENGINEER and installed by MANUFACTURER. snug fit, NO epoxy
SPAX screws shown for outer laminate only, inner laminate to be screwed from below.
4-SPAX screws x350 long supplied by ENGINEER and installed by MANUFACTURER
3751
400
244
260
200
100
70
45
220
175

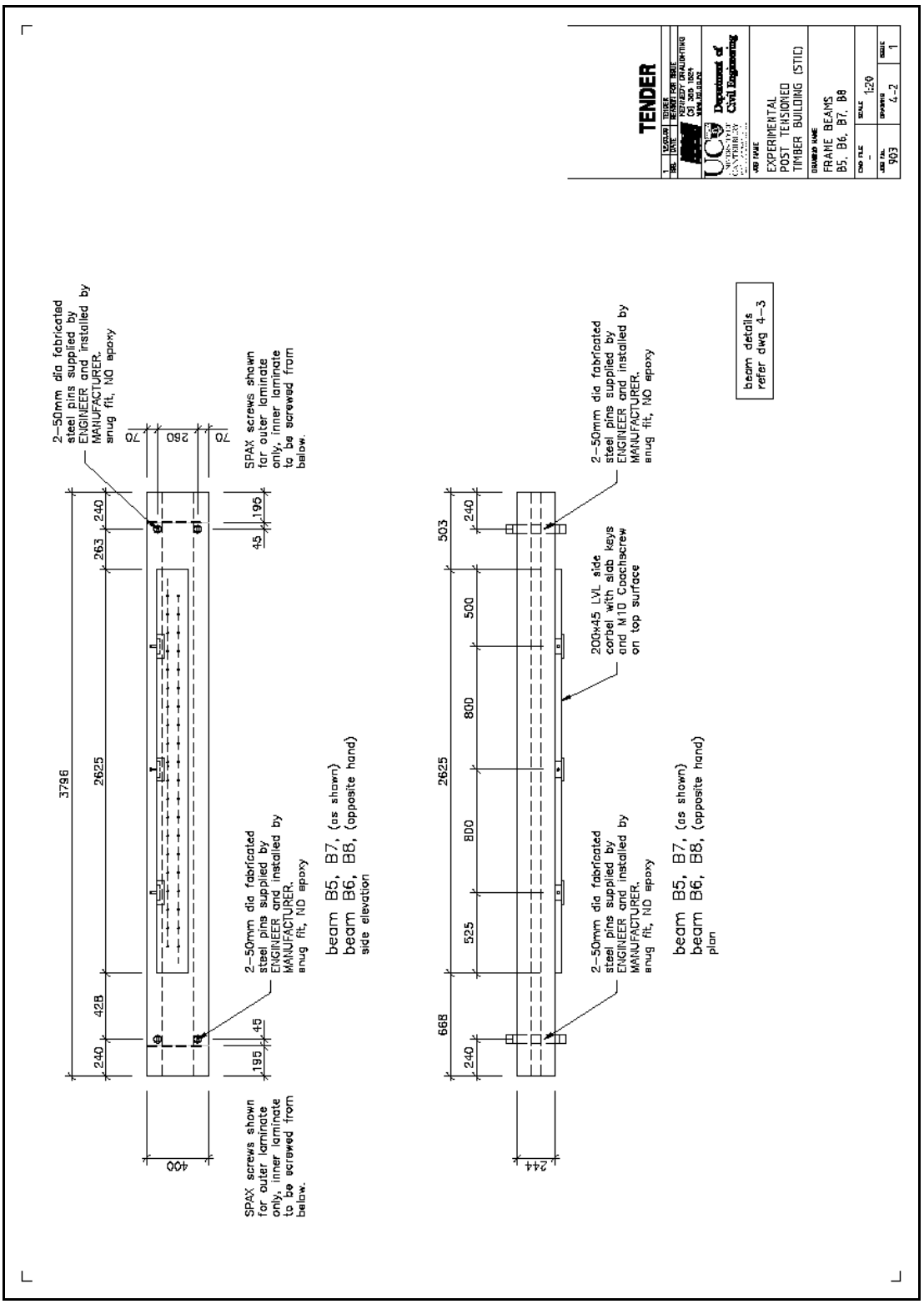
TENDER
Department of Civil Engineering
EXPERIMENTAL POST TENSIONED TIMBER BUILDING (STIC)
FRAME BEAMS B5, B6, B7, B8
1:20
4-2
903
2-50mm dia fabricated steel pins supplied by ENGINEER and installed by MANUFACTURER. snug fit, NO epoxy
SPAX screws shown for outer laminate only, inner laminate to be screwed from below.
2-50mm dia fabricated steel pins supplied by ENGINEER and installed by MANUFACTURER. snug fit, NO epoxy
beam B5, B7, (as shown)
beam B6, B8, (opposite hand)
side elevation
3796
2625
428
240
263
260
70
45
195
400
2-50mm dia fabricated steel pins supplied by ENGINEER and installed by MANUFACTURER. snug fit, NO epoxy
200x45 LVL side corbel with slab keys and M10 Coachscrew on top surface
beam details refer dwg 4-3
beam B5, B7, (as shown)
beam B6, B8, (opposite hand)
plan
503
500
800
525
668
244

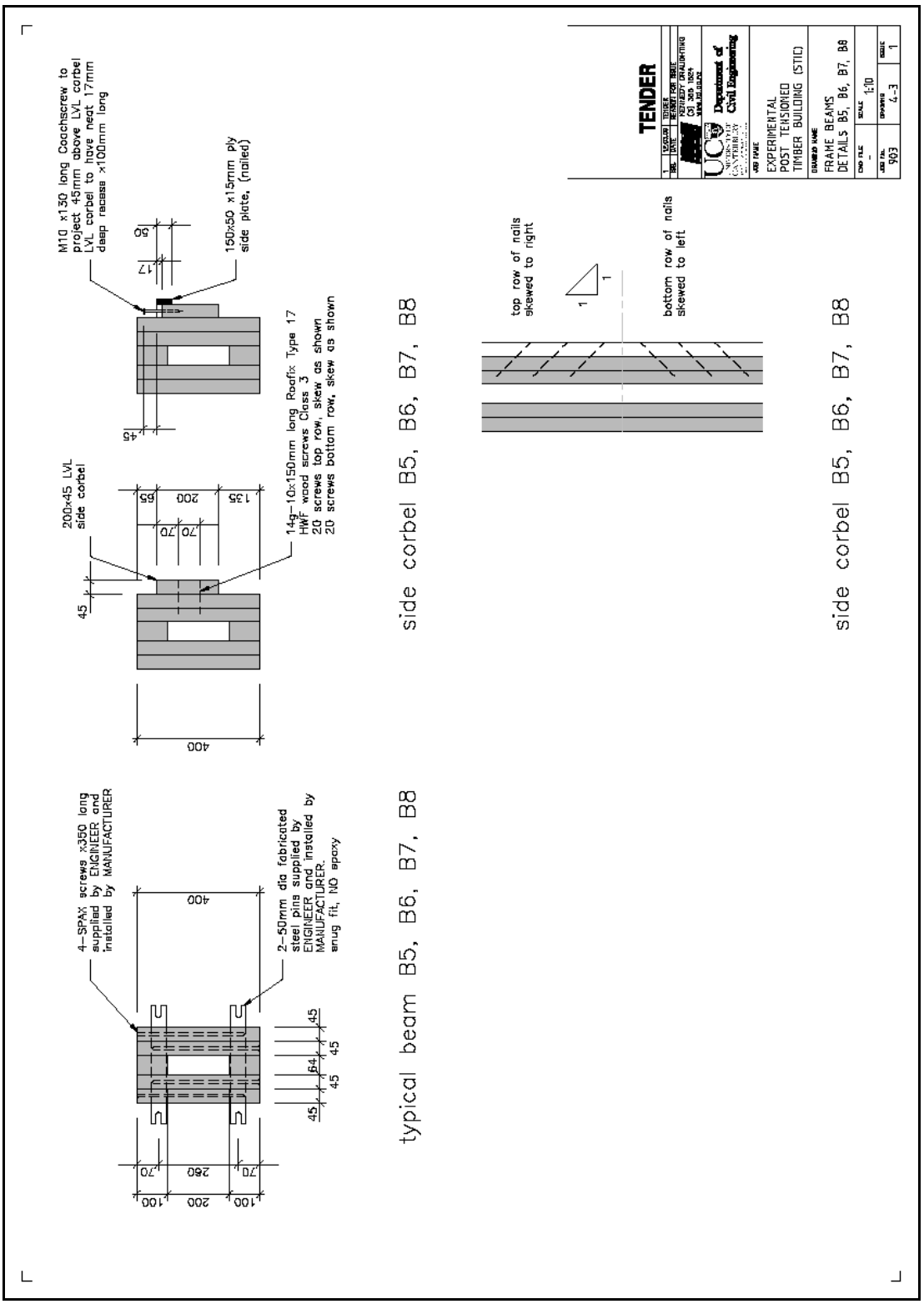
M10 x130 long Coachscrew to project 45mm above LVL corbel
LVL corbel to have neat 17mm deep recess x100mm long
150x50 x15mm ply side plate, (nailed)
50
17
45
200x45 LVL side corbel
14g-10x150mm long Rapfix Type 17 HWF wood screws Class 3
20 screws top row, skew as shown
20 screws bottom row, skew as shown
55
200
135
70
70
45
400
4-SPAX screws x350 long supplied by ENGINEER and installed by MANUFACTURER
2-50mm dia fabricated steel pins supplied by ENGINEER and installed by MANUFACTURER. snug fit, NO epoxy
400
45
64
45
45
45
100
200
100
280
70
70
typical beam B5, B6, B7, B8
side corbel B5, B6, B7, B8
top row of nails skewed to right
bottom row of nails skewed to left
1
1
side corbel B5, B6, B7, B8
TENDER
Department of Civil Engineering
EXPERIMENTAL POST TENSIONED TIMBER BUILDING (STIC)
FRAME BEAMS DETAILS B5, B6, B7, B8
1:10
903
4-3
1

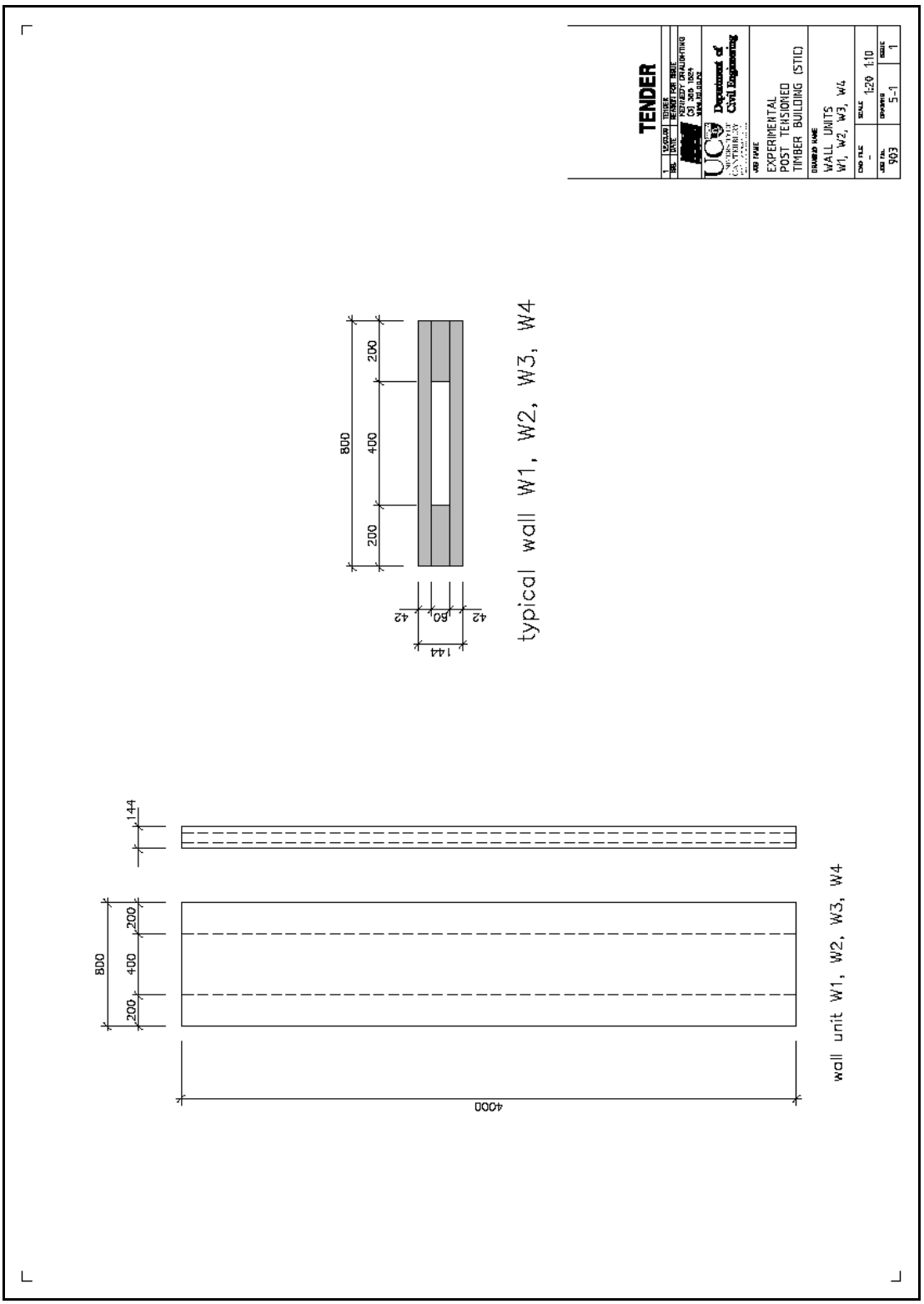
TENDER
Department of Civil Engineering
EXPERIMENTAL
POST TENSIONED
TIMBER BUILDING (STIC)
WALL UNITS
W1, W2, W3, W4
1:20 1:10
903
S-1
typical wall W1, W2, W3, W4
800
200
400
200
144
42
60
42
wall unit W1, W2, W3, W4
4000

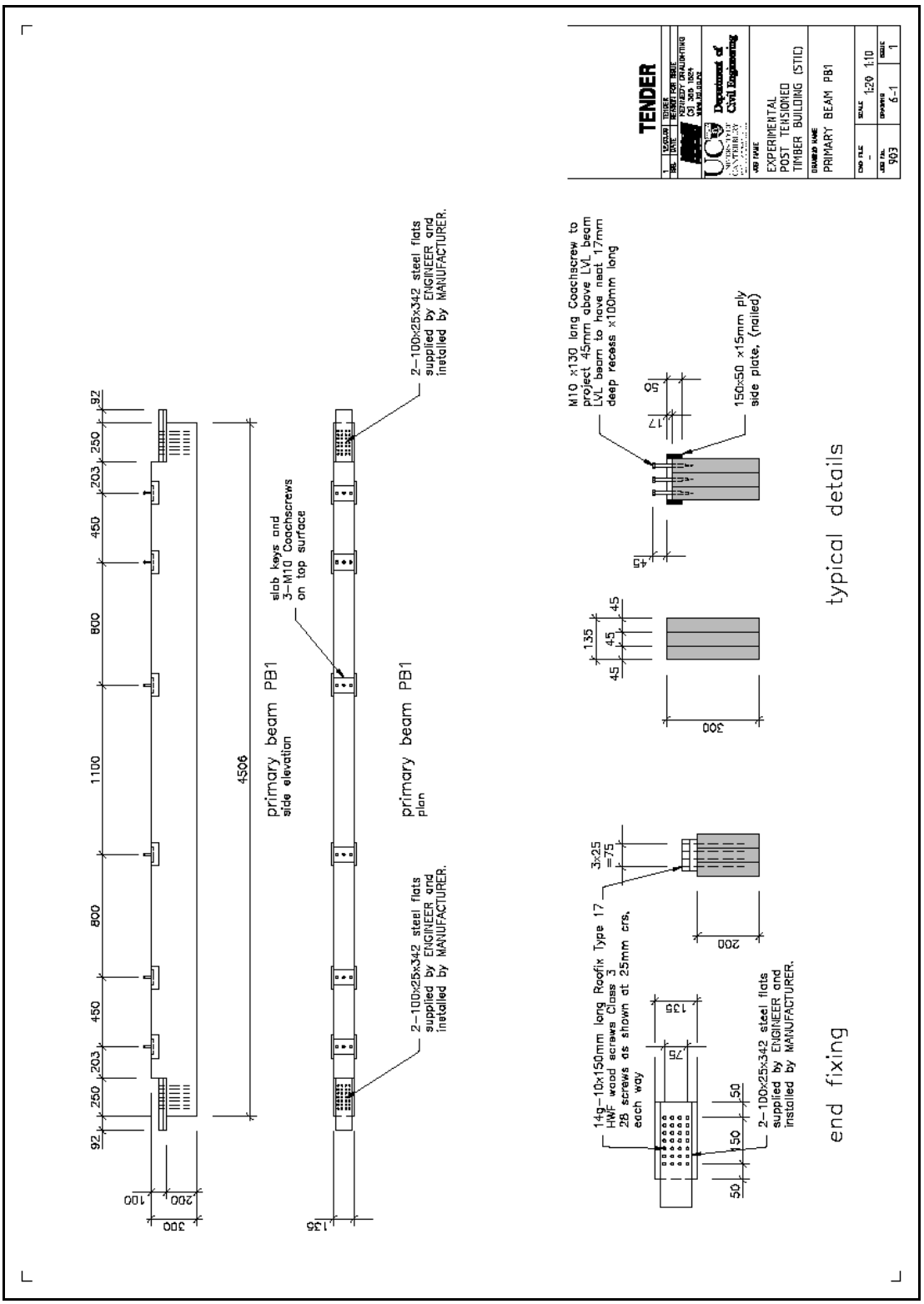
TENDER
Department of Civil Engineering
EXPERIMENTAL POST TENSIONED TIMBER BUILDING (STIC)
PRIMARY BEAM PB1
1:20 1:10
903
6-1
primary beam PB1 side elevation
primary beam PB1 plan
slab keys and 3–M10 Coachscrews on top surface
2–100x25x342 steel flats supplied by ENGINEER and installed by MANUFACTURER.
4506
M10 x130 long Coachscrew to project 45mm above LVL beam deep recess x100mm long
150x50 x15mm ply side plate, (nailed)
typical details
14g–10x150mm long Roofix Type 17 HWF wood screws Class 3 28 screws as shown at 25mm crs. each way
end fixing

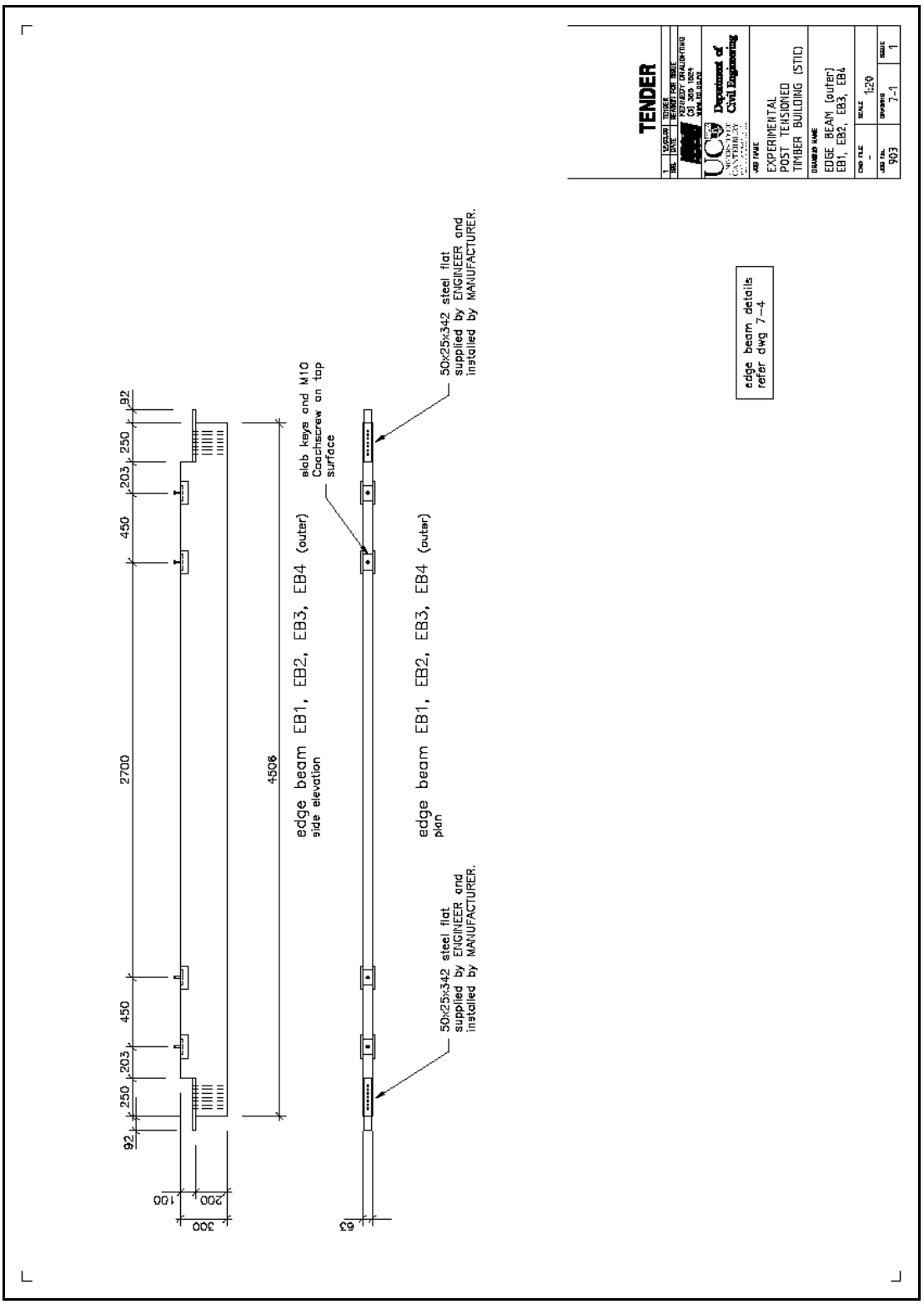
TENDER
ISSUED FOR TENDER
PERMIT FOR TENDER
Department of Civil Engineering
EXPERIMENTAL POST TENSIONED TIMBER BUILDING (STIC)
EDGE BEAM (outer) EB1, EB2, EB3, EB4
903
7-1
1:20
edge beam details refer dwg 7-4
edge beam EB1, EB2, EB3, EB4 (outer) side elevation
edge beam EB1, EB2, EB3, EB4 (outer) plan
slab keys and M10 Coachscrew on top surface
50x25x342 steel flat supplied by ENGINEER and installed by MANUFACTURER.
50x25x342 steel flat supplied by ENGINEER and installed by MANUFACTURER.
92
250
203
450
2700
4506
100
200
300
63

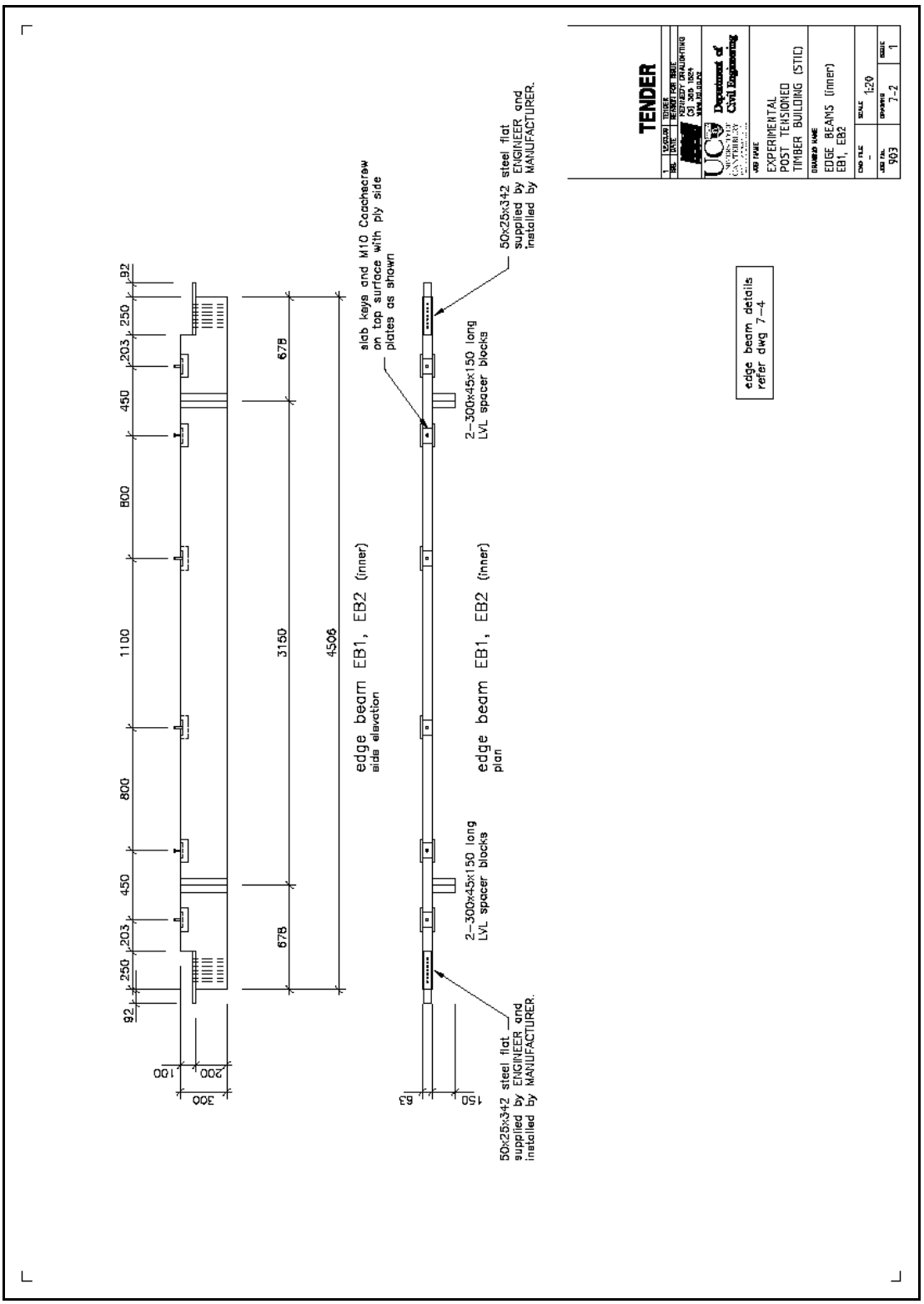
TENDER
Department of Civil Engineering
EXPERIMENTAL POST TENSIONED TIMBER BUILDING (STIC)
EDGE BEAMS (inner) EB1, EB2
edge beam details refer dwg 7-4
edge beam EB1, EB2 (inner) elda elevation
edge beam EB1, EB2 (inner) plan
slab keys and M10 Coachscrew on top surface with ply side plates as shown
2-300x45x150 long LVL spacer blocks
50x25x342 steel flat supplied by ENGINEER and installed by MANUFACTURER.
92
250
203
450
800
1100
800
450
203
250
92
678
3150
4506
300
200
100
63
150

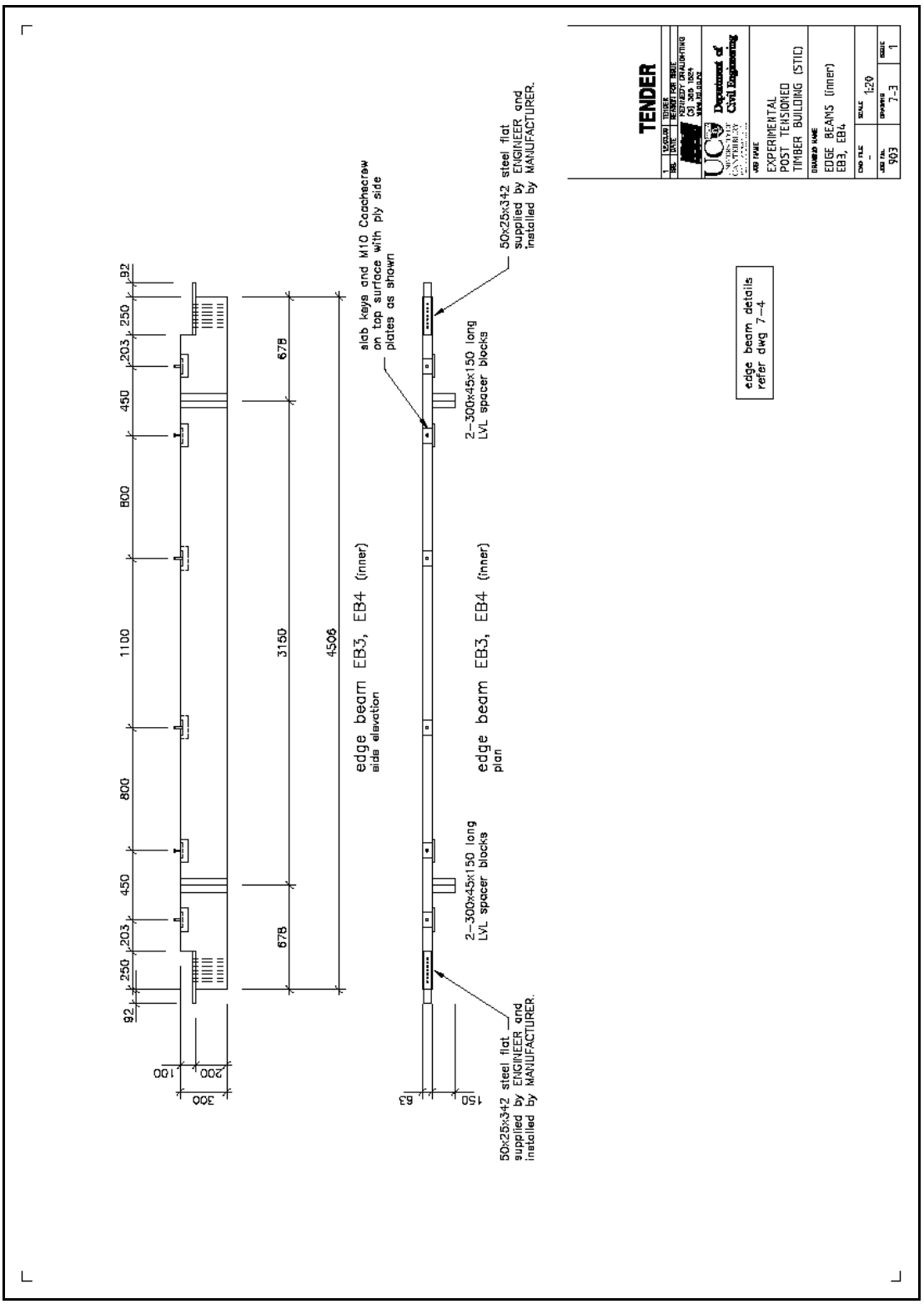
TENDER
Department of Civil Engineering
EXPERIMENTAL POST TENSIONED TIMBER BUILDING (STIC)
EDGE BEAMS (inner) EB3, EB4
1:20
903
7-3
1
edge beam details refer dwg 7-4
edge beam EB3, EB4 (inner) side elevation
edge beam EB3, EB4 (inner) plan
slab keys and M10 Coachscrew on top surface with ply side plates as shown
50x25x342 steel flat supplied by ENGINEER and installed by MANUFACTURER.
2-300x45x150 long LVL spacer blocks
92
250
203
450
800
1100
3150
4506
678
300
200
100
150
63

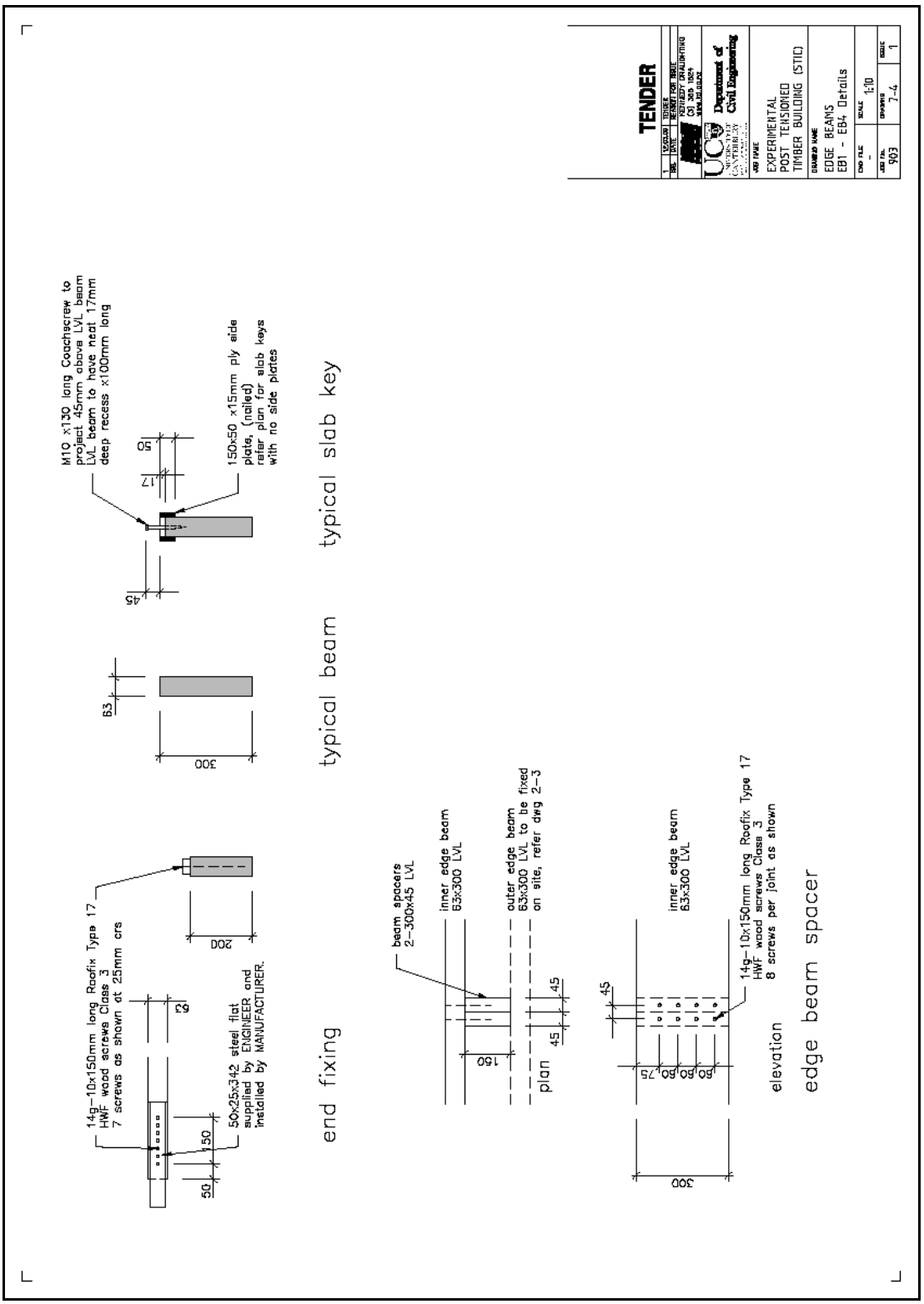
TENDER
Department of Civil Engineering
EXPERIMENTAL POST TENSIONED TIMBER BUILDING (STIC)
EDGE BEAMS
EB1 - EB4 Details
1:10
903
7-4
1
end fixing
typical beam
typical slab key
edge beam spacer
elevation
plan
14g–10x150mm long Roofix Type 17 HWF wood screws Class 3 7 screws as shown at 25mm crs
50x25x342 steel flat supplied by ENGINEER and installed by MANUFACTURER.
M10 x130 long Coachscrew to project 45mm above LVL beam LVL beam to have neat 17mm deep recess x100mm long
150x50 x15mm ply side plate, (nailed) refer plan for slab keys with no side plates
beam spacers 2–300x45 LVL
inner edge beam 63x300 LVL
outer edge beam 63x300 LVL to be fixed on site, refer dwg 2–3
14g–10x150mm long Roofix Type 17 HWF wood screws Class 3 8 screws per joint as shown

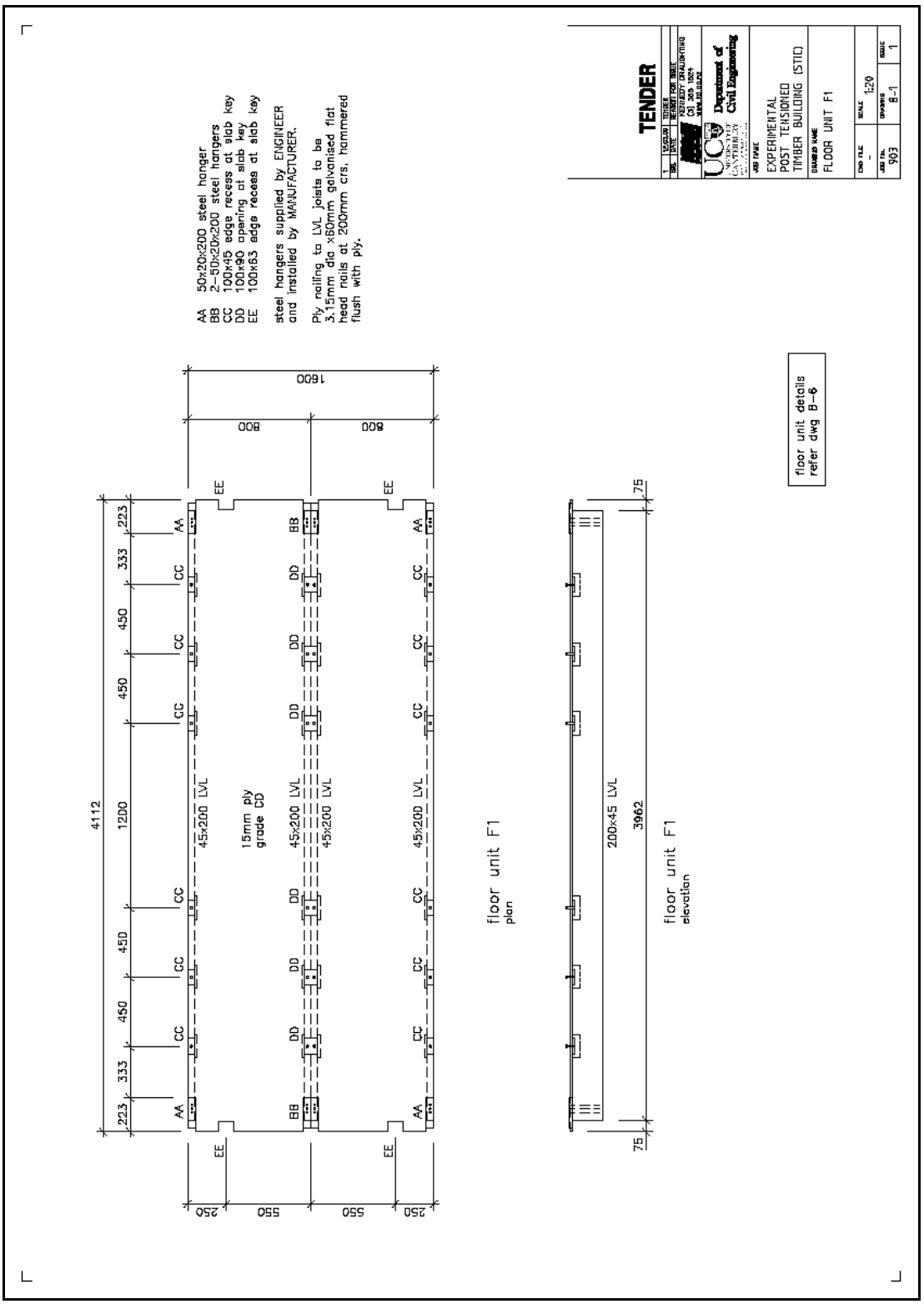
TENDER
ISSUED FOR TENDER
RE-ISSUED DRAWING
Department of Civil Engineering
EXPERIMENTAL
POST TENSIONED
TIMBER BUILDING (STIC)
FLOOR UNIT F1
1:20
903
B-1
AA 50x20x200 steel hanger
BB 2-50x20x200 steel hangers
CC 100x45 edge recess at slab key
DD 100x90 opening at slab key
EE 100x63 edge recess at slab key
steel hangers supplied by ENGINEER and installed by MANUFACTURER.
Ply nailing to LVL joists to be 3.15mm dia x80mm galvanised flat head nails at 200mm crs, hammered flush with ply.
floor unit details refer dwg B-6
15mm ply grade CD
45x200 LVL
4112
1600
800
800
1200
450
450
450
333
223
250
550
550
250
floor unit F1 plan
200x45 LVL
3962
75
75
floor unit F1 elevation

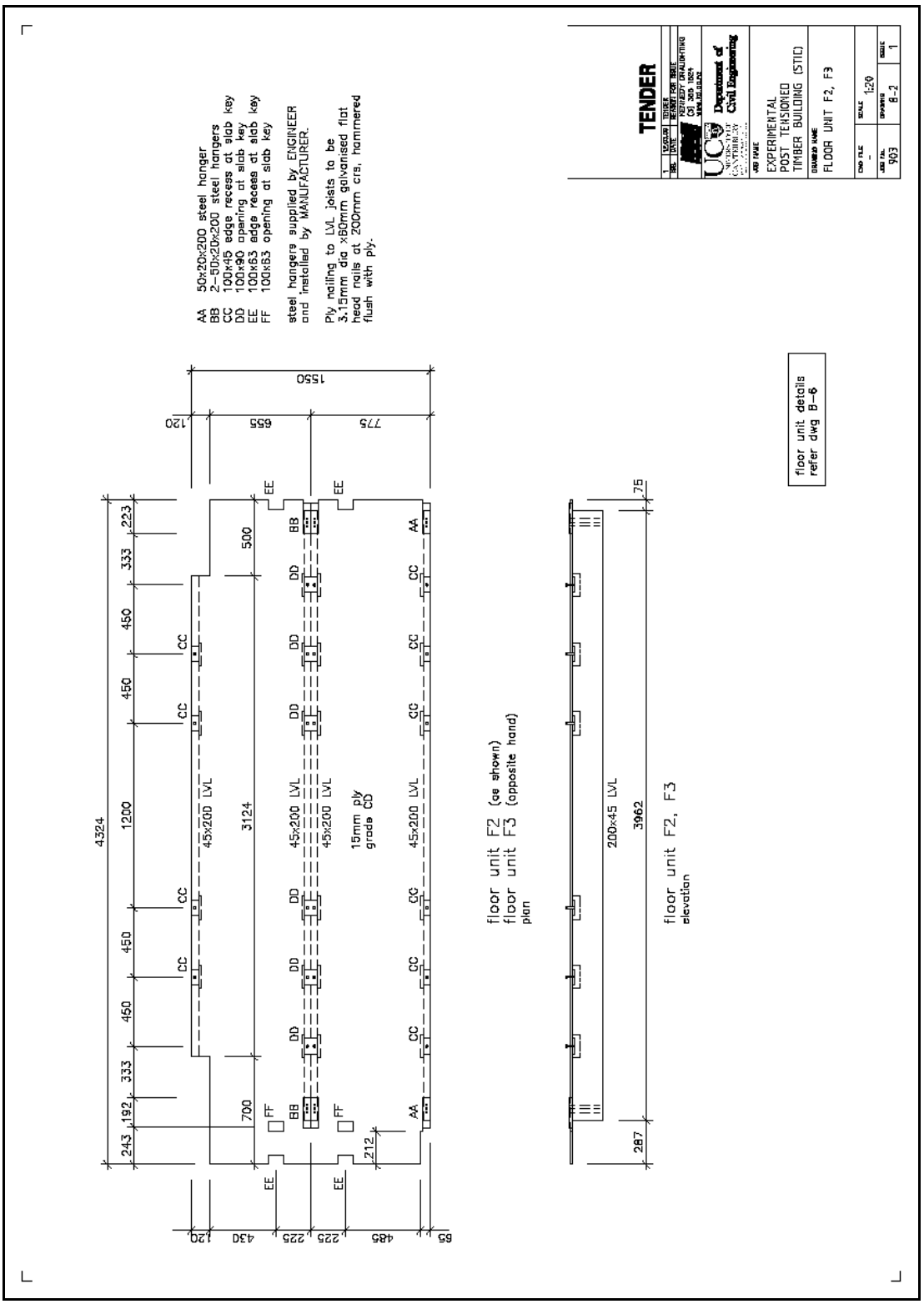
AA 50x20x200 steel hanger
BB 2-50x20x200 steel hangers
CC 100x45 edge recess at slab key
DD 100x90 opening at slab key
EE 100x63 edge recess at slab key
FF 100x63 opening at slab key
steel hangers supplied by ENGINEER and installed by MANUFACTURER.
Ply nailing to LVL joists to be 3.15mm dia x80mm galvanised flat head nails at 200mm crs, hammered flush with ply.
floor unit details refer dwg B-6
floor unit F2 (as shown)
floor unit F3 (opposite hand)
plan
floor unit F2, F3
elevation
45x200 LVL
15mm ply grade CD
200x45 LVL
TENDER
Department of Civil Engineering
EXPERIMENTAL POST TENSIONED TIMBER BUILDING (STIC)
FLOOR UNIT F2, F3
1:20
903
B-2

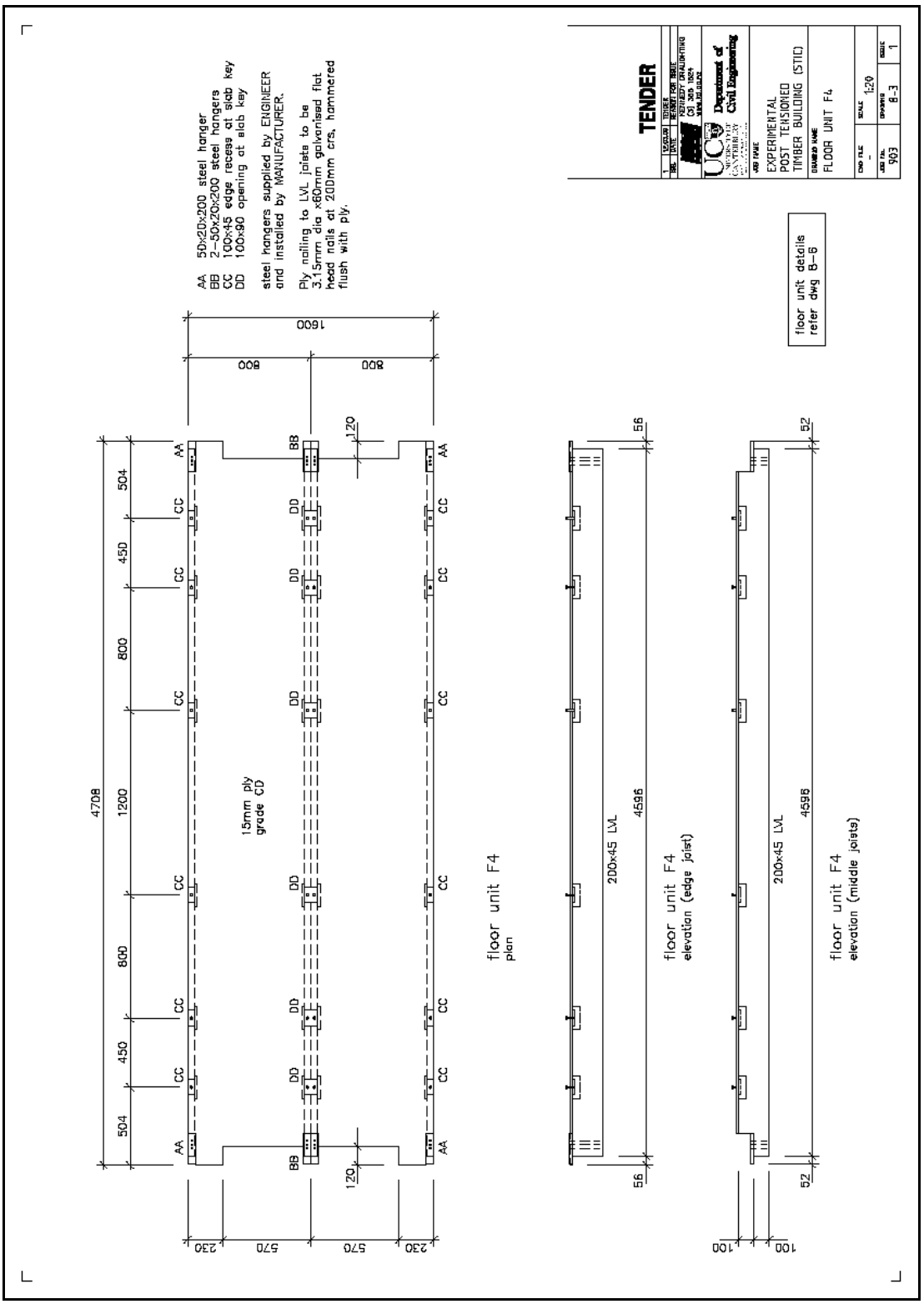
TENDER
Department of Civil Engineering
EXPERIMENTAL
POST TENSIONED
TIMBER BUILDING (STIC)
FLOOR UNIT F4
floor unit details
refer dwg 8-6
AA 50x20x200 steel hanger
BB 2-50x20x200 steel hangers
CC 100x45 edge recess at slab key
DD 100x90 opening at slab key
steel hangers supplied by ENGINEER
and installed by MANUFACTURER.
Ply nailing to LVL joists to be
3.15mm dia x60mm galvanised flat
head nails at 200mm crs, hammered
flush with ply.
15mm ply
grade CD
floor unit F4
plan
200x45 LVL
floor unit F4
elevation (edge joist)
floor unit F4
elevation (middle joists)

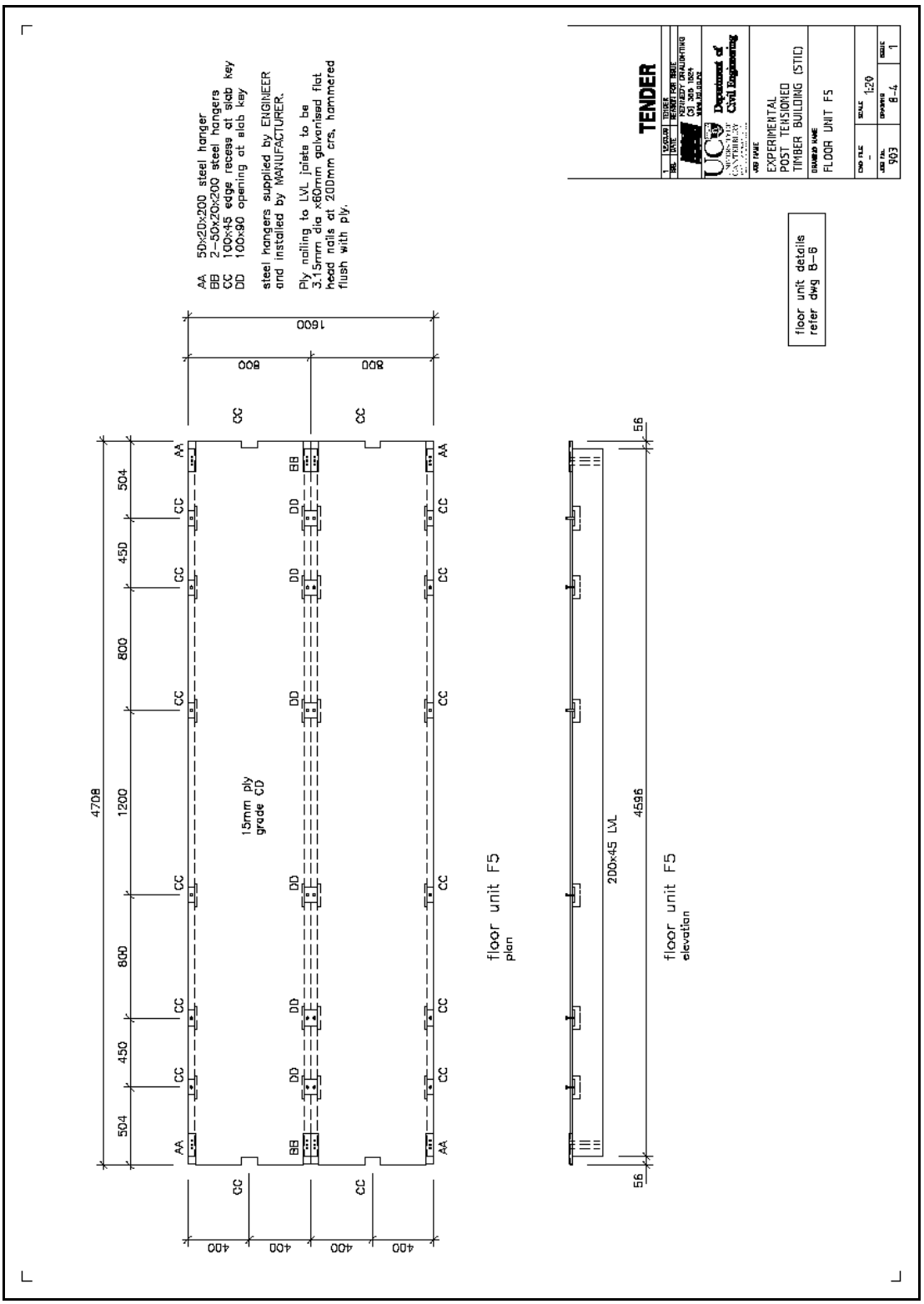
TENDER
Department of Civil Engineering
EXPERIMENTAL
POST TENSIONED
TIMBER BUILDING (STIC)
FLOOR UNIT F5
floor unit details
refer dwg B-6
AA 50x20x200 steel hanger
BB 2-50x20x200 steel hangers
CC 100x45 edge recess at slab key
DD 100x90 opening at slab key
steel hangers supplied by ENGINEER
and installed by MANUFACTURER.
Ply nailing to LVL joists to be
3.15mm dia x60mm galvanised flat
head nails at 200mm crs, hammered
flush with ply.
15mm ply
grade CD
200x45 LVL
4596
4708
1600
800
400
504
450
800
1200
56
floor unit F5
plan
floor unit F5
elevation

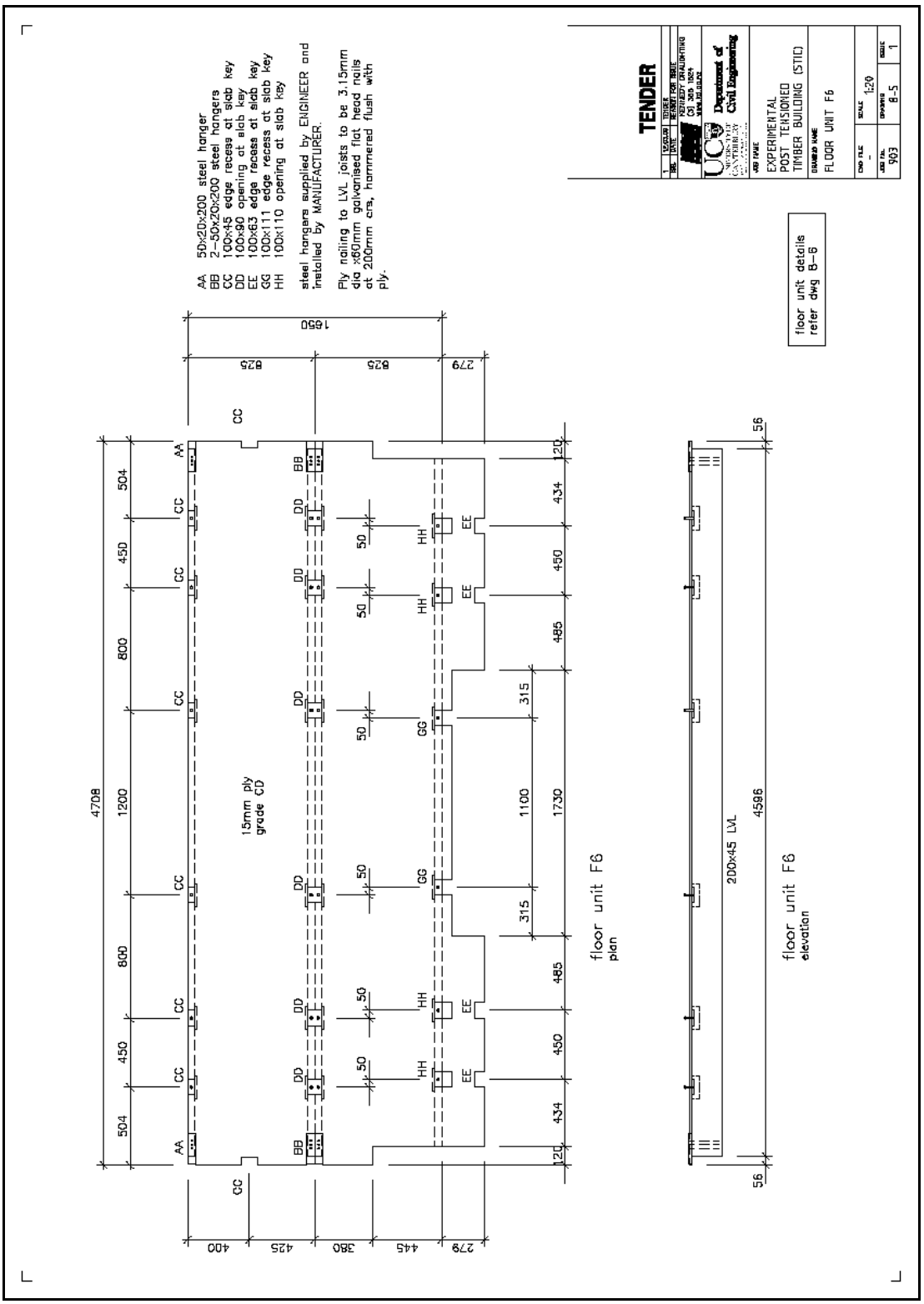
TENDER
Department of Civil Engineering
EXPERIMENTAL POST TENSIONED TIMBER BUILDING (STIC)
FLOOR UNIT F6
floor unit details refer dwg 8-6
AA 50x20x200 steel hanger
BB 2-50x20x200 steel hangers
CC 100x45 edge recess at slab key
DD 100x90 opening at slab key
EE 100x63 edge recess at slab key
GG 100x111 edge recess at slab key
HH 100x110 opening at slab key
steel hangers supplied by ENGINEER and installed by MANUFACTURER.
Ply nailing to LVL joists to be 3.15mm dia x60mm galvanised flat head nails at 200mm crs, hammered flush with ply.
15mm ply grade CD
200x45 LVL
floor unit F6 plan
floor unit F6 elevation

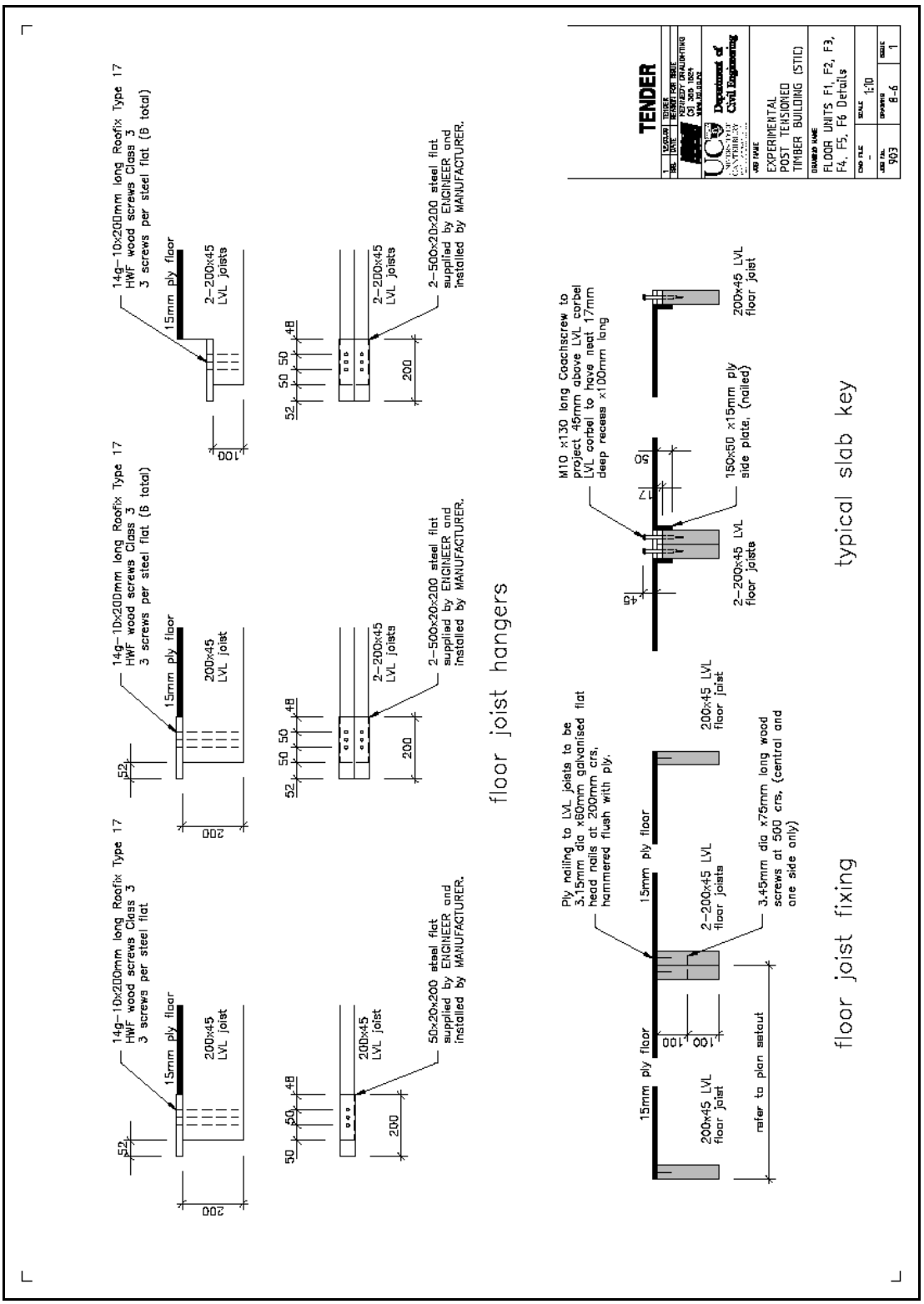
14g–10x200mm long Roofix Type 17
HWF wood screws Class 3
3 screws per steel flat
15mm ply floor
200x45
LVL joist
200
52
50
48
50x20x200 steel flat
supplied by ENGINEER and
installed by MANUFACTURER.
floor joist hangers
14g–10x200mm long Roofix Type 17
HWF wood screws Class 3
3 screws per steel flat (6 total)
2–200x45
LVL joists
100
50 50
2–500x20x200 steel flat
supplied by ENGINEER and
installed by MANUFACTURER.
200
floor joist fixing
Ply nailing to LVL joists to be
3.15mm dia x60mm galvanised flat
head nails at 200mm crs,
hammered flush with ply.
2–200x45 LVL
floor joists
3.45mm dia x75mm long wood
screws at 500 crs. (central and
one side only)
refer to plan setout
M10 x130 long Coachscrew to
project 45mm above LVL corbel
LVL corbel to have neat 17mm
deep recess x100mm long
150x50 x15mm ply
side plate, (nailed)
typical slab key
TENDER
Department of
Civil Engineering
EXPERIMENTAL
POST TENSIONED
TIMBER BUILDING (STIC)
FLOOR UNITS F1, F2, F3,
F4, F5, F6 Details
903
8-6
1:10

A.6.2. Steel components

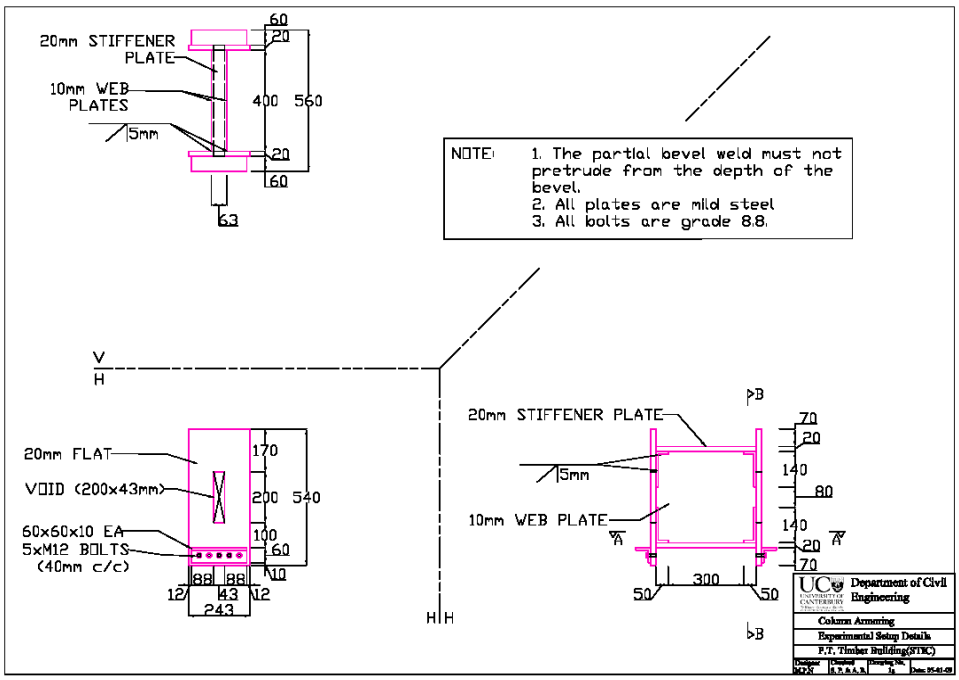

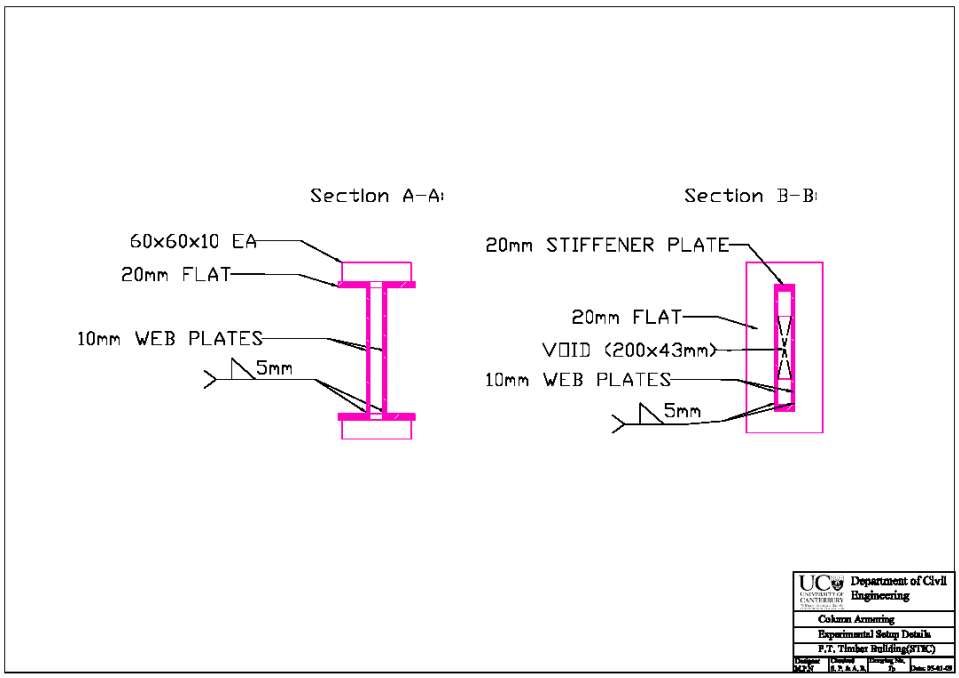

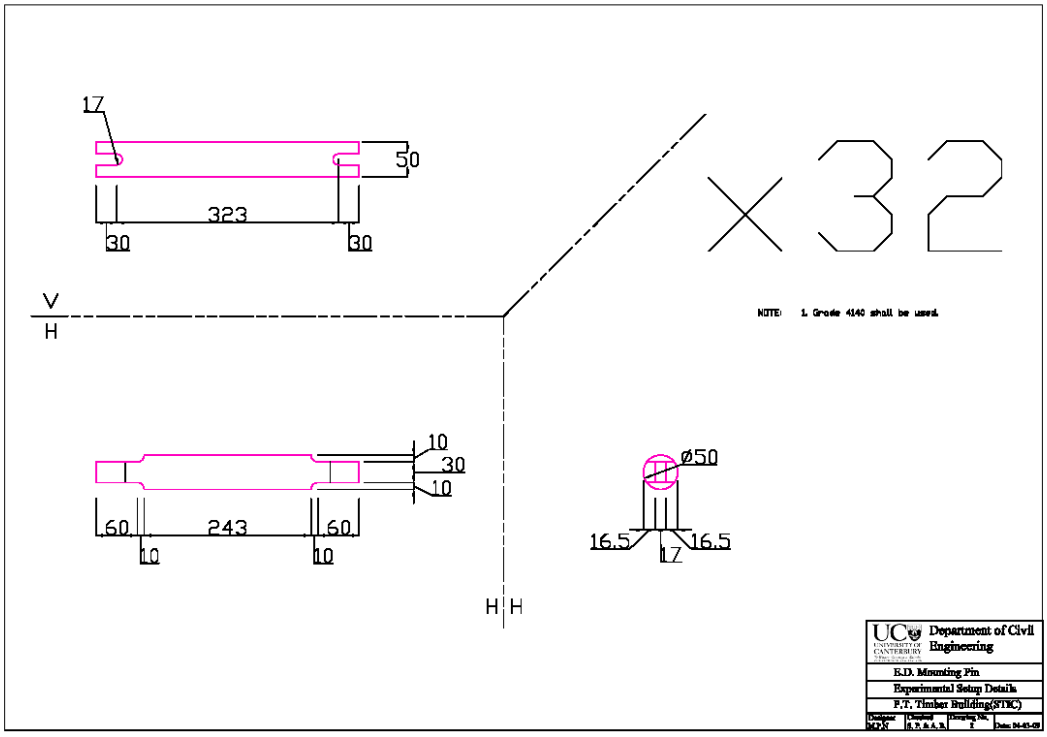
17
50
323
30
30
V
H
×32
NOTE: 1. Grade 4140 shall be used.
10
30
10
60
243
60
10
10
ø50
16.5
16.5
17
H H
Department of Civil Engineering
E.D. Mounting Pin
Experimental Setup Details
P.T. Timber Building(STIC)

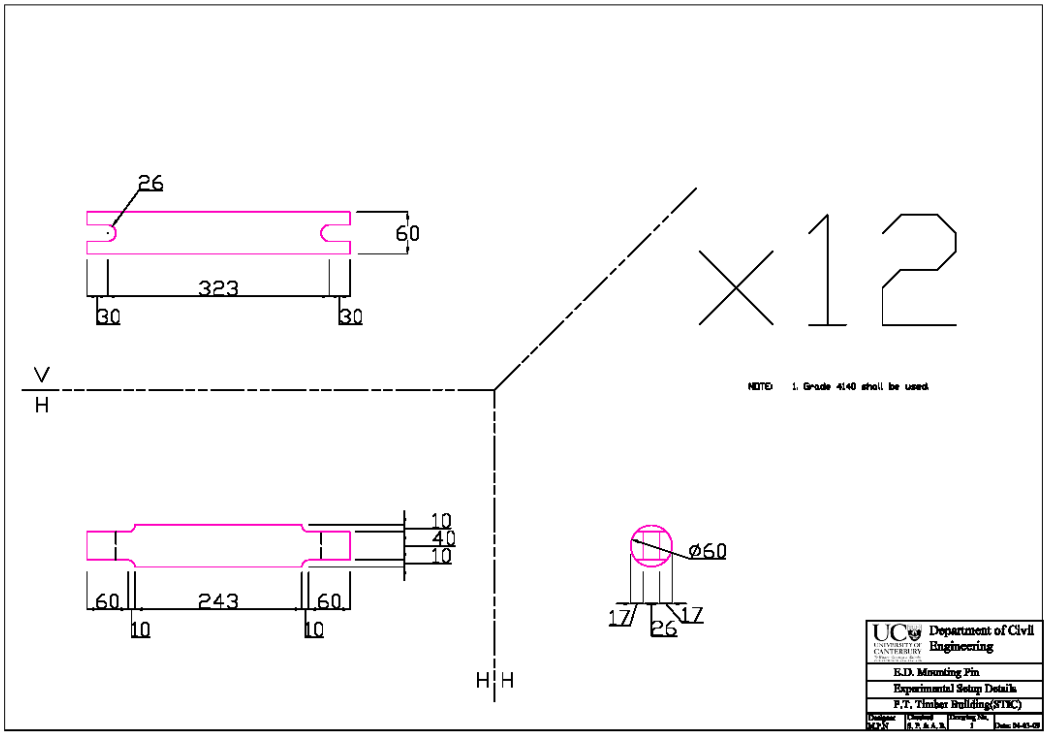
26
60
323
30
30
V
H
×12
NOTE: 1. Grade 4140 shall be used.
10
40
10
60
243
60
10
10
ø60
17
17
26
H H
Department of Civil Engineering
E.D. Mounting Pin
Experimental Setup Details
P.T. Timber Building(STIC)

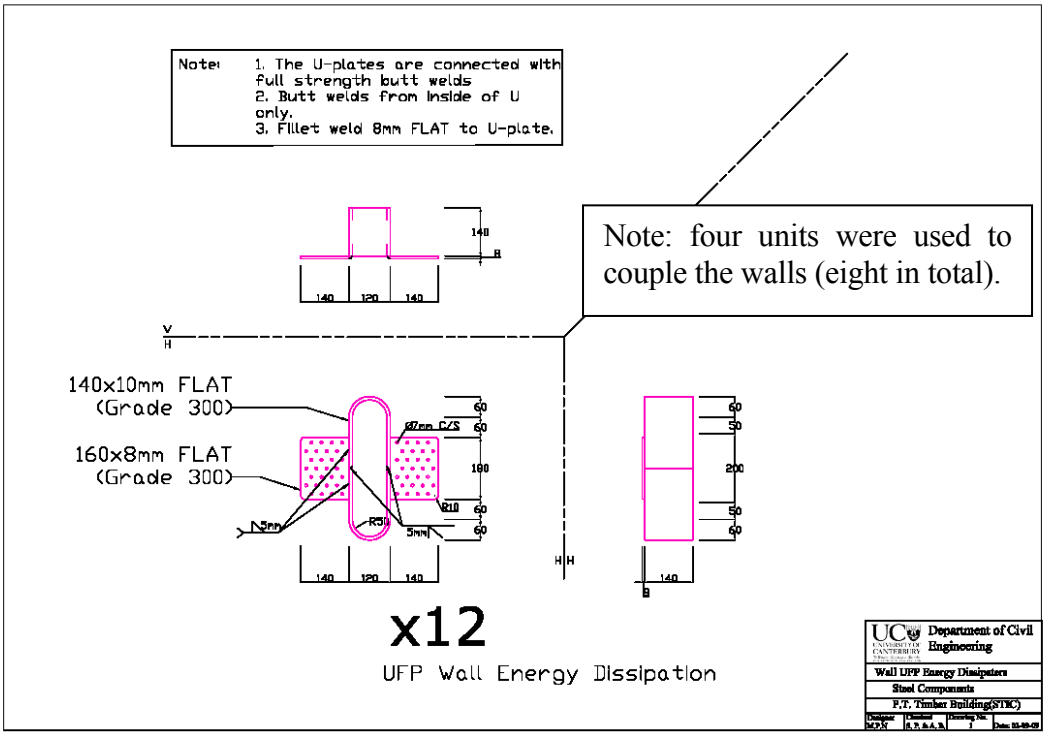
Note:
1. The U-plates are connected with full strength butt welds
2. Butt welds from inside of U only.
3. Fillet weld 8mm FLAT to U-plate.
Note: four units were used to couple the walls (eight in total).
140x10mm FLAT (Grade 300)
160x8mm FLAT (Grade 300)
x12
UFP Wall Energy Dissipation
Department of Civil Engineering
Wall UFP Energy Dissipators
Steel Components
F.T. Timber Building(STIC)

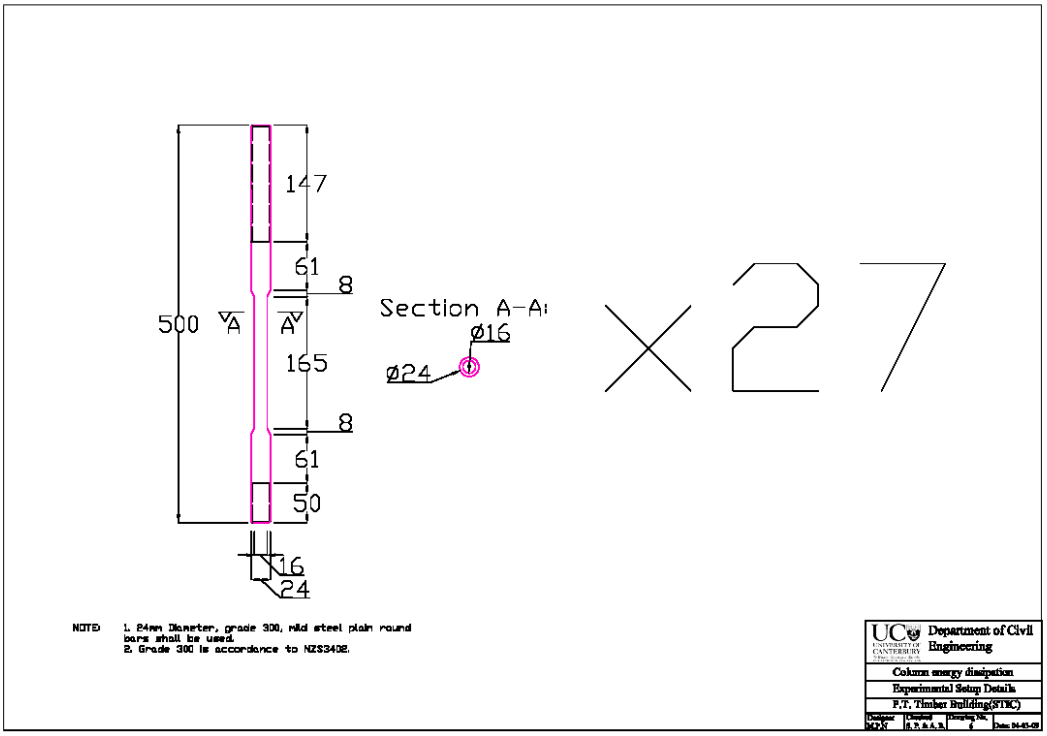
147
61
8
500
165
8
61
50
16
24
Section A-A
Ø16
Ø24
x27
NOTE
1. 24mm Diameter, grade 300, mild steel plain round bars shall be used.
2. Grade 300 is accordance to NZS3402.
Department of Civil Engineering
Column energy dissipation
Experimental Setup Details
F.T. Timber Building(STIC)

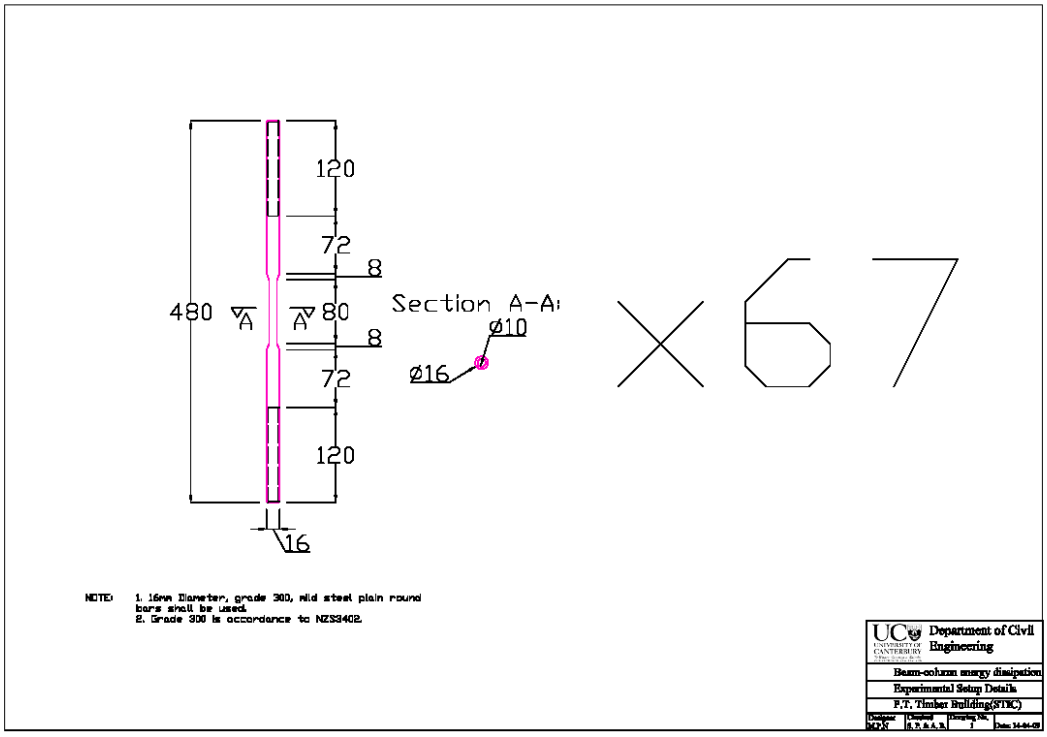
120
72
8
480
A
A
80
8
72
120
16
Section A-A
Ø10
Ø16
×67
NOTE:
1. 16mm Diameter, grade 300, Mid steel plain round bars shall be used.
2. Grade 300 is accordance to NZS3402.
Department of Civil Engineering
Beam-column energy dissipation
Experimental Setup Details
P.T. Timber Building(STIC)

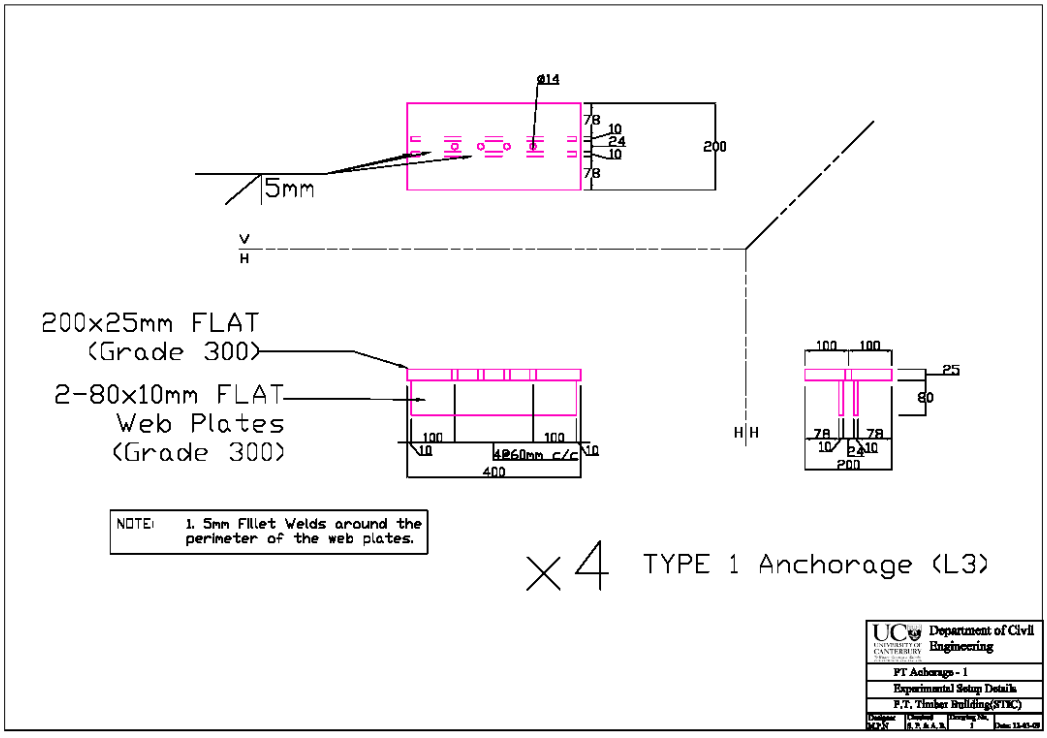
Ø14
78
10
24
10
78
200
5mm
V
H
200x25mm FLAT
(Grade 300)
2-80x10mm FLAT
Web Plates
(Grade 300)
100
100
10
@60mm c/c
10
400
H
H
100
100
25
80
78
78
10
24
10
200
NOTE:
1. 5mm Fillet Welds around the perimeter of the web plates.
×4 TYPE 1 Anchorage (L3)
Department of Civil Engineering
PT Acharage - 1
Experimental Setup Details
P.T. Timber Building(STIC)

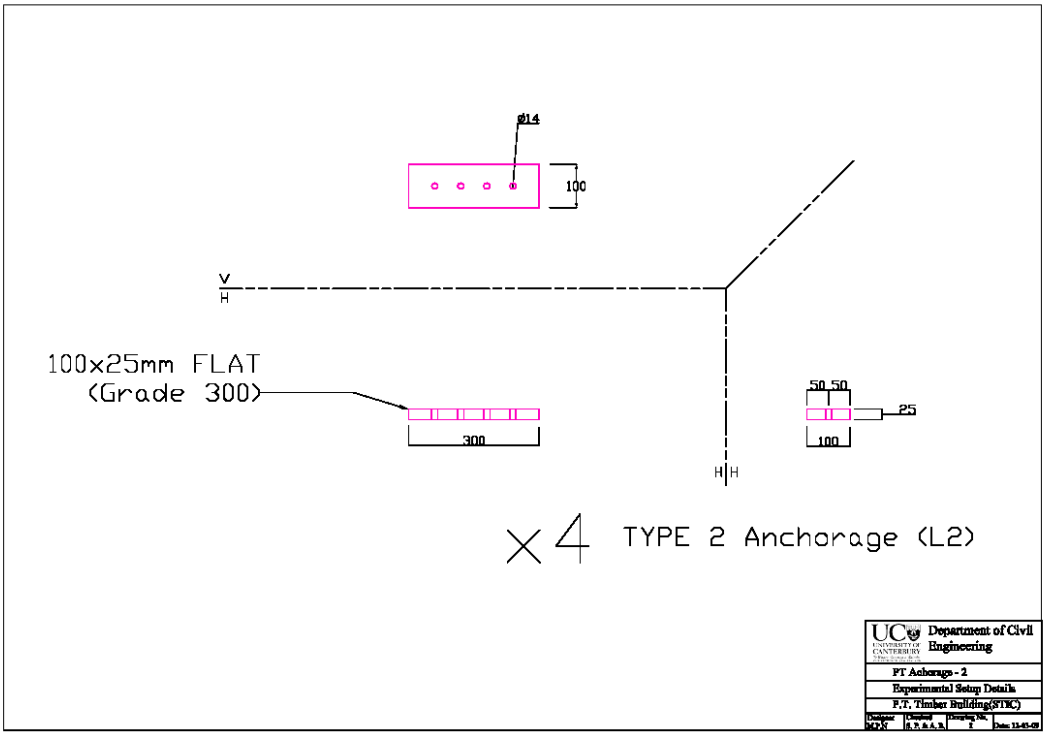
ø14
100
V
H
100x25mm FLAT
(Grade 300)
300
50 50
25
100
H H
4 TYPE 2 Anchorage (L2)
Department of Civil Engineering
PT Acheage - 2
Experimental Setup Details
F.T. Timber Building(STIC)

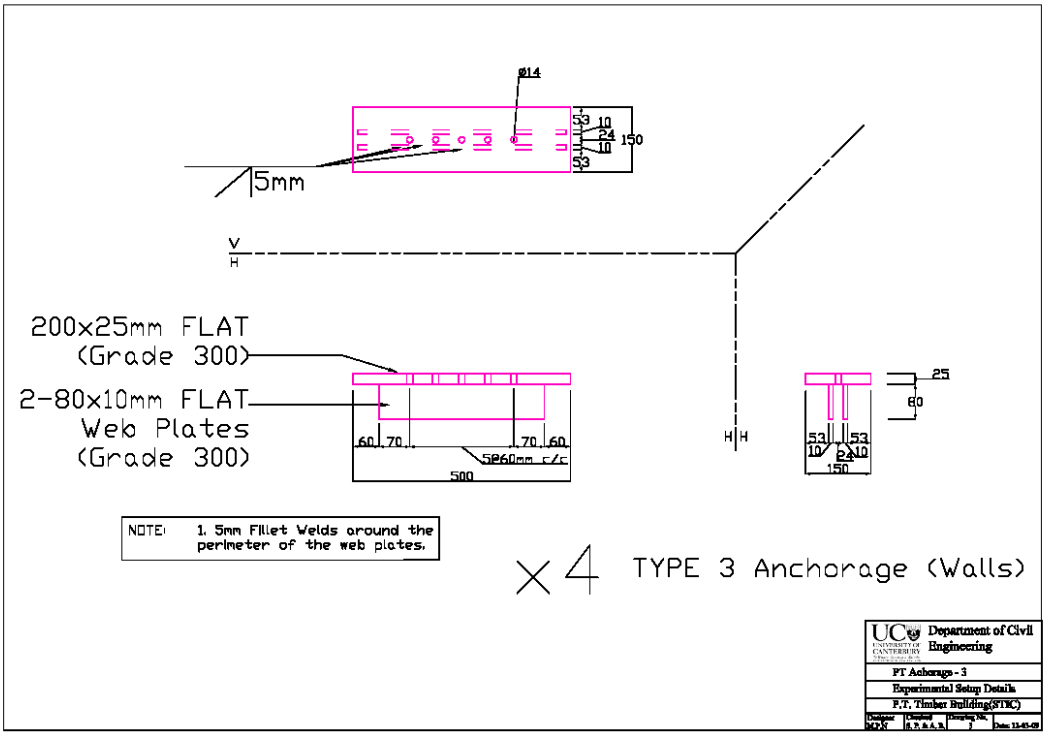
ø14
5mm
53 10 24 10 53
150
V
H
200x25mm FLAT
(Grade 300)
2-80x10mm FLAT
Web Plates
(Grade 300)
60 70
5@60mm c/c
70 60
500
25
60
53 10 24 10 53
150
H H
NOTE: 1. 5mm Fillet Welds around the perimeter of the web plates.
4 TYPE 3 Anchorage (Walls)
Department of Civil Engineering
PT Acheage - 3
Experimental Setup Details
F.T. Timber Building(STIC)

A.6.3. Slab reinforcement

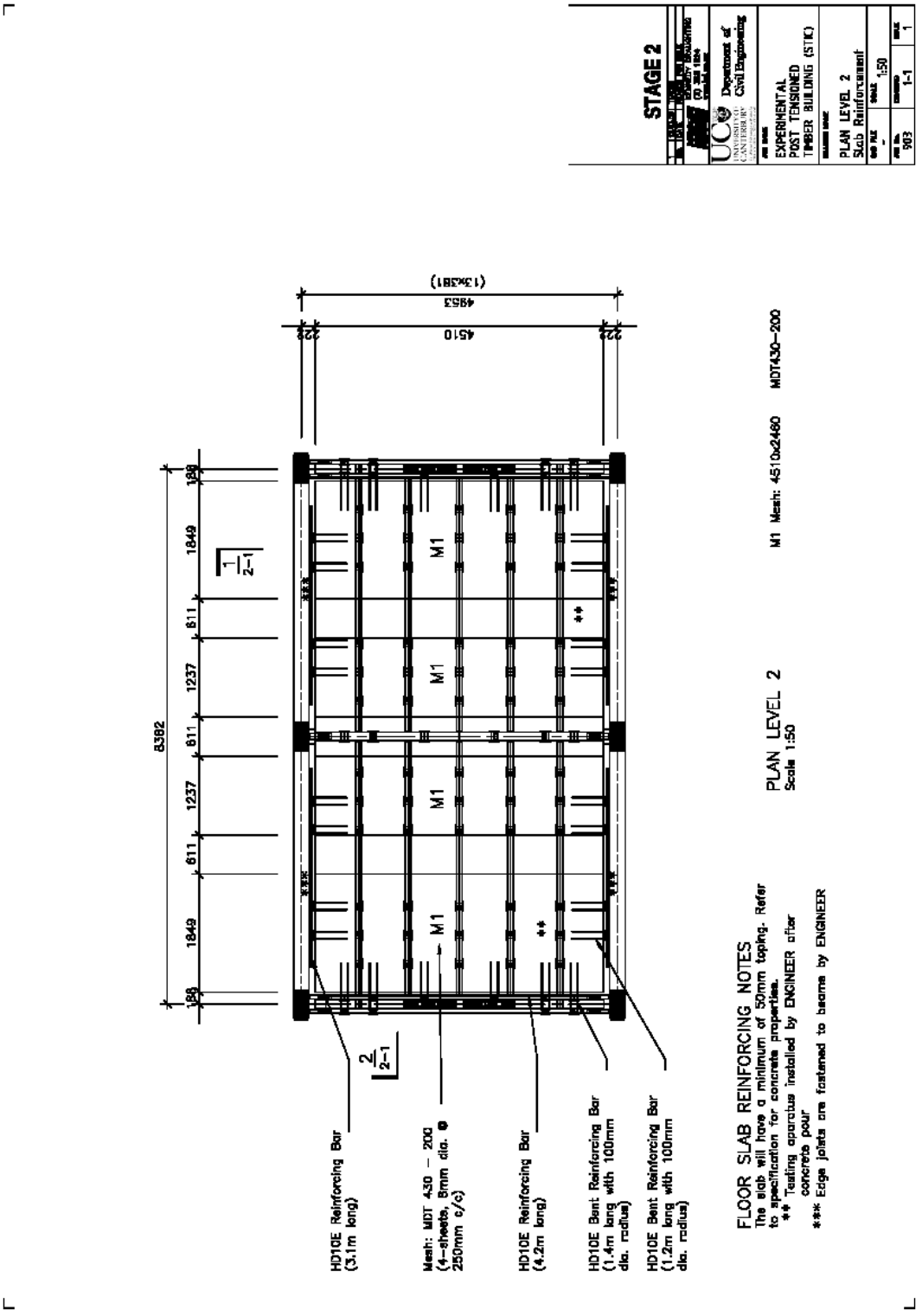
STAGE 2
Department of Civil Engineering
EXPERIMENTAL POST TENSIONED TIMBER BUILDING (STIC)
PLAN LEVEL 2 Slab Reinforcement
scale 1:50
1-1
(13x381)
4853
4510
228
8382
188
1849
611
1237
M1
2-1
HD10E Reinforcing Bar (3.1m long)
Mesh: MDT 430 – 200 (4–sheets, 8mm dia. @ 250mm c/c)
HD10E Reinforcing Bar (4.2m long)
HD10E Bent Reinforcing Bar (1.4m long with 100mm dia. radius)
HD10E Bent Reinforcing Bar (1.2m long with 100mm dia. radius)
PLAN LEVEL 2
Scale 1:50
M1 Mesh: 4510x2460 MDT430–200
FLOOR SLAB REINFORCING NOTES
The slab will have a minimum of 50mm topping. Refer to specification for concrete properties.
** Testing apparatus installed by ENGINEER after concrete pour
*** Edge joists are fastened to beams by ENGINEER

STAGE 2
Department of Civil Engineering
EXPERIMENTAL POST TENSIONED TIMBER BUILDING (STIC)
PLAN LEVEL 3 Slab Reinforcement
1:50
1-2
1
(13438)
4853
4510
222
8362
188
1849
611
1237
611
1237
611
1849
188
M1
M1
M1
M1
M1 Mesh: 4510x2480 MDT430-200
PLAN LEVEL 3
Scale 1:50
HD10E Reinforcing Bar (3.1m long)
Mesh: MDT 430 – 200 (4-sheets, 8mm dia. @ 250mm c/c)
HD10E Reinforcing Bar (4.2m long)
HD10E Bent Reinforcing Bar (1.4m long with 100mm dia. radius)
HD10E Bent Reinforcing Bar (1.2m long with 100mm dia. radius)
FLOOR SLAB REINFORCING NOTES
The slab will have a minimum of 50mm topping. Refer to specification for concrete properties.
** Testing apparatus installed by ENGINEER after concrete pour
*** Edge joists are fastened to beams by ENGINEER

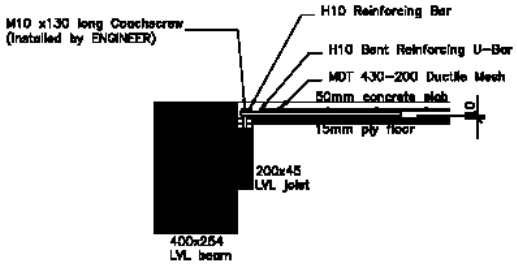

Frame to slab reinforcement

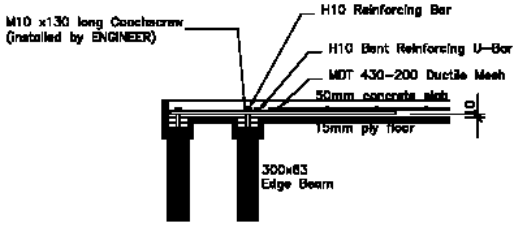

Wall to slab reinforcement

STAGE 2

[redacted]

Department of Civil Engineering

EXPERIMENTAL
POST TENSIONED
TIMBER BUILDING (STIC)

Slab Reinforcing Details

CAD FILE: -	SCALE: 1:10	
JOB No.: 903	DRAWING: 2-1	SHEET: 1

Reinforcing Steel and Mesh:

ITEM	GRADE (MPa)	DIAMETER (mm)	QUANTITY	DIAGRAM
1	500E (Deformed)	10	8	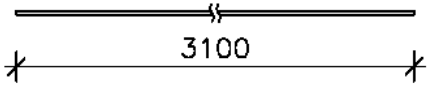
2	500E (Deformed)	10	4	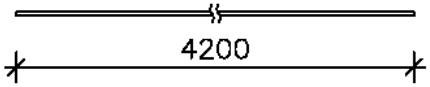
3	500E (Deformed)	10	60	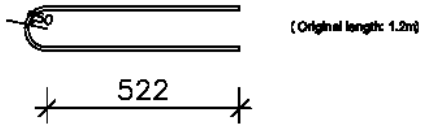
4	500E (Deformed)	10	16	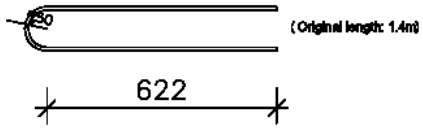
5	MDT 430 (Mesh)	8 @ 250mm (201mm2)	8	

STAGE 2

UC University of Canterbury
Department of Civil Engineering

EXPERIMENTAL POST TENSIONED TIMBER BUILDING (STIC)

Slab Reinforcing Material List

CAD FILE –	SCALE 1:10	
JOB No. 903	DRAWING 3-1	SHEET 1

A.7. DESIGN SPECIFICATIONS OF TEST BUILDING

STRUCTURAL TIMBER FABRICATION

TIM.1 PRELIMINARY
Refer to the Preliminary and General Clauses of this Specification and to the General Conditions of Contract, which are equally binding on all trades. This section of the Specification shall be read in conjunction with all other sections.
In this specification the Principal is the University of Canterbury (UC), the Engineer is the design engineer nominated by the University of Canterbury. The Project Manager is from Mainzeal and is nominated by the University of Canterbury.

TIM.2 SCOPE
This section of the contract includes the following:

(a) Fabrication, supply and delivery of all glued timber members, including beams, columns and structural walls, all manufactured from LVL components with steel brackets and fasteners as detailed.
(b) Fabrication, supply and delivery of all flooring units, manufactured from LVL joists and plywood panels with coach screws and fasteners as detailed.

TIM.3 MATERIALS AND WORKMANSHIP
Wood and wood based products, and construction and workmanship, shall be in accordance with the relevant New Zealand Standards, including the following, as appropriate:

AS/NZS 4357	Structural laminated veneer lumber
AS/NZS1328.1:1998	Glue Laminated Structural Timber Part 1: Performance requirements and minimum production requirements.
AS/NZS1328.2:1998	Glue Laminated Structural Timber Part 2: Guidelines for AS/NZS1328:Part 1
AS/NZS 2269:2004	Structural Plywood
NZS 3602: 2003	Code of practice for specifying timber and wood based products for use in building

TIM.4 TIMBER QUALITY
This clause applies to all Laminated Veneer Lumber (LVL), plywood, and manufactured timber components.

TIM.4.1 Species
All timber shall be Radiata Pine.

TIM.4.2 LVL and Plywood

All LVL shall be manufactured in a factory with a current licence from the Engineered Wood Products Association of Australasia (EWPA), manufactured in accordance with AS/NZS 4357 Structural laminated veneer lumber.

The Contractor shall comply with the requirements of NZS 4357 and AS/NZS 1604.4 for LVL manufacture except where modified by this specification, and use adequate plant and equipment controlled by qualified personnel. Only fabricators certified by the Plywood Association of Australasia, which itself is audited by JAS-ANZ (Joint Accreditation System – Australia and New Zealand) will be considered suitably qualified.

Each piece of LVL shall be branded at least once with the product brand name, the date and time of manufacture, the manufacturer's mill number, and the PAA and JAS-ANZ logos.

All plywood shall be manufactured in a factory with a current licence from the Engineered Wood Products Association of Australasia (EWPA), manufactured in accordance with AS/NZS 2269:2004 Structural Plywood.

TIM.4.3 Treatment
No timber treatment is required.

TIM.4.4 Moisture Content
The moisture content of all timber components shall not exceed 15%. Moisture content variation between adjacent glued laminates must not exceed 2%.

All LVL members shall be provided to the manufacturer true and straight with minimal cupping.

The fabricator shall measure the moisture content before gluing, and inform the Project Manager and Engineer if not within acceptable limits.

TIM.4.5 Grade of LVL
The characteristic modulus of elasticity of LVL must be between 10,000 to 11,000 MPa.

TIM.5 FABRICATED TIMBER

TIM.5.1 Manufacture
All fabricated timber beams, columns and walls shall be fabricated as shown on the drawings and from LVL in accordance with AS/NZS 1328:1998, in a plant holding a current SANZ licence.

Flooring units shall be fabricated as shown on the drawings with plywood nailed to LVL joists.

TIM.5.2 Nominated Manufacturers
Three nominated manufactures shall be used for the fabrication of the columns, beams, walls and floors; MacIntosh Timber Laminates, Timber Bond and Hunters. Table 1 is a possible list of which structural elements each nominated manufacturer may construct. The fabricator may make changes to the list by mutual agreement. Any changes shall be advised to the Engineer.

The position of the structural elements is given in Figure 1.

Table 1. Suggested structural elements to be constructed by nominated manufacturers

Structural element	Number of elements		
	MacIntosh	Timber Bond	Hunters
Frame Beams	2	2	4
Frame columns	2	2	2
Walls	1	2	1
Primary beam	1	-	-
Edge beams	1	2	1
Floor units	4	3	4

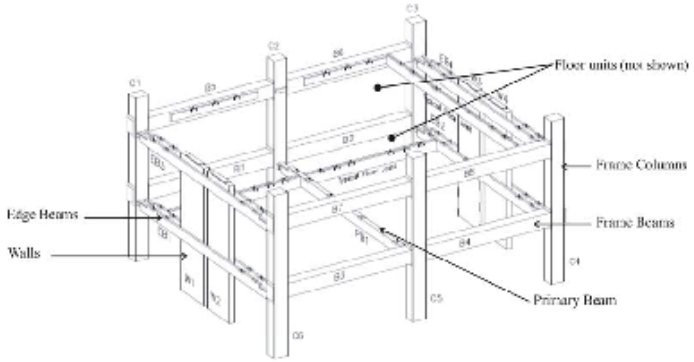

Figure 1. Structural elements

TIM.5.3 Adhesive
The adhesive for all fabricated timber shall be Resorcinol adhesive, as specified in NZS 3606 for Service Class 1. All adhesives shall be mixed, applied and cured strictly in accordance with the manufacturer's recommendations.

TIM.5.4 End Joints
All LVL components shall be provided full length. No end joints are permitted.

TIM.5.5 Testing
Shear blocks from beams, columns and walls shall be tested as specified in AS/NZS 1328.

TIM.5.6 LVL Member Thickness
All LVL members shall be machined on those surfaces to be glued. The finished thickness shall be as necessary to produce the overall beam, column and wall dimensions shown on the drawings.

Extra local machining will be required to fit steel components if the final thickness of the central column laminate is less than 63.5mm.

TIM.5.7 Dimensions and tolerances
The dimensions of the finished timber members shall be as shown on the drawings.
All finished timber members shall be within +/- 3mm of the dimensions shown on the drawings except for the following special tolerances:

Special tolerances are as follows:

Length of beams	+/- 2mm
Thickness of columns	+/- 2mm
Squareness of columns at beam-column joints	+/- 1mm
Squareness of beam end (both ends)	+/- 1mm
Squareness of column and wall end (bottom end)	+/- 1mm
Diameter of drilled holes in beams and in columns at level 3:	< +1.0mm
Squareness of drilled holes in beams and columns	+/- 2 degree
Squareness of pins within the columns and beams	+/- 1 degree

3

The gap between the end grain of the 64mm central laminate and the steel plate insert shall be no more than 1mm.

All dimensions shall be checked before cutting members to final length. Any members not meeting the specified tolerances shall be liable for rejection.

For the holes in the columns drilled adjacent to internal steel components, the hole diameter shall be within 4 mm of the diameter of the pins. If the hole diameter 1mm larger than the diameter of the pins then gaps shall be filled with epoxy according to TIM 5.10.

TIM.5.8 Slots and Holes
All drilling of holes for dowels, and other fixing of bars or brackets, shall be done in the factory.

Flooring units shall have notches in the LVL joists, coach screws, and holes in the plywood sheeting as shown on the drawings.

Where prefabricated steel components are to be inserted into columns, the central column LVL member laminates must be cut to accommodate the steel component, within the tolerances specified in TIM.5.7. Column laminates adjacent to the central lamination may require local machining, according to TIM.5.6. to fit the steel components.

The holes drilled into the columns adjacent to internal steel components may be oversized but shall be filled with epoxy if outside of the tolerances specified in TIM 5.7.

TIM.5.9 Structural steel work items
Take delivery of prefabricated steel plates and pins from the Project Manager or Engineer and build in as detailed in the drawings.

For the pins, holes shall be the same diameter as the steel pins as shown in the drawings.

The pins shall be positioned, as shown in the drawings, so that the u-shaped slots are perpendicular to the column face.

TIM.5.10 Epoxy for gap filling
Epoxy shall be used to keep some pins and column steel components in place, as detailed in the drawings.

Epoxy shall be either of the following listed below unless the Engineer gives written approval for an alternative:

- Araldite 2005 (Nuplex Building Products)
- Araldite K-80 (Nuplex Building Products)
- West System ADR310 / ADH26 (Adhesive Technologies Ltd, Auckland)
- West System Z105 / Z205 or Z105/ Z206 (Adhesive Technologies Ltd, Auckland)
- East 221 epoxy (Polymer Developments, Auckland)

Mix and apply the epoxy in strict accordance with the manufacturer's instructions.

The method of epoxying shall be such that all spaces around the end plate of the steel component and the column face, and the spaces between the pin and the column timber, are thoroughly and completely filled with epoxy. The steel pins within the column adjacent to the internal steel components shall not be bonded to the epoxy. A lubricant shall be used to prevent bonding between the steel pin and epoxy.

Drill injection holes and air holes as required.

TIM.5.11 Camber
No camber is required. All members shall be supplied straight, to the tolerances specified below.

TIM.5.12 Finish
Exposed surfaces shall be finished with a sanded "Standard" finish in accordance with AS/NZS 1328:1998.

Apply one coat of an approved water-resistant sealer to all surfaces before delivery. No other painted surface finishes are required.

Touch up all damaged surfaces and cut ends before delivery. Application of finishes shall be strictly in accordance with the manufacturer's recommendations.

TIM.5.13 Wood fasteners
Wood fasteners shall be used as shown in the drawings.

Nails, Type 17 wood screws and coach screws shall be supplied by the Manufacturer.

All Type 17 wood screws that are 150mm and 200mm long shall have at least 70mm and 100mm of thread respectively.

TIM.5.14 Timber corbels
Timber corbels shall be attached to the beams and columns as shown in the drawings.

In addition to the wood fasteners attaching the corbels, corbels shall be glued to the beams and columns.

TIM.5.15 Cupped member
Members which have cupped shall be straightened to the best of the Manufacturers ability according to the suppliers recommendations.

TIM.6 FLOORING AND GRAVITY BEAMS

TIM.6.1 Joists
Joists shall be constructed including notches and coach screws as shown in the drawings.

TIM.6.2 Plywood
Plywood shall be 15mm untreated 5 ply, CD grade pinus radiata in accordance with AS/NZS 2269.

Plywood shall be nailed with 3.15mm x 60mm galvanised flat head product nails. Plywood is nailed down directly onto LVL joists at no greater than 200mm canters between each nail. Nails in plywood shall be hammered flush with the ply surface.

The top surface of the Plywood and all notches in the LVL joists shall be painted with two coats of approved exterior paint.

TIM.6.3 Joist, Primary Beam and Edge Beam hangers
Take delivery of steel joist and gravity beam hangers from the Project Manager or Engineer.

Attach hangers as shown in the drawings.

If any splitting of the LVL occurs all subsequent holes shall be predrilled.

TIM.7 MARKING
In addition to the requirements of ASNZS 1328 the members shall be marked with a suitable label to indicate their position in the assembled structure.

TIM.8 PROTECTION
Protect all structural timber members and steel components from the weather and from damage of any kind during transit, storage on site and erection.

Wrap or otherwise protect members from exposure to rain or other water. Store well clear of the ground. Discolouration due to differential exposure to sunlight shall be avoided.

Store and handle so that no damage occurs. Any damaged members will be liable for rejection or repair at no cost to the Principal.

TIM.9 DELIVERY TIME
All nominate manufactures shall deliver all structural elements on-site by the date specified by the Project Manager.

If a nominated manufacturer fails to deliver the structural elements by the date specified by the Project Manager the Principle reserves the right to reject the structural elements and nominate another manufacturer at no cost to the Principle.

TIM.10 QUALITY ASSURANCE DUCUMENTATION AND RANDOM TESTING
All nominated manufacturers shall complete quality assurance documentation provided by the Project Manager.

The Project Manager and Engineer shall perform random testing at the nominated manufacturer's facility on a date specified by the project manager.

STRUCTURAL TIMBER ERECTION

ERE.1 PRELIMINARY
Refer to the Preliminary and General Clauses of this Specification and to the General Conditions of Contract, which are equally binding on all trades. This section of the Specification shall be read in conjunction with all other sections.

ERE.2 SCOPE
Stage 1 of the contract includes the erection of the structural timber columns, beams, walls and flooring units and initial post-tensioning.

Stage 2 of the contract includes additional timber fastening, supply and placement of reinforcing mesh and casting of reinforced concrete slabs.

Stage 3 of the contract includes dismantling of the building and re-erection at a new site.

ERE.3 STAGE 1 - ERECTION

ERE.3.1 Members
Take delivery of all structural timber members and erect to accurate line and level as detailed. The members shall be erected as shown on the drawings, in accordance with all dimensions and notes. Where fixings are not shown, consult the Engineer.

All members shall be erected true and plumb and temporary erection bracing shall be introduced wherever necessary to take care of all vertical and lateral loads to which the structure may be subjected. Such bracing shall be left in place until the building is stable. Once all members are in place post-tensioning shall be performed.

Temporary fasteners shall be used to hold the beams in position. These fasteners shall be removed after stressing.

ERE.3.2 Post-tensioning
All initial post-tensioning shall be performed by a nominated subcontractor, BBR Contech Ltd.

All post-tensioning shall be 12.7mm diameter, 7-wire strands. The number of strands, position of strands in the walls and frames and force in the tendons shall be as shown in the drawings.

The force in each strand after stressing shall be +/-10% of the design force indicated on the drawings. The force in the tendons at any time shall not exceed 140 kN. Each tendon shall be stressed twice beyond the design force before the final stressing.

Use specialized tendon anchorages and shims from the Engineer as shown on the drawings.

ERE.3.3 Floor units
Erect floor units in place as shown on the drawings.

If any changes are required to be made to the flooring units dimensions, these shall be made by the contractor at no cost to the Principal.

Once floor units are in place they shall be fastened to the frame and edge beams as shown in the drawings.

Adjacent floor units shall be fastened together using standard removable 75mm wood screws at 500mm centres.

ERE.3.4 Pin connections
Take delivery of pins from Engineer and connect walls as detailed on the drawings.

ERE.3.5 Damage
Any damage on erected units is to be repaired and surface marks removed to the satisfaction of the Engineer.
Any damage to the surrounding site or equipment belonging to the Principal shall be repaired at no cost to the Principal.

ERE.3.6 Lifting equipment
Lifting equipment shall be of adequate capacity to safely lift and maintain work in a stable condition until it is securely braced. The contractor shall check construction loads imparted to the structure during erection. Any damage caused shall be repaired at no cost to the Principal.

ERE.3.7 Erection tolerances
The acceptable tolerances in the completed erected structure are as follows:

Column deviation from vertical line	+/- 5 mm
All other dimensions	+/- 5 mm

ERE.3.8 Temporary members
Temporary members shall be supplied were required to support the corner of floor units as shown in the drawings.
Temporary members shall be fastened using standard removable wood fasteners so that the floor units are safe and stable.

STAGE 2 – CONCRETE SLAB

CON.1 PRELIMINARY
Refer to the Preliminary and General Clauses of this Specification and to the General Conditions of Contract, which are equally binding on all trades. This section of the Specification shall be read in conjunction with all other sections and the structural drawings for stage 2 construction.
In this specification the Principal is the University of Canterbury (UC), the Engineer is the design engineer nominated by the University of Canterbury. The Project Manager and Contractor are from Mainzeal Ltd and are nominated by the University of Canterbury.

CON.2 SCOPE
This section of the Contract includes the following:

(a) Preparation of the concrete slab formworks and propping before the concrete pours.
(b) Supply, casting and curing of all insitu concrete on prefabricated plywood panels erected in Stage 1.
(c) Fabrication, supply and delivery of slab reinforcing bar and mesh.
(d) Fixing of anchor bars and starter bars into concrete.
(e) Requirements for concrete properties for the slab.

CON.3 MATERIALS AND WORKMANSHIP
The Contractor shall adhere to all requirements of NZS 3109:1997 (including Amendments 1and 2), except where specified otherwise herein or instructed otherwise by the Engineer. A copy of this standard shall be kept on the site and relevant parts read with the following clauses of this Specification. Concrete production shall be in accordance with NZS 3104:2003. Cement used in concrete shall be of New Zealand manufacture, complying with all requirements of NZS 3122:1995.

CON.4 INSPECTION
The Engineer may inspect construction in accordance with NZS 3109:1997, Clause 1.3.

CON.5 CONCRETE
Two batches concrete shall be provided, one for each floor of the building. The concrete shall be a special purpose concrete SL as defined in NZS3122.

The concrete shall achieve a slump of between 120mm and 150mm tested over a representative sample in accordance with NZS 3112.1. The Contractor will perform the slump tests. If the concrete does not meet the slump requirements the batch will be rejected.

The 28 day compressive strength of the concrete shall be greater than 25MPa, averaged over 3 samples tested in accordance with NZS 3112.2. The Engineer shall test the samples. Nine test cylinders shall be taken by the Engineer.

The average 56 day drying shrinkage of the concrete shall be no larger than 600 micro strain when tested in accordance with AS 1012.13. The Engineer shall test the samples.

Aggregates shall satisfy the requirements of Clause 6.4 of NZS 3109, and shall be 13 mm maximum size.

All concrete shall be supplied by a ready mixed concrete plant which has a current certificate of audit to demonstrate compliance with NZS 3104:2003. Chloride based accelerators shall not be used in any concrete.

CON.6 REINFORCEMENT
Reinforcement, including all necessary distance pieces required to maintain cover, shall be supplied and fixed by Contractor. The slab reinforcing shall be positioned and bent as per the drawings.

The Contactor, or a competent workman, is to be responsible for checking that reinforcement is not displaced during concreting. Any reinforcement so displaced is to be corrected by the Contractor.

CON.7 VIBRATORS
Vibrators shall be used for the placing of all concrete. Vibrators and their use shall comply with the requirements of NZS 3109, Section 7.6.

Vibrators shall be moved to new positions as frequently as necessary to ensure uniform vibration of the whole mass and fully compacted concrete. On no account shall vibrators come within 12 mm of the face of the formwork. Vibrators shall not be used to transfer concrete from one position to another.

CON.8 FORMWORK AND CONCRETING
Formwork shall be constructed by the Engineer.

Construction joints are not required.

The formwork shall be sealed at joints and edges to avoid any concrete spillage using a silicon gel or equivalent.

Stripping times shall not be less than those in NZS 3109, Clause 5.4 unless otherwise agreed by the Engineer.

CON.9 PROPPING
Propping shall be provided by the Engineer.

Each floor shall be propped before the concrete is poured and shall remain propped for at least 3 days.

CON.10 CONCRETE FINISHES

CON.10.1 Slab Finishes
Finish slabs with a steel trowelled finish as specified in NZS 3114:1987 Grade U3. Floating and subsequent finishing shall be at the correct times and intervals to obtain the quality of compaction and finish required. No trowelling in of fines or dry cement will be permitted.

The Contractor shall arrange the pouring of concrete to allow adequate time for floating and finishing.

All trowelling ridges shall be removed while green or by subsequent light grinding. Slabs not fulfilling the standard of finish required shall be ground smooth or otherwise treated to the satisfaction of the Engineer.

CON.10.2 Curing
All concrete shall be cured as defined in NZS 3109, Clause 7.8.

An acrylic resin curing membrane, Sika Antisol A or equivalent shall be applied over the entire slab.

CON.11 PROTECTION, REPAIRS AND CLEANING
Fairface concrete and slab surfaces shall be protected from damage at all times. Concrete surfaces shall be repaired or remade to the satisfaction of the Engineer at no extra cost.

All concrete work in the building, both insitu and precast, shall be closely inspected for faults in surface finish, damage to corners and edges, dirty marks, splashes or dribbles, and visible imperfections of every kind. Inspections are to be carried out within 14 days of placing the concrete. Any remedial work shall be carried out within a further 14 days.

Significant defects in concrete finish shall be referred to the Engineer for specific instructions on repair work. Patching or filling of concrete and making good broken edges and corners shall be done with coloured sands and cement where necessary, to match precisely the colour of the surrounding concrete when dry. Epoxy or similar adhesives shall be used when required.

The removal of surface markings shall be most carefully done by appropriate methods such as wire brushing, pumice stoning, carborundum stone, or washing and scrubbing; such as will remove the marks without scratching, discolouring or otherwise affecting the surrounding or underlying concrete.

CON.12 CHASES, PENETRATIONS AND UPSTANDS
No concrete shall be cut or hacked unless specific approval is obtained from the Engineer. This includes existing concrete.

A.8. MATERIAL INFORMATION

Material tests were performed on the concrete which was used for the floor slab. This was required to ensure that the concrete satisfied the design specification (see above) in terms of strength and shrinkage. Material tests were not performed on the Laminated Veneer Lumber (LVL) timber in the test building. Because LVL is anisotropic, the material tests required to accurately define the material properties quickly become cumbersome. Furthermore, complicated end bearing effects may significantly alter the apparent strength of the timber. Instead a combination of existing material test data (Newcombe 2008) and manufacturer information were used to approximate the properties of the material.

A.8.1. Laminated Veneer Lumber Timber

Some basic material properties provided by the LVL producers (Futurebuild 2010; NelsonPine 2010) are given in Table A.3. The average modulus of elasticity was determined by considering an factory test data (Banks 2010), rather than lower-bound design values.

Table A.3. Manufacturer specified LVL material properties

Parameter	Symbol	Units	Value
Modulus of elasticity	E	MPa	11000
Shear modulus	G	MPa	660
Bending strength	f_b	MPa	48
Tension parallel to grain	f_t	MPa	30
Compression Parallel to grain	f_c	MPa	45
Shear in beams	f_s	MPa	6.0
Compression perpendicular-to-grain	f_p	MPa	12

The stiffness of the LVL perpendicular-to-grain is not specified by the LVL manufacturers. However, material tests performed by Davies and Fragiacomo (2008), which was documented in Newcombe (2008), suggest a perpendicular-to-grain elastic

modulus of approximately 300MPa. This value is not expected to vary for different grades of LVL, according to the manufacturers (Banks 2010). However, these tests did not consider edge bearing or stress diffusion that would occur in a continuous length of timber (such as a column) subjected to localized compression. Newcombe (2008), showed that edge bearing and stress diffusion effectively increased both the stiffness and strength of the timber element aligned perpendicular-to-grain. Furthermore, LVL material tests presented in Newcombe (2008), indicate the manufacture specified characteristic compressive stresses for LVL are accurate. In Appendix B, experimental data for the test building is analyzed to verify the accuracy of LVL material properties.

A.8.2. Concrete cylinder tests

Ten concrete cylinders were taken halfway through the pour of the floor slabs for the test building. Four cylinders were placed in the fog room and tested at 28days (C1 to C4). Three cylinders were left in ambient air on-site and tested at 28days (C5 to C7). The three remaining cylinders were left in the fog room and tested the same day as seismic testing on the test building began (C8 to C10).

Table A.8.4 – Concrete cylinder tests

Cylinder	Compressive strength (kN)	Compressive strength (MPa)	Average (MPa)
C1	18.6	23.7	
C2	22.8	29.1	
C3	17.8	22.7	
C4	20.8	26.5	**25.5**
C5	19.9	25.4	
C6	18.8	24.0	
C7	19.4	24.7	**24.7**
C8	17	21.7	
C9	25.3	32.3	
C10	20.6	26.3	**26.7**

The overall average 28 day compressive strength was 25.2MPa, marginally within the specification.

A.8.3. Concrete shrinkage tests

Determining the shrinkage of the concrete slab was crucial to the experimental test setup. If the slab shrinkage was significant the floor units would sag. Significant sag would have made it difficult to connect the in-plane loading apparatus and could have caused the floor to buckle.

Standardized shrinkage tests according to AS1012.13 (1992) were performed on the floor slab concrete. As per the standard 3 prism samples (S1, S2 and S3) were taken and the shrinkage was calculated up to 56 days after the concrete pour.

Table A.8.5 – AS1012.13 Shrinkage measurements

Time (days)	Strain (microstrain)			Average (microstrain)
	S1	S2	S3	
0	0	0	0	0
21	412	444	412	423
35	540	552	500	531
56	636	672	628	645

The specified shrinkage limitation for the concrete was 600 microstrain at 56 days (see the specification). Hence, the concrete was not within the specification by 45 microstrain.

A sample of was taken to more accurately determine the actual shrinkage deformation of the timber-concrete composite (TCC) floor. The sample is 500×500×50mm and had similar boundary conditions to the actual concrete slab (see Figure A.8.1) such as a similar surface area to volume ratio (10%) and plywood formwork on the base. No steel reinforcement was included in the sample. All measurements were taken at approximately midday.

Figure A.8.1 – Concrete slab sample

The deformation was recorded for 3 gauge lengths over a period of 150 days. The recorded deformation is plotted below.

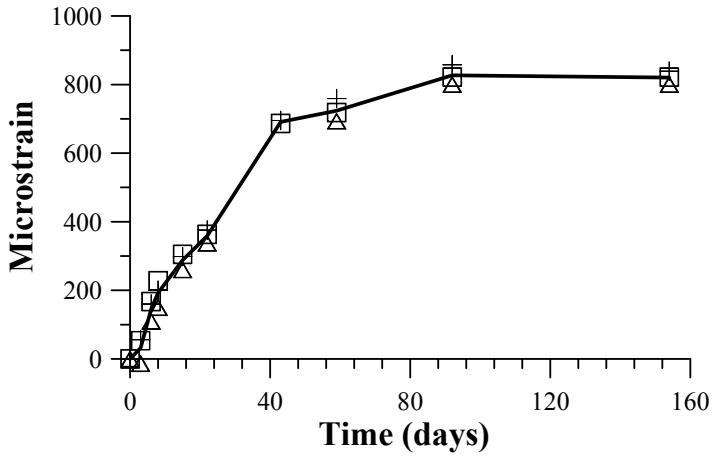

Figure A.8.2 – Shrinkage of concrete slab sample

The following conclusions are drawn:

- The shrinkage strain plateaus at approximately 820microstrain.
- This is significantly larger than the shrinkage of the AS1013.12 samples.
- Using an effective modulus approach (Fenwick and Mackechnie 2009), assuming fully composite action, a 10mm floor deflection is predicted due to shrinkage.

A.9. CONSTRUCTION OF THE TEST BUILDING

All prefabricated timber components were delivered and stacked on-site (see Figure A.9.1a). The timber components were assembled by professional contractors (from Mainzeal) whom have experienced in the construction of concrete and steel buildings. The post-tensioning was applied to the frames and walls by specialist contractors (BBR Contech Ltd). Subsequently, a subcontractor (Allied Concrete Ltd) cast the concrete slab in-situ.

The assembly of the timber components (see Figure A.9.1) took 15 hours (2 working days) using 4 construction workers (less than half of the construction time predicted by Mainzeal). Additional works involved post-tensioning and casting the floor slabs. The post-tensioning (see Figure A.9.1c) was completed in 2 hours (approximately 15% of the assembly time). The concrete pouring, leveling and floating took 1 day (Figure A.9.1d). A pre-camber was not built into the floor system; hence propping was required for 48 hours.

Half of the prefabricated timber components were delivered to site one day late. Notably, this had little impact on the construction time. The modularity and simplicity of the structural system allowed many alternative construction sequences.

The fabrication tolerances (see the above specification) significantly affected the speed of construction. Equivalent buildings in precast concrete typically require that building tolerances are taken up by grout pads between the beam and column faces. Using grout (or epoxy) pads is labor intensive, requires skilled labor and strict quality assurance onsite. By specifying strict tolerances and performing an accurate foundation setout, these measures can be avoided. In addition, strict tolerances ensure that the frames remain straight and the walls remain plumb during stressing.

Aspects of onsite safety and labor significantly increased the construction speed, when compared to steel and concrete. Handrails could be attached to beams before they were lifted in position. Structural elements were significantly lighter, compared to concrete, reducing the required cranage time and risk of injury when positioning elements. Floor

units created a safe working platform and were fastened to beams from the top, avoiding the need for ladders to fasten the joists. Using prefabricated elements reduced onsite clutter and minimized the number of workers on-site, creating a more efficient work environment.

a) **b)**

c) **d)**

e) **f)**

Figure A.9.1 Construction progress a) Start b) At the end of day 1 c) Floor unit d) At end of day 2 e) Applying post-tensioning d) Concrete pour

APPENDIX B

FURTHER DETAIL ON THE EXPERIMENTAL RESPONSE OF THE TEST BUILDING

This appendix provides further details for the experimental response of the test building, summarized in Chapter 5. The global hysteretic results for all tests described and illustrated. Subsequently, the connection-response of the wall and frame system is analyzed in an attempt to evaluate the contribution from each structural component to the total strength of the building.

Other parameters are examined to further characterize the experimental response and performance of the building. These parameters include tendons forces, frame elongation, slab elongation, column and wall inclination, timber properties and floor sagging deformation.

B.1. GLOBAL BUILDING RESPONSE

Within this section, further details (in addition to Chapter 5) are provided on the global response of the test building in terms of overturning moment (OTM) versus drift for all of the seismic tests.

B.1.1. Uni-directional response

Figure B.1.1a shows the hysteretic response of the building with post-tensioned (PT only) frames without floor diaphragms (Stage 1, Test 1). The figure demonstrates that there is limited inelastic response with little hysteretic energy dissipation, as shown in Figure B.1.2a, up to the design level of displacement (2% interstorey drift). There is a slight loss of strength and stiffness observed in Figure B.1.1a. This can be partially

attributed to inelastic deformation of the timber in the west beam-column (BC) connections, induced by concentrated loads applied by the loading apparatus. The presence of inelastic (or permanent) deformation is verified by considering the area-based damping in Figure B.1.2a. There is a significant reduction in the energy dissipation of the frames from the first to the second and third cycles, indicating that permanent deformation of the timber has occurred during the first cycle. Furthermore, some of the column-base connection attachments failed during this test (see Appendix C), which equated to approximately 12% of the frame capacity, and contributed to the loss strength and stiffness for the frame system. This may have also affected the energy dissipation potential of the system.

The frame systems moment capacity is higher than predicted at 2% drift by approximately 17%. However, taking into consideration that some of the column-base connections failed (equating to approximately 215kN.m), this percentage is likely to increase to approximately 35% (430kN.m). The hysteretic damping varies between 5% and 3%, which is much lower than the 12% predicted. This indicates the base connections are not providing as much energy dissipation to the system as expected. This could be due to slippage in the base connections and larger than predicted non-dissipative contributions to the OTM. Furthermore, it is likely that there are modelling inaccuracies associated with the damping predictions (see Appendix A).

External (non-stressed) reinforcement was added to the BC connections, creating a Hybrid system (Stage 1, Test 2). Figure B.1.1b shows that there is minimal loss of stiffness and strength. Considering the hysteretic damping, at small drifts there is little difference between the first and subsequent cycles (see Figure B.1.2b). At drifts in excess of 1%, the hysteretic damping reduces after the first cycle (see Figure B.1.2b). This indicates that further inelastic deformation occurred during this test at Drifts above 1%. The moment capacity is higher than predicted by 36% (480kN.m) at 2% drift. Again, the hysteretic damping varies between 3% and 5% and is significantly under the predicted value (14%). Hence, the BC connections are not providing significant hysteretic damping to the system. There was only a slight increase in frame strength at

2% drift due to the presence the external reinforcement. See Chapter 5 for more detail regarding the effects of external reinforcement.

Figure B.1.1c shows the hysteretic response for the building with post-tensioned (PT only) frames and TCC floor diaphragms (Stage 2, Test 1). There is no significant loss in stiffness and strength. The hysteretic damping only reduces slightly from the first cycle to subsequent cycles (see Figure B.1.2c), indicating minor inelastic response in either the timber elements or the floor slab during this test. This inelastic deformation is likely to be derived from minor cracking of the concrete slab and crushing of the timber at higher drifts (in addition to the crushing that occurred in previous tests). The moment capacity is 46% (570kN.m) higher than predicted. With the floor diaphragm, the difference between the experimental and predicted response at 2% drift is exacerbated. The area-based damping has increased to a maximum of approximately 6% but is well under the predicted value (12%). There was a slight increase in the strength of the frame system due to the presence of the TCC floor. Refer to Chapter 5 for more detail on the influence of the floor on the response of the frame.

For the Hybrid frames (Stage 2, Test 2) with floor diaphragms, the hysteretic response for the building was highly stable, as shown in Figure B.1.1d, with no apparent stiffness or strength degradation. The hysteretic damping is effectively equal for each cycle (Figure B.1.2d), indicating that there is no further significant inelastic deformation of the timber or the floor slab (during this test). The moment capacity is 59% (790kN.m) higher than predicted. The area-based damping varies between 3% and 6% and is well under the predicted value (14%). Again, external reinforcement did not provide significant energy dissipation to the system.

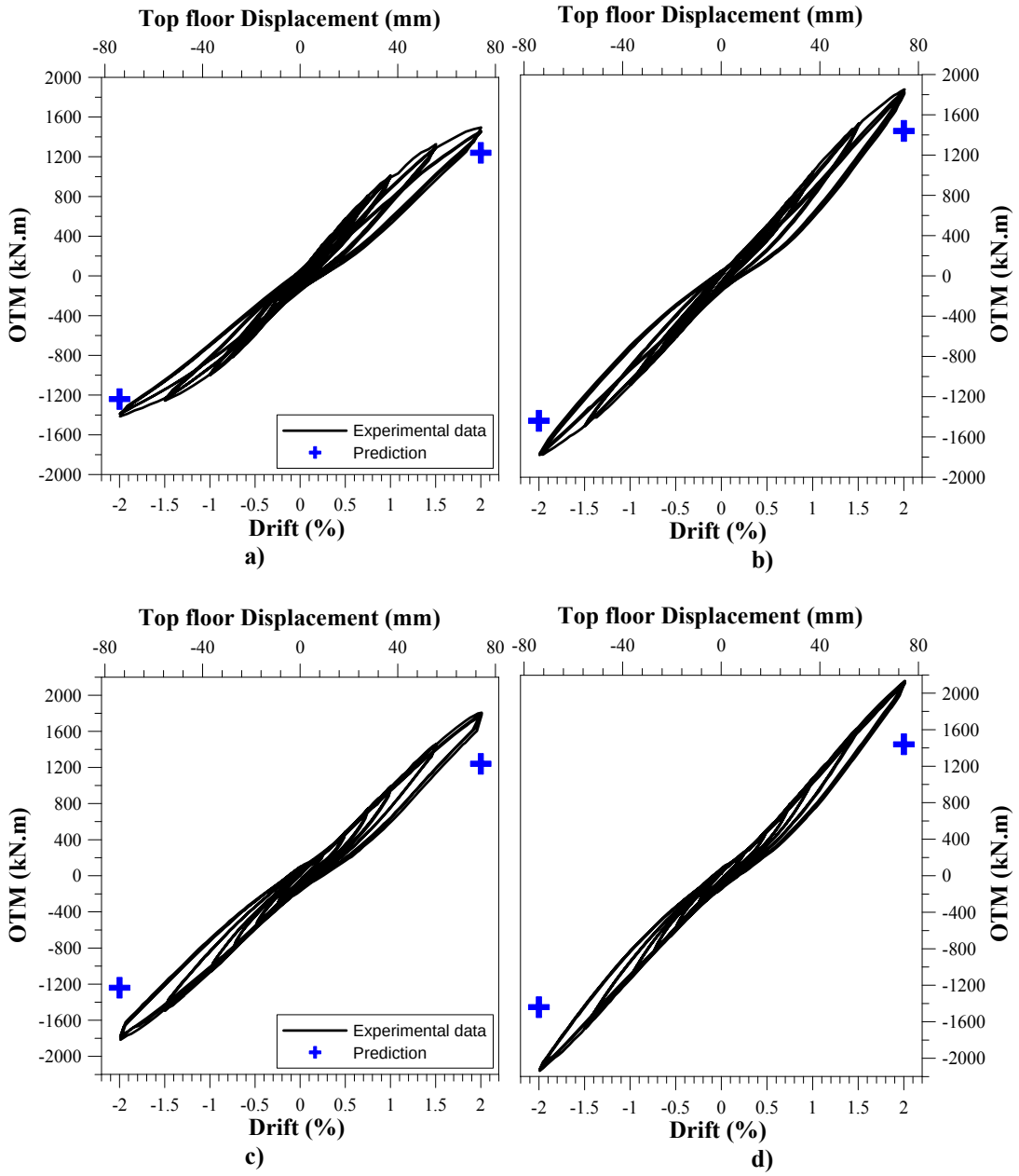

Figure B.1.1. Uni-directional hysteretic response of frames: a) PT only (Stage 1, Test 1) b) Hybrid (Stage 1, Test 2) c) PT only with floor (Stage 2, Test 1) d) Hybrid with floor (Stage 2, Test 2)

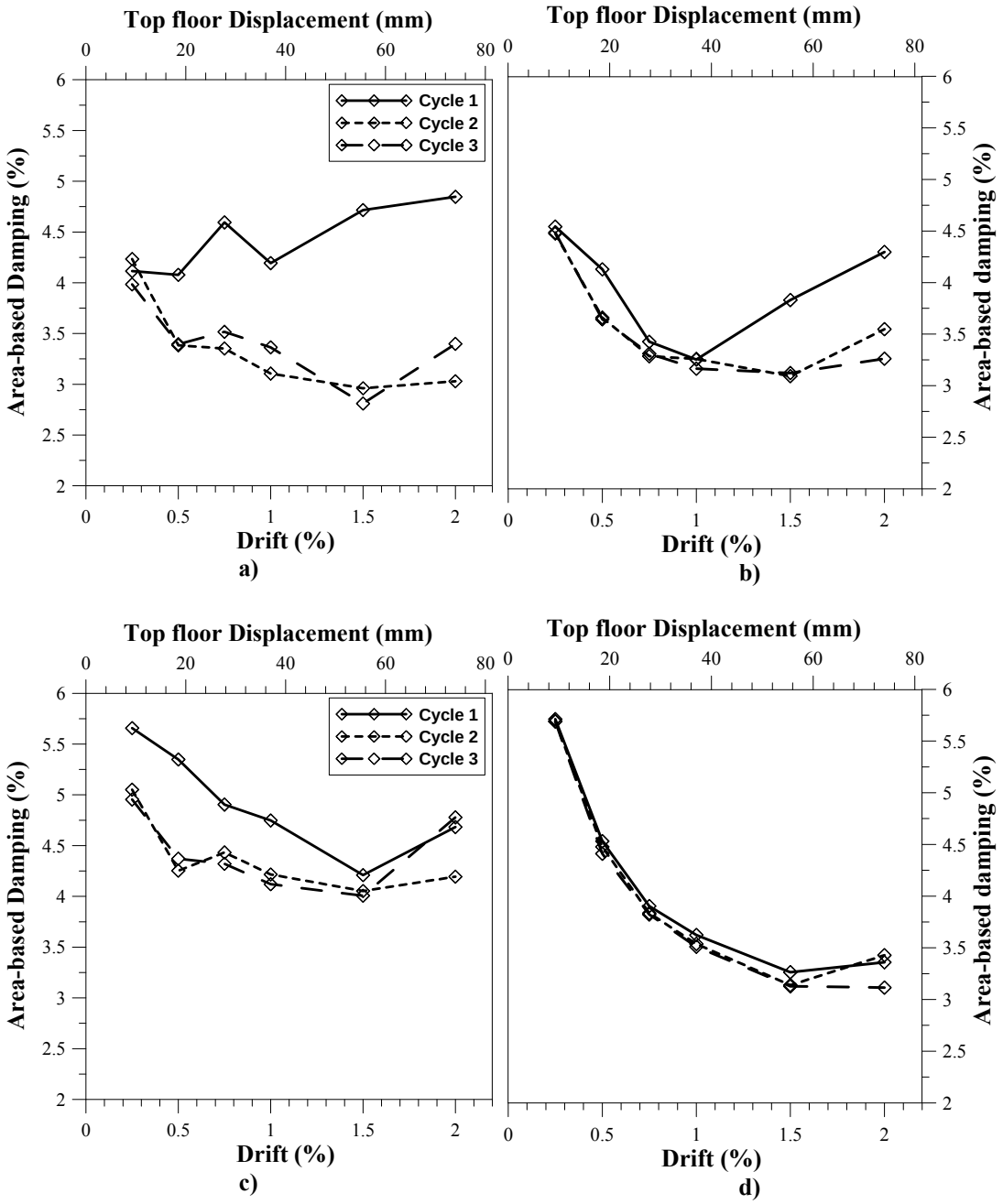

Figure B.1.2. Uni-directional area-based damping of frames: a) PT only (Stage 1, Test 1) b) Hybrid (Stage 1, Test 2) c) PT only with floor (Stage 2, Test 1) d) Hybrid with floor (Stage 2, Test 2)

B.1.2. Uni-directional wall response

The hysteresis loops for all the uni-directional wall tests (from Stage 2) are described below and compared the capacity predictions. During testing, it was determined that there was significant overturning moment capacity derived from the interaction of the floor system and the wall response. Hence, the walls were tested with and without edge beam support to the columns to gauge the relative contribution of edge beams and the floor diaphragm to the capacity of the system.

Figure B.1.3a shows the hysteretic response of building with post-tensioned (PT only) walls with edge beam support (Stage 2, Test 3). The response is essentially elastic up to 2% drift. The hysteretic damping is relatively low (see Figure B.1.4a), compared to the frames, and reduces slightly for the second and third cycles, indicated minor levels of inelastic deformation in the wall elements or the floor slab. The overturning moment capacity of the system is 102% higher than predicted at 2% drift. This can be attributed to the coupling action provided by the floor system and edge beams and the out-of-plane response of the frames. The frame base connections provide approximately 390kN.m of overturning moment acting out-of-plane. Subtracting this from the peak experimental response gives approximately 940kN.m. With this reduction, the experimental response is still 43% (280kN.m) higher than predicted. Hence, the coupling action provided by the floor system and the edge beams increases the system capacity by approximately 40%, assuming that the prediction methodology is accurate. This coupling effect is likely to be amplified due to the short span between frames, which was required due to experimental testing constraints. See Chapter 5 for more detail in the effect of the floor system on the strength of the wall system.

The hysteretic response of the building with Hybrid walls (Stage 2, Test 4) is shown in Figure B.1.3b. The system response is stable and has no significant reduction in hysteretic damping with subsequent cycles (see Figure B.1.4b), indicating that there is no (further) inelastic deformation in the wall elements or slab. The additional reinforcement (UFP couplers) provided limited energy dissipation to the wall system. The hysteretic damping remained effectively similar for each cycle, indicating no

inelastic deformation of the wall elements. The moment capacity of the wall system is 70% higher than predicted at 2% drift. Subtracting the out-of-plane moment capacity of the frame, the experimentally achieved moment is still 31% (320kN.m) higher than predicted. The hysteretic damping varies between 7% and 3%, which is much less than predicted (17%). Because the non-dissipative components of the wall system are much stronger than predicted, the overall system damping is significantly reduced. Refer to Chapter 5 for a comparison of the wall response will and without UFP couplers.

The hysteretic response of the post-tensioned (PT only) wall system, without edge beam supports is presented in Figure B.1.3c (Stage 2, Test 6). Again, the system is stable. There is little hysteretic damping, which varies from 4% to 2% (see Figure B.1.4c). The moment capacity of the wall system is 87% higher than predicted. Subtracting the out-of-plane moment capacity of the frames, the experimental moment capacity is still 28% (190kN.m) higher than predicted.

Figure B.1.3d gives the hysteretic response of the Hybrid wall system without edge beam supports (Stage 2, Test 5). The system is highly stable, exhibiting no significant loss of stiffness or loss of hysteretic energy dissipation potential (Figure B.1.4d). The moment capacity is 58% higher than predicted. Without the moment contribution for the frame acting out-of-plane, the capacity is still 20% (200kN.m) higher than predicted. The achieved hysteretic damping is similar with or without the edge beam supports (3% to 7%), and is much lower than predicted (17%).

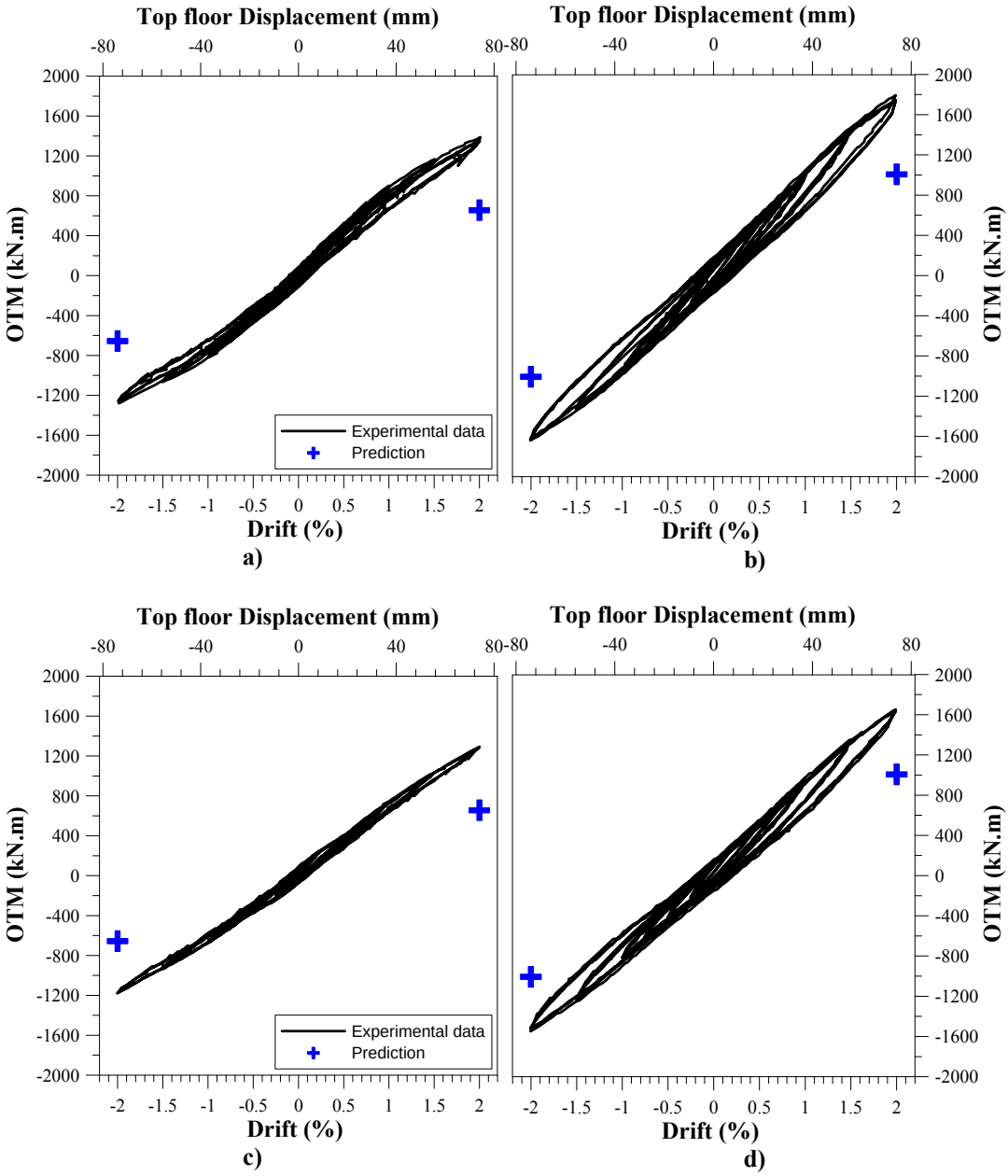

Figure B.1.3. Uni-directional hysteretic response of walls: a) PT only (Stage 2, Test 3) b) Hybrid (Stage 2, Test 4) c) PT only, without edge beam support (Stage 2, Test 6) d) Hybrid, without edge beam support (Stage 2, Test 5)

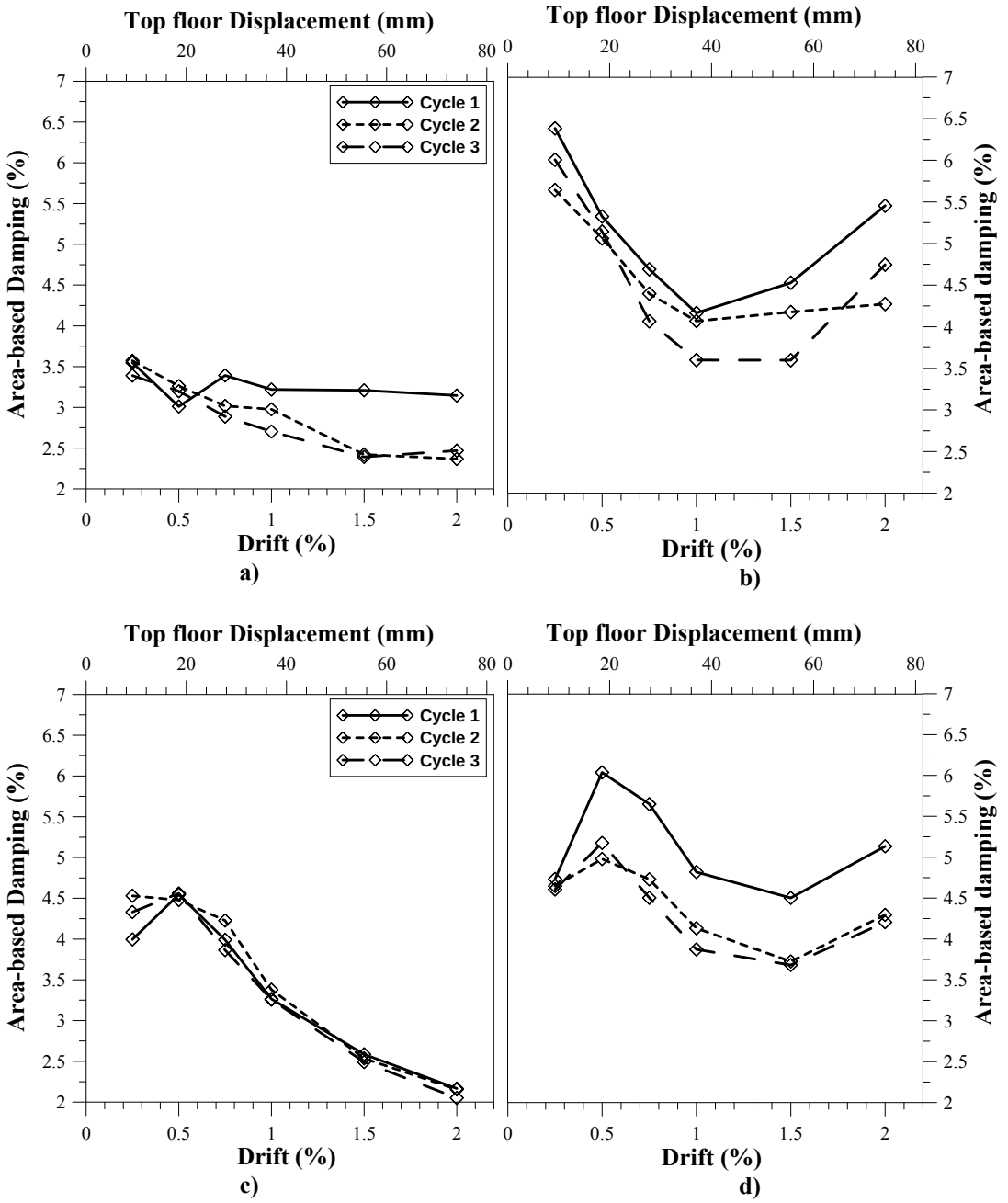

Figure B.1.4. Uni-directional area-based damping of walls: a) PT only (Stage 2, Test 3) b) Hybrid (Stage 2, Test 4) c) PT only, without edge beam support (Stage 2, Test 6) d) Hybrid, without edge beam support (Stage 2, Test 5)

B.1.3. Bi-directional Response

Two bi-directional tests were performed. For the first test (Stage 2, Test 7), additional external reinforcement was present on both the frames and walls. Another test was attempted (Stage 2, Test 7), using only the final displacement amplitude of the loading protocol (corresponding to 3% drift). Fracture of some of the column-base reinforcement occurred due to low cycle fatigue (see Appendix C) after multiple tests, which resulted in the termination of the test after two bi-directional clovers were complete. The global bi-directional response is presented by calculating the total overturning moment (OTM) capacity versus the drift applied to the control columns (termed control drift in Chapter 5), in each orthogonal direction. The area-based damping is plotted for the uni-directional cycle (in the NS and EW direction), subsequent to the bi-directional clover.

Figure B.1.5c and d, show the hysteretic response of building, in the EW and NS direction respectively, with Hybrid frames and walls (Stage 2, Test 7). There is a noticeable loss of strength in the EW (frame) direction above 2% drift, due to a column fracture at the top floor (see Appendix C) and further inelastic deformation in the BC connections. In the NS (wall) direction, there is also some loss of strength and stiffness for the 3% drift cycle, indicating inelastic deformation of the timber wall elements. The area-based damping curves show an increase in energy dissipation at 3% drift, which is likely to be due to increased activation of the UFP couplers and, to a limited extent, inelastic timber deformation at the base of the wall elements. In the frame direction, the overturning moment capacity for the system is 48% higher than predicted at 2% drift. In the wall direction, the moment capacity of the system 58% higher than predicted. The area-based damping is still much less than predicted (see Figure B.1.6).

Figure B.1.5a and c, show the achieved hysteretic response of building, in the EW and NS direction respectively, with post-tensioned (PT only) frames and walls (Stage 2, Test 8). There was significant reduction in stiffness and strength after Test 7. The moment capacity is still approximately 6% and 48% higher than predicted for the frame

and wall directions respectively. The area-based damping values for the one complete cycle are 5% and 7%, still well under the predicted value (12%).

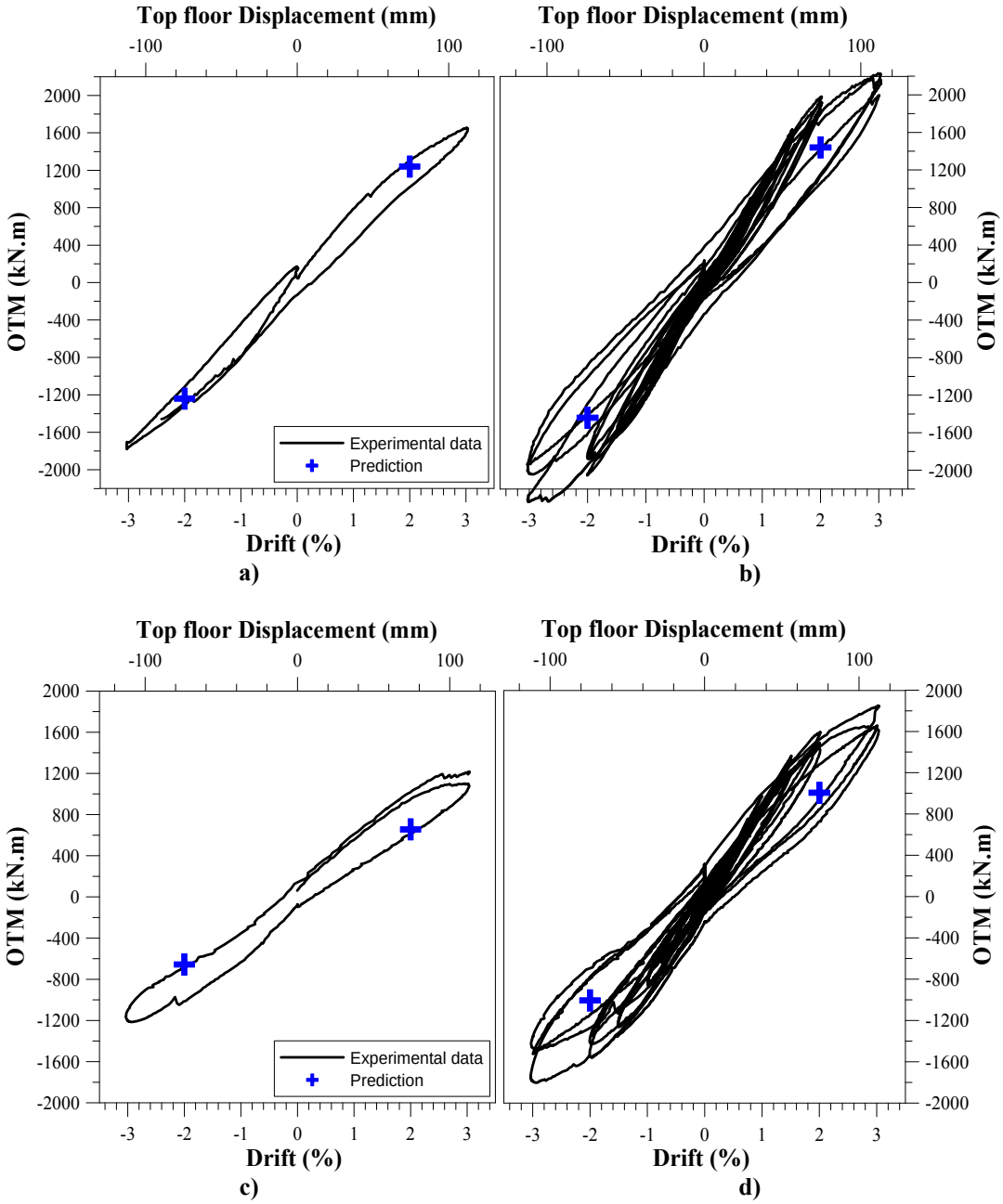

Figure B.1.5. Bi-directional hysteretic response a) EW direction, PT only (Test 8) b) EW direction, Hybrid (Test 7) c) NS direction, PT only (Test 8) d) NS direction, Hybrid (Test 7)

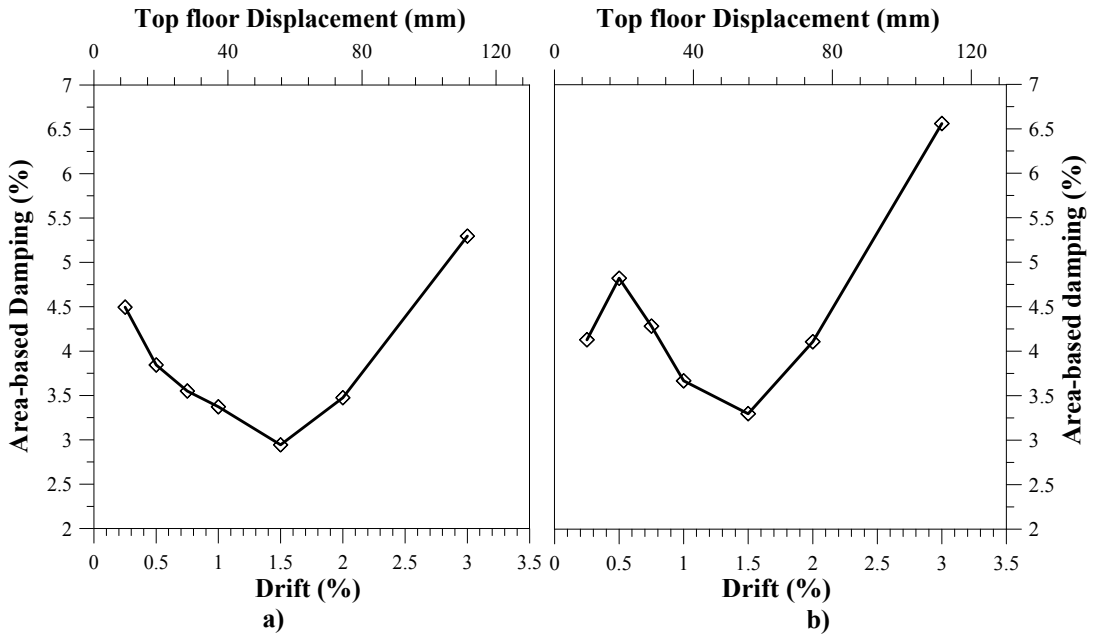

Figure B.1.6. Bi-directional area-based damping: a) EW direction, Hybrid (Test 7) b) NS direction, Hybrid (Test 7)

B.2. CONNECTION RESPONSE

The moment in the connections can be estimated using strain gauges and potentiometers that placed throughout the test building. Curvatures, ϕ, are calculated using the strain gauge or potentiometer data, the second moment of inertia, I, and the modulus of elasticity, E. Hence:

$$M = \phi EI$$

Manufacturers of LVL provide MOE design values that are an estimated lower bound (Futurebuild 2010; NelsonPine 2010). It is likely that the average MOE of LVL is higher than specified. An MOE for the frames and walls was assumed to be 11GPa. This value is recommended by the LVL producers (Banks 2010) based on factory material tests and is within the range in the specification shown in Appendix A.

B.2.1. Uni-directional frame tests

For the north frame, 90mm strain gauges where attached to some of the beams and columns. These are used to estimate the curvatures, and hence moments in the structural elements. Using linear extrapolation, from the position of the strain gauges, the moment at the beam-column (BC) connections can be evaluated. Potentiometers that straddle each BC connections are used to approximate the connection rotation.

Caution was exercised when interpreting the strain gauge data. If the strain gauges were placed in a region where Bernoulli's linear strain assumption does not apply, the evaluated connection moment would be inaccurate. Regions of 'disturbed' strain (NZS3101 2006) surround the BC connection interface. From analysis of the stress flow around a BC connection (see Chapter 6), it is evident that the strain gauges placed on the columns near the BC connections are likely to be in a region of disturbed strain. For the beams, the strain distribution appears to be effectively linear. Hence, the data from the column strain gauges is not considered, other than around the column-base connections.

To present the data each connection in the north frame is labeled, as shown in Figure B.2.1. For each test, the connection moment is calculated and plotted against the control drift and the connection rotation. All moments are taken as being positive for positive drifts. It is noted that connection potentiometers were not present around the connections L2-3 and L3-3 (see Figure B.2.1).

The contribution of connection rotation to the total interstorey drift is investigated. The ratio of the drift due to connection rotation, θ_{con}, and the control drift, θ_D, is plotted. Furthermore, an attempt is made to evaluate the depth of the compression region (neutral axis depth) within the BC connections. However, due to shear distortion in the column, the neutral axis depth is difficult to define accurately, as illustrated in Figure B.2.2.

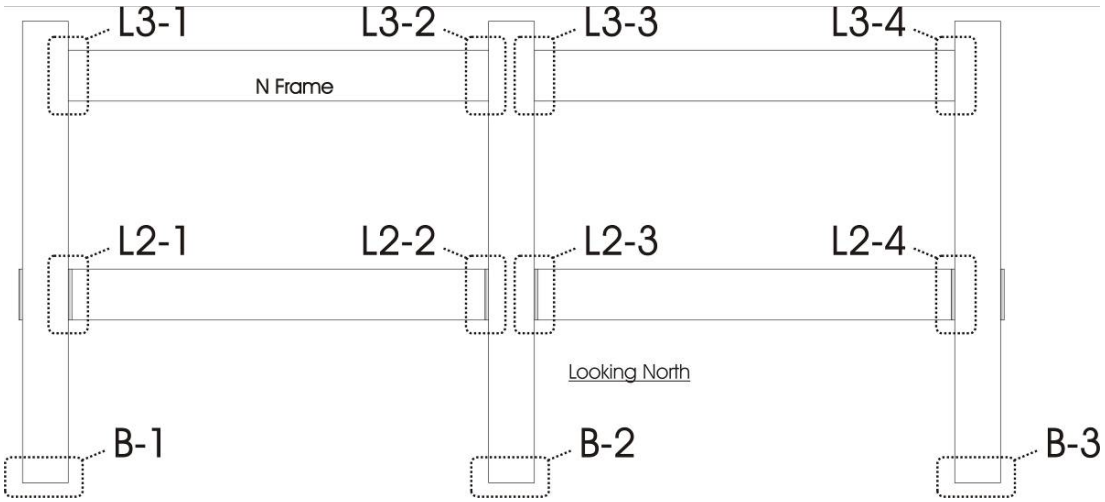

Figure B.2.1. Connection labels on north frame

Stage 1: Test 1 and Test 2

Figure B.2.4a, c and d show the moment-drift response of the frame connections in Test 1. Area enclosed within the hysteresis for the Level 3 (L3) connections on the west side (L3-1 and L3-2) indicate inelastic deformation of the timber for positive drifts. As noted previously, the increased inelastic deformation in the west connections is due to the additional axial forces applied by the loading apparatus. The additional axial force appeared to increase and decrease the moment within the connection for positive and negative drifts respectively. However, there is little difference in connection moment between the west and east connections, which may indicate that inelastic deformation has limited the capacity of the connection to some extent. The hysteretic response for Test 2 is given in Figure B.2.4b, d and f. There is little hysteretic energy dissipation at the L3 connections. Hence, most of inelastic deformation appears to have occurred during Test 1.

The moment-drift response of the Level 2 (L2) connections (see Figure B.2.4c and d) varies significantly for each connection. Intuitively, it is expected that the west connections (L2-1 and L2-2) would have a larger capacity than the east connections (L2-3 and L2-4), due to additional axial load applied by the rams, but the opposite is true. It is possible that either the strain gauge data is inaccurate or secondary effects

have caused additional axial forces in the east bay. This secondary effect could be that axial force from L3 was transferred to the east bay on L2 via shear in the interior column. The higher axial force in the east bay (on L2) could explain the increased moment capacity. Also, each beam-column connection may have had significantly different stiffness, due to alternative fabrication techniques. Half of the columns were manufactured with the internal steel plate arrangement (see Appendix A) epoxied into position. This would have significantly increased the connection stiffness. Additional reinforcement across the BC connections has not provided significant energy dissipation to the frame system on L2 or L3. Refer to Chapter 5, for a discussion on the effectiveness of additional reinforcement.

For Test 1, the column-base connections (see Figure B.2.4e) give a pinched hysteretic response with significant strength loss, indicating that there is anchorage slip and failure of the external reinforcement. For Test 1, the external reinforcement anchorages failed for some connections (most notably B-3), as discussed in the previous section (and illustrated in Appendix C). The connection response partially explains why the frame system has low levels hysteretic damping when compared to predictions (see Chapter 5 for more detail). The exterior connections (B-1 and B-3) show significant variation in moment capacity for positive and negative drifts due variations in column axial forces caused by lateral loading. The column-base connections are more effective for Test 2 (compared to Test 1), as shown in Figure B.2.4f. This is because a pre-tension was applied to the external reinforcement and anchorages were repaired. Yet, the hysteretic energy dissipation provided by the base connections was still much less than predicted (for an elastic-plastic hysteresis), due to pinching (see Chapter 5).

The connection moment versus rotation response is shown in Figure B.2.5. For Level 3, there is much less connection rotation in the positive quadrant (which corresponds to positive drift). This is due to axial forces applied by the rams on the west external columns, which stiffen the connection, resulting in less rotation. For Level 2, the moment-rotation response is variable for each connection and indicates the complex distribution of axial load through the connections or variation in connection flexibility,

as mentioned above. Connections that used non-epoxied internal steel plates exhibit a low initial stiffness. Figure B.2.5c indicates when the ram is in compression, most of the axial force transfers to the east connections increasing the moment and reducing connection rotation. When the ram is in tension, the axial force appears to be highest in the east connections increasing moment and reducing rotation. Comparing Test 1 and 2 (without and with external reinforcement respectively), for Test 2 there is significantly less rotation for both Level 2 and 3 connections due to the presence of additional reinforcement. This is discussed further in Chapter 5.

Figure B.2.6 illustrates the proportion of the connection rotation and total drift (θ_{con}/θ_D) is highly variable (20-60%) for each BC connection. Again, this indicates a complex distribution of axial forces and variable connection stiffness throughout the frame. The experimental data indicates that for many connections there is a finite connection rotation at small interstorey drifts, before the connections have decompressed, contrary to existing precast-concrete theories (Palermo 2004; Pampanin et al. 2001). However, the precision of experimental data at such small displacements is questionable. The connection rotation of the column-base connections is approximately 80% of the interstorey drift at 2% drift.

The neutral axis depth (or compression region) is difficult to accurately define due to deformed profile of joint panel (see Figure B.2.2). However, approximate results are given in Figure B.2.7, using linear extrapolation from potentiometers at the centerline and edges of the beams. The neutral axis depth is slightly larger on Level 3 compared to Level 2. The neutral axis depth for the column-base connections is highly variable, due to the performance of the external reinforcement and significant changes axial load. There is no apparent difference in neutral axis depth, for a given connection rotation, for Test 1 and 2. For the Level 2 and 3 connections the minimum neutral axis depth equates to approximately 80mm and 160mm respectively at 2% drift. This corresponds well with observations, as shown in Figure B.2.3.

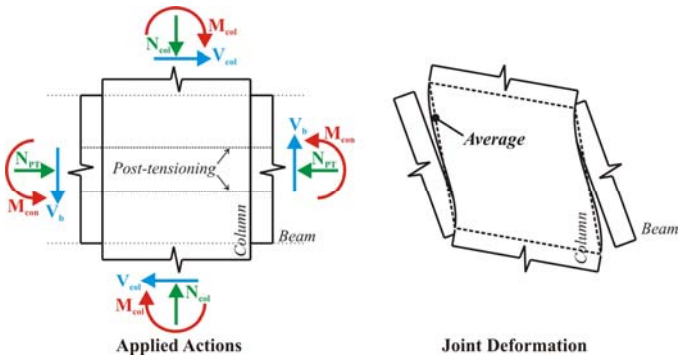

Figure B.2.2. Shear distortion of BC joint panel

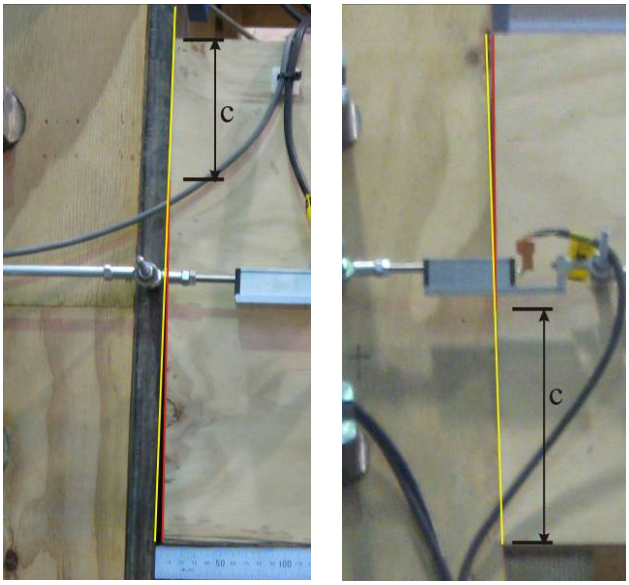

a) **b)**

Figure B.2.3. Photograph of neutral axis for Test 1: a) Level 2 b) Level 3

The connection moments are higher than the predictions (see Appendix A) for the BC connections. Furthermore, for the prediction, the connection deformation was expected to be approximately 60% of the total drift (for Test 1 and 2). Observing the experimental data (see Figure B.2.6); the connection deformation only exceeds 60% for few connections. Hence, for a given connection rotation, the moment capacity of the connections is significantly higher than predicted, especially for Level 3 connections. In addition, the prediction did not capture the significant reduction in connection rotation when the external reinforcement was added. During testing, a pre-load was used for the

energy dissipation to ensure the bars activated under small rotations in tension. This pre-load was not accounted for in the prediction and potentially has increased the shear deformation of the joint panel region.

For the column-base connections, the predictions match relatively well with experimental data, considering that the experimental response was considerably pinched. Furthermore the predictions assumed that the elastic deformation of the column member was insignificant and, hence, the connection rotation was equal to interstorey drift. This assumption gives an error in connection rotation of approximately 20%. Discrepancy between the actual and predicted connection rotation may have also been increased by small amounts of sliding, as well as flexural and shear deformation of the column.

The neutral axis depth was predicted to be 40% and 75% of the beam depth for Level 2 and 3 respectively. The actual neutral axis depth, from experimental data, was significantly less than predicted, giving approximately 30% and 45% for Level 2 and 3 respectively. This further indicates that existing procedures for predicting the connection response (Appendix A) are inaccurate.

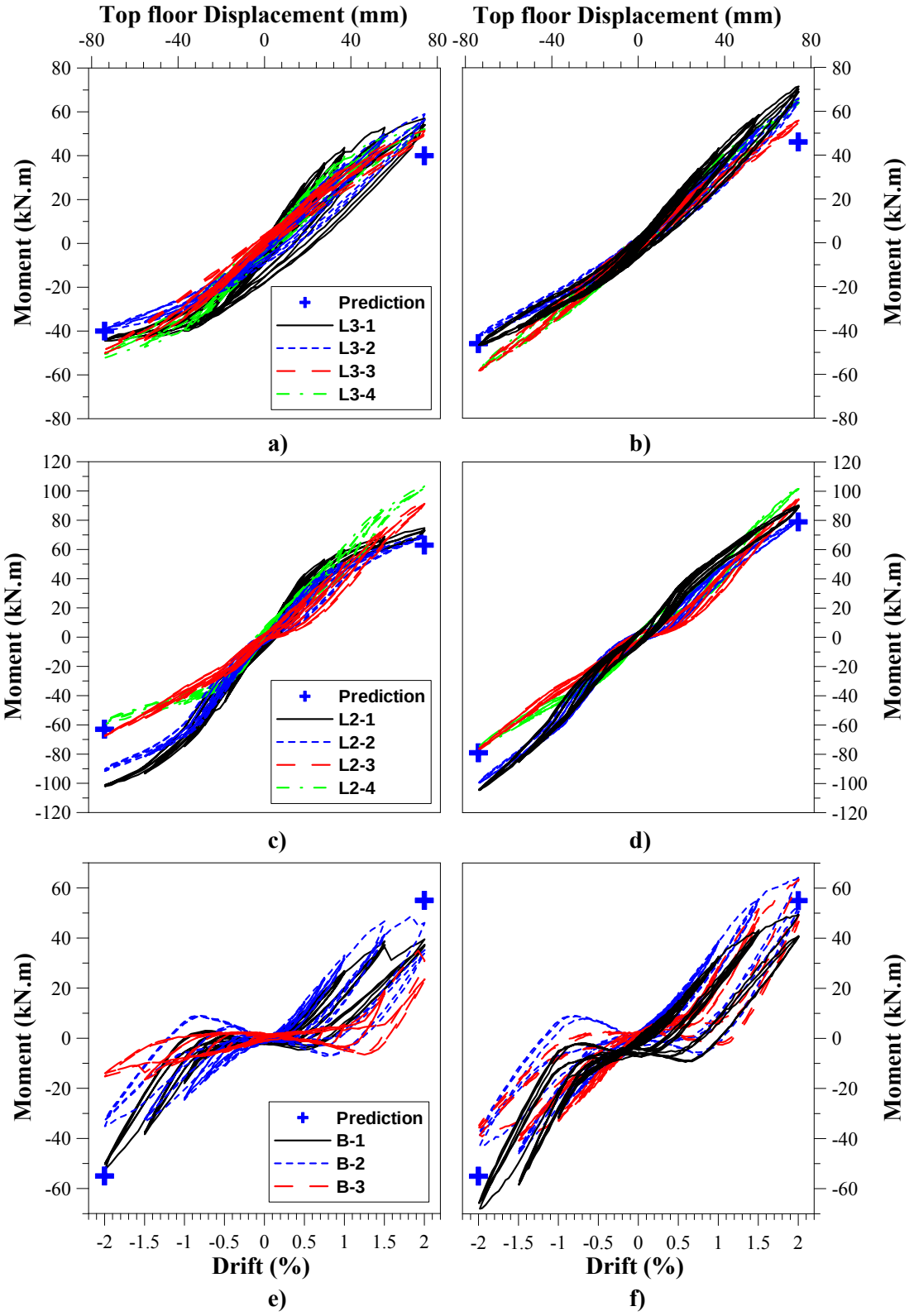

Figure B.2.4. Connection moments versus drift for Stage 1: a) & b) L3 BC connections, c) & d) L2 BC connections, c) & d) Column-base connections for Test 1 and 2 respectively

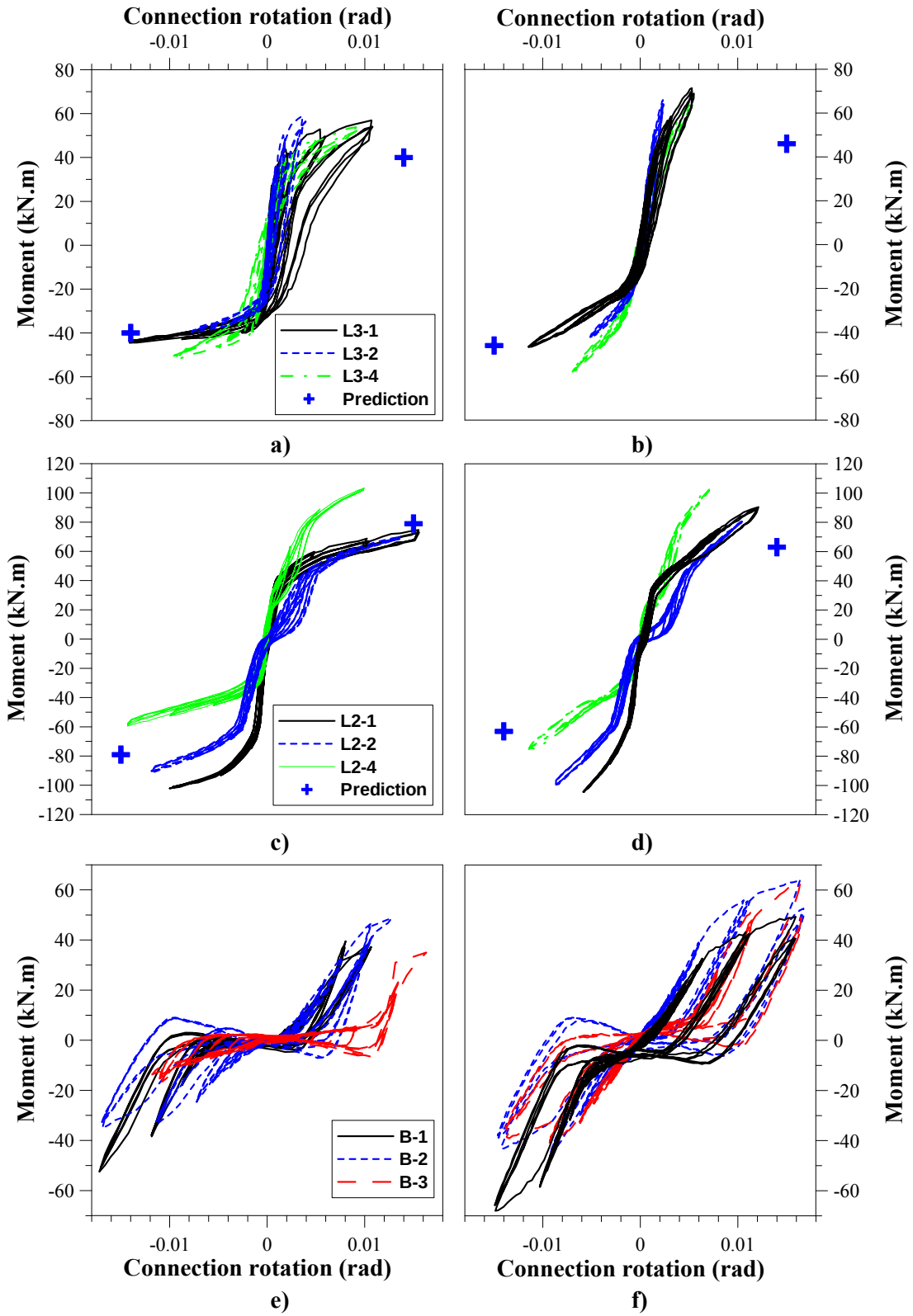

Figure B.2.5. Connection moments versus rotation for Stage 1: a) & b) L3 BC connections, c) & d) L2 BC connections, c) & d) Column-base connections for Test 1 and 2 respectively

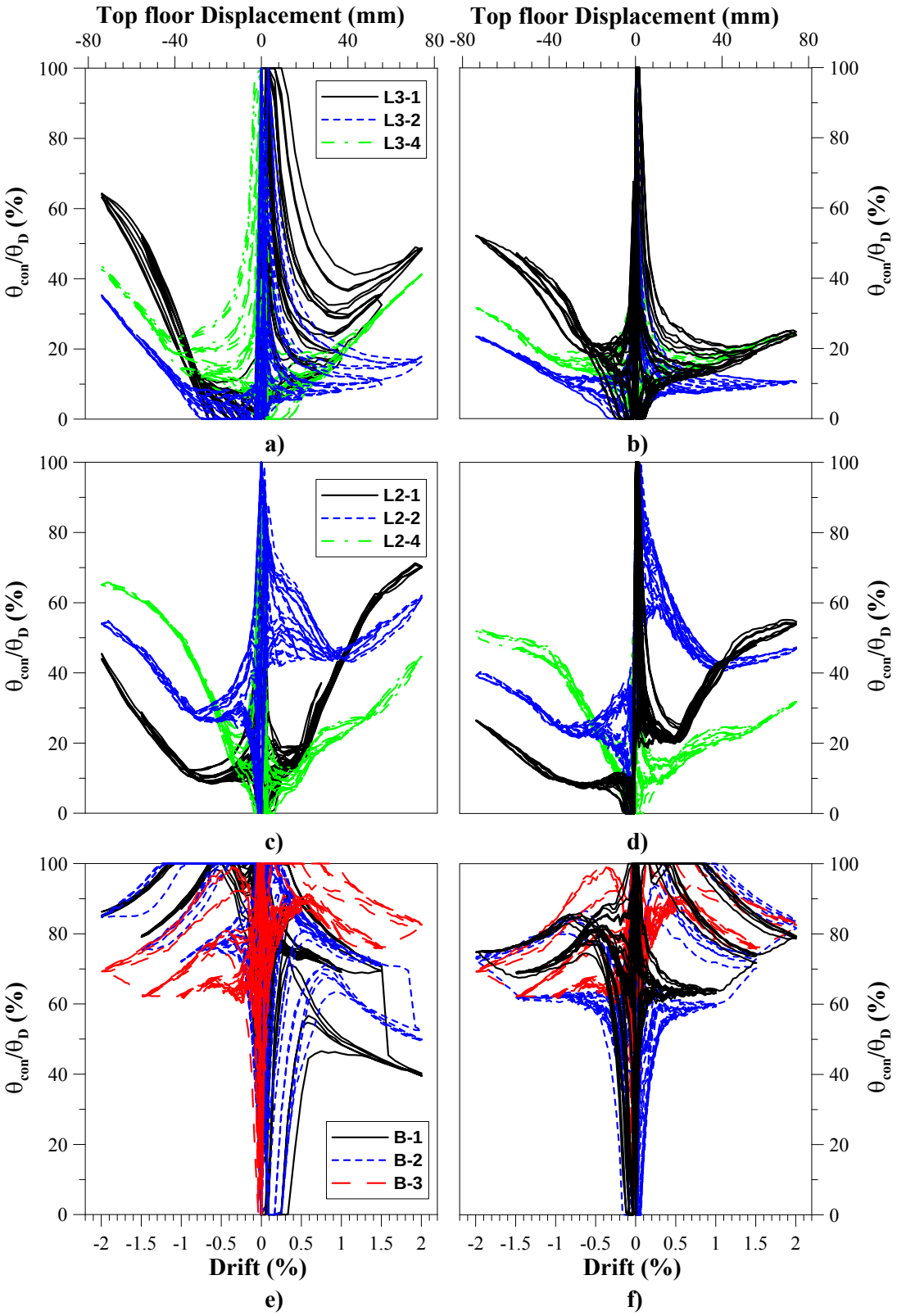

Figure B.2.6. Ratio of connection and total drift for Stage 1: a) & b) L3 BC connections, c) & d) L2 BC connections, c) & d) Column-base connections for Test 1 and 2 respectively

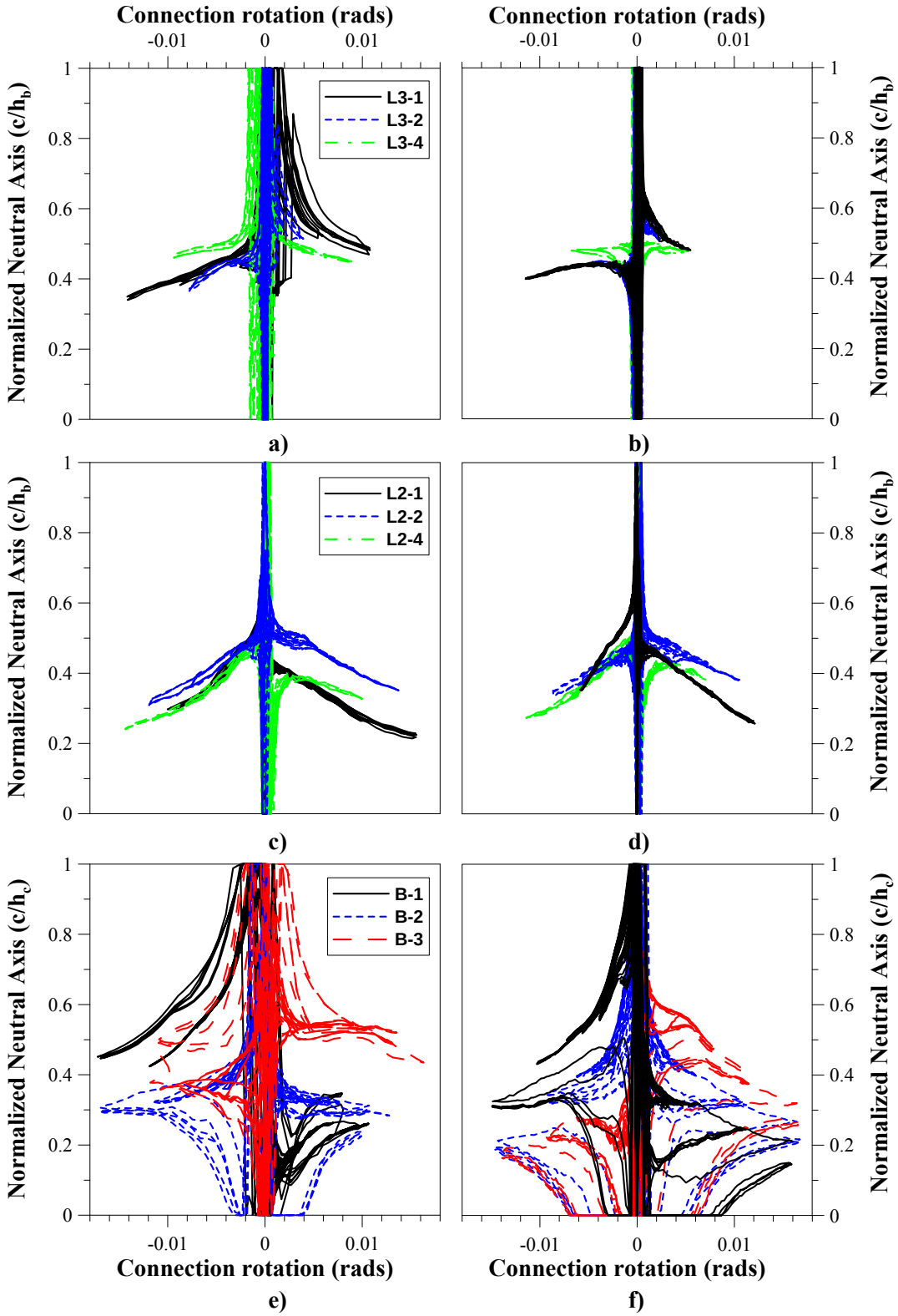

Figure B.2.7. Neutral axis depth for Stage 1: a) & b) L3 BC connections, c) & d) L2 BC connections, c) & d) Column-base connections for Test 1 and 2 respectively

Stage 2: Test 1 and Test 2

Figure B.2.8 shows the moment-drift response of the frame connections for Test 1 and Test 2 of Stage 2, which include a floor diaphragm. There is little hysteretic energy dissipation for L2 and L3 connections. Hence, the majority of inelastic deformation of the timber within the beam column connections has occurred during Stage 1. Generally, the moment response of the BC connections is very similar to Stage 1, with no increase in strength due to the interaction of the floor. Refer to Chapter 5, for a discussion on the influence of floor on the strength of the frame system.

The moment-drift response of each connection is similar for both Test 1 and 2, but the moment-rotation response varies significantly (as discussed above for Stage 1). Again, the external reinforcement appears to have significantly reduced the connection rotation. Refer to Chapter 5, for further discussion on the effects of energy dissipation.

The column-base connections response is highly pinched (see Figure B.2.8e and f) resulting in minor levels of hysteretic energy dissipation. This indicates that in previous tests there has been inelastic deformation of the anchorage pins embedded within the column which has created slop in the connections. This deformation (see Appendix C) has occurred at only approximately 30% of the shear capacity of the pins (640kN) according to EC 5 (EC5 1994). Using a continuous pin through the column appears to provide unsatisfactory performance for cyclic loading (see Chapter 5).

The connection rotation-drift ratio (θ_{con}/θ_D) and the neutral axis depth relationships, shown in Figure B.2.10 and Figure B.2.11, are similar to Stage 1. This further verifies that the presence of the floor diaphragm has little effect on the response of the frame. Note; the neutral axis depth for the column-base connection B-1 could not be defined due to instrument malfunction.

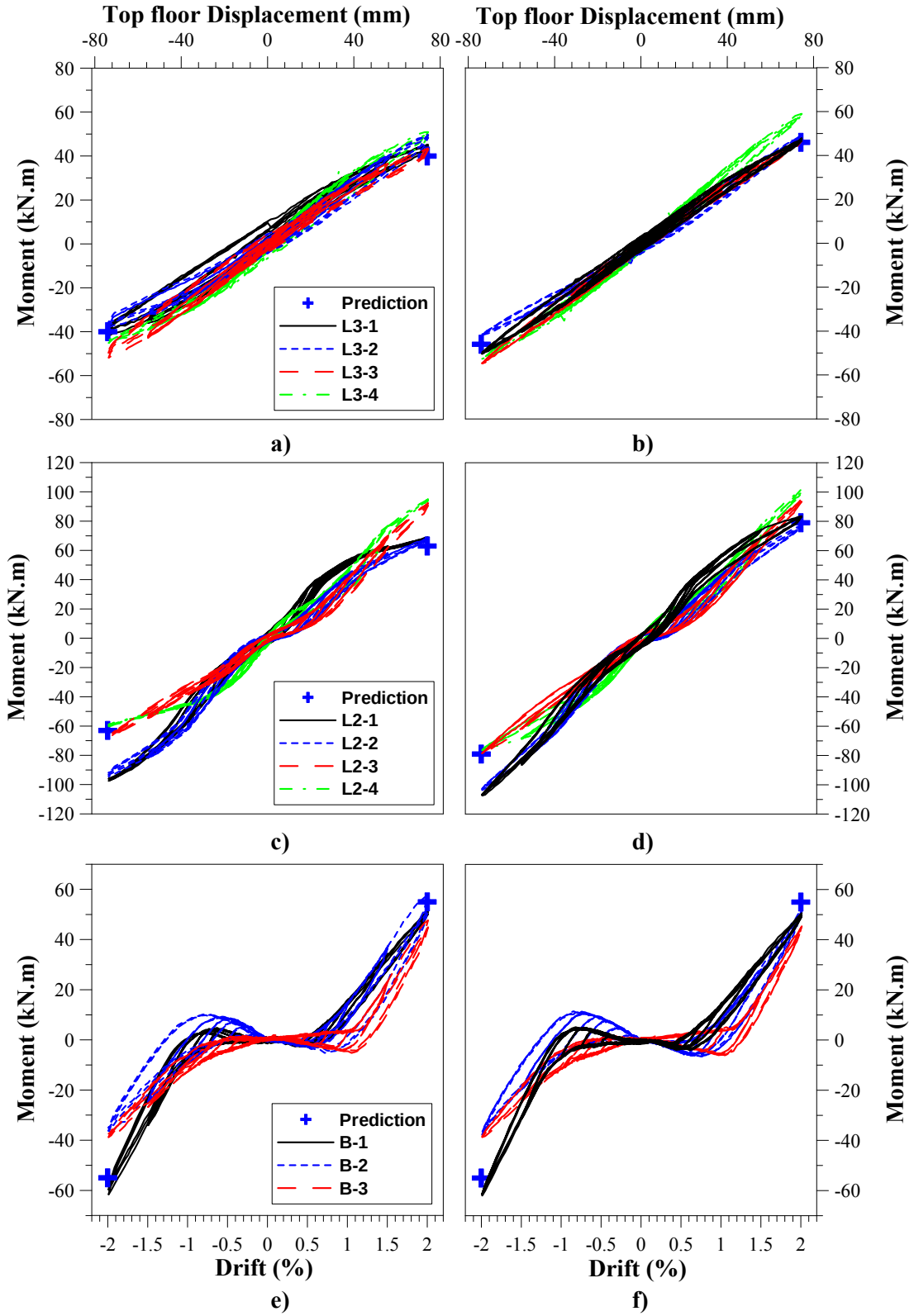

Figure B.2.8. Connection moments for Stage 2: a) & b) L3 BC connections, c) & d) L2 BC connections, c) & d) Column-base connections for Test 1 and 2 respectively

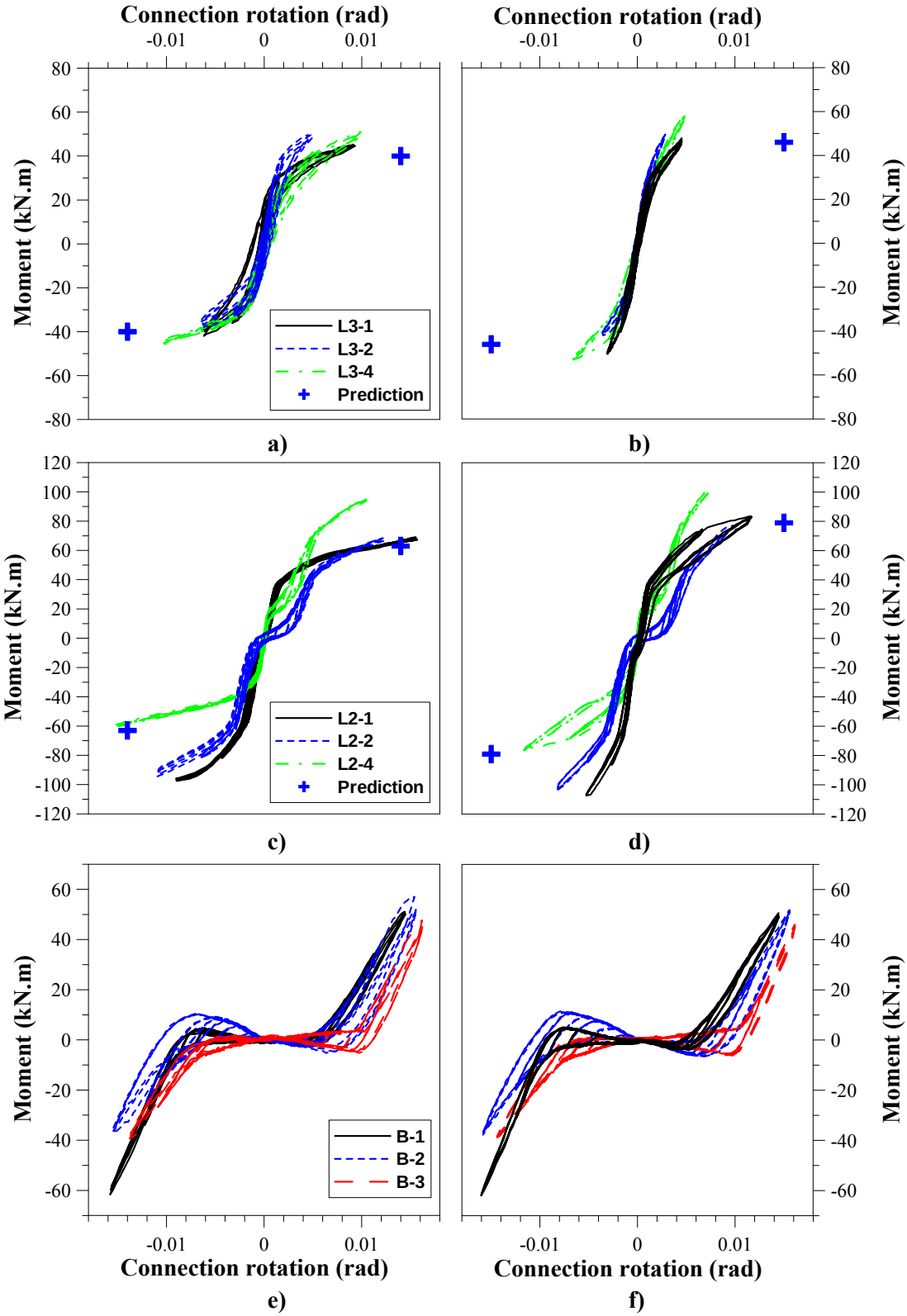

Figure B.2.9. Connection moments versus rotation for Stage 2: a) & b) L3 BC connections, c) & d) L2 BC connections, c) & d) Column-base connections for Test 1 and 2 respectively

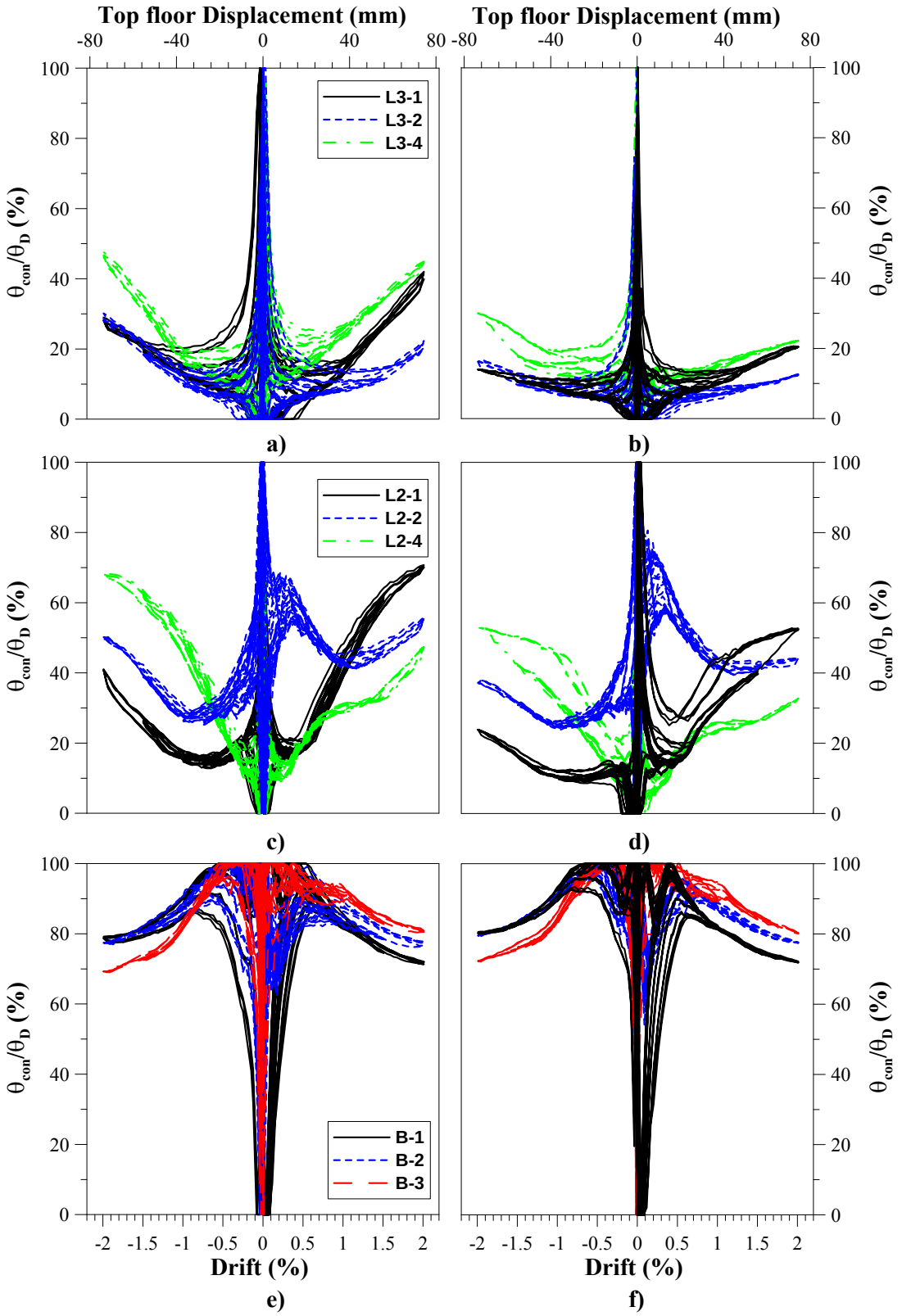

Figure B.2.10. Ratio of connection and total drift for Stage 2: a) & b) L3 BC connections, c) & d) L2 BC connections, c) & d) Column-base connections for Test 1 and 2 respectively

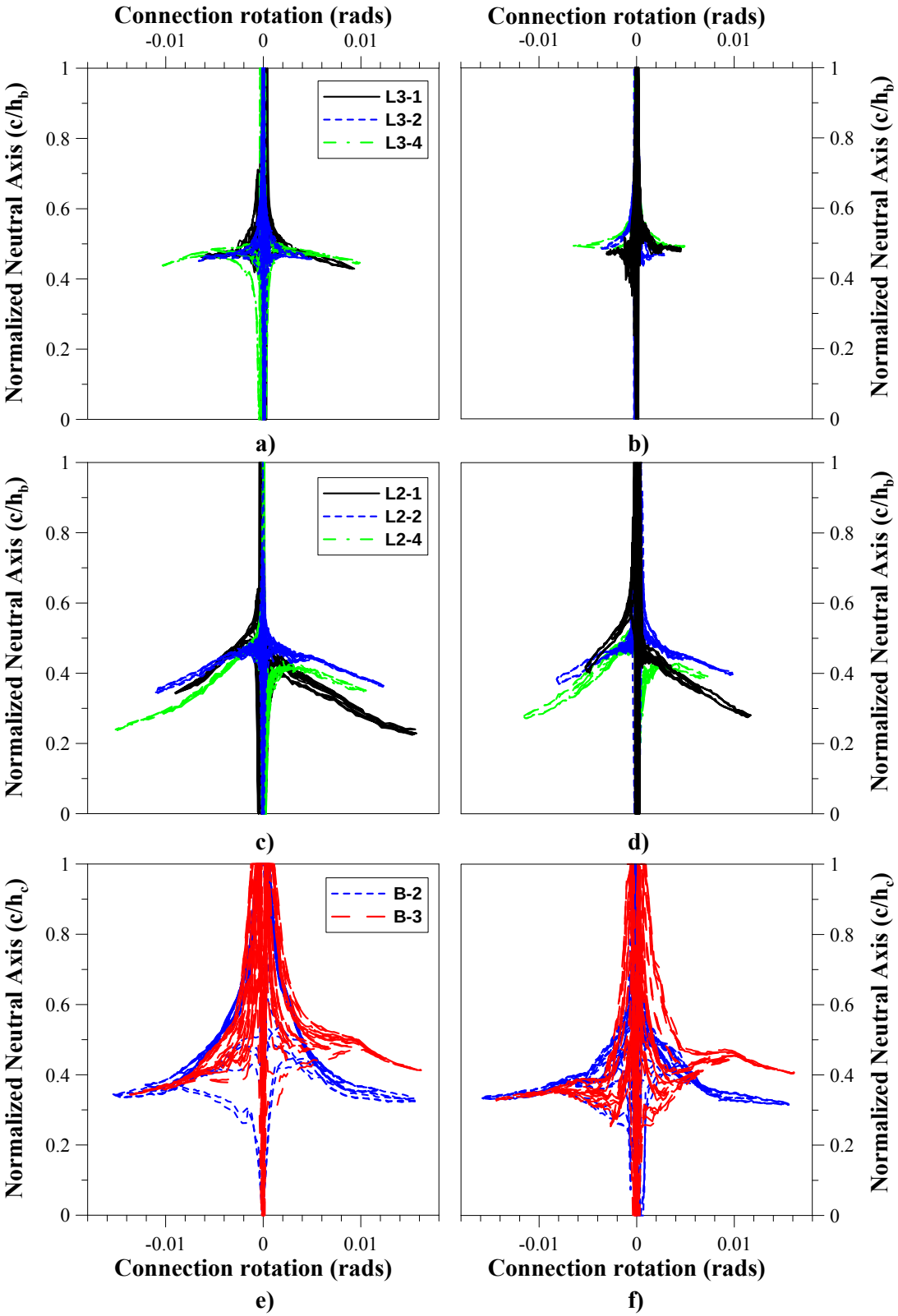

Figure B.2.11. Neutral axis depth for Stage 2: a) & b) L3 BC connections, c) & d) L2 BC connections, c) & d) Column-base connections for Test 1 and 2 respectively

B.2.2. Uni-directional wall tests

Four uni-directional wall tests were performed during Stage 2; Test 3 through 6. The bending moment at the base of the walls was approximated by using potentiometer measurements on the north-west (NW) wall. The curvature over the gauges length is determined, and then multiplied by the elastic modulus (11GPa is assumed) and the second moment of area, giving moment. The moment was determined at two points in the lower part of the wall and projected to the base connection elevation. The moment is plotted versus control drift and connection rotation.

Figure B.2.13a and d shows the wall connection moment versus control drift for the PT only system. The wall appears to respond elastically with little hysteretic energy dissipation. This indicates the hysteretic damping, observable in the global response of the wall system, is derived mostly from friction and cracking of the concrete slab. The experimental response matches well with predictions (see Appendix A).

The moment-drift response of the base connections for the hybrid wall system (Test 4 and Test 5) is given in Figure B.2.13b and c. The moment is slightly higher for positive drifts, due additional axial loads applied by the UFP couplers. Again the connection response matches well with predictions.

Although the predicted connection moment at 2% drift matches well with experimental data, the global OTM of the building (see Figure B.1.3) is significantly under predicted. Therefore, the coupling action provided by the floor diaphragm and edge beams was significant. See Chapter 5 for more detail.

There are some inaccuracies in calculating the rotation at the base of the wall. The deformed profile of the wall section was found to be non-linear from finite element modeling (see Chapter 7) and from experimental data, as shown in Figure B.2.12. From experimental data it was discovered that, depending on which potentiometers (Pots) were used, there was a significant difference in the connection rotation and hence moment-rotation response. Using Pots on the uplifted edge of the wall over-predicted the connection rotation of the wall at the base. A finite element model of the wall found

that Pots A and D (refer to Figure B.2.12) were most appropriate for determining the centerline rotation of the wall due to connection deformation (see Chapter 6 for more detail).

The moment-rotation response of the connections matches relatively well with predictions (see Figure B.2.14) but the connection rotation is over-predicted. The over prediction could be due to inaccuracies in the calculation of the connection rotation from the experimental response and/or due to sliding at the base of the walls.

The accuracy of the neutral axis calculation is also affected by the displacement profile at the base of the wall (see Figure B.2.12). The calculated neutral axis depth for different Pots, versus connection rotation (based on Pots AD), is plotted in Figure B.2.12c. If Pots AB or CD (depending on whether there are negative or positive rotations) are used the neutral axis depth is significantly over-estimated. If Pots AD are used, it is likely that one of the Pots will be in the compression region. This will not affect the accuracy of the result, provided that compression region of the wall has a linear strain profile (as indicated by FEM analysis in Chapter 6). Hence, for all tests Pots AD are used to determine the neutral axis depth. This approach will at least give comparative results between each test.

At 2% drift, the connection rotation is between 50% and 90% of the control drift (see Figure B.2.15). The connection rotation tends to zero for small Drifts, indicating there is a more clearly defined decompression point (compared to the BC connections). Predictions, which suggest that the connection rotation is 80% of drift, match relatively well with the experimental data. Again, the slight over prediction could be due to wall slip or inaccuracies in calculation of the connection rotation.

The experimental neutral axis depth is computed for the NW and SW walls using potentiometers at the edge of each wall, as shown in Figure B.2.16. Based on the experimental data the neutral axis depth is fairly consistent at approximately 0.17 of the wall length at 2% drift. There is a slight variation in neutral axis depth for positive and negative drifts for Test 4 and 5, where the UFP couplers are present. Because there is little variation in neutral axis depth for Test 3 and 6 (without UFPs), it can be inferred

that the wall-floor coupling result in minor variations in axial force in the walls. The predicted neutral axis depth is 0.35 of the wall length at 2% drift, which varies significantly from the experimental results (that give a neutral axis depth of approximately 0.17 of the wall lengths). It is likely that the disparity is due to inaccuracies in the analytical prediction procedure (see Appendix A).

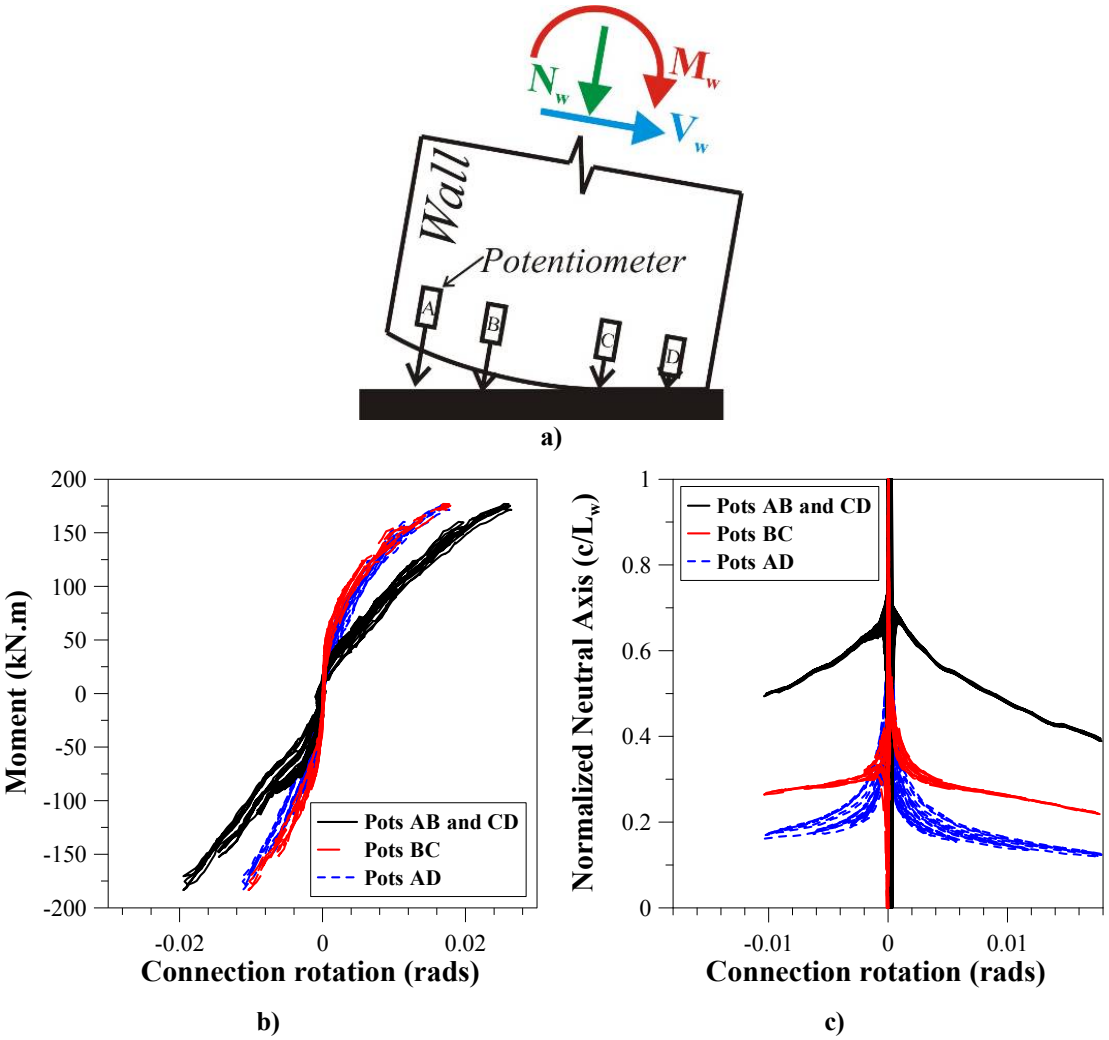

Figure B.2.12. Interpretation of experimental data for wall connection: a) Deformed shape of wall base b) Moment-rotation using different Pots c) Neutral axis depth using different Pots

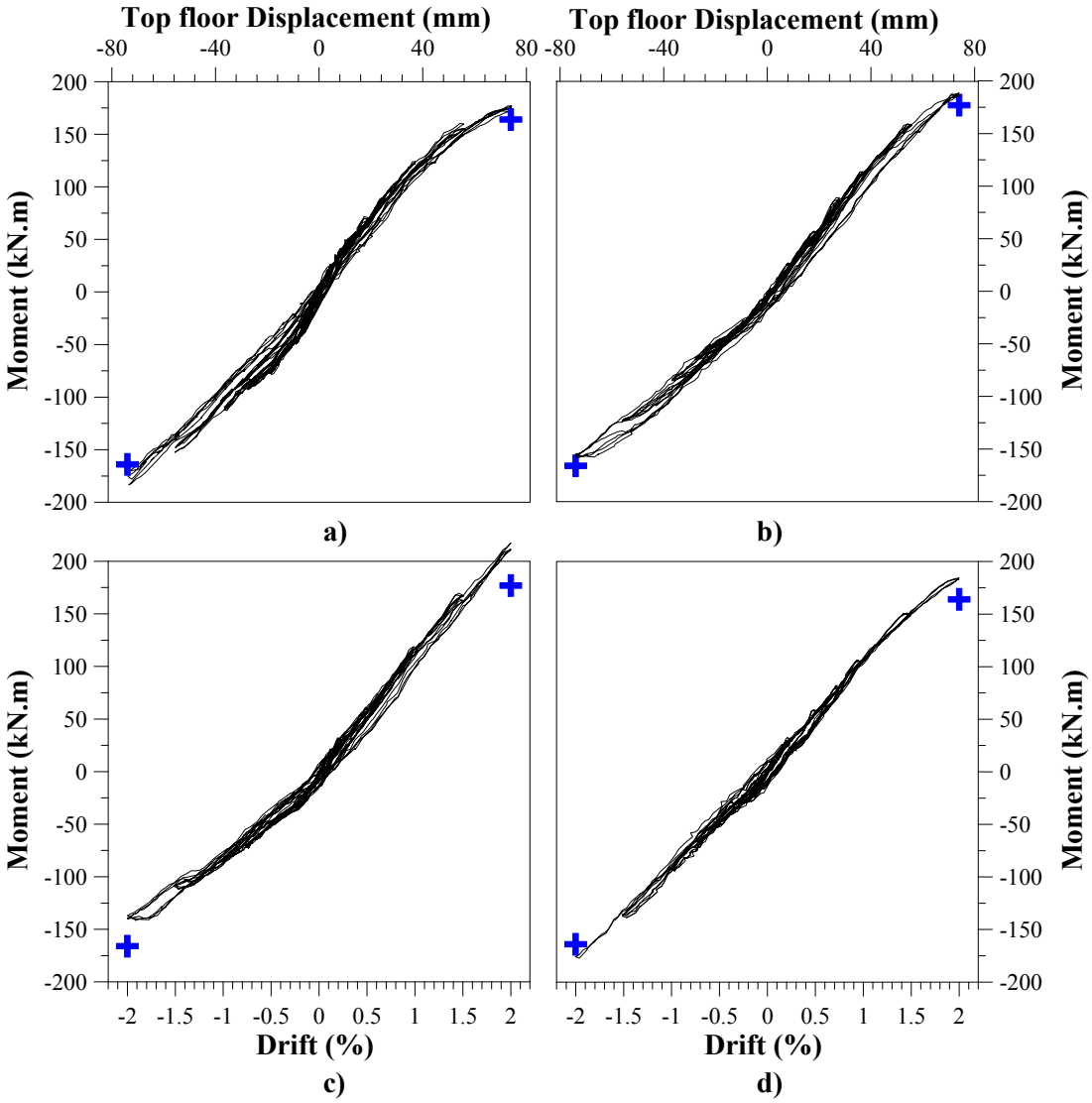

Figure B.2.13. NW Wall connection moments versus Drift: a) Test 3 b) Test 4 c) Test 5 and d) Test 6

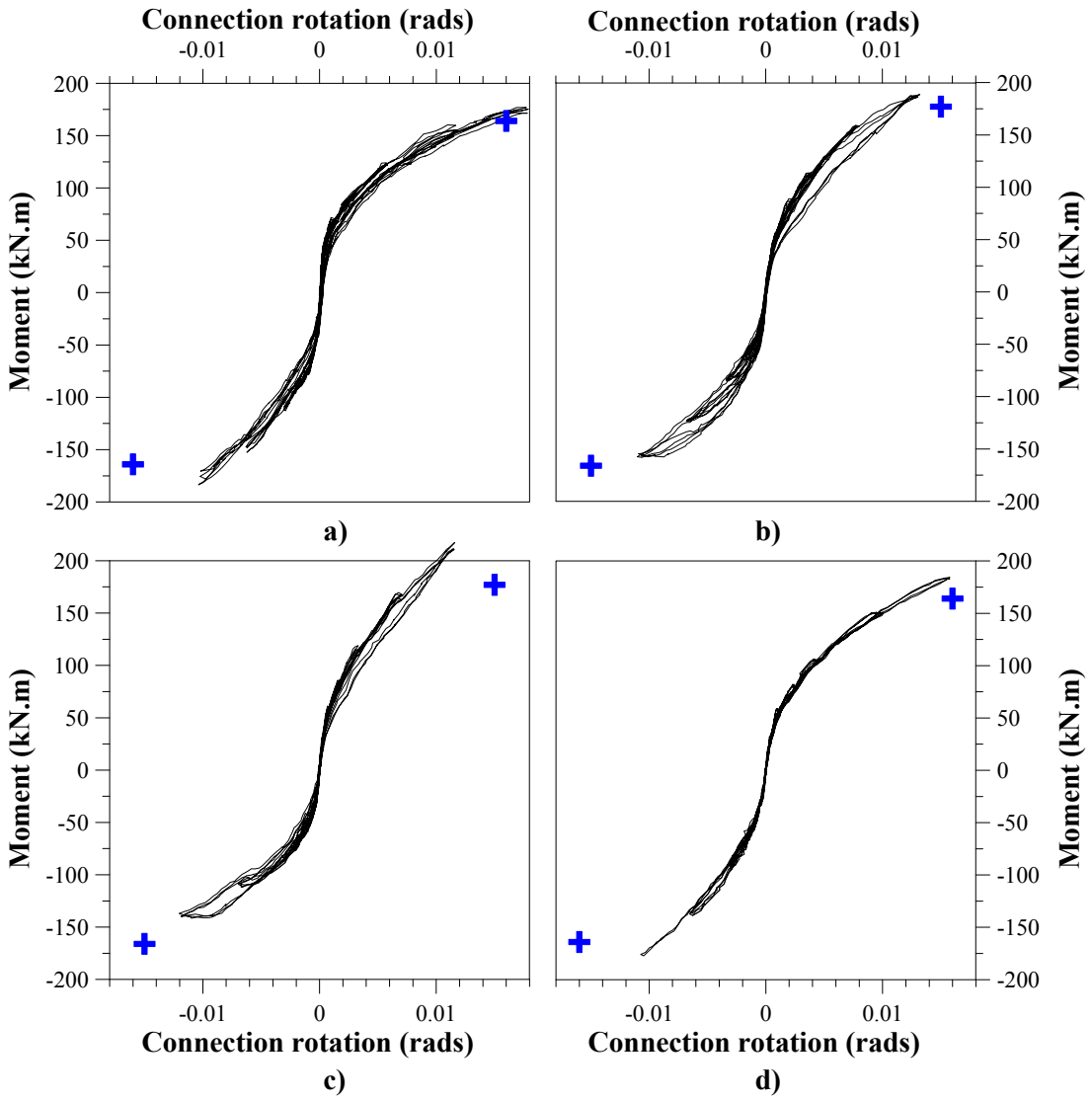

Figure B.2.14. NW Wall connection moments versus connection rotation: a) Test 3 b) Test 4 c) Test 5 and d) Test 6

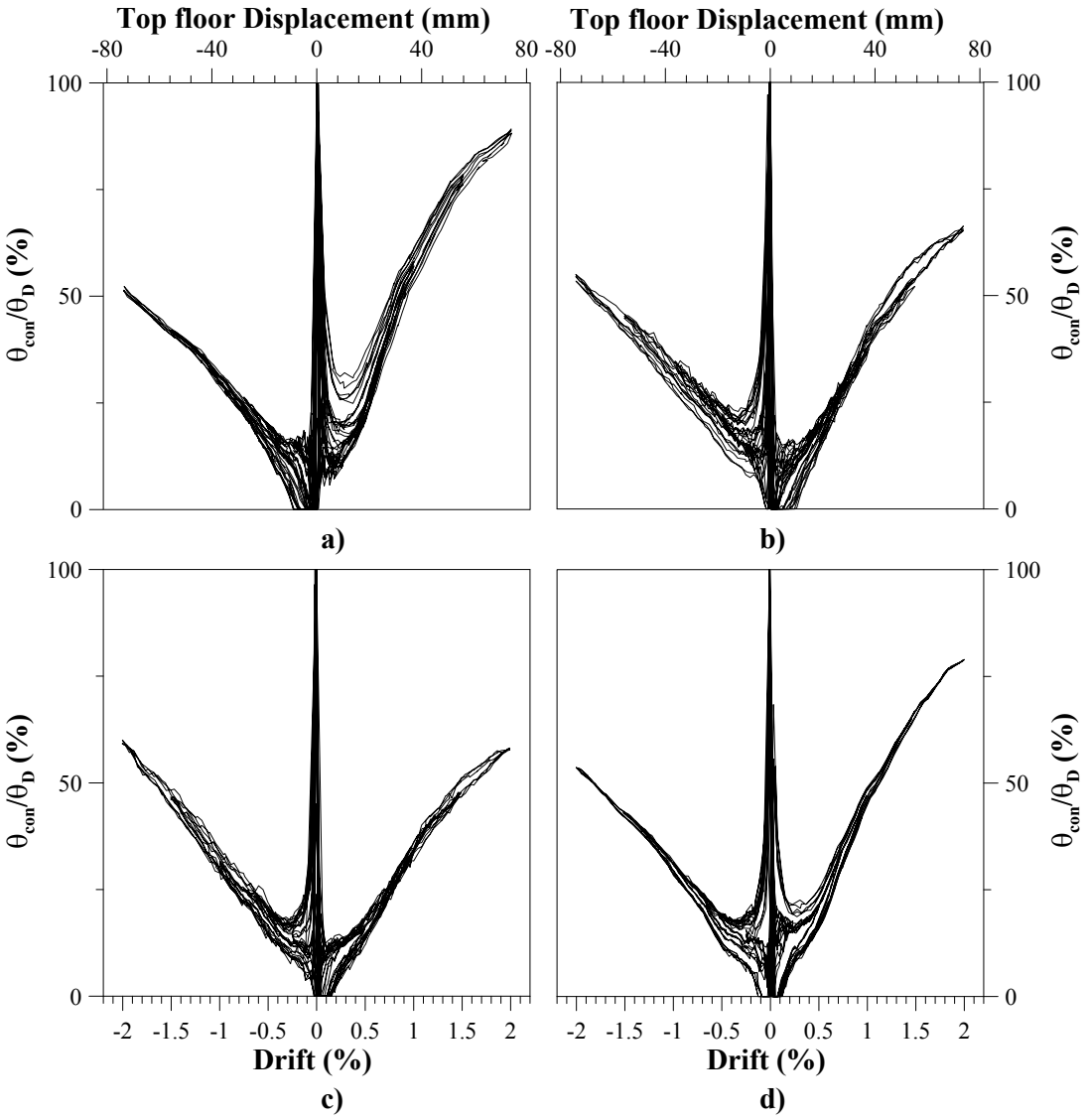

Figure B.2.15. Ratio of connection and total drift for NW wall:
a) Test 3 b) Test 4 c) Test 5 and d) Test 6

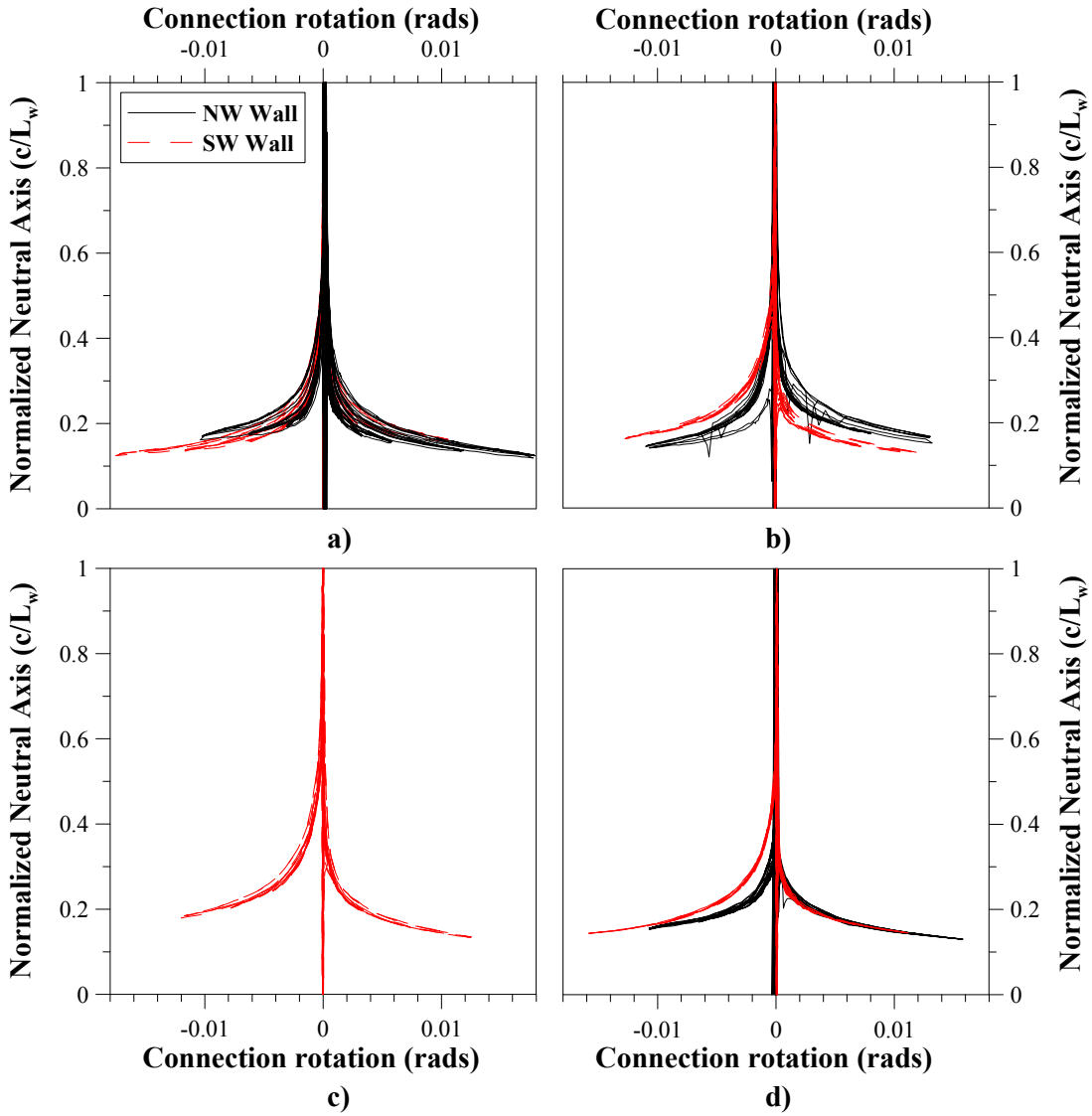

Figure B.2.16. Normalized neutral axis depth versus connection rotation for NW and SW walls: a) Test 3 b) Test 4 c) Test 5 and d) Test 6

B.2.3. Bi-directional tests

The connection response of the wall and frame connections is considered for the bi-directional test (Stage 2, Test 7). Due to the early termination of the second bi-directional test (Test 8), there is limited data available. Hence, only Test 7 is considered here.

Frames

The moment-drift response of the frame connections during the bi-directional test (Test 7) are shown in Figure B.2.17. The BC response was comparable to the uni-directional tests. Notably, the column-base connections provide less moment than in the uni-directional testing. Refer to Chapter 5 for further discussion.

Because 3% peak drift was applied to the structure, the connection rotation was larger than the previous uni-directional tests. With increased connection rotation, BC connections provide a more 'flag-shaped' hysteretic shape with significant hysteretic energy dissipation (see Figure B.2.18). However, the connection rotation is still much less than predicted at 2% drift. The moment within the base-connections are effected by in-plane and out-of-plane drift, hence, it is not possible to compute the connection moment versus rotation in the frame direction.

The ratio connection rotation versus drift and neutral axis depth, shown in Figure B.2.19 and Figure B.2.20 respectively, are similar to uni-directional results.

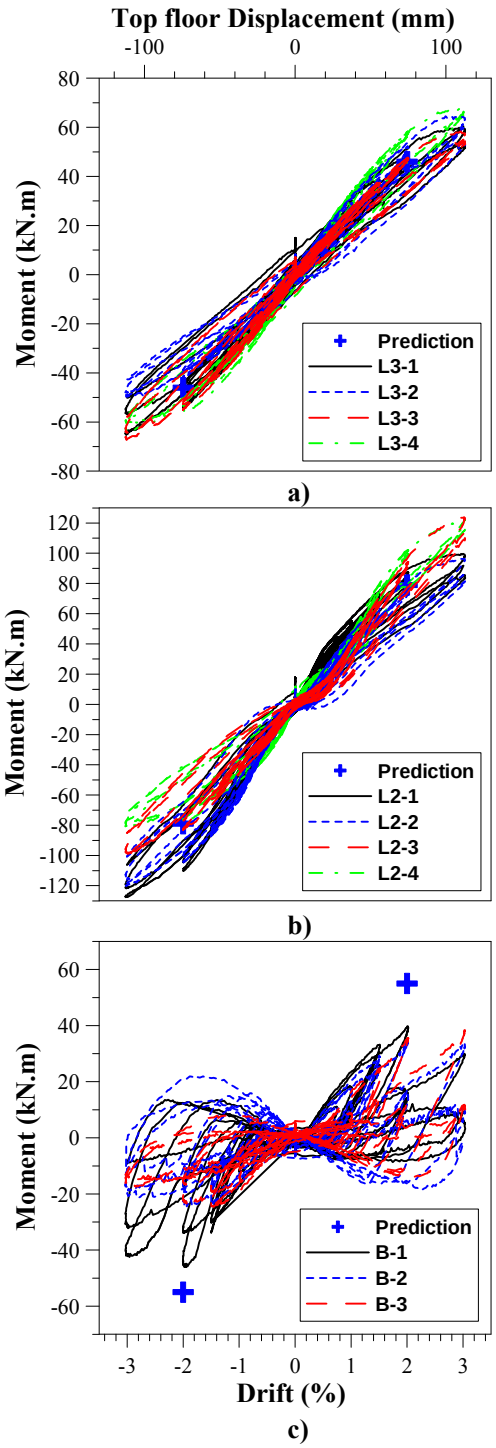

Figure B.2.17. Connection moments versus EW Drift for Stage 2 Test 7: a) L3 BC connections b) L2 BC connections c) Column-base connections

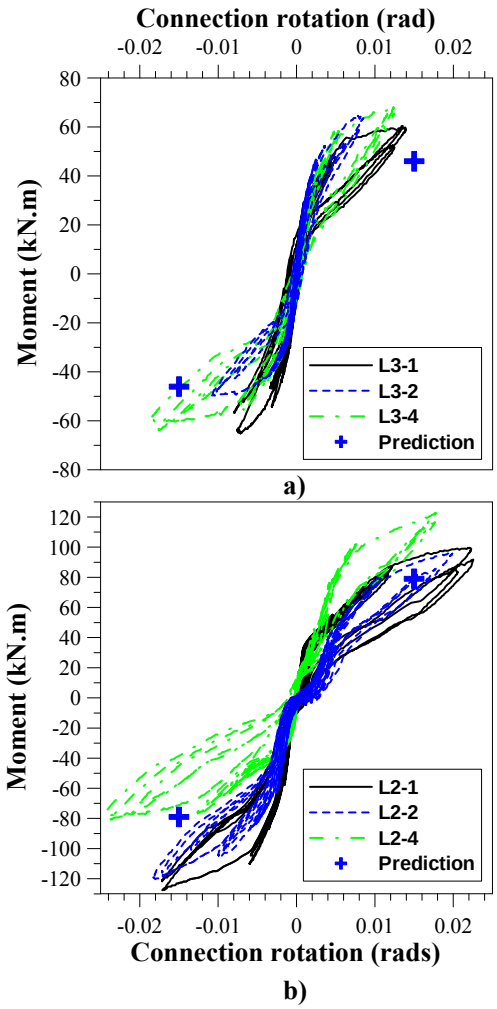

Figure B.2.18. Connection moments versus rotation for Stage 2, Test 7: a) L3 BC connections b) L2 BC connections

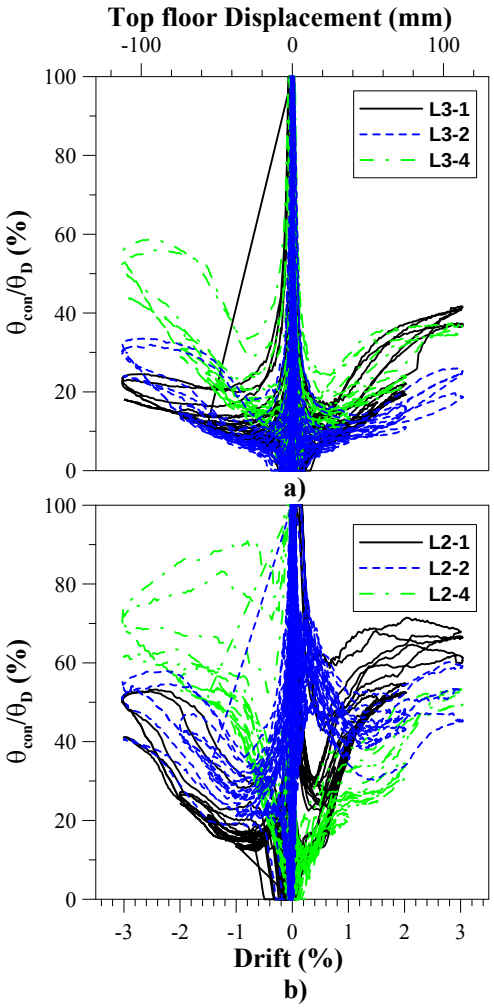

Figure B.2.19. Ratio of connection and total drift for Stage 2, Test 7: a) L3 BC connections, b) L2 BC connections

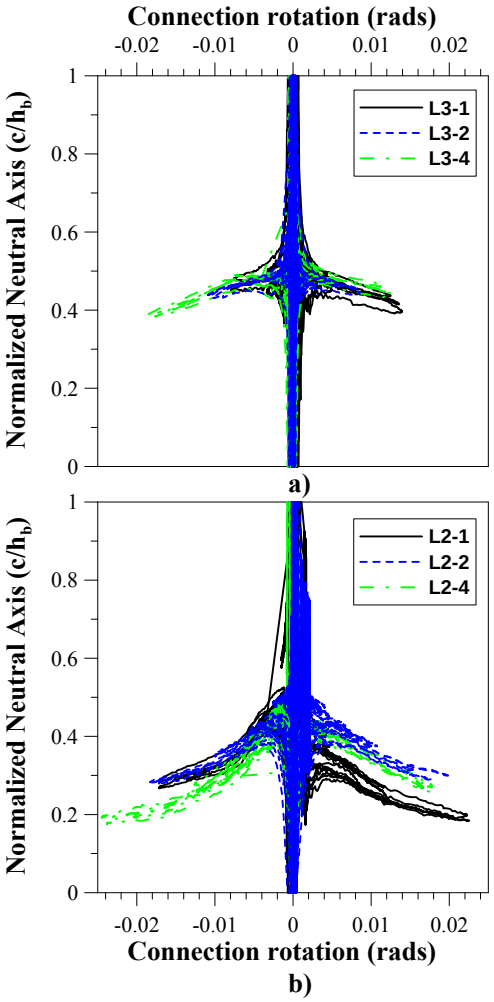

Figure B.2.20. Neutral axis depth for Stage 2, Test 7: a) L3 BC connections, b) L2 BC connections

Walls

The moment-drift response of the NW wall is shown in Figure B.2.21. The UFP couplers provide significant hysteretic damping to the moment-rotation response beyond 2% drift. The accuracy of the estimation of the connection moment appears to be affected by out-of-plane deformation of the wall. In general, the response of the wall system is not significantly affected by bi-directional loading. See Chapter 5 for more detail.

The connection rotation and neutral axis could not be accurately defined for bi-directional loading and is not presented here.

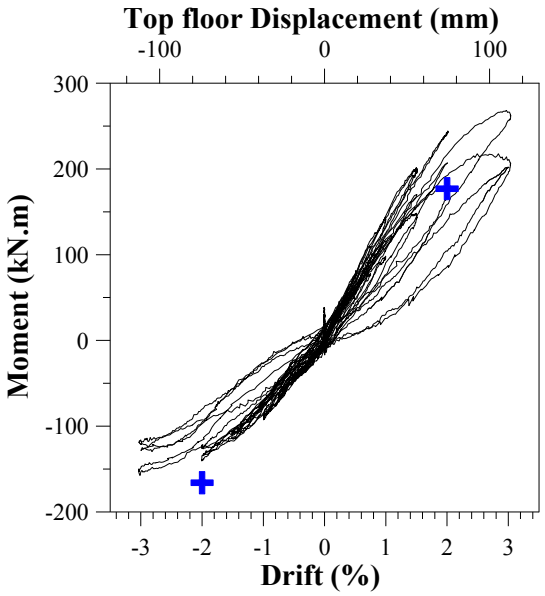

Figure B.2.21. NW Wall connection moments versus NS Drift for Stage 2 Test 7

B.2.4. Out-of-plane moments

Frames

The out-of-plane moment provided by the column-base connections is a component of the global strength of the building in the NS direction. Hence, this contribution is quantified to determine by elimination the influence of the floor system on the response of the building.

Strain-gauges have been placed on the north and south face of the columns on the north frame. The strain-gauges are used to determine the moment provided by the column-base connections, acting out-of-plane, at 2% drift. The average of the column-base moments for the north frame is calculated and plotted in Figure B.2.22 against the interstorey drift for each of the wall tests (Stage 2: Test 3 though 6). The strain-gauges lack the precision to determine the axial force in each column, with which the coupling action provided by the floor and the frame could be quantified.

The moment contribution from the base connections is relatively minor. However, the connection moment shows that there is significant coupling action between the frame and the floor system; for positive drifts the moment is significantly higher than for negative drifts, due to increased axial forces (in the north frame) due to coupling action of the floor. The OTM provided by the base connections at 2% drift can be approximated by taking the average moment for positive and negative base moment, which is approximately 10kN.m per column, and multiplying by the number of columns. Hence, approximately 60kN.m OTM is provided by the column-base connections at 2% drift.

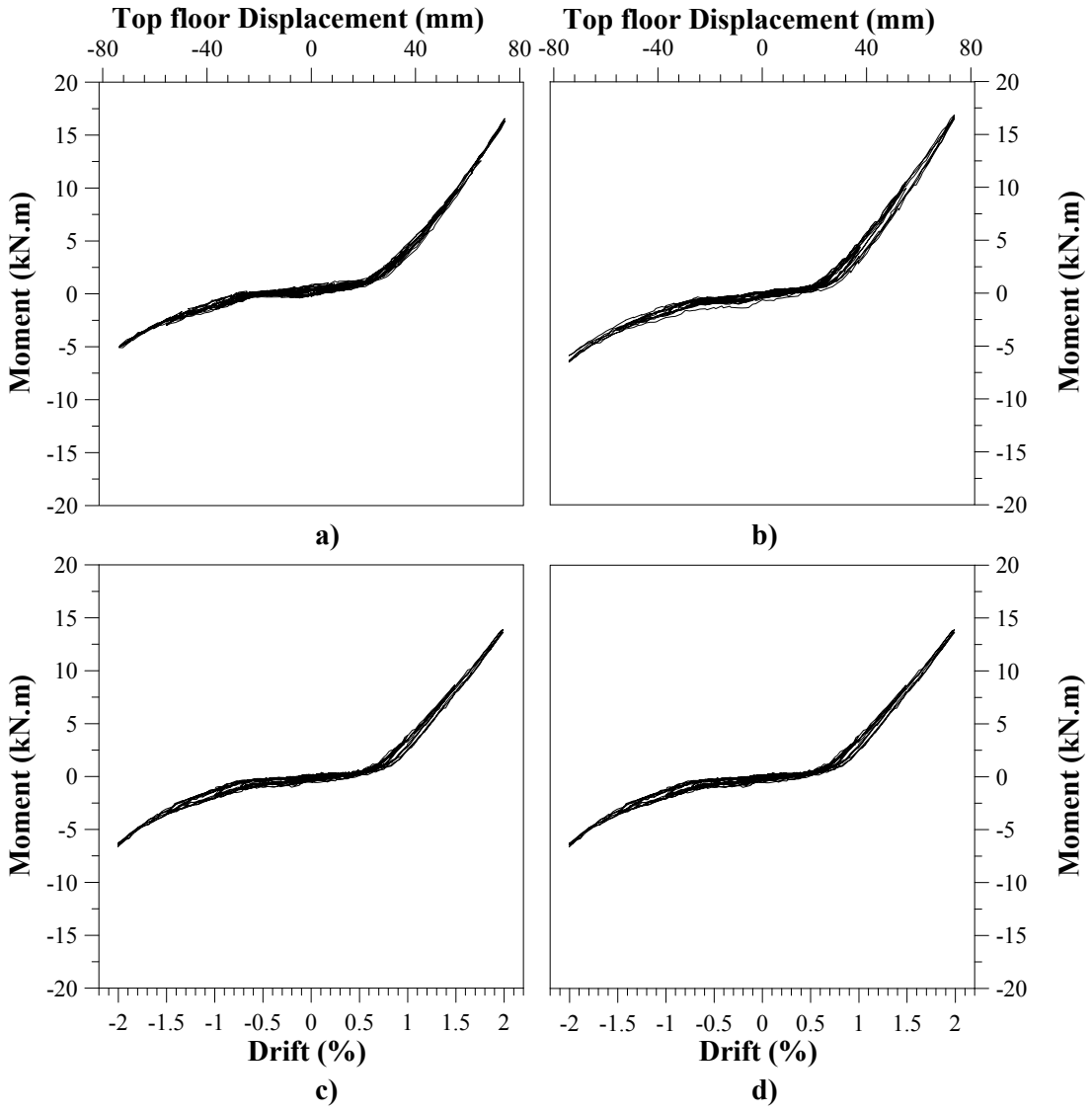

Figure B.2.22. Average out-of-plane moment provided by the column-base connections on the north frame in Stage 2: a) Test 3 b) Test 4 c) Test 5 d) Test 6

Walls

The out-of-plane moment provided by the walls is estimated by using potentiometers on the east and west faces of the NW wall. The moment at the base of the wall is projected from the centerline of the potentiometers assuming a linear moment profile. This moment contribution can subtracted from the total OTM of the building in the EW direction, to determine influence of the floor diaphragm on the building strength (see Chapter 5). The total overturning moment (OTM) contribution provided by the wall acting out-of-plane is approximately 80kN.m at 2% drift.

The axial forces induced by floor-to-wall coupling could not be reliably quantified (other than by elimination) from the experimental data. This mechanism may have provided significant strength to the building, responding the EW direction.

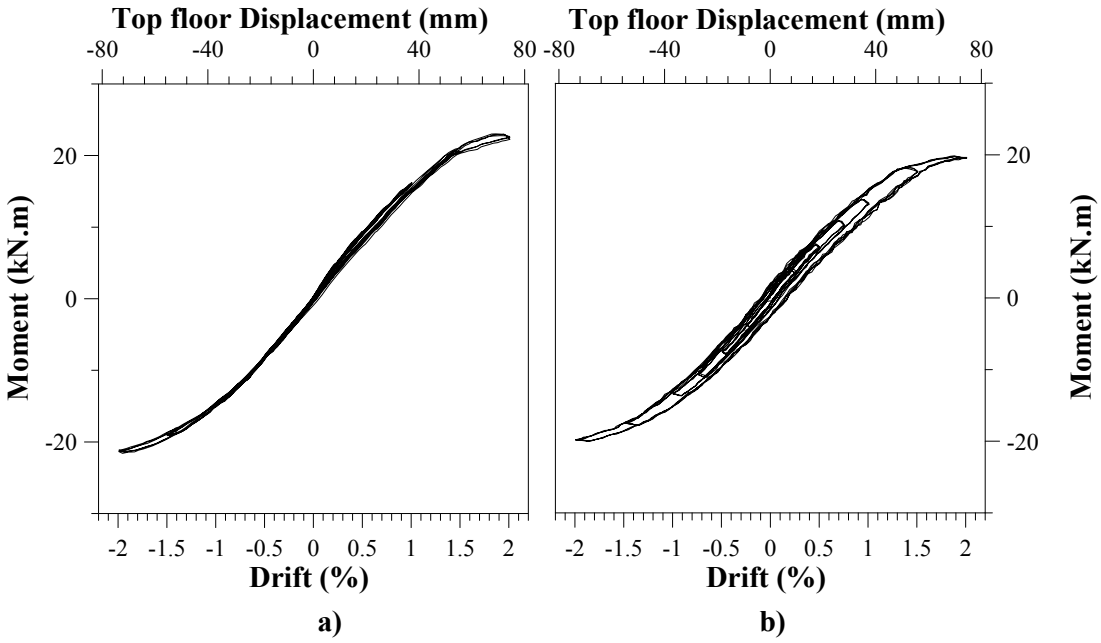

Figure B.2.23. Out-of-plane moment provided by walls in Stage 2: a) Test 1 b) Test 2

B.3. TENDON FORCES

The tendon forces are monitored using load cells on the tendons during the uni-directional and bi-directional tests. Two load cells were used for each tendon group. The load cells were placed on the top and bottom tendons going through the frames, and the north and south tendons going through the walls. These tendons were expected to give the peak tendon force in each group.

B.3.1. Uni-directional frame tests

The tendon forces for Stage 1 (Test 1 and 2) versus drift are shown in Figure B.3.1. For Level 3 tendons, the post-tensioning (PT) force is significantly different for positive and negative drifts. This is due to additional compressive forces applied to the frame by the loading apparatus. For positive drifts, the loading apparatus applies a compressive force, which results in shortening of the frame and loss of post-tensioning force. The reverse is true for negative drifts. For Test 1 (Figure B.3.1a), there is irrecoverable tendon losses because of inelastic deformation of the BC connections adjacent to the application of lateral load. During Test 2, there is no significant loss of PT force, further verifying that there was little further inelastic deformation within the BC connections after Test 1. For the Level 2 tendons, there is no significant variation in force for positive and negative Drifts, or losses in PT force, due to the higher axial stiffness and strength of the BC connections.

For Stage 2, the tendon forces are similar of positive and negative drifts on both Level 2 and 3. This indicates that the Stage 2 loading apparatus effectively distributes lateral forces throughout the structure. Between Stage 1 and 2 there have been slight losses of PT force on Level 3 (due to creep) but effectively none of Level 2. Refer to Neale (2009) for further detail.

For the predictions, it was expected that the tendon forces on Level 2 and 3 would be approximately 110kN and 93kN respectively at 2% drift. Both predictions over-estimate the force in the tendons slightly. This may be because inaccuracies in the

analytical predictions procedures. Namely, because the axial deformation of the members was not taken into account, the predicted force within the tendons was higher. In addition, for both Stage 1 and 2, there is no significant difference in PT force with and without external reinforcement.

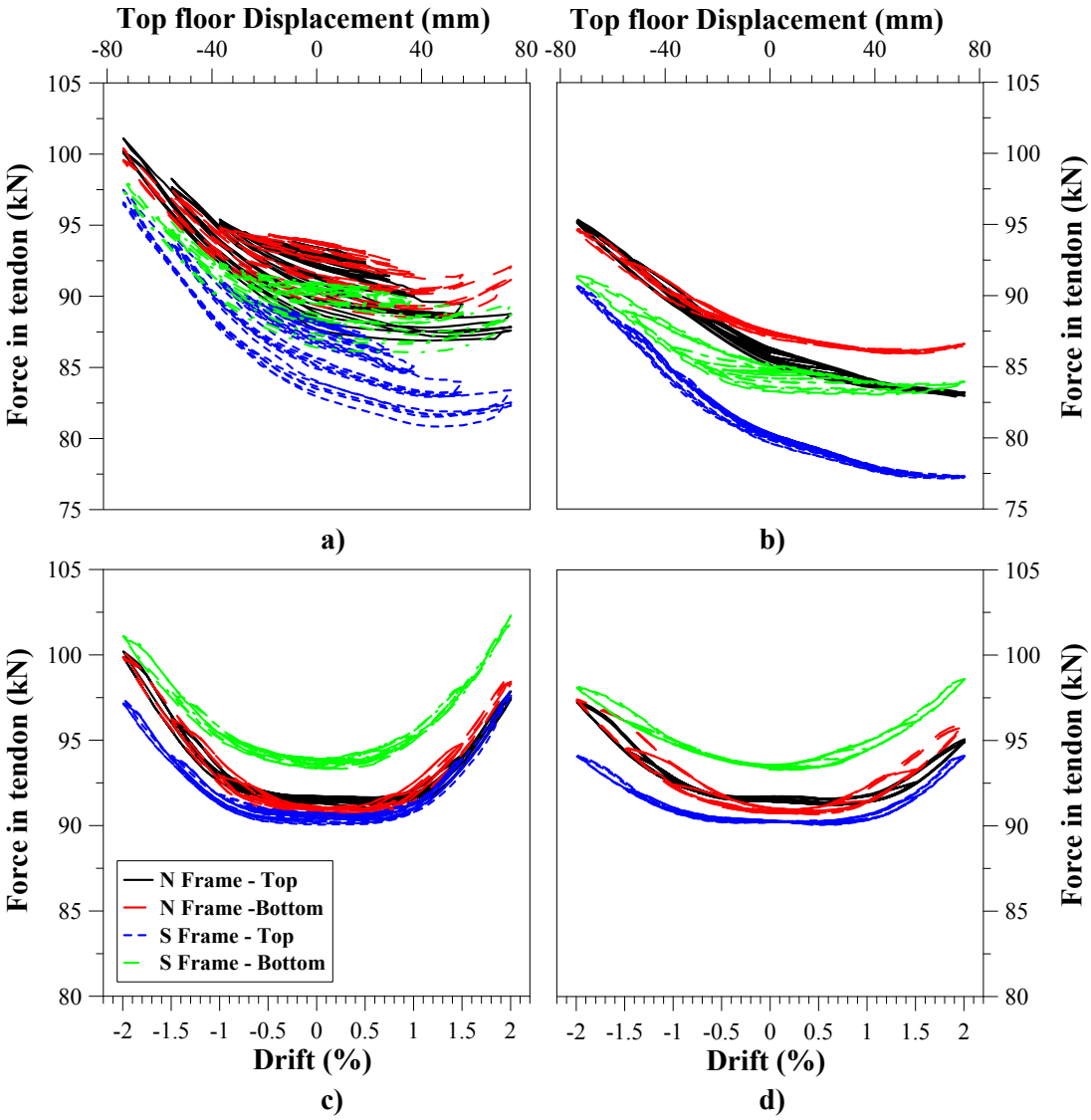

Figure B.3.1. Force in the post-tensioning tendons for stage 1: a) & b) Level 3 tendons, c) & d) Level 2 tendons for Test 1 and 2 respectively

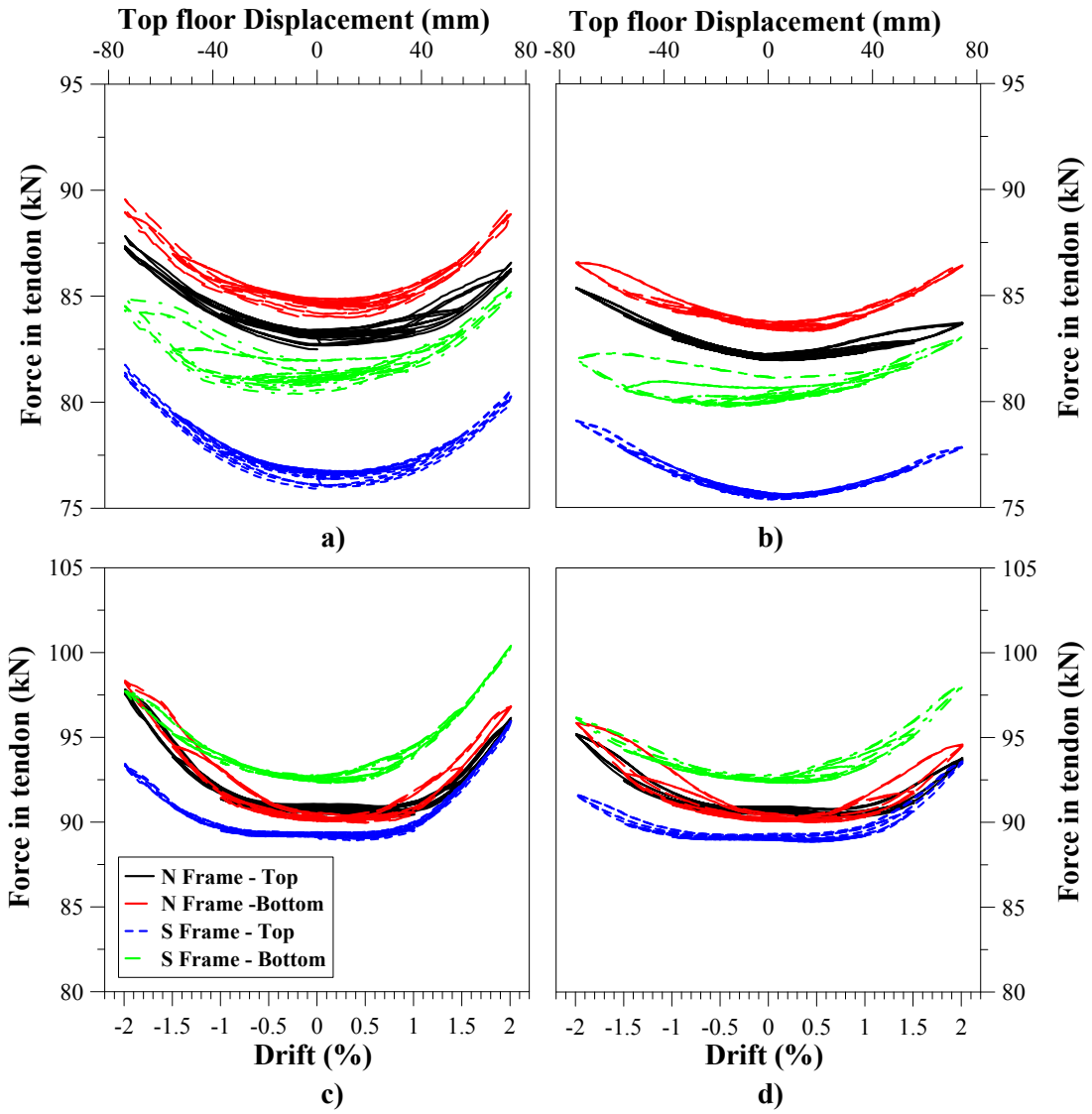

Figure B.3.2. Force in the post-tensioning tendons for stage 2: a) & b) Level 3 tendons, c) & d) Level 2 tendons for Test 1 and 2 respectively

B.3.2. Uni-directional wall tests

Figure B.3.3 shows the forces in the north and south tendons of the NW and SW walls for Tests 3 through 6. During Test 3, there are slight losses in PT force, indicating limited inelastic deformation of the timber. Losses successively reduce for subsequent tests. For the post-tensioned (PT only) walls, which correspond to Test 3 and 6, the PT forces are similar for positive and negative drifts. For Hybrid walls, Test 4 and 5, there

are variations in PT forces between corresponding tendon positions in the north and south walls. This is due to the affects of additional axial load from the UFP couplers. Furthermore to PT force remains higher during unloading for some tendons due to resistance provided by the UFP couplers. The peak PT force was predicted to be approximately 110kN at 2% drift. This corresponds well with experimental results.

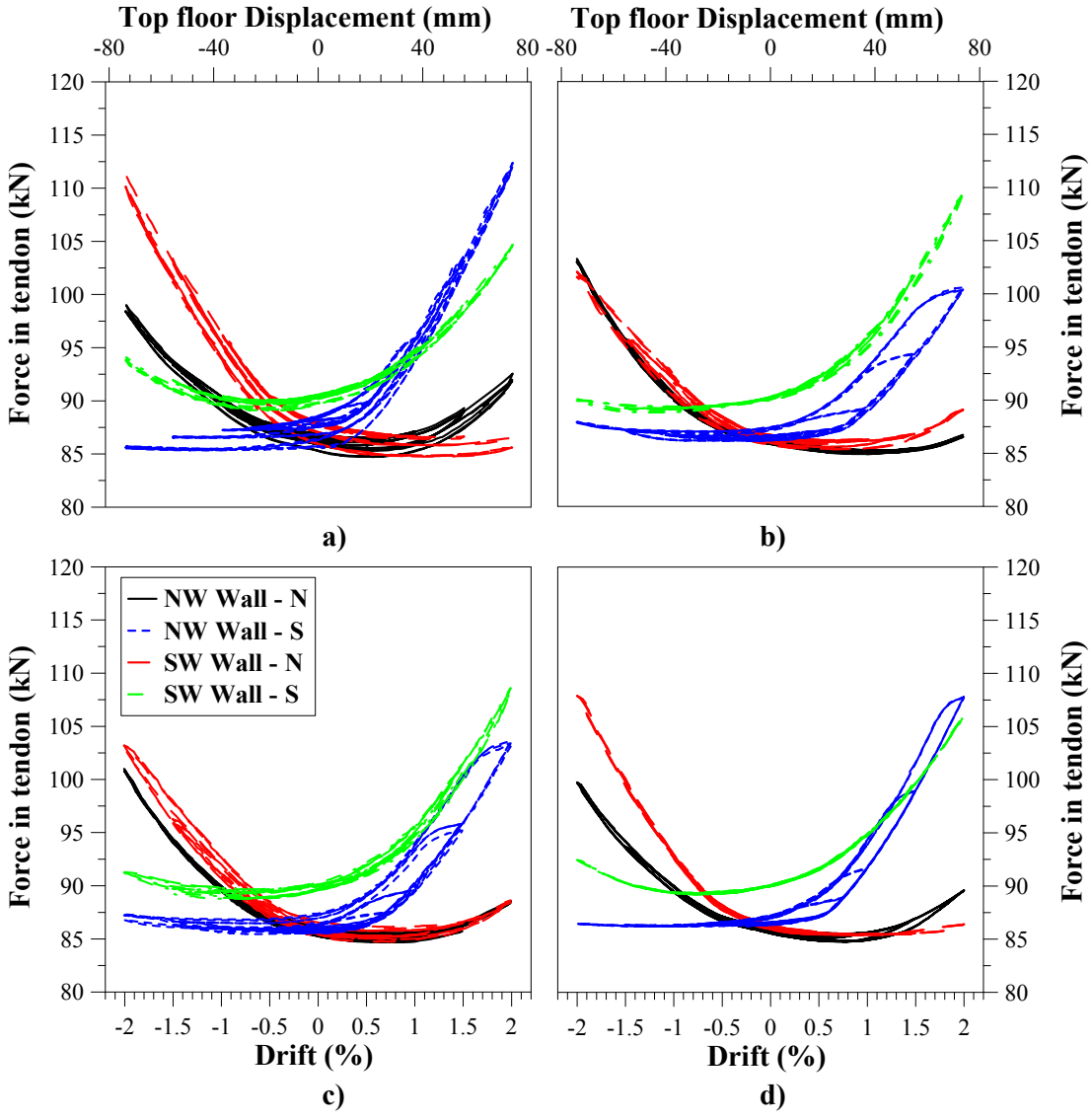

Figure B.3.3. Force in the post-tensioning tendons within the NW and SW walls: a) Test 3 b) Test 4 c) Test 5 d) Test 6

B.3.3. Bi-directional test

The forces in the frame and walls tendons are plotted in Figure B.3.4 and Figure B.3.5 respectively for the bi-directional test (Stage 2, Test 7).

For the frames, there are slight losses in PT force after 2% drift, which indicates further inelastic deformation, especially on Level 3. The peak PT force is approximately 107kN, which is well within the elastic range of the tendon and significantly less than predicted (125kN).

For the walls, the PT forces are similar for all walls except the north tendon in the NE Wall. The initial PT force was higher than specified. Hence, the peak tendon force is dictated by this tendon at 140kN. This PT force is 10% less than the non-linear limit of the tendon, and 23% less than the ultimate tensile strength of the tendon.

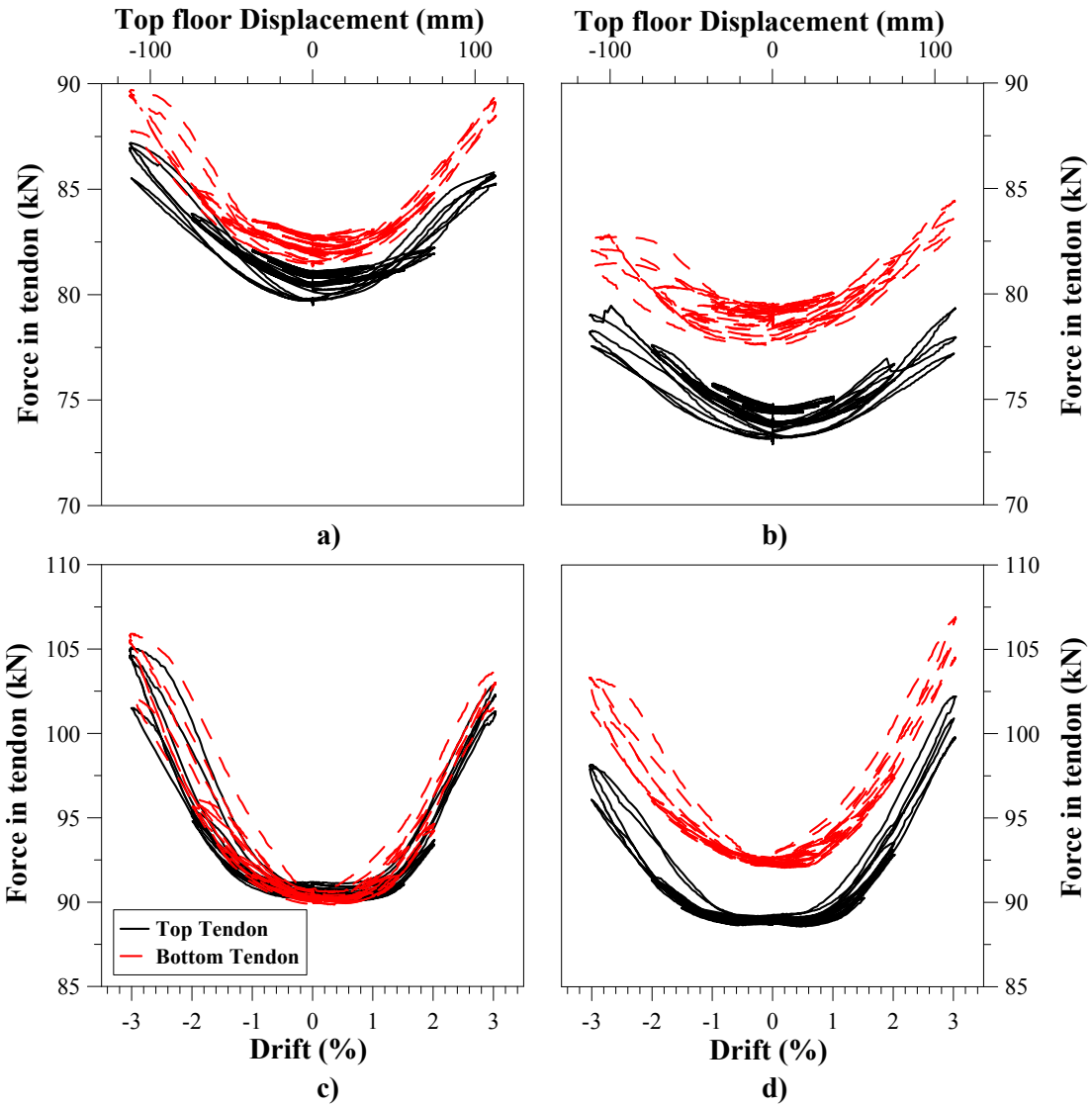

Figure B.3.4. Force in the frame post-tensioning tendons for Test 7: a) & b) Level 3 tendons, c) & d) Level 2 tendons for North and South frames respectively

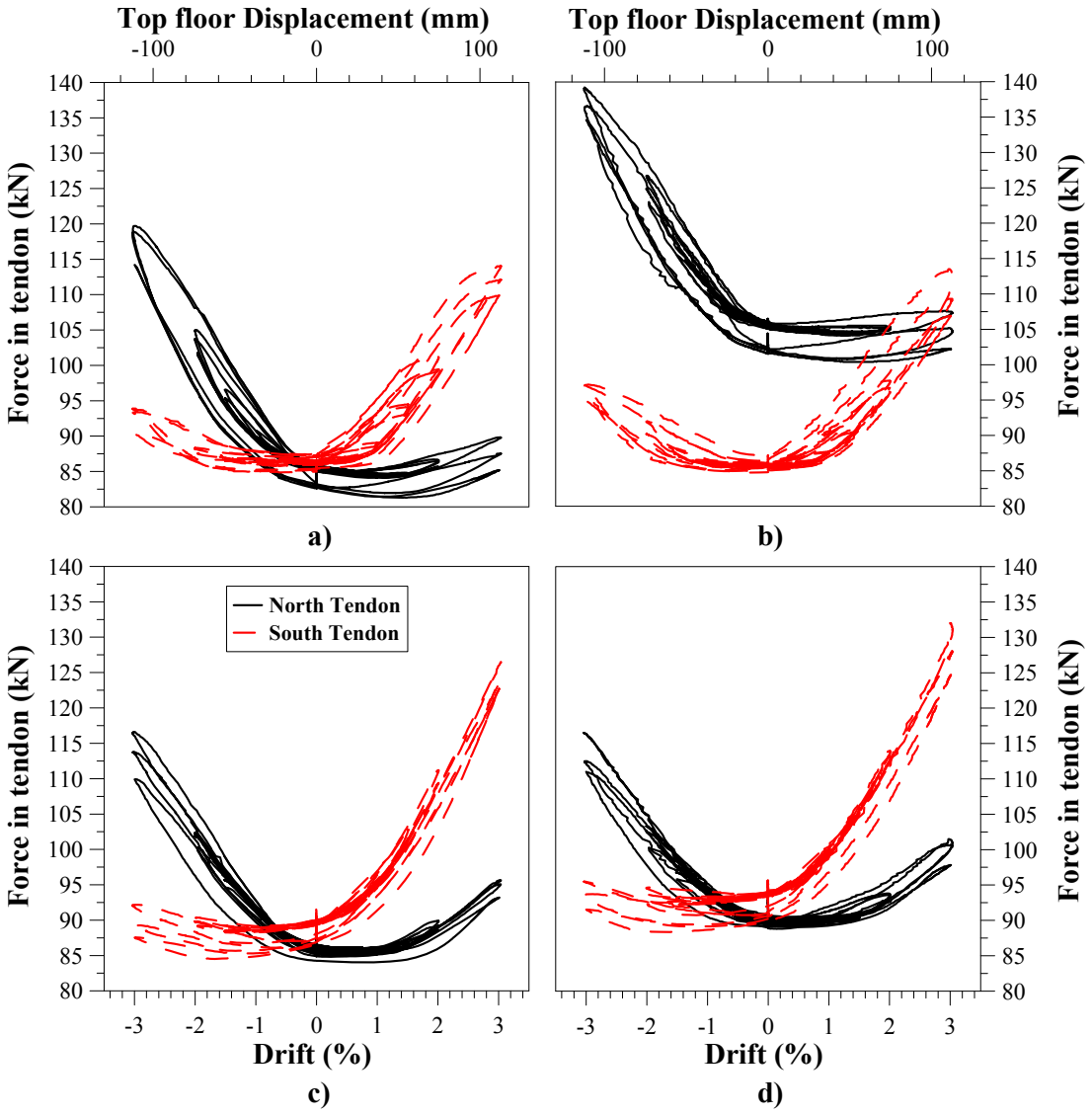

Figure B.3.5. Force in the wall post-tensioning tendons for Test 7: a) NW Wall b) NE Wall c) SW Wall d) SE Wall

B.4. FRAME ELONGATION

The longitudinal elongation/shortening deformation of the frame was recorded using potentiometers, as shown in Figure B.4.1. The total elongation is plotted for each uni-directional frame test from Stage 1 and 2. The elongation/shortening during each test is examined, dividing the total deformation into components. In all graphs, shortening is positive and elongation is negative.

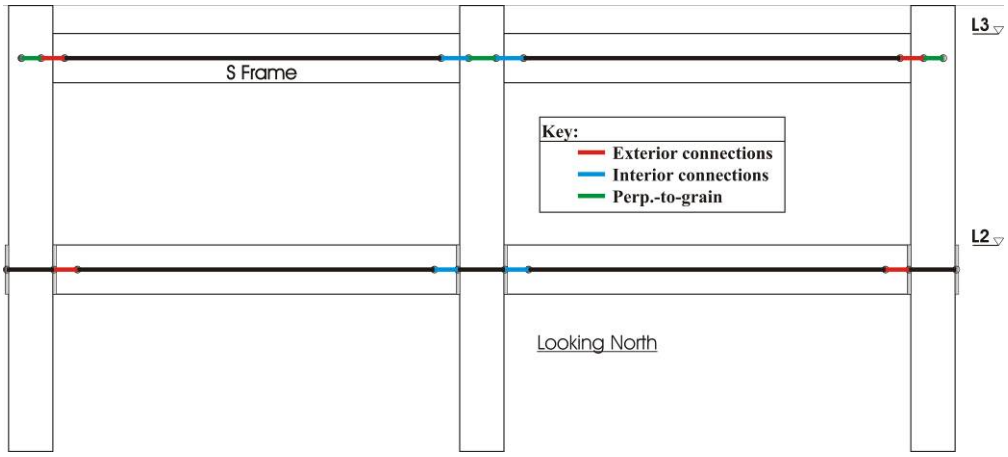

Figure B.4.1. Potentiometers for measuring longitudinal frame deformation

B.4.1. Uni-directional tests

Figure B.4.2 shows the total frame elongation/shortening of Level 2 and 3 for Stage 1, Test 1 and 2. The longitudinal deformation at Level 3 differs for positive and negative drifts, due to application of lateral load from the test apparatus. For negative drifts, the rams is in tension, resulting in increased elongation of the frame. For Test 1, inelastic deformation in the west exterior BC connection results in permanent frame shortening of 3 to 4mm. For Test 2, there is no further permanent shortening. When the ram is in tension, the maximum elongation on Level 3 is 4mm. On Level 2, there is no significant inelastic shortening. A peak elongation of 4mm occurs during Test 1. For Test 2, due to the presence of external reinforcement, the connection rotation is reduced, resulting in less elongation (approximately 2.5mm).

The longitudinal deformation for the frame during the Stage 2 tests (including the floor system) is shown Figure B.4.3. Unlike Stage 1, the longitudinal deformation at Level 3 is similar for positive and negative drifts due to the Stage 2 loading apparatus. The longitudinal deformation of both Level 2 and 3 is similar to that of Stage 1, indicating the floor system did not have a significant affect on the frame elongation. This is because the majority of frame elongation has occurred at the exterior connections which are not connected to the floor diaphragm (as discussed further below).

Differential longitudinal deformation on Level 2 and 3 may have resulted in additional axial forces in the beams. Using simple beam theory and the method of superposition, the worst-case differential elongation of 6mm will result in approximately 40kN compression and 20kN tension at Level 2 and 3 respectively. The increased compressive force would have contributed to the moment capacity of the Level 2 connections (see Figure B.2.4).

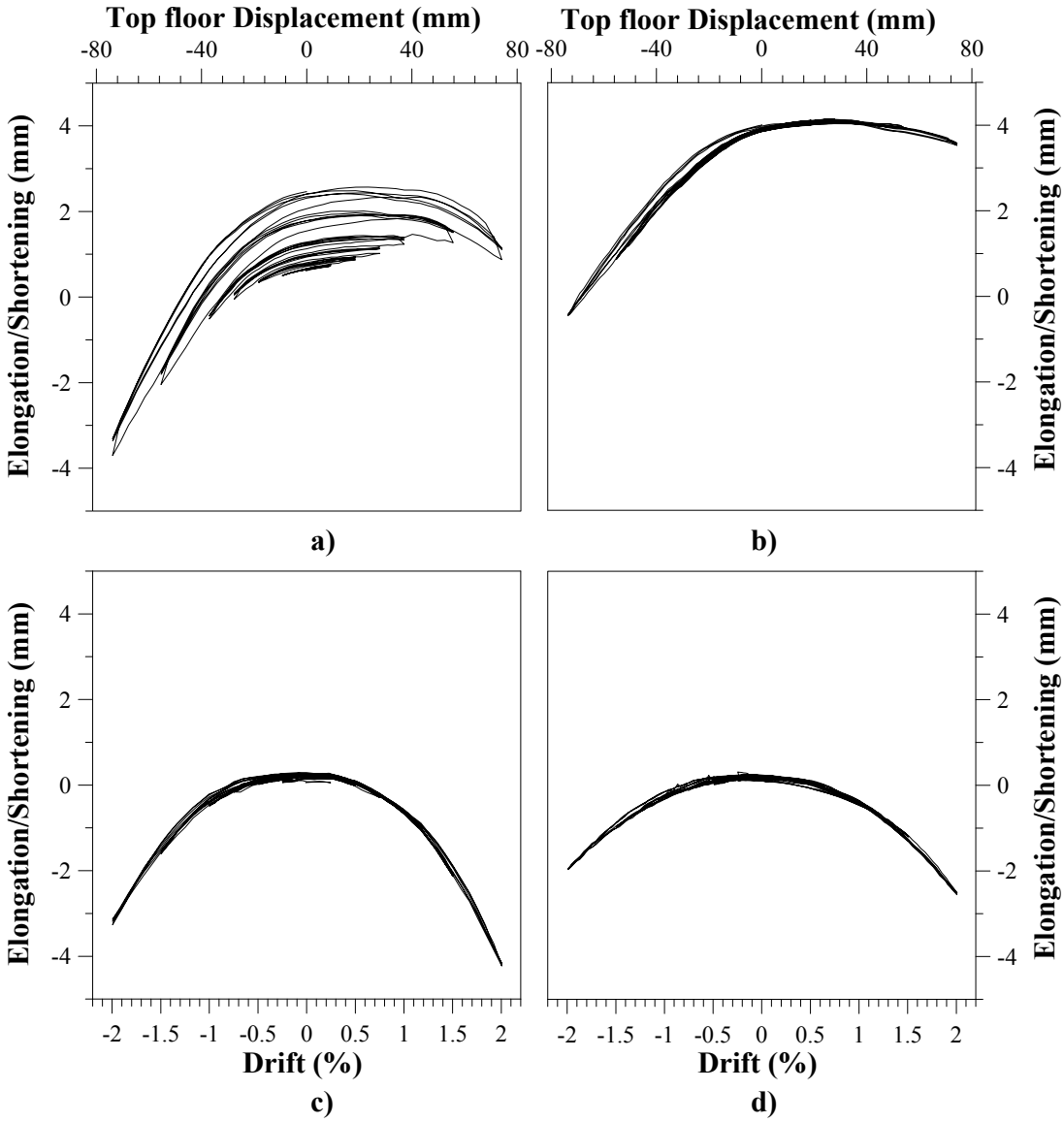

Figure B.4.2. Frame elongation for Stage 1: a) & b) Level 3, c) & d) Level 2 for Test 1 and 2 respectively

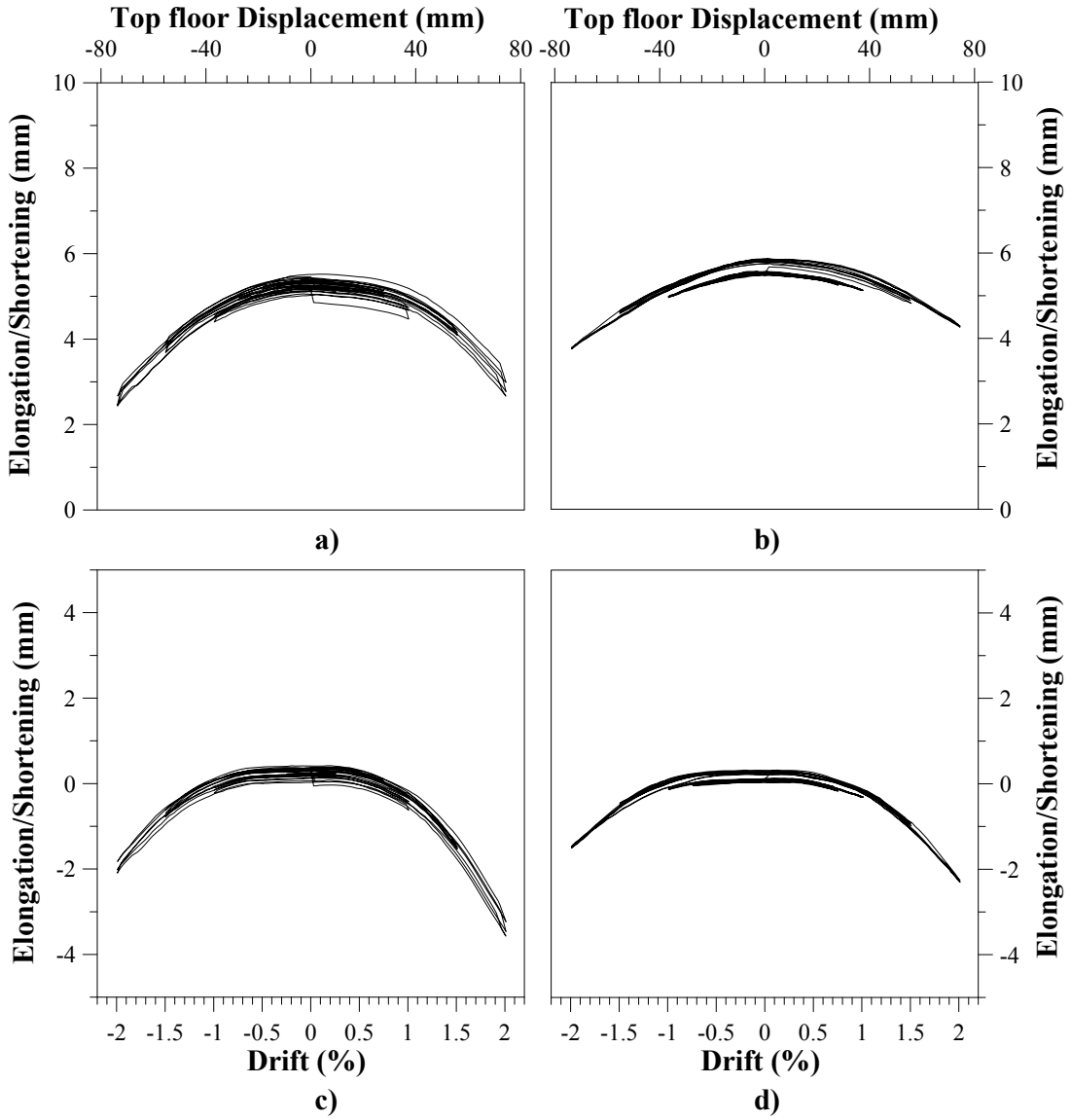

Figure B.4.3. Frame elongation for Stage 2: a) & b) Level 3, c) & d) Level 2 for Test 1 and 2 respectively

The longitudinal deformation is deaggregated into the localized deformation around the exterior and interior BC connections, and the perpendicular-to-grain timber on Level 3, as shown in Figure B.4.1.

For Stage 1 (see Figure B.4.4) the most significant elongation on Level 2 occurs in the exterior connections for both Stage 1 and 2. There is a significantly less longitudinal deformation for Test 2 (Stage 1) due to reduced connection rotation (because of the presence of external reinforcement). On Level 3, the most significant elongation occurs within the exterior BC connections, but this is offset by the permanent compressive deformation in the perpendicular-to-grain timber within the columns. For Test 2, the permanent compressive deformation almost completely offsets the elongation due to connection rotation. There is significantly more elongation in the exterior connections for negative drifts due to forces applied by the experimental apparatus.

The elongation of the interior connections appears to have reduced for Stage 2, compared to Stage 1 on both Levels 2 and 3. On Level 3, this could be attributed to the restraint provided by the floor diaphragm, the different load apparatus for Stage 1 and 2 or inelastic deformation within the connections. However, if the average elongation of the interior connections for positive and negative from Stage 1 is taken, this value compares well with Stage 2. This would indicate the differential elongation in the interior connections is caused by the loading apparatus, and not the restraint provided by the floor. For Level 2, there appears to be slightly less elongation of the internal BC connections for Stage 2. However, any restrain does not appear to have significantly affected the moment resistance provided by the connections.

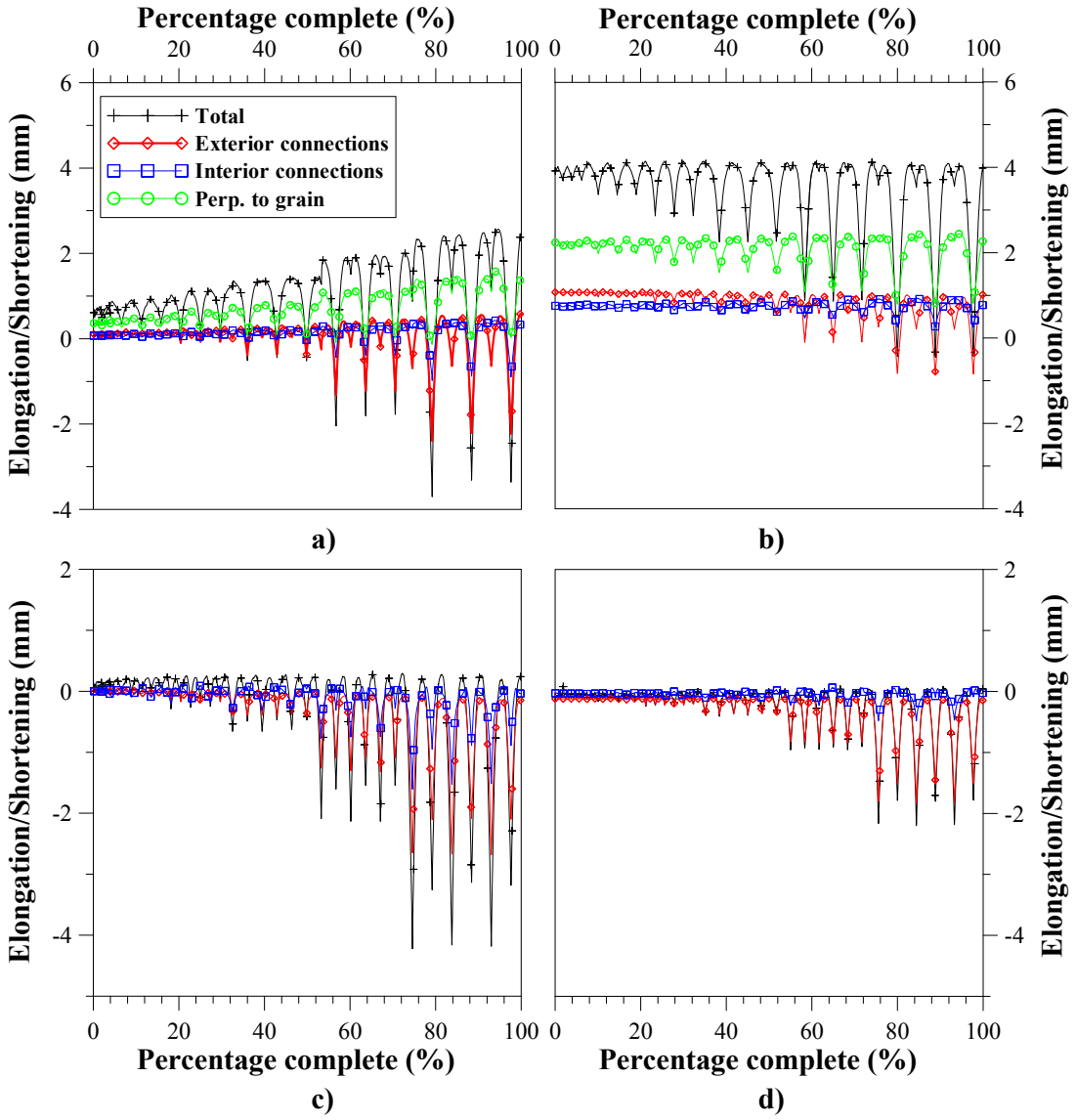

Figure B.4.4. Frame elongation for Stage 1: a) & b) Level 3, c) & d) Level 2 for Test 1 and 2 respectively

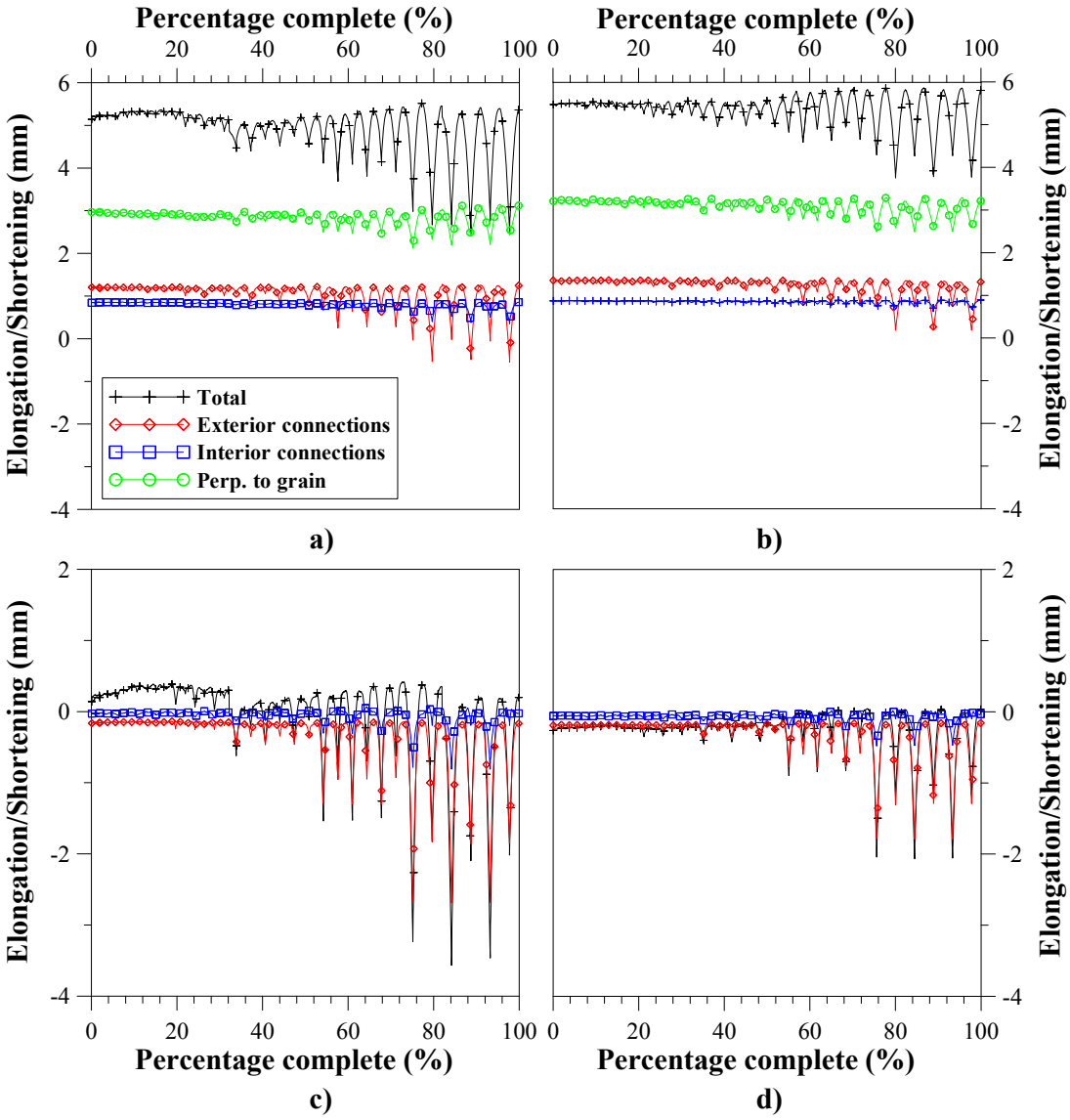

Figure B.4.5. Frame elongation for Stage 2: a) & b) Level 3, c) & d) Level 2 for Test 1 and 2 respectively

B.4.2. Bi-directional test

The total longitudinal deformation of the frame was monitored during the bi-directional test (Test 7), as shown in Figure B.4.6. For the uni-direction part of the bi-directional loading protocol, the elongation is similar to the previous uni-directional frame test up to 2% drift (Stage 2, Test 2). However, under bi-directional loading (during the clover part of the loading protocol) the elongation appears to slightly increase. For Level 3, bi-directional loading appears to increase in the elongation of the frame by 1mm at 2% drift and 2.5mm at 3% drift. For Level 2, the variation between uni-directional and bi-directional cycles is less with 1.5mm at 3% drift. Furthermore, for the NS uni-directional cycles there is an elongation of approximately 1.5mm and 2.5mm during the 3% drift cycle for Level 2 and 3 respectively. This indicates that elongation of the frame is slightly increased by bi-directional loading, which could be caused by bowing of the frame out-of-plane. As the load is applied to the floor diaphragm in the NS direction, it deflects in-plane (like a simply-supported beam), which results in elongation on the frame in the orthogonal direction. Using simple beam theory and assuming a crack section stiffness of 20% of the gross section stiffness for the concrete slab (from Chapter 3), the peak out-of-plane deformation of the floor system is estimated to be 2.5mm on Level 3. Converting the elongation in the NS direction to curvature, the estimated peak displacement of the floor on Level 3 is 7mm. Hence, it is feasible that significant out-of-plane floor deformations have occurred and the calculations would indicate that the stiffness of the floor diaphragm is significantly less than the gross section stiffness.

According to method of superposition, differential elongation of L2 and L3 at 3% drift of 8mm may have resulted in additional compressive and tensile axial forces in the L2 and L3 beams of approximately 50kN and 25kN respectively.

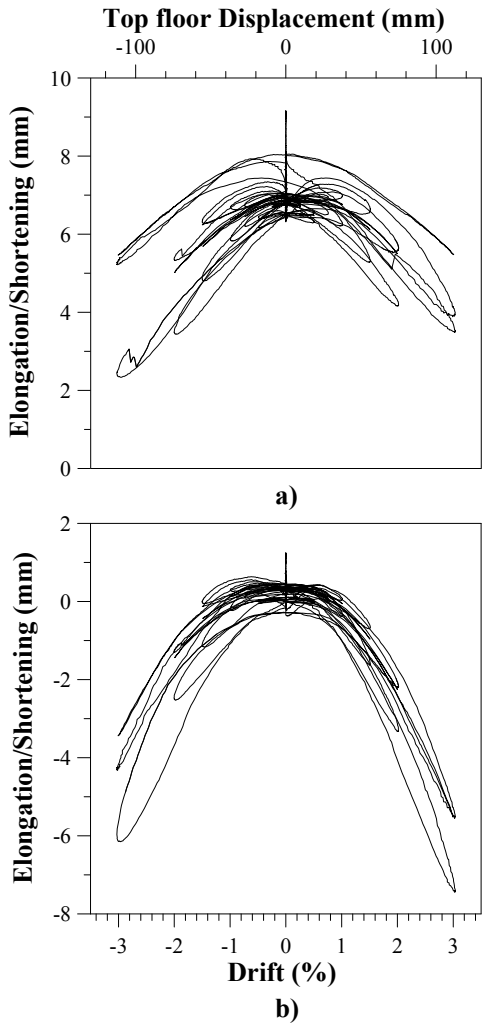

Figure B.4.6. Frame elongation for Stage 2, Test 7: a) Level 3 b) Level 2

B.5. FLOOR SLAB ELONGATION

The floor slab deformations were monitored using a calibrated 'Demec Gauge' and 'Demec Points', as shown in Figure B.5.1. The total elongation of the slab, as determined by summing all the Demec Gauge readings on one line, is given in Table B.8.1. The elongation is deaggregated into the individual readings along the EW (or X) axis of the building (see Figure B.5.1) in Figure B.5.2and Figure B.5.3 for Test 1 and Test 7 respectively.

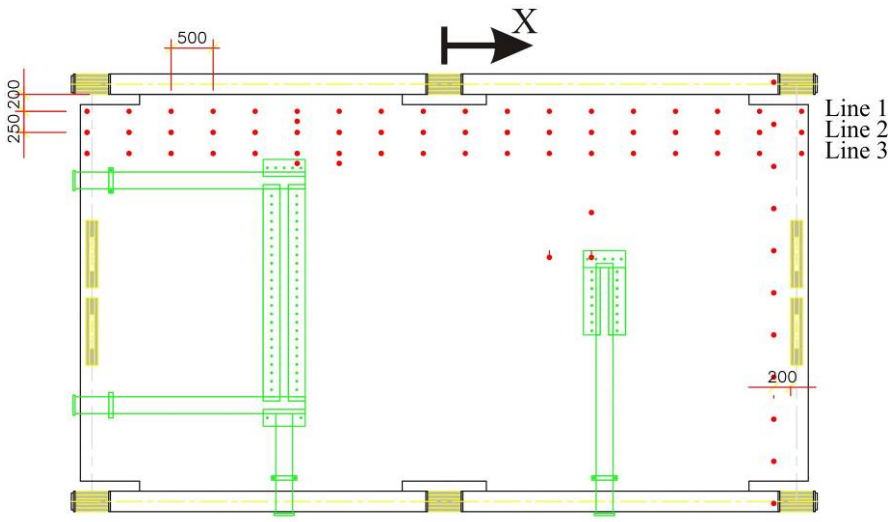

Figure B.5.1. Demec points on floor slab

The peak elongation of the slab over its entire length during uni-directional Test 1 at 2% drift is 1.3mm, with a peak residual deformation of the floor is 0.2mm. Even if the total deformation of the slab was concentrated in one crack, according to FEMA-356 (2000), the slab would not required repair (under immediate occupancy criteria). Observing Figure B.5.2, it is evident that there is significantly more floor slab elongation for negative drifts than positive drifts. This is due to the application of lateral load by the test apparatus. For negative Drifts, the slab is predominately in tension, exacerbating elongation. Most of the deformation that occurs for negative drifts is concentrated around the walls, where the there is deformation incompatibilities between the floor and wall systems, as the building undergoes lateral drift. The residual deformation after Test

1 is relatively uniform, with many areas that have shortened, offsetting areas that have elongated.

Under bi-directional loading (see Table B.5.1 and Figure B.5.3), the residual elongation after 2% drift is larger than for uni-directional loading. This is likely to be due to additional cracking that has occurred due to out-of-plane loading. The most significant residual deformation is adjacent to the walls (at the edges of the floor). The peak residual elongation of the slab after 3% drift is 1.0mm. Again, even if the recorded peak deformation (over a 500mm gauge length) was localized in one crack, the crack would not require repair according to FEMA-356 (2000).

Table B.5.1. Total floor slab elongation/shortening deflection measurements (mm)

Test	Description	Line 1		Line 2		Line 3	
		L2	L3	L2	L3	L2	L3
Test 1	+2.0% Drift	-0.10	0.14	-0.05	0.15	-0.08	0.15
	-2.0%Drift	0.75	1.25	0.88	1.27	0.90	**1.32**
	Residual	-0.04	0.15	0.07	0.18	0.07	0.22
Test 7	Residual after 2% Drift cycle	-0.68	0.69	-0.60	0.86	-0.62	0.96
	Residual after 3% Drift cycle	0.18	1.82	0.15	1.97	0.10	**2.04**

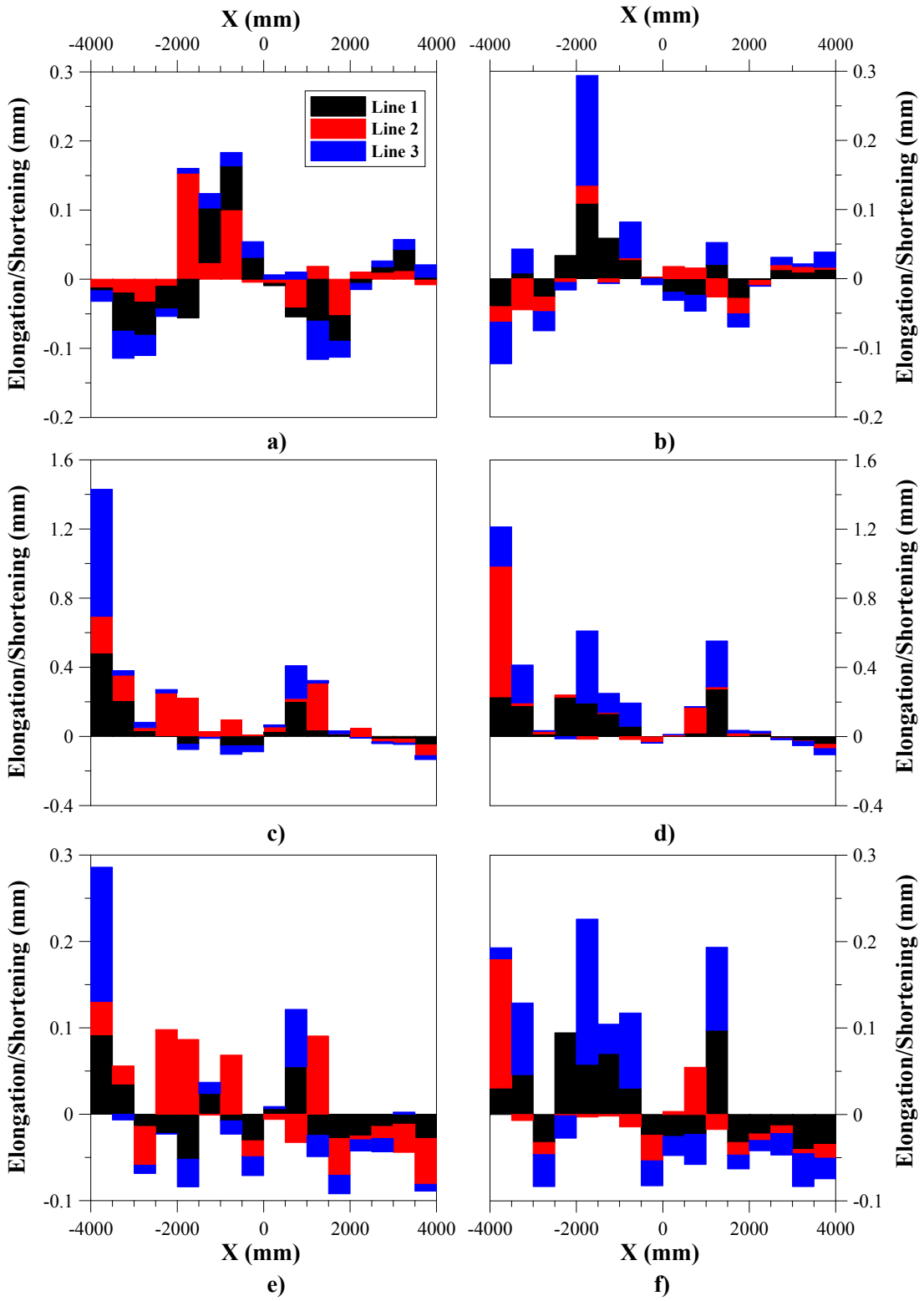

Figure B.5.2. Elongation of the concrete slab for Test 1: a) & b) Positive 2% Drift, c) & d) Negative 2% Drift, e) & f) Residual for Level 2 and 3 respectively

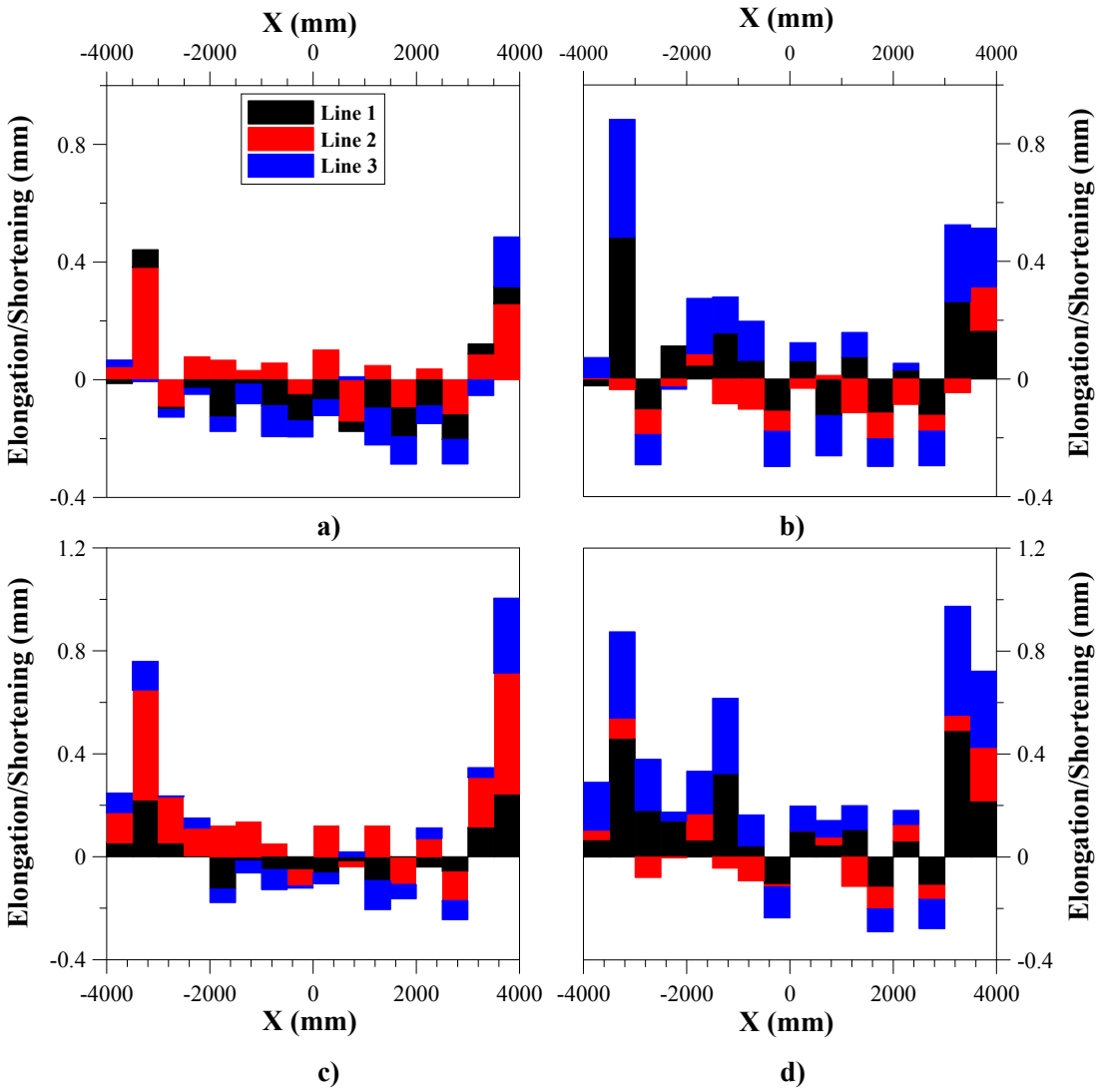

Figure B.5.3. Elongation of the concrete slab for Test 7: a) & b) Residual after 2% Drift, c) & d) Residual after 3% Drift, for Level 2 and 3 respectively

B.6. COLUMN AND WALL INCLINATION

Inclinometers were placed on all of the columns and two of the walls. Each was fixed at the base and at the top of element (in line with L3). The inclinometers have relatively low precision (compared to Potentiometers) but are useful to determine if the rotation of each of the walls and columns are similar. The inclination of the columns or walls can be reduced due to base slippage, which can influence the capacity of the frame and wall systems. Conversely, the inclination of the columns can be increased due to beam elongation.

B.6.1. Uni-directional tests

The ratio of the column and wall rotations and the control Drift (θ/θ_D) for the uni-directional tests are shown in Figure B.6.1. The data precision at small rotations is poor. For larger rotations, the inclination of the columns and walls tests, on average, tends to approximately 95% of the control drift (as defined in Chapter 5). This indicates that the slippage of column bases is minor. Figure B.6.3 shows the column-base slippage for four of the columns for uni-directional tests in the frame and wall direction. The peak slip is approximately 2mm at 2% drift, which equates to 0.05% drift. Hence, column-base slip had little effect on the inclination of the columns. Furthermore, there is no discernible difference between the inclination of the east and west columns. Hence, the outer columns have not splayed due to beam elongation, further indicating that beam elongation was negligible.

For the walls tests, there appears to more variation between the inclination of the walls and the control drift, as illustrated in Figure B.6.1c and d. The variation may be more significant for Test 4, which includes the UFP couplers, due to wall slip at base. It was observed (see Appendix C) that the walls tended to splay at the base due to wedging actions created by the UFP couplers.

To investigate further, the control drift and the inclination of both the columns and walls for the 2% drift cycles are shown in Figure B.6.2. Figure B.6.2a and b. Again, the

inclinations of each column for the uni-directional frame tests are similar to the control drift. There is slightly more instability in the inclination readings for the wall tests but generally good agreement with the control drift. Hence, splaying at the base of the walls does not appear to have been significant.

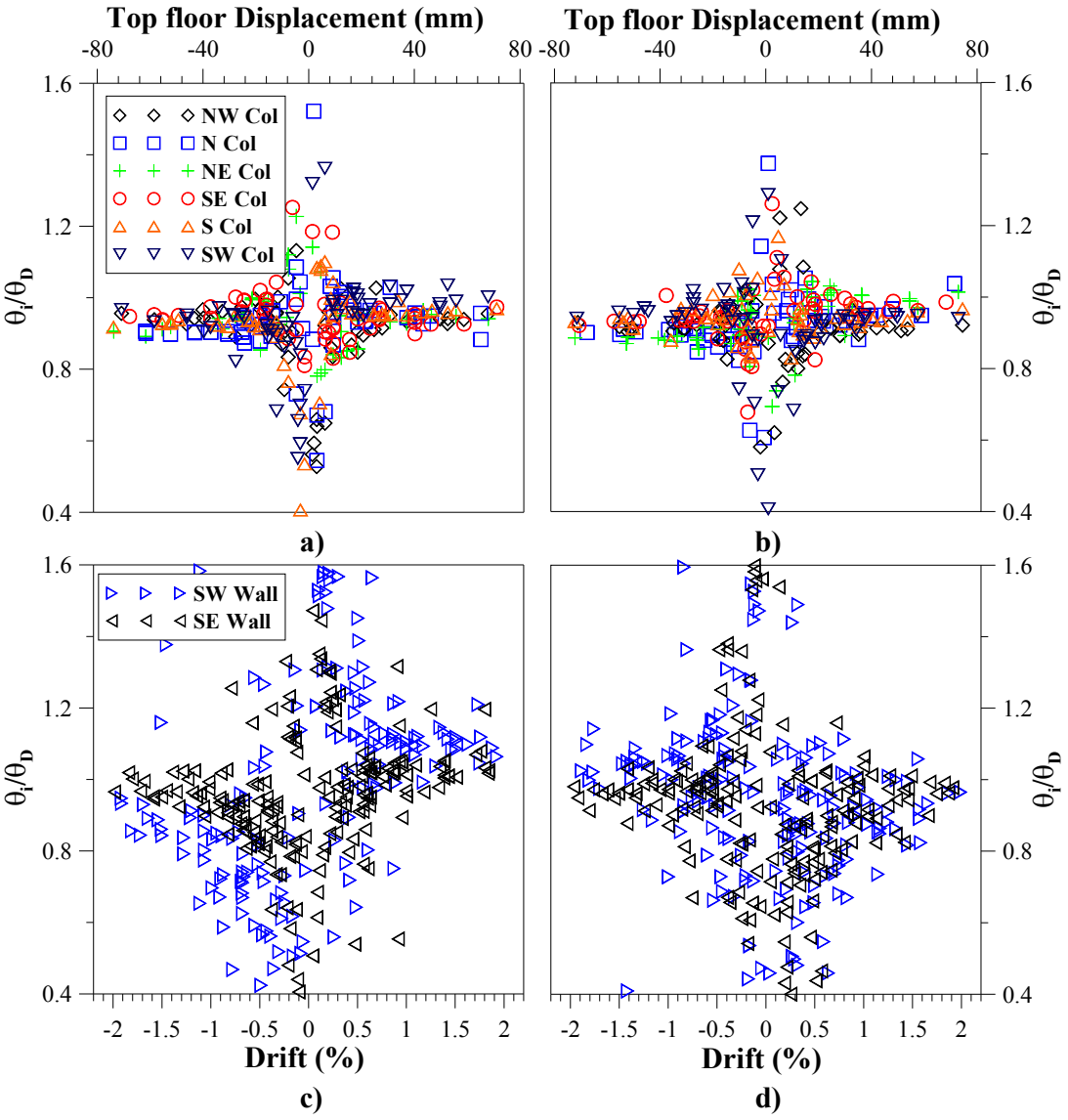

Figure B.6.1. Wall and column inclination versus Drift of the control column (every 40th data point): a) Stage 1, Test 1 b) Stage 2, Test 1 c) Stage 2, Test 3 d) Stage 2, Test 4

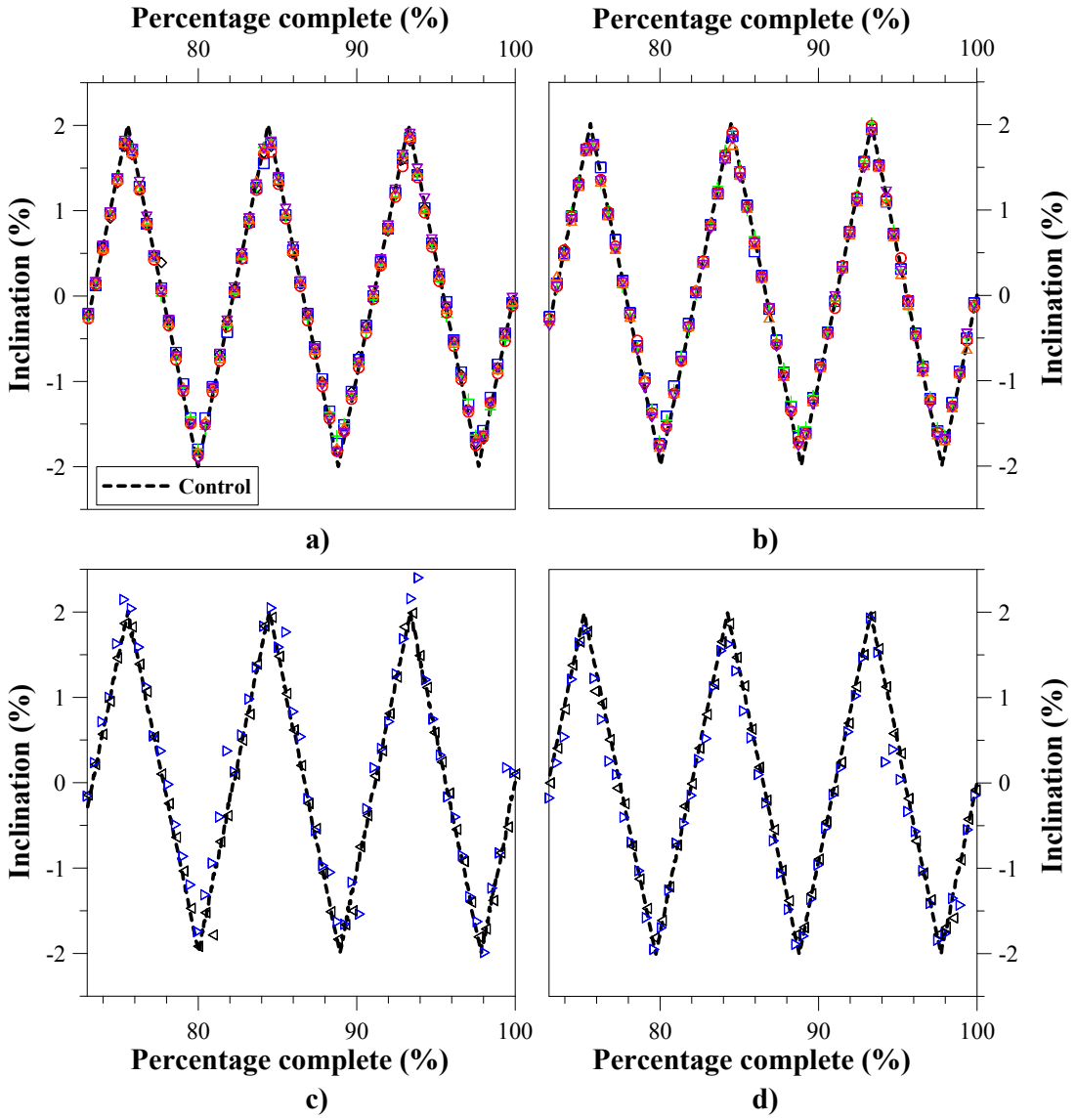

Figure B.6.2. Wall and column inclination for 2% Drift cycles: a) Stage 1, Test 1 b) Stage 2, Test 1 c) Stage 2, Test 3 d) Stage 2, Test 4 (refer to Figure B.6.1 for legend)

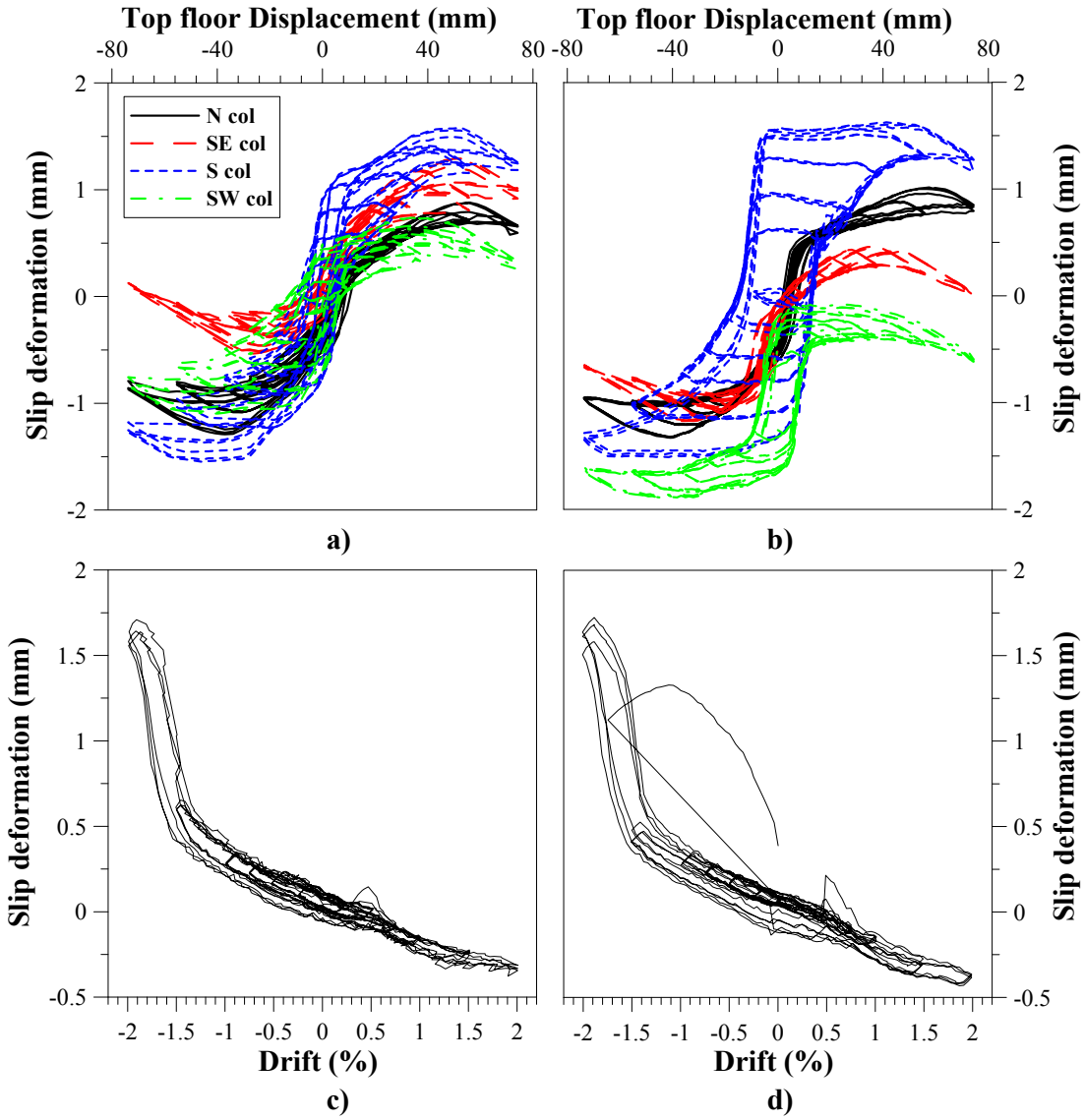

Figure B.6.3. Column-base slip for uni-directional tests a) Stage 1, Test b) Stage 2, Test 1c) Stage 2, Test 3 (NS direction) d) Stage 2, Test 4 (NS direction)

B.6.2. Bi-directional tests

For the bi-directional tests, the inclination of the columns and walls is in general similar to the control drift. While there is imprecision in inclination recordings, the ratio of the column and wall rotation and the control drift (θ/θ_D) tend to unity for both EW and NS loading, as shown in Figure B.6.4. Observing the inclination for columns and walls over the 3% drift cycle (see Figure B.6.5), there is no significant deviation from the control drift, except for the SE column. This is because target drifts were not imposed to the SE column in the loading methodology (refer to Chapter 5). The inclinometer on the SW Wall for EW loading was determined to be faulty and hence does not appear in the figures below.

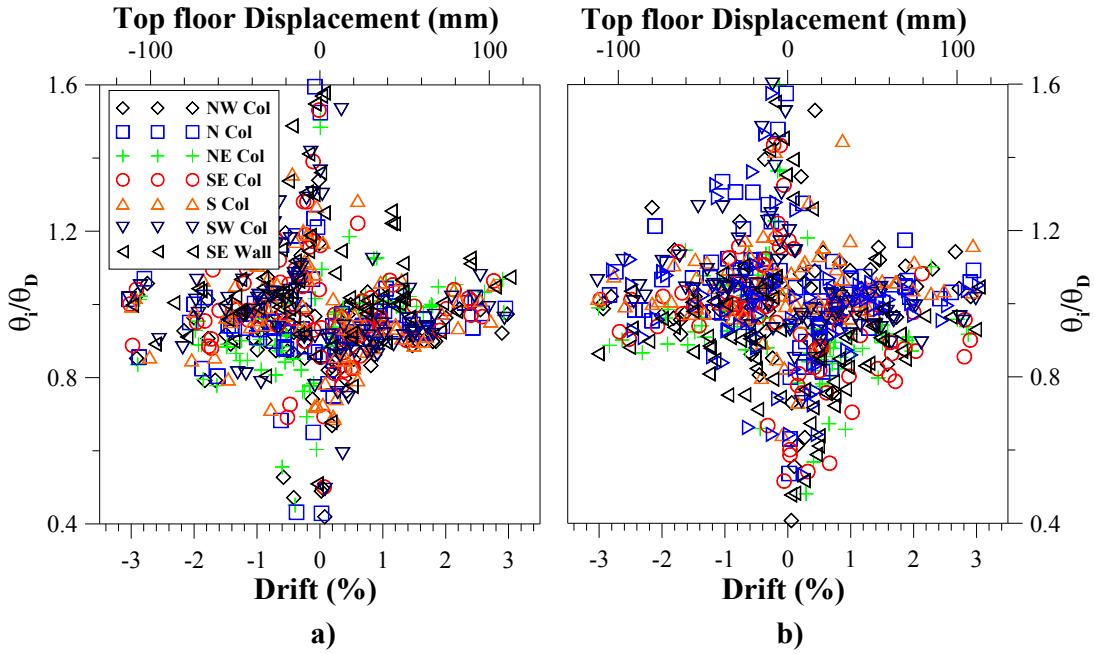

Figure B.6.4. Wall and column inclination versus control Drift for Stage 2, Test 7 a) EW direction b) NS direction

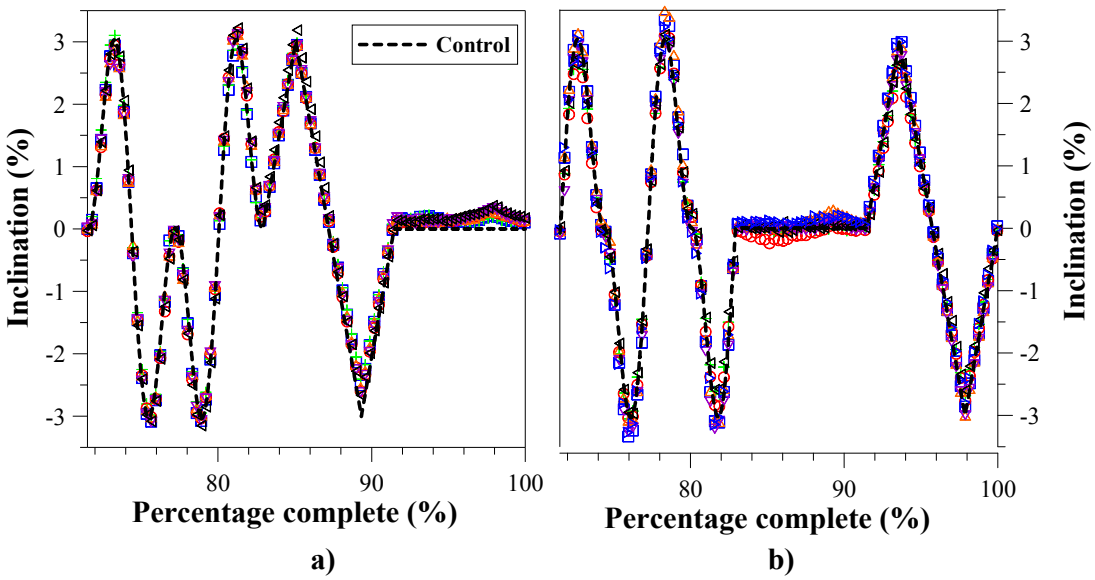

Figure B.6.5. Wall and column inclination for 3% Drift cycles for Stage 2, Test 7: a) EW direction b) NS direction (refer to Figure B.6.4 for legend)

B.7. INVESTIGATION OF TIMBER PROPERTIES

Within this section, experimental data is considered in an attempt to better characterise the material properties of the timber. Key parameters that are investigated are the parallel and perpendicular-to-grain elastic modulus and the shear modulus.

B.7.1. Parallel-to-grain timber stiffness

The elastic modulus of timber parallel-to-grain was characterized using factory test data (Banks 2010), but can be verified by considering experimental data. This is done by considering the axial elastic deformation of the beams and walls that occurred during the application of post-tensioning, as expressed below:

$$E = \frac{F_{pt} L_g}{\Delta_l A}$$

Where: F_{pt} = the axial force applied by the post-tensioning
A = the area of the beam (84800mm^2) or wall (91200mm^2)
L_g = the gauge length of the Pots
Δ_l = the longitudinal displacement of each Pot

Deformation data is provided by potentiometers that are placed longitudinally in the centerline of the beams in the south frame and down either side of the NW wall (see the appended compact disc). The post-tensioning force is determined by using data from load cell placed on the some of the outer tendons and assuming the inner tendons forces are similar.

The experimental data indicates that the elastic modulus of the timber is approximately 12GPa (see Table B.7.1). The data gives values between 10 and 16GPa, indicating that there are some experimental inaccuracies. Hence, for calculation of moments, in the preceding sections, the manufacture specified elastic modulus of 11GPa was used, which is within 15% of the calculated average.

Table B.7.1. Estimated parallel-to-grain Elastic Modulus from experimental data

Location	Pots	A (mm^2)	L_g (mm)	Δ_l (mm)	F (kN)	E (MPa)
NW Wall	17,18,20,21	91200	595	0.210	444	13794
SW Wall	12,13	91200	598	0.239	453	12428
L2-W Beam	163	84800	3390	1.442	371	10285
L2-E Beam	167	84800	3401	1.259	371	11818
L3-W Beam	173	84800	3530	0.953	368	16074
L3-E Beam	177	84800	3520	1.351	368	11307
					Average:	**12618**

B.7.2. Perpendicular-to-grain timber stiffness

The perpendicular-to-grain (perp-to-grain) elastic modulus is difficult to accurately define using experimental data from the test building. While the Level 3 columns were subjected to compression perp-to-grain, the column fibers at the top and bottom of the beam are subjected to tension, which increases the bearing stiffness. Furthermore, the diffusion of compressive stresses into the column and the presence of screw reinforcement may have affected the perceived perp-to-grain elastic modulus of the column. Newcombe (2008), Davies and Fragiacomo (2008), provide some detail on the actual perp-to-grain elastic modulus, without bearing effects at the edges. Newcombe (2008) suggests the perp-to-grain elastic modulus is as low as 300MPa. This is considered as a lower bound, for comparison with experimental data.

The above points notwithstanding, the experimental perp-to-grain stiffness of the column is still important for modeling the frame response (see Chapter 6). The average calculated perp-to-grain elastic modulus is approximately 660MPa. Hence, the combined effect of edge-bearing, diffusion of stresses and screw reinforcement appears to have effectively increased the perp-to-grain stiffness of the timber, according to Newcombe (2008), by approximately 100%.

Table B.7.2. Estimated perpendicular-to-grain Elastic Modulus from experimental data

Location	Pots	A (mm^2)	L_g (mm)	Δ_l (mm)	F (kN)	E (MPa)
L3-SW Col	171	84800	184	1.345	368	594
L3-S Col	175	84800	330	2.462	368	582
L3-SE Col	177	84800	184	0.996	368	802
					Average:	**659**

B.7.3. Shear stiffness

Similar to the parallel-to-grain elastic modulus, the shear modulus may be larger than the value specified by the manufacture (Futurebuild 2010). For the LVL in the test building the manufacturers specify a shear modulus of 660MPa. Here an attempt is made to verify the manufacture specified shear modulus by using experimental data from potentiometers placed on the walls, as shown in Figure B.7.1 below.

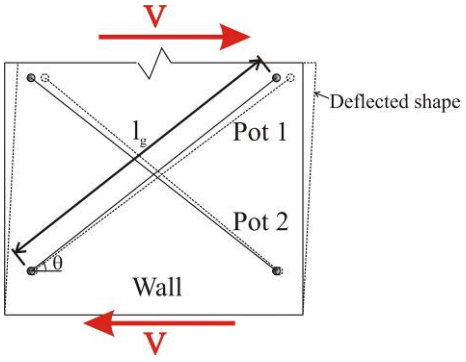

Figure B.7.1. Shear deflection of wall

The shear distortion, γ, can be calculated for the displacement of Pots 1 and 2, δ_1 and δ_2, and the angle of the Pots, θ, as follows:

$$\gamma = \frac{\delta_1 - \delta_2}{2l_g}\left(\tan\theta - \frac{1}{\tan\theta}\right)$$

The shear modulus can be defined as:

$$G = \frac{V}{\gamma A_s}$$

Applying simple beam theory, the shear area, A_s, of the wall sections have been calculated as a function of the total area, A_{tot}. Hence:

$$A_s = 0.85A_{tot}$$

The wall shear force, V, is difficult to accurately define from the experimental data. Some shear resistance will be provided by the columns, acting out of plane. However, the previous estimations of the out-of-plane moment capacity of the frame system indicate the shear resistance provided by the columns is relatively small (approximately 20kN in total) which is approximately 5% of the base shear of the building at 2% drift. Furthermore, due to coupling of the wall and floor system, it is possible that there will be differential shear force in each adjacent wall. To account for the variable in shear resistance provided by each wall the shear deformation of both the NW and SW walls was considered. The shear modulus is then calculated using an average shear force. Taking an average of the calculated shear modulus of the NW and SW wall should provide a good estimate of the actual shear modulus.

The shear modulus is calculated for Test 3 (Stage 2) for all drift values and is plotted in Figure B.7.2. While the precision of the data is relatively poor, the shear modulus appears to be slightly larger than the value specified by LVL producers (Futurebuild 2010) of 660MPa. Taking into account the shear capacity provided by the columns, the shear modulus appears to be between 690MPa and 920MPa. At higher drifts, the accuracy of the calculated shear modulus is expected to be affected by the disturbed strain region at the base of the walls. Hence, for modeling (see Chapter 6 and 7) the shear modulus will be taken as 660MPa.

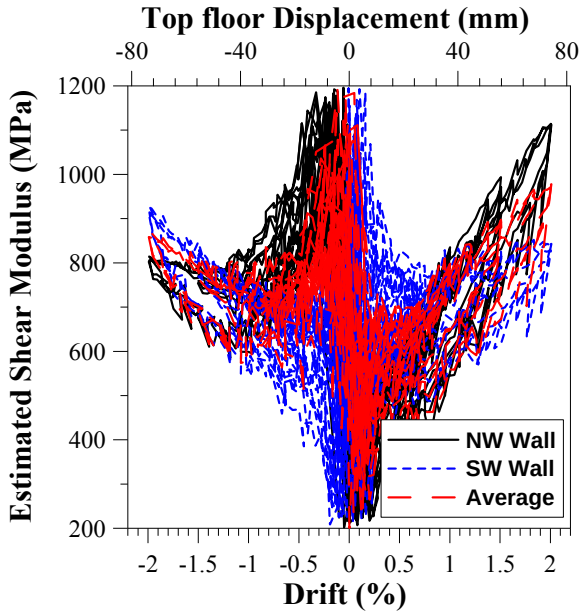

Figure B.7.2. Estimated shear modulus versus Drift (Stage 2, Test 3)

B.8. FLOOR SAGGING DEFORMATION

The floor deformations were monitored using a laser measurement device until the end of testing to ensure the loading apparatus was in alignment and that floor had not buckled due to the in-plane loading. A description of the measurement points for the laser is given in the appended compact disc.

The out-of-plane deformations of the floors are given in Table B.8.1.The seismic tests caused up to +/- 5mm deformation of the floor. The maximum sag for the 1st and the 2nd floor was 14mm and 15mm respectively, which is approximately equal to the span over 300. These values are slightly larger than the (10mm) predicted value by effective modulus approach in Appendix A. Hence, some of the floor distortions are like to be due to the seismic testing and loads applied by the testing apparatus.

Table B.8.1. Floor deflection measurements

Days after pour	Floor	Joist 1	Joist 2	Joist 3	Joist 4	Joist 5	Joist 6	Joist 7	Joist 8	Joist 9	Joist 10	EB1	EB2	PB	Notes:
1	1	1	3	5	6	3	2	4	5	4	2	0	0	4	
	2	2	4	5	3	2	4	5	3	2	N/A	1	0	N/A	
3	1	3	4	7	7	4	3	5	7	5	3	1	0	6	
	2	2	3	7	6	2	2	4	7	5	N/A	1	0	N/A	
6	1	3	7	8	6	4	4	7	8	5	4	0	0	7	
	2	3	7	8	5	2	3	7	8	5	N/A	0	0	N/A	
8	1	3	7	8	9	5	4	8	9	6	4	1	0	8	Steel plates on floor 1 and 2,
	2	3	7	8	8	3	3	8	10	6	N/A	1	-1	N/A	holes drilled in floor.
15	1	5	9	10	11	6	6	10	11	8	5	3	2	9	
	2	5	9	10	9	4	4	9	10	7	N/A	4	2	N/A	Steel plates removed.
22	1	5	10	11	12	7	6	10	11	9	6	3	2	10	Steel plates and square hollow
	2	5	10	11	11	6	5	9	11	9	N/A	4	2	N/A	sections on floors.
43	1	6	10	12	12	8	7	12	12	9	7	3	3	10	Splitter beams and rams
	2	6	10	12	12	8	7	12	12	9	N/A	4	3	N/A	added.
53	1	6	11	13	13	8	6	11	10	8	5	4	1	10	Last cycle in frame test at
	2	7	10	14	15	10	8	12	11	9	N/A	5	2	N/A	+2.0% drift.
53	1	4	8	9	9	5	7	12	12	9	6	1	4	8	Last cycle in frame test at -
	2	5	7	7	9	6	7	11	12	9	N/A	3	4	N/A	2.0% drift.
54	1	6	11	12	13	8	8	13	13	10	7	3	2	11	
	2	8	11	11	14	9	9	13	12	11	N/A	5	2	N/A	After frame test.
76	1	7	12	13	14	8	9	14	14	11	8	3	3	11	
	2	8	12	13	15	10	11	14	15	11	N/A	4	3	N/A	
78	1	7	12	14	14	9	10	15	14	11	8	3	3	12	
	2	8	12	13	14	10	11	15	14	11	N/A	4	2	N/A	
101	1	5	10	12	11	8	6	12	12	9	4	5	3	8	After final test up to 3.0%
	2	1	5	7	10	8	4	9	8	5	N/A	5	3	N/A	bidirectional.

APPENDIX C

EXPERIMENTAL OBSERVATIONS FOR THE TEST BUILDING

In this appendix experimental observations of the test building during each earthquake simulation are recorded using photographs and illustrations. The observations are categorize by those pertaining to the frames, walls, gravity system and floor slab.

C.1. FRAME SYSTEM

C.1.1. Stage 1: Test 1

The frame response at 1% drift was essentially elastic. The only observable inelastic deformation occurred at the west beam column connections on Level 3. At 1.5% drift, the connections appeared to remain within the elastic range. However, localized bearing deformations were observed on the Level 3 connections, which may or may not have been elastic.

At 2% drift, still the frame responded in an essentially elastic manner. However, for the west-exterior beam-column connections on Level 3, bearing failure within the columns (loaded perpendicular-to-gain) became pronounced. Timber crushing and bulging was observed, for positive 2% drift (when the rams were in compression).

a) **b)**

Figure C.1.1. Frame at 1.0% Drift a) 3D view b) S column

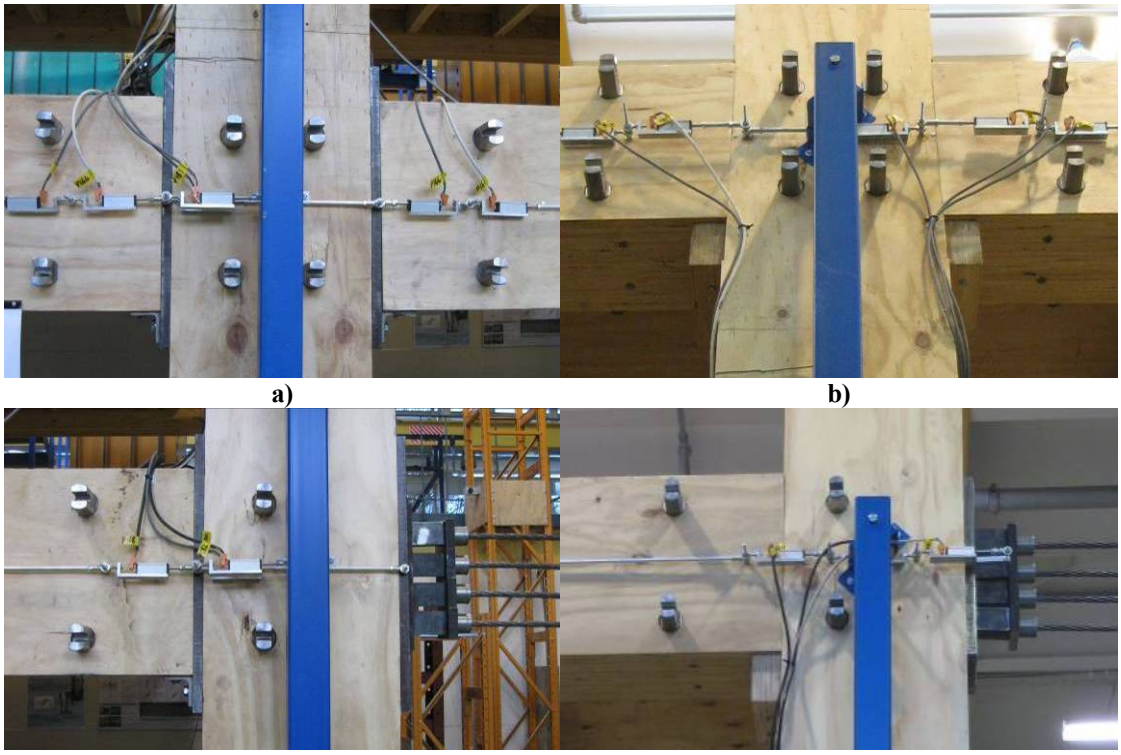

a) **b)**

c) **d)**

Figure C.1.2. Frame connections at 1.5% Drift a) S column L2 b) S column L3 c) SE column L2 d) SE column L3

a) **b)**

Figure C.1.3. Frame at 2.0% Drift a) 3D view b) S column

a) **b)**

Figure C.1.4. Exterior columns at 2.0% Drift a) SW b) SE

a) **b)**

Figure C.1.5. Damage to west columns on L3 at 2% Drift due to loading apparatus a) NW column b) SW column

The beam-column connection gap openings were larger on Level 2 than Level 3. At 2% drift the gap opening was approximately 5mm and between 0 to 2mm for Level 2 and 3 respectively.

During Test 1, the anchorage of the external reinforcement at the column-bases failed at some locations. Welds between steel foundation and anchorage plates fractured, causing a significant reduction in the strength of the frame (see Appendix B).

Screws that were used to provide temporary fixing between the beams and columns during construction were left in-place during testing. The 'Type 17' screws accommodated the deformations at the beam-column connections without fracturing. Hence, these fasteners could also be used for de-construction.

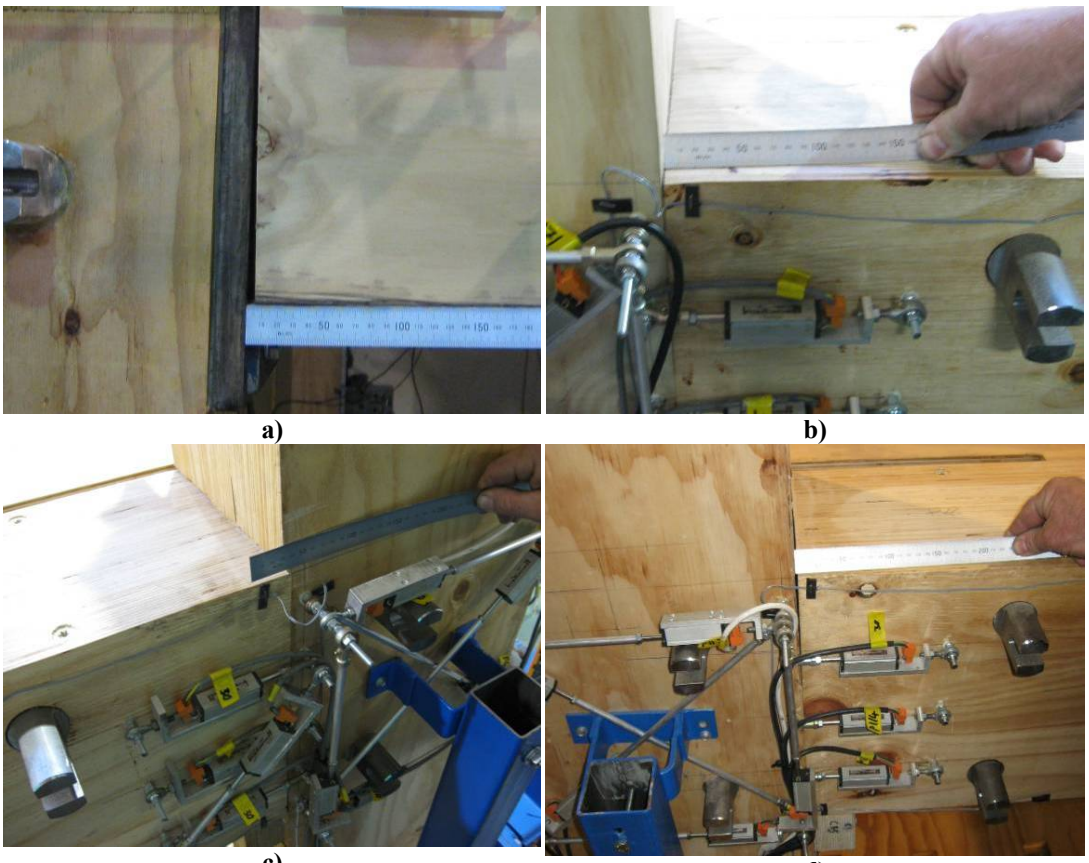

a) **b)**

c) **d)**

Figure C.1.6. BC connection gap opening at 2% Drift a) SW column L2 b) NE column L3 c) NW column L3 d) N column

a) **b)**

Figure C.1.7. Failure of column-base reinforcement anchorages

a) **b)**

Figure C.1.8. Temporary construction screws left in place during testing a) L2 b) L3

C.1.2. Stage 1: Test 2

For Test 2, external reinforcement was connected between the beams and columns. To minimize slop in the connections, the reinforcement was pre-loaded. Hence, the outer nuts were fastened first, to apply a pre-tension (of approximately 120N.m of torque), and then the inner nuts were tightened.

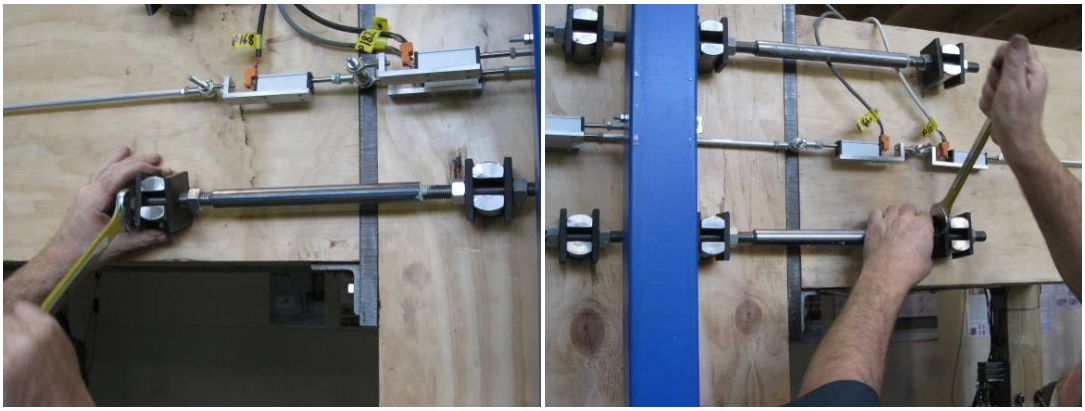

a) **b)**

Figure C.1.9. Attachment of external BC reinforcement

At 2% drift the frame deformation appeared similar to Test 1. On Level 2, the external reinforcement was subjected to elongations in the order of 2 to 5mm. On Level 3, the elongation of the reinforcement appeared to be negligible due to little gap opening.

As shown in figures below, the Level 2 connections deformed differently. Columns that were manufactured by Hunter Laminates Nelson Ltd had the internal steel plate reinforcement that was epoxied in-place, while MacIntosh Timber Laminates Ltd did not. Hence, internal steel plate reinforcement that was not expoxied in-place within the column rotated relative to the column.

a) **b)**

Figure C.1.10. Frame at 2.0% Drift a) 3D view b) S column

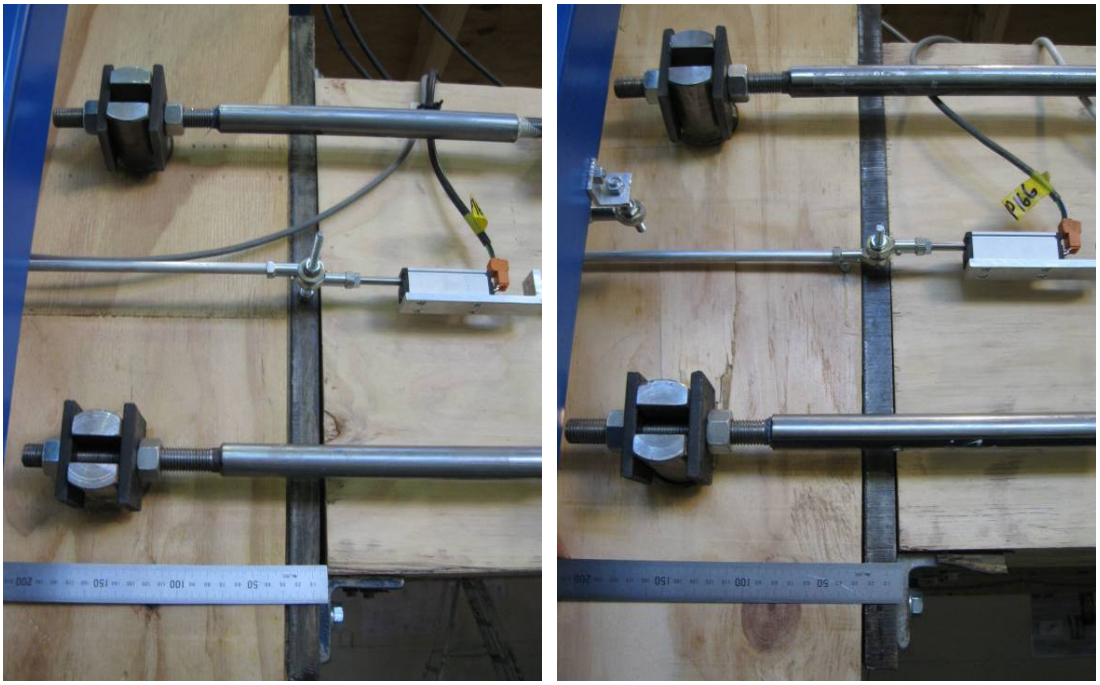

a) **b)**

Figure C.1.11. L2 BC connection gap opening at 2% Drift a) SW column b) S column

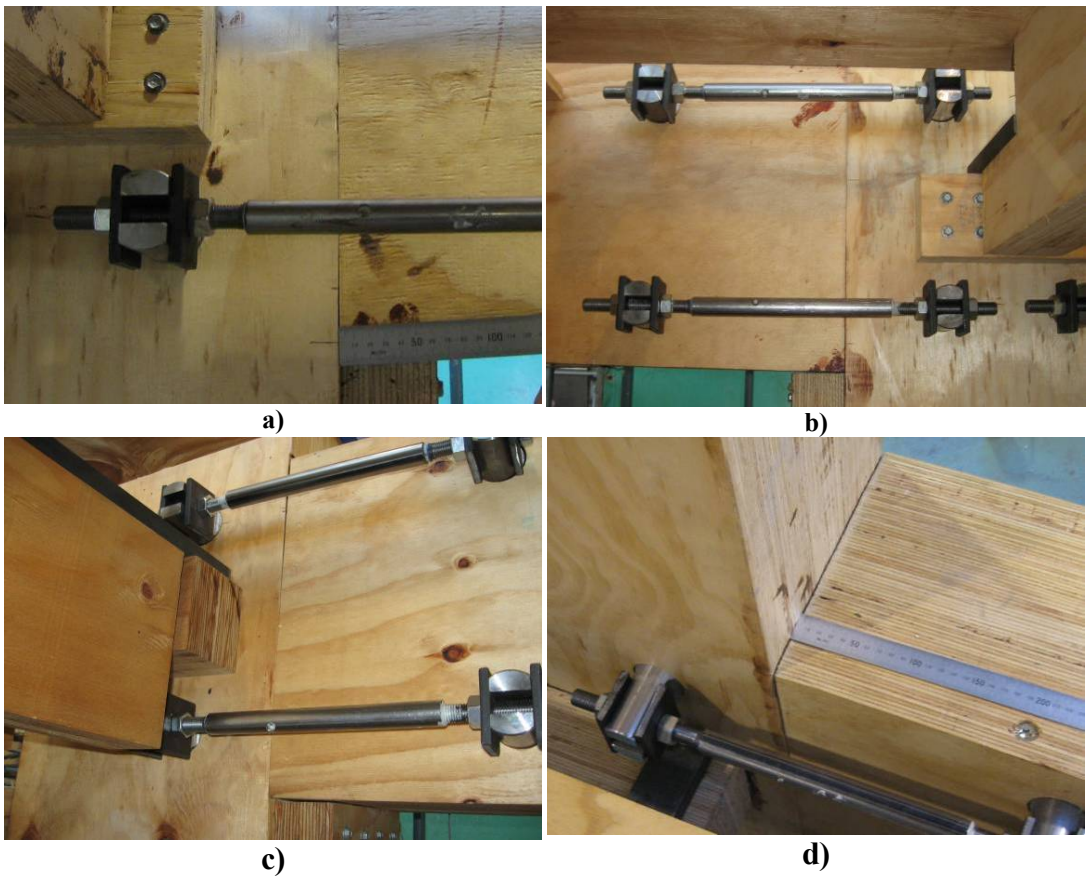

a) b)

c) d)

Figure C.1.12. L3 BC connection deformation at 2% Drift a) & b) S column c) & d) SE column

a) b)

Figure C.1.13. Damage to west columns on L3 at 2% Drift due to loading apparatus a) NW column b) SW column

a) **b)**

Figure C.1.14. Columns at negative 2% Drift a) S column b) SW column

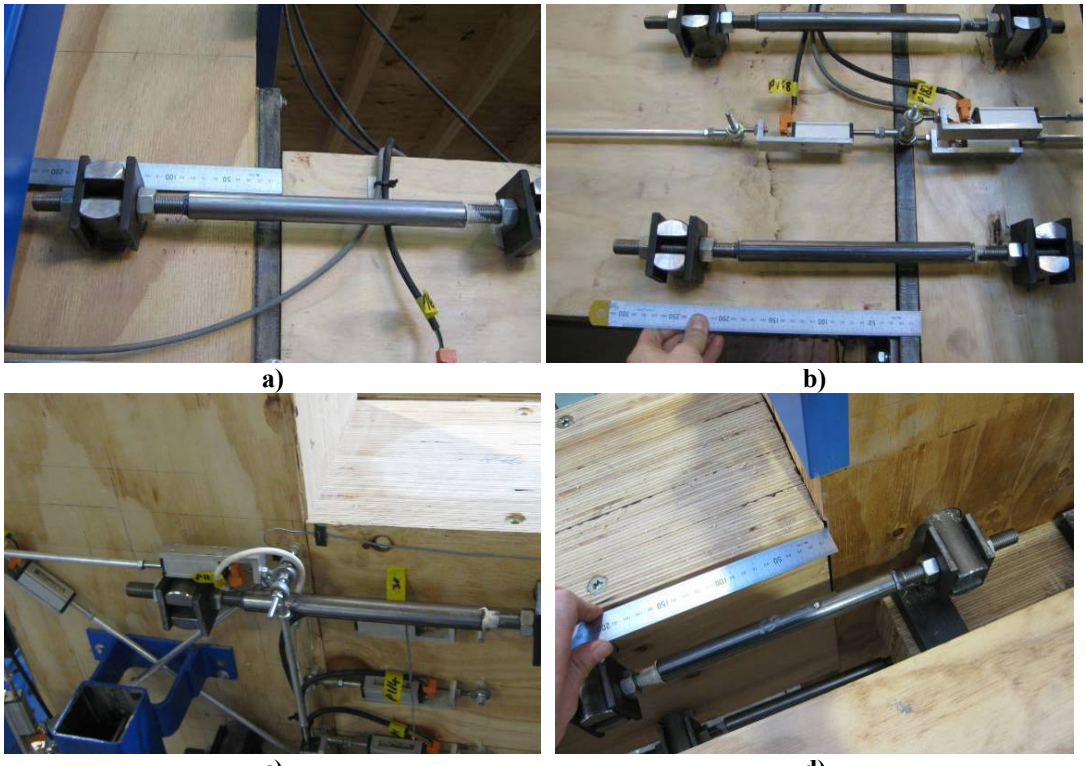

a) **b)**

c) **d)**

Figure C.1.15. BC connection deformation at negative 2% Drift a) SW column L2 b) SE column L2 c) NE column L3 d) SW column L3

At 2% drift, the column-base connections appeared to uplift by approximately 10mm at the unloaded edge of the column. The failure of the external reinforcement anchorages (discussed for Test 1) was noticed during Test 2. Hence, the anchorages were repaired and Test 2 was repeated.

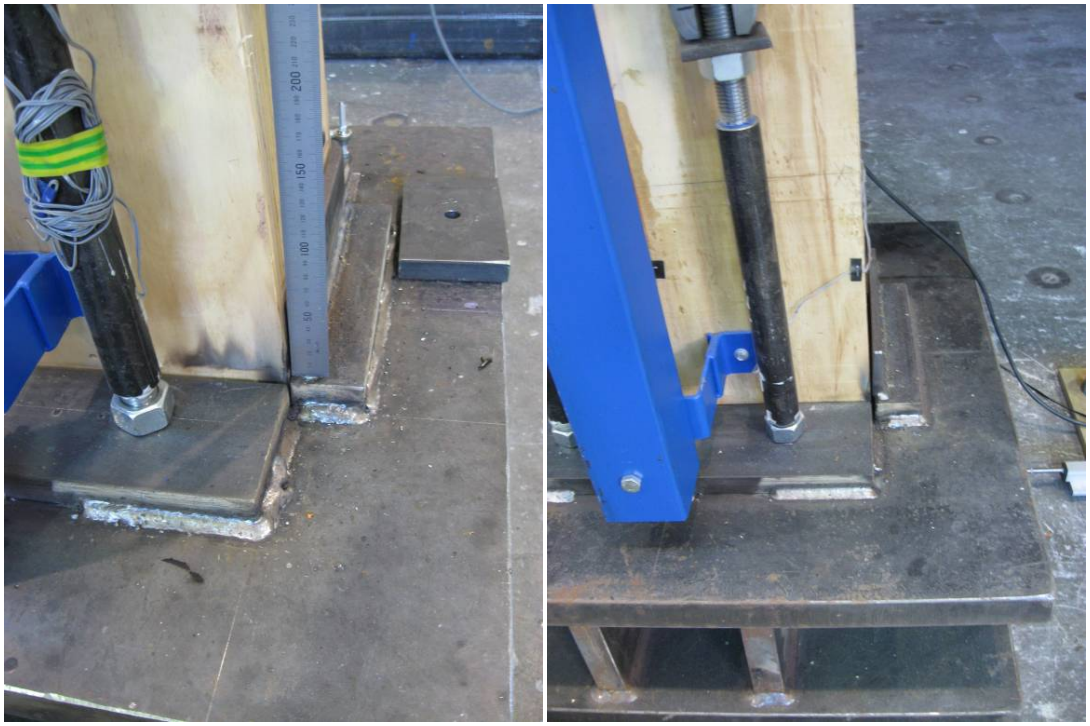

a) **b)**

Figure C.1.16. Column-base connections at negative 2% Drift a) NE column b) SW column

C.1.3. Stage 2: Test 1

The frame deformation was similar with the timber-concrete composite floor (Stage 2). No further inelastic deformation appeared to occur within the beam-column connections and gap openings were similar to Stage 1. Note: all external reinforcement shown in the figures below is loose and hence did not contribute the response of the frames.

a) b)

Figure C.1.17. Frame at 2.0% Drift a) 3D view b) S column

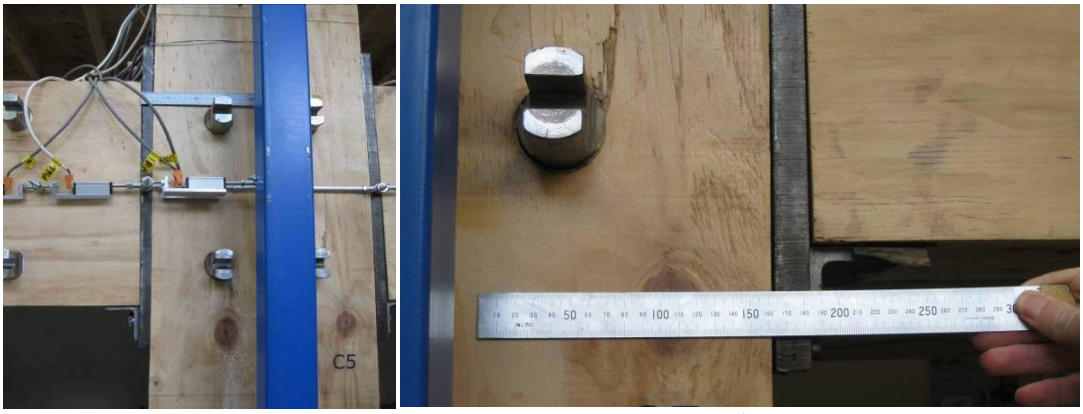

a) b)

Figure C.1.18. L2 BC connection gap opening at 2% Drift a) S column b) S column, east side

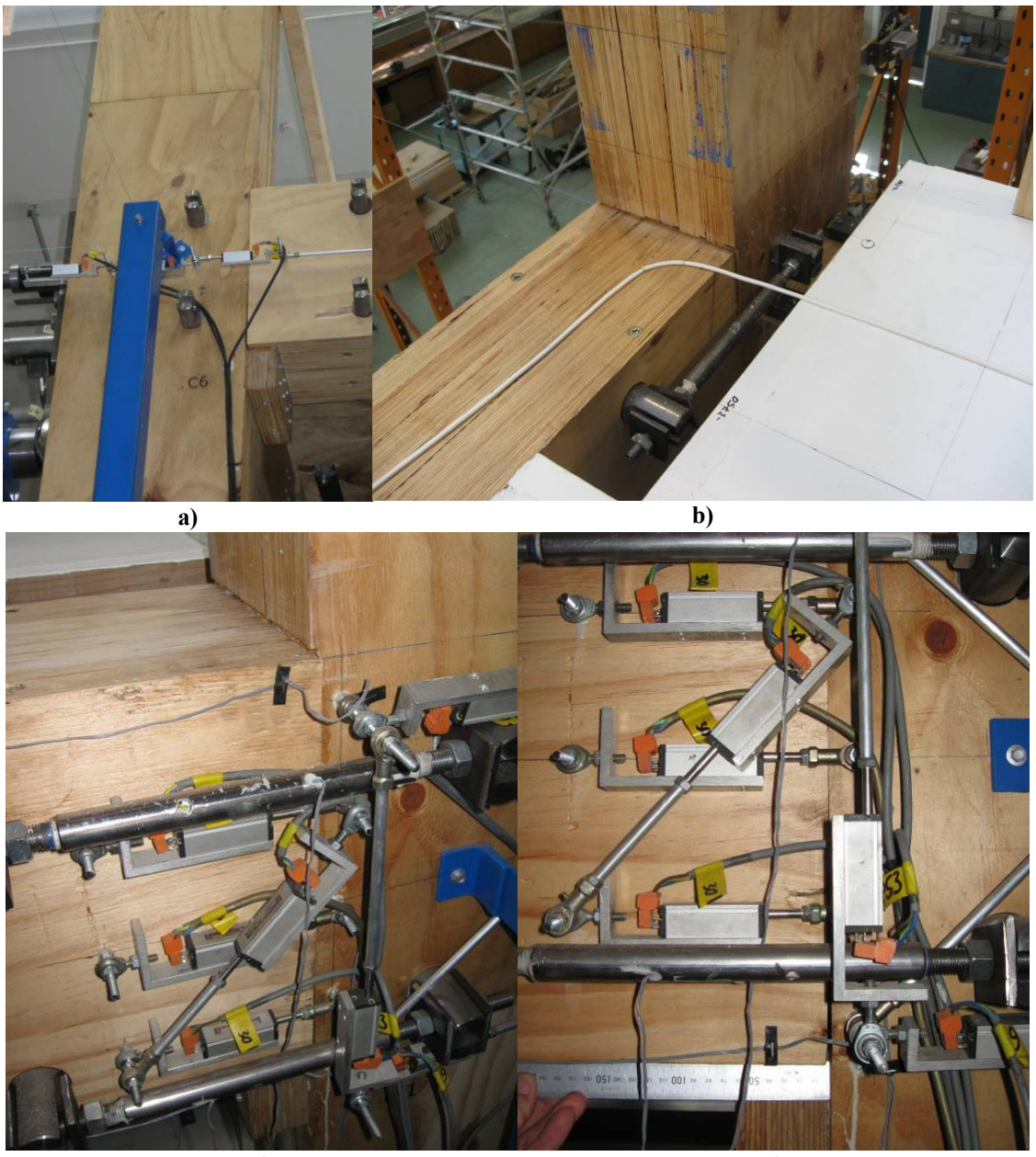

a) **b)**

c) **d)**

Figure C.1.19. L3 BC connection deformation at 2% Drift for west exterior columns a) SW column, looking up b) SW column, looking down c) NW column, top d) NW column, bottom

a) **b)**

Figure C.1.20. L3 BC connection deformation at 2% Drift a) N column b) NE column

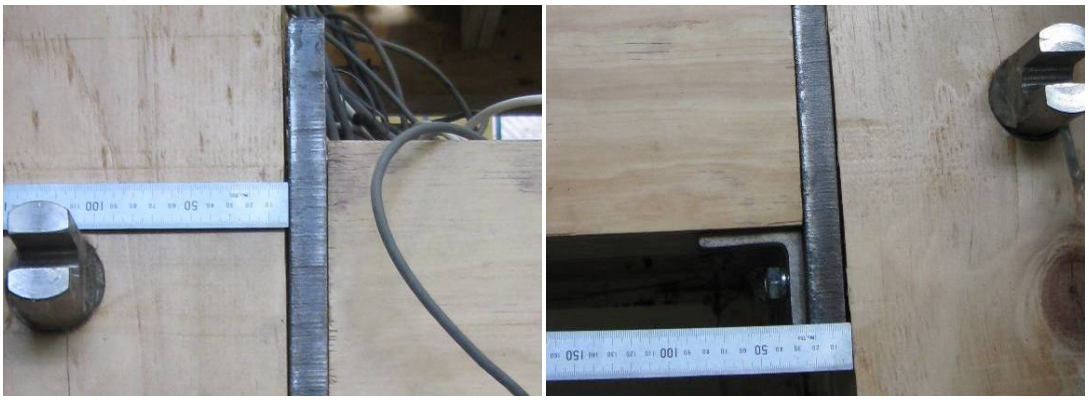

a) **b)**

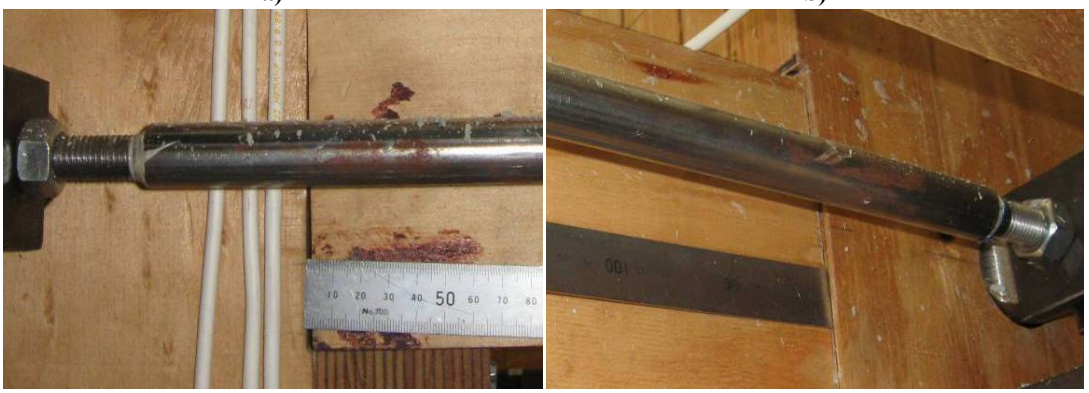

c) **d)**

Figure C.1.21. BC connection deformation at negative 2% Drift a) S column, L2 b) SE column, L2 c) S column, L3 d) SW column, L3

a) b)

Figure C.1.22. Column-base connections at 2% Drift a) SW column b) S Column

The deformation of the edge-joists (used to connect the floor diaphragm to the beams) was monitored during testing. It was shown that there was no significant deformation between the edge-joist and the beam. The position of the edge-joist, relative to the beam, was marked at 1.0% drift. At negative 2% drift the edge joist remained in the same location.

a) b)

Figure C.1.23. L3 edge-joist diaphragm connection at negative 2% Drift a) East bay b) West bay

C.1.4. Stage 2: Test 2

The observed response of the frame with external reinforcement and floor diaphragm was similar to Test 2 from Stage 1. Hence, the floor did not have a noticeable effect.

a) b)

Figure C.1.24. Frame at 2.0% Drift a) 3D view b) S column

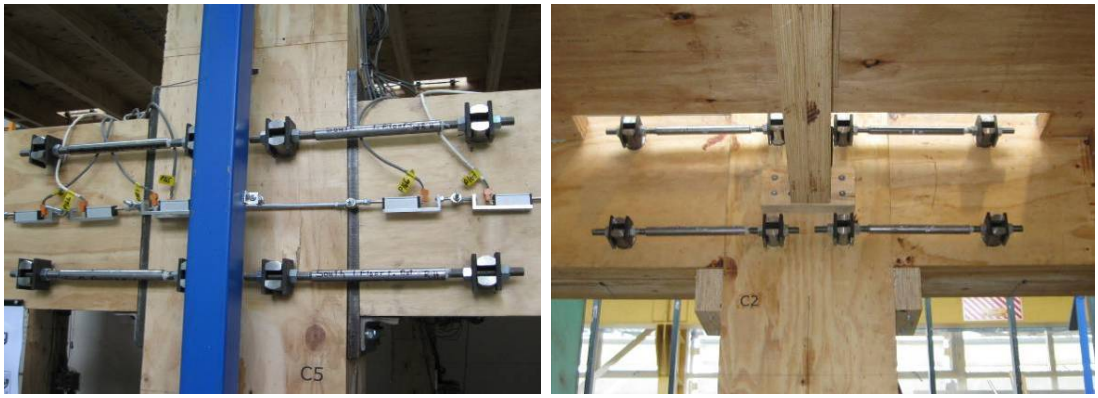

a) b)

Figure C.1.25. External BC connection reinforcement a) S column, L2 b) S column, L3

C.1.5. Stage 2: Test 7

Under the bi-directional loading protocol the frames were subjected to a peak drift of 3% in both the NS and EW direction. The frame is shown in the figures below at the peak bi-directional drift, which is slightly less than 3% drift in both the EW and NS directions.

The beam-column connections appear to respond purely in-plane with the frame. Hence, the connections do not appear to be affected by out-of-plane loading. The gap openings in the beam-column connections were more pronounced (than at 2% drift), resulting in significantly reduce neutral axis depths on Level 3.

The south column fractured at the Level 3 beam-column connection during the second clover at approximately negative 3% drift in the NS and EW direction. The fracture continued to propagate under reversed loading (see Appendix B and Chapter 5 for further discussion).

Cracking was also observed on south column at Level 2. This was caused by the steel pins within the column. The pins were connected to the internal steel plate reinforcing within the column. As the steel plates rotated relative to the column timber, the pins applied high shear stresses to the timber resulting in a localized shear cracking.

a)

b)

Figure C.1.26. Frame and wall at peak bi-directional Drift a) 3D view b) Close 3D view

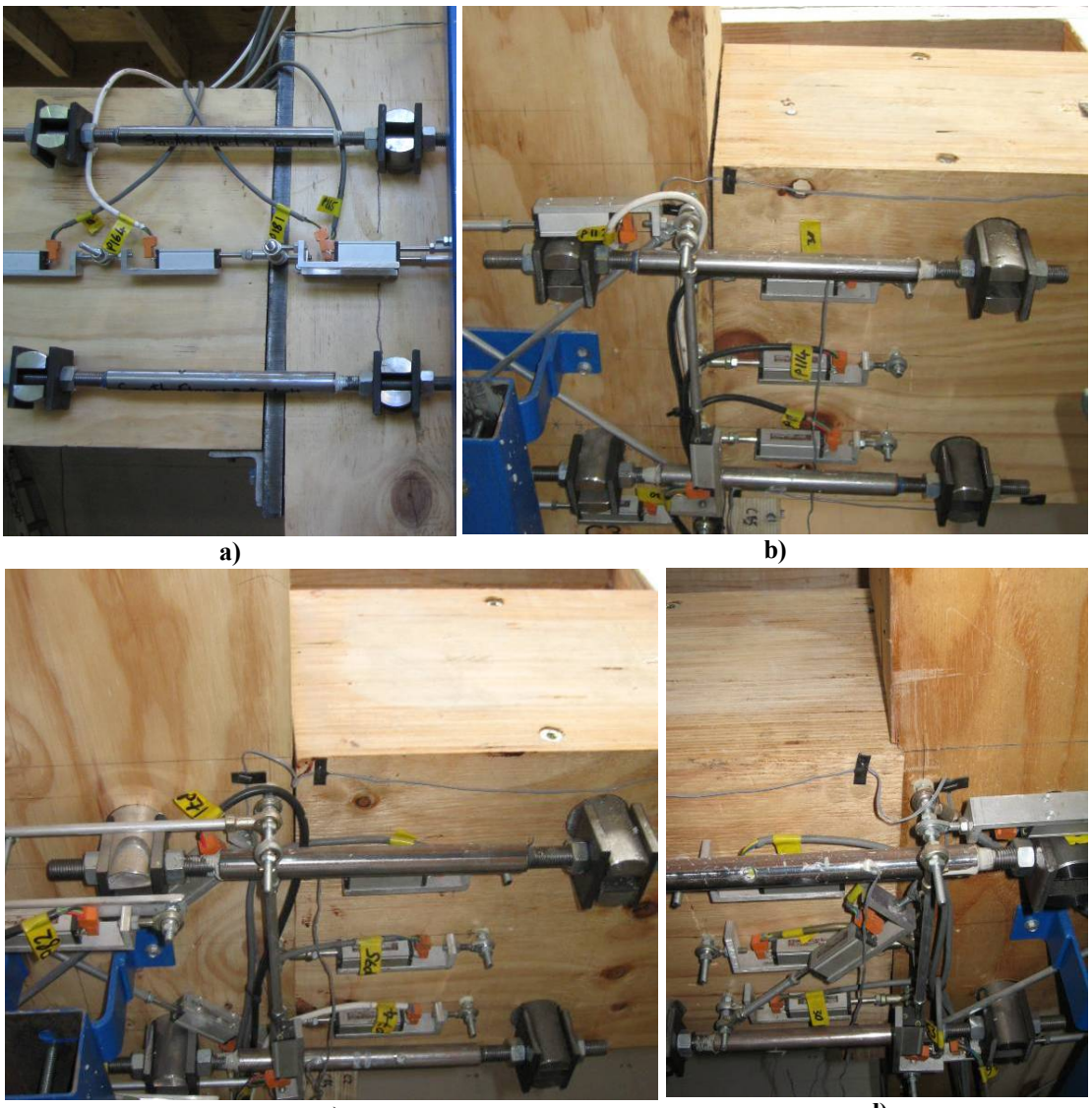

a) **b)**

c) **d)**

Figure C.1.27. BC connection deformation at peak bi-directional Drift a) S column, L2 b) NE column, L3 c) N column, L3 d) NW column, L3

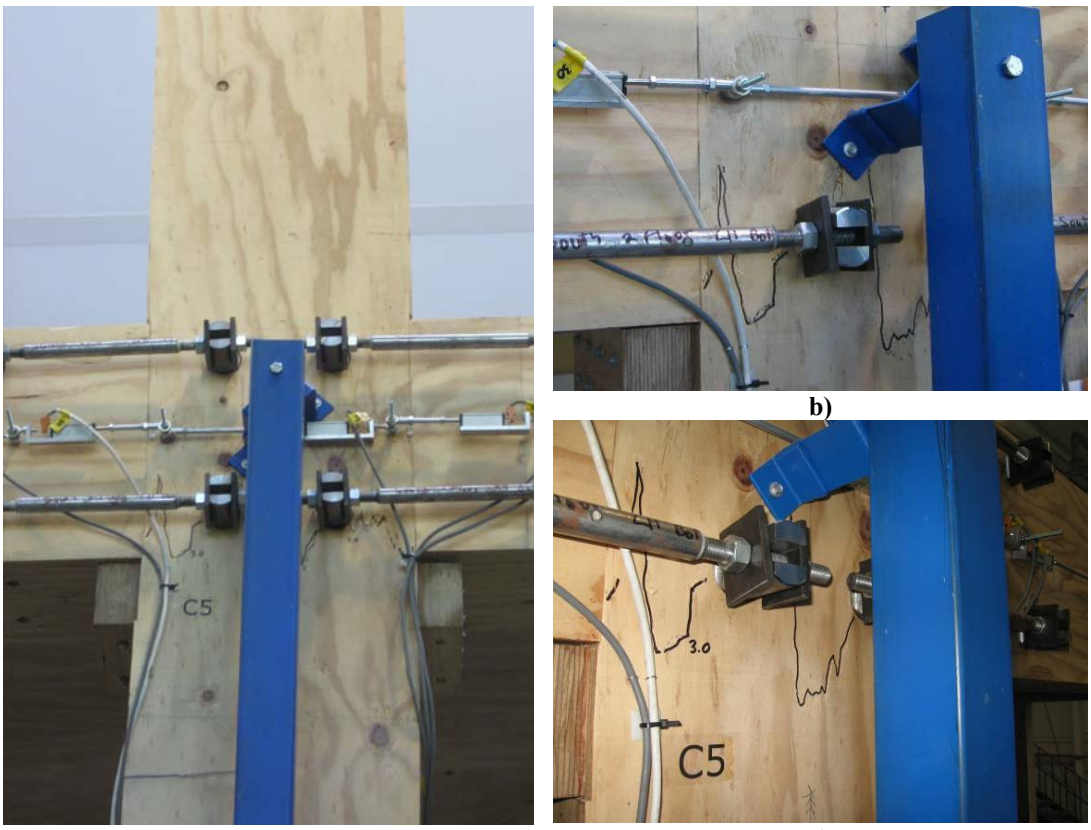

a) **b)** **c)**

Figure C.1.28. S column failure at 3% Drift: a) & b) Looking north c) Looking south

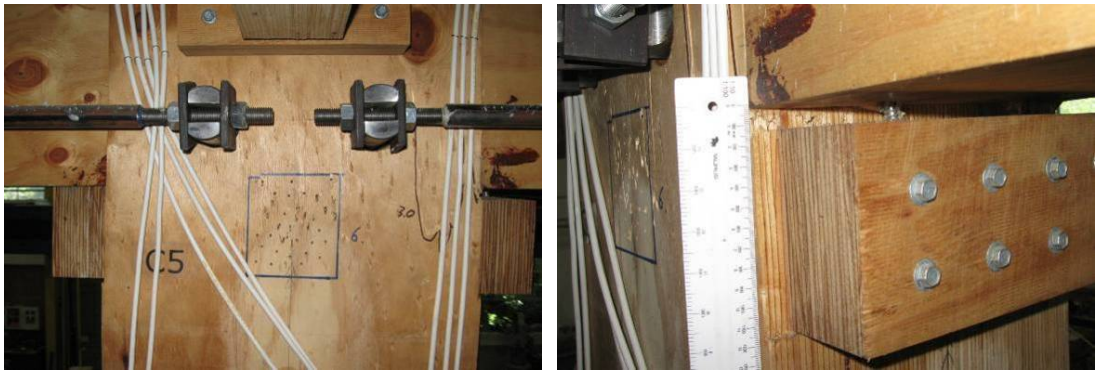

a) **b)**

Figure C.1.29. S column failure at negative 3% Drift

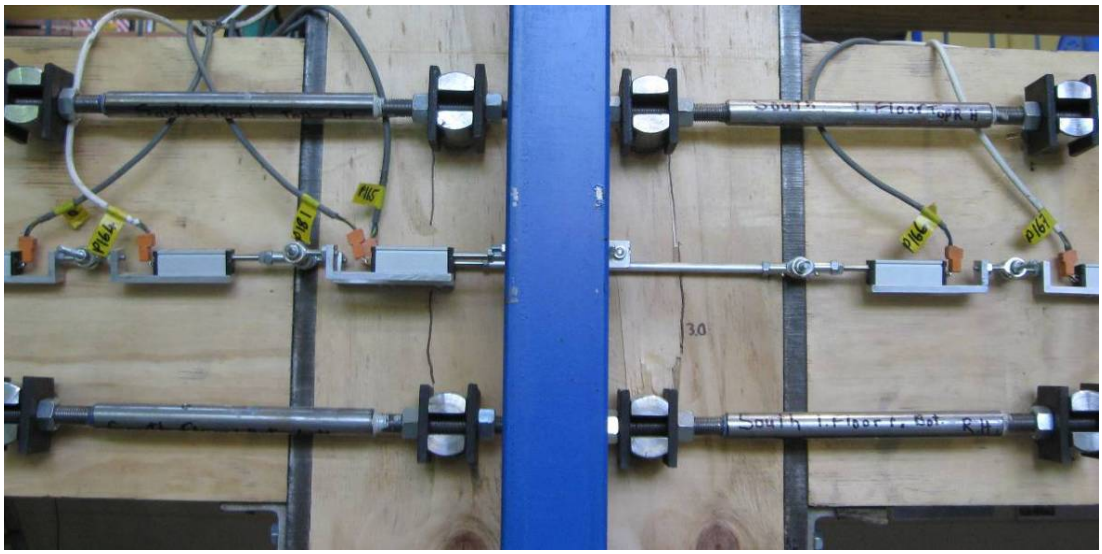

Figure C.1.30. Cracking of S column at 3% Drift (Level 2)

The gap opening of the unloaded edge of the column base at 3% drift was approximately 14mm. The steel plate shear keys at the base of the columns performed as designed. The plates bent above the weld allowing the column to rotate. The perpendicular-to-grain compressive strength of the timber was exceeded, causing minor amounts of crushing.

a) **b)**

Figure C.1.31. Column-base gap opening at 3% Drift (positive in EW and NS direction): a) S column b) SE column

Significant inelastic deformation of the column-base anchorage was observed during testing. Based on experimental data, it is apparent that this deformation also occurred

during the uni-directional tests (see Appendix B). This was not expected because the design axial capacity of the pins was much larger than required (see Appendix A). It appears that uneven tensile forces in the exterior reinforcement resulted in exceedence of the embedment strength at each edge of the pin holes, progressively increasing the slop in the connection. Under bi-direction loading, this mechanism would have been exacerbated, further increasing slop within the base connections.

a) **b)**

Figure C.1.32. Column-base external reinforcement anchorage pin deformation at 3% Drift: a) & b) SE column

C.1.6. Stage 2: Test 8

For Test 8 the 3% drift cycle was attempted, without external reinforcement across the beam-column connections. However, only two complete clovers in the loading protocol were achieved until the column-base connections on the SE column failed (see Appendix B for further details). No further damage to the frame was apparent.

The response of the beam-column connections appeared to be similar with and without external reinforcement.

During this test it was noticed that the flexural deformation of the column out-of-plane was significant.

The external reinforcement at the column-based failed due to low cycle fatigue after being subjected to eight tests up to 2% drift and one test up to 3% drift. For all of these tests the strain within the steel did not exceed 5%.

Figure C.1.33. Frame and wall at peak bi-directional Drift

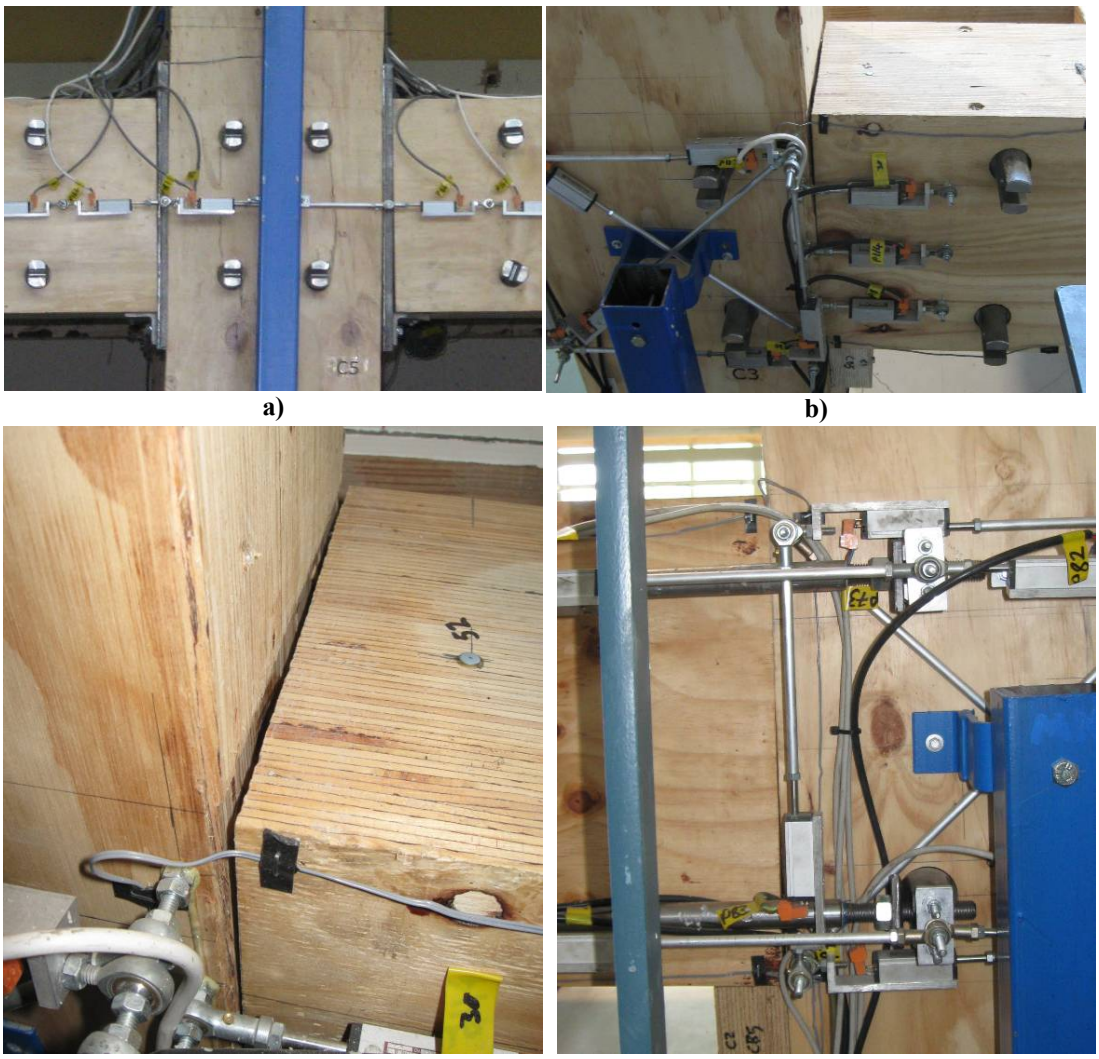

a) **b)**

c) **d)**

Figure C.1.34. BC connection deformation at peak bi-directional Drift a) S column, L2 b) NE column, L3 c) NE column, L3, close up d) NW column, L3

a) b)

Figure C.1.35. Column deformation at peak bi-directional Drift a) S column, in-plane b) NE column, out-of-plane

a)

b)

c)

Figure C.1.36. Column-base external reinforcement failure on SE column

C.1.7. The frame after testing

The damage to column was investigated further after testing was complete. The pin-holes at the column-base had elongated from a diameter of 60mm to 64mm, accounting for the connection slop (apparent in hysteresis from Appendix B).

The column failure appeared to initiate around the heads of the screws used as diagonal and horizontal reinforcement. The diagonal screws appeared to be relatively ineffective at reinforcing the timber against forces induced by the external reinforcement anchorage pin.

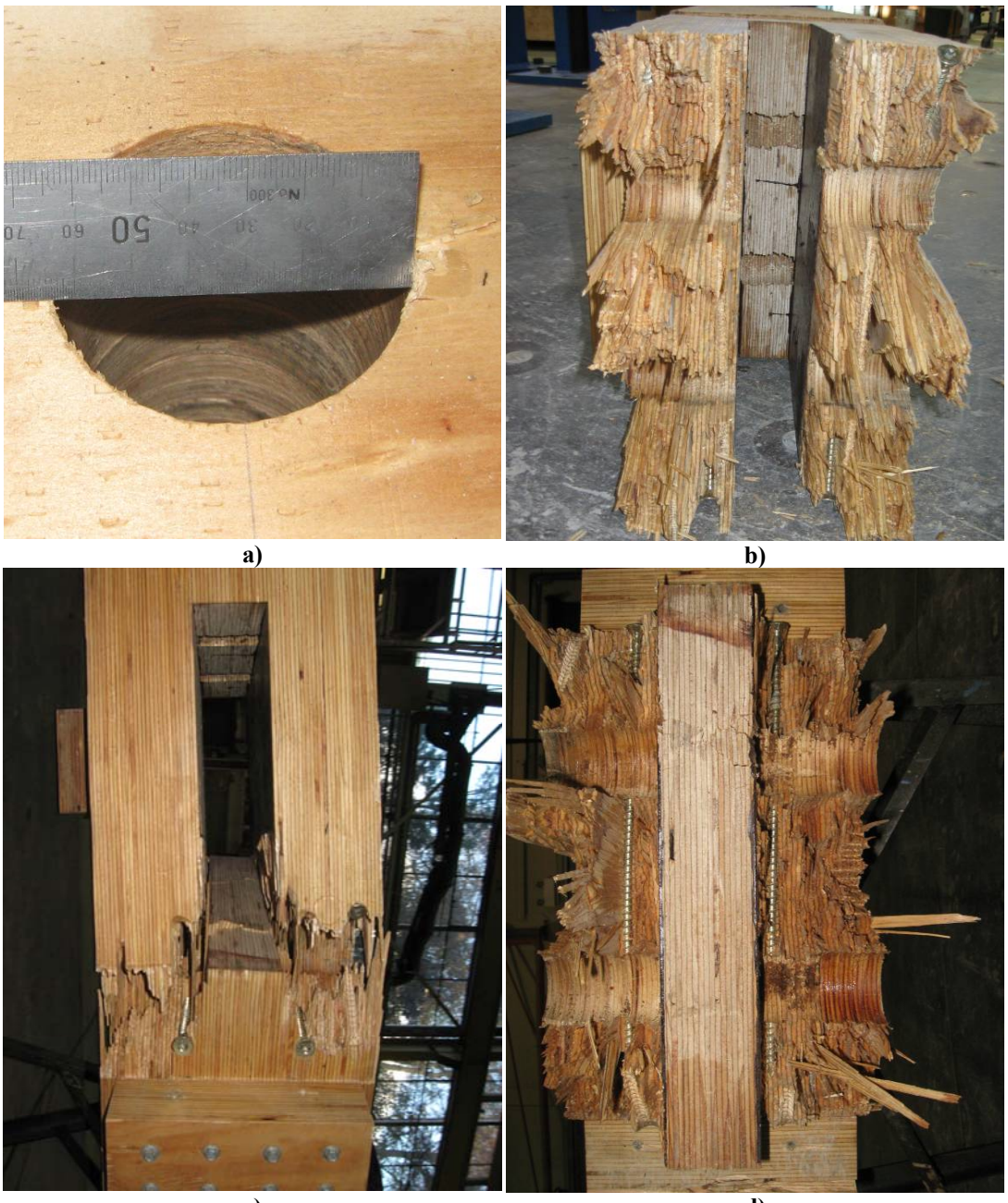

a) **b)**

c) **d)**

Figure C.1.37. Column damage after Testing: a) Pin-holes at column-base for external reinforcement b) Column fracture, looking up c) Column fracture, pulling apart d) Column fracture, looking down

C.2. WALL SYSTEM

C.2.1. Stage 2: Test 3

The observed wall response was almost entirely elastic at 2% drift.

There was some minor perpendicular-to-grain crushing at the wall-base due to shear restraint applied by the shear keys.

The edge beams supports, required for construction (and gravity loading), were subjected to significant compressive loads. Because the edge beam is fixed to each wall, at one end the beam uplifted off the column support, while at the other reacted against the column support. In some cases, the cantilevered steel plate gravity supports began to lever off the edge beam. The uplifted end pulled Type 17 screws from the corbel.

The uplift at the unloaded edge of the base of the wall was in the order of 10mm at 2% drift.

a) **b)**

Figure C.2.1. Wall at 2.0% Drift a) 3D view b) E walls

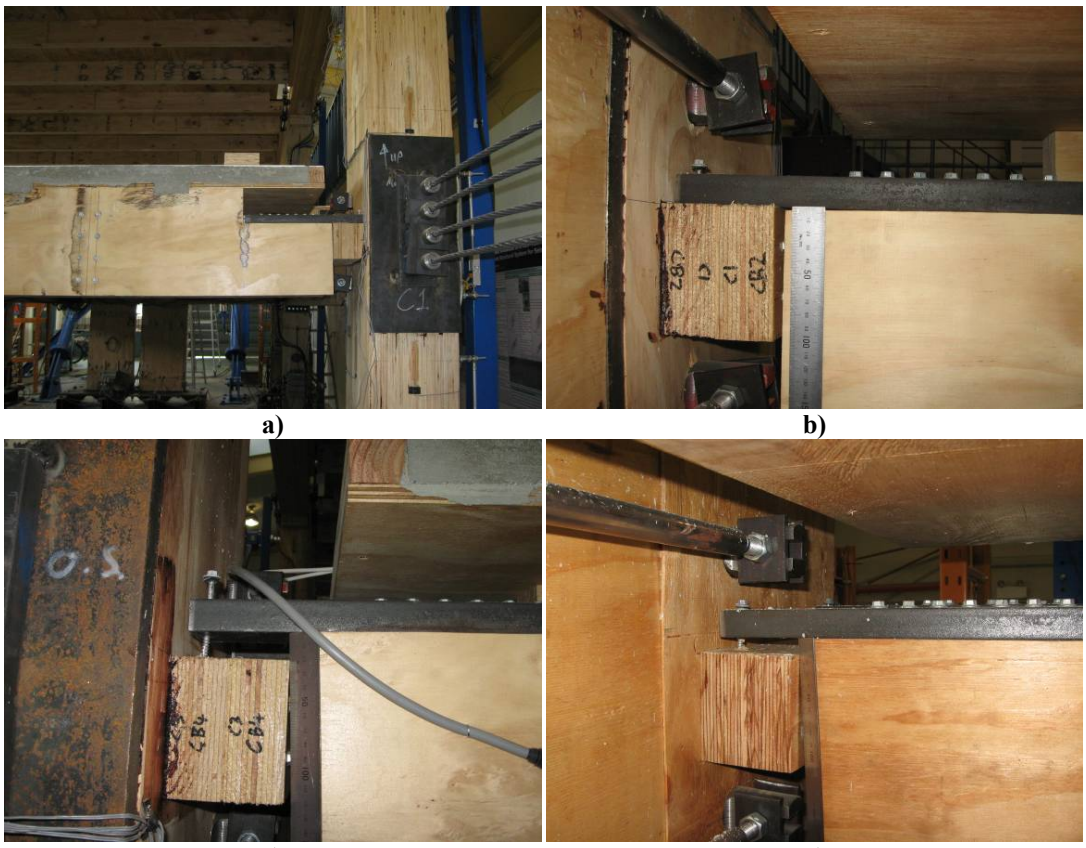

a) **b)**

c) **d)**

Figure C.2.2. Edge beam supports at 2.0% Drift a) NE support b) NE support c) SW support d) NW support

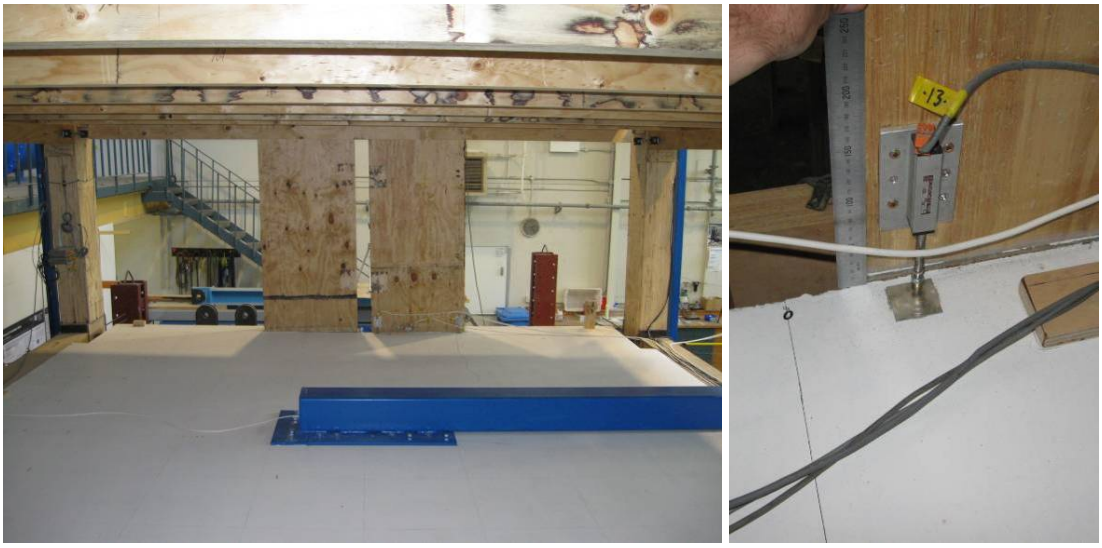

a) **b)**

Figure C.2.3. Wall at 2.0% Drift a) West walls b) Wall rotation relative to slab

a) **b)**

Figure C.2.4. Wall-base at 2.0% Drift a) SE wall, south edge b) NE wall, south edge

a) **b)**

Figure C.2.5. Edge beam supports at negative 2.0% Drift a) SE support b) NW support

a) **b)**

Figure C.2.6. Rotation of edge beam relative to wall a) Looking north b) Looking east

C.2.2. Stage 2: Test 4

For Test 4, UFP couplers were placed between the walls. The observed response of the wall elements appeared to be similar to Test 3. The gap opening at the unloaded edge of the wall-base is approximately 10mm at 2% drift.

a) **b)**

Figure C.2.7. Wall at 2.0% Drift a) 3D view b) E walls

The relative displacement of the anchorage plates at each side of the UFP coupler is approximately 15mm, which includes the gap opening plus compressive deformation of each wall. There was no apparent slip of the anchorage connections. The relative displacement at the centerline of UFP coupler was approximately 6mm, which indicates the UFP couplers did not deform strictly as anticipated.

The deformable wall elements allowed the UFP couplers to deform so that a constant radius was not maintained (as shown below). Hence, the UFP couplers did not yield (or maintain uniform plastic strain) along the entire semi-circle, reducing the effectiveness of the devices to dissipate energy and increasing the yield drift. Also, because the devices were only fixed on the inside of the wall element the elastic deformation of the UFPs would have increased, again reducing the effectiveness of the devices. In

addition, wedging action created by the UFP couplers caused the walls to splay (by 2 to 3mm) at the base. Again, this limited the strain along the UFP plates.

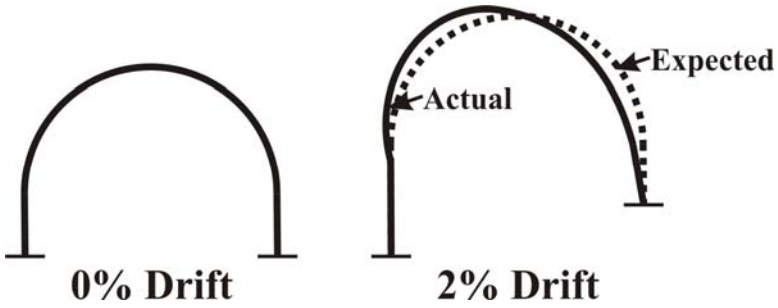

Figure C.2.8. Observed UFP coupler deformation

a) **b)**

Figure C.2.9. Wall uplift at 2.0% Drift a) SE wall, south edge b) SE wall, north edge

a) **b)**

Figure C.2.10. UFP couplers at 2.0% Drift a) E walls, first UFP b) E Wall, second UFP

a) **b)**

Figure C.2.11. Relative wall movements at 2.0% Drift

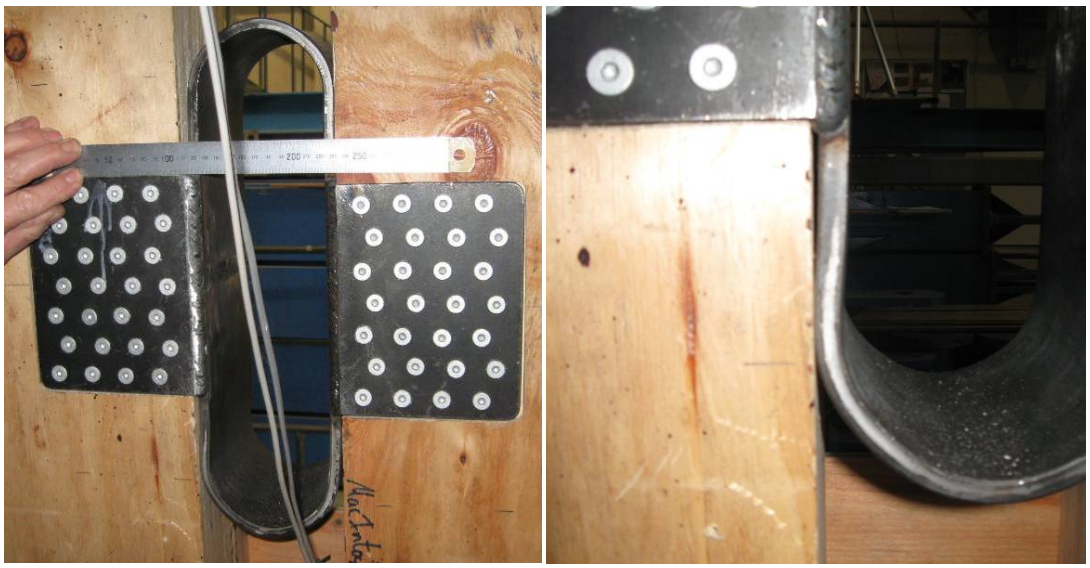

a) **b)**

Figure C.2.12. Deformation of UFP couplers at 2.0% Drift

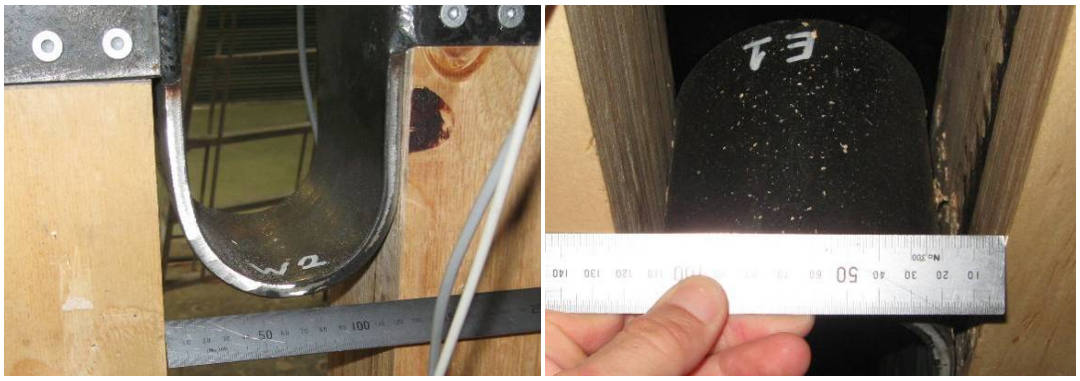

a) **b)**

Figure C.2.13. Wall spreading due to UFP couplers at 2.0% Drift

C.2.3. Stage 2: Test 5

Test 5 was similar to Test 4, except the edge beam supports were removed. This allowed the edge beams to drop below the previous support elevation and avoided reaction forces between the edge beam and column.

a) b)

Figure C.2.14. Wall at 2.0% Drift

Figure C.2.15. Wall spreading due to UFP couplers at 2.0% Drift

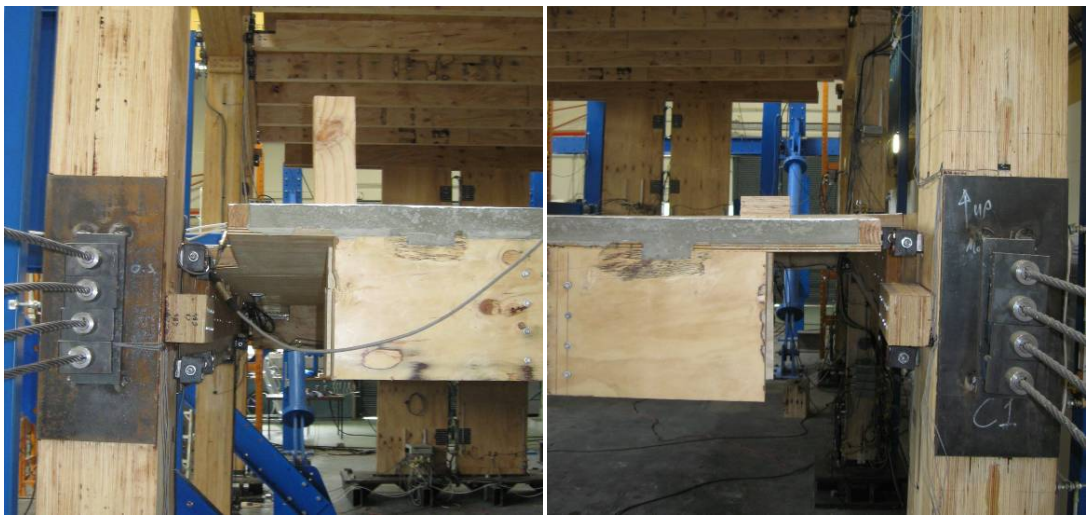

a) **b)**

Figure C.2.16. Edge beams at 2.0% Drift a) South b) North

C.2.4. Stage 2: Test 6

Test 6 was similar to Test 3 but excluded edge beam supports. Further perpendicular-to-grain crushing was evident around the shear keys at the base of the walls. This could have occurred during Test 4 and 5 and may have been exacerbated by the wall splaying induced by the UFP couplers.

Figure C.2.17. West walls at 2.0% Drift

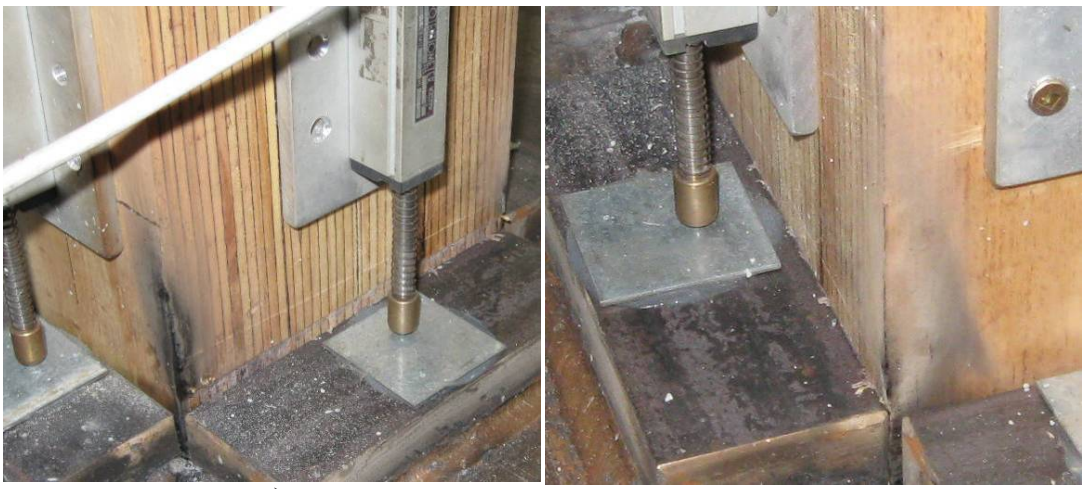

a) b)

Figure C.2.18. Slight crushing at the wall edges

C.2.5. After the uni-directional tests

After the uni-directional walls tests the screws connecting the edge beams to the walls were checked. None of the screws had fractured, and all remained effectively straight with no noticeable signs of inelastic deformation.

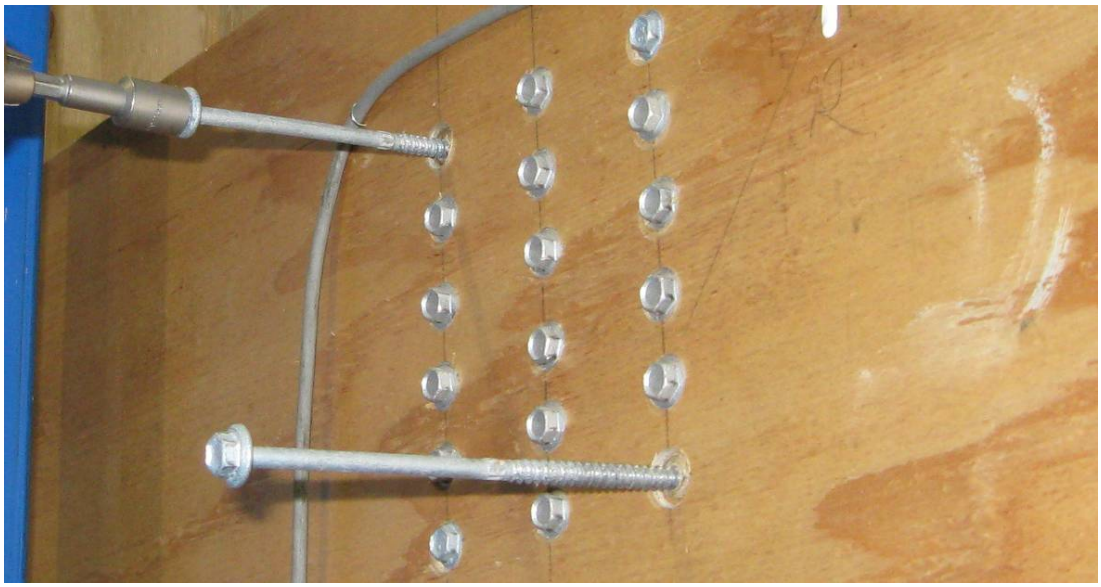

Figure C.2.19. Wall-to-edge beam connection after uni-directional testing

C.2.6. Stage 2: Test 7

Under bi-directional loading up to 3% drift there was no further significant damage to wall system. The displacement incompatibility between the edge-beams and the out-of-plane frames increased. The uplift at the base of the walls increased to approximately 15mm.

The UFP couplers performed in a similar fashion to the uni-directional tests. There were still not signs of movement of the UFP anchorage plates relative to the wall elements.

a) **b)**

Figure C.2.20. Wall at peak bi-directional Drift

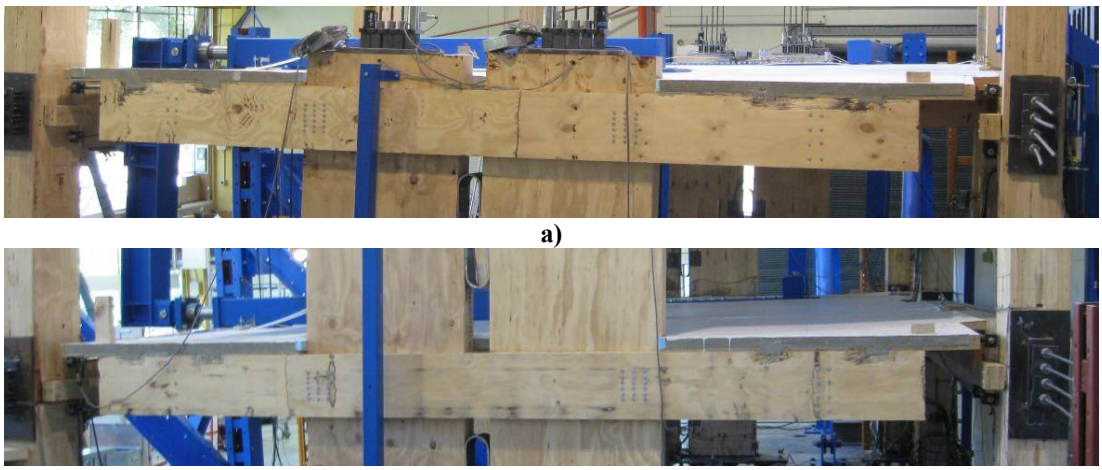

a)

b)

Figure C.2.21. Tilt of edge beams relative to floor a) Level 3 b) Level 2

a) **b)**

Figure C.2.22. SE Wall gap opening

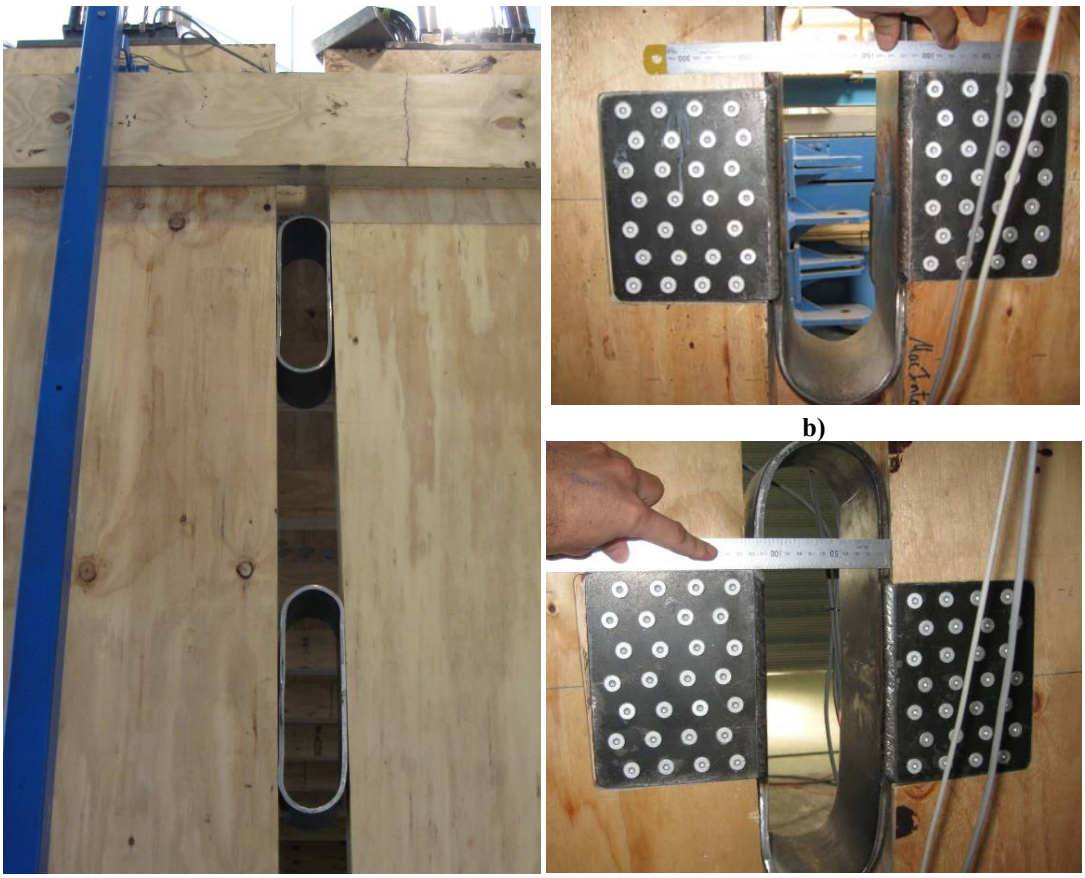

a) **b)** **c)**

Figure C.2.23. Deformation of UFP couplers a) West walls, UFP 3 and 4 b) West walls, UFP 2 c) East walls, UFP 2

C.2.7. Stage 2: Test 8

No further damage to the wall system was noted during Test 8.

a) b) c)

Figure C.2.24. Test 8 a) West walls b) Removed UFP, west side c) Removed UFP, east side

C.2.8. The wall after testing

During de-construction rounding of the wall bases was noticed. A peak permanent inelastic deformation of 1 to 2mm was recorded at the base of the walls.

a)

b)

c)

Figure C.2.25. Rounding at the wall bases: a) Concrete dust showing the rounding at the end b) & c) With a straight edge

C.3. GRAVITY SYSTEMS

C.3.1. Uni-directional frame tests

Considering both Test 1 and 2 of Stage 2, the gravity system (joists and primary beam) performed well up to 2% drift, with no apparent damage.

The top hung support detail incorporated a gap between the supporting elements and the joist. This allowed rotation between the joist and the supporting elements, avoided contact and ensured purely pinned supports (which did not contribute to the lateral strength of the building).

The joists on Level 3 and the primary beam remained fixed to the floor slab, remaining essentially flat as the column rotated.

a) **b)**

Figure C.3.1. Floor joist supports at 2% Drift: a) West edge b) East edge

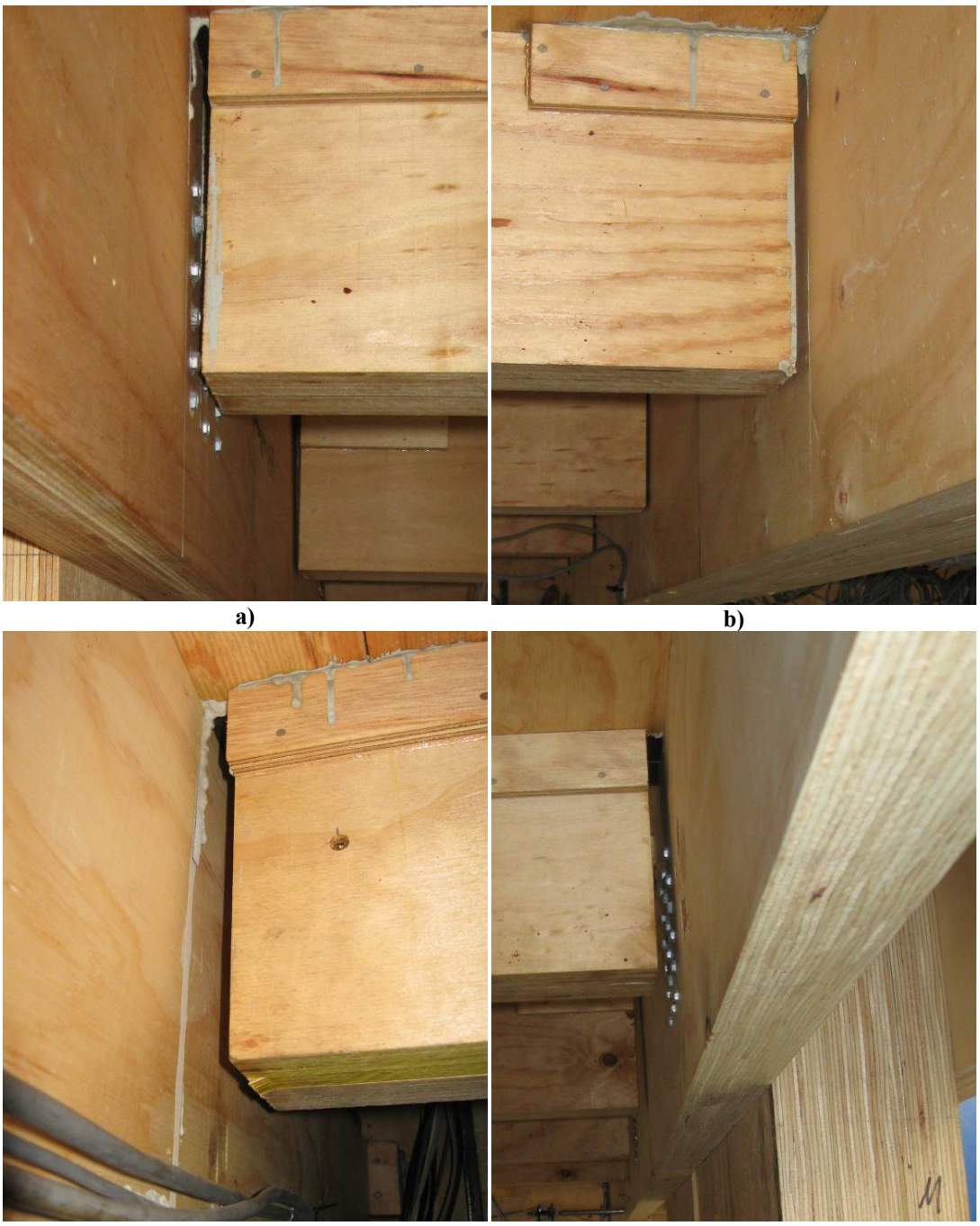

a) **b)**

c) **d)**

Figure C.3.2. Floor joist supports at negative 2% Drift: a) West edge b) West side of primary beam c) East side of primary beam d) East edge

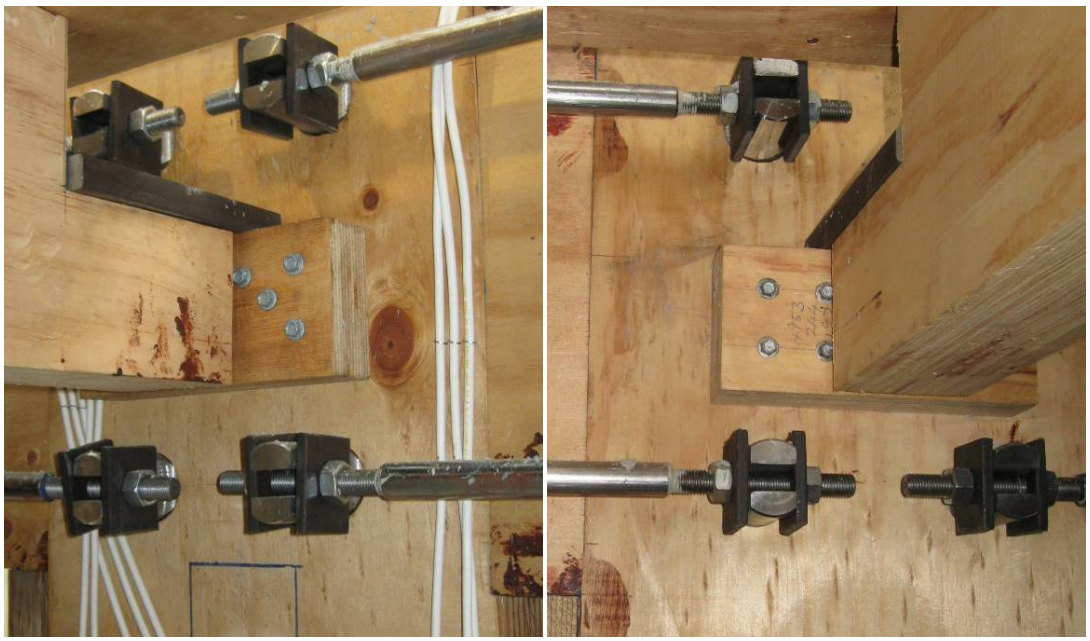

a) **b)**

Figure C.3.3. Floor joist support rotation relative to columns at 2% Drift: a) L3 central joist, looking south b) L3 central joist, looking north

C.3.2. Uni-directional wall tests

Considering Test 3 through 6 of Stage 2, again the gravity system (joists and primary beam) performed well up to 2% drift, with no apparent damage.

a) b)

Figure C.3.4. Floor joist supports at negative 2% Drift: a) South edge b) North edge

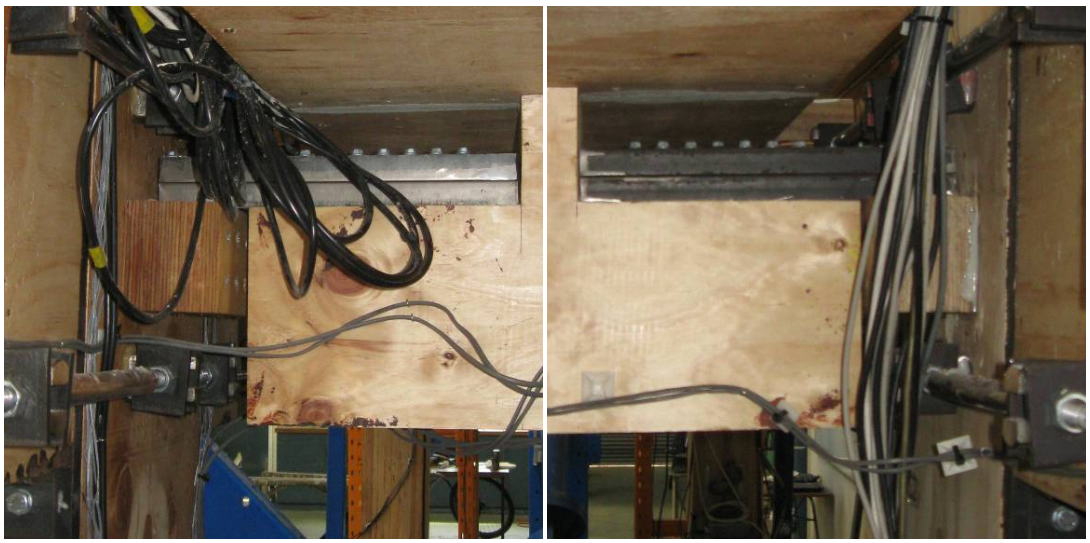

a) **b)**

Figure C.3.5. Primary beam supports at 2% Drift: a) South edge b) North edge

a) **b)**

Figure C.3.6. Level 3 joist rotation relative to frame at 2% Drift: a) Bottom b) Top

C.3.3. Bi-directional test

Considering Test 7, again the gravity system exhibited no apparent damage. There was sufficient gap to accommodate relative rotation between the joists and supporting elements for up to 3% Drift.

a) **b)**

Figure C.3.7. Level 3 joist rotation relative to frame at 3% Drift: a) Bottom b) Top

C.4. FLOOR SLAB

The cracking in the floor was monitored during Stage 2 experimentation. This was done using by sketching the crack propagation on a plan view of each level and using photographs.

C.4.1. Crack patterns

The propagation of cracks across the floor slab was recorded during all tests, except Test 2, 4 and 6. For Tests 2, 4 and 6, the cracks were marked at the end of each test (in black).

Different colors were used to distinguish between cracks that occurred during each test and under positive or negative drifts (as described in the table below).

Table C.4-1. Key for crack patterns

Line colour	Description
Grey	Pre-test cracking
Red	Positive drift in the EW direction
Blue	Negative drift in the EW direction
Black	Cracks that occurred during Test 2, 4 and 6
Purple	Positive drift in the NS direction
Green	Negative drift in the NS direction
Orange	Bi-directional testing

Pre-test cracks were created in the slab by the attachment of the loading apparatus to the floor. The maximum crack width was 0.2mm.

During Test 1, almost all cracks were localized in the corners of the slab around the walls. These cracks were caused by the displacement incompatibility that occurred between the wall system and the floor. The edge beams rotated with walls (up to 2% drift) but the floor slab adjacent to the beams remained horizontal. Because the slab was fixed to the edge beams via notched composite connections (to transfer in plane loads),

the slab cracked. The largest crack of 0.8mm occurred on the SE edge of the slab on Level 3.

Other cracking was observed for negative drifts that extended across the entire slab in the NS direction. This was caused by the loading apparatus. Under negative drifts, the slab is subjected to tension. To transfer this tensile force to the east bay, the concrete cracked, activating the slab reinforcement (see Appendix A). Hence, this cracking was not induced by frame elongation.

For Test 2, the same crack pattern was maintained, with only a few additional cracks being observed.

During Test 3, when the building was subjected to NS loading, again there was a displacement incompatibility between the wall system and floor. The edge beams remained effectively fixed to the wall system, causing uplift of the corners of the floor slab at one end of the edge beam. Adjacent to the beam (from the frame) the slab remained in-line with the top of the beam (due to the composite connections) causing cracking that extended in either the NS or EW direction. Corbels on the columns forced the edge beams to bend, allowing the slab to remain at the same elevation as the top of the beam. This reduced cracking. The maximum crack width of 0.2mm was recorded during testing.

After Test 4, very little additional cracking was observed in the floor slab.

For Test 5, once the edge beam support had been removed, the slab was able to drop below the top of beam (with the edge beam) at the corners. This significantly increased the number of cracks in the slab adjacent to the walls. The maximum crack was similar to Test 3.

There were very few additional cracks during Test 6.

During Test 7, in general the crack pattern remained similar to the previous uni-directional tests but the number and size the cracks increased. The maximum residual crack width was approximately 1mm. There were several more cracks surrounding the loading apparatus, due to increased lateral forces that were applied to the structure.

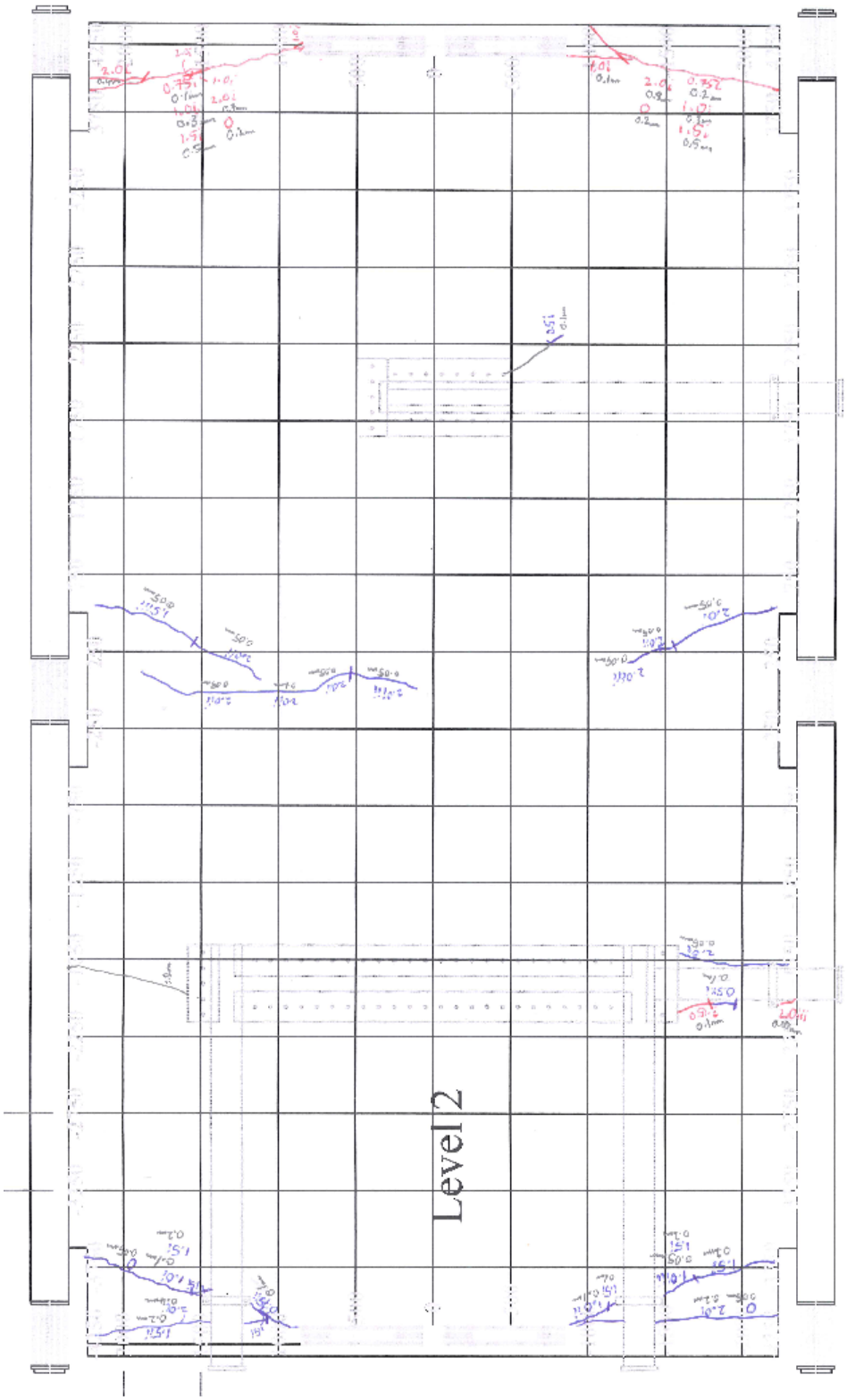

Figure C.4.1. Crack pattern after Test 1: Level 2

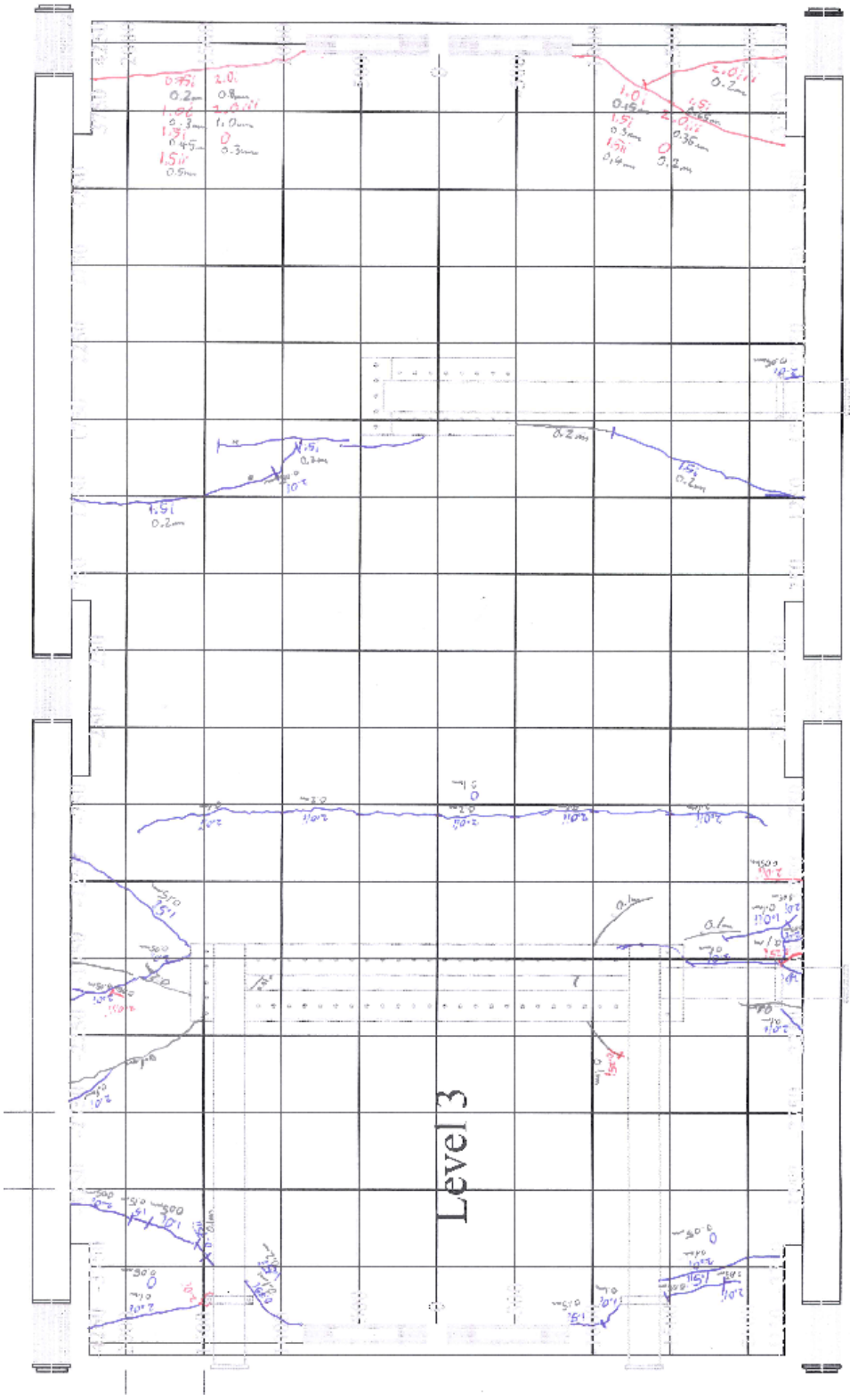

Figure C.4.2. Crack pattern after Test 1: Level 3

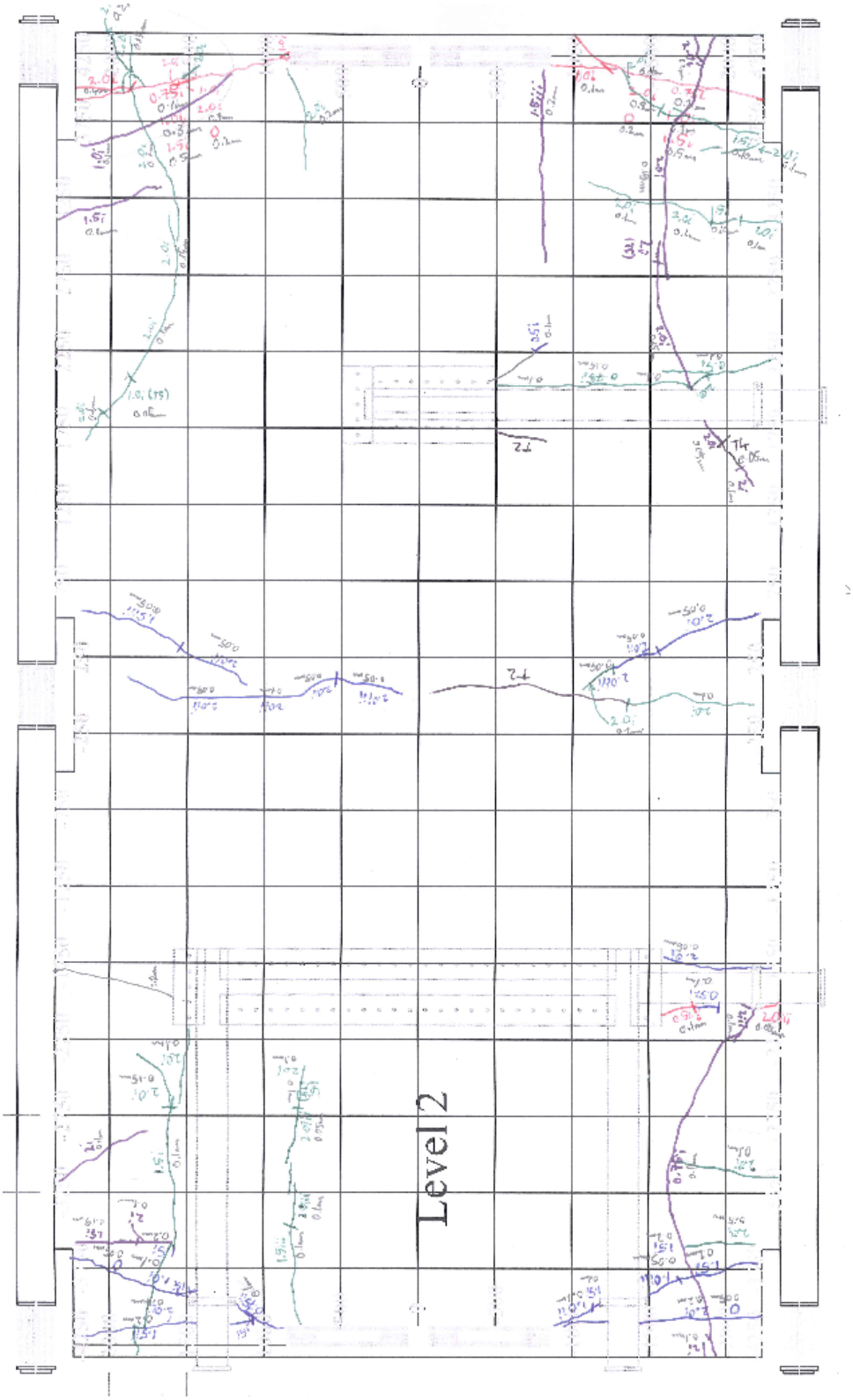

Figure C.4.3. Crack pattern after Test 4: Level 2

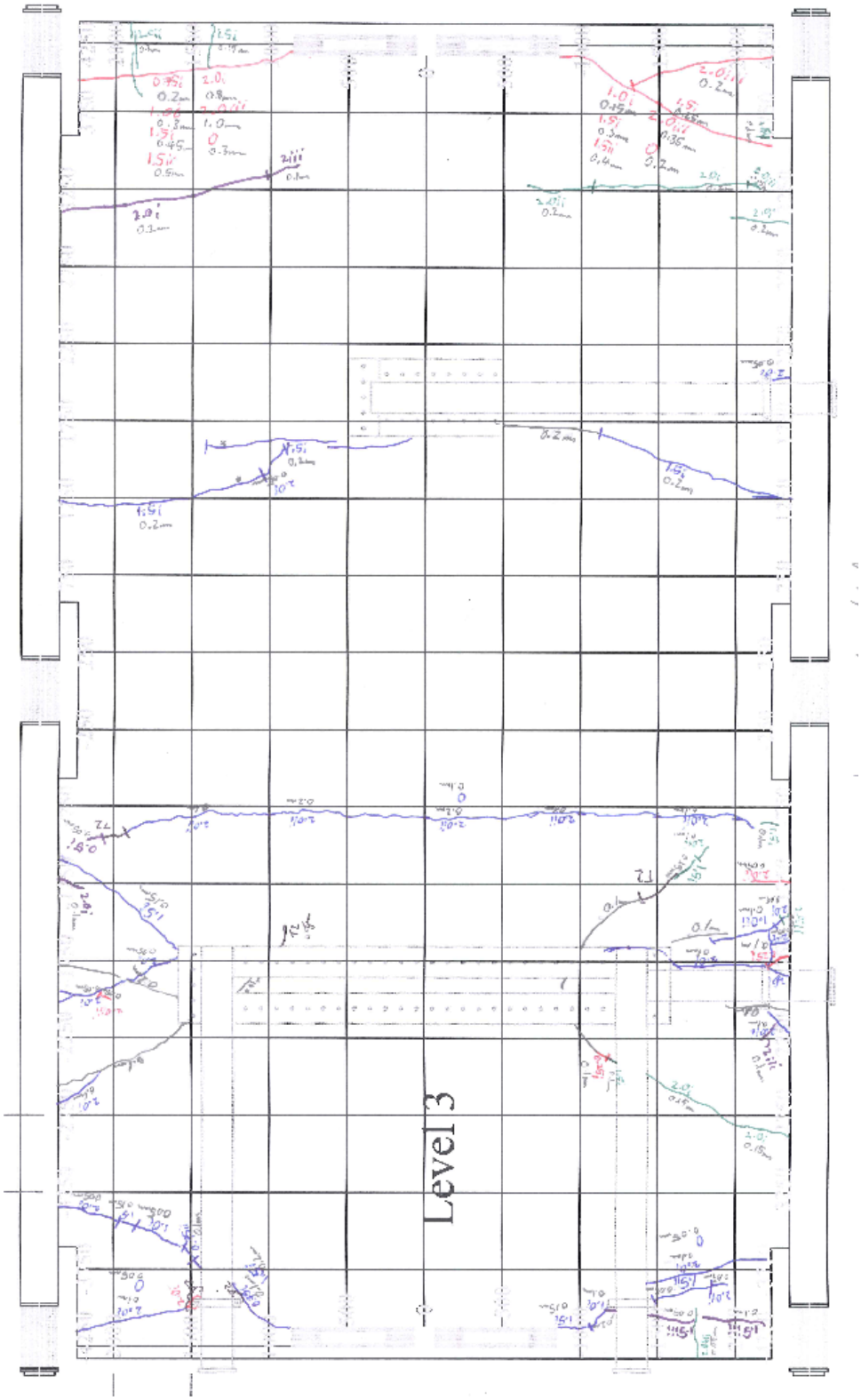

Figure C.4.4. Crack pattern after Test 3: Level 3

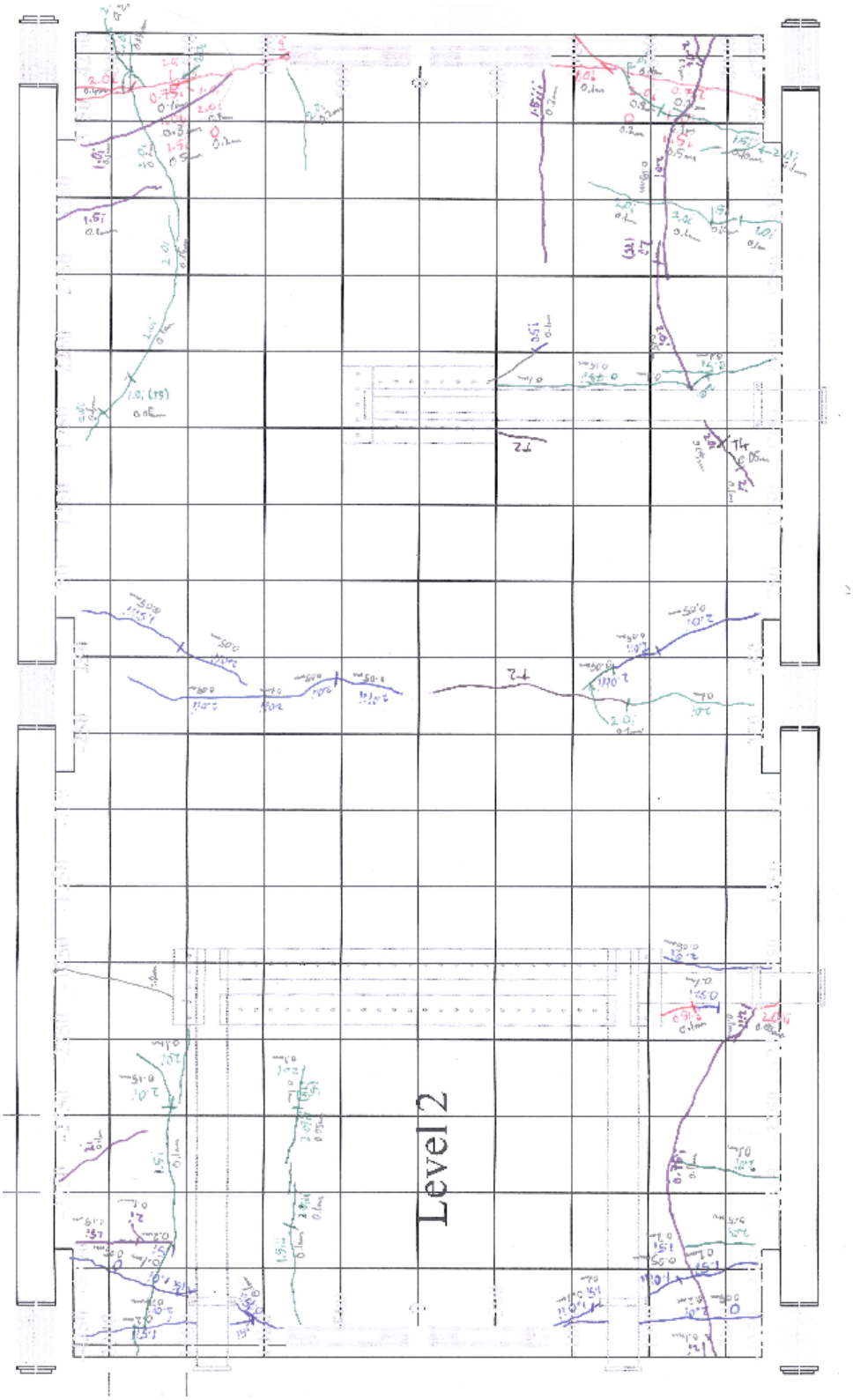

Figure C.4.5. Crack pattern after Test 3: Level 2

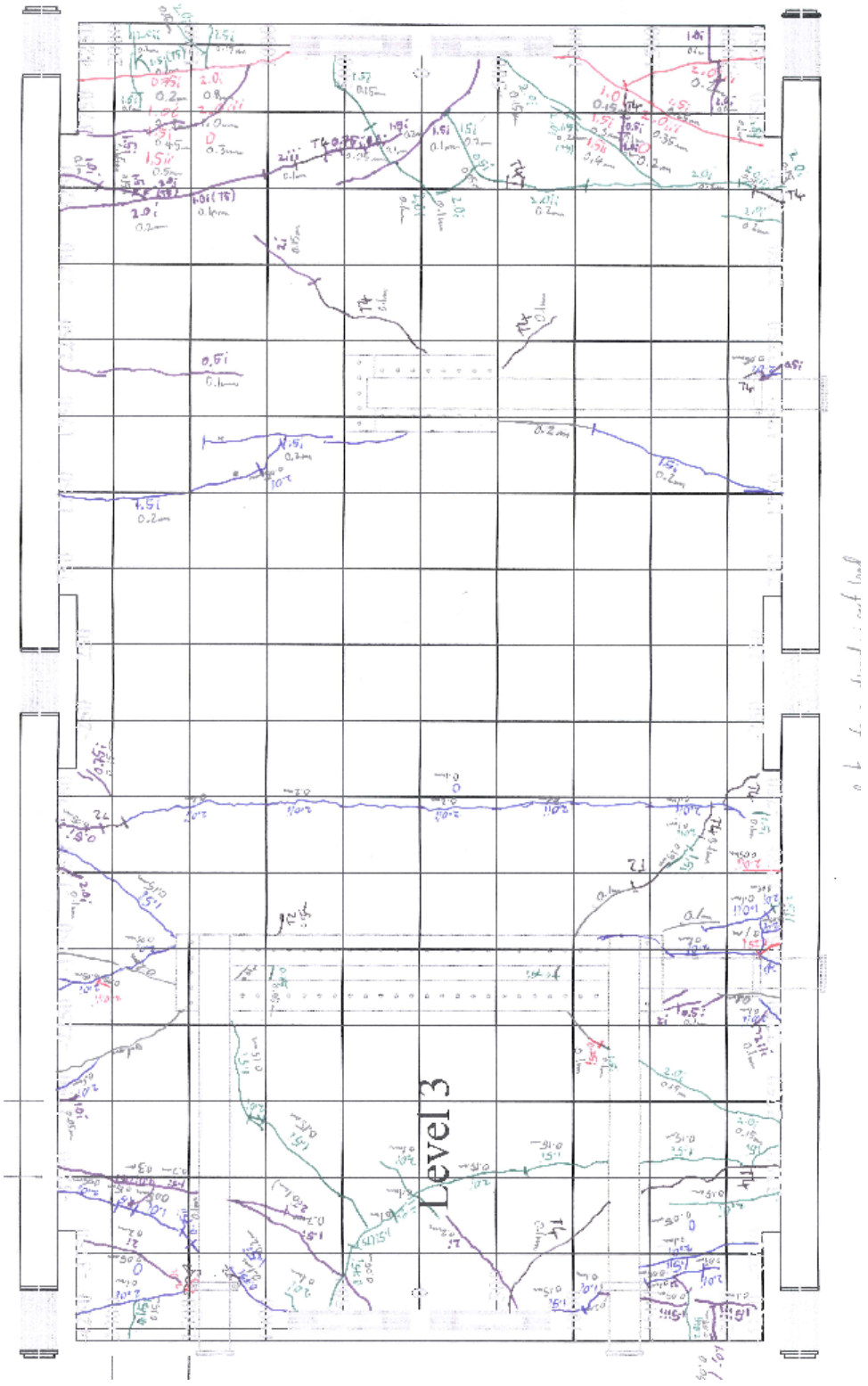

Figure C.4.6. Crack pattern after Test 5: Level 3

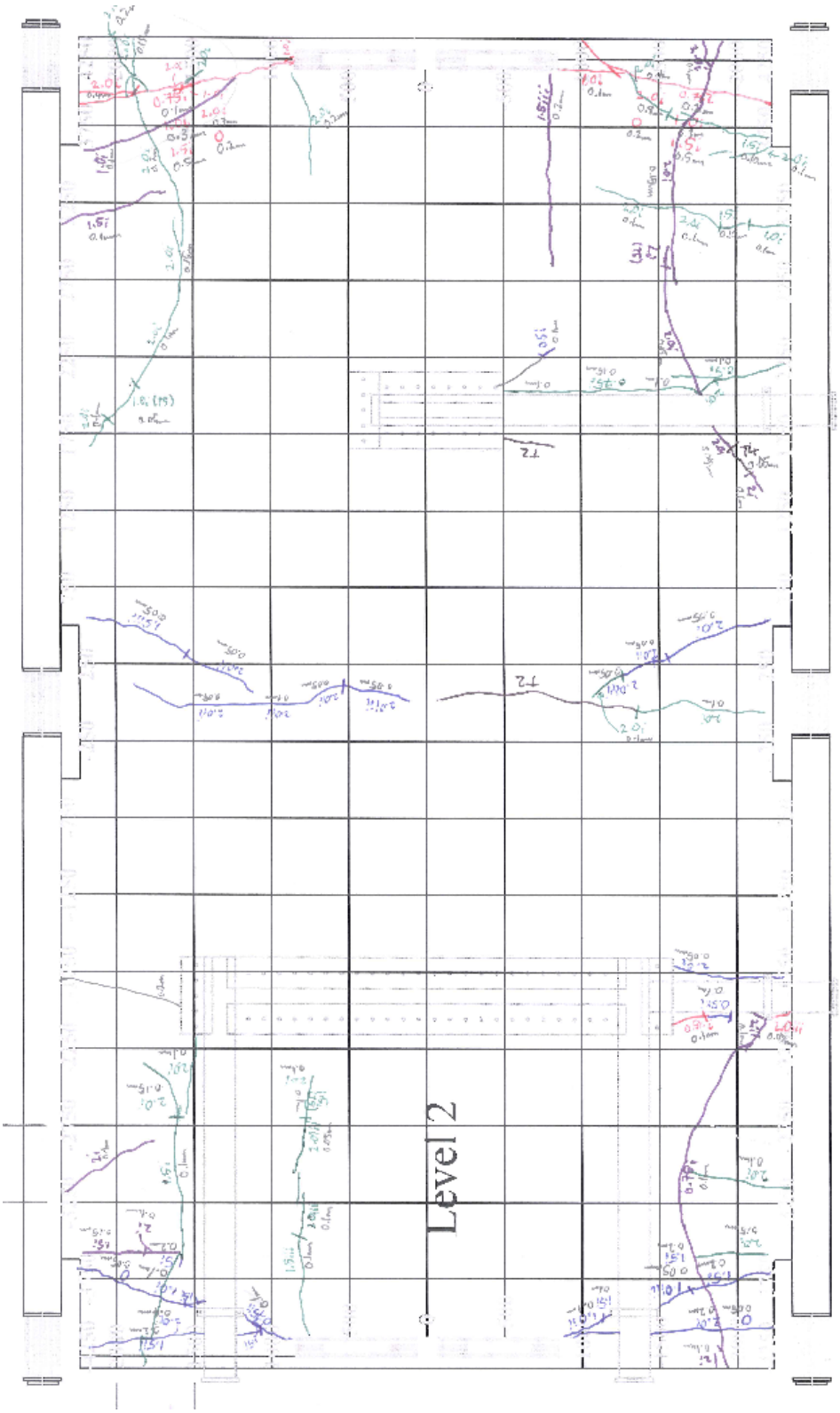

Figure C.4.7. Crack pattern after Test 5: Level 2

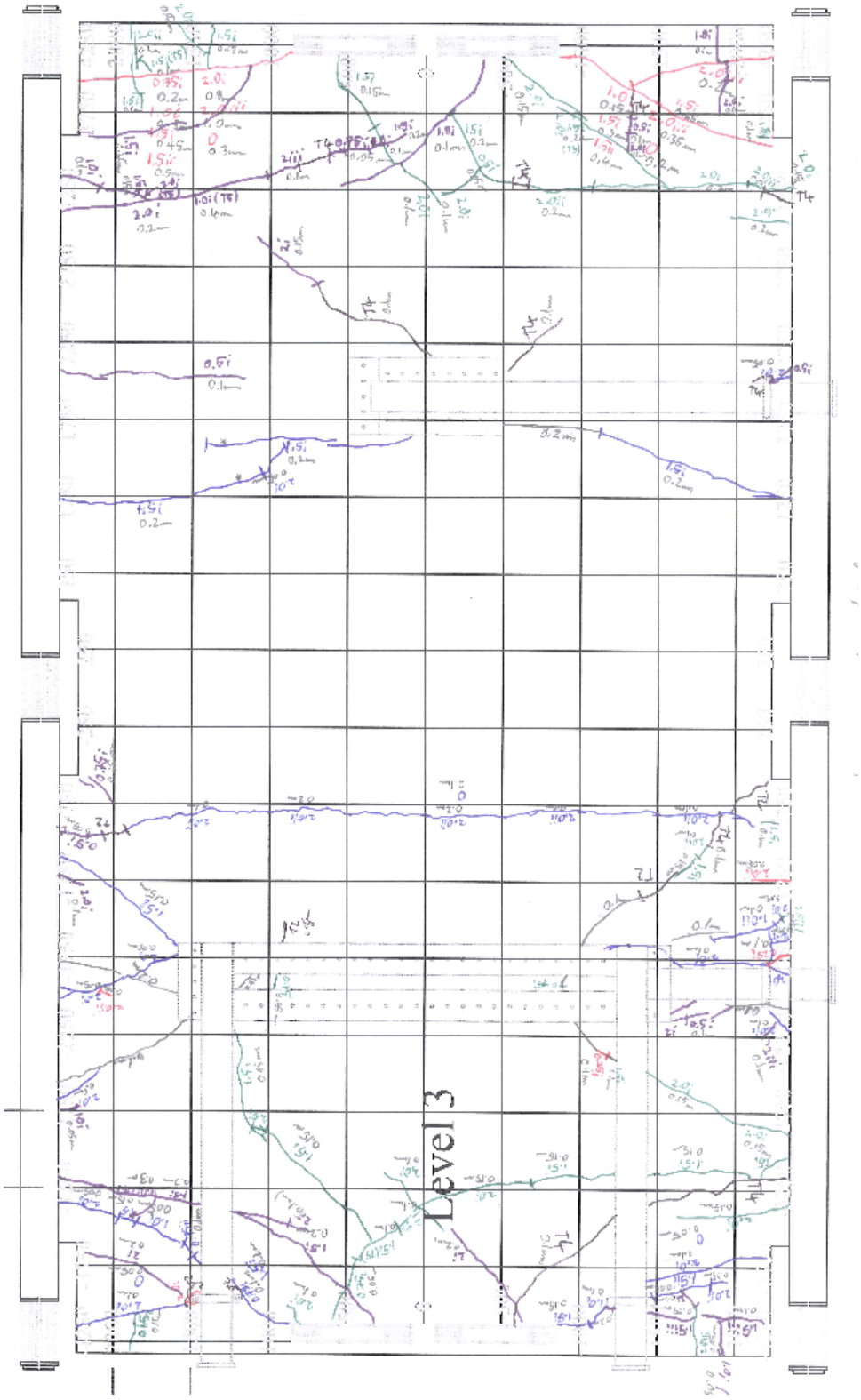

Figure C.4.8. Crack pattern after Test 6: Level 3

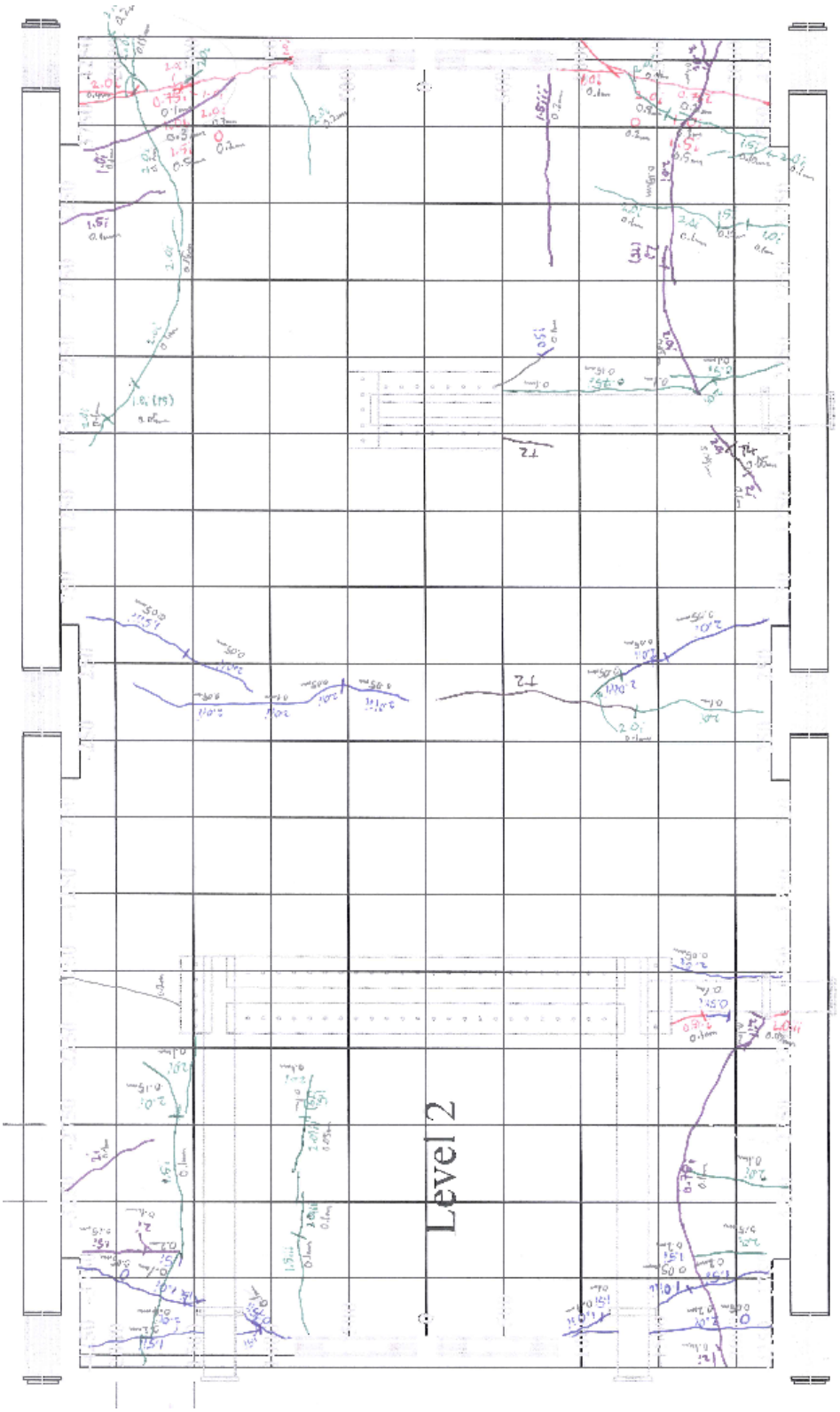

Figure C.4.9. Crack pattern after Test 6: Level 2

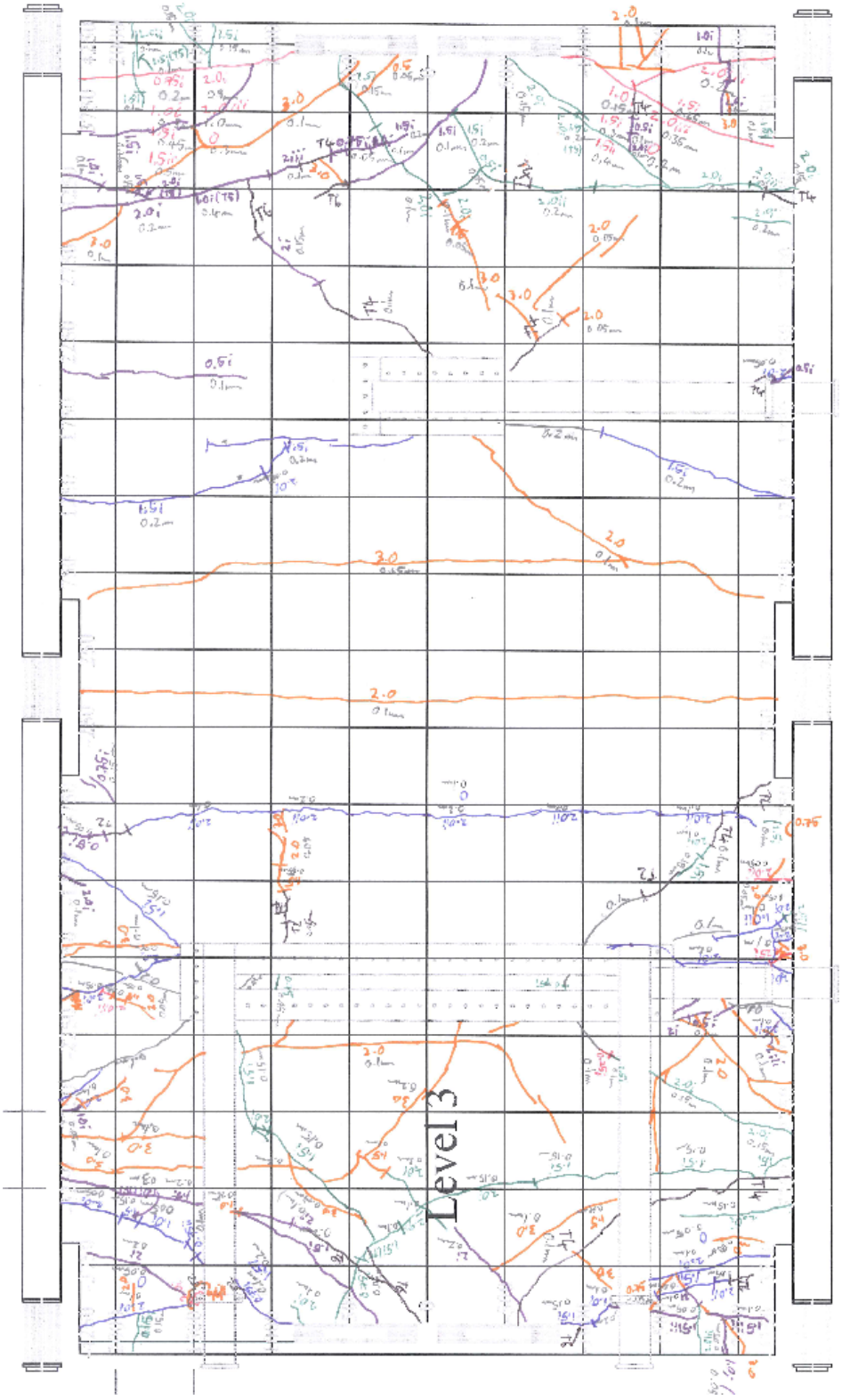

Figure C.4.10. Crack pattern after Test 7: Level 3

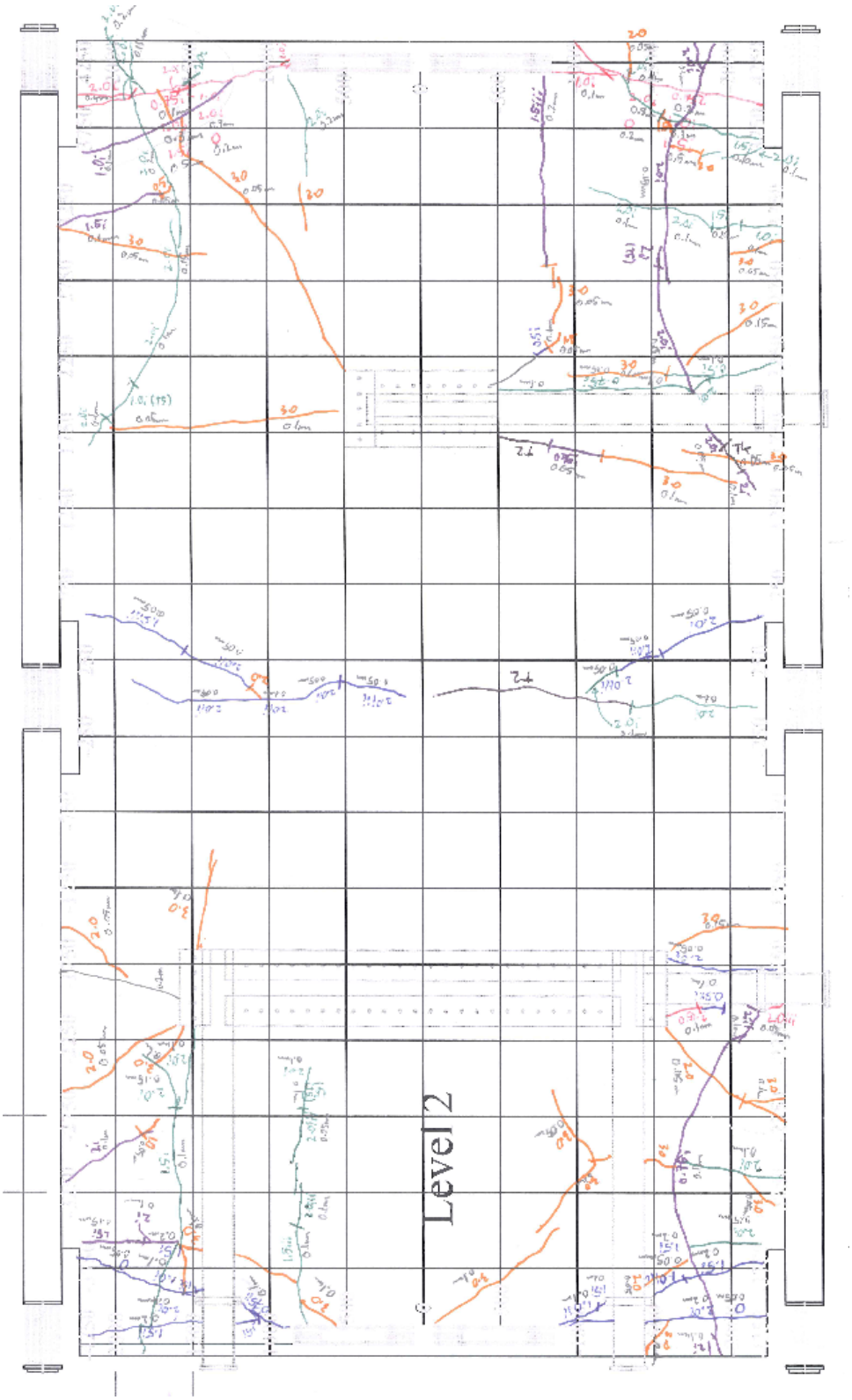

Figure C.4.11. Crack pattern after Test 7: Level 2

C.4.2. Localized damage

Pre-test cracking

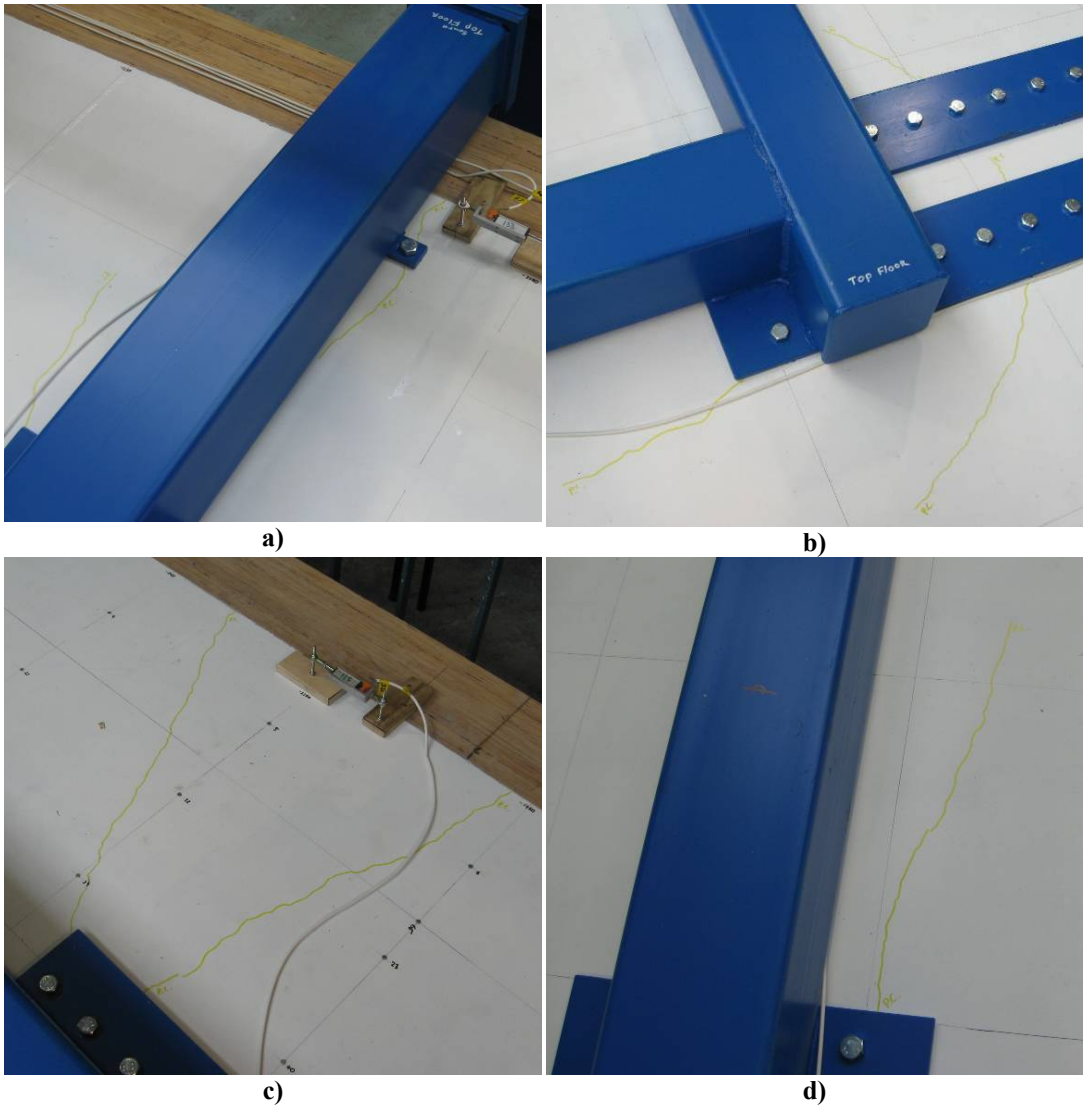

a) **b)**

c) **d)**

Figure C.4.12. Pre-test cracking due to loading apparatus on Level 3: a) & b) SW bay c) NW bay d) SE bay

Test 1

During Test 1, cracking was observed in the corners of the floor slab (as discussed above).

a) **b)**

Figure C.4.13. Cracking around edge beams at 0.75% Drift on Level 3: a) & b) NE corner

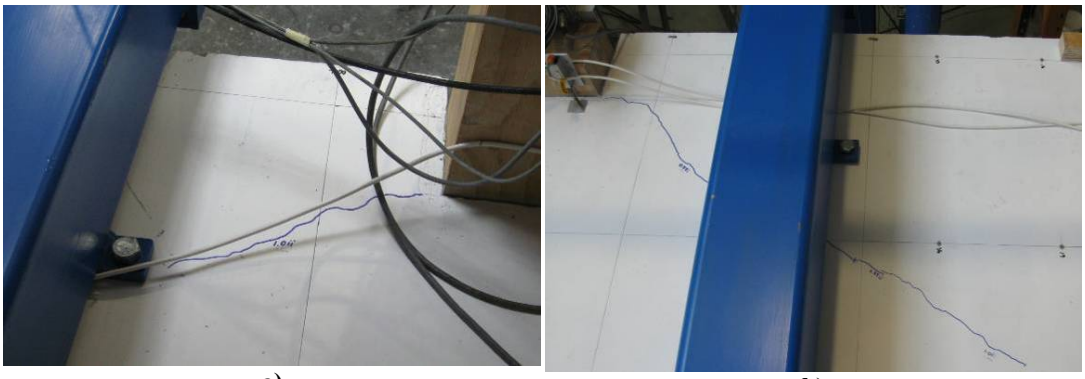

a) **b)**

Figure C.4.14. Cracking around edge beams at negative 0.75% Drift: a) Level 2, SW corner b) Level 3, NW corner

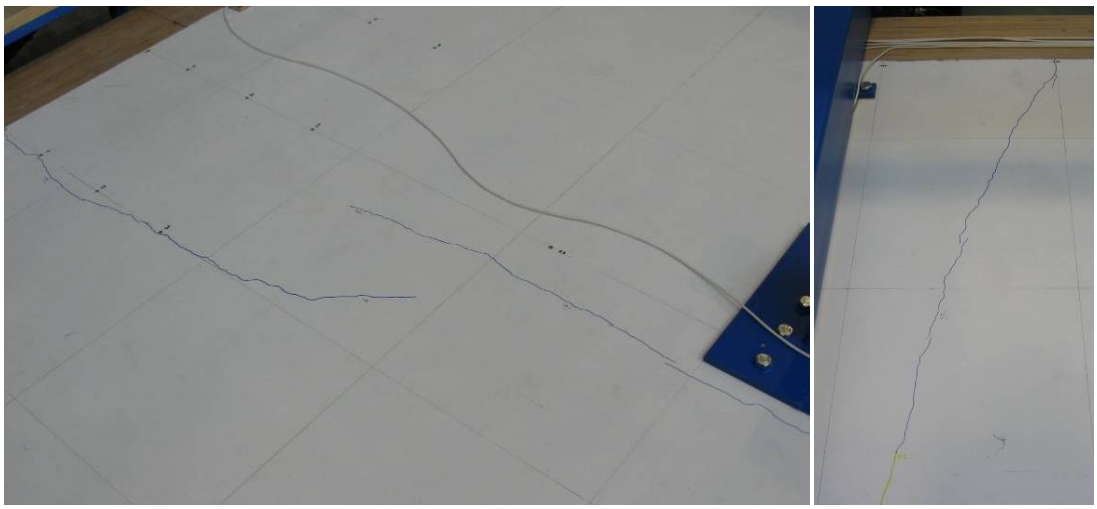

a) **b)**

Figure C.4.15. Cracking induced by loading apparatus on Level 3 at negative 1.5% Drift: a) SE bay b) NE bay

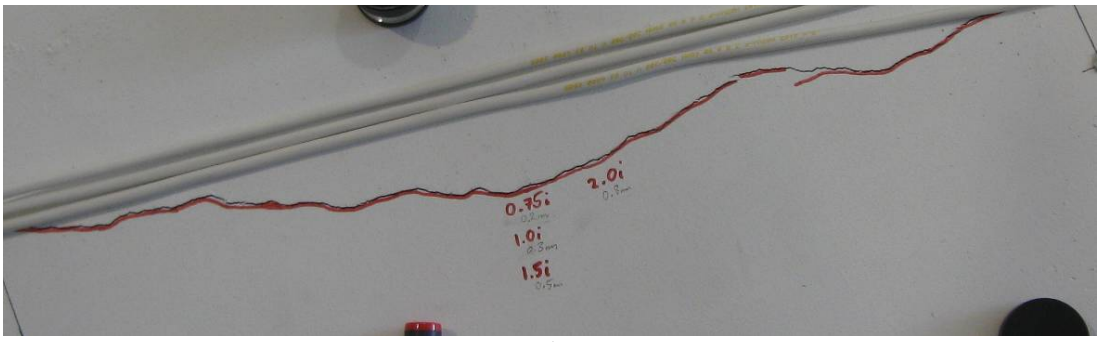

a)

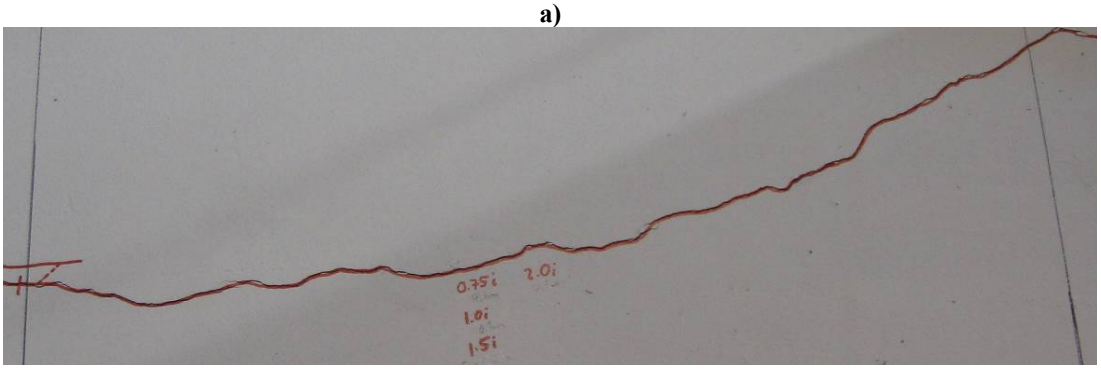

b)

Figure C.4.16. Cracking around edge beams over a 500mm grid at 2.0% Drift: a) NE bay b) SE bay

Additional cracking was induced by the loading apparatus. Due to eccentricities between the slab and the application of load, a partial pull-out failure of a bolted connection was observed at the NW corner of the slab on Level 3.

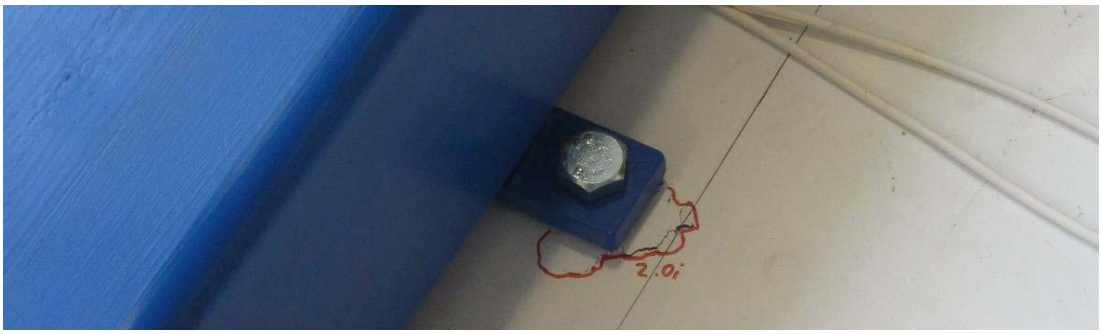

Figure C.4.17. Cracking due to loading apparatus hold-down at 2.0% Drift

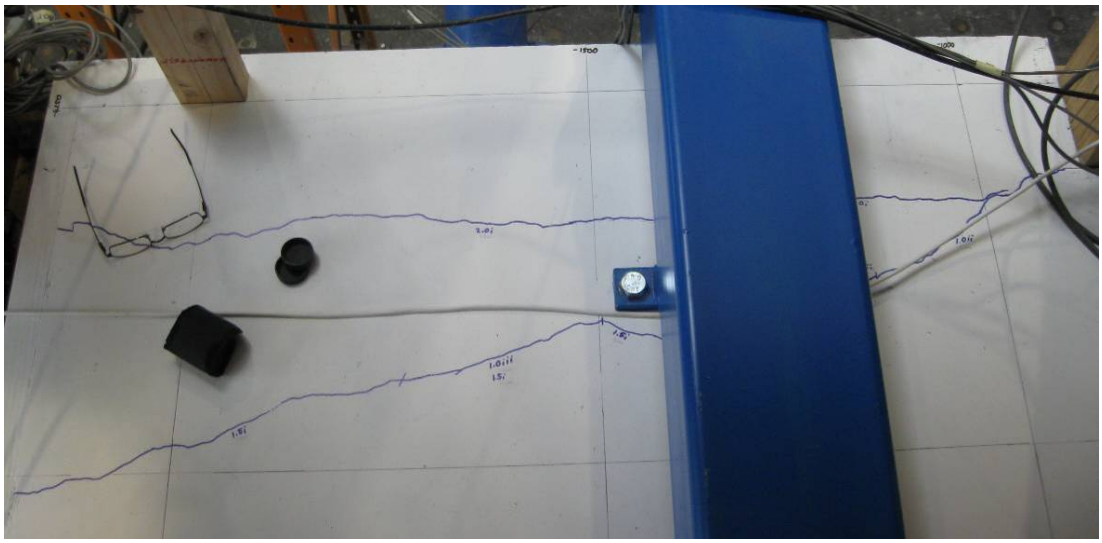

a)

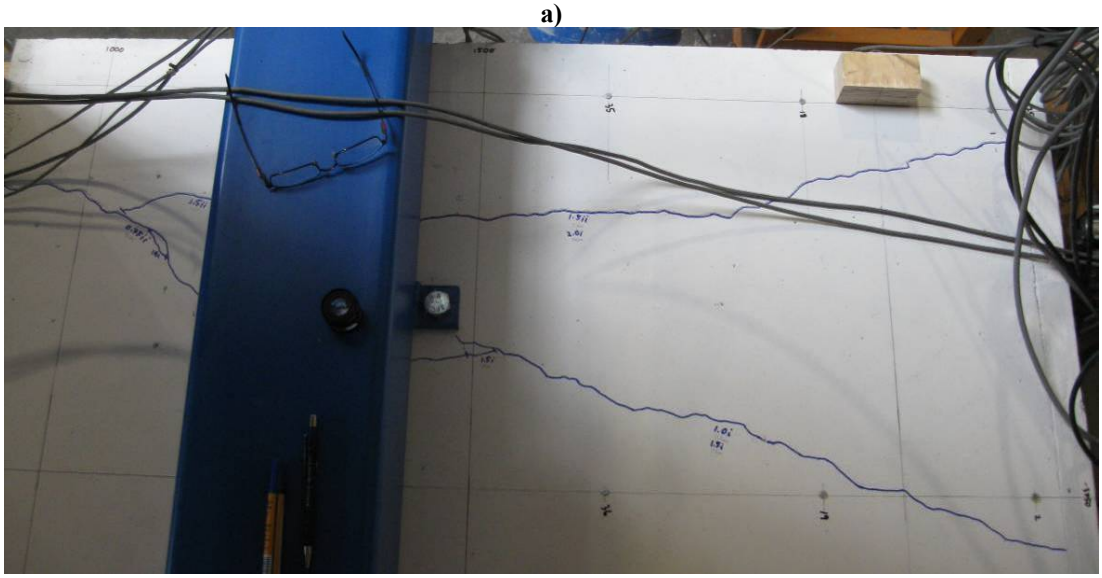

b)

Figure C.4.18. Cracking around edge beams at negative 2.0% Drift: a) SW bay b) NW bay

Test 2

Few additional cracks were observed during Test 2. However, the pull-out failure due to the loading apparatus grew slightly.

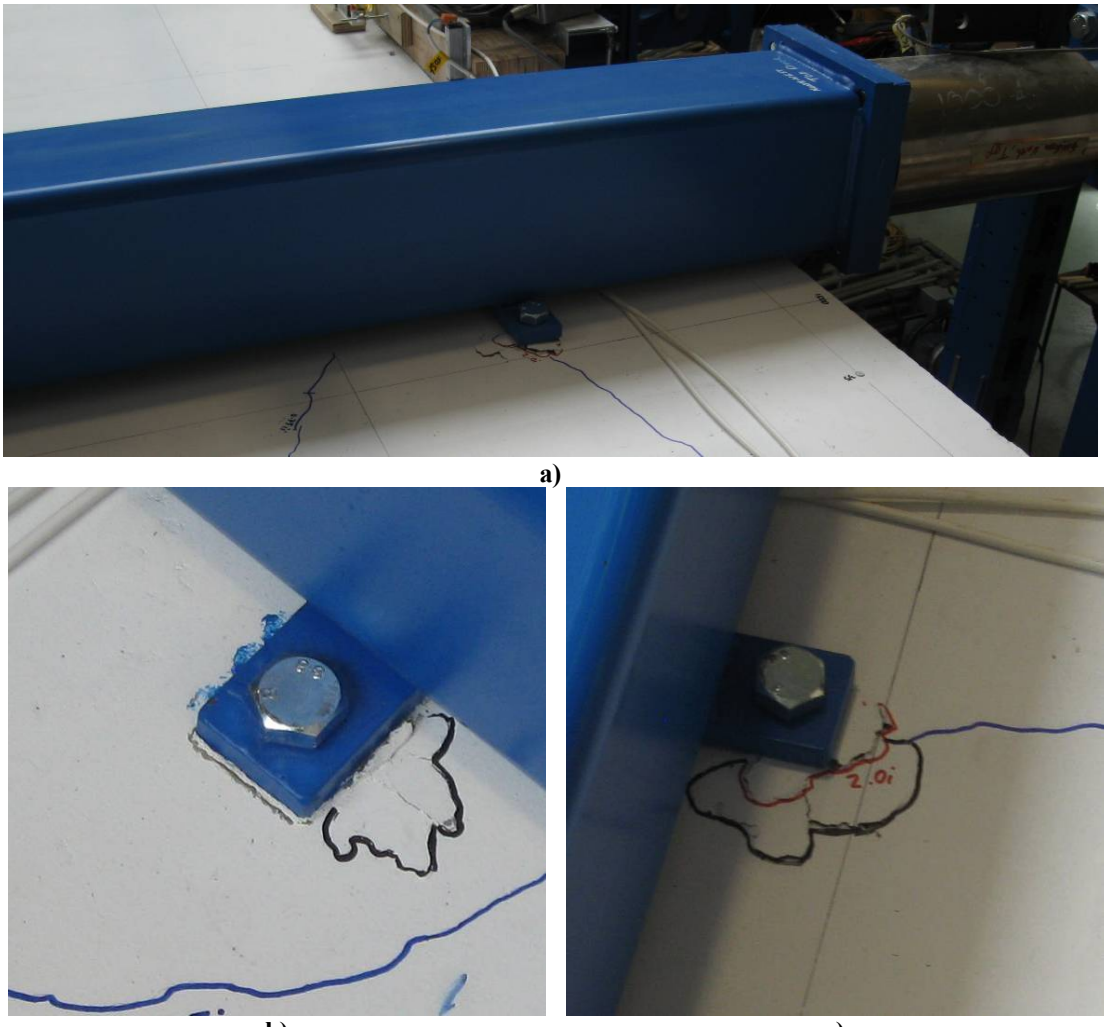

a)

b) **c)**

Figure C.4.19. Further cracking due to loading apparatus hold-down at 2.0% Drift

Test 3

During Test 3, cracking was observed in the corners of the floor slab (as discussed above).

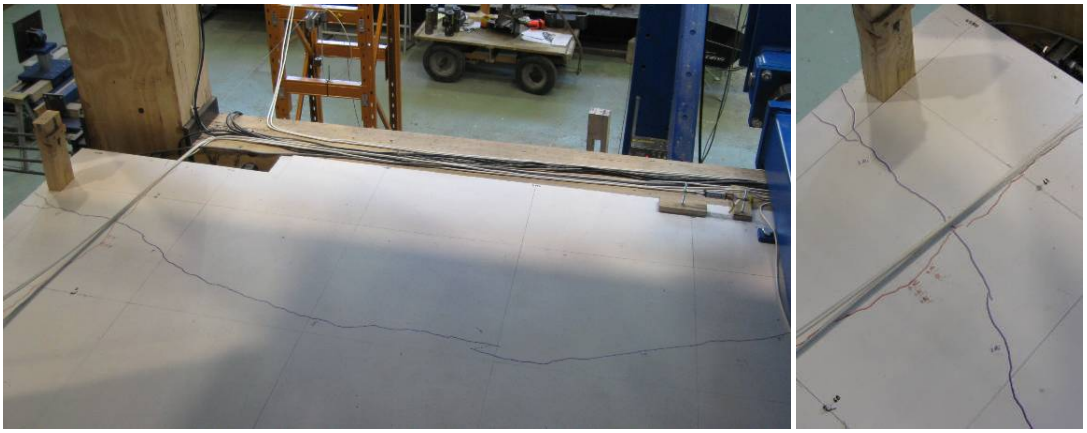

a) **b)**

Figure C.4.20. Cracking due to bending of the slab on Level 2 at 2.0% Drift: a) & b) SE bay

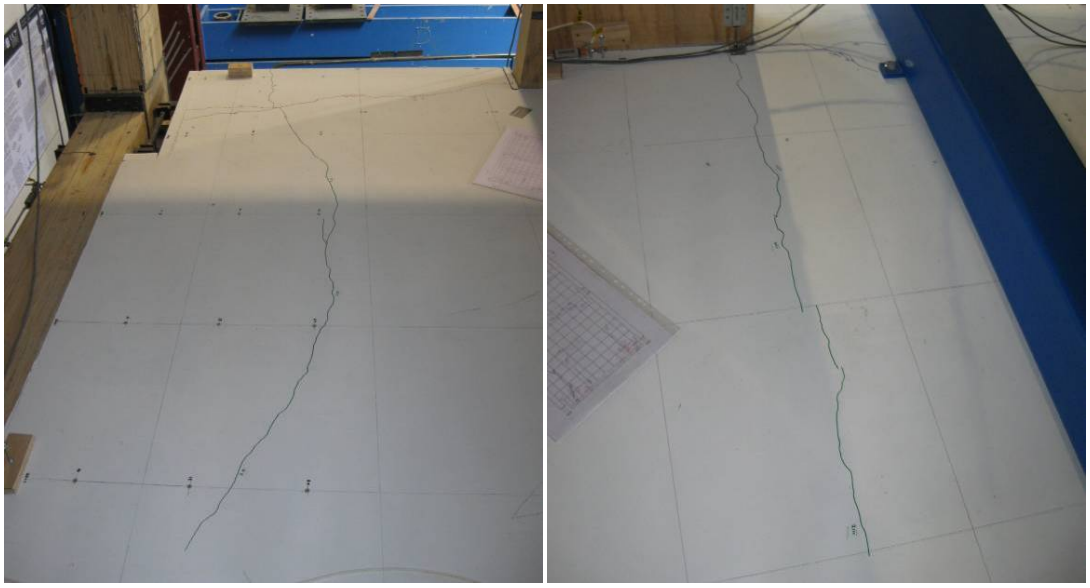

a) **b)**

Figure C.4.21. Cracking due to bending of the slab on Level 2 at negative 2.0% Drift: a) & b) SE bay

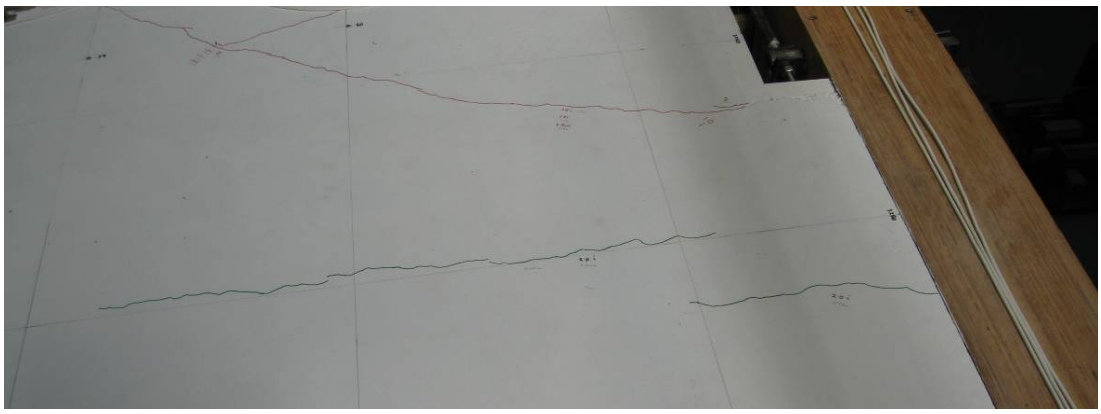

Figure C.4.22. Cracking due to bending of the slab on Level 3 at negative 2.0% Drift in the SE bay

Foam spacers were effective at preventing crushing and damage to the floor slab at the walls rotated.

a) **b)**

Figure C.4.23. Deformation around wall edges: a) Position of flexible foam spacer b) Deformation around spacer at 2% Drift

The frame system rotated out-of-plane relative to the floor slab. This resulted in the gap opening between the beam and the slab, avoiding cracking of the slab. However, this deformation would have caused bending in the coach screws that were used for the timber-concrete composite diaphragm connection.

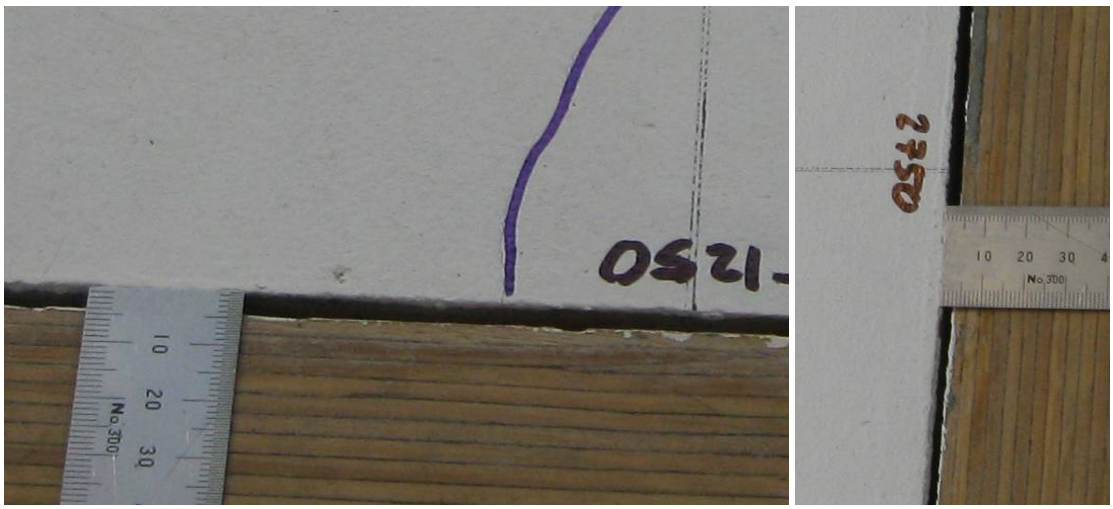

a) b)

Figure C.4.24. Gap opening between slab and beam 2.0% Drift: a) NE bay b) NW bay

a) b)

Figure C.4.25. Slab uplift relative to the beam at negative 2.0% Drift: a) & b) NE bay

Test 4

During test 4, floor cracking slightly increased, but generally in the same locations as Test 3.

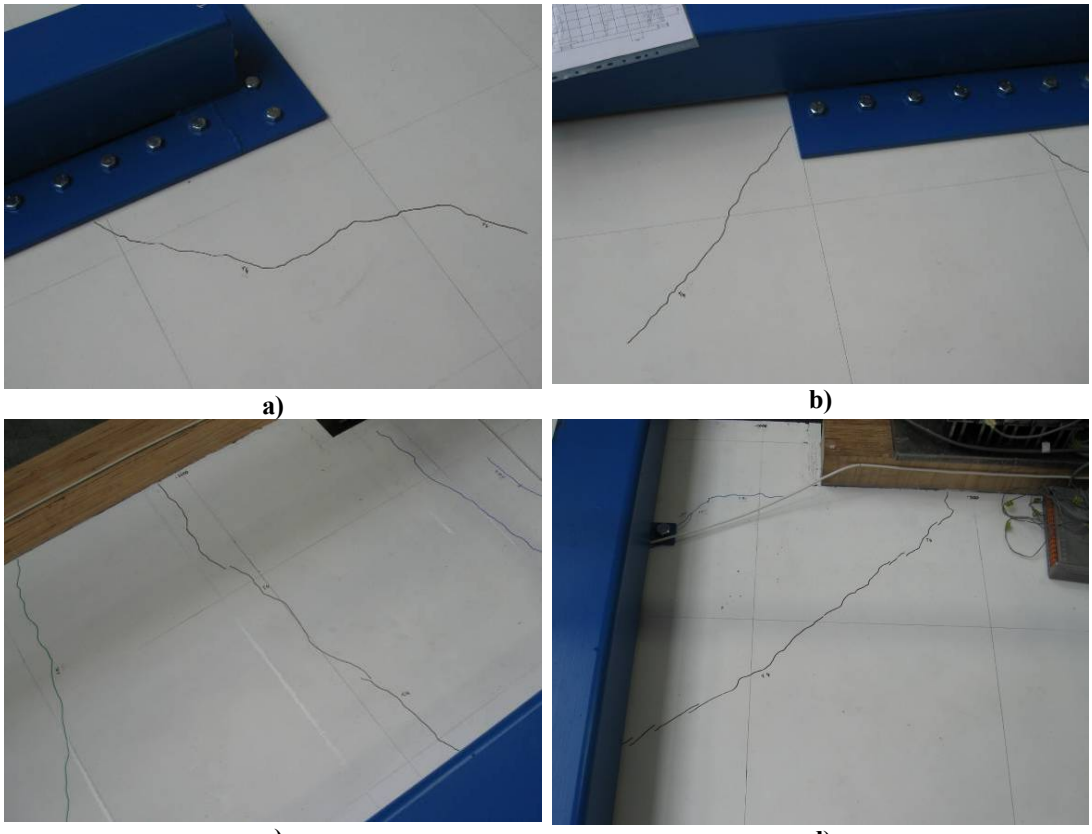

a) **b)**

c) **d)**

Figure C.4.26. Further cracking during Test 4: a) & b) East bay, Level 3 c) & d) West bay, Level 3

Test 5

The cracking pattern changed slightly due to the absence of the edge beam supports. The slab was able to drop below the beams, resulting in more visible cracking. Crack around the supporting corbel were created when the slab depressed with the edge beam.

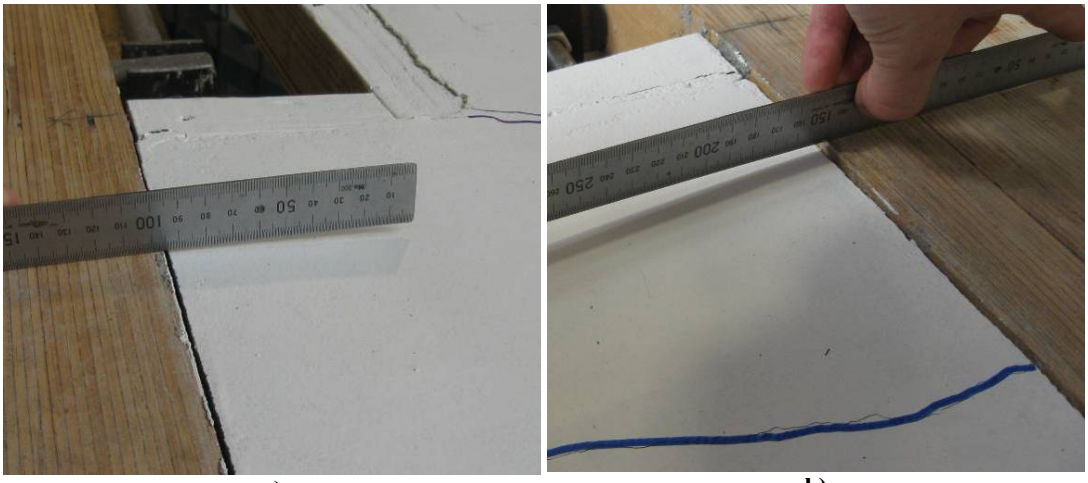

a) b)

Figure C.4.27. Slab depression relative to the beam at 2.0% Drift on Level 3: a) NE bay b) NW bay

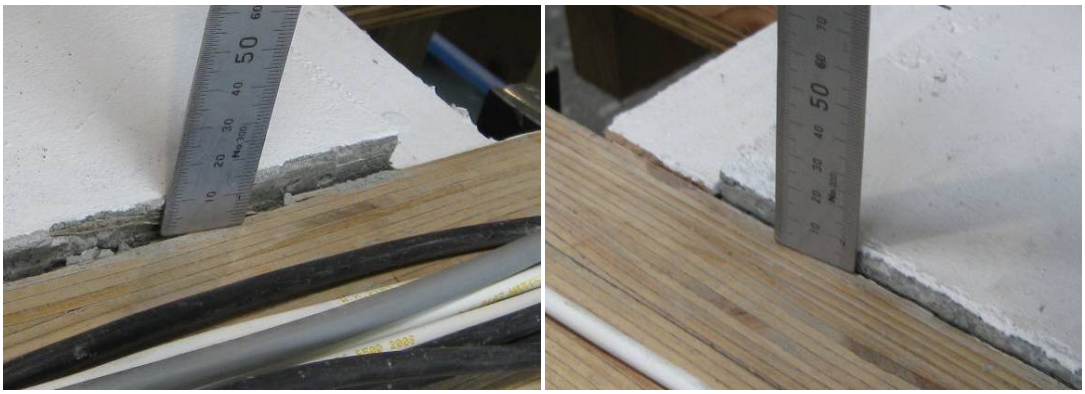

a) b)

Figure C.4.28. Slab uplift relative to the beam at 2.0% Drift on Level 3: a) NE bay b) NW bay

a) **b)**

Figure C.4.29. Slab uplift relative to the beam at negative 2.0% Drift on Level 3: a) NW bay b) NE bay

Test 6

There were no significant changes in the crack patterns during Test 6. Some cracking was noticed between edge-beams and concrete slab. Similar cracking was not observed on Level 3, where the in-plane forces are double that at Level 2. This indicates that the cracking was caused by restraint of the edge of the floor slab as the edge beam dropped below the height of the beam, which acted to delaminate the slab from the formwork.

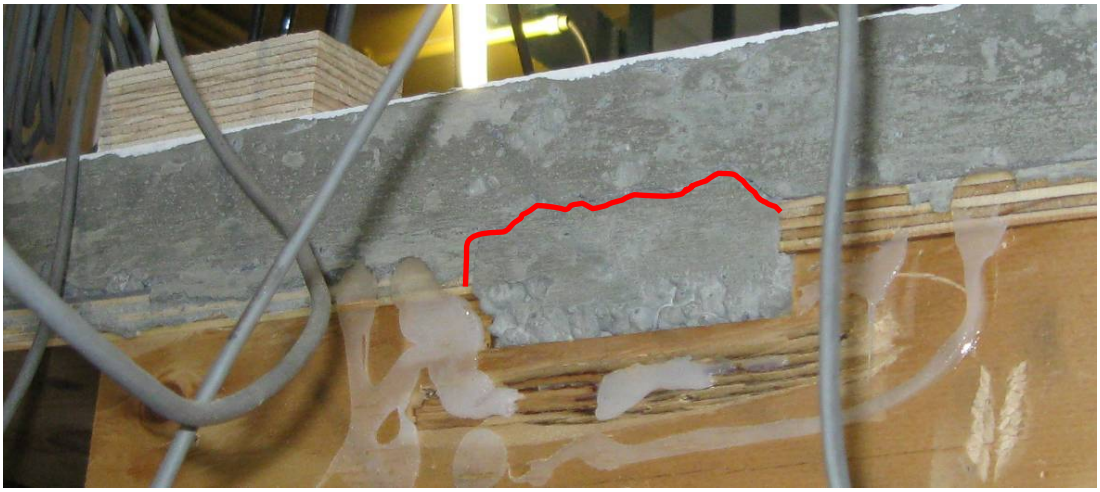

Figure C.4.30. Slab cracking around edge beam connection at SE corner on Level 2

Test 7

For the bi-directional testing, cracking patterns were similar to the uni-directional tests. Generally cracks increased in length, became more numerous in certain areas and increased in width. No new trends in crack development were noted.

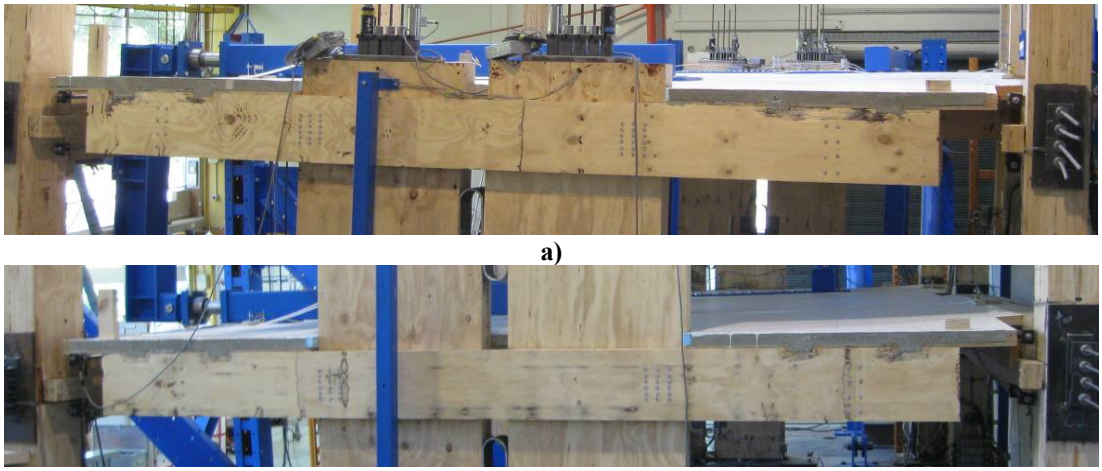

a)

b)

Figure C.4.31. Slab distortion at peak bi-directional Drift: a) Level 3 b) Level 2

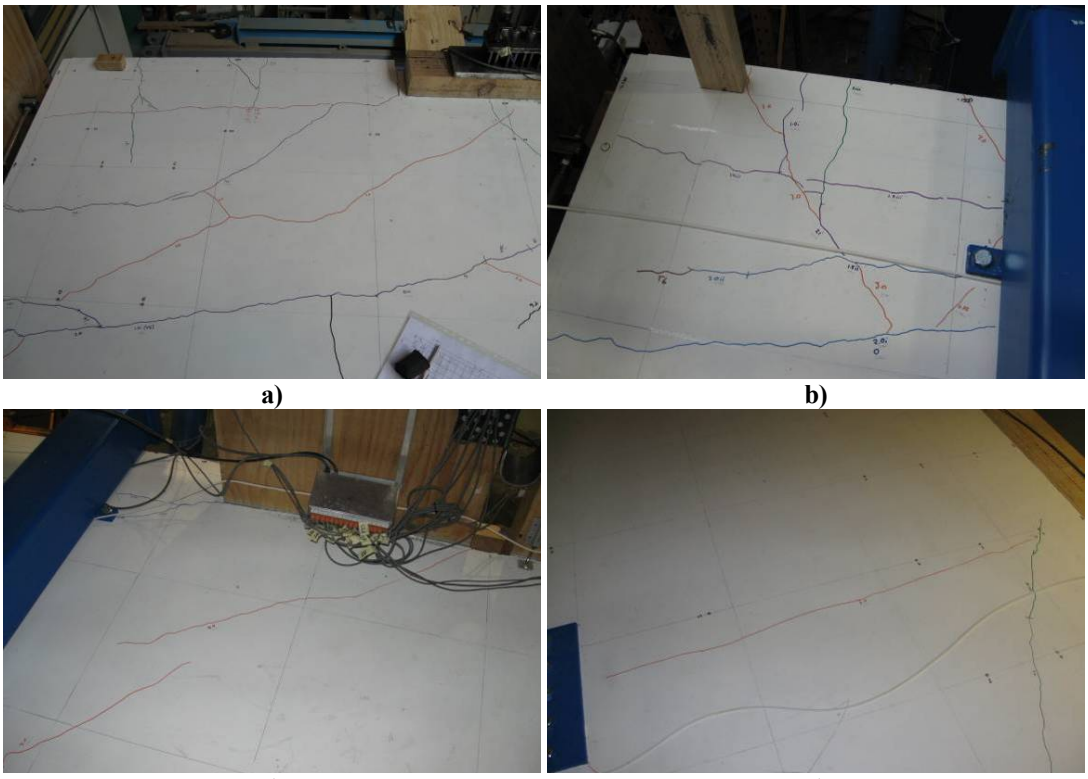

a) **b)**

c) **d)**

Figure C.4.32. Further cracking during Test 4: a) & b) East bay, L3 c) & d) West bay, L3

APPENDIX D

MODELLING FRAME SYSTEMS

This appendix focuses on the modeling the response of post-tensioned timber frames. The predicted response of the frames is compared with complex finite element models (FEM) and experimental data.

D.1. COLUMN DEFORMATION USING FEM

In the section, the analytical predictions of the column deformation are compared with the results of finite element model (FEM) created in SAP 2000 (2005). For the numerical model, it was not possible to separate the individual components of column deformation into joint panel, column deformation, as considered for analytical modeling. Instead, a combination of joint panel and column deformation was considered, as illustrated in Figure D.1.2. A small sensitivity study is performed in which several different parameters are varied, to ensure the accuracy of the analytical equations.

D.1.1. The finite element model

The model is a two-dimensional representation of the column which consists of orthotropic elastic shell elements. A fine mesh was required to achieve convergence of displacements from model, as shown in Figure D.1.1. A benchmark model was specified, and key parameters were altered to determine their effect on the accuracy of the analytical predictions. The material properties and dimensions for the benchmark model are given in Table D.1.1.

The boundary conditions are pin supports at the top and bottom of the column. The nodes at the top and bottom edges of the column are constrained to the same rotation and can not deform transversely; hence, a linear strain profile is enforced.

For the benchmark model, the applied loads are linearly distributed, and provide a connection moment of 150kN.m. The distance between extreme top and bottom point loads is the beam depth. The beam shear is calculated for a 6m bay length and is simulated by using uniformly distributed point loads within the simulated compression region (or neutral axis depth).

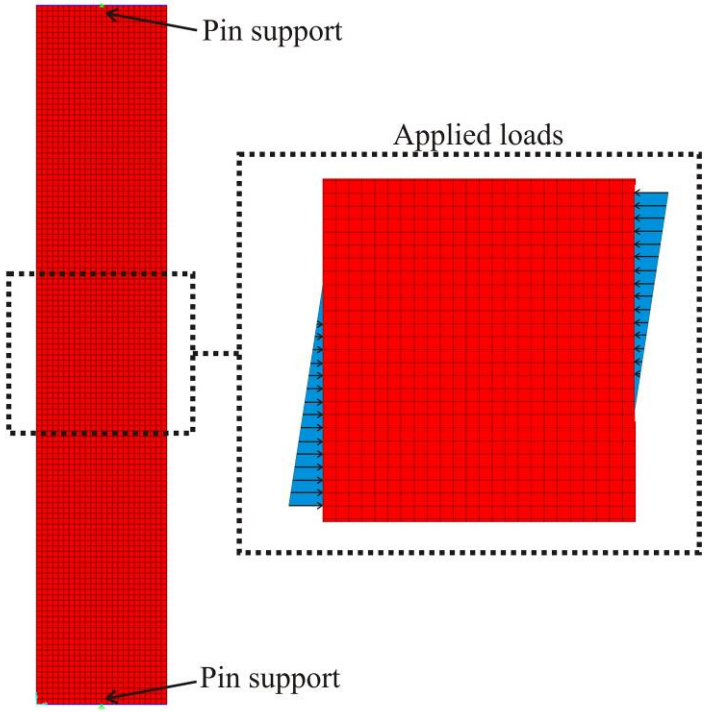

Figure D.1.1. Boundary conditions and applied loads for the benchmark FEM of the column

Table D.1.1 – Material properties and geometry of the benchmark column model

Parameter	Symbol	Units	Value
Elastic modulus – Parallel to grain	E_{para}	MPa	13200
Elastic modulus – Perp. to grain	E_{perp}	MPa	660
Poisson's ratio*	υ	-	0.3
Shear modulus	G	MPa	600
Column height	H	m	3.2
Column depth	h_c	mm	600
Column width	b_c	mm	380
Beam depth	h_b	mm	600
Bay length	L_b	mm	6000

*Based on research performed on Pine by Murray (2007).

D.1.2. Comparison of the model and the analytical equations

The FEM deformation can be compared with the analytical model, to a limited extent. Because the boundary conditions for the FEM are different to those assumed for the analytical equations, it is not possible to simply compare the sum of joint and column deformation, as defined in Chapter 6. This is illustrated in Figure D.1.2.

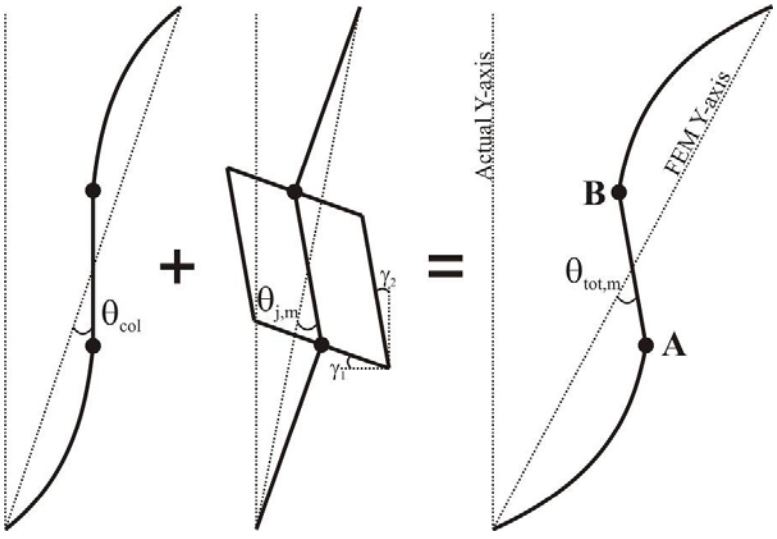

Figure D.1.2. Deformation components of FEM column

The total rotation of the FEM, as shown in Figure D.1.2, is:

$$\theta_{tot,m} = \theta_{col} + \theta_{j,m} = \frac{\Delta_A - \Delta_B}{h_b}$$

To allow comparison, $\theta_{tot,m}$, must be defined with analytical equations. The column rotation, θ_c, was defined in Chapter 6 as:

$$\theta_c = \frac{\phi_c}{H}\left(\frac{(H-h_b)^2}{6} + \frac{E_t}{G}\frac{h_c^{\,2}}{4}\right)$$

Where: $\phi_c = \frac{M_{con}}{E_t I_c}\frac{L_b(H-h_b)}{H(L_b-h_c)}$.

The rotation due to joint panel rotation, $\theta_{j,m}$, can be derived using simple trigonometry as:

$$\theta_{j,m} = \frac{H-h_b}{H}\gamma$$

Where: $\gamma = \frac{\overline{V_{jh}}}{GA_{sh}}$

$\overline{V}_{jh} = \frac{2M_{con}}{h_b} - V_{col}$;

$A_{sh} = b_c h_c$.

Hence, for the analytical comparison:

$$\theta_{tot,m} = \theta_{col} + \theta_{j,m} = \theta_{col} + \frac{H-h_b}{H}\gamma$$

D.1.3. Results from the sensitivity study

In this section, the results of the sensitivity study on the column deformation are considered. For each FEM permutation, key findings are presented and the deformation of the column is compared with the analytical predictions in Table D.1.2.

FEM 1 (Benchmark)

The deformed shape, transverse, longitudinal and shear stresses are shown in Figure D.1.3. The shear, transverse and longitudinal stresses range from -3 to 5, -11 and 0 and -35 and 11 respectively. In Figure D.1.3, the minimum and maximum values correspond to purple and blue respectively.

The analytical prediction for the benchmark model was 9% greater than that of the FEM, as shown in Table D.1.2. It is preferable that the equations are slightly conservative, as is the case here, because the connection rotation and therefore the design strength of the frame is conservative.

FEM 2

For FEM 2, the only alteration from the benchmark models was the neutral axis depth, which was halved. This modification had no significant effect on the accuracy of the analytical predictions (which was 8% larger than the deformation of the FEM).

The shear stresses within the joint panel are shown in Figure D.1.4, over the same range as the benchmark model. The angle of the compression strut does not appear to significantly affect the accuracy of the predictions. The shear stresses due to the applied loads are concentrated mainly with the joint. However, there is some diffusion of shear stress to outside the joint panel, which may account for the slight inaccuracy of the predictions.

FEM 3

For FEM 3, the only alteration from the benchmark models was the stress distribution. Instead of a linear stress distribution, a uniform stress distribution was applied, which gave the same connection moment as the benchmark model. This modification had no significant effect on the accuracy of the predictions.

FEM 4

For FEM 4, the connection moment is doubled and the neutral axis depth is halved from the benchmark model. These modifications had no significant effect on the accuracy of the predictions.

FEM 5

For FEM 5, the neutral axis depth is halved and the column depth is reduced by one-third from the benchmark model. In this case, the prediction improved in accuracy but slightly underestimated the column deformation by 5%. Due to the increased aspect ratio of the joint panel, it is expected that the contribution of flexural deformation increased. Flexural deformations are not considered in the analytical predictions.

FEM 6

For FEM 6, the neutral axis depth is halved and the column depth is increased by two-thirds from the benchmark model. The prediction significantly over-estimates the column deformation by 44%. There is significant diffusion of stresses into the column, outside the joint panel zone. The diffusion of stresses results in a less pronounced compression strut and less overall column deformation, and consequently, conservative predictions.

FEM 7

For FEM 7, the neutral axis depth is halved and the beam depth is reduced by one third from the benchmark model. The prediction is 23% larger than the deformation of the FEM. Similar to FEM 6, there is significant stress diffusion and a less defined compression strut, which appears to have increased the joint panel stiffness. The effect of stress diffusion is not as significant as FEM 6, because the neutral axis depth is larger relative to the height of the beam.

FEM 8

For FEM 8, the neutral axis depth is halved and the beam depth is increased by two-thirds from the benchmark model. The prediction is only 1% larger than the deformation of the FEM.

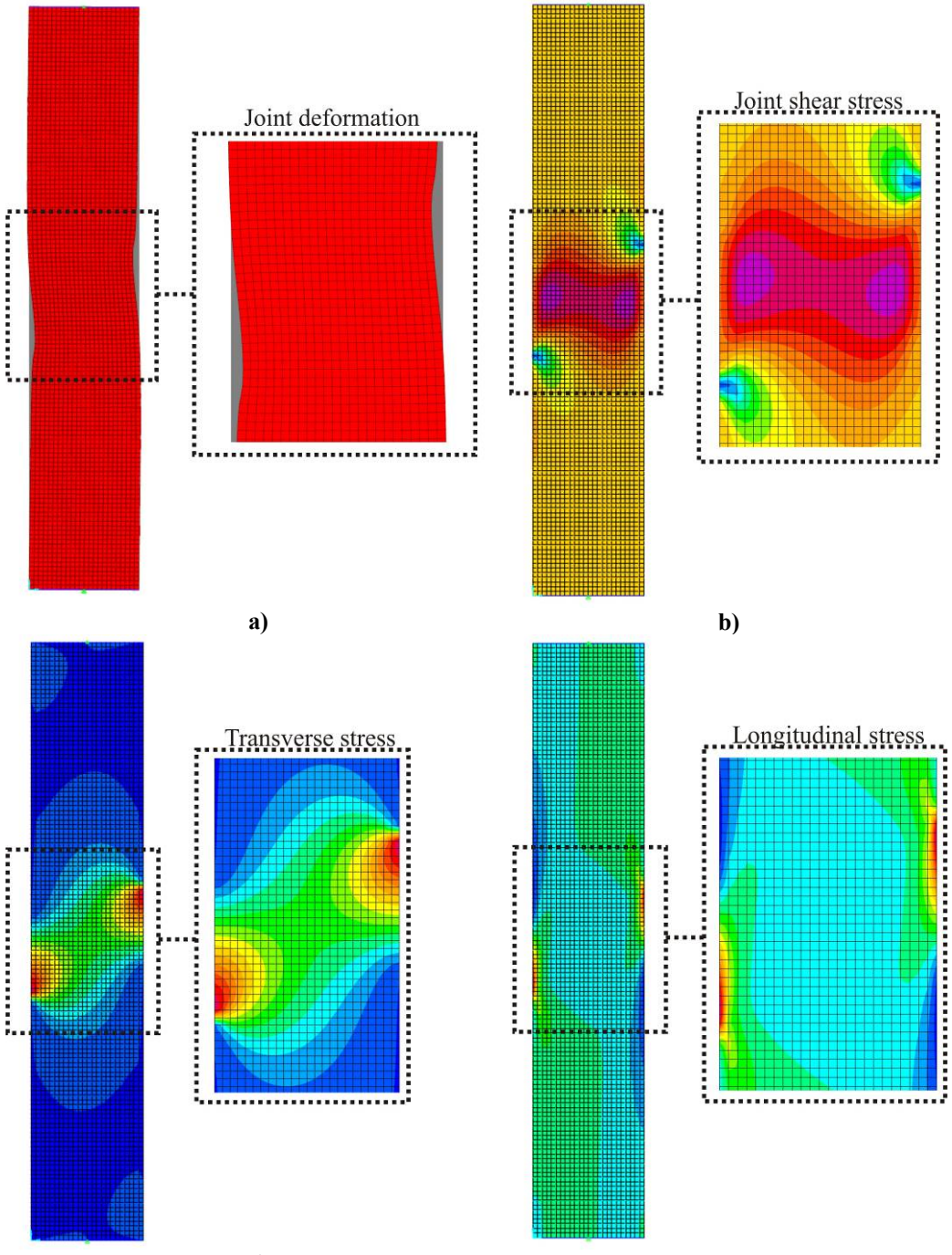

Figure D.1.3. Results of for benchmark FEM: a) Deformed shape b) Shear stresses c) Transverse stresses d) Longitudinal stresses

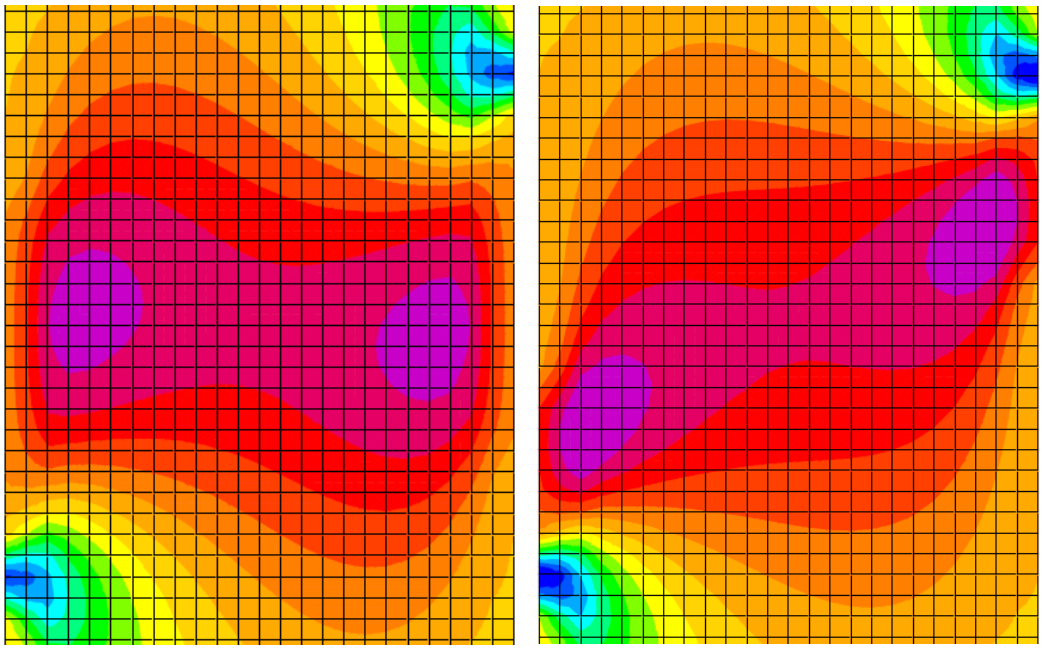

a) **b)**

Figure D.1.4. Shear stresses in joint panel: a) Benchmark b) FEM 2

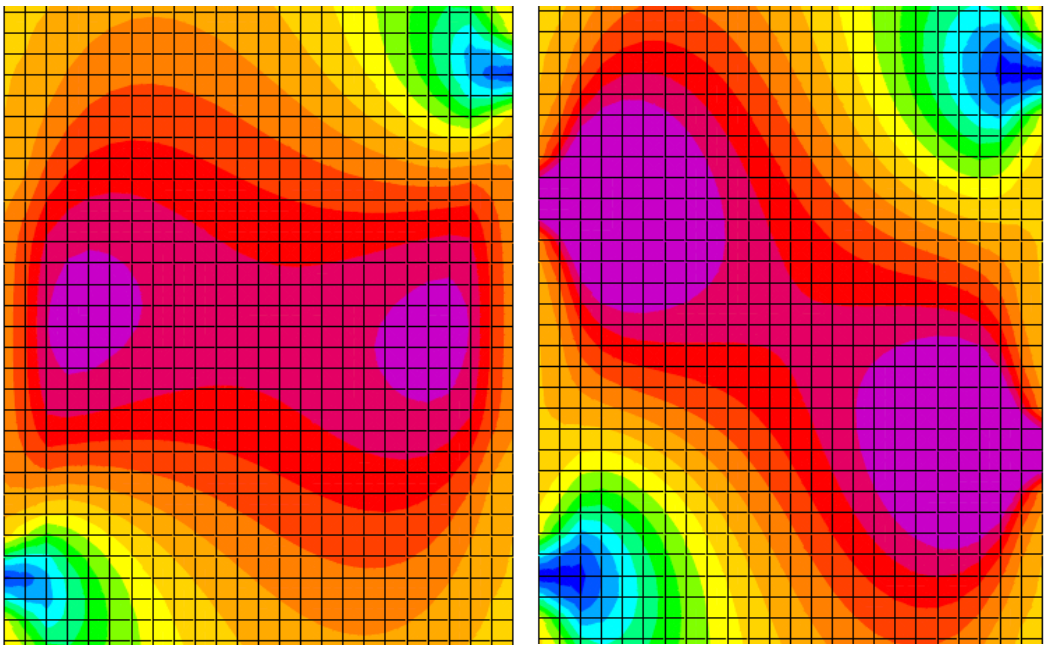

a) **b)**

Figure D.1.5. Shear stresses in joint panel: a) Benchmark b) FEM 3

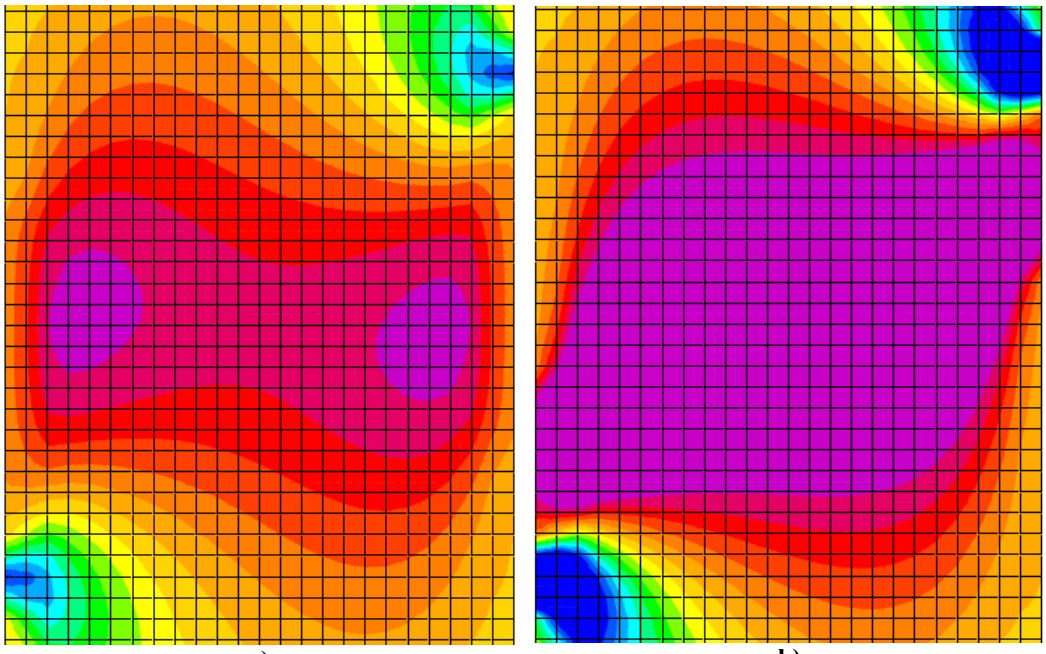

a) **b)**

Figure D.1.6. Shear stresses in joint panel: a) Benchmark b) FEM 4

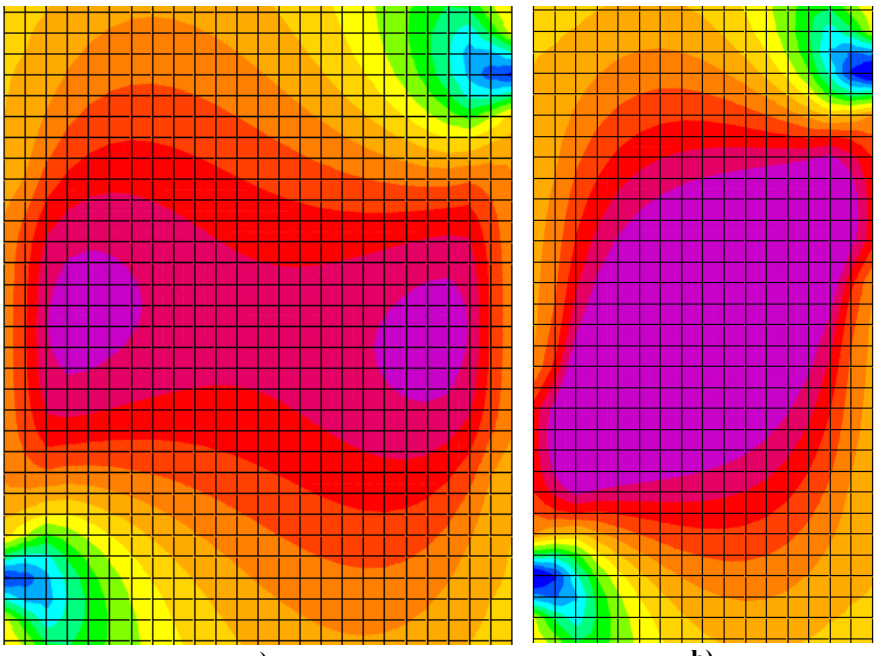

a) **b)**

Figure D.1.7. Shear stresses in joint panel: a) Benchmark b) FEM 5

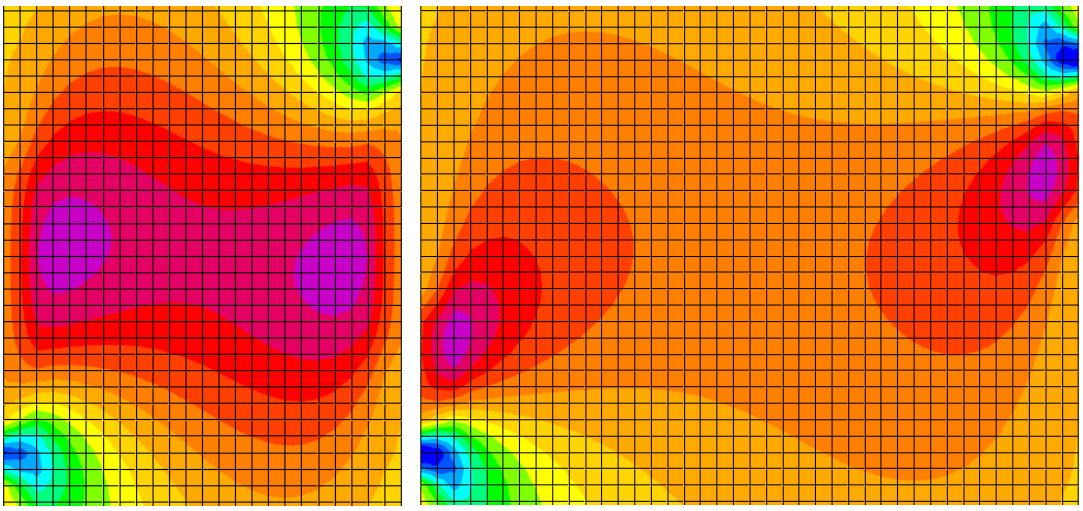

a) **b)**

Figure D.1.8. Shear stresses in joint panel: a) Benchmark b) FEM 6

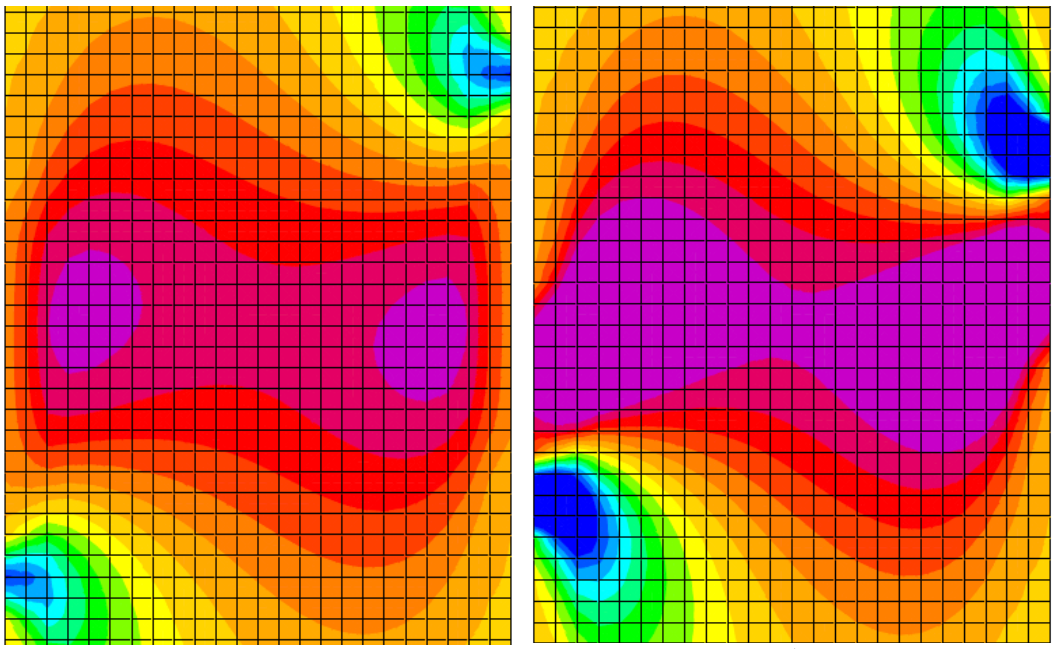

a) **b)**

Figure D.1.9. Shear stresses in joint panel: a) Benchmark b) FEM 7

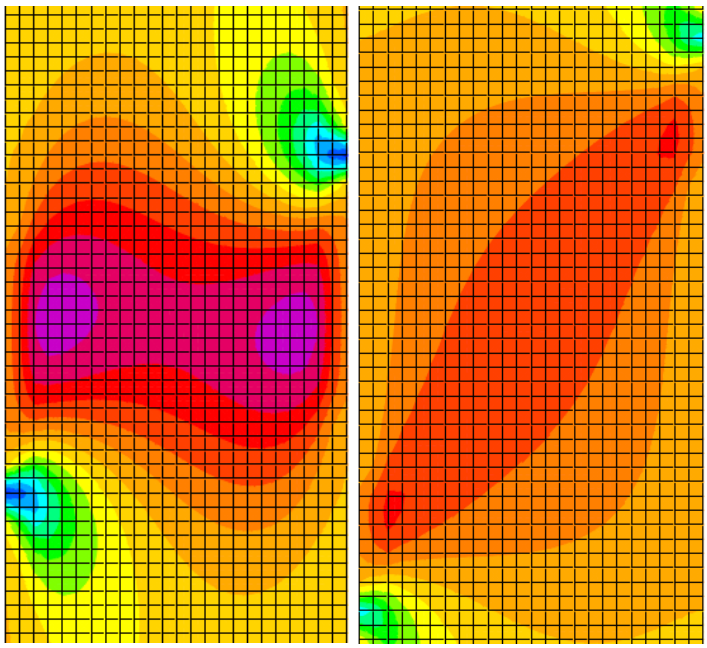

a) **b)**

Figure D.1.10. Shear stresses in joint panel: a) Benchmark b) FEM 8

Summary of the sensitivity study

Based-on the results in Table D.1.2, the analytical predictions are sufficiently accurate. For joint panels that have an aspect ratio (h_b/h_c) of less than one, the analytical predictions will be conservative for design.

Table D.1.2 – Summary of the column FEM results and comparison with predictions

FEM Model	Change from benchmark	θ_c (rad)	γ (rad)	$\theta_{tot,m}$ (rad)		Accuracy*
		Eqn.	Eqn.	Eqn.	FEM	
1	Benchmark	0.00132	0.00299	0.00374	0.00351	7 %
2	Half neutral axis	0.00132	0.00299	0.00374	0.00345	8 %
3	Uniform stress	0.00132	0.00299	0.00374	0.00347	8 %
4	Double M_{con} Half neutral axis	0.00263	0.00597	0.00749	0.00690	9 %
5	Half neutral axis 2/3 column depth	0.00287	0.00448	0.00651	0.00687	-5 %
6	Half neutral axis 5/3 column depth	0.00061	0.00179	0.00206	0.00143	44%
7	Half neutral axis 2/3 beam depth	0.00150	0.00482	0.00572	0.00464	23 %
8	Half neutral axis 5/3 beam depth	0.00100	0.00152	0.00204	0.00202	1 %

*Positive percentages indicate that the column deformation is over predicted.

D.2. JOINT PANEL DEFORMATION USING EXPERIMENTAL DATA

For further verification, the predicted joint panel zone deformation is compared with experimental data from subassembly tests. The joint panel deformation is determined using diagonal potentiometers placed on the joint panel, as shown in Figure D.2.1. The joint panel shear distortion, γ, is calculated as:

$$\gamma = \frac{\Delta_2 - \Delta_1}{2L_g}\left(\tan\theta + \frac{1}{\tan\theta}\right)$$

Where: Δ_1 and Δ_2 is the displacement of Pot 1 and 2;
L_g is the gauge length of the potentiometers.

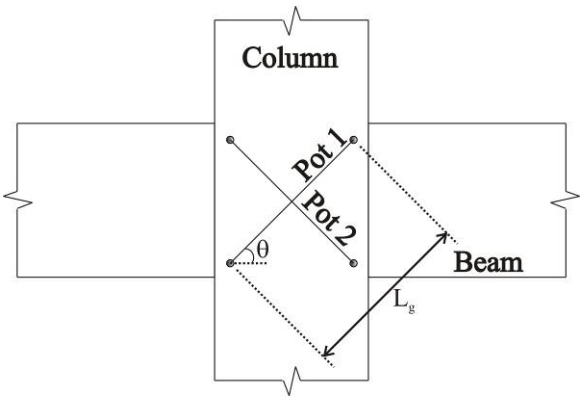

Figure D.2.1. Diagonal potentiometers to determine shear distortion

However, caution should be exercised when interpreting the joint panel deformation from experimental data for timber frames. There is significant perpendicular-to-grain strain (ε_z) that occurs near the compression regions. This has the effect of artificially increasing the measured joint distortion, γ, as illustrated in Figure D.2.2. To minimize inaccuracies in measurement (due to the transversal strains in the column), the potentiometers should be located at the center of joint panel and have a short gauge length. Alternatively, additional potentiometers should be placed transversely, at the top and bottom of the joint panel. This will enable the transverse deformation of the column and the resultant rotation, γ_c, to be quantified, and then subtracted from the measured joint panel deformation, γ_{tot}. Therefore:

$$\gamma = \gamma_{tot} - \gamma_c = \frac{\Delta_2 - \Delta_1}{2L_g}\left(\tan\theta + \frac{1}{\tan\theta}\right) - \frac{\delta_c}{h_b}$$

Where: δ_c is the difference in displacement between the top and bottom transverse potentiometers.

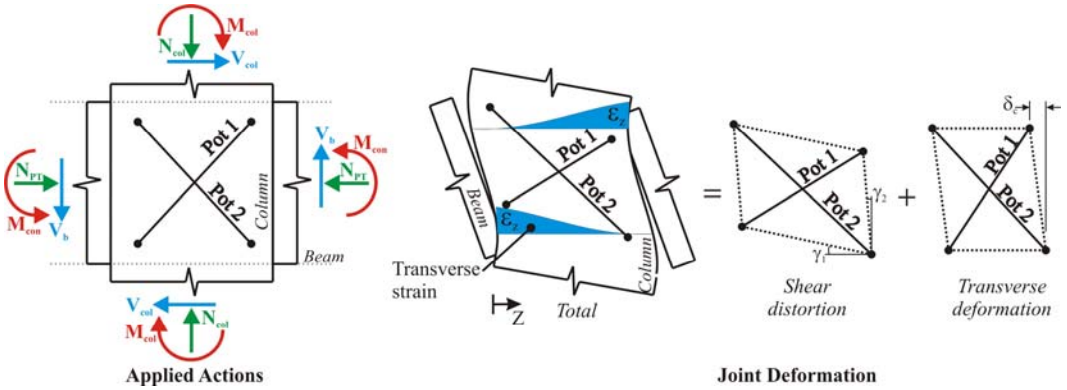

Figure D.2.2. The effect of transverse strain on the measure joint panel deformation

To-date no experimental tests have adequately taken into account the interaction of shear and transversal deformation, and hence, placed potentiometers away for the compression regions. Therefore, the comparison of the FEM and the analytical model is likely to be the most robust for now.

Persevering with experimental data, an approximate evaluation of the accuracy of the analytical model can be made by considering external and internal beam-column subassembly tests (Cusiel 2010; Green 2010; Iqbal et al. 2010). Experimental data from the test building, as discussed in Chapter 5, is not as reliable due to the approximate means of calculating the connection moments (using strain gauges). A summary of the subassembly tests considered is given in Table D.2.1 and Figure D.2.3. In Table D.2.1, the area of beam, A_b, the force in the post-tensioning tendons, T_{pt}, and the initial stress applied the column, f_i, is also given.

The experimental data from the subassembly tests is compared with analytical predictions in Figure D.2.4. For the predictions, as shear modulus of 660MPa is assumed. For subassembly 1 (Sub 1) from Green (2010), two pair of diagonal potentiometers are used to measure the joint panel deformation (see Figure D.2.3a).

This arrangement effectively reduces the contribution of transverse deformation to the shear distortion, by average the joint distortion between the two diagonal pairs of potentiometers. Because the perpendicular-to-grain stresses are relatively low for Test 1A and 3 (see Table D.2.1), the transverse deformation is further reduced. Consequently, the predictions match relatively well with the experimental data, as shown in Figure D.2.4a and b.

For Sub 2 (Cusiel et al. 2010), the predicted panel stiffness is significantly higher than indicated by experimental data. This is expected due to the proximity of the diagonal potentiometers to large transverse deformations. Furthermore, inelastic deformation is apparent in Figure D.2.4c, associated with the transverse deformations, which are actually linked to the rocking connection response. Therefore, contrary to recent research (Cusiel et al. 2010), the joint panel deformation should not provide any additional damping to the frame system and should be considered as part of the rocking connection response.

For Sub 3 (Iqbal et al. 2010), top and bottom potentiometers were present in the joint panel region (see Figure D.2.4c and d). This meant that the joint deformation could be approximately decoupled into transversal and shear distortion, as shown in Figure D.2.4d. The resultant joint deformation, γ, matches well with the analytical prediction. While there appears to be some hysteresis with the pure shear distortion, it is likely that this is due to inconsistent zero positions for the horizontal and diagonal potentiometers.

Table D.2.1 – Summary of the subassembly test considered for joint response

Sub.	Test	Description	A_b (mm^2)	T_{pt} (kN)	f_i (MPa)
1	Test 1A	External - No armouring	72000	62	0.9
	Test 3	External - No armouring	72000	186	2.6
2	Test 1	Internal - No armouring	55800	240	4.4
3	Test 3	External - Armoured	223000	870	3.9

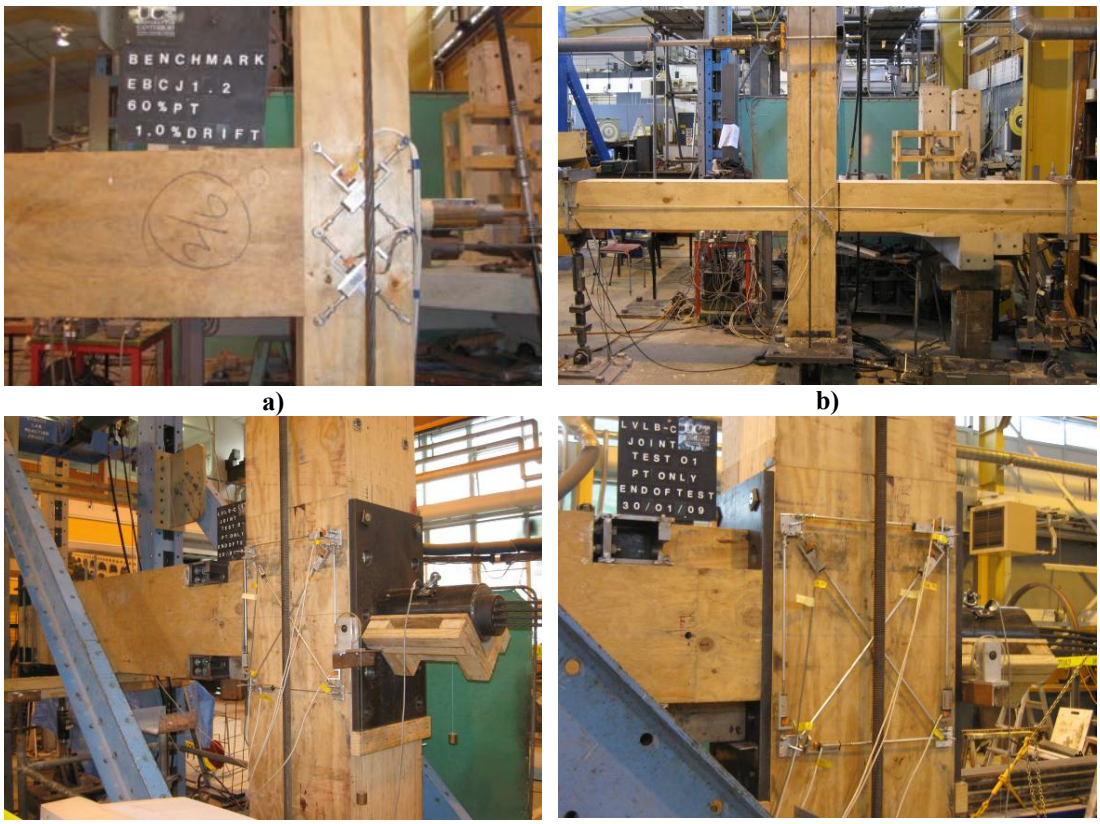

a) **b)**

c) **d)**

Figure D.2.3. Subassembly tests considered for joint panel moment-rotation response: a) Sub 1 (Green 2010) b) Sub 2 (Cusiel et al. 2010) c) and d) Sub 3 (Iqbal et al. 2010)

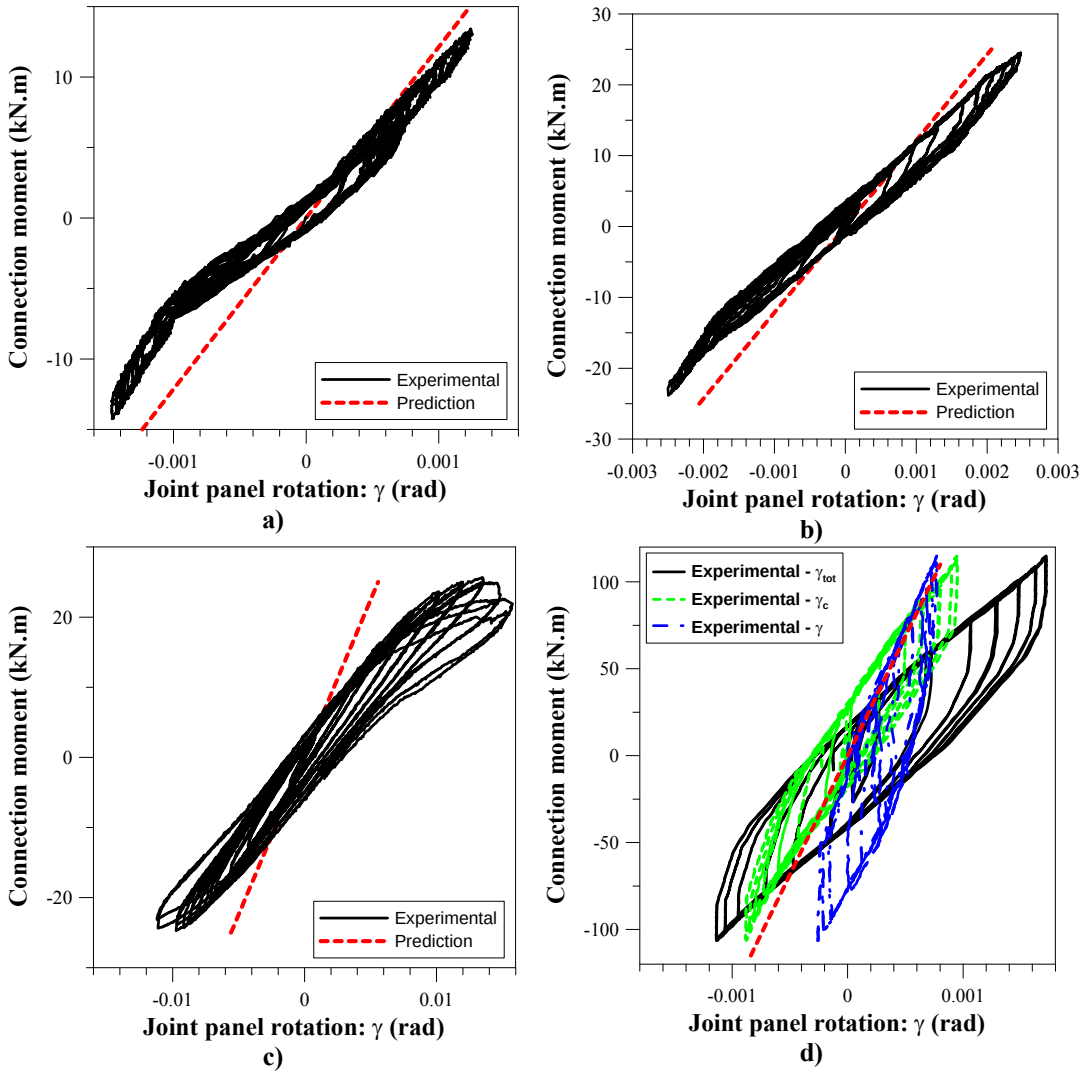

Figure D.2.4. Experimental and predicted joint response for subassembly tests: a) Sub 1 - Test 1 b) Sub 1 - Test 3 c) Sub 2 - Test 1 d) Sub 3 - Test 3

D.3. CALIBRATION OF THE PASTERNAK MODEL

The Pasternak Model, as applied to timber by Tanahashi *et al* (2006), is proposed for defining the connection response of non-armoured post-tensioned timber frames (see Chapter 6). The Pasternak Model accounts for shear deformation of the column adjacent to beam-column interface (see Figure D.3.1), termed henceforth as 'edge-effect'. To do this, the parameter, α, must be calibrated for the specific material properties of the timber. The parameter α is related to Φ and, in turn, η.

The parameters η and Φ, define the strain profile into the column depth, as shown in Figure D.3.1. A two-dimensional finite element model is created in SAP 2000 (2005) to determine η and Φ for Laminated Veneer Lumber (LVL), with the same material properties as shown in Table D.1.1. A sensitivity study of the FEM models is performed and the results are summarized in Table D.3.1.

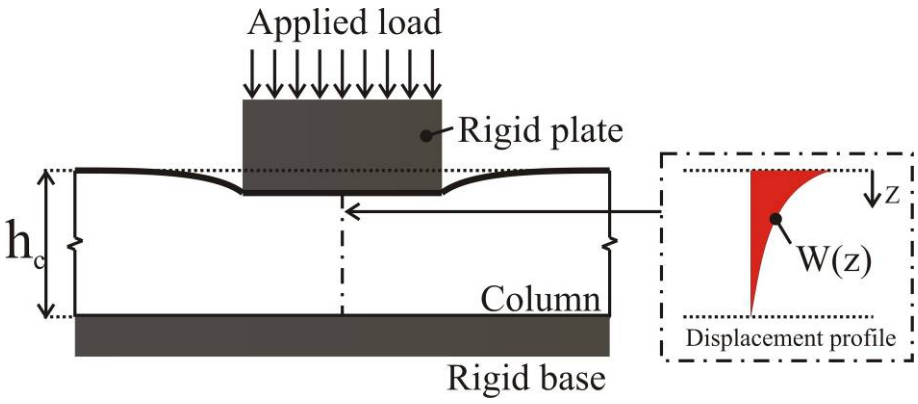

Figure D.3.1. Calibrated parameters for Pasternak Model

To determine η and Φ, the displacement profile for the Pasternak model is calibrated to the displacement profile from the FEM. From Tanahashi *et al* (2006), the displacement profile is:

$$W(z) = W_0 \frac{\sinh\left(\eta\left(1-\frac{z}{h_c}\right)\right)}{\sinh\eta}$$

Where: W_0 is the surface displacement.

And:

$$\Phi = \eta\sqrt{\frac{\sinh\eta\cosh\eta+\eta}{\sinh\eta\cosh\eta-\eta}}$$

The shape of the displacement profile, outside the compression region is related to the parameter, Φ, according to the equation:

$$\alpha = \sqrt{\frac{E_{perp}}{(1-\nu_{LT}\nu_{TL})G}}\frac{\Phi}{h_c}$$

Where: ν_{LT} and ν_{TL} are the Poissons Ratios in the longitudinal and transversal directions;
G is the shear modulus (in the longitudinal and transverse directions).

For this study the poisons ratios, ν_{LT} and ν_{TL}, are assumed to be 0.3, based on research performed on Radiata Pine by Murray (2007).

D.3.1. Results of the sensitivity study

The sensitivity study is performed by creating a benchmark model and modifying one parameter at a time within realistic bounds. The material properties of the timber were assumed to remain fixed. Hence, this study is only applicable to Laminated Veneer Lumber, with the properties given in Table D.1.1. In this section, key results from the sensitivity study are provided.

FEM 1 (Benchmark)

The deformed shape of the model is illustrated in Figure D.3.2a. The displacement profile at the centreline of the FEM and the calibrated Pasternak Model representation is shown in Figure D.3.2b.

FEM 2

The support conditions were altered from FEM 1. Instead of a rigid supports on the left hand side of the column, supports were provided at the top and bottom of the column, as shown in Figure D.3.3a. This resulted in a different displacement profile (see Figure D.3.3b), that could not be accurately represented by the Pasternak Model. Therefore, the interaction of longitudinal bending stresses result in an altered displacement profile in the transverse direction. This is not considered by Tanahashi *et al* (2006). Possibly, because the bending stresses are equal and opposite above and below the centreline of the beam, the support conditions of the benchmark model are appropriate for calibration of the Pasternak Model. Further research is required.

FEM 3

In this model, the compression area is halved. This altered the displacement profile slightly, as shown in Figure D.3.4.

FEM 4

In this model, the column depth is halved. The displacement profile is almost linear. Hence, the model is tending towards a state of full compression and the displacement profile in the centre is essentially unaffected by the diffusion of stresses above and below the compression region.

FEM 5

In this model, the column depth is doubled. The displacement profile is similar to FEM 3.

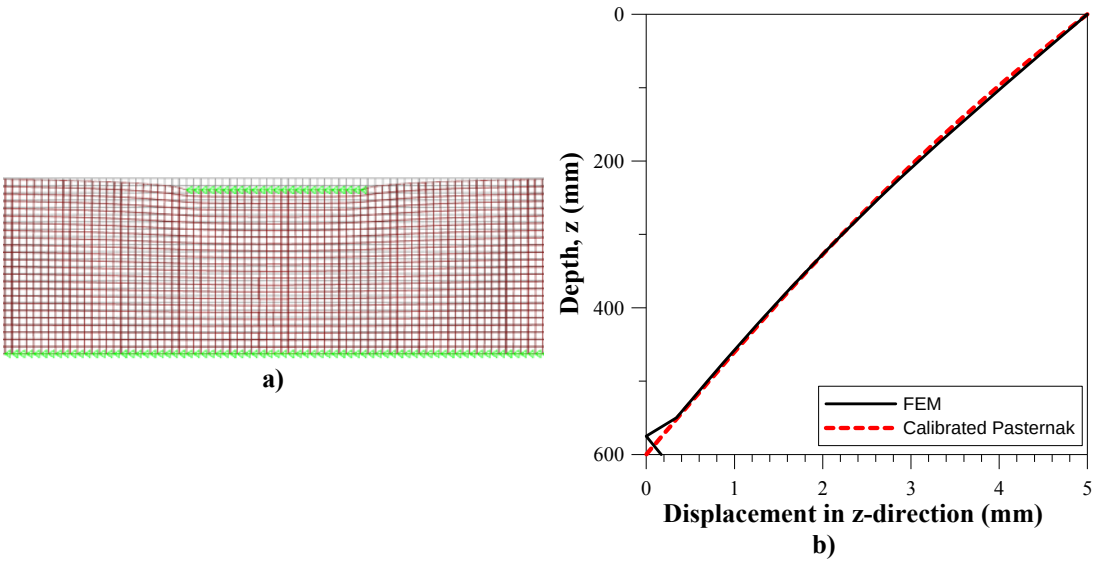

Figure D.3.2. Deformation of benchmark model: a) FEM b) The calibrated Pasternak Model and FEM displacement profile

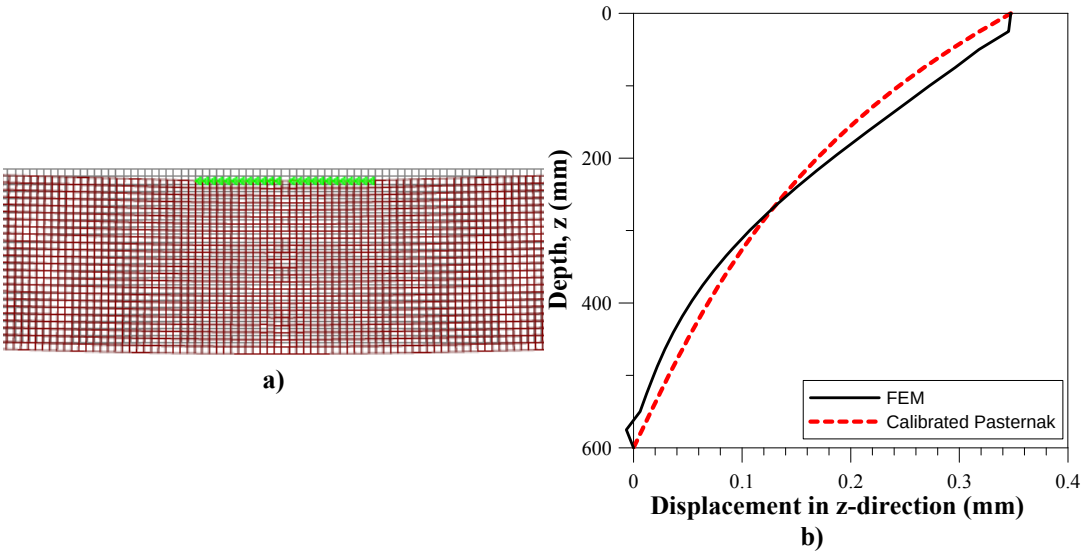

Figure D.3.3. Deformation of FEM 2: a) FEM b) The calibrated Pasternak Model and FEM displacement profile

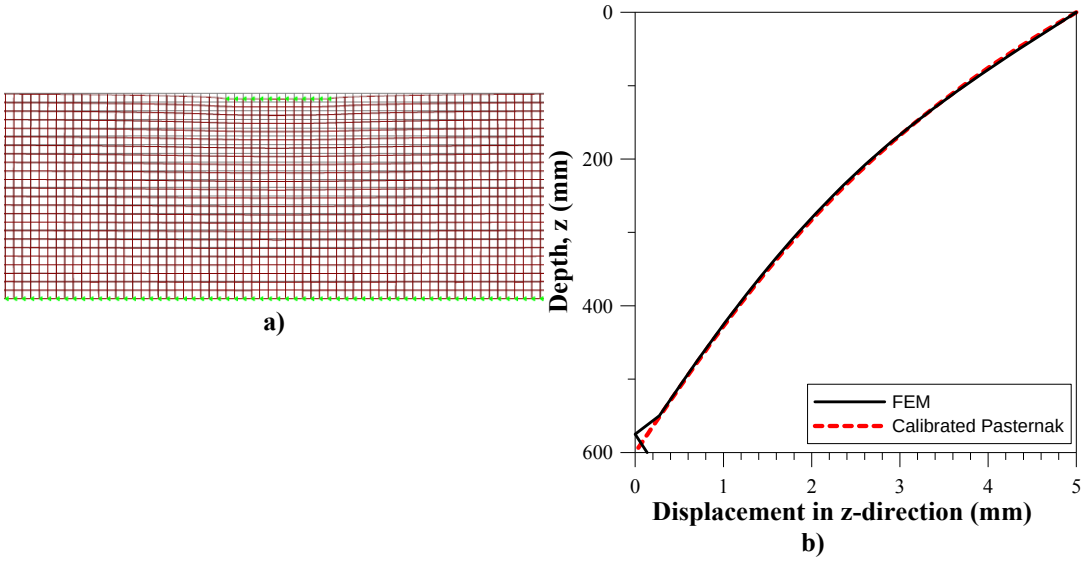

Figure D.3.4. Deformation of FEM 3: a) FEM b) The calibrated Pasternak Model and FEM displacement profile

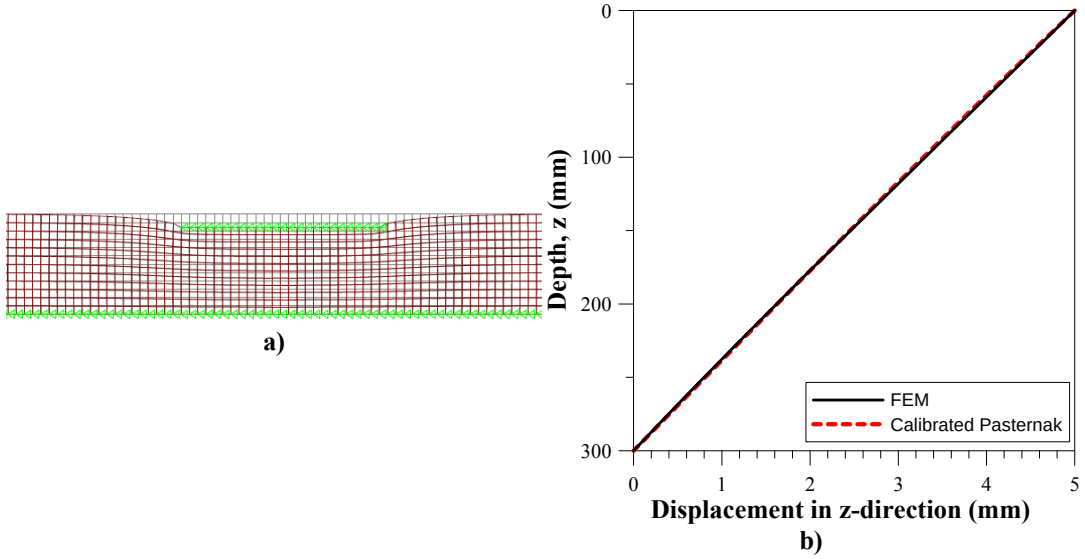

Figure D.3.5. Deformation of FEM 4: a) FEM b) The calibrated Pasternak Model and FEM displacement profile

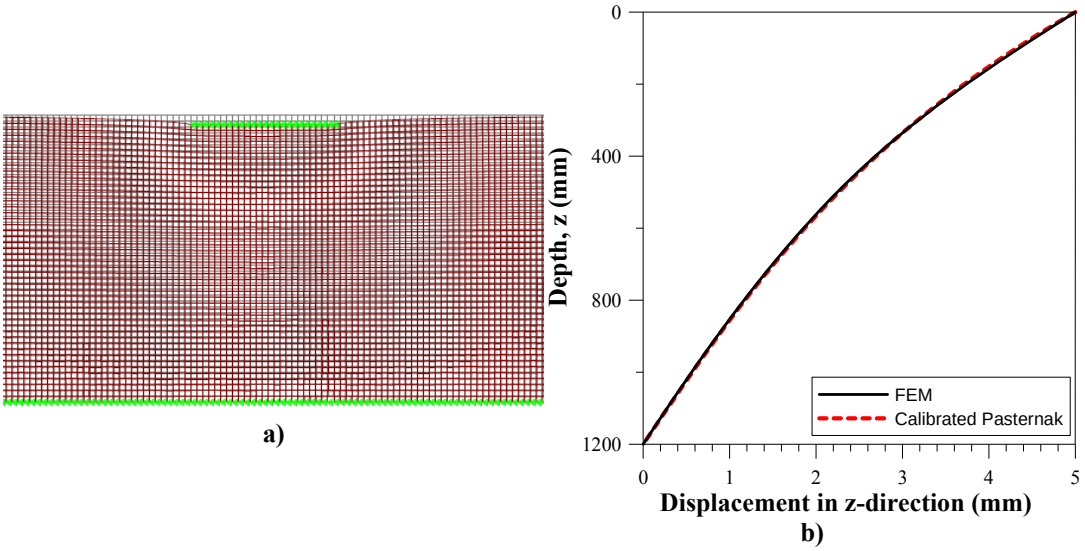

Figure D.3.6. Deformation of FEM 5: a) FEM b) The calibrated Pasternak Model and FEM displacement profile

D.3.2. Summary of the sensitivity study

The results of the sensitivity study are shown below. Firstly, it is evident that the aspect ratio of the column depth to the length of the compression area affects the parameter, η and Φ. For a rocking connection, the depth of the compression region will change as the connection rotation increases, but the depth of the column is constant. To minimise variation of Φ, a constant ratio of $\alpha \cdot h_c$ of 2.0 is considered. The implication of choice on the moment-rotation response is examined in Chapter 6.

Table D.3.1 – Summary calibrated values for the Pasternak Model

FEM Model	Change from benchmark	η	Φ	α	$\alpha \cdot h_c$
1	Benchmark	1.0	1.86	0.0034	2.04
2	Altered support conditions	2.0	2.32	0.0043	2.55
3	Halved compression area	1.6	2.09	0.0038	2.30
4	Halved column depth	0.4	1.75	0.0064	1.92
5	Double column depth	1.6	2.09	0.0019	2.30

D.4. BEAM-COLUMN CONNECTION RESPONSE USING FEM

Here the accuracy of analytical relationships, derived in Chapter 6, for modeling non-armoured PT beam-column connections are evaluated. Firstly, the proposed relationship between the neutral axis depth, c, and the imposed connection rotation, θ_{imp}, is considered. This expression is repeated below:

$$\theta_{imp} = \frac{T_{pt} h_c}{E_{perp} b_b \left(c^2 + \frac{2c}{\alpha} \right)}$$

Where: T_{pt} is the force applied by the post-tensioning;
α defines the displacement profile on the column face (see Chapter 6);

Secondly, the stresses distribution applied to the column face are investigated. It is proposed that the peak stress applied to the column is approximately:

$$f_t = \frac{2T_{pt}}{cb_b}$$

Analytical expressions are compared with the results of sensitivity study using finite element models created in SAP 2000 (2005). This model is an extension of the column model from section D.1 and includes beam elements, as shown in Figure D.4.1. The sensitivity study considers variation in several parameters, to ensure a robust evaluation of the accuracy of the analytical connection rotation versus neutral axis depth (θ_{imp}-c) predictions and peak stresses. This study is limited to the elastic response of the timber within the beam-column connections.

D.4.1. The finite element model

Again, a benchmark beam-column subassembly model was specified, and key parameters were altered to determine their effect on the accuracy of the θ_{imp}-c predictions and the peak stresses. The material properties and dimensions for the benchmark model were similar to the column model in section D.1, given in Table

D.1.1. The beam and the column have identical material properties and section size, but the beam was orientated at 90 degrees to the column. The bay length was 6 meters.

The boundary conditions consist of a pin support at the bottom of the column and vertical restraint at the end of the beams. Lateral loads are applied to the top of the column, which create a known connection moment. Axial loads, of 1020kN for the benchmark model, are applied to the end of the beams to simulate the compression provided by the post-tensioning.

To simulate the rocking beam-column connection, any shell elements in tension at the connection interface were deleted, as shown in Figure D.4.1. This was an iterative process, which required shell elements to be deleted or added until the transverse stress at the edge of the neutral axis was approximately zero. The fineness of the mesh was enhanced around the beam-column interface to improve the accuracy of the model and to avoid instability due to the interaction of shell elements which represent the parallel and perpendicular-to-grain timber.

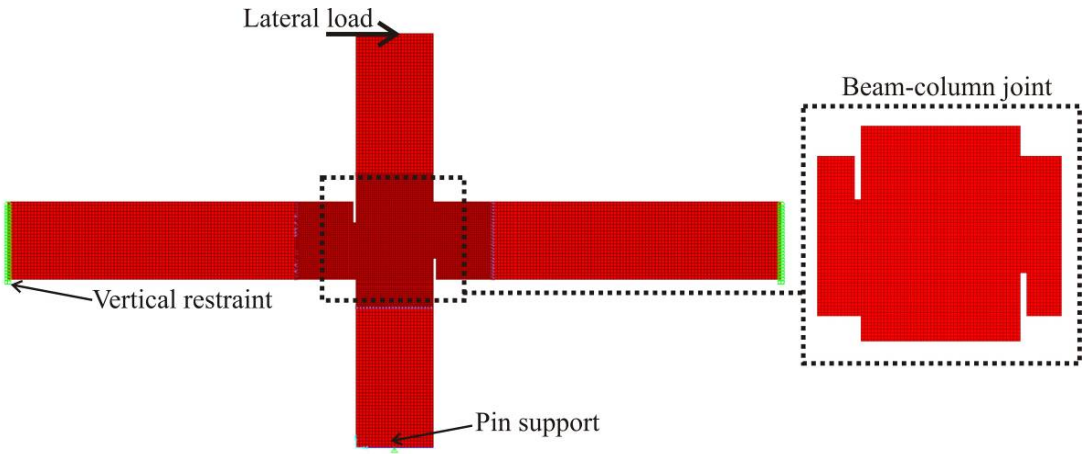

Figure D.4.1. Boundary conditions and applied loads for the benchmark FEM of the beam-column subassembly

D.4.2. Comparison of the model and the analytical equations

To evaluate the accuracy of the analytical θ_{imp}-c relationship, the results from the FEM must be interpreted accurately. The neutral axis depth can be readily interpreted by observing the transverse stresses, but the imposed connection rotation is more problematic. This is because the joint panel deformation and the connection deformation are difficult to decouple in the FEM.

One approach (Approach 1) is to deduce the connection rotation by subtracted the member deformation from the total deformation, Δ_{tot}, of the subassembly (measured at the top of the column). It was shown in section D.1 that the member deformation could be predicted with sufficient accuracy using analytical equations (from Chapter 6).

Hence:

$$\theta_{con} = \frac{\Delta_{tot}}{H} - \left(\theta_b + \theta_c + \theta_j\right)$$

And:

$$\theta_{imp} = \frac{\theta_{con}}{\left(1 - \frac{h_c}{L_b}\right)}$$

Furthermore, using this approach evaluates the accuracy of the overall analytical frame modeling procedure, because it incorporates the member and connection deformations.

An alternative approach (Approach 2) is to determine the imposed rotation by taking the difference between average rotation of the column centerline and the rotation of the column surface under compression (see Figure D.4.2). This approach becomes less accurate as the neutral axis depth becomes smaller. When the neutral axis depth is small, the displacement profile on the surface of the column is affected by shear distortion of the joint panel and the axial deformation of the beam.

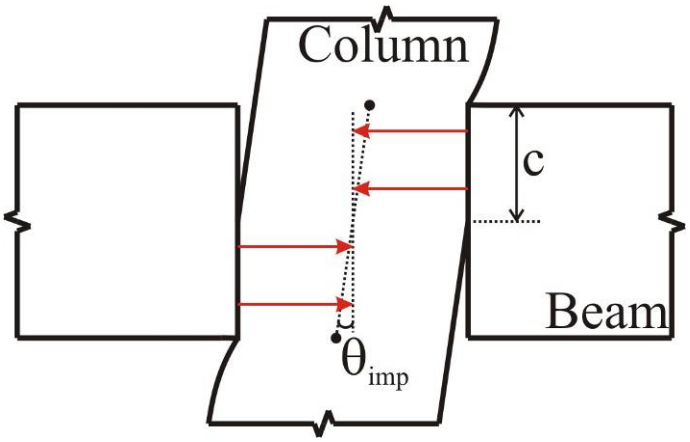

Figure D.4.2. Interpretation of the connection rotation from the FEM

Both approaches are considered to evaluate the imposed rotation from the FEM analyses.

The stresses applied to the column face in the FEM analyses were determined by recording the element joint forces. To avoid numerical instabilities created by the interaction of parallel and perpendicular-to-grain elements, the joint forces were recorded at 12.5mm into the column.

D.4.3. Results from the sensitivity study

The sensitivity study considered many parametric variations. Hence, only key results are presented. A summary of the study is given in Table D.4.1.

Benchmark response

The benchmark response for a connection moment of 150kN.m is shown below in terms of deformation, horizontal stresses, vertical stresses and shear stresses. The displacement profile of the column-face appears to correspond well with that assumed by the Pasternak Model (see Figure D.4.3). Furthermore, the diffusion of transverse stresses is shown in Figure D.4.4.

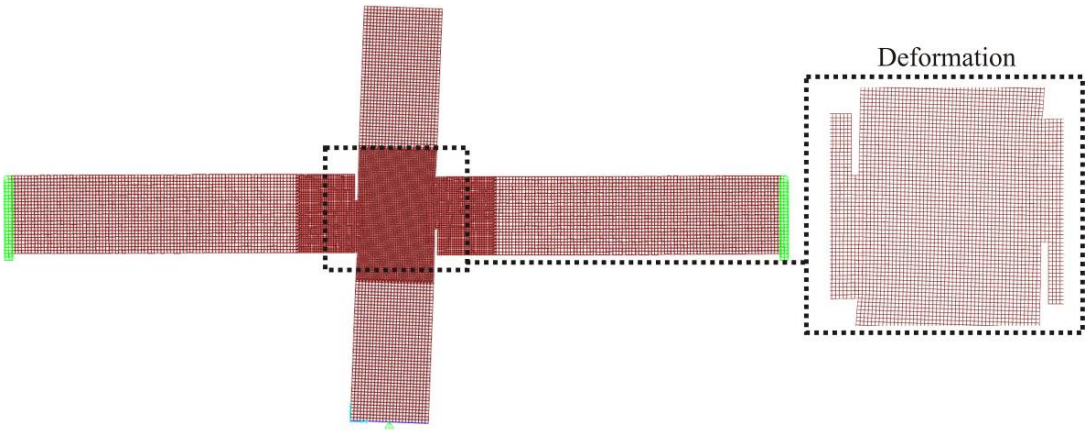

Figure D.4.3. Results of benchmark FEM: Deformed shape

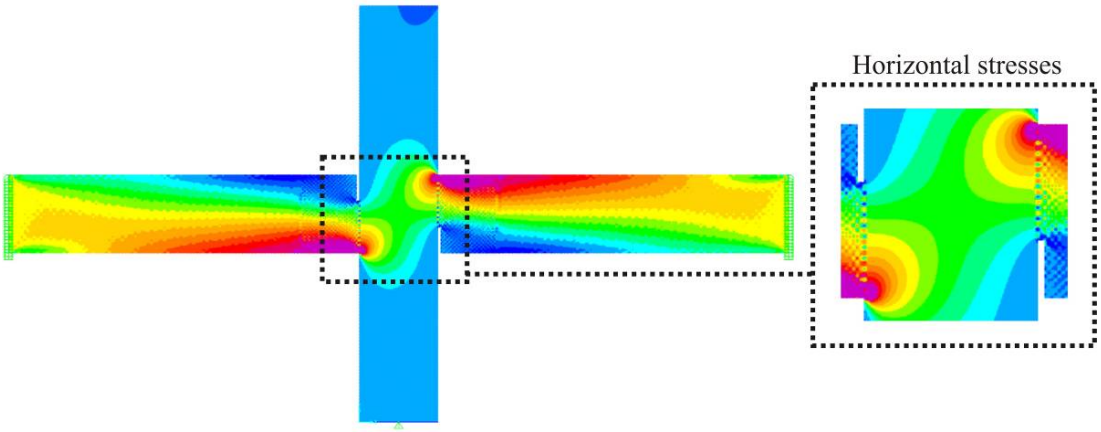

a)

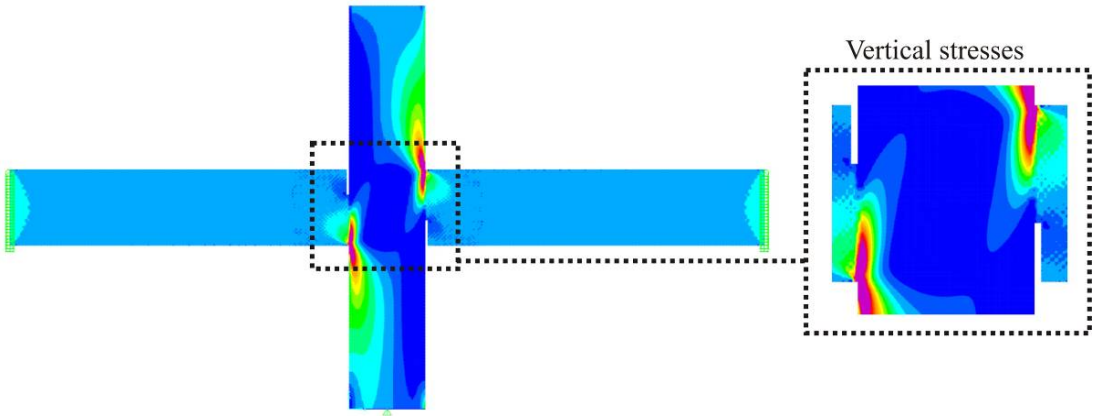

b)

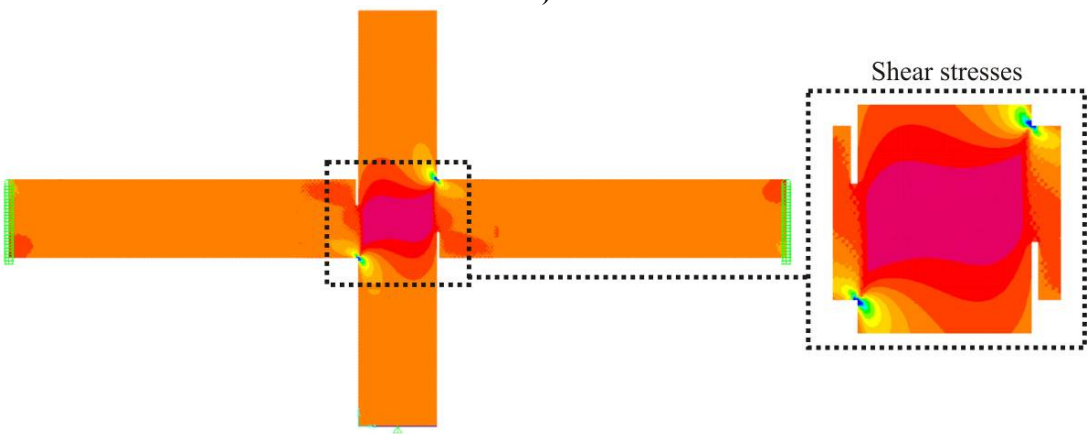

c)

Figure D.4.4. Results of benchmark FEM: a) Horizontal stresses b) Vertical stresses c) Shear stresses

The θ_{imp}-c relationship

Three models were subjected to several different moment demands; model 1, 2 and 3 from Table D.4.1. This enabled the relationship between the neutral axis depth and the imposed connection rotation to be established for each of these models, as shown in Figure D.4.5. The θ_{imp}-c equation appears to give a slightly larger neutral axis depth for a give rotation, and therefore, is conservative when predicting the moment provided by the connections.

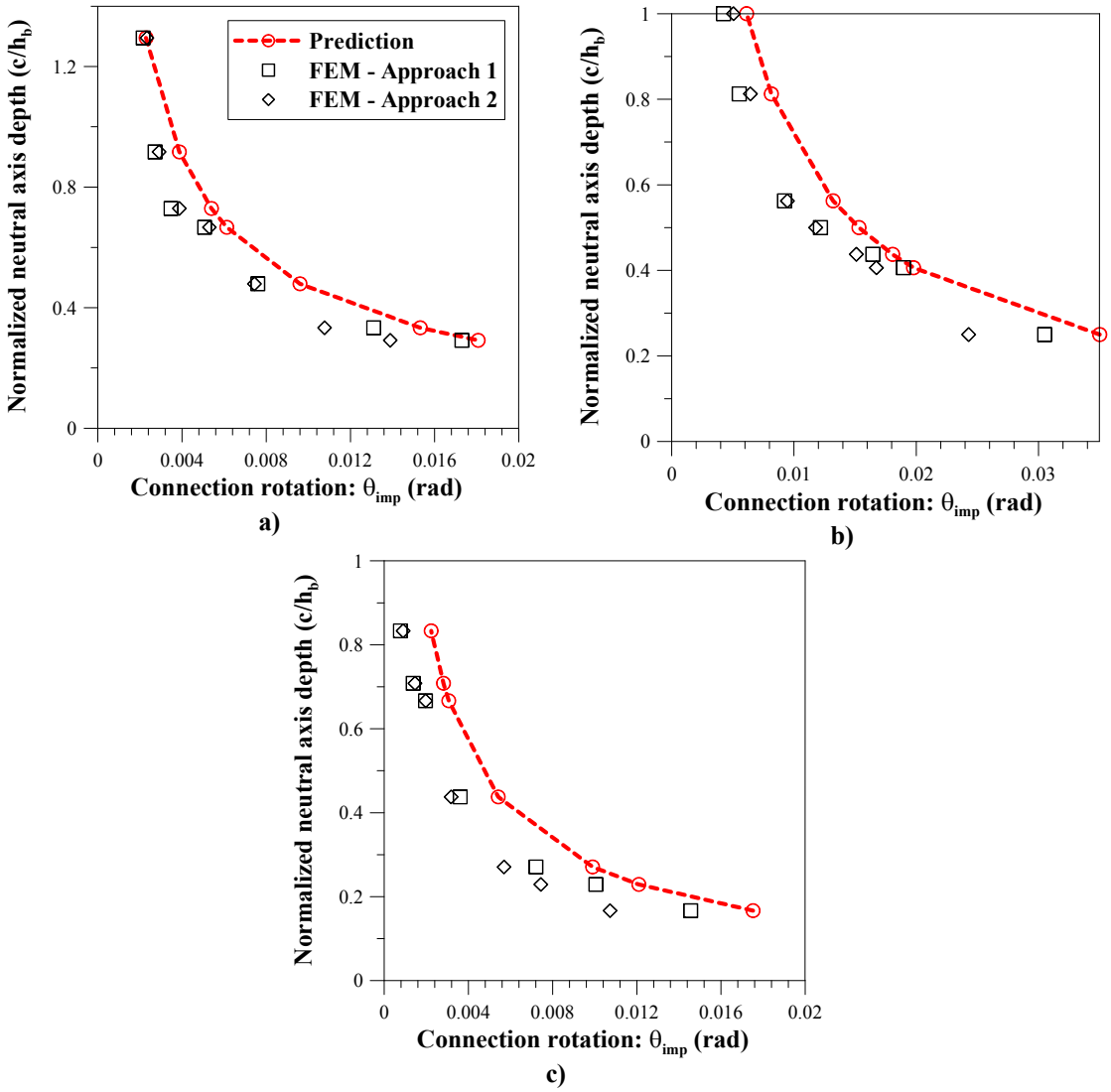

Figure D.4.5. Normalized neutral axis depth versus connection rotation: a) FEM 1 b) FEM 2 and c) FEM 3

The accuracy of the analytical θ_{imp}-c relationship was evaluated for different transverse (or perpendicular-to-grain) elastic moduli in the column. It was determined that there were significant discrepancies when the transverse elastic modulus increased and tended to the parallel-to-grain elastic modulus. This is because the assumed surface displacement profile, from the Pasternak Model, is not appropriate for high transverse elastic moduli.

The column deformation, magnified by ten, is shown in Figure D.4.6 for four different transverse moduli. It can be observed that there is a less shear distortion adjacent to compression edge of the beam (or edge-effect) as the transverse elastic modulus increases. Or more specifically, α (as defined in Chapter 6), appears to be larger. Furthermore, Figure D.4.7 shows that there is less diffusion of the transverse stresses as the elastic modulus increases.

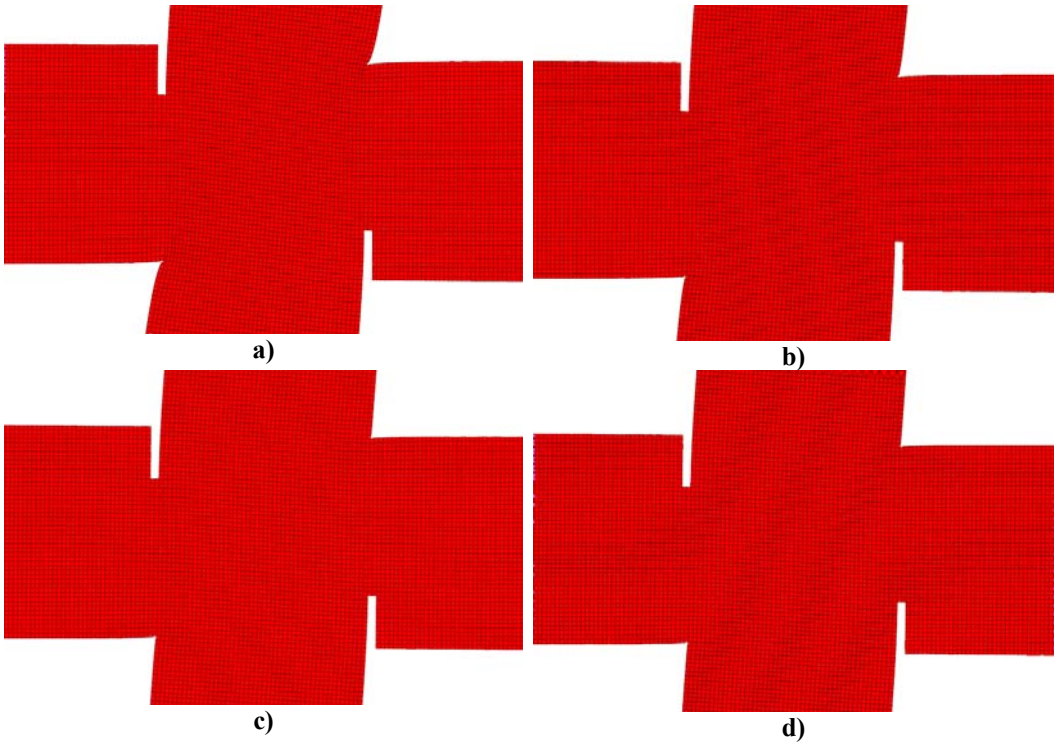

Figure D.4.6. Connection deformation for different transverse elastic moduli (E_{perp}): a) 400 MPa b) 1320 MPa c) 8000 MPa d) 13200 MPa

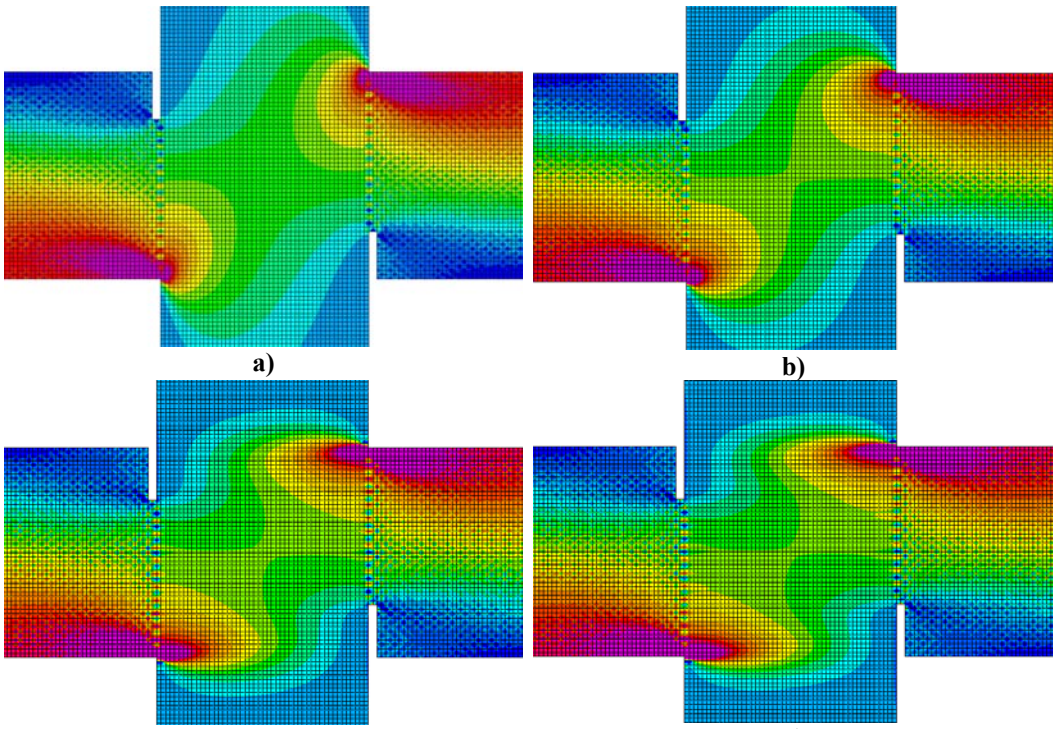

Figure D.4.7. Transverse stresses for different transverse elastic moduli (E_{perp}): a) 400 MPa b) 1320 MPa c) 8000 MPa d) 13200 MPa

Therefore, it is proposed that the edge-effect, accounted for in the Pasternak Model, can be ignored if the transverse timber in the column is aligned parallel-to-grain. Therefore:

$$\theta_{imp} = \frac{T_{pt} h_c}{E_{perp} b_b c^2}$$

However, when the transverse elastic modulus in the column tends toward the parallel-to-grain elastic modulus in the beam, it is no longer reasonable to assume the beam is effectively rigid compared to the column, as assumed in Chapter 6 for the Pasternak Model. The contribution of the beam to the flexibility of the connection is difficult to accurately define or interpret from FEM. The flexibility is derived from the compressive strains at the beam end, which are in excess of longitudinal strains due to flexure. Therefore, several different FEM analyses are run with a parallel-to-grain (13200MPa) transverse elastic modulus to calibrate the appropriate axial stiffness of the connection. The θ_{imp}-c relationship is shown in Figure D.4.8 (and compared with the

benchmark model). For the θ_{imp}-c prediction, it is tentatively proposed that the axial stiffness of the beam should be one third of the axial stiffness of the column, and hence:

$$\theta_{imp} = \frac{3}{2}\frac{T_{pt}h_c}{E_{perp}b_b c^2}$$

From Figure D.4.8, it is noted that there are larger discrepancies between Approach 1 and 2 for calculation of imposed rotation from the FEM. This is because the beam-end and column-face have a similar axial stiffness. Deformation of the beam end adds to the imposed rotation, but is not accounted for by Approach 2. Furthermore, the deformations of the beam end are non-linear, further complicating the computation of the imposed rotation. Hence, Approach 1 is considered more robust for these analyses.

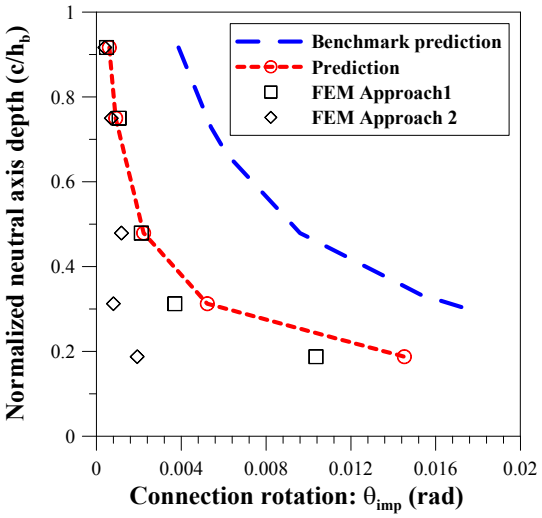

Figure D.4.8. Normalized neutral axis depth versus connection rotation: FEM 4

The addition of a steel plate to the column face effectively increases edge-effects, distributing deformation further outside the beam-column connection. This is shown in Figure D.4.9, by analyzing the column section with uniform transverse displacement at the beam position, as done in section D.3. Similar observations are made for the beam-column FEM model in Figure D.4.10. The increased edge-effect is also evident when observing the transverse stresses in the column, which are distributed further above and below the connection (see Figure D.4.11). This results in significantly reduced perpendicular-to-grain stresses.

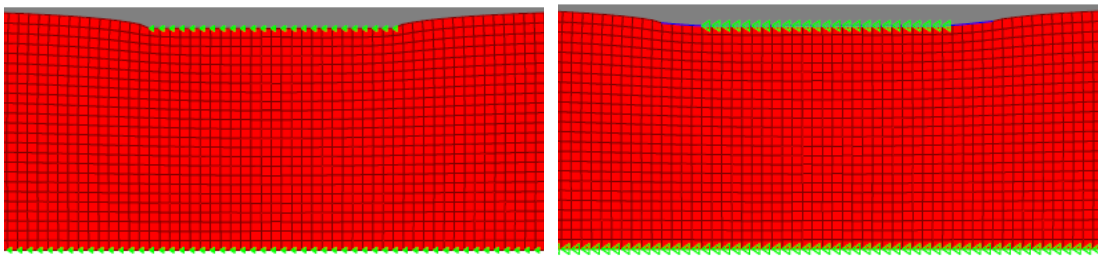

a) **b)**

Figure D.4.9. Displacement profile for the Pasternak Model with a steel armouring plate: a) Benchmark b) With a 30mm steel plate

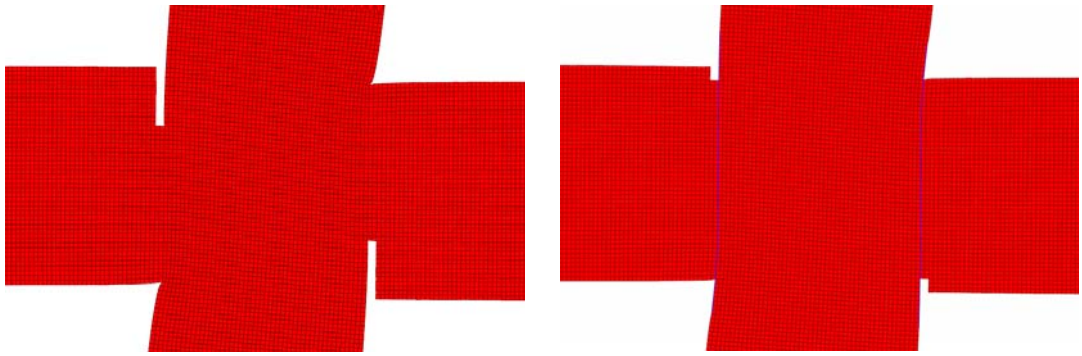

a) **b)**

Figure D.4.10. Connection deformation (magnified by 10) with a steel armouring plate: a) Benchmark b) With a 30mm steel plate

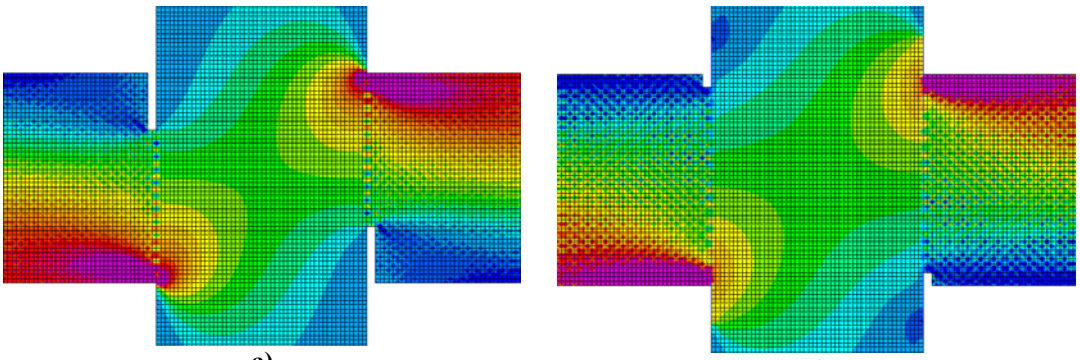

a) b)

Figure D.4.11. Transverse stresses with a steel armouring plate: a) Benchmark b) With a 30mm steel plate

To adequately account for steel plate armoring using the Pasternak Model, the displacement profile at the surface of the column needs to be defined. This will depend on the thickness of the steel plate and the distance that the plate extrudes outside of the beam column connection. An example of how the displacement profile may look is given in Figure D.4.13. A conservative design approach is to ignore the presence of the steel plate, for the calculation of the θ_{imp}-c relationship. The consequence of this assumption is examined in Figure D.4.12, for a 30mm thick plate with 100mm extrusion at the top and bottom of the beam (FEM 16). In Figure D.4.12, the benchmark prediction ignores the presence of the plate. It is apparent that the imposed rotation is significantly over-predicted for a given neutral axis depth.

Again, it is noted that Approach 2, for determination of the imposed rotation, is inaccurate due to deformation at the end of the beam. Furthermore, the accuracy of Approach 1 may be affected by the addition of the steel plates in the FEM. In the model, the steel plates are fully connected to the column and will contribute to the flexural and shear stiffness of the column. This will decrease column deformation and result in an underestimation of the imposed connection rotation using Approach 1. In reality, the steel plates are able to slide on the column face and can detach from the column surface. Hence, further analysis is required to characterize the θ_{imp}-c relationship with steel plate armouring.

If the plate is designed to be effectively rigid, the displacement profile in the column can be readily defined, as shown in Figure D.4.13. Following the same procedure from Chapter 6, the θ_{imp}-c relationship can be re-defined as:

$$\theta_{imp} = \frac{T_{pt} h_c}{E_{perp} b_b (c + e_p)\left((c + e_p) + \frac{2}{\alpha}\right)}$$

Where: e_p is distance that the plate extrudes outside of the beam-column connection.

The above θ_{imp}-c relationship is compared with the results of FEM 16 in Figure D.4.12. The accuracy of the prediction appears to have improved significantly, but remains conservative due to the inaccuracies of calculating the imposed rotation from the FEM.

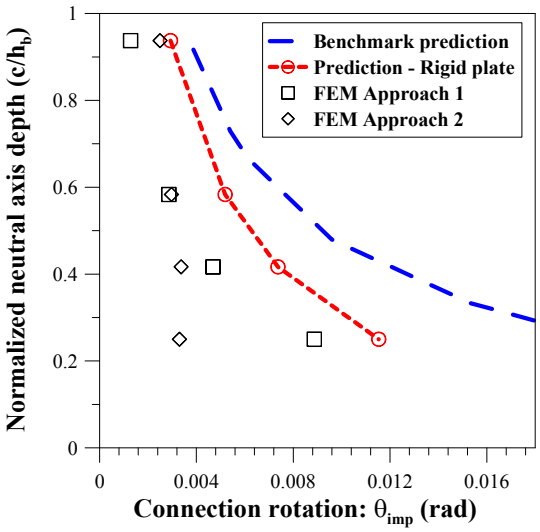

Figure D.4.12. Normalized neutral axis depth versus connection rotation with steel armouring plates (FEM 16)

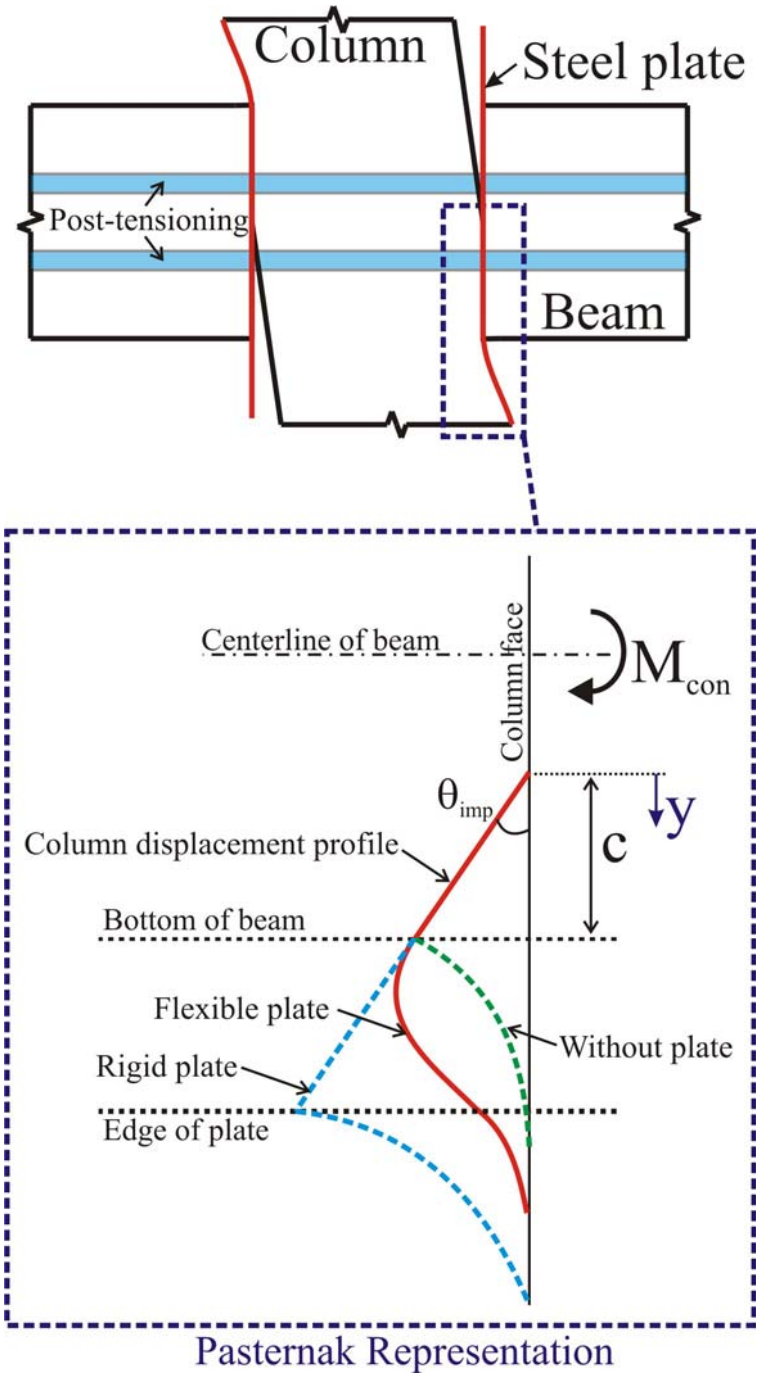

Figure D.4.13. Displacement profile of column face with steel armouring

Three FEM analyses (FEM 17) investigated whether the θ_{imp}-c relationship varied for an external beam-column connection. One of the beams from the benchmark model was removed. A tendon anchorage was represented using a 30mm thick steel plate on the face of the column, as shown in Figure D.4.14a.

The predicted θ_{imp}-c relationship, which is identical to the benchmark subassembly, matched well with the FEM analysis results (see Figure D.4.14b). It is noted that Approach 1 for interpreting the FEM results is less accurate for an external beam-column subassembly. This is because the deformation at the top of the column, due to joint panel deformation cannot be accurately defined. However, for Type 1 (unarmoured) connections, the FEM results for the benchmark model according to Approach 1 and 2 are similar. Therefore, it can be inferred that Approach 2 is fairly accurate for the external subassembly. Furthermore, the computed joint panel deformation is relatively small.

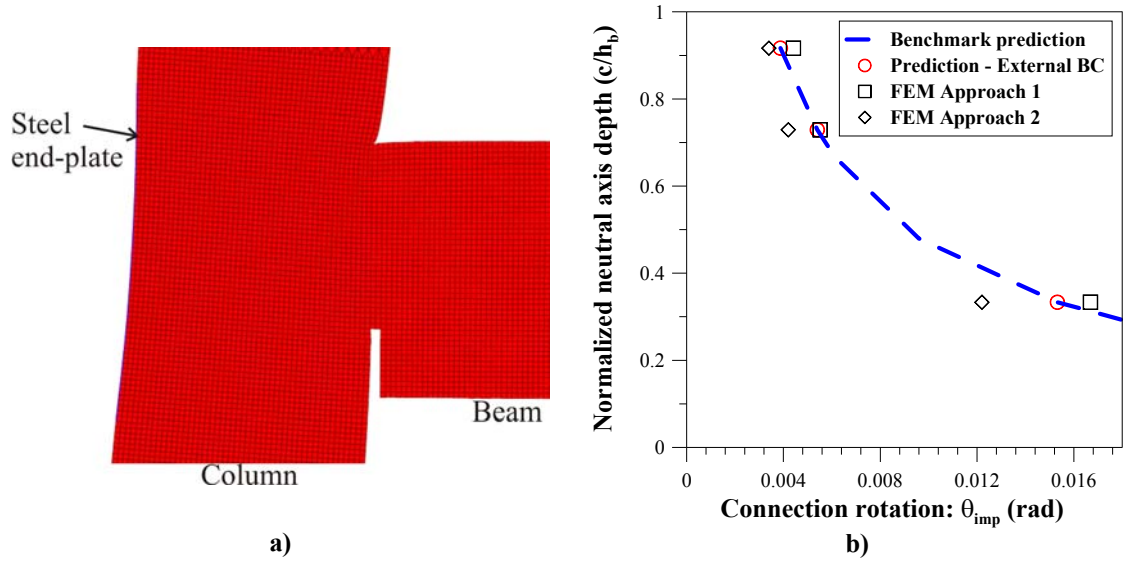

Figure D.4.14. External beam-column connection: a) Deformation (magnified by 10) with steel end plate b) Neutral axis depth

The modification of beam depth, post-tensioning force, column depth and shear modulus did not appear to affect the accuracy of the proposed θ_{imp}-c relationship. Perhaps the lack of sensitivity to the shear modulus is counter-intuitive. It would be expected that as the shear modulus increased that the diffusion of transverse stresses

into the column would be more significant. However, it is inferred that the perpendicular-to-grain elastic modulus is the most important parameter in defining the column displacement profile for the Pasternak Model. A more comprehensive sensitivity analysis is required in future research. These studies should focus more heavily on the connection response for armoured columns.

The applied stress distribution

As introduced in Chapter 6, the applied stress distribution at the column face is not equal to the average transverse stress distribution within the column. The Pasternak Model inherently assumes a shear resistant layer which distributes applies stress to the column, to satisfy a certain displacement profile. If the applied stress distribution were linear, the peak stress at the extreme fiber of the beam is:

$$f_t = \frac{y}{c}\frac{2T_{pt}}{cb_b}$$

Where: y is distance from the neutral axis position into the compression region.

The above expression is compared with the results of the FEM sensitivity study, as shown in Figure D.4.15. For the unarmoured connections (FEM 1, 2 and 3), the stress distribution appears to be non-linear. Hence, the peak stresses are higher than predicted toward the extreme compression fiber and lower than predicted towards the neutral axis position. This is likely to be result of interaction with the shear distortion of the joint panel region, which also has a non-linear deformed shape. However, the predictions still provide reasonable estimates of the peak stress. Furthermore, under cyclic loading the extreme compression fibers will yield, causing redistribution of stresses, which will result in a more linear stress profile. Finally as the timber strain increases, an elasto-plastic stress distribution may be appropriate. Also, the non-linearity of the stresses may have been exacerbated by inaccuracies in the FEM model. The finite elements on the extreme compression edge of the beam have half the stiffness of elements within the section, resulting in a reduction of peak stress at the extreme fiber (see Figure D.4.15).

For connections with parallel-to-grain timber running transversely through the column, there is no significant affect on the shape of the stress distribution, as shown in Figure D.4.15c for FEM 4. However, armouring will steel plates significantly reduces the non-linearity and magnitude of the applied stress. The steel plate is analogous to the shear layer used in the Pasternak Model, and distributes applied stresses throughout the column. If the steel plate is thick enough, the parallel-to-grain timber in the beam yields before the perpendicular-to-grain timber in the column. This was the case for FEM 16.

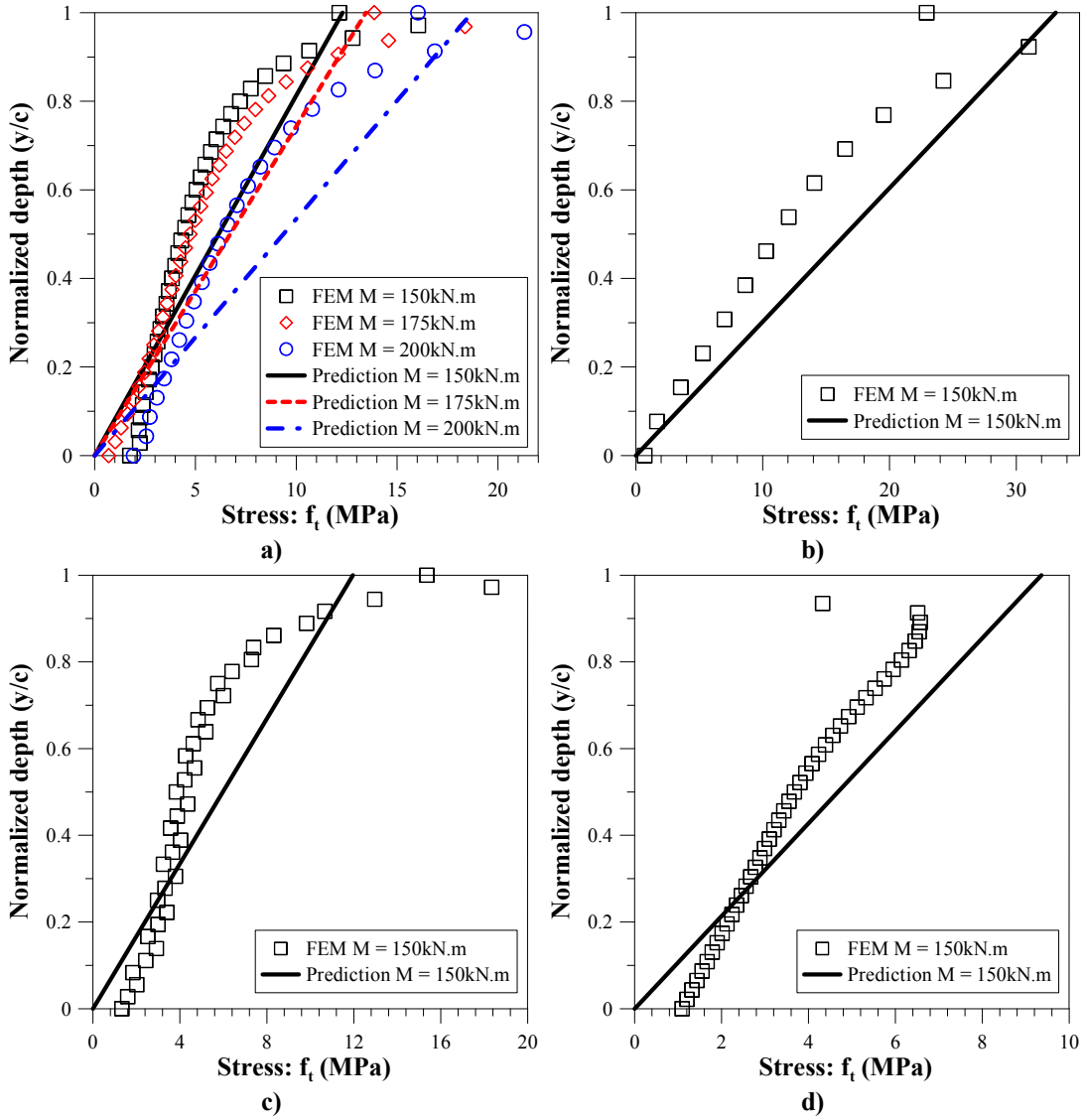

Figure D.4.15. Stresses applied to column face: a) Benchmark (FEM 1) b) FEM 2 c) FEM 4 d) FEM 16

Summary of the sensitivity study

The θ_{imp}-c relationship predicted by Pasternak Model is in good agreement with the FEM sensitivity study. Three analytical equations are used for the sensitivity study.

For traditional PT timber frames (where compression is applied to perpendicular-to-grain timber without armouring):

$$\theta_{imp} = \frac{T_{pt} h_c}{E_{perp} b_b \left(c^2 + \frac{2c}{\alpha} \right)}$$

If parallel-to-grain timber is aligned transversely within the column:

$$\theta_{imp} = \frac{3}{2} \frac{T_{pt} h_c}{E_{perp} b_b c^2}$$

If an effectively rigid steel plate is used to amour the column face:

$$\theta_{imp} = \frac{T_{pt} h_c}{E_{perp} b_b \left(c + e_p \right) \left(c + e_p + \frac{2}{\alpha} \right)}$$

The predicted imposed rotation from the above equations is compared with the results of the sensitivity study in Figure D.4.16.

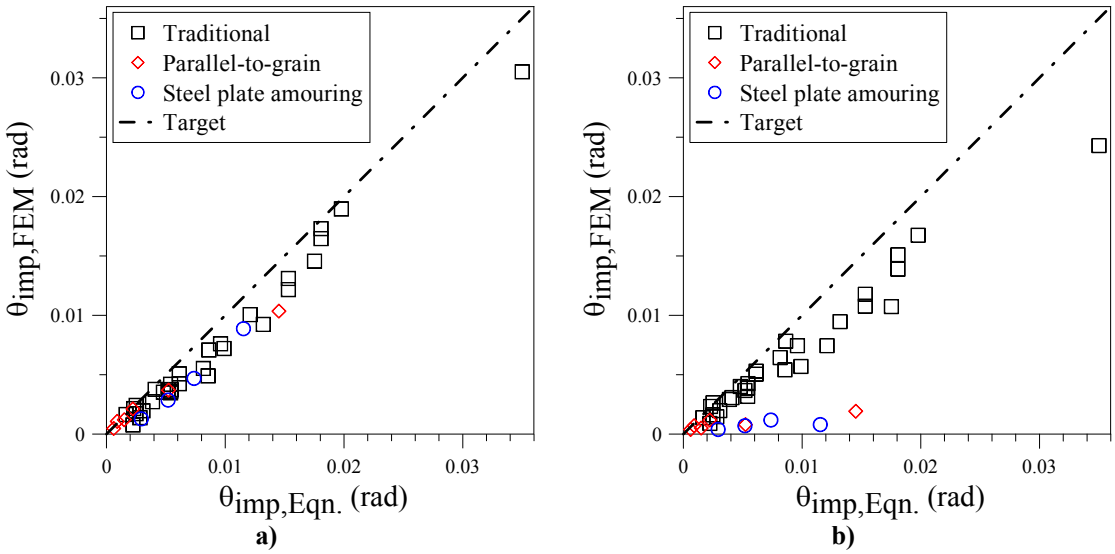

Figure D.4.16. Correlations between the predicted and FEM imposed connection rotation: a) Approach 1 b) Approach 2

The stresses applied to the column face are predicted reasonably accurately by the analytical expression, repeated below.

$$f_t = \frac{y}{c}\frac{2T_{pt}}{cb_b}$$

For timber-to-timber connections peak stresses at the extreme fiber are slightly underestimated. For connections with steel armouring the applied stresses are slightly underestimated.

Table D.4.1 – Summary beam-column FEM

FEM Model	Change from benchmark	M_{con} (kN.m)	c/h_b	θ_{imp}		
				FEM1*	**FEM2***	**Eqn.**
1	Benchmark	100	1.30	0.0021	0.0023	0.0023
		125	0.92	0.0027	0.0029	0.0039
		150	0.73	0.0035	0.0039	0.0054
		175	0.67	0.0051	0.0053	0.0061
		200	0.48	0.0076	0.0074	0.0096
		225	0.33	0.0131	0.0108	0.0153
		250	0.29	0.0173	0.0139	0.0181
2	Beam height reduced to 400mm.	160	0.25	0.0305	0.0243	0.0350
		145	0.41	0.0190	0.0167	0.0198
		135	0.44	0.0165	0.0151	0.0181
		125	0.50	0.0122	0.0118	0.0153
		100	0.56	0.0092	0.0095	0.0132
		80	0.81	0.0055	0.0064	0.0082
3	Half of the post-tensioning force.	125	1.00	0.0042	0.0051	0.0061
		120	0.17	0.0146	0.0107	0.0175
		115	0.23	0.0101	0.0074	0.0121
		100	0.27	0.0072	0.0057	0.0099
		80	0.44	0.0036	0.0032	0.0054
		70	0.67	0.0020	0.0020	0.0031
		50	0.71	0.0014	0.0015	0.0028
4	E_{perp} of the column 13200MPa (aligned parallel-to-grain).	100	0.83	0.0008	0.0009	0.0006
		150	0.92	0.0005	0.0004	0.0009
		200	0.75	0.0011	0.0007	0.0022
		225	0.48	0.0021	0.0012	0.0052
		250	0.31	0.0037	0.0008	0.0145
5	Beam height increased to 800mm.	150	0.19	0.0104	0.0019	0.0025
6	Col. height decreased to 400mm.	150	0.92	0.0017	0.0016	0.0041
7	Col. height increased to 1000mm.	150	0.77	0.0038	0.0031	0.0048
8	E_{perp} of the column 400MPa.	150	0.92	0.0035	0.0040	0.0086
9	E_{perp} of the column 1320MPa.	150	0.75	0.0049	0.0054	0.0025
10	E_{perp} of the column 8000MPa.	150	0.77	0.0024	0.0026	0.0015
11	E_{para} of col. and beam 8000MPa.	150	0.75	0.0012	0.0005	0.0052
12	G of col. and beam 400 MPa.	150	0.75	0.0038	0.0037	0.0054
13	G = 1400MPa, E_{perp} = 2000MPa.	150	0.73	0.0042	0.0039	0.0016
14	70% of the post-tensioning force.	150	0.77	0.0016	0.0014	0.0086
15	150% of the post-tensioning force.	175	0.40	0.0071	0.0078	0.0054
16	Steel plate armouring: plate thickness 30mm and 100mm extrusions.	150	0.96	0.0037	0.0043	0.0029
		200	0.94	0.0013	0.0025	0.0052
		225	0.58	0.0029	0.0030	0.0074
		250	0.42	0.0047	0.0034	0.0115
17	External beam-column connection	125	0.92	0.0044	0.0034	0.0039
		150	0.73	0.0055	0.0042	0.0054
		225	0.33	0.0167	0.0122	0.0153

* FEM 1 and 2 are the imposed rotations obtained by Approach 1 and 2 respectively.

D.5. VERIFICATION OF THE CONNECTION PROCEEDURE

In Chapter 6, analytical modeling approaches are proposed for post-tensioned timber beam-column connections. Within this section, the predictions are compared with experimental data for several subassembly tests. The input parameters used for each subassembly are given in Table D.5.1.

D.5.1. Axial stiffness corrections for the post-tensioning

As discussed in Chapter 6, compression of the perpendicular-to-grain timber within the column reduces the strain, and therefore, the force in post-tensioning tendons. For the predictions, this was taken into account by increasing the apparent unbonded length of the post-tensioning tendons. If the connections remain elastic the following expression can applied to estimate the corrected unbonded length:

$$l_{pt,c} \approx E_{pt} A_{pt} \left(\frac{1}{K_{beam}} + \frac{1}{K_{col}} + \frac{1}{K_{pt}} \right)$$

Where: K_{beam}, K_{col}, K_{pt} is the axial stiffness of the beam, column and post-tensioning respectively;
E_{pt} is the elastic modulus of the tendon;
A_{pt} is the area of the tendon.

If the connection goes into the inelastic range, the above expressions will under-estimate the flexibility of the column. Therefore, if the timber is inelastic the unbonded length is calibrated to approximately match the tendon force from the experimental data.

D.5.2. Experimental-Analytical Comparison

Several frame subassembly tests are considered to verify the accuracy of the proposed connection design procedure. Due to lack of experimental data, only unarmoured beam-column connections are considered. All the post-tensioned frame subassemblies

constructed to date, have been subjected to multiple quasi-static tests, which have resulted in inelastic deformation of the timber. Because of stiffness degradation, the first test on a given subassembly is most appropriate for comparison with the design procedure.

Subassembly 1

Subassembly 1 is an approximate two-third scale external beam-column joint. Two tests are considered; Test 1 and 3.

For Test 1, there were significant losses in tendon forces. Hence, an upper and lower bound prediction were made with an initial post-tensioning force of 31kN and 23kN per tendon respectively. The elastic modulus of the perpendicular-to-grain timber was 600MPa. The perpendicular-to-grain compressive strength of the timber was taken as 6MPa. Due to axial deformation of the timber, the unbonded length of the tendons was increased to 3000mm, to match with experimental data.

The connection moment, neutral axis depth and tendon forces are shown in Figure D.5.1. The connection moment and post-tensioning force matches well with the experimental data. The upper bound prediction appears to overestimate the moment provided by the connection at small rotations. This may be because the yield strain of the timber, according to the analytical procedure, is exceeded at a rotation of only 0.005 rad. This may have caused significant losses of post-tensioning force at even small displacement cycles. The prediction with the lower-bound post-tensioning force appears to match the initial stiffness well. As discussed in Appendix B, it is difficult to obtain an accurate neutral axis depth relationship from experimental data and therefore, inaccuracies in the experimental neutral axis depth are likely. This is verified by observing Figure D.5.1d, which shows the connection interface at 4% connection rotation. The inferred neutral axis depth from this figure is approximately 18% of the beam depth, which provides good agreement with the analytical predictions.

For Test 3, the post-tensioning force was increased to 93kN per tendon. Observing Figure D.5.2a, the connection moment is over predicted at small rotations. This is due to strength and stiffness degradation that has occurred in previous tests. Loss of post-

tensioning force (for the tendon within the neutral axis) also indicates that permanent deformation of the column face has occurred (see Figure D.5.2b). The analytical predictions indicate the yielding of timber may have begun at as low as 0.0025rad.

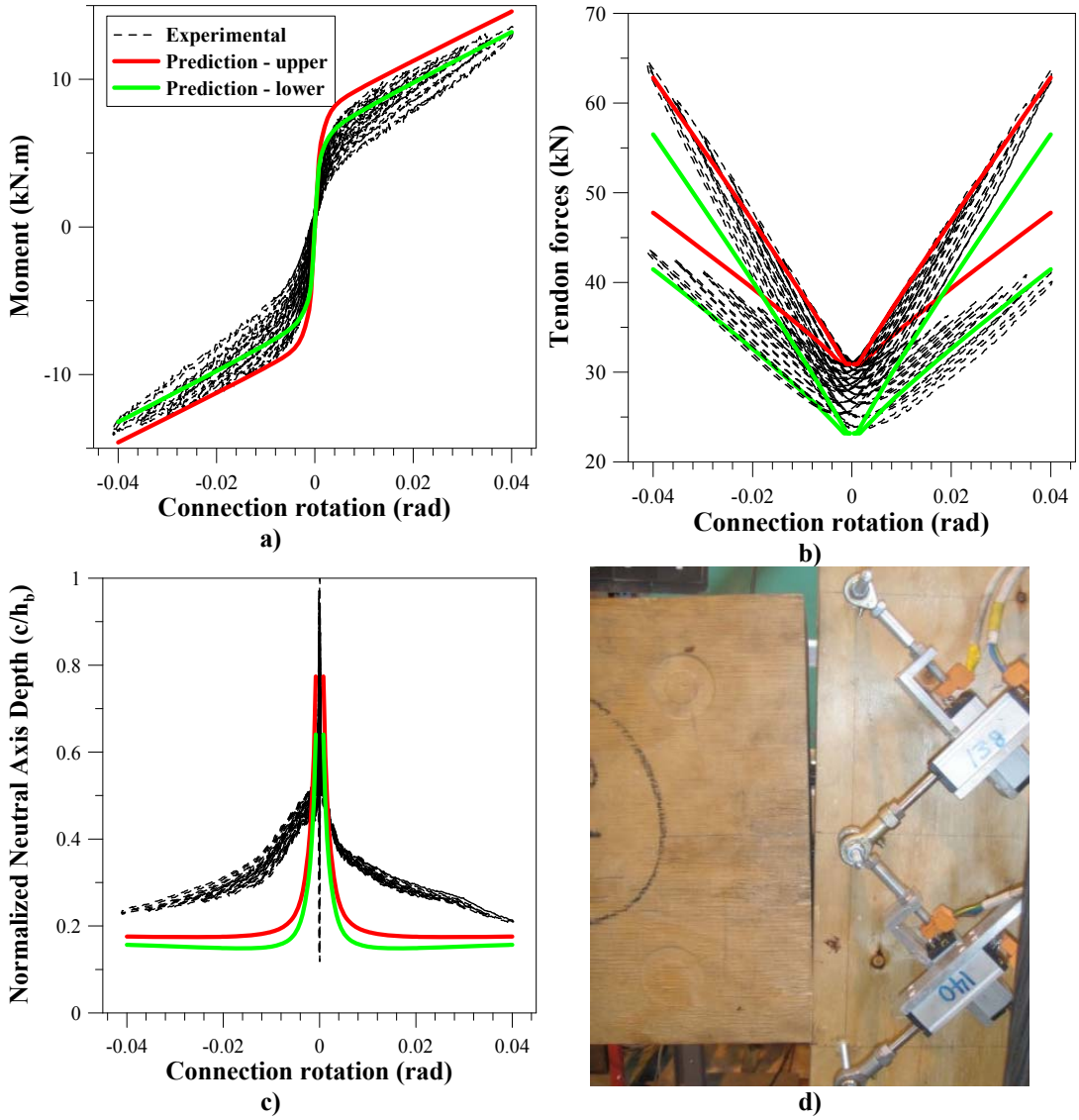

Figure D.5.1. Experimental – analytical comparison for Subassembly 1, Test 1A: a) Connection moment b) Tendon forces c) Neutral axis depth d) Neutral axis depth at 4% rotation

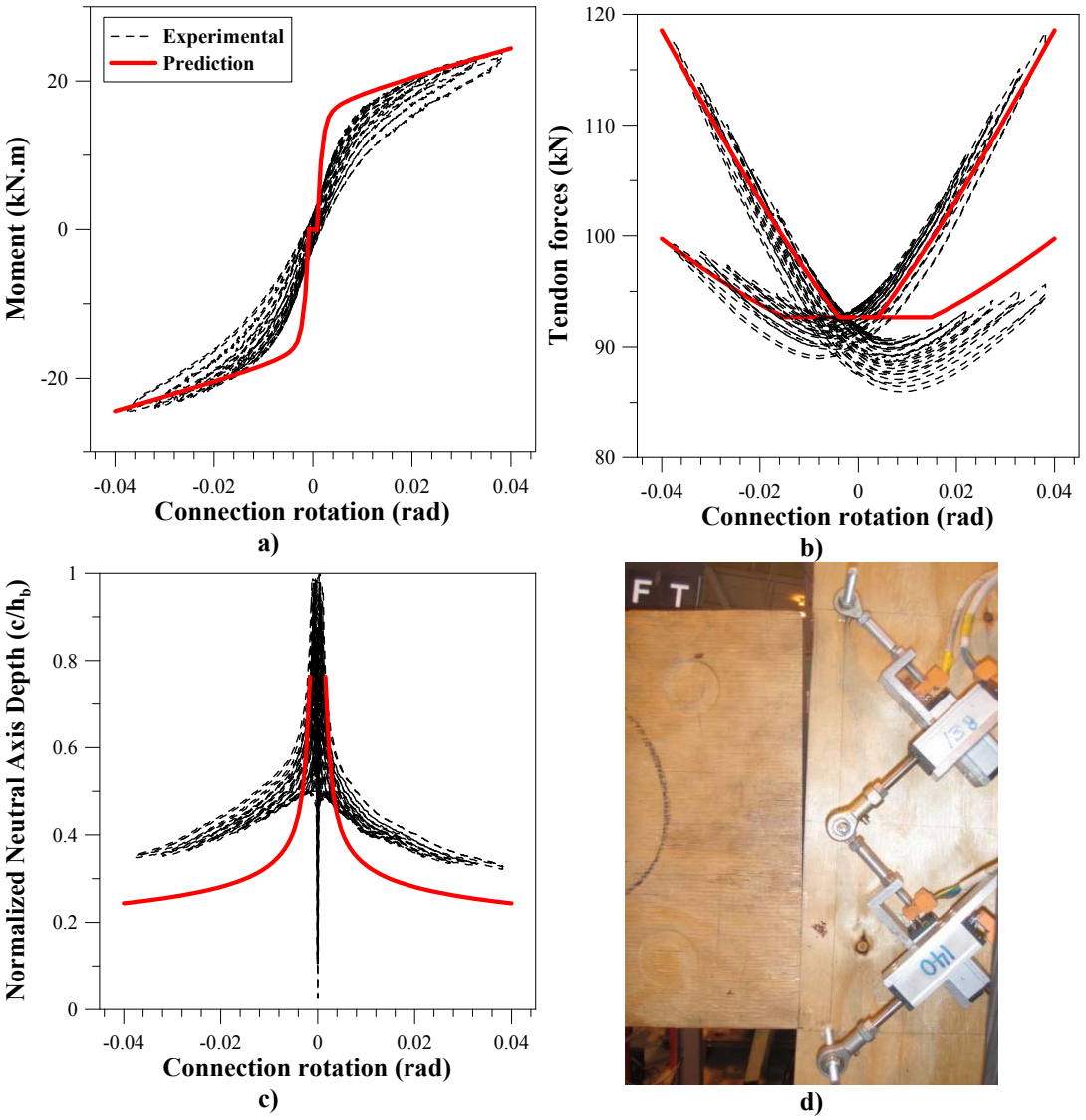

Figure D.5.2. Experimental – analytical comparison for Subassembly 1, Test 3: a) Connection moment b) Tendon forces c) Neutral axis depth d) Neutral axis depth at 4% rotation

Subassembly 2

Subassembly 2 is an approximate two-thirds scale internal beam column joint. One test is considered. The connection moment, neutral axis depth and tendon forces are shown in Figure D.5.3. The connection moment is over predicted. It is likely that this is due to significant inelastic deformation of the timber and losses in the post-tensioning force. The analytical prediction indicates that the yield stress of the timber is exceeded at only 0.0025rad. The bi-linear stress-strain law, used for the timber in compression, may need refinement when there is significant inelastic deformation. For the prediction procedure a bi-linear factor of 0.1 is assumed. To illustrate the effect of the timber stress-strain law another prediction is made with a bi-linear factor of 0, which is plotted in Figure D.5.3a. This prediction matches much more closely with the experimental data.

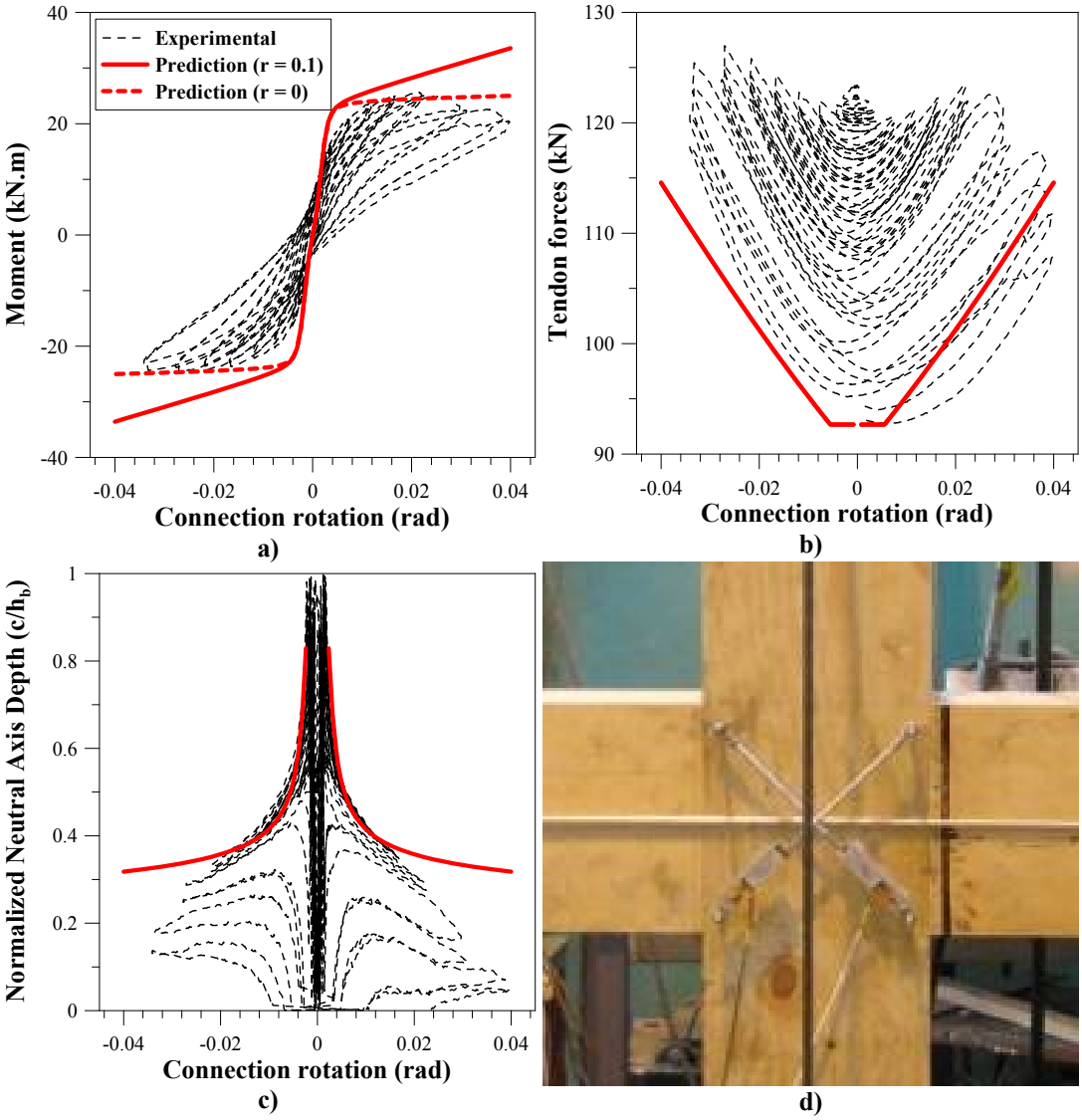

Figure D.5.3. Experimental – analytical comparison for Subassembly 2: a) Connection moment b) Tendon forces c) Neutral axis depth d) Beam-column connection

Subassembly 3

Subassembly 3 is an approximate two-thirds scale external frame. For more information refer to Palermo *et al* (2005a). The connection moment and tendon force is shown in Figure D.5.4. Due to errors in data acquisition, it is not possible to show the connection rotation or the neutral axis depth. Hence, the total frame drift, rather than connection rotation, is considered. Hence, the elastic deformation of the column, beam and joint panel is taken into account. There is good agreement between the analytical predictions and experimental data.

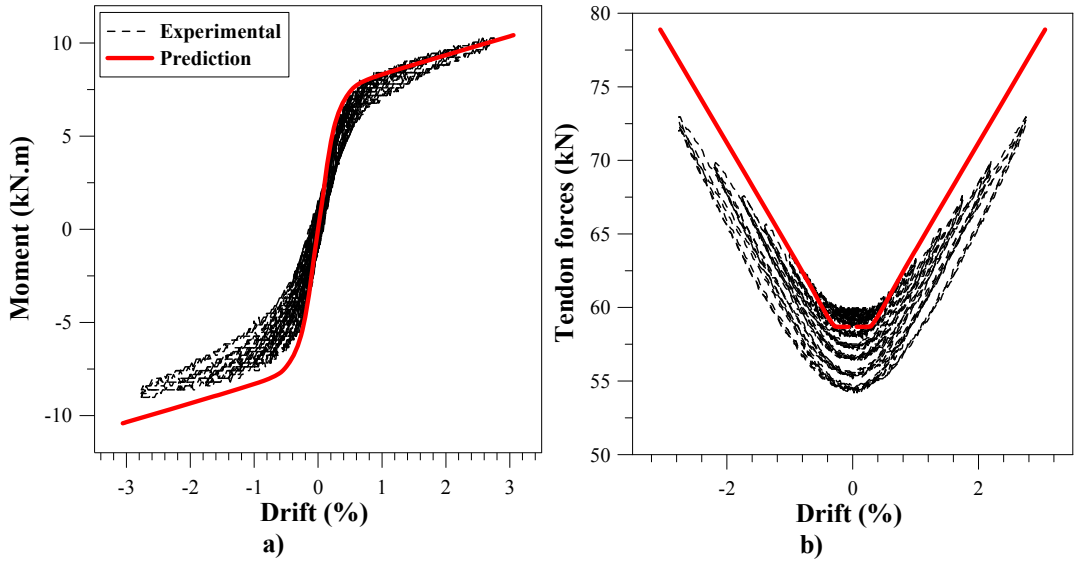

Figure D.5.4. Experimental – analytical comparison for Subassembly 4: a) Connection moment b) Tendon forces

Table D.5.1 – Summary of frame subassembly tests

Sub.	Test	Date (m/y)	L_b (mm)	H (mm)	h_b (mm)	b_b (mm)	h_c (mm)	b_c (mm)	E_{perp} (MPa)	$f_{y,t}$ (MPa)	T_{pt} (kN)	E_{pt} (MPa)	$l_{ub,c}$ (mm)	y_{pt} (mm)
1	1A Exterior	01/10	3000	2000	300	255	195	255	600	8	31;31	190000	3000	120;180
	3 Exterior	01/10	3000	2000	300	255	195	255	600	8	93;93	190000	3000	120;180
2	1 Interior	01/10	3100	2000	300	216	300	216	600	8	124;124	190000	4650	170;230
3	1 Exterior	01/05	3000	2000	300	255	200	255	600	8	60	190000	3000	150

APPENDIX E

MODELLING WALL SYSTEMS

This appendix concentrates on modeling the connection response of post-tensioned timber walls. Analytical predictions, that are proposed in Chapter 7 are compared with complex finite element models (FEM) and experimental data.

E.1. WALL- BASE CONNECTION RESPONSE USING FEM

Here the accuracy of analytical relationships, derived in Chapter 7, for modeling PT wall-base connections are evaluated. Firstly, the proposed relationship between the neutral axis depth, c, and the imposed connection rotation, θ_{imp}, is considered. This expression is repeated below:

$$c = \left(\frac{2L_e \sum N}{\theta_{imp} E_{para} t_w} \right)^{0.5}$$

Where: $\sum N = T_{pt} + N \pm V_{CE}$ is the sum of the axial force from the post-tensioning, axial load and coupling elements;
E_{para} is the parallel-to-grain elastic modulus of the timber;
t_w is the thickness of the wall.

The effective length, L_e, was calibrated as:

$$L_e \approx 65\left(\frac{l_w}{c} - 1 \right) \quad (mm)$$

The peak stress at the toe of the wall is:

$$f_t = \frac{2\sum N}{cb_b}$$

Analytical expressions are compared with the results of sensitivity study using finite element models created in SAP 2000 (2005). The sensitivity study considers variation in several parameters, to ensure a robust evaluation of the accuracy of the analytical (θ_{imp}-c) predictions and peak stresses. This study is limited to the elastic response of the wall-base connections.

E.1.1. The finite element model

A benchmark wall subassembly model was created, as shown in Figure D.4.1, and key parameters were altered to determine their effect on the accuracy of the θ_{imp}-c predictions and the peak stresses. The material properties and dimensions for the benchmark model are given in Table E.1.1. The geometry of the benchmark model was actually based on column dimensions. This is allows a more gradual change in neutral axis depth with connection rotation, and hence, more accurate calibration.

The boundary conditions consist of a pin supports at the base of the wall, which resist only longitudinal compression and shear forces. Hence, support nodes are deleted if tension forces occur, which is an iterative process. A lateral load is applied to the top of the wall, which create a known connection moment. This lateral load is distributed evenly throughout the top of the wall section. Axial loads (730kN for the benchmark model) are applied to the top of the wall to simulate the compression provided by the post-tensioning and gravity loads. This is kept constant throughout the analysis.

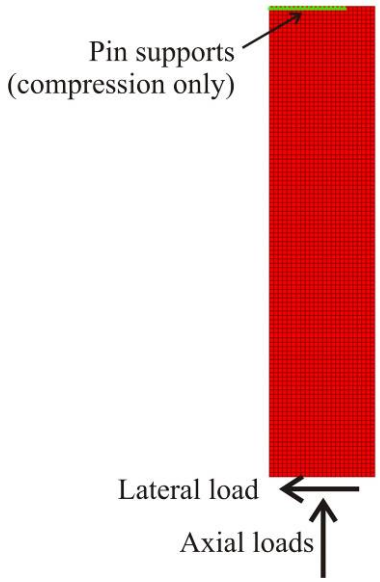

Figure E.1.1. Boundary conditions and applied loads for the benchmark FEM of the wall

Table E.1.1 – Material properties and geometry of the benchmark wall model

Parameter	Symbol	Units	Value
Elastic modulus – Parallel to grain	E_{para}	MPa	13200
Elastic modulus – Perp. to grain	E_{perp}	MPa	660
Poisson's ratio*	υ	-	0.3
Shear modulus	G	MPa	600
Wall height	H	m	2.7
Wall length	l_w	mm	600
Wall thickness	t_w	mm	380

*Based on research performed on Pine by Murray (2007).

E.1.2. Comparison of the model and the analytical equations

To evaluate the accuracy of the analytical θ_{imp}-c relationship, the results from the FEM must be interpreted accurately. The neutral axis depth can be readily interpreted by observing the longitudinal stresses, but the imposed connection rotation is slightly more problematic. This is because the base of the wall does not remain linear. This is also reported from experimental results in Appendix B.

The connection rotation is deduced by taking the total deformation of the wall, Δ_{tot}, and subtracted the member deformation. Hence:

$$\theta_{imp} = \frac{\Delta_{tot}}{H} - \left(\theta_f + \theta_s\right)$$

The flexural and shear deformation of the wall is approximated using simple beam theory. Therefore:

$$\theta_f = \frac{\Delta_f}{H} = \frac{FH^2}{3E_{para}I_w} \;\&\; \theta_s = \frac{\Delta_s}{H} = \frac{F}{GA_{sw}}$$

Where: F is the lateral force applied to the model;
I_w is the second moment of inertia of the wall;
$A_{sw} = \frac{2}{3} l_w t_w$ is the shear area of the wall.

Models are created with and without shear deformation. This is because the shear area used in simple beam theory is an only approximation, which can affect accuracy of the computed imposed rotation. If shear deformation is ignored, the imposed rotation at the connection can be determined more accurately. However, if the shear modulus significantly affects neutral axis depth, the accuracy of the proposed θ_{imp}-c relationship may be affected. This is investigated as part of the sensitivity study.

E.1.3. Results from the sensitivity study

The sensitivity study considered many parametric variations. Only key results are presented. A summary of the study is given in Table D.4.1.

Benchmark response

The benchmark response, for a connection moment of 150kN.m, is shown below in terms of deformation, horizontal stresses, vertical stresses and shear stresses.

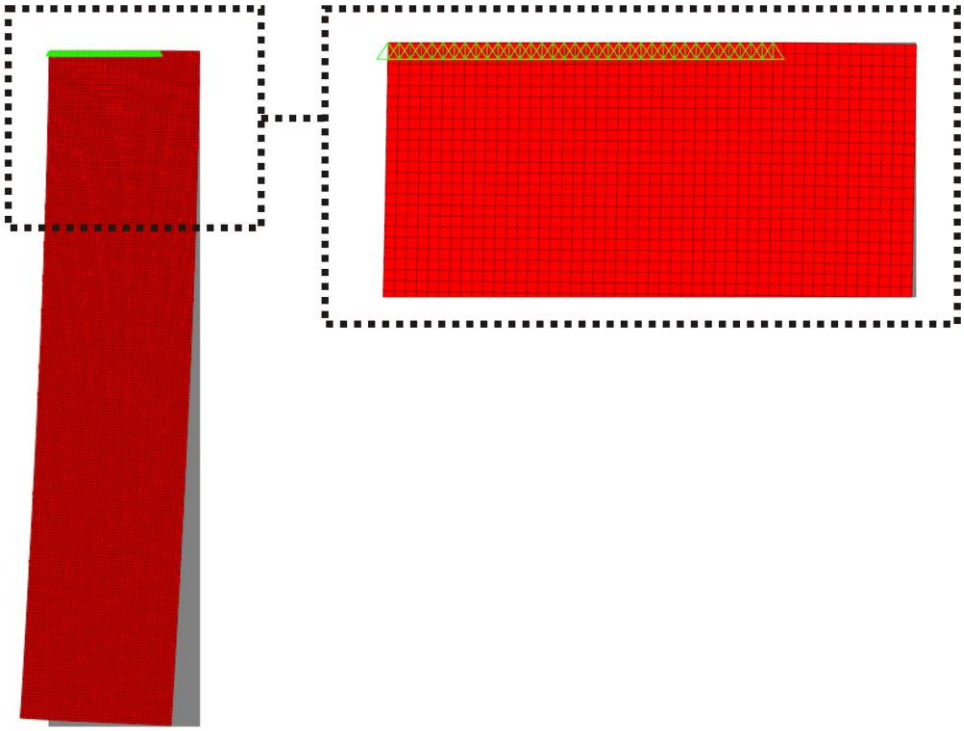

Figure E.1.2. Results of benchmark upside-down FEM wall: Deformed shape (magnified by 20)

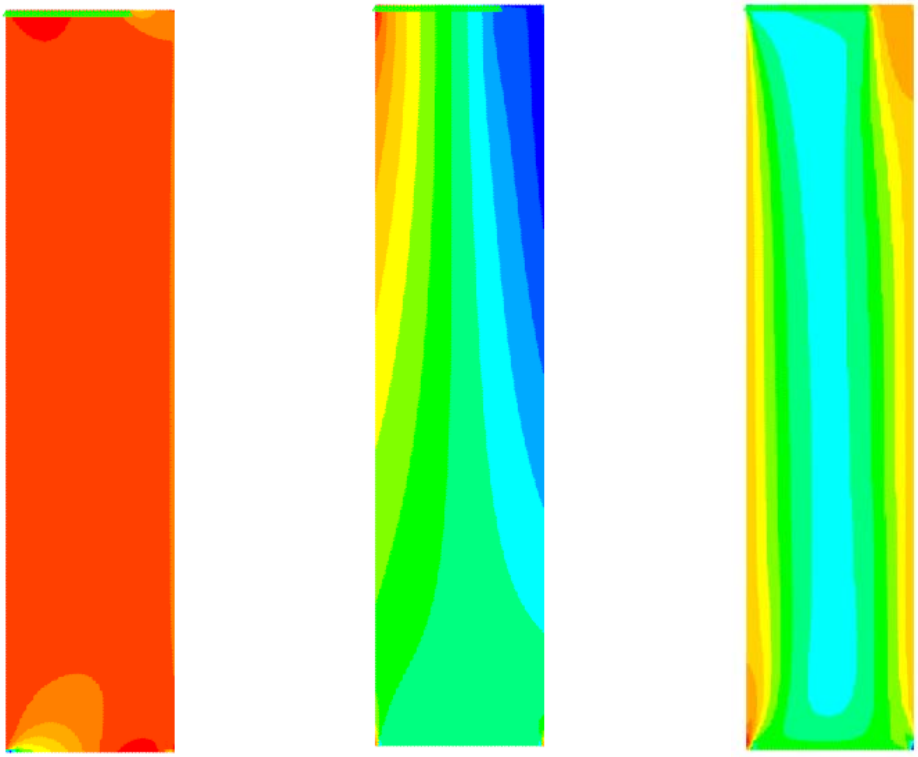

a) **b)** **c)**

Figure E.1.3. Results of benchmark FEM: a) Horizontal stresses b) Vertical stresses c) Shear stresses

The compressive stress distribution at the connection interface is shown in Figure E.1.4. This is determined by dividing the force applied by the pinned supports by the area of the each shell element. The analytical expression (shown above) for timber stresses is compared with the results of the benchmark FEM. Assuming that applied stress distribution is linear the stress in the timber can be re-written as:

$$f_t = \frac{y}{c}\frac{2\sum N}{cb_b}$$

Where: y is distance from the neutral axis position into the compression region.

Observing Figure E.1.4 it is evident that the timber stresses are effectively linear. Hence, it is reasonable to assume both linear stress and strain in the connection design procedure.

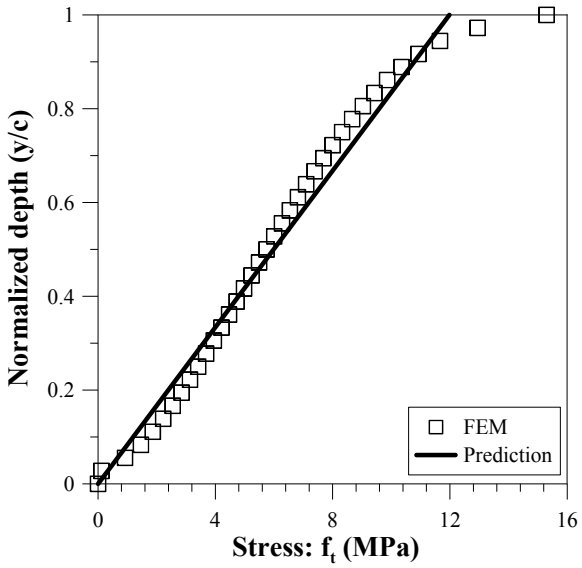

Figure E.1.4. Predicted and FEM timber stresses for benchmark model

The θ_{imp}-c relationship

Several models were created (see Table D.4.1) to compare the proposed relationship for the neutral axis depth with FEM results. To gauge the accuracy of the proposed θ_{imp}-c relationship, the predicted normalised neutral axis depth is plotted against that obtained from FEM (for a given connection rotation), as shown in Figure E.1.5.

In Figure E.1.5, the data is divided into models that do and do not consider shear deformation, and models that vary the material properties of the timber. The proposed neutral axis depth formulation matches well with the FEM data. The same trend is apparent with and without shear deformation in the model. Hence, the shear modulus does not significantly affect the θ_{imp}-c relationship. However, there is more dispersion in the results when shear deformation is considered. It is likely that this due to inaccuracy in calculating the shear deformation, which leads to inaccuracy in interpreting the connection rotation. Changing the material properties of the timber appears to slightly influence the accuracy of the proposed θ_{imp}-c relationship. Further research is necessary to determine if this is actually the case.

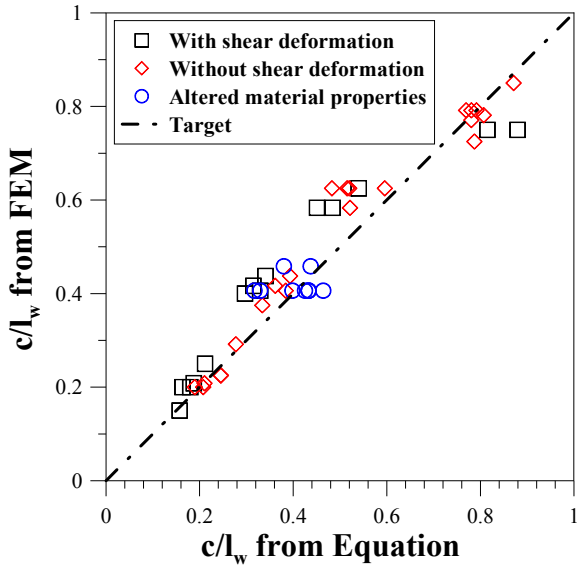

Figure E.1.5. Correlation between the predicted and FEM neutral axis depth

The proposed θ_{imp}-c relationship is plotted for FEM model 7 (see Table D.4.1) and compared with three FEM data points in Figure E.1.6. The proposed θ_{imp}-c relationship appears reasonable and matches well with the FEM results.

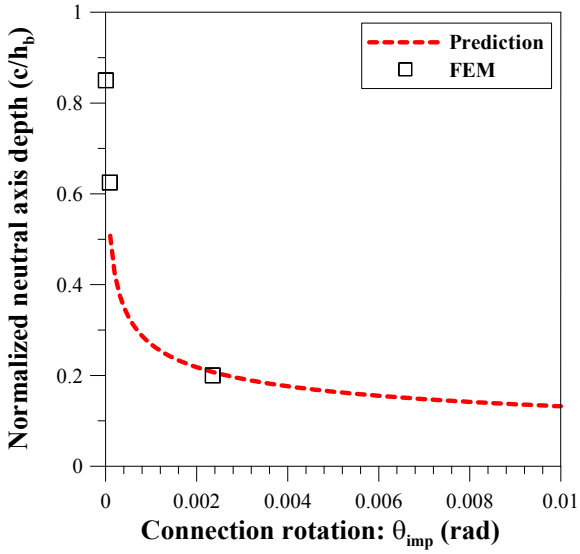

Figure E.1.6. Normalized neutral axis depth versus connection rotation for FEM 7

Table E.1.2 – Summary wall FEM

FEM Model	Change from benchmark	M_{con} (kN.m)	Shear def. (Y/N)	c/h_b	θ_{imp}
1	Benchmark	150	N	0.79	0.00003
		225	N	0.42	0.00100
2	Lw = 400mm	150	N	0.44	0.00165
3	Lw = 400mm, 150% Tpt	150	N	0.78	0.00009
		180	N	0.63	0.00048
4	Lw = 400mm, Lcant = 5400mm	150	N	0.41	0.00180
5	80% Tpt	150	N	0.63	0.00027
6	60% Tpt	150	N	0.29	0.00150
7	Lw = 1000mm	225	N	0.85	0.00001
		300	N	0.63	0.00009
		450	N	0.20	0.00235
8	Lw = 1000mm, 60% Tpt	150	N	0.73	0.00001
9	Lw = 1000mm, 40% Tpt	150	N	0.38	0.00019
10	Lw = 1000mm, 35% Tpt	150	N	0.23	0.00048
11	Lw = 1000mm, 35% Tpt, tw = 180mm	150	N	0.23	0.00095
12	Lw = 1000mm, Lcant = 6400mm	451	N	0.20	0.00316
13	Lcant = 2200mm	150	N	0.79	0.00003
14	Lcant = 2200mm, 80% Tpt	150	N	0.58	0.00020
15	Lcant = 3200mm	150	N	0.79	0.00004
16	Lcant = 3200mm 80% Tpt	150	N	0.63	0.00021
17	Lcant = 6400mm	270	N	0.21	0.00623
18	Lw = 400mm	150	Y	0.44	0.00276
19	Lw = 400mm, 150% Tpt	150	Y	0.75	0.00009
20	Lw = 400mm, Lcant = 5400mm	150	Y	0.41	0.00311
21	67% Tpt	150	Y	0.42	0.00108
22	Lw = 1000mm	300	Y	0.63	0.00008
		450	Y	0.20	0.00373
23	Lw = 1000mm, 40% Tpt	150	Y	0.40	0.00029
24	Lw = 1000mm, 35% Tpt	150	Y	0.25	0.00077
25	Lw = 1000mm, 60% Tpt, tw = 180mm	266	Y	0.15	0.00688
26	Lw = 1000mm, Lcant = 6400m	451	Y	0.20	0.00508
27	Lw = 600mm, Lcant = 2200mm, 80% Tpt	150	Y	0.58	0.00027
28	Lcant = 3200mm	150	Y	0.75	0.00001
29	Lcant = 3200mm, 80% Tpt	150	Y	0.58	0.00035
30	Lcant = 6400mm	281	Y	0.21	0.00947
31	Eperp = 8000MPa	225	N	0.46	0.00050
32	Epara = 8000MPa	225	N	0.46	0.00138
33	Lw = 400mm, Lcant = 5400mm, Eperp = 8000MPa	150	N	0.41	0.00089
34	Lw = 400mm, Lcant = 5400mm, Epara = 8000MPa	150	N	0.41	0.00261
35	Lw = 400mm, Lcant = 5400mm, G = 400MPa	150	Y	0.41	0.00355
36	Lw = 400mm; Lcant = 5400mm, Isotropic E=13200	150	Y	0.41	0.00116
37	Lw = 400mm, Lcant = 5400mm, Isotropic E=8000	150	Y	0.41	0.00191
38	Lw = 400mm, Lcant = 5400mm, Isotropic E = 5000	150	Y	0.41	0.00306
39	Lw = 400mm, Lcant = 5400mm, Isotropic, $\upsilon = 0$	150	Y	0.41	0.00124

E.2. VERIFICATION OF THE CONNECTION PROCEEDURE

In Chapter 7, analytical modeling approaches are proposed for post-tensioned timber wall-base connections. Within this section, the predictions are compared with experimental data from subassembly tests (Iqbal et al. 2007; Smith et al. 2007). Rather than considering the connection rotation, which is difficult to accurately define from experimental data (see Appendix B), the total drift of the subassembly is considered. Hence, the analytical predictions consider the flexural and shear deformation of the wall elements. The input parameters used for each subassembly are given in Table E.2.1.

Subassembly 1

Subassembly 1 is an approximate two-third scale post-tensioned wall. The connection moment, neutral axis depth and tendon forces are shown in Figure E.2.1. The connection moment and post-tensioning force matches well with the experimental data. As discussed in Appendix B, it is difficult to obtain an accurate neutral axis depth relationship from experimental data due to the non-linear displacement at the base of the wall. Therefore, there are likely to be inaccuracies in the experimental neutral axis depth. Furthermore, due to experimental calibration error the neutral axis depth could only be calculated for positive drifts. However, the accuracy of the predicted neutral axis depth is verified by observing Figure D.5.1d, which shows the connection interface at 2.5% drift. The inferred neutral axis depth from this figure is approximately 10% of the wall length, which is in agreement with the analytical predictions.

At 2.5% drift, the peak stress is only 60% of the yield stress of the timber parallel-to-grain. Hence, in many situations it may be possible to avoid any yielding in the wall elements.

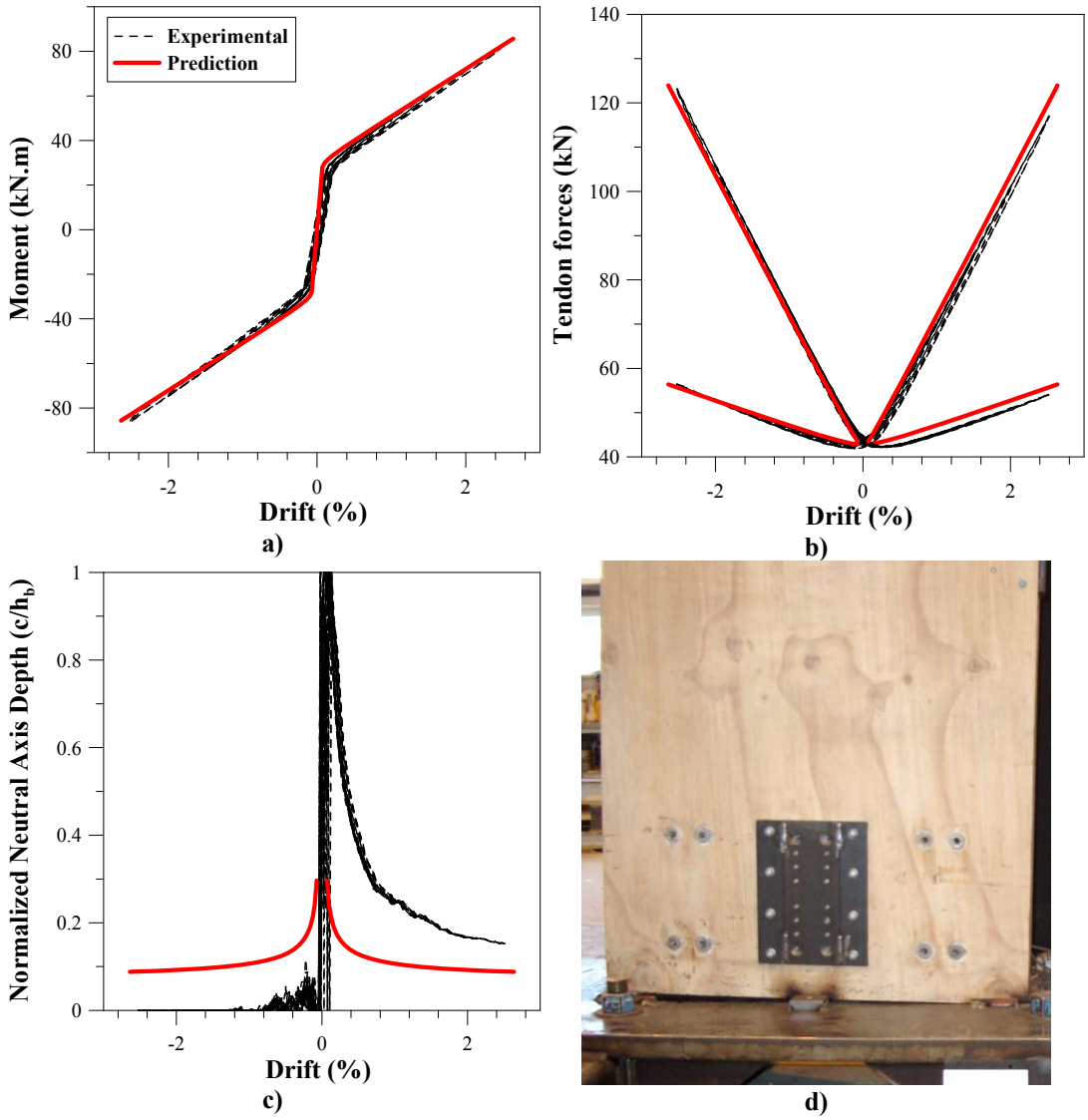

Figure E.2.1. Experimental – analytical comparison for Subassembly 1: a) Connection moment b) Tendon forces c) Neutral axis depth d) Neutral axis depth at 2.5% drift

Subassembly 2

Subassembly 2 is another two-third scale post-tensioned wall. The connection moment and tendon forces are shown in Figure E.2.2. The neutral axis depth is not compared, due to errors associated with interpreting the neutral axis depth from experimental data (see Appendix B) and experimental calibration errors. The connection moment and post-tensioning force matches well with the experimental data. There was some wall sliding during the experiment, which accounts for the differences in connection moment between the experimental data and the prediction at low rotations.

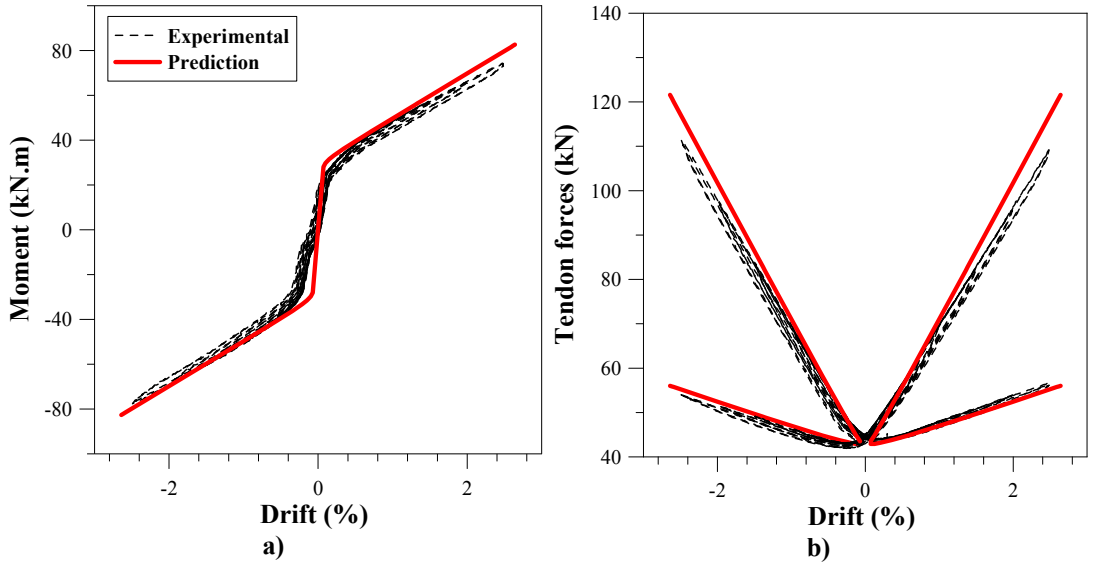

Figure E.2.2. Experimental – analytical comparison for Subassembly 1: a) Connection moment b) Tendon forces

Table E.2.1 – Summary of wall subassembly tests

Sub.	Test	Date (m/y)	l_w (mm)	t_w (mm)	H (mm)	E_{para} (GPa)	G (MPa)	$f_{y,t}$ (MPa)	T_{pt} (kN)	E_{pt} (GPa)	$l_{ub,c}$ (mm)	y_{pt} (mm)
1	8	10/06	790	195	2000	10.5	600	45	43;43	190	3200	160;640
2	1	08/06	790	195	2000	10.5	600	45	43;43	190	3400	160;640

APPENDIX F

EARTHQUAKE RECORDS

This appendix provides a summary of the earthquake records used within thesis for numerical time-history analysis. Details are provided on location, distance to source and the employed scaling approaches.

F.1. EARTHQUAKE SET 1

Earthquake set 1 consists of 15 earthquakes, with a mixture near field and far field records. The characteristics of the earthquake records are provided in Table F.1.1.

The records were chosen to satisfy, and scaled according to, New Zealand Standards criteria (NZS1170.5 2004) within a period range of 0.64 to 3s. This was to match with case study building used in Chapter 8 to determine the effects of floor flexibility. The scaling factors for 2% damping and 1/500 year, Wellington City, Soil type C, earthquake intensity are shown in Table F.1.1. For 2% damping the spectral response varies significantly and therefore the limitations on scaling (0.3 to 3) according to NZS1170.5 (2004) were violated for 3 earthquakes. The goodness-of-fit criteria according to NZS1170.5 (2004), which specify that the normalized sum of the lognormal difference between the earthquake spectra and the design spectra must be less than $\log_{10}(1.5)$, were satisfied for all earthquakes. The scaled displacement and acceleration spectra for 2% of critical damping are shown in Figure D.1.1, Figure F.1.2 and Figure F.1.3.

Table F.1.1 – Properties of earthquake set 1

EQ Number	Near field/ Far field	Location	Distance to source (km)	Soil type (NEHRP)	Component	PGA (g)	Scale factor ξ_{el} = 2% 1/500 year
1	NF	Northridge, Los Angeles Dam	5.92	A	334	0.35	1.2
2	NF	Norhtridge, Sylmar - Olive view Med Ctr	5.3	D	360	0.84	0.6
3	FF	Tabas, Iran (BOS_L1)	26.1	D	LP1 (P)	0.107	4.49
4	FF	Nothridge, N Hollywood – Coldwater Can	14.6	C	270	0.271	2.18
5	FF	Northridge, Canoga Park – Topanga Clan	15.8	D	106	0.356	1.82
6*	N/A	Artificial record	-	-	-	0.53	1.22
7	FF	Superstition Hills, El Centro Imp. Co. Cent	13.9	D	0	0.2899	2.16
8	FF	Superstition Hills, Plaster City	21	D	135	0.155	4.49
9	FF	Cape Mendocino, Fortuna Fortuna Blvd	23.6	C	0	0.116	2.68
10	NF	Loma Prieta, Los Gatos Pres Center	3.88	A	0	0.563	0.55
11	FF	Northridge, LA – N Faring Rd	23.9	D	0	0.273	3.22
12	NF	Chi Chi, TCU068	9.96	D	270	0.57	0.56
13	FF	Landers, Yemo Fire Station	24.9	D	0	0.2095	2.65
14	FF	Loma Prieta, Hollister Diff. Army	25.8	D	0	0.2762	1.29
15	NF	Tabas, Iran	2	D	TR	0.852	0.85

*Earthquake 6 is an artificial record using SIMQKE

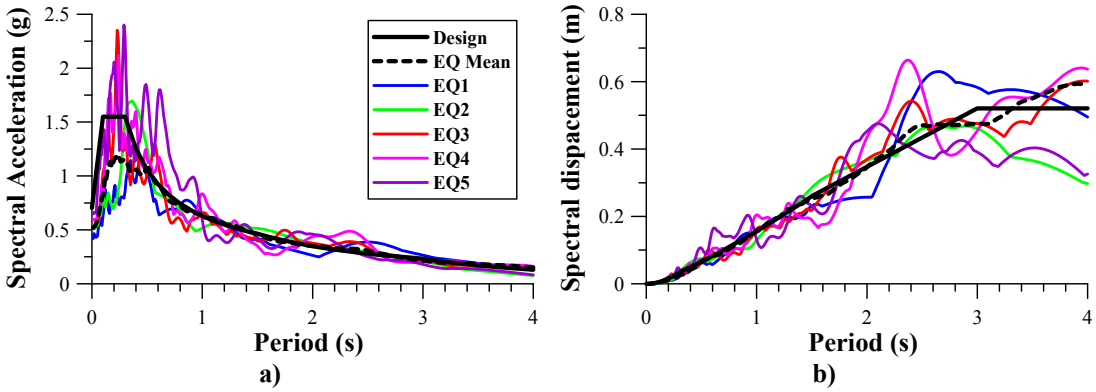

a) b)

Figure F.1.1. Set 1 spectra for EQ 1 to 5: a) Acceleration b) Displacement

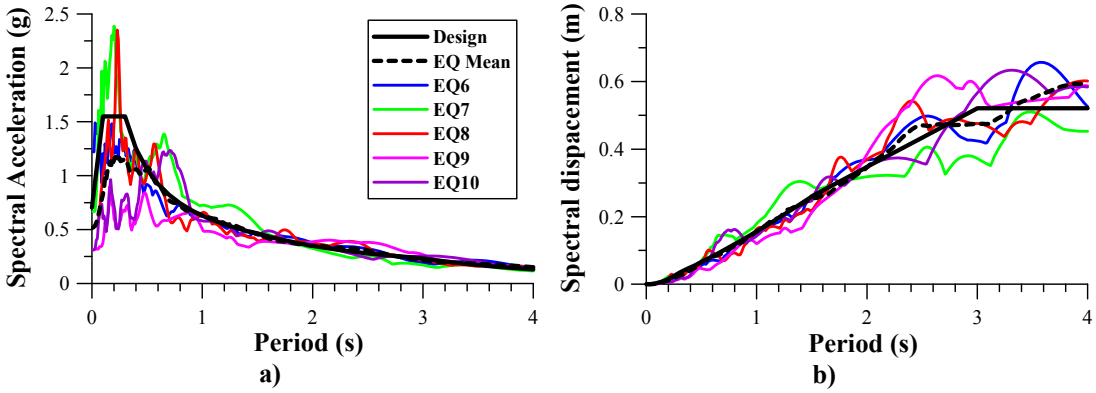

a) b)

Figure F.1.2. Set 1 spectra for EQ 6 to 10: a) Acceleration b) Displacement

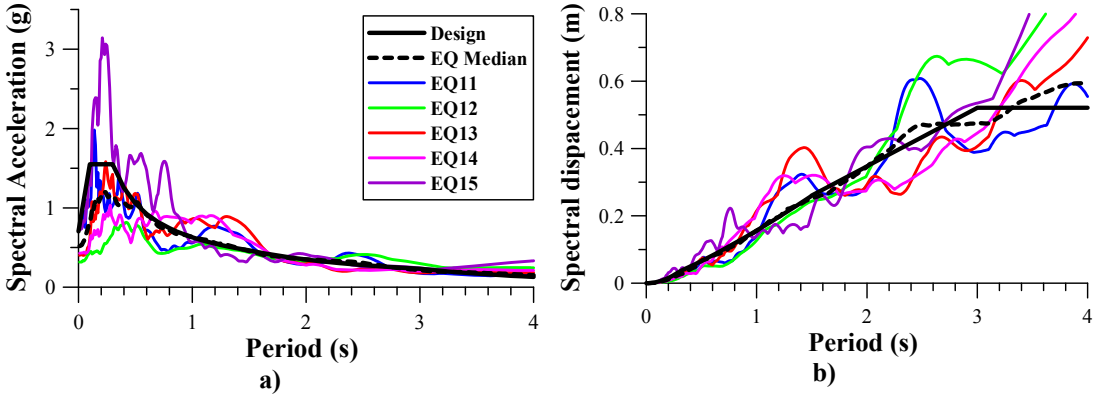

a) b)

Figure F.1.3. Set 1 spectra for EQ 11 to 15: a) Acceleration b) Displacement

F.2. EARTHQUAKE SET 2

Earthquake set 2 consists of 15 earthquakes records that are a mixture near field and far events. Several earthquakes from Set 1 were also used in Set 2. However, earthquake Set 1 under represented the design spectral demand at low periods. Hence, both far field and near field records were added which increase the spectral demand at low periods. This is to ensure that higher mode amplification factors, developed in Chapter 10, are conservative. The characteristics of the additional five earthquakes are provided in Table F.2.1.

The records were chosen to satisfy, and scaled according to, New Zealand Standards criteria (NZS1170.5 2004) within a period range of 0.2 to 3.5s. This range was expected to encompass the modal periods that would significantly contribute to the response of the frame and wall models from Chapter 10 and 11. The scaling factors for 2% and 5% damping and 1/500 year earthquake, Wellington City, Soil type C, intensity are shown in Table F.2.2. The displacement and acceleration spectra for each record, for 5% of critical damping, are shown in Figure F.2.1, Figure F.2.2 and Figure F.2.3.

Table F.2.1 – Properties of earthquake set 2

EQ Number	Near field/ Far field	Location	Distance to source (km)	Soil type (NEHRP)	Component	PGA (g)
1	NF	Northridge, Los Angeles Dam	5.92	A	334	0.35
2	NF	Norhtridge, Sylmar - Olive view Med Ctr	5.3	D	360	0.84
3	FF	Tabas, Iran (BOS_L1)	26.1	D	LP1 (P)	0.107
4	FF	Nothridge, N Hollywood – Coldwater Can	14.6	C	270	0.271
5	FF	Northridge, Canoga Park – Topanga Clan	15.8	D	106	0.356
6*	N/A	Artificial record	-	-	-	0.53
7	FF	Superstition Hills, El Centro Imp. Co. Cent	13.9	D	0	0.2899
8	FF	Superstition Hills, Plaster City	21	D	135	0.155
9	FF	Northridge, LA – N Faring Rd	23.9	D	0	0.273
10	FF	Landers, Yemo Fire Station	24.9	D	0	0.2095
11	NF	Tabas, Iran	2	D	TR	0.852
12	FF	Superstition Hills, Brawley	18.2	D	-	0.134
13	NF	Dinar, Turkey	3.4	C	180	0.285
14	FF	LA - Hollywood Stor FF	25.5	D	90	0.231
15	FF	El Cent. Imp. Val. Niland Fire Station	35.6	D	90	0.087

*Earthquake 6 is an artificial record using SIMQKE

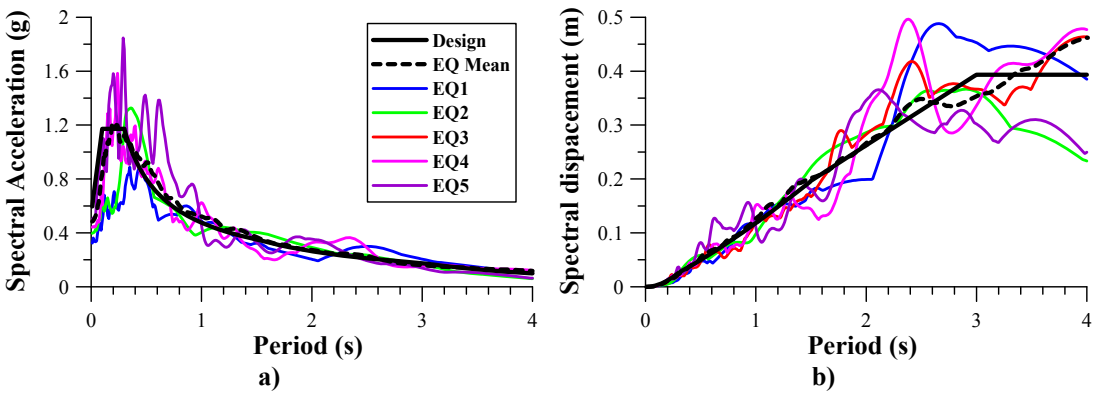

a) b)

Figure F.2.1. Set 2 spectra for EQ 1 to 5 for 5% damping: a) Acceleration b) Displacement

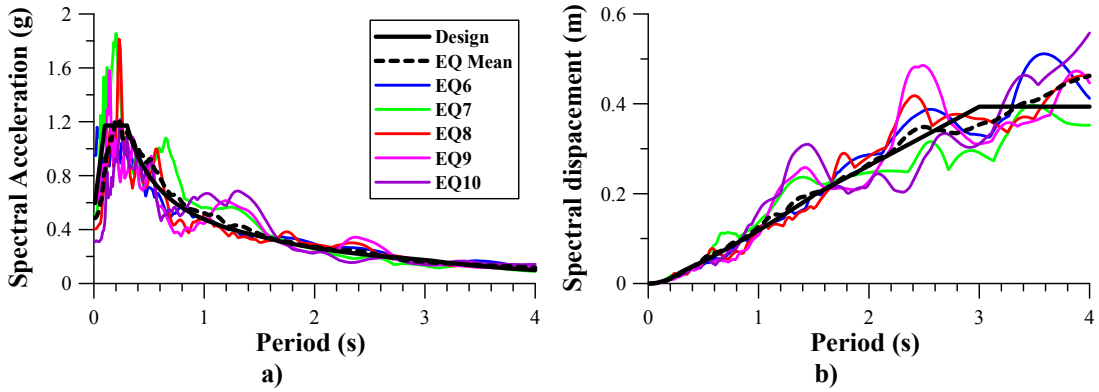

a) b)

Figure F.2.2. Set 2 spectra for EQ 6 to 10 for 5% damping: a) Acceleration b) Displacement

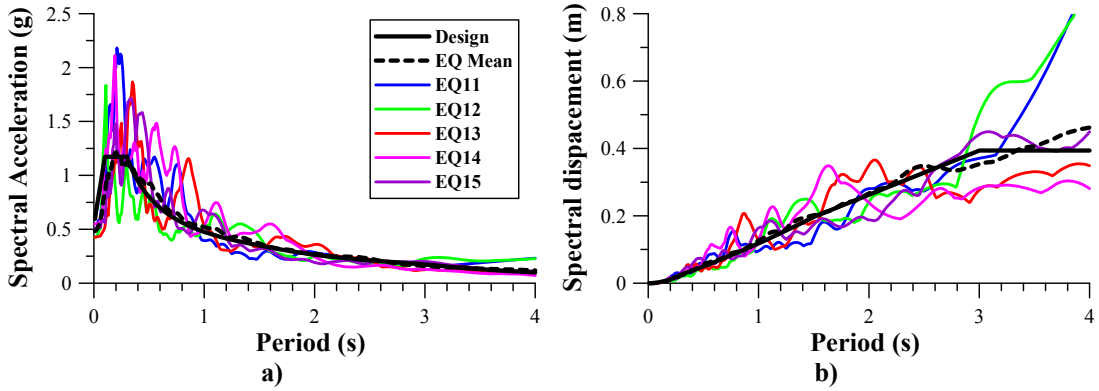

a) b)

Figure F.2.3. Set 2 spectra for EQ 11 to 15 for 5% damping: a) Acceleration b) Displacement

Table F.2.2 – Scale factors for earthquake set 2

EQ Number	Scale factor ξ_{el} = 5% 1/500 year	Scale factor ξ_{el} = 2% 1/500 year
1	0.93	1.23
2	0.47	0.62
3	3.46	4.58
4	1.63	2.15
5	1.40	1.85
6	0.95	1.25
7	1.68	2.22
8	3.46	4.58
9	2.57	3.41
10	2.04	2.69
11	0.59	0.79
12	3.65	4.83
13	1.51	2
14	2.37	3.14
15	4.67	6

APPENDIX G

DESIGNS FOR TIME-HISTORY ANALYSIS VERIFICATION

Within this appendix the design of post-tensioned timber frame and wall buildings from Chapter 10 and 11 is documented. These designs are divided post-tensioned timber frames, cantilever walls and coupled walls. The lateral force design, member design and connection design are provided.

G.1. FRAMES

As described in Chapter 10, three frame geometries were considered, termed frame 1, 2 and 3. The frames are designed using lateral force design procedures from Chapter 9 and frame design procedures from Chapter 6.

G.1.1. Lateral force design

The lateral force design procedure is shown below for frame 1. Because a similar approach was followed for frame 2 and 3 for brevity only the results are provided herein.

Frame 1

Step 1: The design displacement Δ_d, the effective mass m_e and effective height H_e is determined.

The peak design displacement for the SDOF representation:

$$\Delta_d = \sum_{i=1}^{n}\left(m_i\Delta_i{}^2\right)\Big/\sum_{i=1}^{n}\left(m_i\Delta_i\right)$$

Where:

$$\Delta_i = \delta_i \frac{\Delta_1}{\delta_1}$$

And:

$\frac{\delta_i}{\delta_1} = \frac{H_i}{H_n}$ = the mode shape (linear displacement profile)

So:

$$\Delta_i = \frac{H_i\Delta_1}{H_n}$$

And:

$$\Delta_1 = H_1 \cdot \theta_d = 3.81 \times 0.02 = 0.0762m$$

The effective mass:

$$m_e = \sum_{i=1}^{n}\left(m_i\Delta_i\right)\Big/\Delta_d$$

The effective height:

$$H_e = \sum_{i=1}^{n}\left(m_i\Delta_i H_i\right)\Big/\sum_{i=1}^{n}\left(m_i\Delta_i\right)$$

Table G.1.1 – DBD calculations

Storey, i	Height, Hi (m)	Weight, wi (KN)	Mass, mi (tonnes)	Δi (m)	mi*Δi	mi*Δi^2	mi*Δi*Hi
3	11.43	630	64.2	0.229	14.7	3.36	167.8
2	7.62	693	70.6	0.152	10.8	1.64	82.0
1	3.81	693	70.6	0.076	5.4	0.41	20.5
Sum		**3360**	**205.4**		**30.9**	**5.41**	**270.3**

Therefore:

$$\Delta_d = \sum_{i=1}^{n}\left(m_i\Delta_i{}^2\right)\Big/\sum_{i=1}^{n}\left(m_i\Delta_i\right) = \frac{5.41}{30.9} = 0.175m$$

$$m_e = \sum_{i=1}^{n}\left(m_i\Delta_i\right)\Big/\Delta_d = \frac{30.9}{0.175} = 176tonne \text{ (85\% of the total mass)}$$

$$H_e = \sum_{i=1}^{n}\left(m_i\Delta_i H_i\right)\Big/\sum_{i=1}^{n}\left(m_i\Delta_i\right) = \frac{270.3}{30.9} = 8.77m \text{ (77\% of the total height)}$$

Step 2: Determine the system damping

An elastic damping, ξ_{el}, of 5% of critical damping is assumed, based on findings from Chapter 9.

$$\xi_{eq} = \xi_{el} + \xi_{hyst} = 5\% + 0 = 5\%$$

Step 3: Determine the effective period from the design displacement spectrum

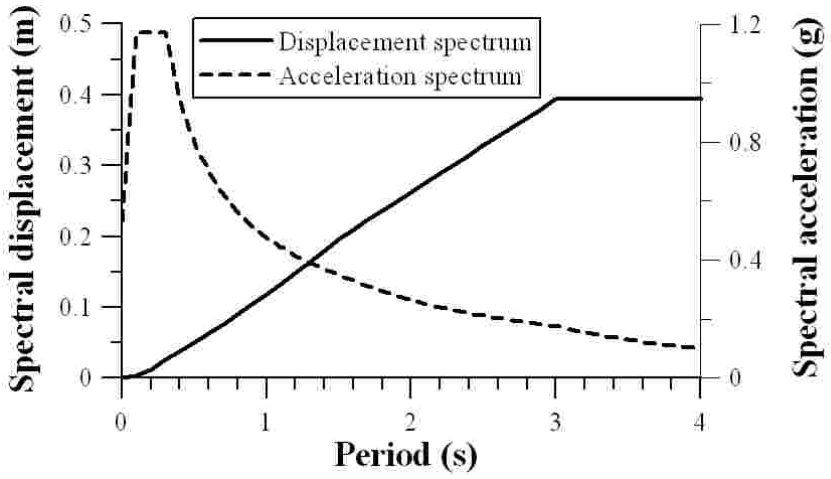

Figure G.1.1 – Design acceleration and displacement spectrum for 5% damping

By entering the displacement spectrum with the design displacement the effective period is obtained: $\mathbf{T_e = 1.37s}$.

Step 4: Obtain the equivalent lateral stiffness

$$K_e = \frac{4\pi^2 m_e}{T_e^2} = 4\pi^2 \frac{176}{1.37^2} = 3691 kN/m$$

Step 5: Determine the base shear

$$V_b = K_e \Delta_d = 3691 \times 0.175 = 647 kN$$

Step 6: Distribute the base shear up the structure

The base shear is distributed up the structure as equivalent lateral forces, which are proportional to the mass and displacement at each floor. Priestley *et al* (2007) suggests that an additional allocation of force shall be added to roof, to account of higher modes of vibration. However, this is only suggested for taller frames. This measure is said to be conservative for frames below 10 storeys. To be consistent with the specified displacement profiles (see Chapter 9), an additional 10% of the base shear is added to the roof level for frames over 4 storeys. Therefore, for Frame 1:

$$F_i = V_b \left(m_i \Delta_i\right) \Big/ \sum_{i=1}^{n} \left(m_i \Delta_i\right)$$

Table G.1.2 – Design lateral forces for Frame 1

Storey, i	Floor Force (KN)
3	308
2	226
1	113
Sum (Vb)	**647**

Frame 2

The resultant base shear and distributed lateral forces from the displacement-based design for Frame 2 are given Table G.1.3. The frame has effective period of 2.03s.

Table G.1.3 – Design lateral forces for Frame 2

Storey, i	Floor Force (KN)
6	288
5	191
4	161
3	127
2	89
1	46
Sum (Vb)	**901**

Frame 3

The resultant base shear and distributed lateral forces from the displacement-based design for Frame 2 are given Table G.1.4. The frame has effective period of 3.26s, which is above the corner period from NZS1170.5. To determine the effective period, a linear projection of the displacement spectrum below the corner period was considered, as discussed in Chapter 9.

Table G.1.4 – Design lateral forces for Frame 3

Storey, i	Floor Force (KN)
10	218
9	129
8	118
7	107
6	94
5	81
4	67
3	51
2	35
1	18
Sum (Vb)	**918**

G.1.2. Determination of frame actions

The moments and shears throughout the frame must be determined. To do this an equilibrium-based approach (Priestley et al. 2007) is used. As for the lateral force design, the procedure for determining the frame actions is only shown for Frame 1. Key results are provided for Frame 2 and 3.

Frame 1

Step 1: Determine the total overturning moment (OTM)

$$OTM = \sum_{i=1}^{n} F_i H_i$$

Table G.1.5 – Calculation of OTM

Storey, i	Hi (m)	Fi (kN)	Fi.Hi (kN.m)
3	11.43	308	3524
2	7.62	226	1723
1	3.81	113	431
Sum		**V_b=647**	**OTM=5677**

Step 2: Decide how much of the OTM will be taken by the column bases:

$$OTM = \sum_{j=1}^{n} M_{c,j} + TL_{base}$$

Where: $\sum_{j=1}^{n} M_{c,j}$ = the sum all column-base moments

T = the tension force induced by lateral load in the exterior column

L_{base} = the total frame length (to column centrelines)

Hence, the sum of the column base moments must be decided. As mentioned in Chapter 10, it is decided that the base connections have a contra-flexure point at approximately 60% the first interstorey height.

Hence:

$$\sum_{j=1}^{n} M_{c,j} = 0.6 V_b H_1 = 1479 kN.m$$

Step 3: Determine the remaining tension and compression force in the exterior columns:

$$T = C = \frac{OTM - \sum_{j=1}^{n} M_{c,j}}{L_{base}} = \frac{5677 - 1479}{35} = 120.0 kN$$

Step 4: Proportion the seismic axial forces to each beam up the height of the building

A rational way to proportion the seismic axial forces into beam shears, is to use the total shear force diagram (Priestley et al. 2007). This will ensure that the assumed displacement profile is maintained. Hence:

$$V_{B,i} = T \frac{V_{S,i}}{\sum_{i=1}^{n} V_{S,i}}$$

Where: $V_{B,i}$ = the beam shear at the ith floor

Table G.1.6 – Calculation of beam shears

Storey, i	Fi (kN)	Vsi (kN)	VBi (kN)
3	308	308	24.8
2	226	534	43.0
1	113	647	52.1
Sum	**V_b=647**	**∑Vsi=1489**	**∑VBi=120.0**

Step 5: Calculate beam design moments

$$M_{B,i} = V_{B,i} \frac{L_b}{2}$$ (At the column centerlines)

Where L_b = the length of the bay from column centerline to column centerline (7m)

The beam-column connection design moments at the column face are:

$$M_{con,i} = M_{B,i} \frac{L_b - h_c}{L_b}$$

Where h_c = the column width (600mm assumed)

Table G.1.7 – Calculation of beam moments

Storey, i	VBi (kN)	MBi (kN.m)	Mcon (kN.m)
3	24.8	86.8	79.4
2	43.0	151	138
1	52.1	182	167

Step 6: Calculate column design moments

The sum of the column moments above and below a given floor must equal the sum of the beam moments.

$$\sum M_{c,i,above} + \sum M_{c,i,below} = \sum M_{B,i}$$

It is reasonable to assume that the column moments, immediately above and below the ith floor, are equal. Making this assumption, the following equations are appropriate:

For the 1st and 2nd storey:

$$\sum_{j=1}^{n} M_{C,j} = n_b M_{B,i}$$

For the 3rd storey (the Roof):

$$\sum_{j=1}^{n} M_{C,j} = 2n_b M_{B,i}$$

Where n_b = the number of bays

Table G.1.8 – Calculation of total column moments

Storey, i	MBi (kN.m)	∑Mc (kN.m)
3	79.4	868
2	138	753
1	167	912
0	0	1479

The worst-case column moment is at the base of the frame. By equilibrium, the moments induced in the interior and exterior columns can be determined:

$$M_{c,\text{int}} = \sum_{j=1}^{n} M_{C,j} \Big/ n_b$$

$$M_{c,ext} = \sum_{j=1}^{n} M_{C,j} \Big/ 2n_b$$

Table G.1.9 – Calculation of interior and exterior column moments

Storey, i	Mc,ext (kN.m)	Mc,int (kN.m)
3	86.8	174
2	75.2	151
1	92.2	184
0	148	296

Frame 2

The distributed actions for Frame 2 are given Table G.1.10. It is assumed that the column depth is 700mm.

Table G.1.10 – Design actions for Frame 2

Storey, i	VBi (kN)	MBi (kN.m)	Mcon (kN.m)	∑Mc (kN.m)	Mc,ext (kN.m)	Mc,int (kN.m)
6	27.0	94.5	85.0	945	94.5	189
5	44.9	157	142	786	78.6	157
4	60.0	210	189	1051	105	210
3	71.9	252	227	1259	126	252
2	80.3	281	253	1405	140	281
1	84.6	296	266	1481	148	296
0	-	-	-	2060	412	206

Frame 3

The distributed actions for Frame 3 are given Table G.1.10. Again, it is assumed that the column depth is 700mm.

Table G.1.11 – Design actions for Frame 3

Storey, i	VBi (kN)	MBi (kN.m)	Mcon (kN.m)	∑Mc (kN.m)	Mc,ext (kN.m)	Mc,int (kN.m)
10	21.7	75.9	68.3	759	75.9	152
9	34.5	121	109	604	60.4	121
8	46.3	162	146	811	81.1	162
7	57.0	199	179	997	99.7	199
6	66.3	232	209	1161	116	232
5	74.4	260	234	1302	130	260
4	81.0	284	255	1418	142	284
3	86.1	302	271	1507	151	302
2	89.6	314	282	1569	157	314
1	91.4	320	288	1600	160	320
0	-	-	-	2099	420	210

G.1.3. Frame and post-tensioning design

As for the lateral force design, only the design of the Frame 1 is described in full. Key results are provided for Frame 2 and 3.

Frame 1

Step 1: Estimate frame geometry

As mentioned in Chapter 10, it is assumed that the frame geometry is constant up the entire height of the building. A solid section of 300mm wide by 600mm deep is assumed for both the beam and column.

Step 2: Evaluate member deformation

The deformation of the beam, column and joint panel at every level can be determined using equations from Chapter 6. The resulting member deformation of each level is given in Table G.1.12.

For the beam and column deformation for each level is:

$$\theta_b = \frac{\phi_b}{L_b}\left(\frac{(L_b - h_c)^2}{6} + \frac{E_t}{G}\frac{h_b^{\,2}}{4}\right)$$

$$\theta_c = \frac{\phi_c}{H}\left(\frac{(H - h_b)^2}{6} + \frac{E_t}{G}\frac{h_c^{\,2}}{4}\right)$$

Where: E_t and G are the bending and shear elastic modulus respectively;
L_b is the length of the bay;
H is interstorey height;
h_b and h_c is the depth of the beam and column respectively.

The bending and shear modulus is taken as 11000 MPa and 600MPa respectively. The curvature in the beam and column is a function of the applied moment in the connection (M_{con}) and the frame geometry:

$$\phi_b = \frac{M_{con}}{E_t I_b} \;\&\; \phi_c = \frac{M_{con}}{E_t I_c}\frac{L_b(H - h_b)}{H(L_b - h_c)}$$

For joint panel deformation:

$$\theta_j = \frac{\overline{V_{jh}}}{GA_{sh}}\left(1 - \frac{h_c}{L_b} - \frac{h_b}{H}\right)$$

Where: $\overline{V}_{jh} = \frac{2M_{con}}{h_b} - V_{col}$;

$A_{sh} = b_c h_c$.

Note that at the roof level, the column moment is approximately double the connection moment but only half an interstorey height is deforming. Hence, the above equation for column deformation is also appropriate for the roof level, provided that the column curvature is also calculated as shown above. However, this assumes that the contraflexure point is at the half height of the column.

Therefore, the total member deformation is:

$$\theta_{mem} = \theta_c + \theta_b + \theta_j$$

Table G.1.12 – Member deformation

Storey, i	θb (rad)	θc (rad)	θj (rad)	θmem (rad)
3	0.0016	0.0022	0.0015	0.0053
2	0.0028	0.0019	0.0027	0.0074
1	0.0034	0.0023	0.0032	0.0089

Step 3: Determine the allowable connection rotation

The difference between the allowable drift per floor and member deformation, gives the allowable connection rotation, which is used for connection design.

$$\theta_{imp} \le \frac{\theta_D - \left(\theta_b + \theta_c + \theta_j\right)}{\left(1 - \frac{h_c}{L_b}\right)}$$

Table G.1.13 – Design connection rotation

Storey, i	θimp (rad)
3	0.0160
2	0.0138
1	0.0121

Step 4: Evaluate connection moment capacity

The connection moment is evaluated, using modeling procedures from Chapter 6, repeated here as Figure G.1.2. The connections are designed with half of the section comprised of parallel-to-grain timber armouring. One post-tensioning tendon group is positioned at the half height of the beam section. The connections were designed to remain essentially elastic until the design drift of 2%. A bi-linear stress-strain law is applied for the timber in compression, with a yield stress of 45MPa.

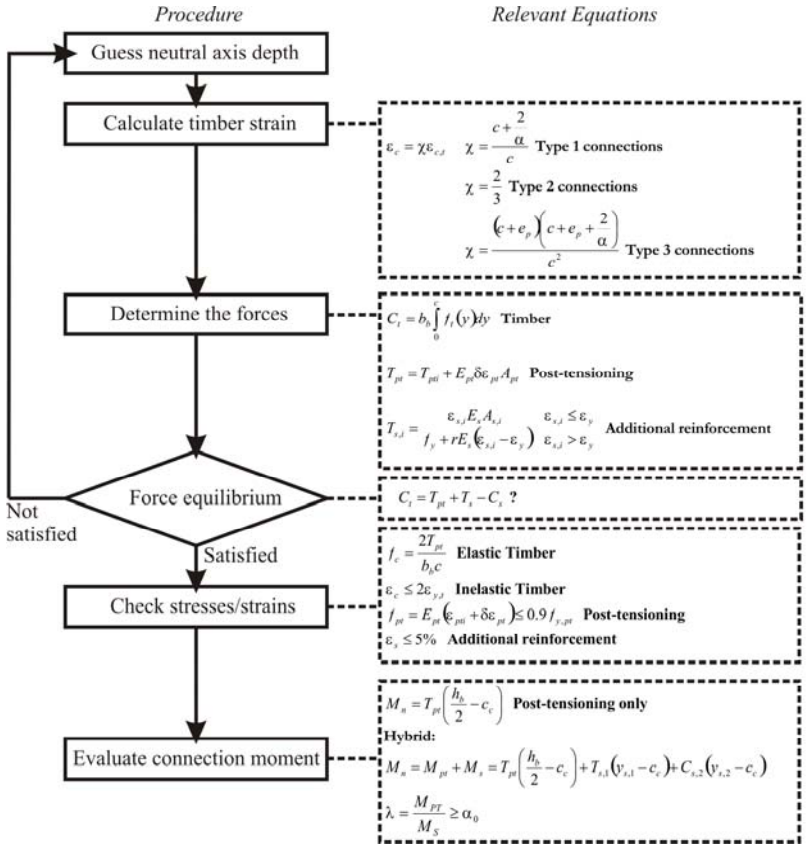

Figure G.1.2. Connection response procedure for frames

The moment-rotation curves for the beam-column connection on each level are shown in Figure G.1.3. Each curve satisfies the design connection moment and rotation from above. The post-tensioning area and force from each analysis is given in Table G.1.14.

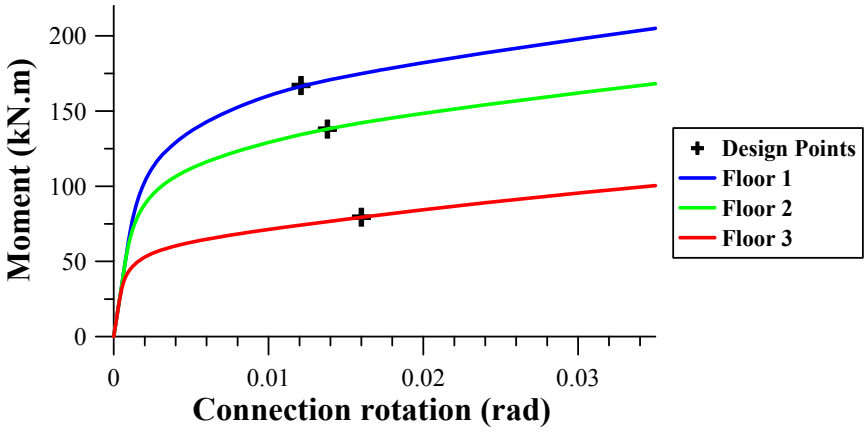

Figure G.1.3. Connection response for frame 1

Table G.1.14 – Post-tensioning area and force from connection design of Frame 1

Storey, i	Apt (mm^2)	Tpt (kN)
3	297	246
2	495	494
1	693	638

Step 5: Detailed design

The flexural and shear capacity of the beam and column is checked for ultimate limit state loading. Because this is not a critical step for defining the frame models for time-history analysis, the detailed design is not shown here. In general, the deflection criteria are more critical than the ultimate limit state strength demands.

Frame 2

For frame 2, the same process (shown above for Frame 1) is repeated. The design results in a solid section of 300mm wide by 700mm deep for both the beam and column. Again, the beam-column connections are armoured with parallel-to-grain timber, which is half the width of the column. Further information is given in Figure G.1.4 and Table G.1.15.

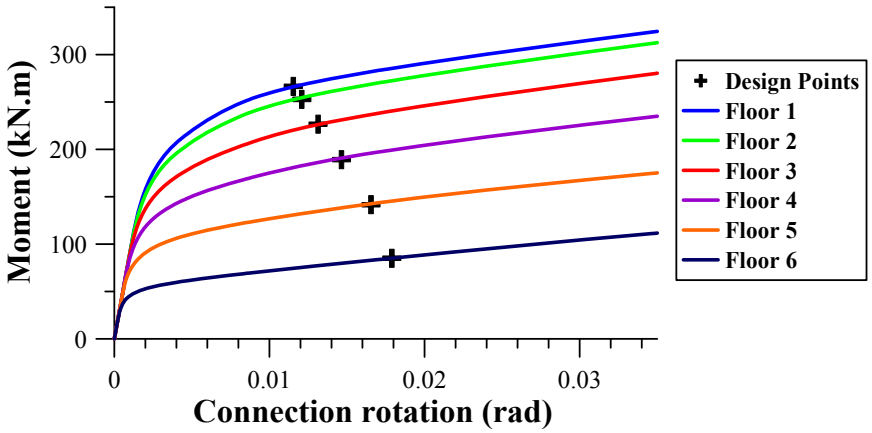

Figure G.1.4. Connection response for frame 2

Table G.1.15 – Design parameters for Frame 2

Storey, i	θimp (rad)	Apt (mm^2)	Tpt (kN)
6	0.0179	297	196
5	0.0165	396	389
4	0.0146	594	565
3	0.0131	792	717
2	0.0121	891	862
1	0.0115	891	931

Frame 3

For Frame 3, a solid section 300mm wide by 700mm deep is required for both the beam and column. Again, the beam-column connections are armoured with parallel-to-grain timber, which is half the width of the column. Further information is given in Figure G.1.5 and Table G.1.16.

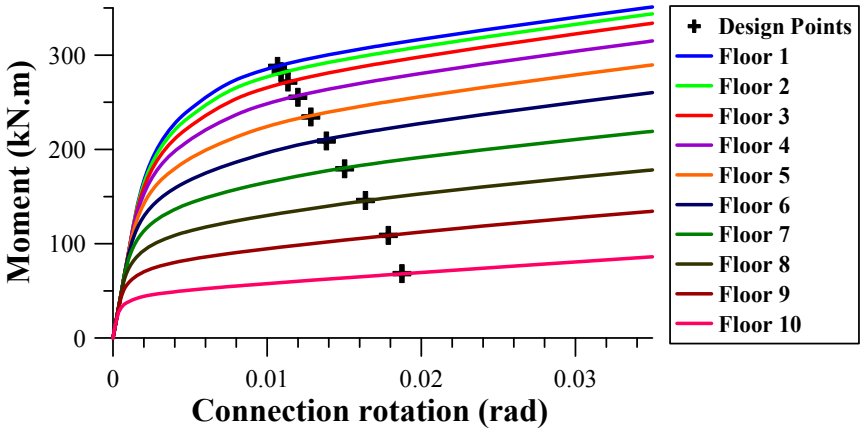

Figure G.1.5. Connection response for frame 3

Table G.1.16 – Design parameters for Frame 3

Storey, i	θimp (rad)	Apt (mm^2)	Tpt (kN)
10	0.0187	198	157
9	0.0179	297	278
8	0.0164	396	402
7	0.0150	495	533
6	0.0138	693	649
5	0.0128	792	766
4	0.0120	891	876
3	0.0113	990	958
2	0.0109	990	1019
1	0.0107	990	1066

G.1.4. Column-base connection design

As discussed in Chapter 10, the column-base connections are designed as PT connections, without additional reinforcement. The internal column-base connections are considered for design. The design process is similar to that for the frames with horizontal post-tensioning but additional gravity axial loads are taken into account. Under the earthquake combination (from NZS1170.5:2004) the gravity induced axial forces on the interior columns are 416kN, 832kN and 1387kN for Frame 1, 2 and 3 respectively. The exterior columns have half the axial force of the interior columns.

The exterior columns are assumed to provide half the moment of the interior columns, under gravity axial loads. As discussed in Chapter 10, the effects tension and compression axial forces induced by seismic loading are ignored, as it has little effect on the average moment provided by the exterior columns.

Frame 1

Step 1: Defined geometry

The column is a solid section of 300mm wide by 600mm deep.

Step 2: Evaluate member deformation

The deformation of the column can be estimated by considering the assumed contra-flexure point at 60% of the first interstorey height.

$$\theta_c = \frac{\phi_{c,b}}{0.6H_1}\left(\frac{(0.6H_1)^2}{3} + \frac{E_t}{G}\frac{{h_c}^2}{8}\right)$$

The curvature at the column-base is:

$$\phi_{c,b} = \frac{M_{\text{int},b}}{E_t I_c} = \frac{0.6V_b H_1}{n_b}\frac{1}{E_t I_c} = 4.98\times10^{-6}\,\frac{1}{mm}$$

Therefore, the total column deformation is:

$$\theta_c = \frac{4.98\times10^{-6}}{2286}\left(\frac{2286^2}{3}+\frac{11}{0.6}\frac{600^2}{8}\right) = 0.0038 + 0.0018 = 0.0056$$

Step 3: Determine the allowable connection rotation

The difference between the allowable drift per floor and member deformation, gives the allowable connection rotation, which is used for connection design.

$$\theta_{imp} \le \theta_D - \theta_c = 0.0144$$

Step 4: Evaluate connection moment capacity

The connection moment is evaluated, using modeling procedures from Chapter 7, repeated here as Figure G.1.6. The post-tensioning tendons are positioned 50mm outside the column section, on both sides (see Chapter 10). The connections were designed to remain essentially elastic until the design drift of 2%. A bi-linear stress-strain law is applied for the timber in compression, with a yield stress of 45MPa.

The moment-rotation curve for the interior column-base connections is shown in Figure G.1.7. The curve satisfies the design connection moment and rotation from above. The same process is repeated for the exterior column-base connection. The required area and force for each tendon is given in Table G.1.17.

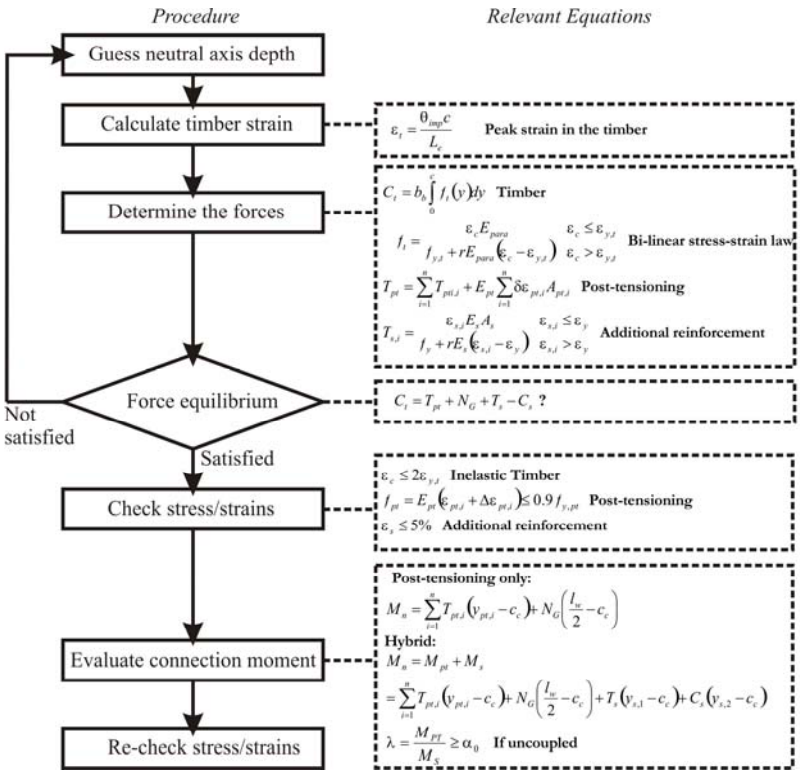

Figure G.1.6. Connection response procedure for walls

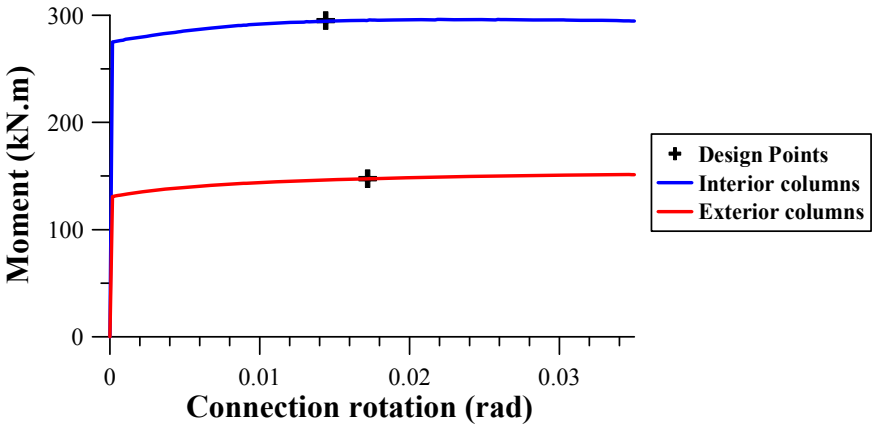

Figure G.1.7. Column-base connection response for frame 1

Table G.1.17 – Post-tensioning area and force for Frame 1 column-base connections

Storey, i	Apt (mm^2)	Tpt (kN)
Interior	495	401
Exterior	297	185

Step 5: Detailed design

The flexural and shear capacity of the column is checked for ultimate limit state loading. Because this is not a critical step for defining the frame models for time-history analysis, the detailed design is not shown here. In general, the deflection criteria are more critical than the ultimate limit state strength demands.

Frame 2

For column-based connections of frame 2, the same process, shown above for Frame 1, is repeated. The imposed rotation in the connection is 0.0145 and 0.0173 for the interior and exterior columns respectively. The moment-rotation curve is shown in Figure G.1.8. The post-tensioning area and force is given in Table G.1.18.

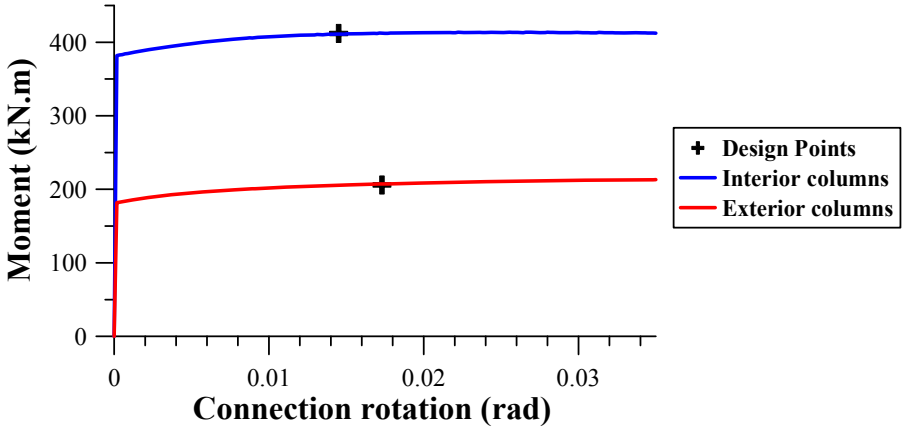

Figure G.1.8. Column-base connection response for frame 2

Table G.1.18 – Post-tensioning area and force for Frame 2 column-base connections

Storey, i	Apt (mm^2)	Tpt (kN)
Interior	396	309
Exterior	198	136

Frame 3

For column-based connections of frame 3, the imposed rotation in the connection is 0.0144 and 0.0172 for the interior and exterior column respectively. The moment-rotation curve is shown in Figure G.1.9.The post-tensioning area and force is given in Table G.1.19. Note; the gravity induced axial force for the exterior columns is so large that post-tensioning is not unnecessary. Furthermore, this is only possible if the seismic induced tension force (648kN) is less than the gravity induced axial force (694kN), which is the case here. For actual design, non-stresses reinforcement should be provided to ensure structural robustness for larger earthquake events.

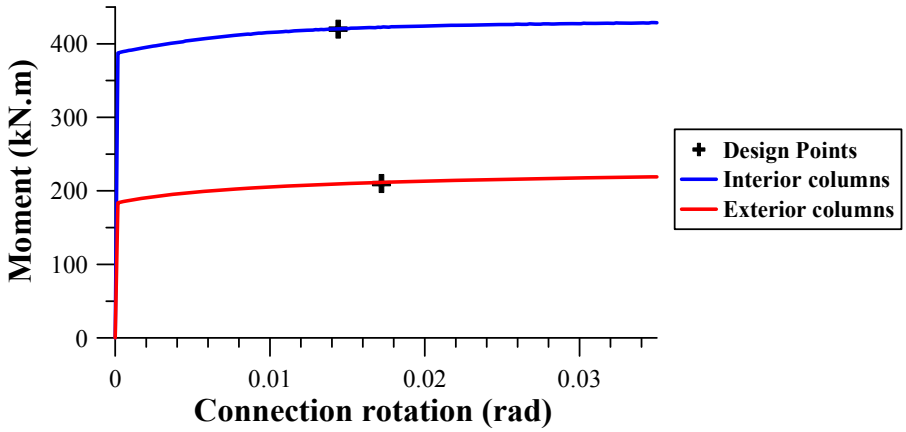

Figure G.1.9. Column-base connection response for frame 3

Table G.1.19 – Post-tensioning area and force for Frame 3 column-base connections

Storey, i	Apt (mm^2)	Tpt (kN)
Interior	396	309
Exterior	0	0

G.1.5. Frame design with pinned column-base connections

As discussed in Chapter 9, a designer may choose to pin the column-base connections to minimizing foundation demands and/or to potentially reduce construction costs. In Chapter 9, it is suggested that an essentially linear displacement profile can be maintained. This is provided that the stiffness of the first floor is increased to compensate for the increased flexibility of the columns between the basement and the first floor. Within this section, a brief description of the design process necessary to ensure a linear displacement profile is presented. Frame 2 from Chapter 10 is considered.

Determination of frame actions

Again, an equilibrium-based approach (Priestley et al. 2007) is used to distribute strength throughout the frame. However, because the column-base connections are pinned the moment demand at the top of the columns is defined. The first floor moment demand must also increase to ensure a consistent bending moment diagram up the height of the frame.

Step 1: Determine the total overturning moment (OTM)

$$OTM = \sum_{i=1}^{n} F_i H_i$$

Step 2: Decide how much of the OTM will be taken by the column bases:

$$OTM = \sum_{j=1}^{n} M_{c,j} + TL_{base}$$

The sum of the column base is zero for pinned-base columns. Hence:

$$\sum_{j=1}^{n} M_{c,j} = 0$$

Step 3: Determine the tension and compression force in the exterior columns:

$$T = C = \frac{OTM - \sum_{j=1}^{n} M_{c,j}}{L_{base}}$$

Step 4: Determine the design moment first floor beams

A rational approach is to make the first floor beam moment and the column moments equal. Hence:

$$M_{B1} = \frac{V_b H_1}{n_b}$$

This gives a beam shear of:

$$V_{B1} = \frac{2M_{B1}}{L_b}$$

Step 5: Proportion the seismic axial forces to each beam up the height of the building

The beam shear for the first floor has already been defined. A rational way to proportion the remaining seismic axial forces into beam shears, is to use the shear force diagram (Priestley et al. 2007). This will ensure that the assumed displacement profile is maintained. Hence:

$$V_{B,i} = (T - V_{B1}) \frac{V_{S,i}}{\sum_{i=2}^{n} V_{S,i}}$$

Step 6: Calculate the remaining beam design moments

$M_{B,i} = V_{B,i} \frac{L_b}{2}$ (At the column centerlines)

The beam-column connection design moments at the column face are:

$$M_{con,i} = M_{B,i} \frac{L_b - h_c}{L_b}$$

Step 7: Calculate column design moments

For all storeys, other than the roof:

$$\sum_{j=1}^{n} M_{C,j} = n_b M_{B,i}$$

For the roof:

$$\sum_{j=1}^{n} M_{C,j} = 2n_b M_{B,i}$$

For Frame 2, a summary of the frame actions are given in Table G.1.20. Note that for the lateral force design of this frame a linear displacement profile is assumed.

Table G.1.20 – Design actions for Frame 2 with pinned column-bases

Storey, i	VBi (kN)	MBi (kN.m)	Mcon (kN.m)	∑Mc (kN.m)	Mc,ext (kN.m)	Mc,int (kN.m)
6	14.2	49.5	45.3	495	49.5	99.1
5	27.1	94.9	86.8	475	47.5	94.9
4	37.5	131	120	656	65.6	131
3	45.3	159	145	793	79.3	159
2	50.5	177	162	883	88.3	177
1	153	534	465	2670	267	534
0	-	-	-	0	0	0

Due to the pinned column-base connections, the moment demand on the first floor beams and columns is significantly higher than the other levels. Hence, it is likely with such a design that the section size of the beams and columns at the first floor will need to be increased.

Frame and post-tensioning design

A similar process is followed for both pinned and moment resisting column-based connections. However, for the connection design at the first floor, the elastic deformation of the column over the entire first floor interstorey height and half the second floor interstorey height is considered.

Step 1: Estimate frame geometry

Step 2: Evaluate member deformation

The deformation of the beam, column and joint panel at every level other than the first level can be determined using equations from Chapter 6 (see above). For the first floor, the elastic deformation of the beam and column is:

$$\theta_b = \frac{\phi_b}{L_b}\left(\frac{(L_b - h_c)^2}{6} + \frac{E_t}{G}\frac{h_b^{\,2}}{4}\right) \text{ (as before)}$$

$$\theta_c = \frac{\phi_c}{H}\left(\frac{(2H - h_b)^2 + (H - h_b)^2}{12} + \frac{E_t}{G}\frac{h_c^{\,2}}{4}\right)$$

Where:

$$\phi_b = \frac{M_{con}}{E_t I_b} \;\&\; \phi_c \approx \frac{M_{con}}{E_t I_c}\frac{L_b(1.5H - h_b)}{1.5H(L_b - h_c)}$$

For joint panel deformation:

$$\theta_j \approx \frac{\overline{V_{jh}}}{GA_{sh}}\left(1 - \frac{h_c}{L_b} - \frac{h_b}{1.5H}\right)$$

Therefore, the total member deformation is:

$$\theta_{mem} = \theta_c + \theta_b + \theta_j$$

Step 3-5: See above. The remainder of the design procedure is similar to frames with moment-resisting column-base connections.

The above design procedure results in a solid section of 300mm wide by 900mm deep for the beams and columns on the first floor. For the remainder of the frame, the beams and columns are 300mm wide by 600mm deep. Further information is given in Figure G.1.4 and Table G.1.15.

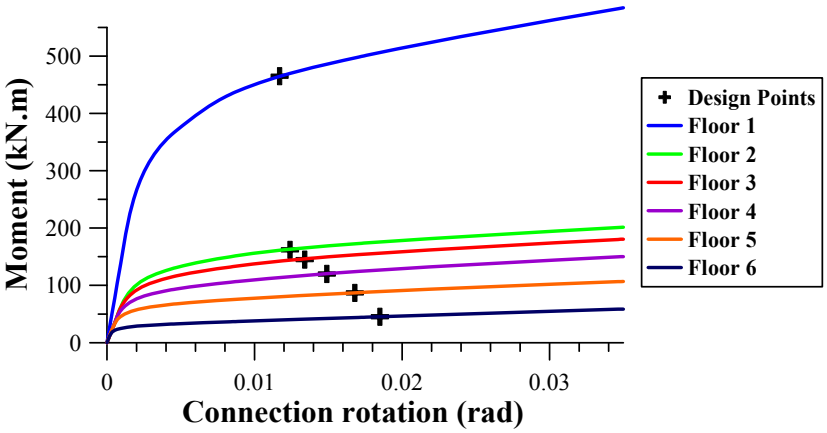

Figure G.1.10. Connection response for frame 2 with pinned column-bases

Table G.1.21 – Design parameters for Frame 2 with pinned column-bases

Storey, i	θimp (rad)	Apt (mm^2)	Tpt (kN)
6	0.0185	198	117
5	0.0168	297	273
4	0.0149	495	402
3	0.0134	594	528
2	0.0124	693	616
1	0.0117	1386	1254

G.2. WALLS

As described in Chapter 11, six wall geometries are considered, termed wall 1, 2, 3, 1c, 2c and 3c, where the 'c' stands for coupled. The walls are designed using lateral force design procedures from Chapter 9 and wall design procedures from Chapter 7. The lateral force design, wall design and connection design for each of these walls is documented below.

G.2.1. Lateral force design

The lateral force design procedure is similar to frames (see section G.1). Therefore, only the key results for the lateral force design of each wall are given here. For all designs a linear displacement profile is assumed. The design actions for the coupled walls are simply double that of the cantilever walls. A hysteretic damping of 8% is specified for the hybrid coupled wall systems.

Wall 1

The resultant base shear and distributed lateral forces from the displacement-based design for Wall 1 are given Table G.2.1. The wall has effective period of 1.10s.

Table G.2.1 – Design lateral forces for Wall 1

Storey, i	Floor Force, Fi (KN)	Shear, Vsi (kN)	Moment, Msi (kN.m)
3	115	115	0
2	84	199	438
1	42	241	1196
0		**(Vb =) 241**	**(OTM=) 2115**

Wall 2

The resultant base shear and distributed lateral forces from the displacement-based design for Wall 2 are given Table G.2.2. The wall has effective period of 1.88s.

Table G.2.2 – Design lateral forces for Wall 2

Storey, i	Floor Force, Fi (KN)	Shear, Vsi (kN)	Moment, Msi (kN.m)
6	78	78	0
5	71	149	297
4	57	206	865
3	43	249	1651
2	29	278	2600
1	14	292	3658
0		**(Vb =) 292**	**(OTM=) 4770**

Wall 3

The resultant base shear and distributed lateral forces from the displacement-based design for Wall 3 are given Table G.2.3. The wall has effective period of 3.05s. A linear projection of the displacement spectrum beyond the corner period is assumed, as discussed in Chapter 9.

Table G.2.3 – Design lateral forces for Wall 3

Storey, i	Floor Force, Fi (KN)	Shear, Vsi (kN)	Moment, Msi (kN.m)
10	49	49	0
9	49	98	188
8	43	142	563
7	38	180	1103
6	33	212	1789
5	27	240	2598
4	22	261	3511
3	16	278	4507
2	11	289	5565
1	5	294	6664
0		**(Vb =) 294**	**(OTM=) 7785**

Wall 1c

The resultant base shear and distributed lateral forces from the displacement-based design for Wall 1c are given Table G.2.4. The moment applied due to UFP couplers and the wall elements is determined by assuming a β_{CE}-value of 0.4. For the moment applied to the wall elements, the absolute maximum moment at a given floor is considered. The wall has effective period of 2.20s.

Table G.2.4 – Design lateral forces for Wall 1c

Storey i	Floor Force Fi (KN)	Shear Vsi (kN)	Moment Msi (kN.m)	Moment Mufp (kN.m)	Moment Mw (kN.m)
3	57	57	0	104	104
2	42	99	216	207	320
1	21	120	593	311	697
0		**(Vb =) 120**	**(OTM=) 1048**	**311**	**737**

Wall 2c

The resultant base shear and distributed lateral forces from the displacement-based design for Wall 2c are given Table G.2.5. The wall has effective period of 4.10s. Again, a linear projection of the displacement spectrum beyond the corner period is assumed, as discussed in Chapter 9.

Table G.2.5 – Design lateral forces for Wall 2c

Storey i	Floor Force Fi (KN)	Shear Vsi (kN)	Moment Msi (kN.m)	Moment Mufp (kN.m)	Moment Mw (kN.m)
6	33	33	0	69	69
5	30	63	125	137	57
4	24	87	364	206	227
3	18	105	695	275	489
2	12	117	1095	343	821
1	6	123	1540	412	1197
0		**(Vb =) 123**	**(OTM=) 2008**	**412**	**1596**

Wall 3c

The resultant base shear and distributed lateral forces from the displacement-based design for Wall 3c are given Table G.2.6. The wall has effective period of 6.65s, which is well above the corner period. Again, a linear projection of the displacement spectrum is assumed. Note; it is likely that serviceability limit state wind would govern the design (see Chapter 9) of this wall system.

Table G.2.6 – Design lateral forces for Wall 3c

Storey i	Floor Force Fi (KN)	Shear Vsi (kN)	Moment Msi (kN.m)	Moment Mufp (kN.m)	Moment Mw (kN.m)
10	21	21	0	56	56
9	21	41	79	112	33
8	18	60	237	167	126
7	16	76	465	223	298
6	14	89	753	279	530
5	11	101	1094	335	815
4	9	110	1478	391	1143
3	7	117	1898	446	1508
2	5	122	2343	502	1897
1	2	124	2806	558	2304
0		**(Vb =) 124**	**(OTM=) 3278**	**558**	**2720**

G.2.2. Wall and post-tensioning design

The design of the Wall 1 and 1c is described in full. Key results are provided for Wall 2, 2c, 3 and 3c.

Wall 1

Step 1: Estimate wall geometry

As mentioned in Chapter 11, it is assumed that the wall geometry is constant up the entire height of the building. A solid section of 2400mm wide by 180mm thick is assumed.

Step 2: Evaluate wall deformation

The deformation of the wall is a combination of the flexural deformation and shear deformation and is approximated as:

$$\theta_w = \theta_f + \theta_s = \frac{V_b H_e^{\,2}}{3EI_w} + \frac{0.8V_b}{GA_{sw}} = 0.0027 + 0.0011 = 0.0038$$

Step 3: Determine the allowable connection rotation

The difference between the allowable drift and the wall deformation, gives the allowable connection rotation, which is used for connection design.

$$\theta_{imp} \le \theta_D - \theta_w = 0.020 - 0.0038 = 0.0162$$

Step 4: Evaluate connection moment capacity

The connection moment is evaluated, using modeling procedures from Chapter 7, repeated here as Figure G.2.1. The post-tensioning is assumed to be positioned at the centerline of the wall section. The connections are assumed to remain elastic. The connection moment is evaluated for the combined axial load from the post-tensioning and gravity load. The gravity induced axial load is 480kN.

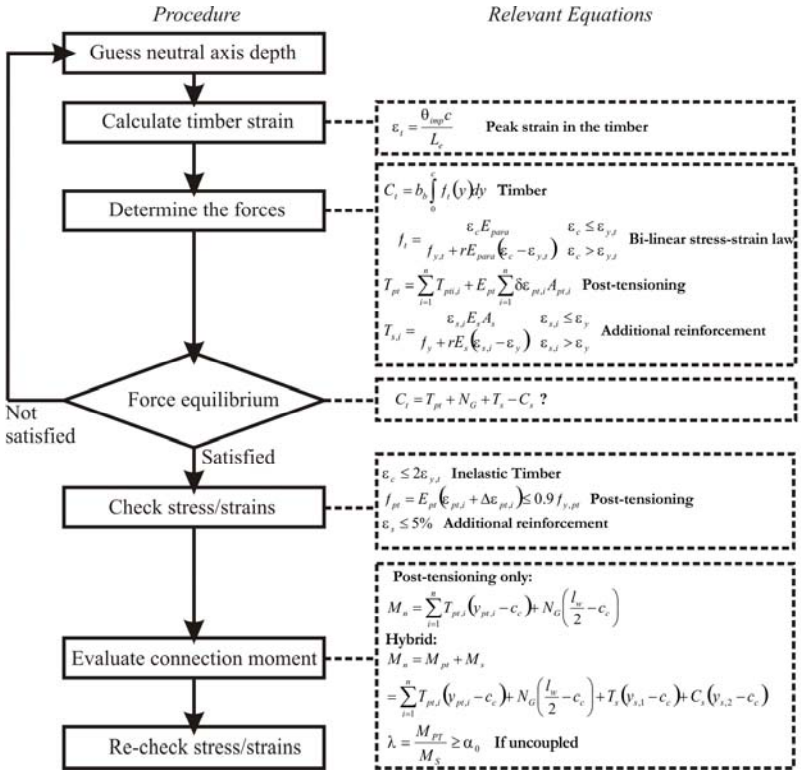

Figure G.2.1. Connection response procedure for walls

The moment-rotation curve for the wall-base connection is shown in Figure G.2.2. The curve satisfies the design connection moment of 2115kN.m within the imposed rotation of 0.0162. The post-tensioning area and force from each analysis is 1089mm^2 and 1164kN respectively.

Step 5: Detailed design

The flexural and shear capacity of the wall is checked for ultimate limit state loading. Because this is not a critical step for defining the wall models for time-history analysis, the detailed design is not shown here. In general, the deflection criteria are more critical than the ultimate limit state strength demands on the wall elements.

Wall 2

For wall 2, a similar process, shown above for Wall 1, is repeated. A solid section of 3000mm wide by 180mm thick is required. The moment-rotation curve for the wall-base connection is given in Figure G.2.2. The imposed connection rotation at the base of the wall is 0.0131rad. The post-tensioning area and force from each analysis is 2079mm^2 and 2222kN respectively. The gravity induced axial load on the wall is 975kN.

Wall 3

For wall 3, a solid section of 4000mm wide by 180mm thick is required. The moment-rotation curve for the wall-base connection is given in Figure G.2.2. The imposed connection rotation at the base of the wall is 0.0127rad. The post-tensioning area and force from each analysis is 2079mm^2 and 2342kN respectively. The gravity induced axial load on the wall is 1635kN.

Wall 1c

Wall 1c is the first of the coupled walls. The deflection is determined based on the average moment and shear demand per wall. The design moment for the wall-base connections is 314kN.m. This moment demand is satisfied, ignoring axial forces induced by the coupling elements, as discussed in Chapter 7. A solid section of 1200mm wide by 180mm thick is required. The moment-rotation curve for the wall-base connection is given in Figure G.2.2. The imposed connection rotation at the base of the wall is 0.0162rad. The post-tensioning area and force from each analysis is 297mm^2 and 301kN respectively. The gravity induced axial load is 230kN.

Wall 2c

For wall 2c, the design moment for the wall-base connections is 602kN.m. A solid section of 1800mm wide by 180mm thick is required. The moment-rotation curve for the wall-base connection is given in Figure G.2.2. The imposed connection rotation at the base of the wall is 0.0162rad. The post-tensioning area and force from each analysis is 198mm^2 and 207kN respectively. The gravity induced axial load is 488kN.

Wall 3c

For wall 3c, the design moment for the wall-base connections is 983kN.m. A solid section of 2200mm wide by 180mm thick is required. The moment-rotation curve for the wall-base connection is given in Figure G.2.2. The imposed connection rotation at the base of the wall is 0.0147rad. The post-tensioning area and force from each analysis is 198mm^2 and 124kN respectively. The gravity induced axial load is 818kN. Hence, the axial load is providing most of the base-moment.

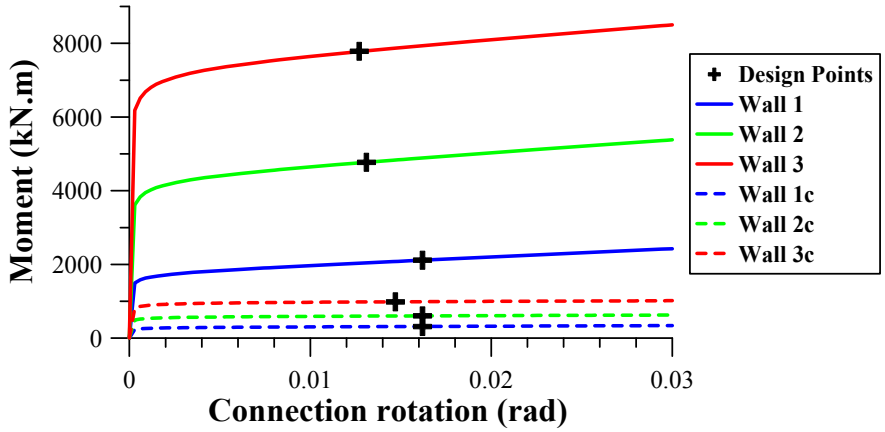

Figure G.2.2. Connection response for wall 1, 2, 3, 1c, 2c and 3c

G.2.3. Calibration of the multi-axial-springs

To model the wall-base and splice connections in RUAUMOKO, the axial stiffness of the multi-axial-springs must be calculated (see Chapter 11) to match the analytical predictions (described in Chapter 7). The axial stiffness of the multi-axial-spring (MS) is determined by interpreting the neutral axis depth from the analytical prediction and calculating the effective length, L_e, as shown in Chapter 7. The calculated axial stiffness for the MS model, K_A, for each wall is shown in Table G.2.7.

Table G.2.7 – MS Axial stiffness calculation

Wall	c/Lw	Le (mm)	K_A (kN/m)
1	0.1072	541	8.41E6
2	0.1205	474	11.95E6
3	0.1074	540	13.99E6
1c	0.1139	506	4.48E6
2c	0.0944	624	5.45E6
3c	0.0933	632	6.58E6

G.2.4. UFP Coupler design

For Wall 1c, 2c and 3c the UFP couplers must be designed. There are several approaches that can be followed, as discussed in Chapter 9. Here the UFP couplers are designed for a set β_{CE} – value (0.4), which was defined in Chapter 9 as the ratio of the over-turning moment provided by the coupling elements and the total overturning moment.

To determine the required strength of the UFP couplers the following equation is applied. It is assumed, based on analytical modeling (see Chapter 7), that the maximum variation of the center of compression, c_c, in each wall is 2% of the wall length, l_w.

$$V_{ufp} = \frac{\beta_{CE} OTM}{l_{cc}}$$

Where: $l_{cc} = l_{cl} - (c_{c,1} - c_{c,2}) \approx l_{cl} - 0.02 l_w$ is the distance between center of compression of each wall;
l_{cl} is the distance between the centerline of each wall;
$c_{c,1}$ & $c_{c,2}$ is the distance from the extreme compression fiber to the center of compression of each wall, $c_{c,1}$ is the wall with maximum compression.

The shear provided from the couplers is then divided evenly to each floor (giving $V_{ufp,i}$). As discussed in Chapter 11, an elastic-perfectly-plastic hysteresis rule is used to model the UFP couplers. The axial stiffness of the coupling elements, K_{ufp}, can be determined from the design shear force, $V_{ufp,i}$, and the assumed slip. It is assumed that there is 1mm slip per UFP anchorage. Hence, the yield point is at 2mm of axial displacement. A summary of the above calculations is given in Table G.2.8.

Table G.2.8 – UFP coupler strength and stiffness

Wall	OTM (kN.m)	lcl (m)	Vufp (kN)	Vufp,i (kN)	Kufp (kN/m)
1c	1048	1.35	316	105	52690
2c	2008	1.95	420	69.9	34970
3c	3278	2.35	569	56.9	28430

G.2.5. Verification of the modelled hysteretic damping

In Chapter 11, a cyclic adaptive pushover analysis is used to ensure that the assumed hysteretic damping from the displacement-based design (15%) is achieved by the UFP couplers. The hysteretic damping values achieved from the cyclic pushover analysis are shown in Table G.2.9.

Table G.2.9 – Achieved hysteretic damping values

Wall	ξhyst (%)
1c	19.4
2c	21.2
3c	21.1

All hysteretic damping values are in excess of the values assumed by the displacement-based design by up to 40%. However, according to displacement based design process (discussed in Chapter 9), using a hysteretic damping of 21.2% rather than 15% will result in a base shear that is 13% less. Notably, the hysteretic damping correction factor in the ductility ranges of the coupled wall systems (5 to 7) from Priestley *et al* (2007) are approximately unity for the flag-shaped hysteresis.

An alternative approach to verify the hysteretic damping is to use the analytical modelling approaches (from Chapter 7). To do this the yield deformation of the wall system must be estimated. As discussed in Chapter 9, the yield deformation can be estimated using empirical expressions, which are repeated below. These empirical relationships are compared with the results from the pushover analysis to ensure they are sufficiently accurate.

$$\Delta_{y,e} = \Delta_{ufp,e} + \Delta_{w,e}$$

Where: $\Delta_{y,e}$ = the total yield deformation at the effective height;

$\Delta_{ufp,e}$ = the yield deformation due to couplers at the effective height;

$\Delta_{w,e}$ = the yield deformation due to the wall at the effective height;

The yield deformation due to the coupler is given below. It is assumed that the slip of the UFP couplers relative to the walls is 2mm.

$$\Delta_{ufp,e} = 2H_e \frac{\Delta_{ufp}}{l_w}$$

Where: H_e is the effective height of the wall;
Δ_{ufp} is the slip of the UFP coupler relative to the walls.

The wall deformation is approximated using the following expression:

$$\Delta_{w,e} = \frac{0.43V_b H_e}{\gamma_{LS} GA_{sw}} + 2H_e V_{ufp}\left(\frac{1}{GA_{sw,v}} + \frac{1}{l_w}\frac{H_n}{EA_w}\right)$$

Where: γ_{LS} is 1.0 and 1.25 for serviceability and ultimate limit state design respectively;
V_b is the base shear of a double wall system;
A_{sw} is the horizontal shear area of one wall element;
$V_{ufp} \approx \frac{\beta_{CE} OTM}{l_{cl}}$ is the total shear from the UFP couplers;
l_{cl} is the centerline distance between each wall;
$A_{sw,v}$ is the vertical shear area of one wall element;
G is the shear modulus of the timber;
H_n is total height of the wall;
A_w is the cross sectional area of one wall element.

The yield displacement predicted by the above equations is compared with the results from the pushover analyses in Table G.2.10. However, because the finite element model uses Giberson frame elements, vertical shear distortion is not possible. Therefore, the vertical shear distortion, in the above expression, is ignored.

The estimated yield rotation is larger than the results from the pushover analysis by 40% on average. This is desirable from a design point of view, as it results in

conservative estimates for the hysteretic damping of the system. Furthermore, it is likely that the numerical model does not include all of the significant deformation contributions.

Table G.2.10 – Yield deformation from analytical model and pushover analysis

Wall	Δufp,e (m)	Δw,e (m)	Δy,e (m)	θy,e (%)	
				Est.	Pushover
1c	0.0146	0.0260	0.0406	0.46	0.37
2c	0.0182	0.0532	0.0714	0.44	0.31
3c	0.0241	0.1245	0.1486	0.56	0.34

APPENDIX REFERENCES

ACI. (2001). "Acceptance Criteria for Moment Frames Based on Structural Testing and Commentary." American Concrete Institute Innovation Task Group 1 and Collaborators, American Concrete Institute, Farmington Hills, MI.

AS1012.13. (1992). "Methods of testing concrete - Determination of the drying shrinkage of concrete for samples prepared in the field or in the laboratory." Australian Standards, SAI Global Ltd, Sydney, Australia.

Banks, W. (2010). "Personal communication: The average LVL Elastic Modulus from Factory Data, Carter Holt Harvey Wood Products." M. P. Newcombe, ed., December 12, Manukau, New Zealand, Recommended Elastic Modulus based on Carter Holt Harvey factory data

Bejtka, I., and Blass, H. J. "Joints with inclined screws." *CIB Working Commission W18 - Timber Structures*, Meeting 35, Kyoto, Japan.

Blandon, C. A., and Priestley, M. J. N. (2005). "Equivalent viscous damping equations for Direct Displacement-Based Design." *Journal of Earthquake Engineering*, 9(2), pp 257-278.

Carradine, D., Newcombe, M. P., and Buchanan, A. H. "Screwed corbel connections in Laminated Veneer Lumber." *World Conference on Timber Engineering*, Riva del Garda, Italy, pp. 8.

Carradine, D. M., Newcombe, M. P., and Buchanan, A. H. "Using Screws for Structural Applications in Laminated Veneer Lumber." *CIB-W18 Conference Proceedings*, Dubendorf, Switerland, Paper 42-7-7.

Cusiel, M. R. (2010). "Personal communication: Experimental test data for internal beam-column joint subassembly." M. P. Newcombe, ed., Christchurch, New Zealand.

Cusiel, M. R., Newcombe, M. P., Pampanin, S., Buchanan, A. H., and Palermo, A. "The effect of joint flexibility on the seismic response of post-tensioned LVL frames." *The 14th European Conference on Earthquake Engineering* Ohrid, Macedonia, pp. 8.

Davies, M., and Fragiacomo, M. (2008). "Long-Term Behaviour of Laminated Veneer Lumber Members Prestressed with Unbonded Tendons " *New Zealand Timber Design Journal*, 16(3), pp. 13-20.

EC5. (1994). "Eurocode 5: Design of Timber Structures - Part 1-1: General - Common rules and rules for buildings." ECS, Brussels, Belgium.

FEMA-356. (2000). "Prestandard and Commentary for the Seismic Rehabilitation of Buildings." Prepared by the American Society of Civil Engineers for the Federal Emergency Management Agency, Washington, D.C.

Fenwick, R. C., and Mackechnie, J. (2009). "Analysis and creep, shrinkage and thermal effects in concrete structures." *SESOC Journal*, 22(2), pp. 72-87.
Futurebuild. (2010). "The Futurebuild Range." Carter Holt Harvey Woodproducts New Zealand, website: www.chhwoodproducts.co.nz/futurebuild-lvl.
Green, J. (2010). "Seismic performance of enhanced hybrid subassemlies," STIC Laboratory Test Report, University of Canterbury, Christchurch, New Zealand.
IBC. (2003). "International Building Code." International conference of building officials, Whitter, CA, 2003.
Iqbal, A., Pampanin, S., Buchanan, A., Fragiacomo, M., and Palermo, A. "Application of Hysteretic Dampers in LVL Coupled Walls for Improved Seismic Performance." *Proceedings, 8th Pacific Conference of Earthquake Engineering, Singapore*.
Iqbal, A., Pampanin, S., and Buchanan, A. H. "Seismic Performance of Prestressed Timber Beam-Column Sub-Assemblies." *New Zealand Society of Earthquake Engineering Conference*, Wellington, New Zealand.
Jacobsen, L. S. "Damping in composite structures." *2nd World Conference on Earthquake Engineering*, Tokyo and Kyoto, Japan, pp. 1029-1044.
Kelly, J. M., Skinner, R. I., and Heine, A. J. (1972). "Mechanism of Energy Absorption in Special Devices for Use in Earthquake Resistant Structures." *Bulletin New Zealand Society of Earthquake Engineering*, Vol. 5(3), pp. 63-88.
Marriott, D. (2009). "The development of high-performance post-tensioned rocking systems for seismic design of structures," Doctorate thesis, University of Canterbury, Christchurch, New Zealand.
Murray, Y. D. (2007). "Manual for LS-DYNA wood material model 143." *Report number: FHWA-HRT-04-097*, APTEK Inc., Colorado Springs, U.S.A.
Neale, A. (2009). "Long term performance of post-tensioned timber buildings." *Third Pro. Report*, University of Canterbury, Dept. of Civil and Nat. Res. Engineering, Christchurch, New Zealand.
NelsonPine. (2010). "Nelson Pine Laminated Veneer Lumber: NZ LVL 11." *NPIL/LVL 03*, Nelson Pine, Nelson, New Zealand.
Newcombe, M. P. (2008). "Seismic Design of Multistorey Post-Tensioned Timber Buildings," Masters Thesis, University of Pavia, Pavia, Italy.
Newcombe, M. P., Pampanin, S., Buchanan, A., and Palermo, A. (2008). "Section Analysis and Cyclic Behavior of Post-Tensioned Jointed Ductile Connections for Multi-Storey Timber Buildings." *Journal of Earthquake Engineering*, 12(Special Issue), pp. 83-110.
NZCS. (2010). "NZCS PRESSS Design Handbook." Ed. Stefano Pampanin, New Zealand Concrete Society, Wellington, New Zealand.
NZS1170.5. (2004). *Structural Design Actions - Part 5 - Earthquake Actions*, New Zealand Standards, Wellington.
NZS3101. (2006). *Concrete Structures Standard*, New Zealand Standards, Wellington, New Zealand.
NZS3404. (1997). *Steel Structures Standard: Part 1 and 2*, New Zealand Standards, Wellington.
NZS3603. (1999). *Timber Structures Standard*, New Zealand Standards, Wellington.

Palermo, A. (2004). "Use of Controlled Rocking in the Seismic Design of Bridges," Doctate Thesis, Technical Institute of Milan, Milan.

Palermo, A., Pampanin, S., Buchanan, A., and Newcombe, M. "Seismic Design of Multi-Storey Buildings using Laminated Veneer Lumber (LVL)." *2005 New Zealand Society of Earthquake Engineering Conference*, Wairaki, New Zealand, pp. 8.

Palermo, A., Pampanin, S., and Carr, A. "Efficiency of Simplified Alternative Modeling Approaches to Predict the Seismic Response of Precast Concrete Hybrid Systems." *fib Symposium: "Keep Concrete Attractive", Budapest, Hungary*, pp. 7.

Pampanin, S., Priestley, M. J. N., and Sritharan, S. (2001). "Analytical Modelling of the Seismic Behavior of Precast Concrete Frames Designed with Ductile Connections." *Journal of Earthquake Engineering*, 5(3), pp. 329-367.

Priestley, M. J. N., Calvi, G. M., and Kowalsky, M. J. (2007). *Displacement-Based Seismic Design of Structures*, IUSS PRESS, Pavia, Italy.

SAP2000. (2005). "Structural Analysis Package 2000, Version 10.0.1." Computers and Structures Inc., Berkeley, California.

Smith, T., Ludwig, F., Pampanin, S., Fragiacomo, M., Buchanan, A., and Deam, B. "Seismic response of Hybrid-LVL coupled walls under quasi-static and pseudo-dynamic testing." *NZSEE Conference, Palmerston North, New Zealand.*, pp. 8.

Tanahashi, H., Shimizu, H., and Suzuki, Y. "Formulation of Elasto-Plastic Moment-Resisting Performance of Timber Connections Using Pasternak Model." *World Conference on Timber Engineering*, Postland, Oregon.

TDG. (2008). *Timber Design Guide, Editted by A. H. Buchanan*, New Zealand Timber Industry Federation Christchurch, New Zealand.

UBC. (1997). "Uniform Building Code." International conference of building officials, Whitter, CA, 1997

Yeoh, D. E. C. (2010). "Behaviour and design of timber-concrete composite floor system," PhD Thesis, University of Canterbury, Christchurch, New Zealand.